23 Mar 1994

1994 OURE report, including the 4th Annual UMR Undergraduate Research Symposium -- Entire Proceedings

University of Missouri--Rolla

Recommended Citation

University of Missouri--Rolla, "1994 OURE report, including the 4th Annual UMR Undergraduate Research Symposium -- Entire Proceedings" (1994). *Opportunities for Undergraduate Research Experience Program*. 1.
https://scholarsmine.mst.edu/oure/1

OPPORTUNITIES FOR

UNDERGRADUATE RESEARCH

EXPERIENCE PROGRAM

(OURE)

University of Missouri-Rolla
1994

ACKNOWLEDGEMENTS

The Opportunities for Undergraduate Research Experience program began in 1990. This volume constitutes the proceedings of the fourth annual OURE program. The goals of the program are: (1) to expand opportunities for a more active form of learning by students; (2) to encourage the direct interaction of undergraduate students with faculty through research; (3) to expand the level of research activity on the campus; (4) to help encourage superior students to pursue graduate study; and (5) to reinforce the idea that teaching and research are compatible and mutually reinforcing at a research university.

The OURE program continues to achieve its goals--UMR students have performed research on a wide variety of topics, have worked closely with faculty and have experienced first-hand both the excitement and the frustration of performing research.

This volume contains papers presented at the fourth annual UMR Undergraduate Research Symposium held on March 23, 1994, and final reports of students participating in the 1993-94 OURE program. Students in the OURE program are encouraged to participate in the Symposium and participation increased substantially this year.

On behalf of all involved, I would like to express appreciation to those who continue to make this program successful. A special thanks goes to the members of the 1993-94 OURE Selection Committee. They are:

> Dr. Donald Sparlin, Chair
> Dr. Neil Book
> Dr. Shari Dunn-Norman
> Dr. Richard Miller
> Dr. Christopher Ramsay
> Dr. Jerome Westphal

Through programs such as this, the University of Missouri-Rolla, Missouri's Technological University, continues to provide opportunities for its undergraduate students to further their research experiences in preparation for their future endeavors.

<div align="right">

Walter J. Gajda, Jr.
Vice Chancellor for Academic Affairs

</div>

Contents

Undergraduate Research Symposium Papers

UMR OURE Papers

UNDERGRADUATE RESEARCH

SYMPOSIUM PAPERS

MACROCYCLIC ANTIBIOTICS AS A NEW CLASS OF CHIRAL SELECTORS FOR LIQUID CHROMATOGRAPHY

Christina S. Bagwill, Chemistry Department

ABSTRACT

In the field of chromatographic separations, the need for new chiral stationary phases is always in demand. Many stationary phases already exist, some of the more popular being cyclodextrin or protein based phases. During this research, a new class of chiral selectors were discovered and evaluated for chiral recognition. Vancomycin, thiostrepton, and rifamycin B all belong to the macrocyclic antibiotic family. Not only can this new class of chiral selectors be used to resolve compounds that cannot be separated on any other column, but it is also more stable and has much greater capacity than protein based columns.

INTRODUCTION

In order to understand the significance of this research, some relevant information is needed regarding the importance of chiral separation technology. All of the stationary phases mentioned previously are selective for chiral compounds. A chiral compound is one that is not superposable on its mirror reflection (e.g., your left and right hands are mirror images but are not superposable on one another). Some examples of compounds which have chiral centers are listed in Table 1 and Table 5. Mirror image compounds that are not superposable are called enantiomers. They have identical physical and chemical properties in an isotropic environment. Since they have identical properties it is difficult to distinguish one from another through 'normal' chemical methods. However, using a chromatography column containing a chiral selector sometimes allows certain enantiomers to be successfully separated. Choosing a chiral selector is dependent upon the functionality of the enantiomer and the interactions taking place between the enantiomers and the stationary phase.

A typical enantiomeric separation is given in Figure 1. The notation system for distinguishing between two enantiomers use the letters: (R), (S) or (D), (L). The (D) and (L) labeling is the older system but is still used today. This notation is usually used with amino acids, sugars and related compounds. The (R) and (S) system is newer and more widely used. The letter (R) is for the Latin "rectus" (i.e., right or clockwise) and (S) "sinister" is for left or counter clockwise. These terms are used to describe the absolute conformation of a chiral compound according to their sequence rules.

Chiral separations are very important to the pharmaceutical, food and beverage, and environmental industries. Many drugs that the pharmaceutical industries produce are chiral. Over the past two years chiral drug

4

technology have been given the cover story in several issues of *Chemical and Engineering News*. The September 27, 1993 issue talks about the effects of enantiomers on the pharmaceutical industry. When antibiotic drugs are produced by fermentation they will only consist of one enantiomer. However when chemists synthesize chiral compounds without including a chiral enantiomeric reagent or chiral catalysts, the result is a 50-50 mixture of enantiomers which is called a racemate or a racemic mixture. Usually one enantiomer is responsible for the pharmacological activity, and the other may be inactive or toxic. Until recently, because of cheaper production costs, drug researchers were satisfied with manufacturing racemic forms of the chiral drugs. Ibuprofen is an example of a drug which has been produced as a racemic mixture. Independently, several companies are preparing to market the S (+) enantiomer of ibuprofen because it is the "active" enantiomer. Conversely, both enantiomers of ketoprofen play different medicinal roles. The S-(+)-ketoprofen is used an analgesic/anti-inflammatory whereas the (R) enantiomer of ketoprofen is active against bone loss in periodontal disease.[2]

Carvone is an example of a chiral compound that is both a natural or synthetic chiral flavor and fragrance component found in most foodstuffs. The (R) enantiomer of carvone smells like mint, and the (S) enantiomer smells like caraway. Enantiomeric analyses allow the only accurate evaluation of flavors and fragrances.[6]

EXPERIMENTAL SECTION

Materials. All racemic analytes resolved in this study were obtained from Aldrich (Milwaukee, WI) or Sigma (St. Louis, MO). All HPLC grade solvents and N,N-dimethylformamide (DMF) were obtained from Fisher (Pittsburgh, PA). All organosilane compounds were obtained from Petrarch (Bristol, PA). Cyclic antibiotics containing amine, hydroxyl or carboxylic acid functionalities can be linked to silica gel in a variety of different ways. The three cyclic antibiotics discussed in this work (vancomycin, thiostrepton and rifamycin B from Sigma) all contain one or more of these functional groups. Structures for these compounds are shown in Figure 2. Carboxylic acid terminated organosilanes (e.g., 10-carbomethoxy)-ethylmethyldichlorosilane, 2-(carbomethoxy)-ethyltrichlorosilane, etc.) can be used to immobilize vancomycin, and thiostrepton while amine terminated organosilanes (e.g., 3-amino-propyldimethylethoxysilane, 3-aminopropyltriethoxysilane, etc) can be used for rifamycin B. In a typical reaction, four grams of dry silica gel is slurried on 50 mL of dry toluene in a 250 mL 3 neck flask. Two grams of the desired organosilane is dissolved in approximately 15 mL of dry toluene contained in a dropping flask. The organosilane

5

solution is added drop-wise over approximately 30 minutes to the refluxing toluene-silica gel slurry. The mixture is allowed to reflux (~ 110°C) for two hours, then cooled, filtered and washed with methanol, 50% aqueous methanol, methanol again, and then dried. The silanized silica gel can be slurried in anhydrous DMF. One gram of the appropriate cyclic antibiotic is added along with an appropriate carbodiimide dehydrating agent. After six hours the chiral stationary phase material is filtered and washed with methanol and then aqueous methanol.

The cyclic antibiotics also can be attached to silica gel via epoxy terminated organosilanes as has been described previously for cyclodextrin.[3] Another approach involves reacting the macrocycle with a 2 to 3 molar excess of an isocyante terminated organosilane (e.g., 3-isocyanatopropyltriethoxysilane) in anhydrous DMF. This product is then added to a dry DMF slurry of silica gel (approximately 2 grams of modified cyclic antibiotic to 4 grams of silica gel). The solution is stirred and allowed to react for 20 hours at 107°C. Subsequently the chiral stationary phase was filtered and washed as indicated previously. Although other attachment chemistries are possible, these are the ones used in the initial studies.

Methods. The cyclic antibiotic chiral stationary phases (5 µ particles) were slurry packed into 5 cm x 0.44 cm i.d. stainless steel columns. Separations were achieved using a Shimadzu LC 6A liquid chromatograph with UV detection (254 nm) and a C-R3A chromatopac data station or with a Waters model 590 HPLC with a 745B data module. Separations were carried out at a flow rate of 1.0 mL/min. and at room temperature (~ 22°C) unless noted otherwise. Mobile phase compositions are listed in the appropriate tables and figures.

RESULTS AND DISCUSSION

Vancomycin is produced by *Streptomyces orientalis* (Figure 2).[7] It has a molecular weight of 1,449. There are three macrocyclic portions to the molecule which also contains five aromatic rings. Also, there are two side chains, one of which is a carbohydrate dimer and the other a N-methyl-amino acid. Upon heating in neutral or basic conditions, aspartic acid is lost thereby opening at least one of the macrocyclic rings. This is thought to occur during the silica gel immobilization reaction step. Native vancomycin contains 18 stereogenic centers, 9 hydroxyl groups, 2 amine groups, 7 amido groups and 2 chlorine moieties. These groups are known to be useful for stereoselective molecular interactions with chiral analytes.

Rifamycin B is produced by *Nocardia mediterranei* and has a molecular weight of 755.8 (Figure 2).[8,9] It

6

has 9 stereogenic centers, 4 hydroxyl groups one carboxylic acid moiety and one amide bond. This particular macrocycle may be particularly useful as a chiral mobile phase additive for the separation of chiral amino-alcohols.

Thiostrepton is produced by *Streptomyces azureus* and consists of two joined macrocyclic rings.[10,11] It has a molecular weight of 1,665. It has 17 stereogenic centers, 5 hydroxyl groups, 10 amide linkages and one secondary amine.

All of the cyclic antibiotic stationary phases were tested for stability by switching back and forth between normal and reversed phase modes. All appeared to by stable in both chromatographic modes. Also the enantioselectivity of these stationary phases appears to be different in the two chromatographic modes. Hence, chiral recognition mechanism in the reversed phase mode is not the same as that in the normal phase mode. Table 1 lists a number of reversed phase data for the macrocyclic antibiotic columns.

Optimization of reversed phase separations are done in much the same way as for cyclodextrin-based columns.[3,4,5] Retention is adjusted by controlling the amount of organic modifiers added. Selectivity is effected by both the type of organic modifier and the pH of the mobile phase. Efficiency and selectivity can be effected by ionic strength, buffer type, other additives, and flow rate (Table 4). Lower temperatures usually enhance chiral separations (i.e., increase α, Table 3).

The effect of pH on enantioselective retention can be seen in Table 2. Ionizable solutes such as coumachlor are significantly affected by pH while nonionizable molecules, such as devrinol are not as affected. However, it should be noted that since these chiral stationary phases are ionizable as well, pH effects for neutral molecules are possible if they result from changes in the chiral selector. Coumachlor, as seen in Table 2, is best resolved at acidic pHs where it exists as the protonated neutral molecule. Clearly the enhanced resolution of coumachlor from pH 7.6 to 4.5 is mainly due to greater efficiency and somewhat longer retention times. The selectivity changes (αs) are not appreciable in this region. Below pH 4.5 there is a discontinuity for both the retention (k') and α. Since this occurs for the neutral molecule devrinol it is believed that is due to the protonation of the vancomycin stationary phase. Unlike proteins, macrocyclic antibiotics can be used in the normal phase mode without denaturation or any irreversible change in enantioselectivity. Table 5 lists a number of normal phase data for the macrocyclic antibiotic columns. The racemates resolved in the normal phase mode generally cannot be resolved in the reversed phase mode

and vice versa. Again some of these separations have not been achieved on any other chiral stationary phase (Compound 8, PROXYL, Table 5). Also because of the lower molecular weight and greater loadability of the macrocyclic chiral stationary phases, as compared to proteins, semipreparative and preparative scale-ups are much more feasible.

CONCLUSIONS

Macrocyclic antibiotics are viable chiral selectors for HPLC. They can be bonded to silica gel via linkage chains using a variety of chemistries. They can be used in either the reversed phase mode or the normal phase mode and have different enantioselectivities in each. Also, cyclic antibiotics can be derivatized in order to change interactions taking place between the analyte and the stationary phase. Macrocyclic antibiotic bonded phases have many of the characteristics of protein-based stationary phases, but with greater stability and much higher capacities. As a results of their relatively small size and the fact that their structures are known, basic studies on chiral recognition should be feasible.

ACKNOWLEDGEMENTS

REFERENCES

(1) Armstrong, D. W.; Tang, Y.; Chen, S.; Zhou, Y.; Bagwill, C.; and Chen, J.-R. Anal. Chem. Accepted for publication May 1, 1994.

(2) Stinson, S. *Chemical and Engineering News* September 27, 1993.

(3) Armstrong, D. W.; DeMond, W. *J. Chromatogr. Sci.* **1984**, 22, 411

(4) Armstrong, D. W.; Stalcup, A.M.; Hilton, M. L.; Duncan, J.D.; Faulkner Jr., J. R.; Chang, S.-C. *Anal. Chem.* **1990**, 62, 1612.

(5) Armstrong, D. W.; Hilton, M.; Coffin, L. *LC-GC* **1992**, 9, 646.

(6) Armstrong, D.W.; Chang, C.-D.; Li, W. Y. *Journal of Agricultural and Food Chemistry* **1990**, 38, 1674

(7) Higgins, H. M.; Harrison, W. H.; Wild, G. M.; Bungay, H.R.; McCormick, M. H. *Antibiotics Ann.* **1958**-59, 906.

(8) Sensi, P. et al., *Antibiotics Ann.* **1959**-60, 262.

(9) Rinehart, Jr., K. L.; Shield, L S. *Fortschitte Chem. Naturstoffe* **1976**, 33, 231.

(10) Pagano, J.F.; Weinstein, M.J.; Stout, H.A.; Donovick, R, *Antibiotics Ann.* **1955**-56, 554.

(11) Vandeputte, J.; Dutcher, J. D. *Antiobiotics Ann.* **1955**-56, 560.

A

TIME, MIN

Figure 1

VANCOMYCIN

RIFAMYCIN B
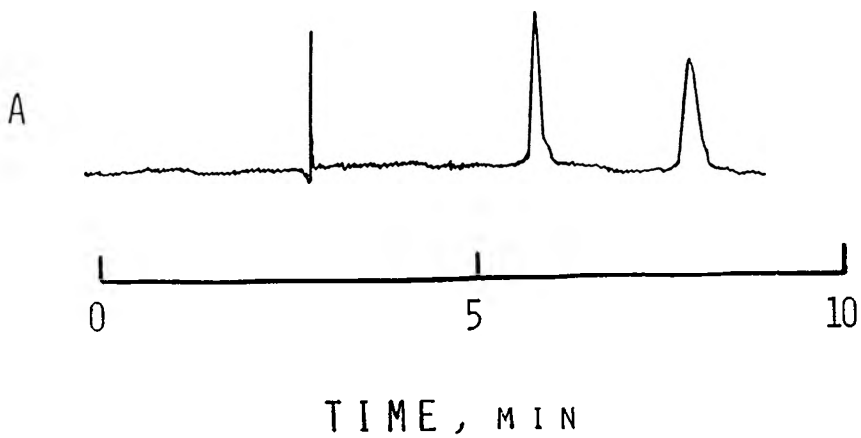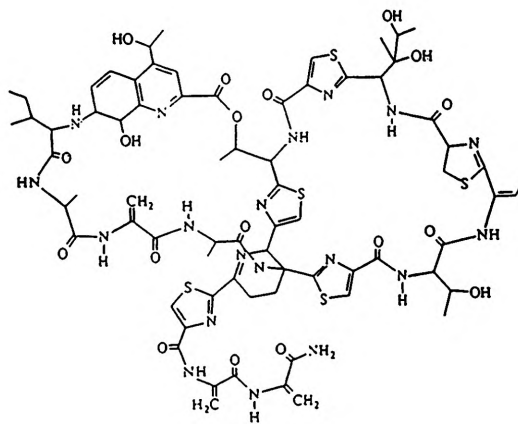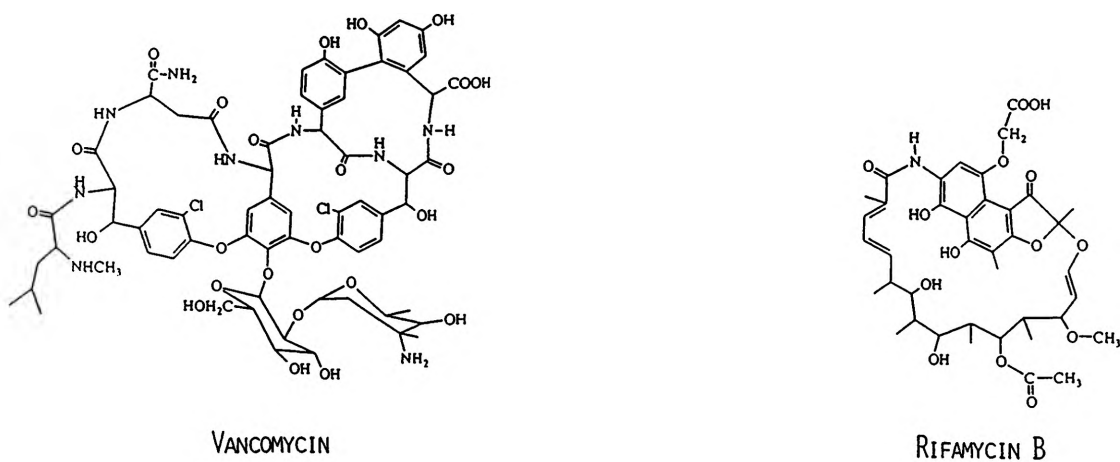
THIOSTREPTON

Figure 2

10

Table 1. Chromatographic Data for the Reversed-Phase Resolution of Racemic Compounds on Macrocyclic Antibiotic Bonded Stationary Phases

compounds[a,e]		k_1' [b]	α	mobile phase[c]	pH	column[d]
(1) coumachlor		3.27	2.0	10:90	4.1	Van
(2) warfarin		1.98	1.70	10:90	7.0	Van
		2.27	1.44	10:90	4.1	Van
(3) devrinol		1.40	1.62	10:90	4.1	Van
(4) 5-methyl-5-phenylhydantoin		0.38	1.41	10:90	7.0	Van
		0.24	1.36	10:90	4.1	Van
(5) proglumide		1.17	1.40	10:90	7.0	Van
		1.18	1.75	10:90	4.1	Van
(6) α-(1-aminoethyl)-4-hydroxybenzyl alcohol	$HOC_6H_4CH[CH(NH_2)CH_3]OH$	0.39	1.30	10:90	7.0	Van
(7) bendroflumethiazide		1.58	1.25	10:90	7.0	Van
(8) bromacil		0.67	1.21	10:90	7.0	Van
(9) idazoxan		0.38	1.21	10:90	7.0	Rif
(10) 3-methyl-5-cyano-6-methoxy-3,4-dihydro-2-pyridone		0.32	1.21	10:90	7.0	Van
(11) pyridoglutethimide		0.84	1.20	10:90	7.0	Van
(12) N-carbamyl-D,L-phenylalanine		0.31	1.20	10:90	4.1	Van
(13) aminoglutethimide		0.79	1.15	10:90	7.0	Van
(14) N-benzoylalanine methyl ester		0.47	1.15	10:90	4.1	Van
(15) coumafuryl		0.68	1.15	10:90	7.0	Van
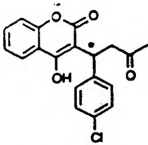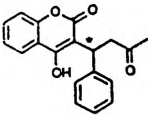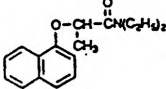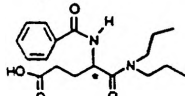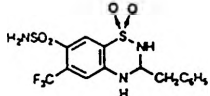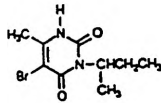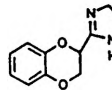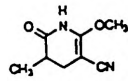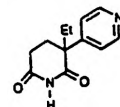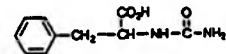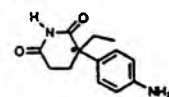
11
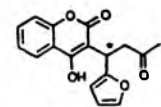
Table 1 (Continued)

compounds[a,e]		k_1' [b]	α	mobile phase[c]	pH	column[d]
(16) dansyl-α-amino-n-butyric acid	H_5C_2—CH—CO_2H \ NHR$_3$	3.29	1.15	10:90	4.1	Van
(17) dansylaspartic acid	HO_2C—CH—CH_2—CO_2H \ NHR$_3$	3.00	1.15	10:90	4.1	Van
(18) N-(3,5-dinitrobenzoyl)phenylglycine		1.55	1.15	10:90	4.1	Van
(19) thioridazine		22.0	1.15	10:90	7.0	Thio
(20) dansylnorleucine	CH_3—$(CH_2)_3$—CH—CO_2H \ NHR$_3$	6.17	1.14	10:90	4.1	Van
(21) 5-(4-hydroxyphenyl)-5-phenylhydandoin		0.78	1.14	10:90	7.0	Van
(22) dansylserine	HO—CH_2—CH—CO_2H \ NHR$_3$	2.09	1.12	10:90	4.1	Van
(23) indapamide		1.35	1.12	10:90	7.0	Van
(24) benzoin methyl ester	$C_6H_5CH(OCH_3)COC_6H_5$	0.80	1.11	10:90	7.0	Van
(25) N-benzoylleucine	$(CH_3)_2CH$—CH_2—CH—CO_2H \ NHR$_2$	1.90	1.10	10:90	4.1	Van
(26) N-(3,5-dinitrobenzoyl)leucine		1.44	1.10	10:90	4.1	Van
(27) methsuximide		0.39	1.10	10:90	7.0	Van
(28) dansylvaline	$(CH_3)_2CH$—CH—CO_2H \ NHR$_3$	3.97	1.09	10:90	4.1	Van
(29) indoprofen		1.55	1.09	10:90	4.1	Van
		2.85	1.06	10:90	7.0	Van
(30) N-benzoylphenylalanine		2.10	1.08	10:90	4.1	Van
(31) N-benzoylvaline	$(CH_3)_2CH$—CH—CO_2H \ NHR$_2$	0.68	1.08	10:90	4.1	Van
(32) 1,1-binaphthyl-2,2'-diyl hydrogen phosphate		3.75	1.07	10:90	4.1	Van
		1.63	1.05	10:90	7.0	Van
(33) N-t-Boc-p-chlorophenylalanine		2.06	1.07	10:90	4.1	Van

[a] The compounds in this table are listed in order of their α-values (from highest to lowest. [b] This is the k' of the first eluted enantiomer. [c] The mobile-phase compositions indicated are the volume ratios of acetonitrile to 1% triethylammonium acetate buffer. [d] The abbreviations for the columns are as follows: Van, vanocomycin bonded stationary phase; Thio, thiostrepton bonded stationary phase; Rif, rifamycin B bonded stationary phase. [e]

12
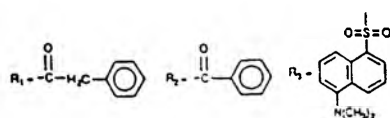
Table 2. Effect of pH on the Chromatographic Retention and Separation of Coumachlor and Devrinol on a 25 cm × 0.44 cm (i.d.) Vancomycin CSP[a]

	coumachlor			devrinol		
pH	k'	α	Rs	k'	α	Rs
7.6	1.00	1.69	1.6	1.15	1.80	3.2
6.2	1.21	1.64	2.0	1.16	1.77	3.3
5.5	2.00	1.60	2.7	1.36	1.76	3.5
4.5	3.00	1.64	4.1	1.46	1.70	3.6
3.6	1.65	2.42	3.9	1.19	1.41	3.7

[a] The mobile phase was 10:90, acetonitrile–1% triethylammonium acetate buffer (by volume). The temperature was 22 °C.

Table 3. Effect of Temperature on the Reversed-Phase Retention and Resolution of Enantiomers of Proglumide, 5-Methyl-5-phenylhydantoin , and N-Carbamyl-D,L-phenylalanine[a]

temp (°C)	k'	α	Rs
	Proglumide		
0	1.33	2.27	3.6
5	1.33	2.11	3.3
15	1.31	1.87	2.4
22	1.18	1.75	2.1
35	0.93	1.57	1.8
45	0.76	1.44	1.6
	5-Methyl-5-phenylhydantoin		
0	0.35	1.38	1.5
5	0.27	1.36	1.0
22	0.24	1.34	1.0
35	0.24	1.30	0.9
45	0.19	1.32	0.7
	N-Carbamyl-D,L-phenylalanine		
0	0.51	1.39	1.5
5	0.39	1.34	1.3
15	0.38	1.23	1.0
22	0.31	1.20	0.8
35	0.27	1.11	0.7
45	0.22	1.00	0

[a] The column was a 25 cm × 0.44 cm (i.d.) vancomycin CSP. The mobile phase was 10:90 acetonitrile–1% triethylammonium acetate buffer (pH 4.1). The flow rate was 1.0 mL/min.

Table 4. Effect of Flow Rate on the Normal-Phase Enantiomeric Separation of 3a,4,5,6-Tetrahydrosuccinimido[3,4-b]acenaphthen-10-one[a]

flow rate (mL/min)	α	Rs
0.50	1.31	1.28
0.75	1.31	1.19
1.00	1.27	1.14
1.50	1.30	1.13
2.00	1.29	1.11

[a] The column was a 25 cm × 0.44 cm (i.d.) vancomycin CSP. The mobile phase was 50:50 2-propranol–hexane (by volume).

Table 5. Chromatographic Data for the Normal-Phase Resolution of Racemic Compounds on Macrocyclic Antibiotic Bonded Stationary Phases

compounds[a]		k_1' [b]	α	mobile phase[c]	column[d]
(1) 5-methyl-5-phenylhydantoin		2.50	1.67	50:50	Van
(2) mephobarbital		0.58	1.62	50:50	Van
(3) hexobarbital		0.75	1.61	50:50	Van
(4) N-(3,5-dinitrobenzoyl)-α-methylbenzylamine	$C_6H_5CH(CH_3)NHCOC_6H_3(NO_2)_2$	0.82	1.36	50:50	Van
(5) altniazide		5.30	1.35	65:35	Thio
(6) 1-benzoyl-2-tert-butyl-3-methyl-4-imideazolidinone		2.67	1.35	50:50	Van
(7) N-(3,5-dinitrobenzoyl-α-methylbenzylamine	$C_6H_5CH(CH_3)NHCOC_6H_3(NO_2)_2$	2.00	1.33	10:90	Van
(8) 3-[2-(2-bromoacetamido)acetamido]-PROXYL		2.63	1.30	50:50	Van
(9) mephenytoin		1.64	1.30	10:90	Van
(10) phensuximide		3.84	1.26	10:90	Van
(11) 3a,4,5,6-tetrahydrosuccinimido[3,4-b]acenaphthen-10-one		2.00	1.25	50:50	Van
(12) bendroflumethiazide		2.95	1.24	50:50	Van
(13) 4-benzyl-2-oxazolidinone		4.2	1.10	65:35	Thio
		1.30	1.21	50:50	Van
(14) coumafuryl		0.30	1.20	50:50:10[e]	Rif
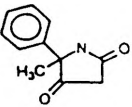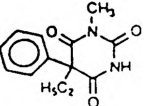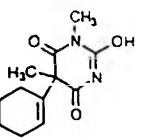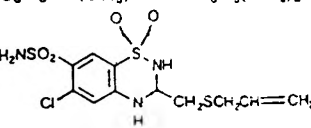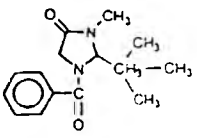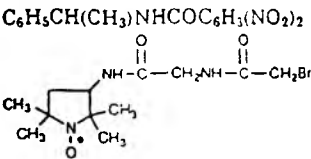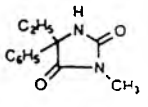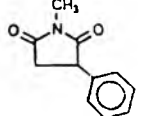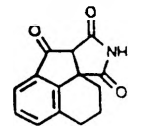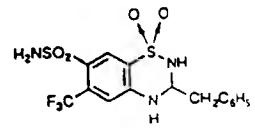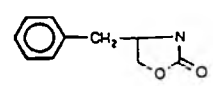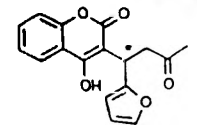
Table 5 (Continued)

compounds[a]	k_1' [b]	α	mobile phase[c]	column[d]
(15) ethyl-2-pyrrolidone-5-carboxylate	3.05	1.15	50:50	Van
(16) N,N'-bis(α-methylbenzyl)sulfamide	0.66	1.13	10:90	Van
(17) indapamide	2.5	1.13	50:50	Van
(18) α-carbethoxy-γ-phenyl-γ-butyrolactone	0.58	1.12	50:50	Van
(19) CGA-40919	0.72	1.11	10:90	Van
(20) ftorafur	4.68	1.11	50:50	Van
(21) 5-(4-Methylphenyl)-5-phenylhydantoin	6.00	1.10	90:10	Van
(22) 1,1'-bi-2-naphthol	0.80	1.09	10:90	Van
(23) α-methyl-α-phenylsuccinimide	3.02	1.09	10:90	Van
(24) laudanosine	2.37	1.13	10:90	Rif
(25) γ-phenyl-γ-butyrolactone	4.43	1.08	40:60	Van
	4.05	1.08	10:90	Van
(26) mandelamide	2.50	1.04	50:50	Van
(27) 3-(2-naphthyl)alanine	1.28	1.04	50:50	Van
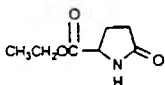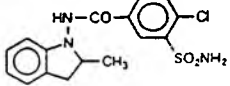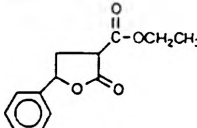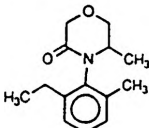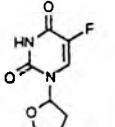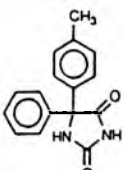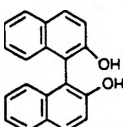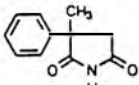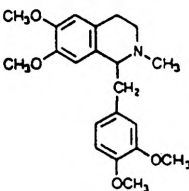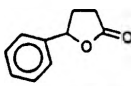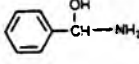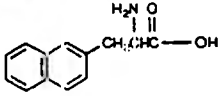
[a] The compounds in this table are listed in order of their α-values from highest to lowest (except for the last four compounds which use a different mobile phase). [b] This is the k' of the first eluted enantiomer. [c] The mobile-phase composition represents the volume ratio of 2-propanol to hexane. [d] The abbreviations for the columns are as follows: Van, vancomycin bonded stationary phase; Thio, thiostrepton bonded stationary phase; and Rif, rifamycin B bonded stationary phase. [e] This mobile phase composition represents the volume ratios of 2-propanol–hexane–acetonitrile.

15

MODIFIED RECYCLED GLASS AS AN ADDITIVE IN COATINGS APPLICATIONS

Garth D. Brown

Chemistry Department

ABSTRACT

The feasibility of using chemically modified, finely pulverized recycled glass as an additive in coatings was investigated. The ground glass was added as partial replacement for the conventional pigment titanium dioxide (TiO_2). The loss of TiO_2 pigment was compensated with an optical brightening agent (OB agents). OB agents can help contribute to a coating's hiding capacity by absorbing light in the UV range, releasing light of a lower energy in the visible spectrum. Glass supplemented coatings were formulated and common paint tests were performed. The glass changed the optical and physical properties of the coating formulations. The results of the project demonstrated the feasibility of using recycled glass as an additive in coatings.

INTRODUCTION

This project was conducted to investigate the feasibility of using chemically modified recycled glass as an additive in coatings. The chemical modification tested in this project involved the addition of an optical brightening agent (OB agents). This type of usage of recycled glass could be beneficial for several reasons including development of a possible market for recycled glass plus the reduction of other more expensive pigments in coatings such as titanium dioxide (TiO_2).

An OB agent is a chemical that can absorb light in the ultraviolet region and then re-emit light in the visible region. The OB chemicals are

also called Fluorescent Whitening Agents (FWA's). [1] Addition of these agents contribute to the hiding capacity of a coating and can also yield an entirely new type of pigment for coatings.

With the replacement of the commonly used pigment TiO_2 by glass, the new coating will display changed properties. The changes in optical properties include hiding capacity and maximum reflectance of light. Altered physical properties include scrub resistance and viscosity.

POSSIBLE ENVIRONMENTAL IMPACT

A potentially significant impact of this project is finding a new market for recycled glass. The U.S. produces a large amount of glass and could benefit economically with a new market for recycled glass. The annual amount of waste glass generated in the Ozark Rivers Solid Waste Management District is listed in Table I. [2]

TABLE I

WASTE GLASS GENERATED ANNUALLY IN OZARK RIVERS SOLID WASTE MANAGEMENT DISTRICT

Amber Glass	1,128 Tons
Green Glass	1,025 Tons
Clear Glass	3,280 Tons
TOTAL	5,433 Tons*

*The total waste glass generated is equivalent to 360 lbs/per person/ year.

This amount of glass could potentially be utilized and help reduce some of the 1 million tons of TiO_2 used in the coatings industry.

METHODS OF PROJECT

The first step was grinding the glass. This was done by a local company and provided to us by Mo-Sci Corporation. The grinding of the glass used in this project was done with a roller mill and was obtained in a variety of sizes. Other glass samples were obtained from treatment with an air cyclone. This latter glass was not used because it was not of high enough quality, having a gray tint, and it did not consist of sufficient small particles. A list of the sizing of the glass is shown in Table II.

Table II.

PERCENT OF GLASS IN EACH SIZE RANGE - COMPARISON OF TWO GRINDING METHODS

Size in μM	Milling	Cyclone
> 150	43.11%	53.85%
150 - 106	10.86%	13.19%
160 - 75	16.33%	12.93%
75 - 45	12.90%	11.28%
< 45	16.80%	8.75%
Total	612.4 grams	890.2 grams

Two different phases of the project were conducted once the glass was milled. The first phase was performed to determine if untreated glass could be added to a coating without drastically changing the performance properties of the paint. This involved preparing and testing various formulation of water-based latex paints. The glass replaced the TiO_2 in 2.5% increments by weight up to 20% of the TiO_2 pigment, which is approximately 2.5 pounds per gallon of paint. The Table III lists the basic paint formulation used in the study.

TABLE III

COATING FORMULATION

Chemical	Amount Used in Grams
Natrosol 250 HBR	1.8
Water	12.9
Tamol 850	112.0
Trition N-101	4.6
Colloid 643	1.0
KTTP	0.5
Minex 4	125.0
Optiwhite	25.0
Combination of TiO_2 and glass added in 2.5% increments	125.0
UCARA 525	214.0
Butyl Cellosolve	8.5
Colloid 643	1.3
Nept 95	4.5
NH_4OH	1.8

Tests were then performed on the coatings for each formulation to determine what properties changed with each addition incremental of glass. The tests performed included grind to measure the particle size, scrub resistance, viscosity, and flexibility on a metal panel.

The second phase of the project was the incorporation of the OB agent onto the surface of the glass. The chemical used for this was 2,5-bis(5-tert-butyl-2-benzoxazolyl)thiophene (BBTP), whose structure is shown in Figure I.

FIGURE I
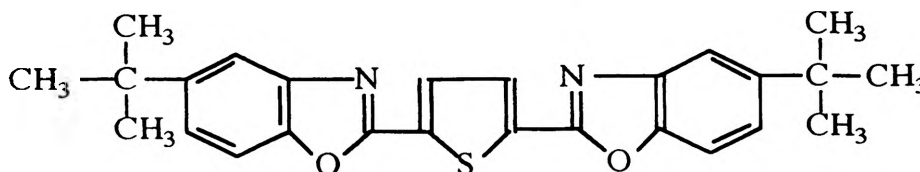
CHEMICAL FORMULA OF THE OPTICAL BRIGHTENING AGENT

The BBTP organic molecule was bonded to the inorganic surface of the glass with the use of a silane coupling agent. Silane coupling agents are commonly used to bond organic material to inorganic material. The silane coupling agents have two main groups and have a generic form of X_3-Si-RY. The 'X' determines the bond to which the inorganic material and the 'RY' is an organic segment with functionality 'Y,' which is used to bond to the organic molecule. In this case, the organic molecule was the OB agent. Exact information of how this is done is considered proprietary, because a patent may be sought on the OB glass.

Once glass was treated with the OB agent, new coating formulations were developed and tested. Coatings were made of the same formulation in Table I, but with 5%, 10%, and 20% substitution of OB modified glass. These three formulations were compared to the same percentages of untreated glass. Two other formulations were made for the Missouri Highway Department and then tested against their specifications.

RESULTS

The coatings made with the variable amount of glass showed several different physical properties. The increase in glass caused a rise in the viscosity of the formulation. With the incorporation of the hard glass into the coating, the scrub resistance was improved although the flexibility was reduced with a high loading of glass. The decrease in some properties, such as an increase in viscosity and grind, with the higher loadings of glass will probably limit the amount of glass that can be added into a formulation. The main optical property of concern, hiding capacity, was lowered with the inclusion of the OB glass and plain glass when compared to no glass substitution for TiO_2. When the same percentages of OB glass were compared to plain glass, the OB glass did have more hiding capacity than the plain glass.

Some tests were performed using test specifications developed by the Missouri Highway Department. Test formulations met most of these requirements as shown in Table IV. With additional revision of the experimental formulations, all of the test requirements should be met. The results of the OB glass in two model traffic formulations are shown in Table IV.

TABLE IV

MODEL TRAFFIC PAINT FORMULATIONS COMPARED TO MISSOURI HIGHWAY DEPARTMENT SPECIFICATIONS TTP-1952B

TEST	REQUIREMENT	WHITE	REQUIREMENT	YELLOW
Viscosity	70-90 KU	70 KU	70-90 KU	71 KU
Storage Stability	70-90 KU	73 KU	70-90 KU	69 KU
Total Solids	50% min	57%	67-75%	69%
Drying Time	75 min max	pass	75 min max	pass
Flexibility	pass (1/8")	pass	pass (1/8")	pass
Scrub Resistance	400 cycles	390 cycles	400 cycles	380 cycles
Dry Opacity	0.92 min	0.96	0.92 min	0.97
72 hour Water Resistance	pass	pass	pass	pass
Freeze Thaw, 3 cycles	pass	pass	pass	pass

* Formulation with a 20% substitution of glass for TiO2

Tests were done to show that the OB agent was bonded to the glass, including infrared red (IR) and ultraviolet (UV) spectroscopy, shown in Figure 2 and Figure 3 respectfully. The evidence to qualitatively show that the OB agent was attached to the surface of the glass was the appearance of the modified glass. The OB agent is a bright yellowish-green powder and the glass is a white powder. The modified glass was a yellow-green powder. When the modified glass was placed inside a UV-black box, it would fluoresce in a similar manner to the OB agent.

The spectroscopic test to determine the OB to glass loading were not conclusive. Inferred spectra were run on a sample of the OB modified glass and compared to the untreated glass. The spectra were almost identical and the spectra inclusive, as can be shown from comparison of the two spectra shown in Figure 2. The UV spectra of the two samples also did not show any significant differences, as shown in Figure 3.

FIGURE II

Comparions of Spectra of OB modified Glass And Untreated Glass

FIGURE III

UV Spectra
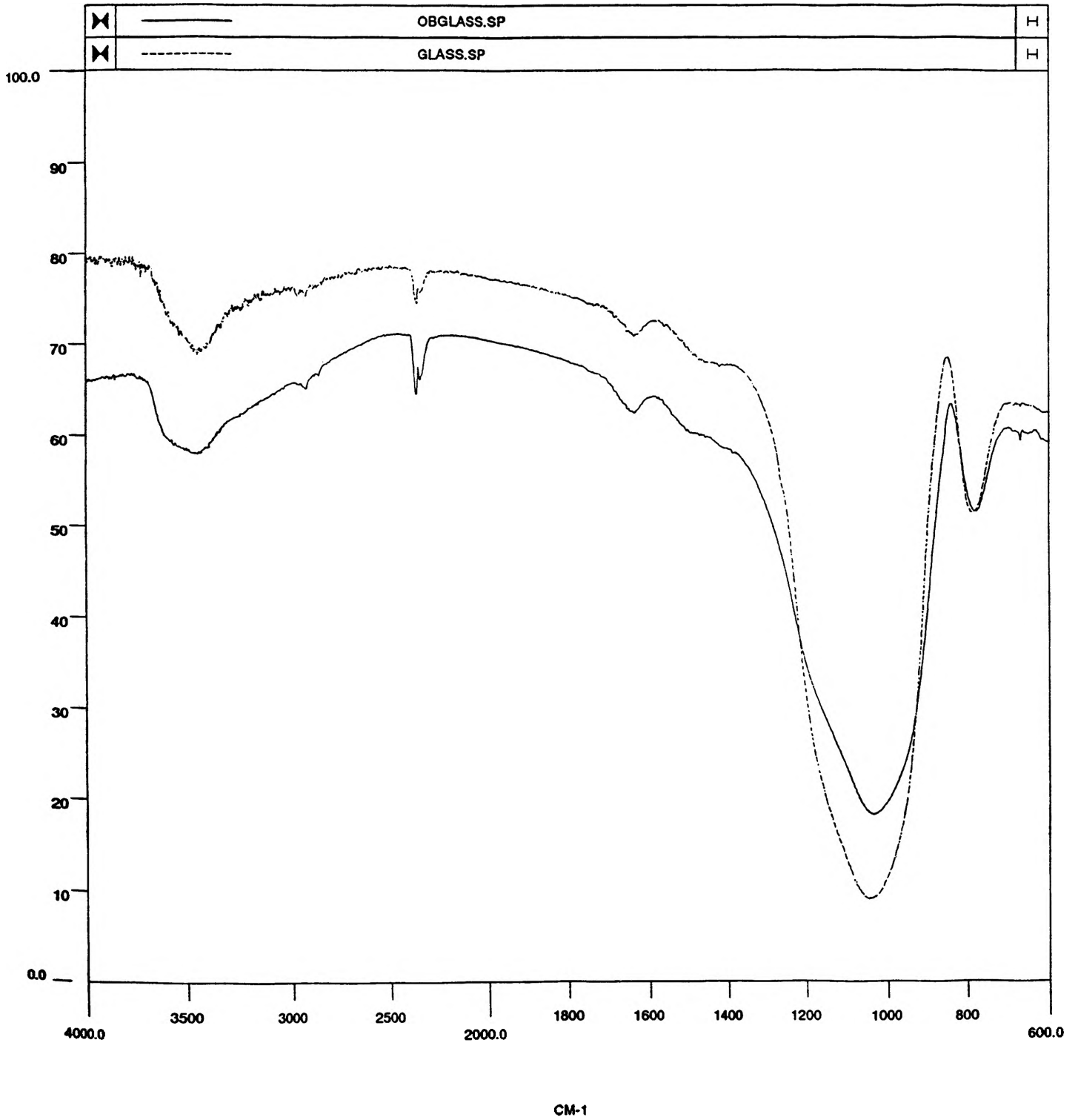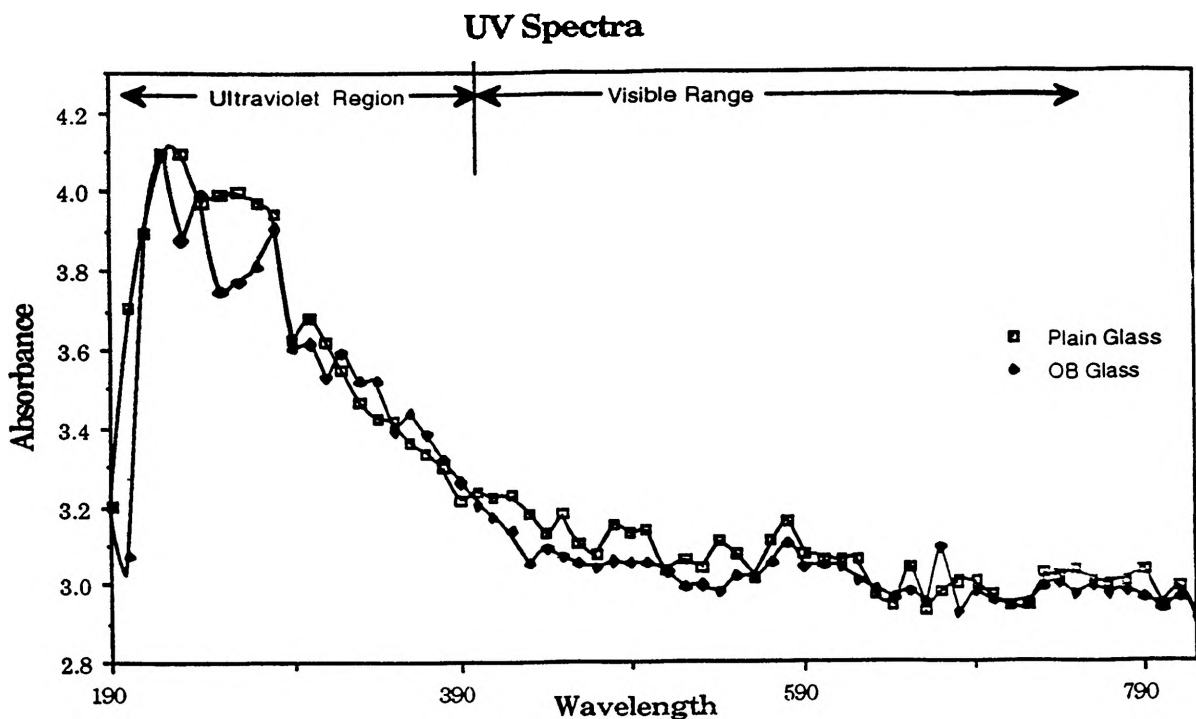
The inconclusiveness of the tests comes from a few factors. The largest factor was the concentration of the OB agent on the glass surface. When each spectrum was run, the samples had to be of a low concentration within a suspending material. The suspending material for the IR was potassium bromide (KBr) and for the UV spectra, the suspending material was in a nujol mol, a gel to suspend a solid allowing a spectra to be obtained. Within the samples, the concentration of the OB agent would be very small and unmeasurable with the instrumentation used. Another factor may have resulted from the glass absorbing some of the light. This was more important in the UV spectra where glass will absorb ultra violet light and is therefor opaque in the UV spectrum.

24

CONCLUSION

In this project, the feasibility of using modified recycled glass was studied. It was shown that recycled glass can be added to some coatings without a large change in the performance properties of the coating. The OB agent was also shown to be attached to the surface of the glass and to partially compensate for the reduced amount of TiO_2 in experimental coatings.

When the experimental paint was applied to the test surfaces, the glass particles caused a rough texture. This roughness makes the coatings applicable to be used in traffic coatings, where the artistic value of the coating is not as important. The use of these coatings for highway traffic coatings is of interest to the Missouri Highway Department. This roughness could be lowered by using a smaller particle sizes of glass and by allowing the paint to be ground up longer during formulation.

If glass is incorporated into formulations, the project could have a positive environmental impact. It will allow for a recycled product to have a new market and reduce the need for other newly processed material.

REFERENCES

1 Lambourne, R. Paint and Surface Coatings. 1987.

2 Information provided Ozark Rivers Solid Waste Management District

3 Petrarch Systems. Silicon Compounds. 1987.

ACKNOWLEDGMENTS

An Artificially Intelligent Word Recognizer to Control Appliances and Switches:

The home that listens to your every command

authors: Joseph Bauer and Rick Steurer

Department of Electrical Engineering

University of Missouri - Rolla

January 1994

CONTENTS

ABSTRACT

The most natural and informal means of communication and control is speech communication. Therefore, it also goes to say that control of home appliances, stereo, computer, and heating thermostat to name a few will naturally tend to this form of control.

A word recognition home controller was designed, constructed, and tested successfully. This paper will discuss the low-cost overall design, implementation, and results of a presently constructed and working "home controller." The results of this successful project in voice control are very promising and agree with the original hypothesis: A home that listens to your command is very much a part of the reality of the future.

INTRODUCTION

From day one man has dreamed of hands-off-control. Even science fiction portrays human interaction with machines using word recognition as the interface. Now fast becoming realizable, many applications to word recognition control devices are starting to become apparent: controls in industrial systems, aids for the handicapped, jet fighter controls, computerized telephone operators, academic learning tools, and even word recognition controlled Windows software.

The system designed by the authors uses a standard IBM compatible 486, a Sound Blaster Sound Card with Digital Signal Processor, and Radio Shack's "Plug In Power." The major tasks in the project's design and implementation fell into three areas:

1. Software control of a Digital Signal Processor to look for a word and digitize sound samples into memory.

2. Software to compress and recognize isolated words from a trained dictionary of words.

3. Designing a circuit interface to allow the computer to control a Radio Shack Transmitter. This transmitter transmits a tone or frequency through standard house wiring, where upon a Radio Shack receiver, set to filter for that tone, triggers the selected device or appliance.

While some sections are fairly detailed, do not expect to find a step by step "how to" process. The intent of the authors is to inform its audience and give them a better understanding of one implementation of the up-and-coming technology.

DESIGN AND IMPLEMENTATION

This section of the report discusses, in a logical layout, the design from the spoken command to the appliance control. Each portion of the design and a description of the devices involved is summarized. The basic blocks of the system step through each portion of the sound input to computer memory (Figure 1a) and from the computer to the appliance (Figure 1b) The overall flowchart of the design can be found in the appendix (page 16).

> *important note: all programming was handled in one high level language called TURBO PASCAL with device driver calls in assembly language to handle hardware interrupts.*

FIGURE 1(a): Block diagram of the microphone, analog to digital convertor, and input to the computer memory.
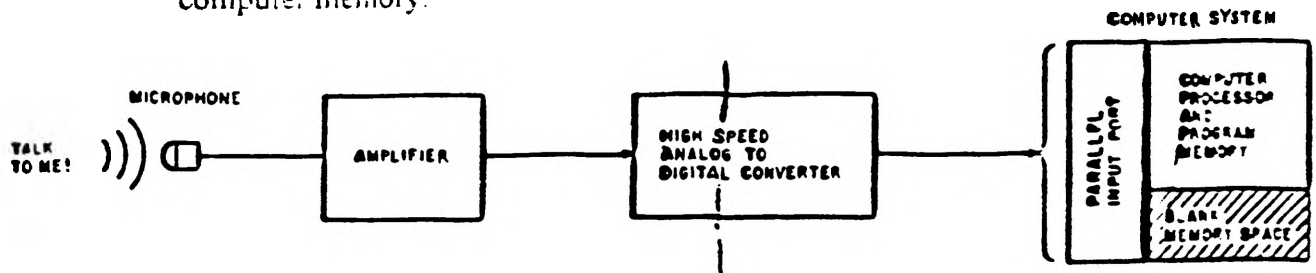
FIGURE 1(b): Block diagram of the computer control through AC house wiring

33
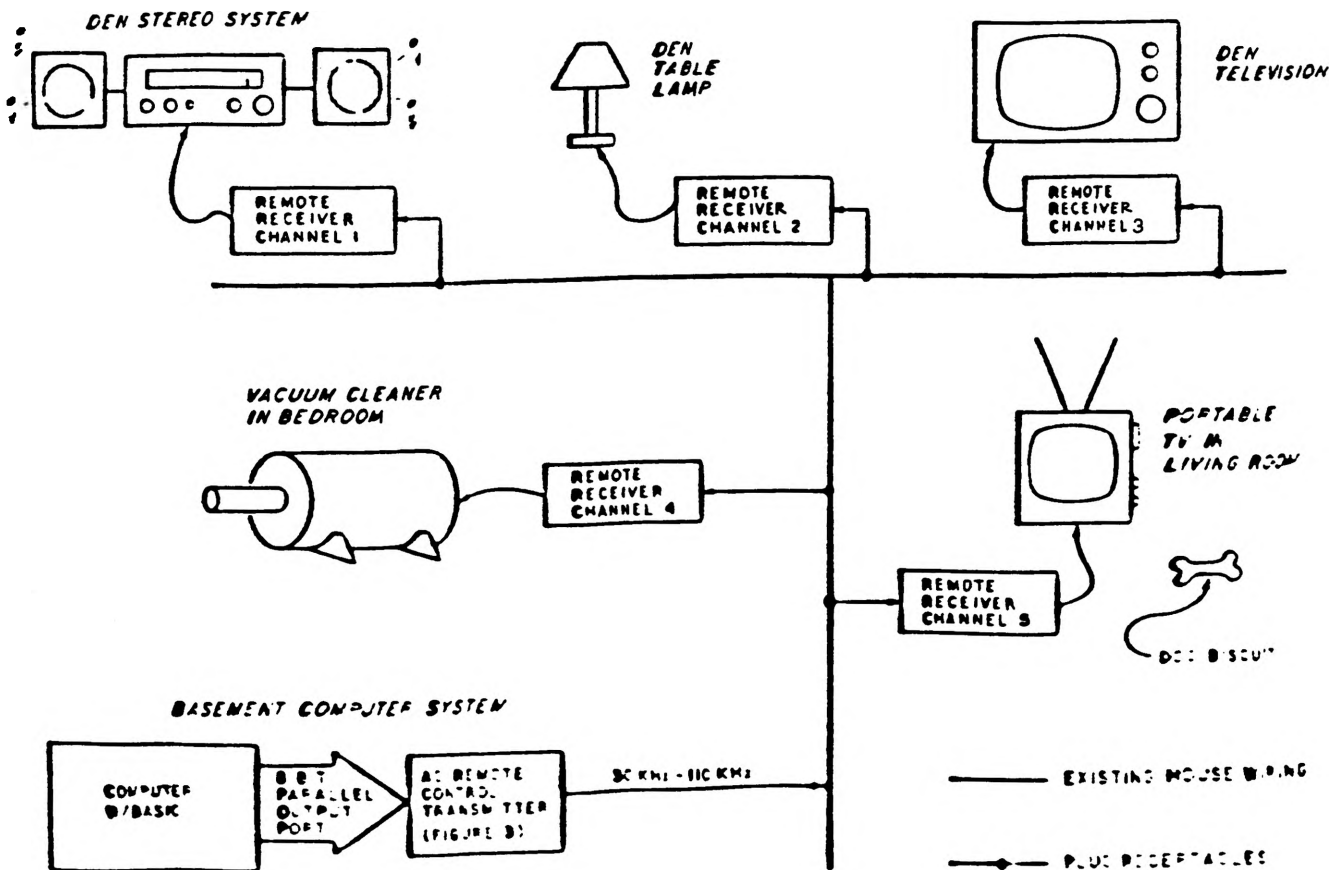
Microphone Input

To receive voiced input into a personal computer for further processing, speech must first be input into a microphone. A microphone's task is fairly simply explained. It takes a sound's time-varying loudness and air pressure differences and converts them linearly into a time-varying voltage signal (see figure 2).

FIGURE 2: an electrical time-varying signal as would be seen on an oscilloscope.
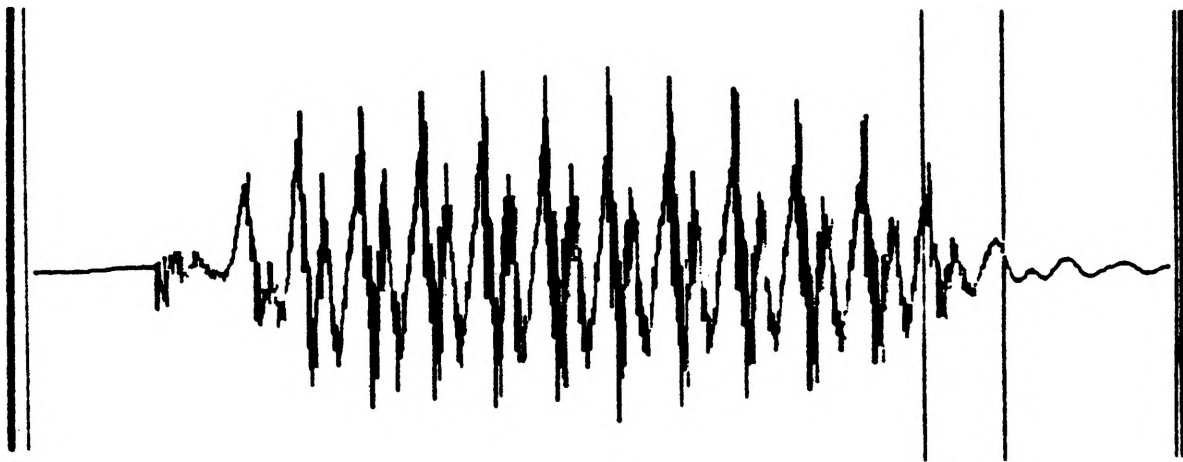
Analog To Digital Conversion and Digital Signal Processing

Once sound is converted to a time-varying voltage signal it can be sampled.* Sampling

* before the signal is sampled it is passed through an Automatic Gain Control (AGC). Once an AGC picks up a signal it holds that signal at a constant gain even when the signal slowly weakens. This aids in speaker recognition while a speaker is moving or varying voice loudness. *While this improves results it is not necessary.*

34

converts a continuous signal into a number of discrete samples. Since most of the frequency range for a voiced signal is under 5 kHz the Nyquist criterion states that the sampling rate must be at least twice the maximum frequency, therefore a sampling range of 6k to 10k samples/sec will suffice. Because Creative Labs Sound Blaster Sound Card is arguably the most-used Digital Signal Processor (DSP) for the personal computer it was chosen to perform the digital signal sampling. Each sample was taken as a 16-bit Compact Disc quality sample. Control of the DSP is accessed through device drivers [1] (low level code summoned from a higher level language to control a card) and the samples are placed in memory. The signal is next low pass filtered to remove 60Hz hum and high pass filtered to remove high frequency noise. The filtering is internal to the programming (i.e. digital filtering is employed).

Word Detection

Word detection is handled by calculating a simple ten ms energy and comparing to a threshold to check if there is energy above and beyond background noise. This energy calculation takes valuable time to perform and part of the word may have already passed by the time the word is detected. Therefore employing two Direct Memory Access buffers* will allow tacking on the previously stored memory buffer to the present buffer being checked if a word is detected. While the computer is checking samples from one memory buffer the DSP is recording to the other buffer.

Once the word is detected again a device driver is employed to record one second's worth of samples to memory. Again these samples are tacked on to the previously stored short-time samples used for the word detection.

*DMA entails the Sound Blaster peripheral storing its speech samples directly to a buffer set up in the computer's Random Access Memory (RAM). Since the microprocessor is not tied up in storing bytes to memory it can perform sequential operations even while speech is being recorded.

Speech Signal Compression

The signal for a spoken word looks fairly random (figure 3a), however upon closer inspection, fairly uniform frequencies and energy can be seen in a voiced signal (figure 3b). These uniformities and other uniform aspects of the voiced signal allow the possibility for compression of a word without losing vital information that describes the word. In fact, with proper compression and decompression the original signal can be recovered from the compressed parameters. This compression, in appropriate applications, can allow for much faster and less frequency bandwidth data transmission. As an example of compression consider a Cosine signal, a continuous signal consisting of an infinite amount of points, can be totally described by its Amplitude and frequency.

FIGURE 3(a): The spoken word signal looks fairly random in nature
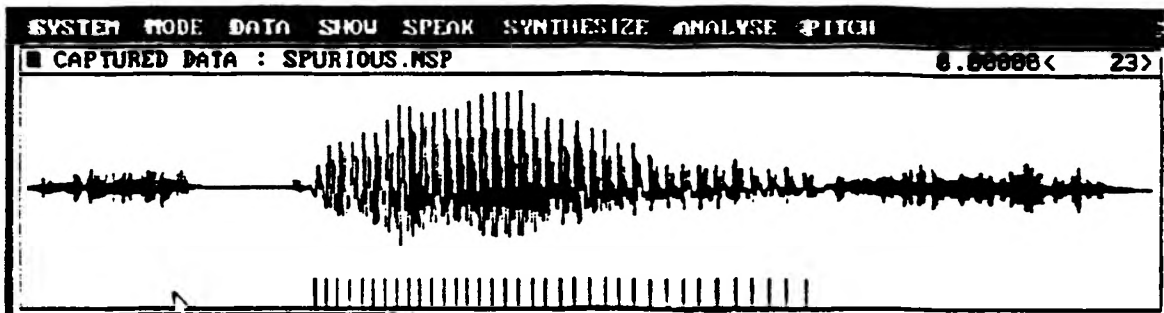
FIGURE 3(b): Closer inspection of the signal reveals uniform frequency and gain
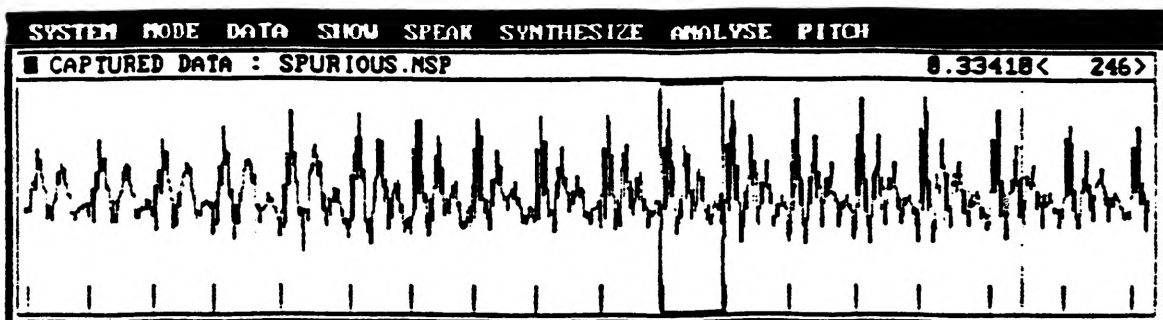
Before compression can take place the endpoint of the word has to be located and word framing performed. End point of the word recorded is found similar to finding the start of the word. The endpoint is found by calculating consecutive ten ms energies until background noise levels are reached [2]. Framing of a word is like chopping the word into smaller portions and then analyzing each portion. The word is framed into thirty-two frames of 256 samples each. This number does not vary with word length which means frames must overlap by an amount dependent on word length. This type of word framing linearly adjusts to the word's size without the computation involved in more complex techniques such as Dynamic Time Warping (DTW). Each frame of samples is then windowed by a hamming window to prevent aliasing.

For the compression of the word certain parameters must be chosen to represent the word. Each frame of the thirty-two frames will have eight parameters to describe it. Since each frame is 256 samples in length originally and now the frame can be represented by 8 parameters, this is a 32:1 compression ratio. (This compression will later allow much less computation in the recognition of the word.) The eight parameters chosen for this application are the same as those chosen in a successful word recognition study performed at the University of Purdue by M. Daniel Tom and M. Renando Tenorio [3]. The eight parameters for each frame of interest are four Linear Predictive Coding coefficients, normalized prediction error, the peak sampled value, the number of zero crossings, and the root-mean-squared energy*. A thorough discussion of these parameters would not help meet the objective of this paper. The book Speech Communication is a very good reference for a further discussion of these parameters [4]. These parameters that describe the word being analyzed will be fed into an artificially intelligent word recognizer for word recognition.

*Note: with these eight parameters it is not possible to recover the original signal totally. However, with word recognition our intent is only to recognize the word..

Artificially Intelligent Word Recognizer

There are many techniques and types of word recognition systems in existence that have met with a certain degree of success: phoneme classifiers, complex computer algorithms, series of bandpass filters, loaded dictionary comparators [4] to name a few. Choices for a recognizer can depend on speed, cost, complexity and/or recognition percentage.

For this application a neural network paradigm (i.e. artificial intelligence) was chosen for a number of reasons:

(1) Neural networks have been tested in word recognition systems and work well with small (~ <50) isolated word vocabularies. This is ideal for a small control specific language;

(2) Neural networks can continue to learn as a speaker's voice changes over the years. In fact, its word recognition accuracy will increase with each additional use;

(3) Neural networks can be easily trained with multiple speakers to achieve a word recognizer with speaker independent recognition.

(4) Another important reason for choosing an artificial intelligence-based word recognizer is that a programmer need not write massive algorithms that can discern a vocabulary of words. This is because it is totally up to the neural network through a process of trial and error to learn the words of its vocabulary.

Accordingly, of the many neural network paradigms, the back propagation neural network paradigm was chosen because:

(1) It is a good at finding general pattern similarities among its training inputs;

(2) The back propagation neural network is fairly straight forward to program;

(3) The back propagation neural network is the most widely used of the paradigms and it has many well documented research applications (even though neural networks are a relatively new field of study).

The back propagation neural network was modeled after the brain's interconnected network of neurons and has an input and an output. Training of the back propagation neural network is accomplished by giving it a known input and comparing the neural network's output to the actual desired output (in this case the correct word that corresponds to the known input). The amount of difference between the desired output and the neural networks output is the error [5]. By propagating this error backwards into the "brain neurons" and changing the neurons proportionally to the amount they erred, the neural network learns. Never has the saying been so true "to error is to learn" as it pertains to neural networks.

Using a ten word vocabulary for training and saying each word only once, the neural network was able to decipher a spoken word correctly 85% of the time. However near 100% recognition was achieved by simply saying each word of the vocabulary twice. This adds more training records to the training process for the neural network to learn with.

Computer Parallel Port Output

Each word of the established vocabulary is given a coded eight bit hexadecimal number to be outputted out of the parallel port of the personal computer upon recognition of the spoken word (e.g. "lamp on" --> hexadecimal code: 02h   "lamp off"--> hexadecimal code: 20h). This hexadecimal code will activate a switch on a peripheral Radio Shack Transmitter connected to the parallel port. The transmitter then transmits a corresponding Pulse Code Modulated signal through the house wiring.

The Frequency Transmitter and Receiver

The transmitter and receiver are a design of Radio Shack Plug in Power. By pressing an input on a selection panel the transmitter sends Pulse Code Modulated signals over standard house wiring. The device that is desired to be controlled is plugged into a Radio Shack receiver. The receiver upon receiving the signal will demodulate and filter the signal, then activate the device. Plug in appliances as well as *switches* can be controlled using these special receivers. The transmitter had to be redesigned to allow interface to the computer.

Computer - Transmitter Interface

Analyzing the selection panel led to a design for a computer integrated controller of the devices (as seen on the next page figures 4a and 4b). The selection panel switches were connected in parallel with computer activated optoisolators, so the switches on the transmitter could be closed either manually or by the computer. These optoisolation devices have basically two tasks: First, the optoisolators, stimulated by a parallel port output code act as solid state relays, closing switches. Second they isolate the computer from any possible spikes coming from the direct transmitter hookup to house wiring. The data stream from the parallel port is connected to this interface via a stripped printer cable.

40

FIGURE 4(a): Block schematic of the computer to transmitter interface.
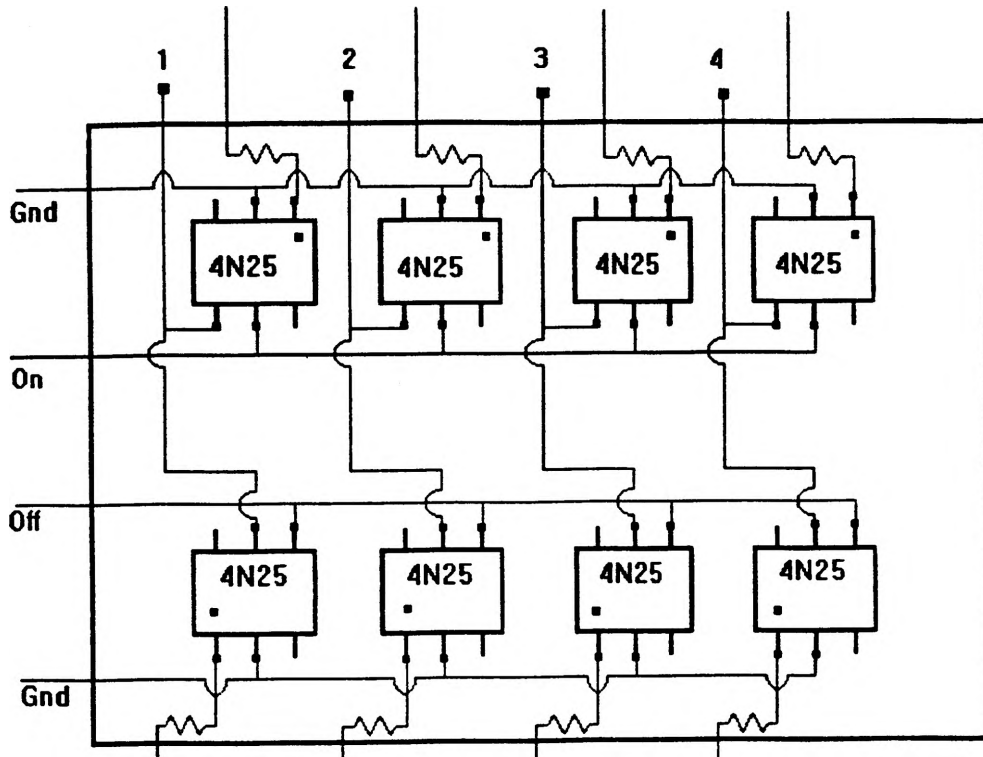
FIGURE 4(b): Photograph of the computer to transmitter interface.

41
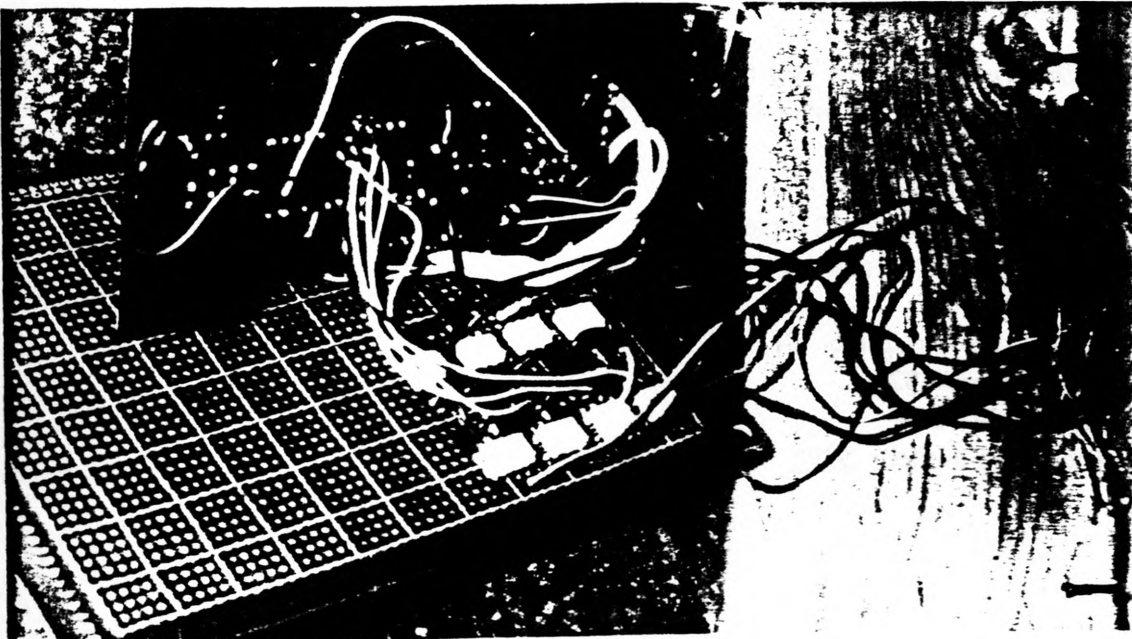
RESULTS AND COST ANALYSIS

research and development costs

        costs of miscellaneous circuitry for scrapped design - $235

        breadboards - $50

        wires, resistors, LED's - $28

        Sound Blaster programming information (Creative Labs Developers Kit) - $105

        Radio Shack transmitter - $15

        Radio Shack 8 receivers - $10 a piece

        16 optoisolator chips - $2 a piece

        2 decoder chips - $2 a piece

        Creative Labs Sound Blaster 16 DSP- $209

        Printer Cable - $15

TOTAL prototype model $671

actual costs to build a production model

(1) Not including the cost of a Sound Blaster Card (computer assumed)

        Radio Shack transmitter - $15

        Radio Shack 8 receivers - $10 a piece

        16 optoisolator chips - $2 a piece

        2 decoder chips - $2 a piece

        circuit board - $1

        miscellaneous wiring etc. $1

        circuit package - $2

        Printer Cable - $15

TOTAL production model $118

(2)Including the cost of a Sound Blaster Card

        Creative Labs Sound Blaster 16 DSP ~$209

        transmitter - $15

        8 receivers - $10 a piece

        16 optoisolator chips - $2 a piece

        2 decoder chips - $2 a piece

        circuit board - $1

        miscellaneous wiring etc. $1

        circuit package - $2

        Printer Cable - $15

TOTAL production model $295

Product's good qualities and bad qualities

Product Good Points

1. no need for additional house wiring

2. near 100% isolated word recognition accuracy

3. cost of a production model is very reasonable

4. easy of use and installation

Product Problems

1. range only good for over a certain circuit breaker

2. requires a dedicated computer while the program is running

3. three and a half second delay time (1 second for record and playback time, 1.5 second for word compression, and 1 second for Radio Shack device switching time)

FURTHER DEVELOPMENTS AND ENHANCEMENTS

>Use two microphones setup properly on opposite sides of a room with Automatic Gain Control to improve recognition of a speaker being located at any point in the room.

>Use a cheap, very low power Frequency Modulated transmitter attached to the shirt of the person in control, with an FM receiver near the computer to demodulate and input spoken commands into the computer. This is a second solution to allow recognition of speaker from any point in the house.

>Design and build a custom board with a DSP, microprocessor, and memory capability. This will decrease the delay time, eliminate the need for a dedicated computer (except to program and initialize the chips), and eliminate the need for the Sound Blaster card.

>Increase transmitted power to allow control over the entire house.

>Put the executable software into resident memory so that, much like a screen saver, the software can always be running even while running other programs (this is another solution to not dedicating the computer to the sole task of running this software).

CONCLUSION

A word recognition home controller was designed and tested successfully, showing great promise for this type of device control. The design's ease of use, excellent isolated word recognizer, and low cost make it an appealing and marketable consumer product. However, certain aspects of the word recognition controller need improvement including increasing the transmitters power, shortening the delay time, and constructing a dedicated microprocessor and Digital Signal Processor board so as not to dedicate a computer to one sole task. Future work by both authors hope to make the necessary improvements.

REFERENCES

[1] Developer Kit for Sound Blaster Series 2nd edition. Creative Labs, 1993

[2] L.R. Rabiner and M.R. Sambur, "An Algorithm for Determining the endpoints of Isolated Utterances," The Bell System Technical Journal, vol. 54 No.2, pp.297-315, Feb. 1975

[3] M. Daniel Tom and M. Ferando Tenorio, "A Spatio-Temporal Pattern Recognition Approach to Word Recognition," School of Electrical Engineering Purdue University, pp. 351-355, 1989

[4] Douglas O'Shaughnessy. Speech Communication: Man and Machine. Addison Wesley Pub. Co., 1987

[5] James A. Freeman, David M. Skapura. Neural Networks: Algorithms, Applications, and Programming Techniques. Addison-Wesley Publishing Co., 1991.

APPENDIX: Flowchart of the implemented design

46
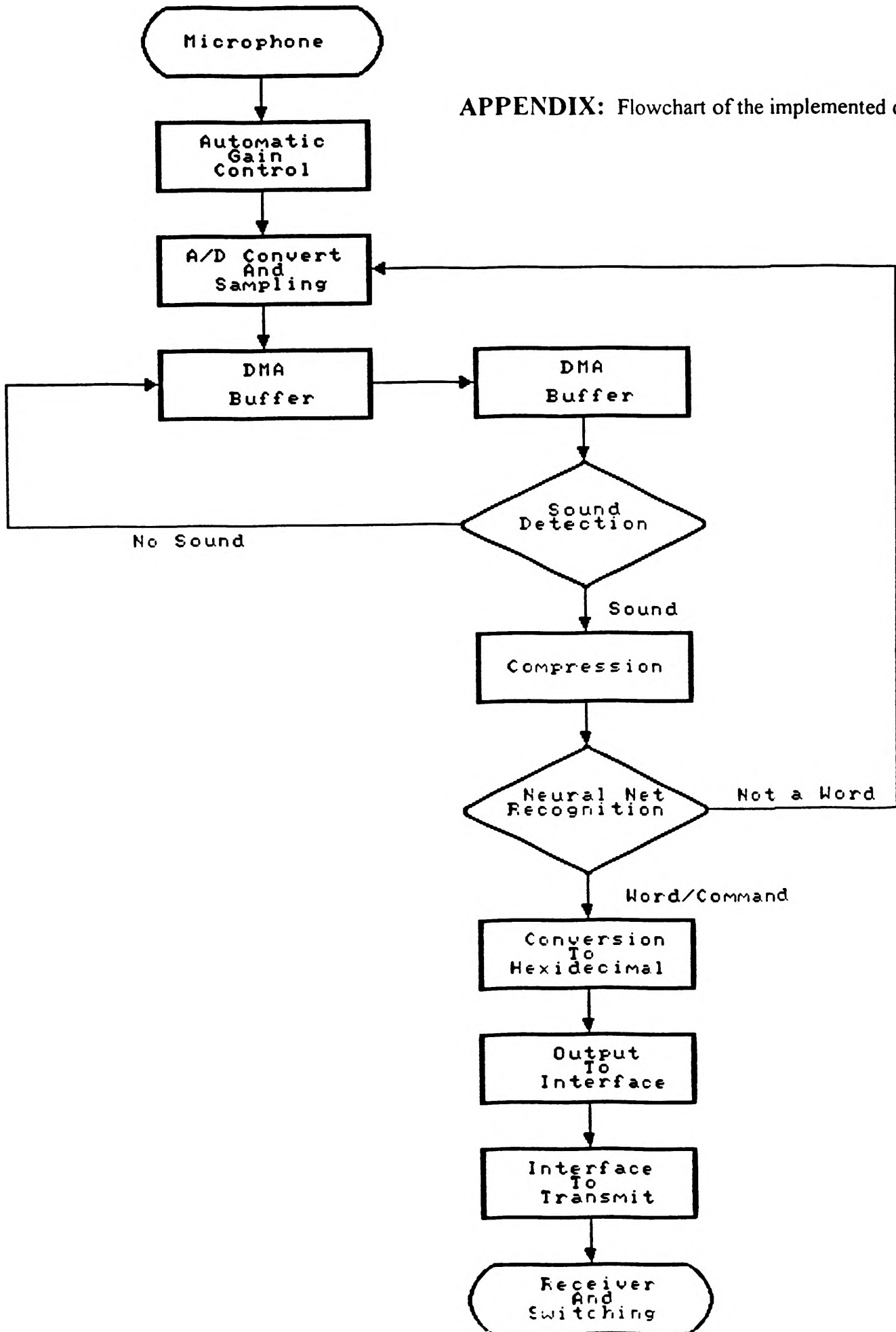
A DESIGN METHODOLOGY FOR A MULTI-FPGA BASED RAPID PROTOTYPING SYSTEM

WILLIAM EATHERTON

DEPARTMENT OF ELECTRICAL ENGINEERING

ABSTRACT

The movement of universities from university-created digital design software to commercial design tools has resulted in a need for a revision of existing rapid prototyping systems. The rapid prototyping system created at North Carolina State University (NCSU) and centered on a FPGA-based board (called the Anyboard), was revised to use Mentor Graphics, a sophisticated industrial EDA tool, rather than board specific software. To provide a guide for future students at UMR and other schools using the Anyboard, an example design was created with Mentor Graphics to route data between a PC bus, SRAMs, and an arithmetic logic unit.

INTRODUCTION

The Anyboard[1,2,3,4,5], developed at North Carolina State University (NCSU) was a large step forward in the field of rapid prototyping. With six field programmable gate arrays (FPGAs), a PC bus connection, a sixty pin external connection, and three static RAMs, the board can be used to implement a wide variety of designs. FPGAs are programmable digital chips that store a design temporarily like a memory chip. These chips have revolutionized the rapid prototyping industry since designs can be implemented in a manner of minutes instead of months. Previously when digital design classes wished to implement their designs, chips had to be fabricated for each student at a cost of around $500. Now with one expenditure of around $500 a board can be constructed for the PC using programmable VLSI chips that can be used for virtually an unlimited number of designs. Unfortunately all designs developed for the board thus far seem to be using text based board specific software[3,4].

Since the general goal of most engineering students is to get an industrial job, training in design entry methods like schematic capture and logic synthesis from equations that is used in industry would be more useful than special purpose academic design methods. With industrial tools like Mentor Graphics, the experience gained designing for the Anyboard can be applied to other design implementation platforms. With this research project, the most advanced technology in rapid prototyping has been united with the most popular design package in electrical engineering. The result will be a system for rapid prototyping that can be used both for research at UMR and for the training of students in digital design with real industrial tools.

So that future students creating designs with Mentor Graphics do not have to have to learn the Anyboard specific language (SOLDER [4]) developed at NCSU, an example covering the various functions of the Anyboard is needed. A major point of interest with the example will be the manual routing of I/O lines between FPGA chips since the NCSU software automatically partitions a large design among

the five FPGA chips. Soon third party companies are promising software to partition designs across multiple FPGAs for use with packages like Mentor Graphics.

This paper describes the design, simulation, and testing of a digital system based on the 74LS181 arithmetic logic unit (ALU), and implemented on the Anyboard. Two SRAMs are used to store the inputs for the ALU obtained from the PC bus. A third SRAM stores the output of the ALU for retrieval by the PC bus later. As the system ALU is developed, the new design process for the Anyboard is laid out.

ANYBOARD DESCRIPTION

The Anyboard is useful for the rapid prototyping of digital systems. The feature of the Anyboard that lends itself to the breadboard qualities is the ring of five Xilinx type FPGAs available for user designs. A sixth FPGA controls and protects the PC bus from faulty designs, downloads designs to the other chips, and controls the timing of the other chips. This interface chip is loaded by an EPROM on boot up. The design for the interface chip was created by the designers of the board at NCSU and therefore the details of the above mentioned functions do not have to be taken on by student designers. Chip 3 receives the PC data bus and control signals from the interface chip and therefore is referred to as the PC interface in designs to be implemented on the Anyboard. The conceptual layout of the Anyboard is shown in Figure 1.
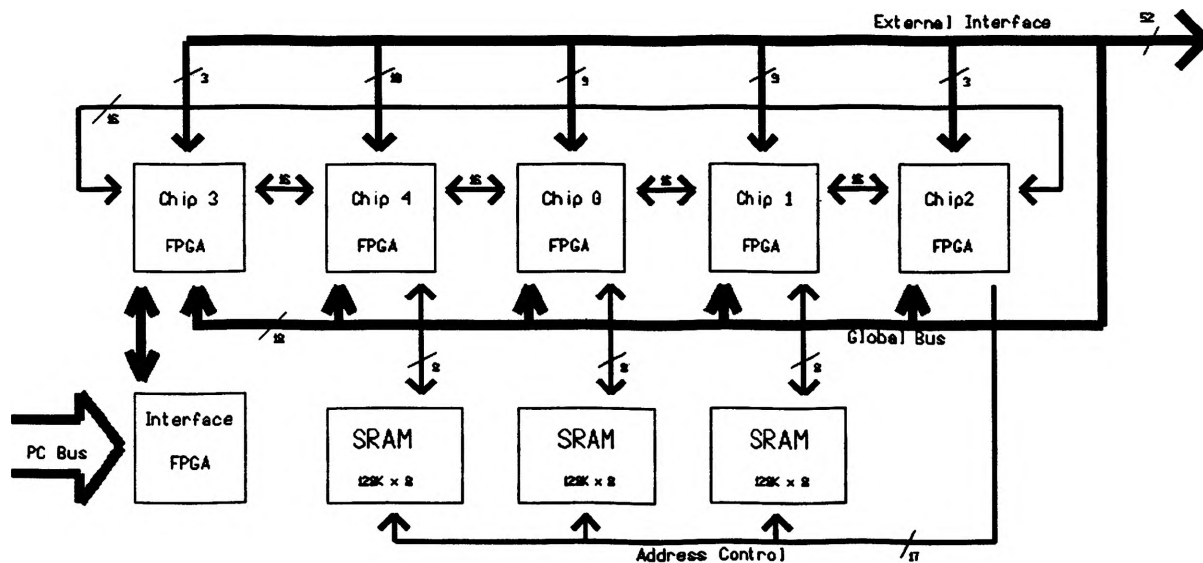
Figure 1 Anyboard Conceptual Layout

SYSTEM OVERVIEW

A system block diagram appears in Figure 2. The global bus connects the PC bus through chip 3 to the other four chips. It contains an eight bit data bus for data transfer with the SRAMs, and for loading the ALU function register on chip 0. Also the global bus contains a five bit control bus that is sent by chip 3 from a system function register. Dclk and OE are the clocks on the global bus for the writing and reading of data between the PC bus and the SRAMs along with clocking of data from SRAMs A and B to SRAM C. The final signal on the global bus is the clear signal. Both the clocks and the clear signal are logic combinations of PC bus control lines.

The 'C' algorithm that describes the overall ALU system would look like:

$$\text{for } (i=0 ; i <= n ; i ++)$$
$$\{ C(i) = A(i) \text{ op } B(i) \} .$$

In this paper the operation is add. The A, B, and C variables represent the memory contents of the respective SRAMs at i address.

48
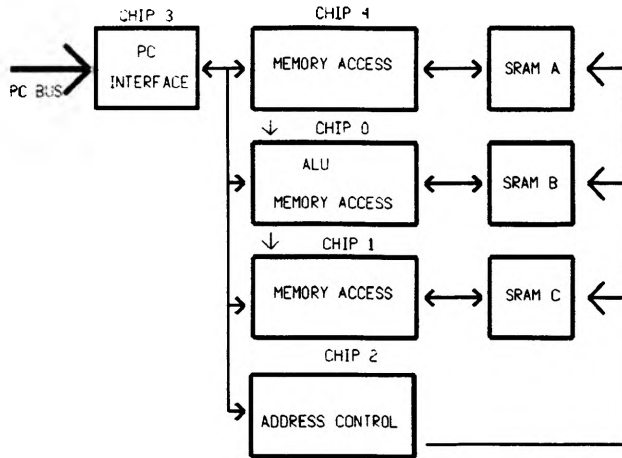
Figure 2 Block Diagram of System ALU

SYSTEM DESIGN

The chip designs were done with a component of Mentor Graphics called Design Architect. Xilinx supplied libraries of SSI and MSI parts were used with schematic capture. In Figure 3 below is a screen from Mentor Graphics that shows a schematic Layout for chip 0. As can be seen from the screen, the layout of a chip schematically is easy to conceptually grasp. This illustrates one advantages of graphical packages like Mentor Graphics over academic textual design tools. Following the schematic is a brief description of each of the five FPGA designs for the chips in Figure 2.
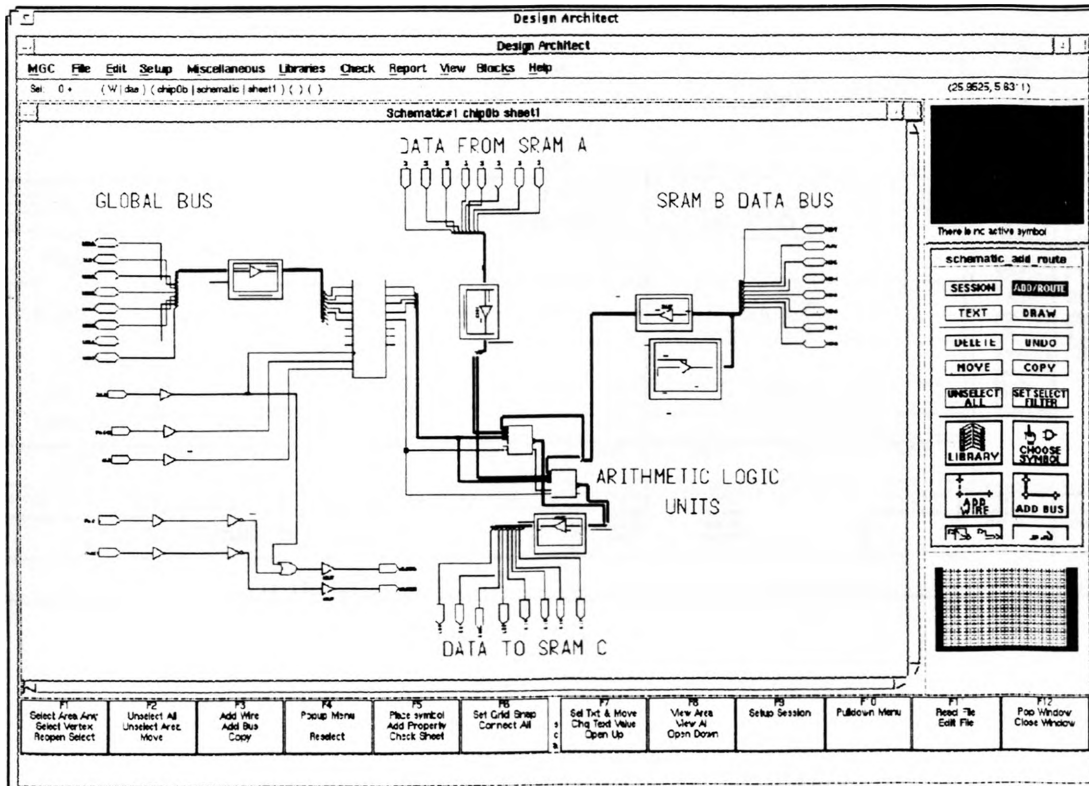
Figure 3 Mentor Graphics Schematic Capture

Chip 3

Chip 3 provides the interface to the PC bus. Using information from the PC bus, chip 3 generates the control lines on the global bus (shown in Figures 2 and 3). One eight bit register on chip 3 stores the system control word and several primitive gate (and, or, nor) combinations do address decoding.

To clock in a command word to the system function register, the adr{0} line is used which goes high when the specific I/O address 301 is used. A system command word is sent to 301, and then 300 is used for all the rest of the reading and writing of data.

Chip 4

Chip 4 routes data from the global bus to its adjacent SRAM called A in the system overview), it also moves data from the SRAM to the ALU on chip 0 through a local bus. The control of the SRAM is done using the control lines present on the global bus and several basic logic gates.

Chip 1

Chip 1 routes data from the ALU on chip 0 to the SRAM adjacent to chip 1 (called B in the overview), and then routes data from the SRAM to the global bus. Like chip 4, this chip uses the global bus control lines and basic gates to perform it functions.

Chip 0

Chip 0 appears in Figure 3 as a schematic, and Figure 4 as a block diagram. It contains the ALU and an ALU function register. To implement this chip, an eight bit register was used to store the function of the ALUs. Using a schematic of the LS'181[7] an equation file was written starting at the lowest level nodes and working up to the outputs. A program called eqn2xnf was then used to generate a Xilinx format netlist(XNF) file. When this was completed, a Mentor schematic was generated with the program gensch8. The final step in the ALU construction was to add input and output ports and create a symbol of the ALU for use on the Design Architect schematic of chip 0.
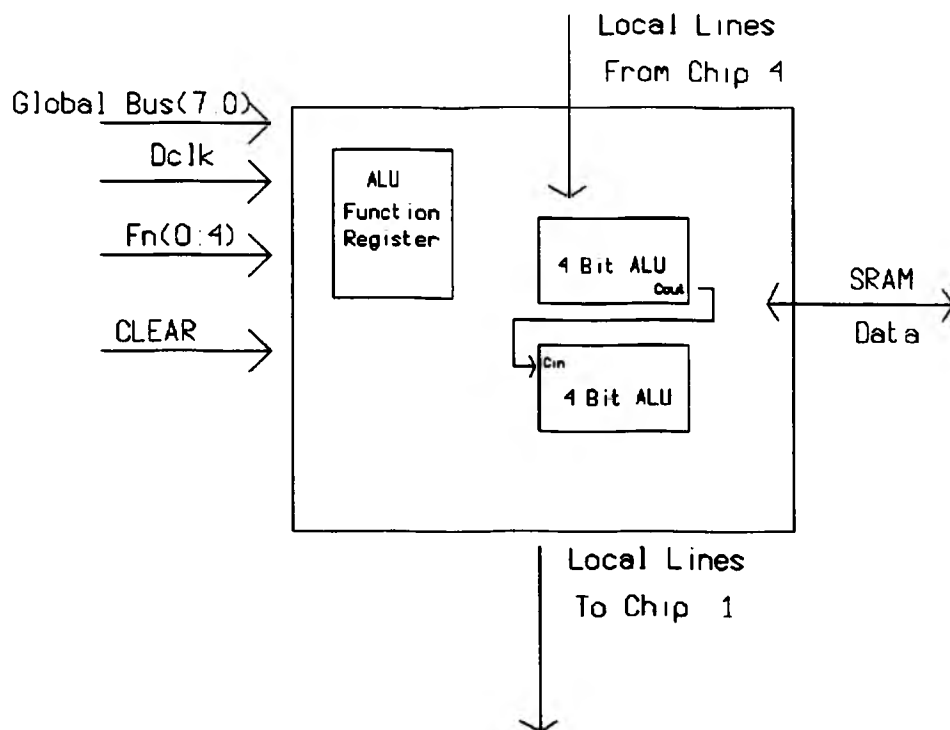
Figure 4 Block Diagram for Chip 0

Chip 2

Chip 2 stores the current address for SRAMs A, B, and C. Then the chip multiplexes the relevant address onto the single address bus. The C SRAM will fill up starting at the 0 address with results of operations between data from SRAMs A and B which were previously loaded. When a read operation is performed on the C SRAM, the C counter is decremented. The A and B counters are permanently up enabled so that after filling up the SRAMs, the counter will flip over and start writing over the hopefully already used first run data. One way to look at it is that the A and B counters are FIFO while the C counter is LIFO. This chip was implemented with 12 eight bit counters and multiple primitive logic gates.

CHIP SIMULATIONS

The chips were simulated using QuicksimII the Mentor Graphics digital simulator. Figure 5 below shows the quicksim screen and the testing of chip 0. Notice that both the schematic and simulation results appear on the same screen to make testing of any net on the schematic possible.

Before beginning simulation, the chips had to go through the Xilinx chip partitioning tools. Then the information regarding signal delays was back annotated into the original schematics to improve simulation accuracy.
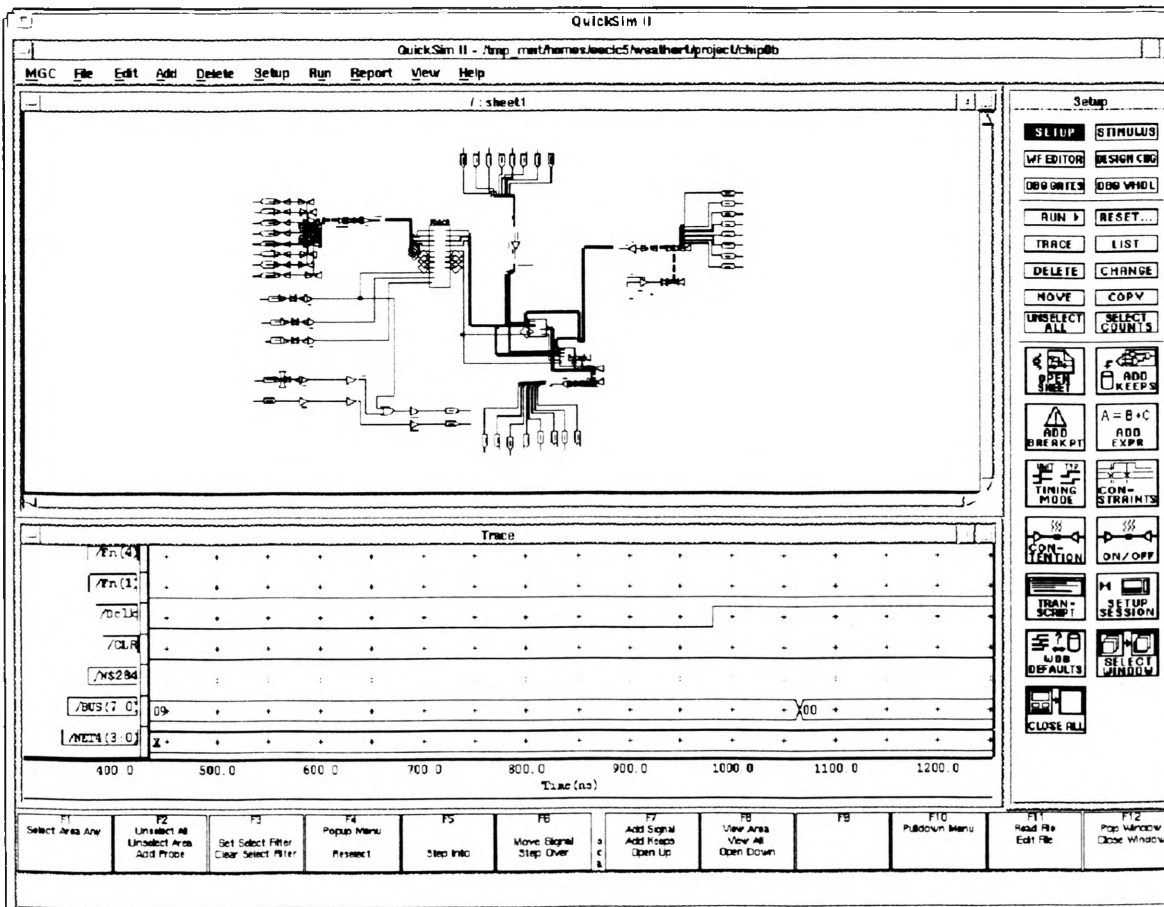
Figure 5 Mentor Graphics Digital Simulation

51

SYSTEM TESTING

Now that the chips have successfully been simulated it is desirable to determine if the system functions properly. A system simulation would only be as good as a very rough approximation of the PC bus. Therefore, it was decided to only conduct a system simulation if an actual test of the design failed. The ability to reiterate the design and test cycle quickly is what makes rapid prototyping systems based on FPGAs useful. To obtain a file for download to the Anyboard, all five chips underwent a procedure similar to the one for back annotation of timing information. The chip designs were first converted to xnf, then the Xilinx Xmake program was run on the xnf files resulting in five bit files. Since many times a single EPROM supplies the bit file for multiple Xilinx chips, Xilinx includes a tool called Makeprom that can concatenate several bit files together into one bit stream. The command from the tutorial supplied by NCSU was adapted and the resulting command for concatenation was 'Makeprom -t -v -s 32 -u 0 chip0.bit chip1.bit chip2.bit chip3.bit chip4.bit -o SYSAALU.mcs'. The '.mcs' file is always about fifty thousand bytes for five 3042 chips concatenated together no matter what the size of the designs (this is because the bit files must specify a 1 or 0 for each programmable piece of the Xilinx chip no matter how much of the chip is used).

A 'C' program was then written to test out the system ALU by first writing two sets of data and then reading back the summed set of data. The test eventually worked after a few redesign and implementation cycles.

CONCLUSION

The system ALU described in this paper has already been used in two student projects as a guide on how to route I/O between chips, transfer data to memory, address memory, and interface with the PC from the Anyboard. This allows the use of traditional design tools (in this case Mentor graphics and Octtools were used), for rapid prototyping at no additional hardware expense. The new design cycle for the Anyboard appears below as Figure 6.
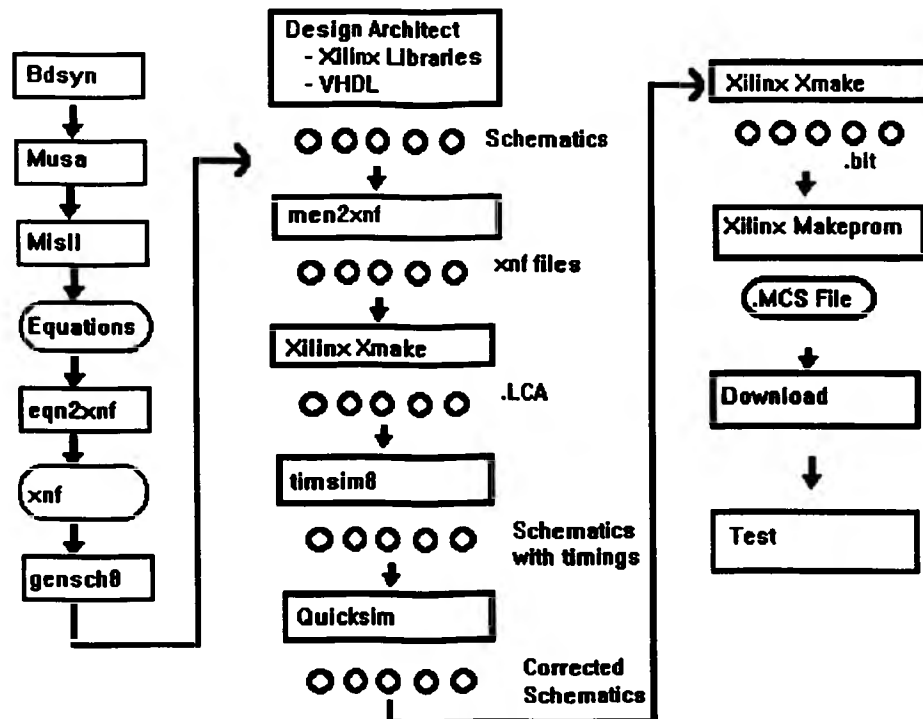
Figure 6 New Rapid Prototyping System

52

FUTURE RESEARCH

The conclusion about the design of systems using multiple FPGAs and SRAMs, is that manual partitioning of designs can make straight forward digital concepts more complex. Until software for the partitioning of designs across multiple FPGAs becomes more available, a board designed with only one or two large Xilinx chips would be more useful. Two Xilinx 4013 chips would have more equivalent gates (about 26 thousand) than the Anyboard (about 20 thousand) and would be much easier to design for since there would be much less manual partitioning of the design. Since most industrial design packages run on workstations rather than PCs, a board designed for a popular workstation bus (like SBUS or VME) would speed up the design cycle considerably.

Continuing the research described in this paper, a new project will begin this summer involving three undergraduate students with the author coordinating. The first step of the project will be to design a new card for the Sun workstations similar to the Anyboard but with more capabilities. Then a software front end based in Mentor Graphics will be developed specifically for the Sun card. The result will be one of the fastest and most powerful rapid prototyping systems available at cost.

ACKNOWLEDGMENTS

REFERENCES

[1] D.E. Van den Bout et al, "Anyboard: An FPGA-Based, Reconfigurable System", *IEEE Design & Test of Computers,* pages 21-30, September 1992.

[2] Joseph N. Morris, "Hardware design of a rapid prototyping reconfigurable system", Master's thesis, North Carolina State University, ECE Dept., Box 7911, Raleigh, NC 27695-7911, 1992.

[3] M. Scot Wingo, "DOOD: The digital object oriented database for the Anyboard environment", Master's thesis, North Carolina State University, ECE Dept., Box 7911, Raleigh, NC 27695-7911, 1992.

[4] Scott C. Labrozzi, "Solder: An object oriented environment for the description and event-driven simulation of structural and behavioral digital designs", Master's thesis, North Carolina State University, ECE Dept., Box 7911, Raleigh, NC 27695-7911, 1992.

[5] D.E. Van den Bout et al, "Tutorial: Using the Anyboard Environment", Unpublished, North Carolina State University, ECE Dept., Box 7911, Raleigh, NC 27695-7911, July 10, 1993.

[6] Royer, J. P., *Handbook of Software & Hardware Interfacing for IBM PCs,* Prentice-Hall, Inc., Englewood Cliffs, New Jersey, 1987.

[7] Signetics, 811 East Arques Avenue, P.O. Box 3409, Sunnyvale, California 94088-3409. *TTL Data Manual,* 1984.

[8] Wakerly, J. F., *Digital Design Principles and Practices,* Prentice-Hall, Inc., Englewood Cliffs, New Jersey, 1990.

[9] XILINX, 2100 Logic Drive, San Jose, California, 95214. *The Programmable Gate Array Book,* 1993.

The Synthesis and Characterization of Poly(1,1'-Divinyl-2,2'-Biimidazole)

Submitted to OURE by:
Timothy S. Evenson
Chemistry Department
University of Missouri-Rolla

ABSTRACT

The monomer 1,1'-divinyl-2,2'-biimidazole was prepared using a previously published procedure (1). The new divinyl biimidazole polymer was then synthesized from this monomer. The polymer was characterized by infrared and ultraviolet-visible spectroscopy. Nuclear magnetic resonance confirms the structure of the polymer. Also, gel permeation chromatography was used to determine molecular weight, while differential scanning calorimetry was used to determine the glass transition temperature and crystalline melting point of the polymer.

INTRODUCTION

Polymers that can bind metals or conduct electricity are being sought for a wide variety of uses. These polymers are often used in models of physiological processes. This is especially true of compounds containing the imidazole ring because the imidazole ring is found in the histidyl group of some amino acids. Metal binding polymers can also be used for selective metal chelating. Electrically conducting polymers are desired as light-weight semi-conducting materials. An electrically conducting polymer is even being used to create artifical neural networks (2). Poly(1,1'-divinyl-2,2'-biimidazole) was produced to determine its metal binding ability and electrical conductivity. This research characterized the polymer so that the subsequent evaluation of chelating and conducting ability can be made.

Poly(divinyl biimidazole) should have the ability to bind metals. The biimidazole molecule has already been shown to form complexes with many different metals (3). The incorporation of biimidazole in to this polymer should yield a metal binding polymer.

Conducting polymers have been researched since the 1970's. In 1977, polyacetylene was shown to have a conductivity around 1000 $(ohm \cdot cm)^{-1}$ after it was exposed to oxidizing or reducing agents (dopants)(4). Other polymers have been made with varying degrees of conductivity. Their use in batteries looks promising because they are light weight and can be used at both electrodes. Conducting polymers tend to have a large number of pi electrons in close proximity and a large ultraviolet extinction coefficient (5). Polyvinylimidazole is one of the polymers with some conductivity (6). Due to its similar structure, Poly(divinyl biimidazole) should also be a conducting polymer.

EXPERIMENTAL

The dimethyl sulfoxide and methanol used in this research were from the Fisher Chemical Company. The dimethyl formamide, ethanol, and acetone were from the Aldrich Chemical Company. The glyoxal, ammonium hydroxide, and potassium hydroxide were also from Aldrich. The hydroquinone inhibitor was from Aldrich, and azobisisobutyronitrile (AIBN) initiator was from Eastman-Kodak. The deuterated dimethyl formamide and tetramethyl silane used in the nuclear magnetic resonance (NMR) experiments were from Aldrich. The potassium bromide used for infrared spectroscopy (IR) was also from Aldrich.

The reactor used for making divinyl biimidazole was the Parr micro reactor model number 4591. The Jeol 100 megahertz FT-NMR was used for NMR. The IR spectra were produced using a Perkin-Elmer Fourier Transform infrared spectrometer model number 1750. Ultraviolet-Visible (UV-Vis) spectra were produced by a Hewlett-Packard diode array spectrophotometer model number 8452A. Differential Scanning Calorimetry (DSC) was performed using a Perkin-Elmer DSC-4. The gel permeation chromatography (GPC) was performed using a Beckman spherogel column, dimethyl formamide solvent, and polystyrene molecular weight standards.

2,2'-Biimidazole was produced by the reaction of ammonium hydroxide and glyoxal (7). The biimidazole was purified by recrystallization from boiling water. The 1,1'-divinyl-2,2'-biimidazole was produced by the reaction of biimidazole with 20 psi of acetylene in dimethyl sulfoxide with a potassium hydroxide catalyst (1). This product was recrystallized from boiling ethanol. Product identification was confirmed by melting point and NMR. The monomer was polymerized by refluxing in a methanol solution containing AIBN for 48 hours. The polymer was then precipitated from solution using acetone. This is similar to the solution polymerization of vinyl imidazole (8). These reactions are shown in Figure 1.

The divinyl biimidazole monomer was characterized by IR and NMR. The divinyl biimidazole polymer was characterized by IR, NMR, UV-Vis, DSC, and GPC.

RESULTS

Proton nuclear magnetic resonance spectra are given for the monomer and polymer-Figures 2 and 3, respectively. The multiplet peaks at 7 ppm and 8 ppm are from the overlap of peaks for four hydrogen atoms. The doublets at 5.0 and 5.6 ppm are due to vinylic hydrogens. These peaks are smaller in the polymer NMR because the vinyl groups have reacted to yield methylene groups instead. This is shown by the appearance of a peak at 2.2 ppm characteristic of a methylene hydrogen. Because the vinyl peaks have not completely disappeared, complete cross-linking of the polymer did not occur; however, polymer branching is high. Peak size indicates about 20% of the vinyl groups did not react, but this figure can probably be controlled by varying polymerization conditions. Other NMR peaks can be attributed to solvent effects.

Infrared spectra of monomer and polymer are included-Figures 4 and

5, respectively. A UV-Vis spectrum of the polymer in a dimethyl formamide solution is also included as Figure 6. The UV absorbance of this solution peaks at a wavelength of 288 nanometers. The large UV absorbance is directly proportional to a very large extinction coefficient.

The polymer's glass transition temperature (Tg) was found to be 110 ºC. The crystalline melting point (mp) was 145 ºC. The DSC curves are Figures 7 and 8, and show the two peaks corresponding to Tg and mp.

Polymer molecular weight (weight average) was estimated to be 120,000 grams per mole. This estimate was made using a polystyrene standard curve. Molecular weight, however, can be controlled by varying polymerization conditions.

DISCUSSION

The NMR spectra help show that this is a highly branched polymer. The IR spectra are helpful in showing the polymer identity also. The unusually large UV absorbance at 288 nanometers is an indicator that this polymer might conduct electricity. The polymer color should be noted as well. The monomer is a brown powder and the polymer has a much darker brown color. Molecular weight is characteristic of this type of polymer; however, it must be stressed that the molecular weight given here is an estimate only based on polystyrene standards, and that this value will change upon variation of polymerization conditions. The crystalline melting point shows that there is some degree of crystallinity in the polymer.

There is a good possibility that this polymer will conduct electricity. Metal binding may increase crystallinity and conductivity. The extent of metal binding is the next step of this research. The measurement of electrical conductivity of the polymer, uncomplexed and complexed, would then be considered in the research of this polymer system.
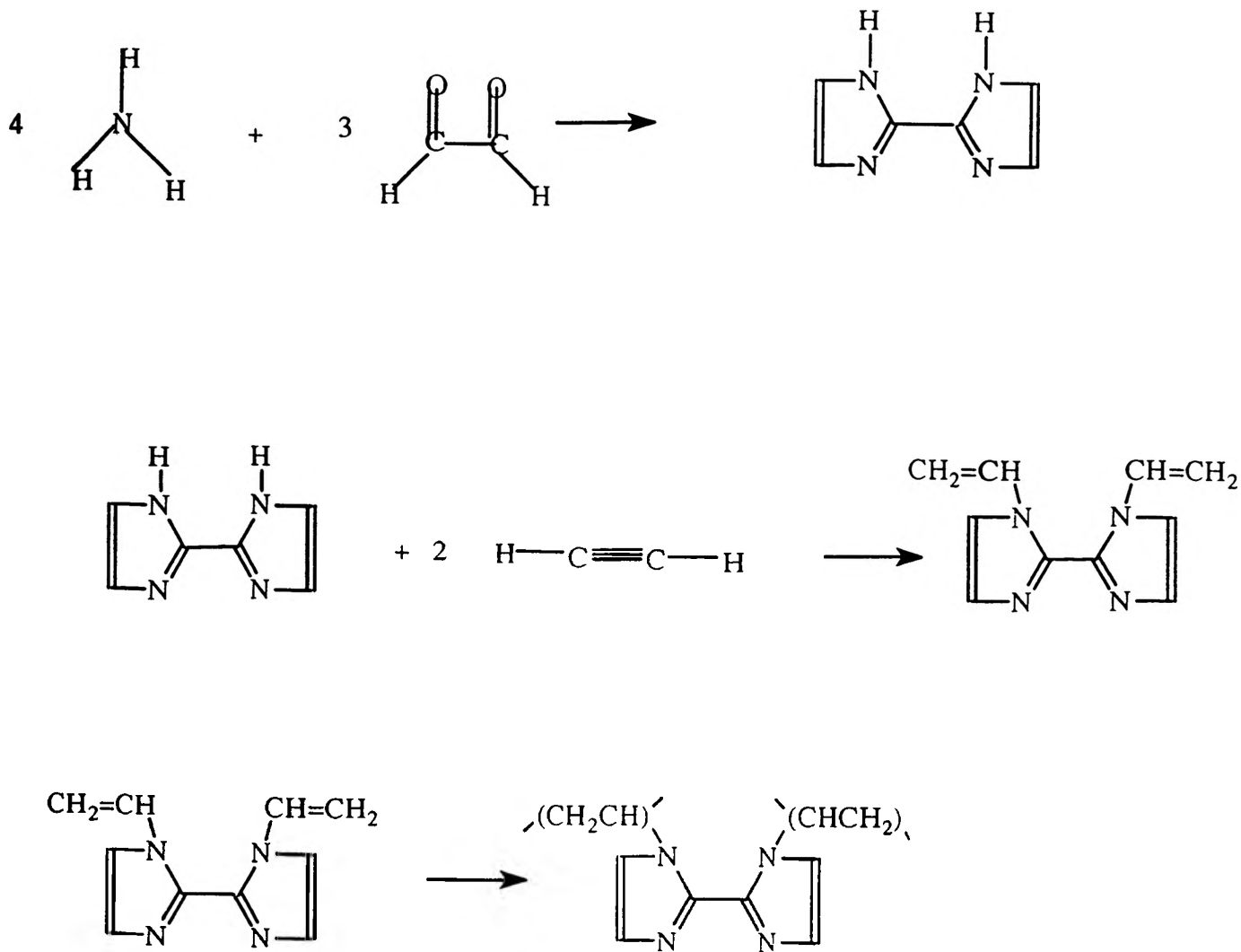
Figure 1 - Reactions.

Obs Freq	99.601900(		ppm	
SW +/-	600.0	#	Start	Stop
FREQU	1200.0	2	8.47	7.77
FILTER		1	7.58	6.97
OBFRQ	99.55	3	5.81	5.46
OBSET	51.9000	4	5.15	4.87
IRMOD	NON			
IRSET	51.50			
No. Scans	32			
No. Points	4096			
Last Delay	1.00e+00			
Line Brdng	0.00			
Nucleus	H1			
Sequence	single H1			
Filename	Tim-3/7/9			
Acq. Time	3.41e+00			

File created:
InteMonday, March 7, 1994
10:17 AM

umr
nmr

3.90   4.00

1.10 1.13
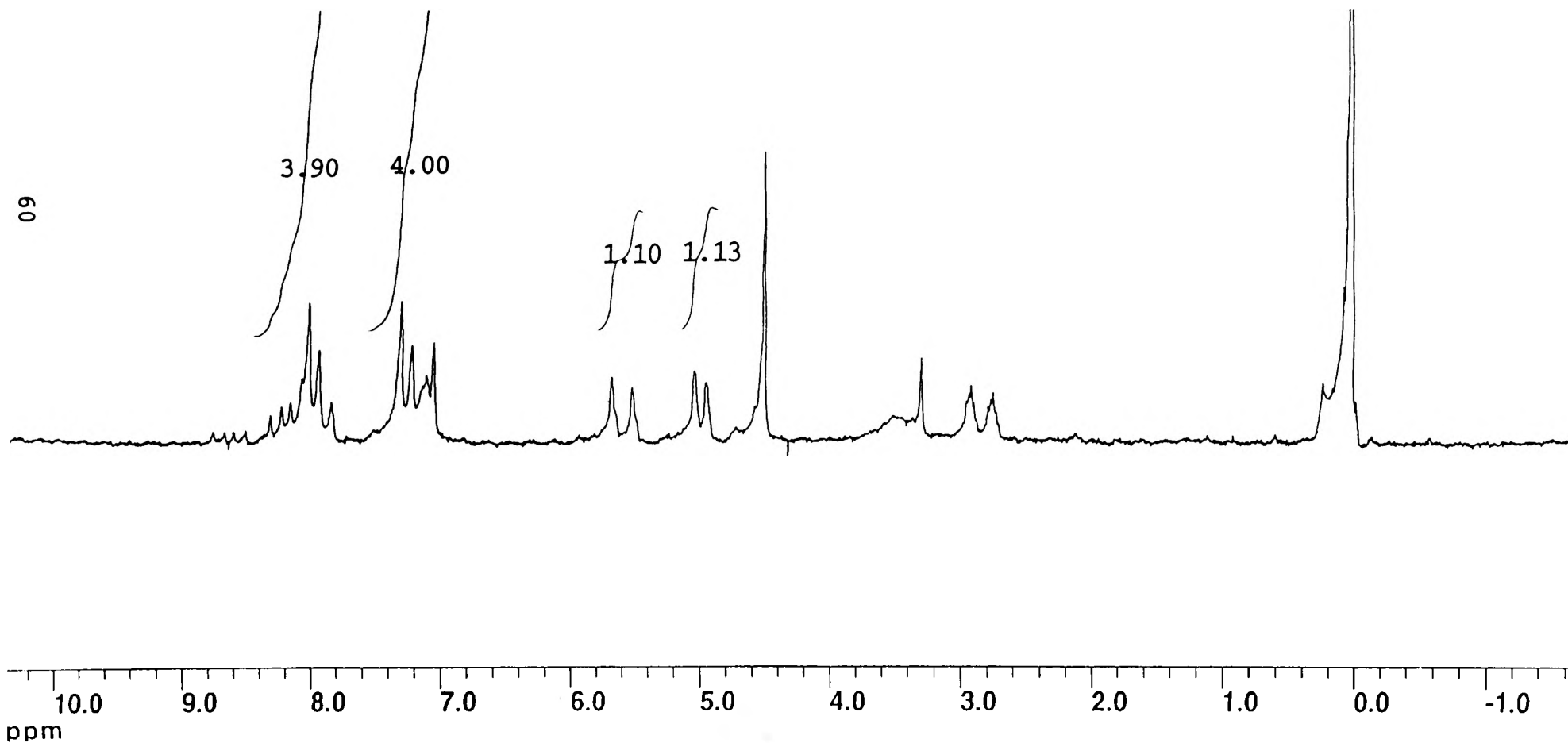
Figure 2 — monomer NMR

MONOMER.SP
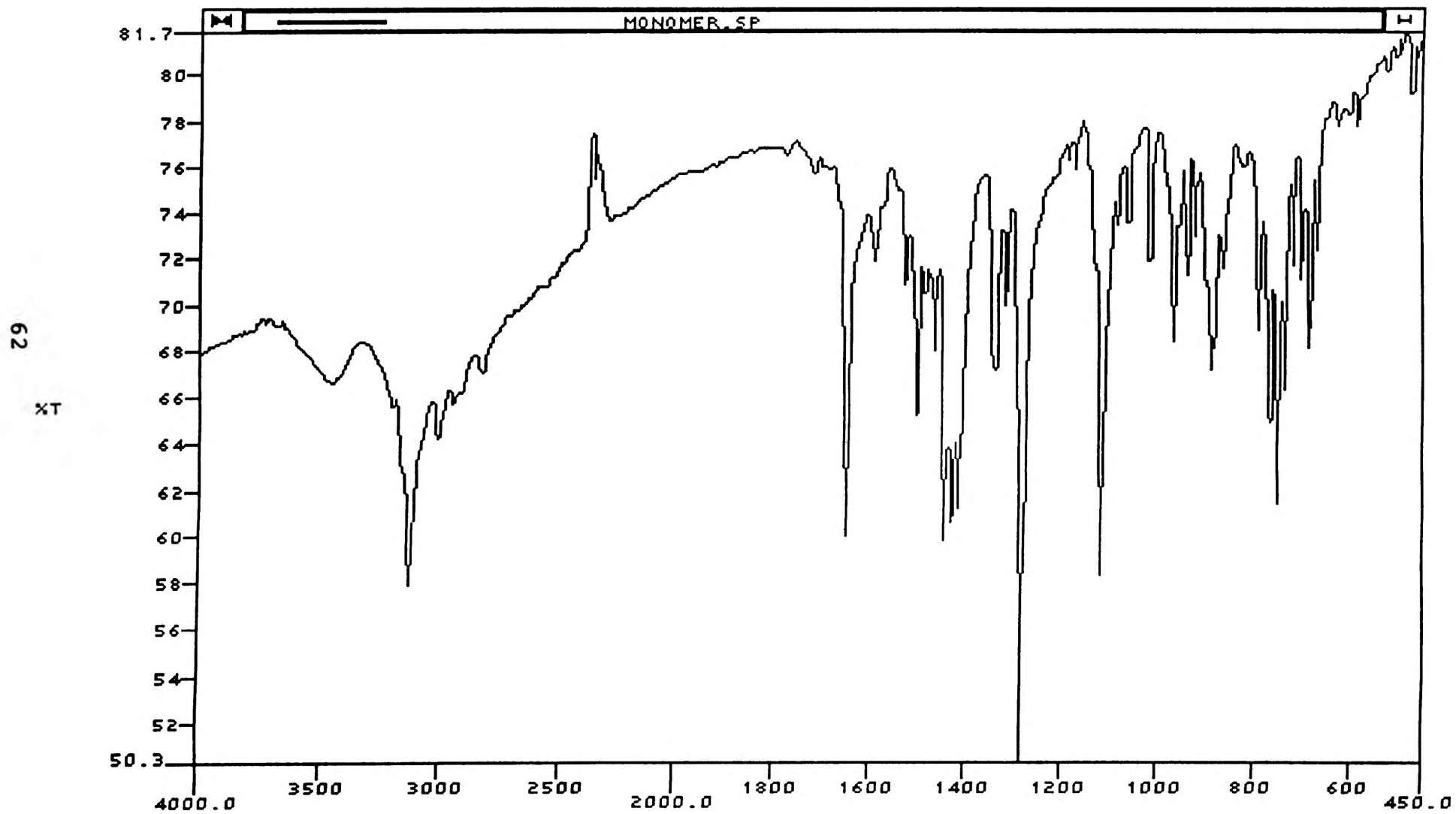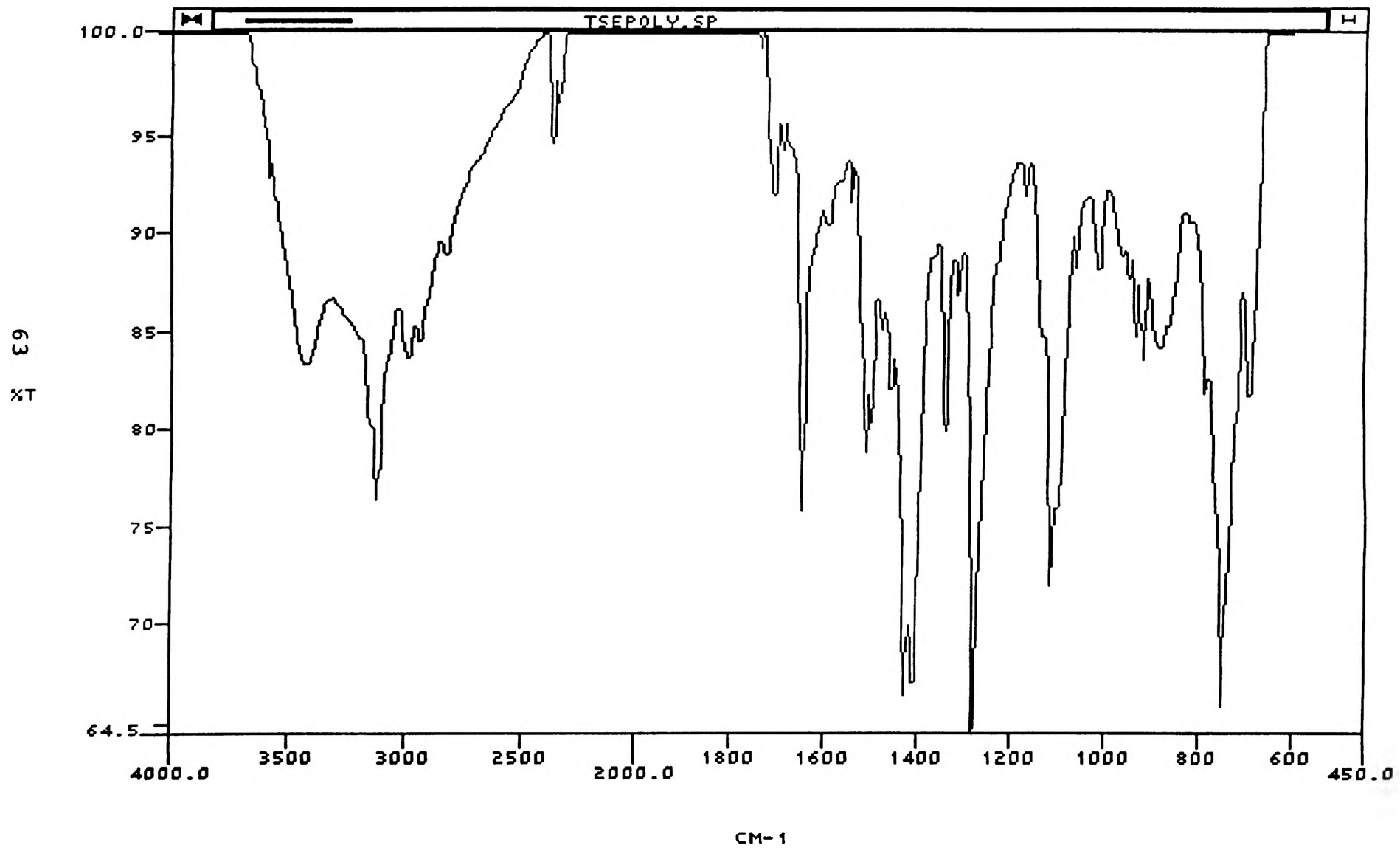
Figure 5 - IR spectrum of polymer.

UV-Vis spectrum of a 0.1g/L solution of Poly(1,1'-Divinyl 2,2'-Biimidazole)
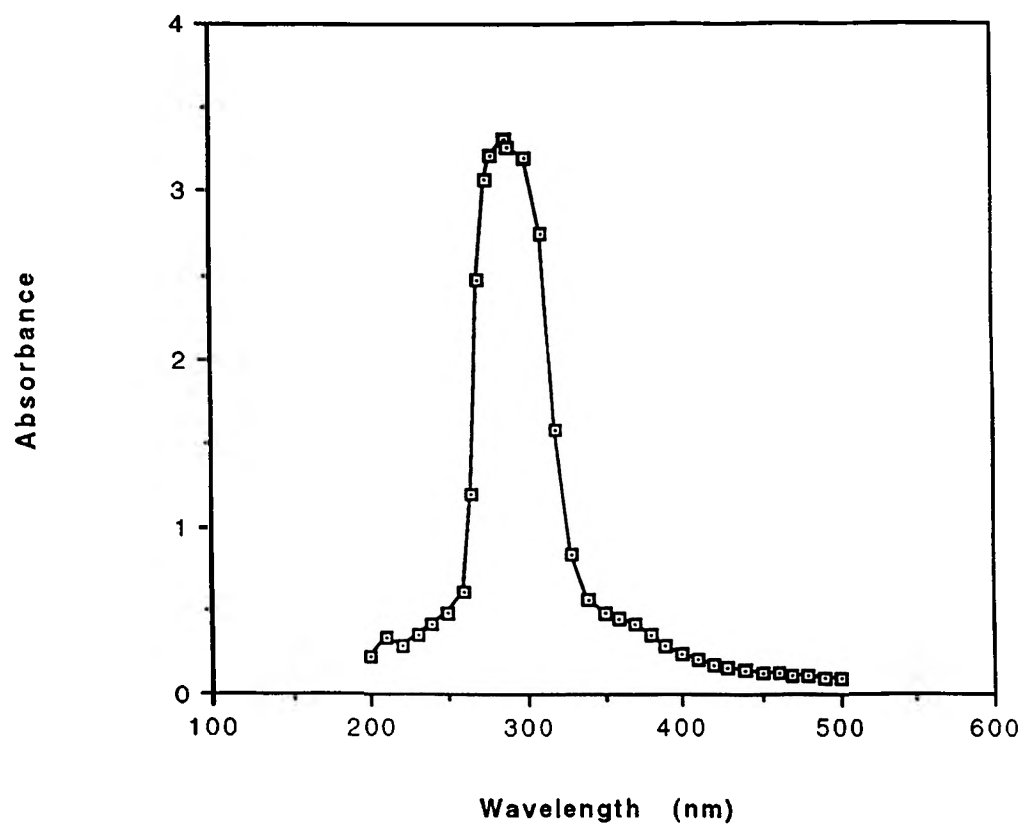
Figure 6 – UV-Vis spectrum of polymer.

Figure 7 - DSC of polymer.

DIVINYLBIIM

WT: 0.00 mg

SCAN RATE: 10.00 deg/min

T/G FROM: 140.38
        TO: 155.2
ONSET: 145.55
MIDPOINT: 148.1

ENDO>

MCAL/SEC

99

1.00

0.50

0.00

60.00   80.00   100.00   120.00   140.00   160.00
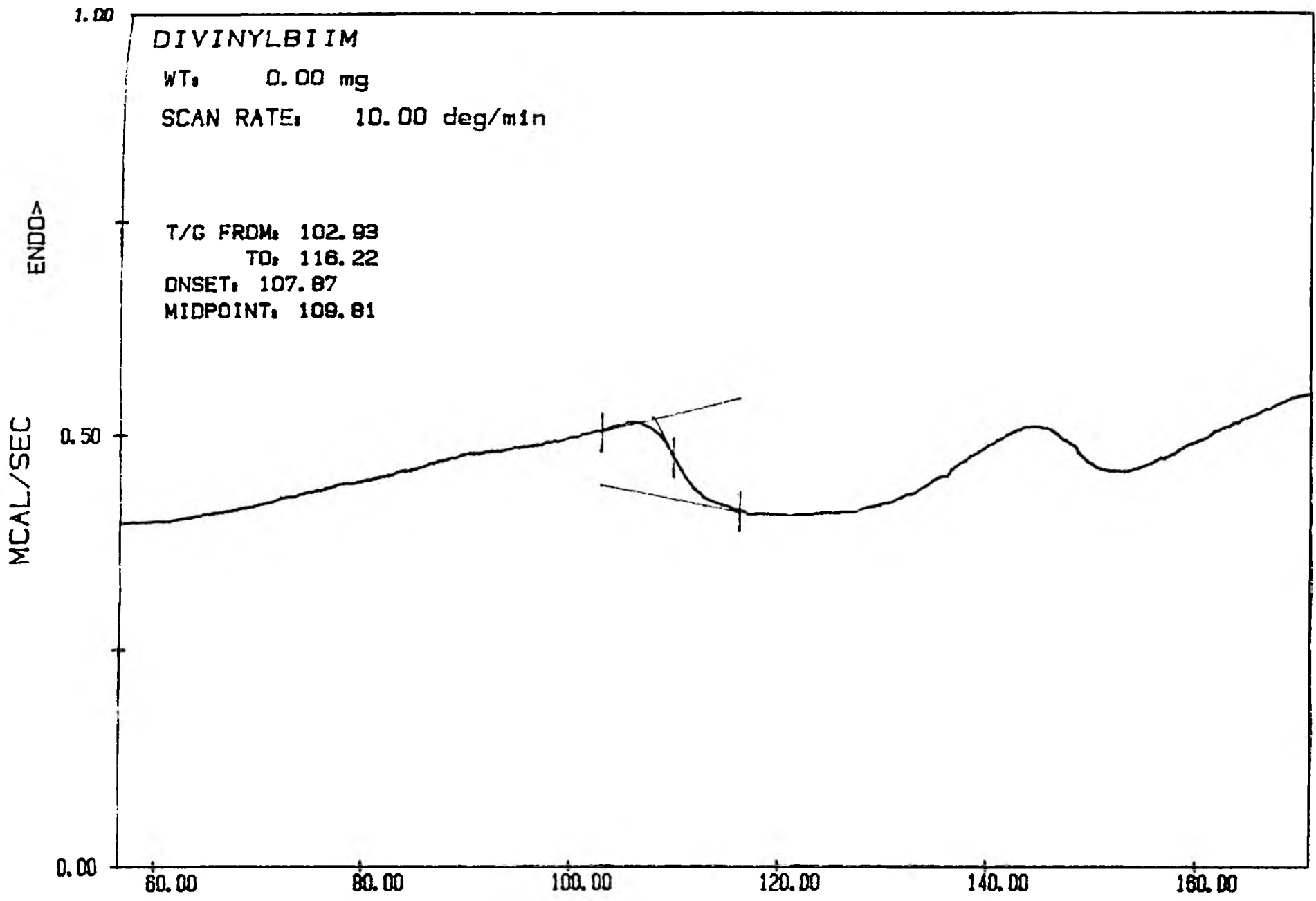
EVENSON   FILE: QSAVE.D4   TEMPERATURE (C)   DSC
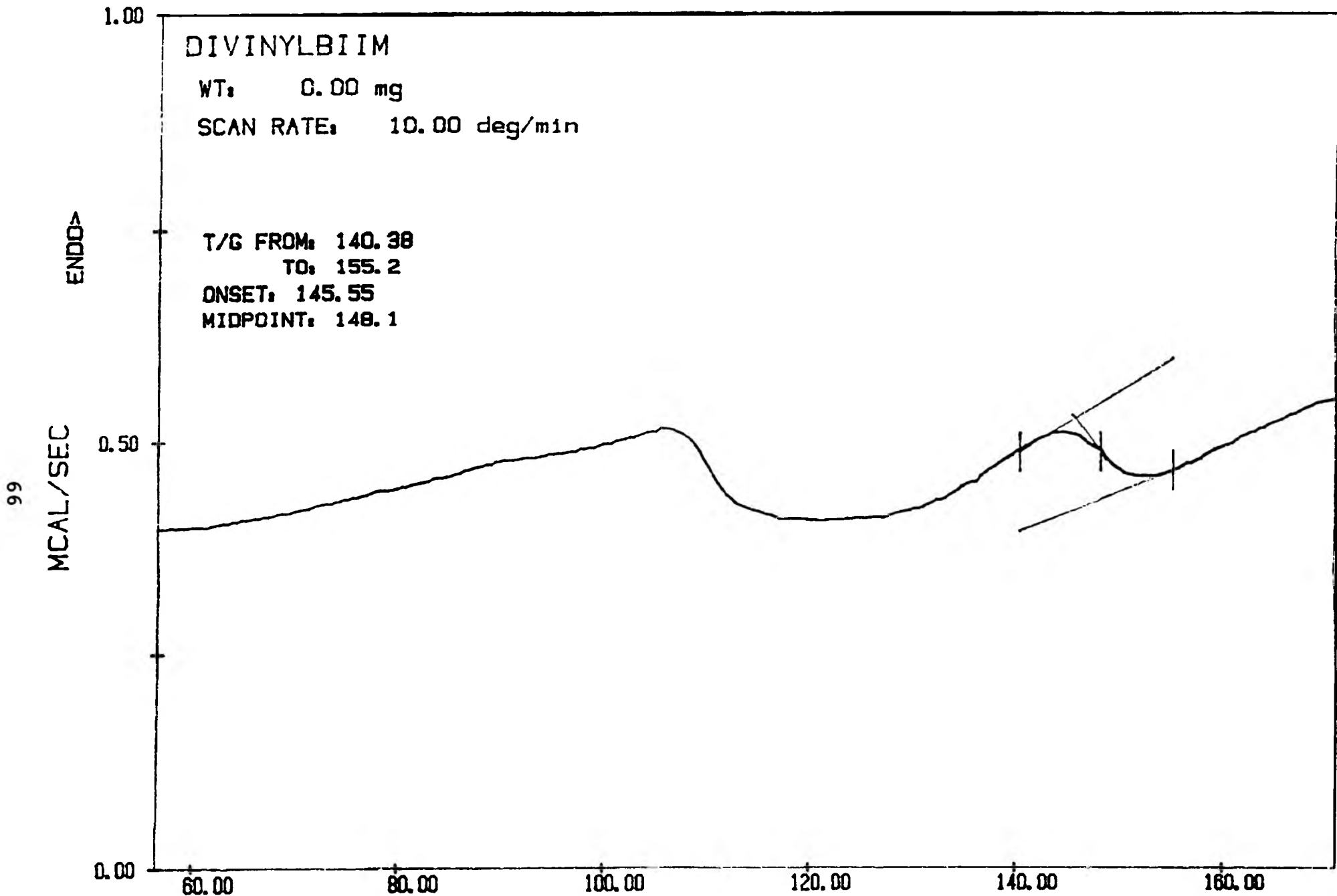
REFERENCES

1. G.G.Skvortsova, et.al. *Izvestiya Akademii Nauk*, SSSR. Seriya Khimicheskaya. Oct 1980. pp. 2339-42.

2. Kittleson, White, Wrighton. *Journal of the American Chemical Society*. 106. 1984. p. 7389.

3. P.J.Steel. *Coordination Chemistry Reviews*. 106. 1990. pp. 227-265.

4. C.K.Chiang, et.al. *Applied Physics Letters*. 33(1). 1978.

5. Bredas, Street. *Acc. Chem. Res.* 18. 1985. pp. 309-315.

6. N.Koyama. Japanese Patent. Japan Kokai Tokyo Koho JP59311,565 [8431,565]. 1984.

7. H.Debus. *Justice Liebigs Ann. Chem.* 107. 1859. p.199.

8. Kham, Deratani, Gal. *New Journal of Chemistry*. 16:4. 1992. pp.505-509.

ACKNOWLEDGEMENTS

SYNTHESIS EVALUATION OF NEW HIGH PERFORMANCE POLYMER SYSTEMS INVOLVING TETRACHLOROHYDROQUINONE

JASON A. GILES

UNIVERSITY OF MISSOURI-ROLLA CHEMISTRY DEPARTMENT

ABSTRACT:

New high performance transparent polymers are in demand in the aerospace and automotive industries to replace current glass and composite systems. Tetrachlorohydroquinone (TCHQ) was used as the base monomer for various copolymer formulations. Different acid chloride monomers lead to polyester formation with TCHQ. Polycarbonates were formed with triphosgene and diethyl carbonate. This base monomer added rigidity, transparency, and high temperature resistance, however, resulting polymers were brittle and difficult to process. Polymers were characterized by IR and DSC.

INTRODUCTION

During the year of 1992 a joint DARPA project (1) between the Materials Research Center and the Polymer and Coating Chemistry department of the University of Missouri- Rolla produced interesting results. The project goal was to develop transparent glass/plastic composites with unique, high performance characteristics for application as a glass replacement material in supersonic transport and fighter plane canopies and windows. Characteristics of the polymer consisted of optical transparency as well as specific infrared wavelength transmittance. The composite was required to have a working temperature range above 250° C while maintaining desired strength factors.

The Opportunities for Undergraduate Research Experience program provided an excellent chance for an investigation to develop a new high performance transparent polymer which could be used in a similar composite system. Using the basic concept of aromatic polymer chains giving better thermal properties combined with the idea that halogenated polymers are generally transparent, thermally stable, and chemically resistant provides a specific path for the research. By focusing on a starting monomer and performing standard polymer chemistry polymerization techniques with that monomer the qualitative results indicate the development of new polymers. These polymers achieved the project goals of high temperature stability, transparency, and chemical resistance. As always an undertaking like this takes many hours and the potential of this project has yet to be exhausted.

A. Details of a High Performance, Transparent Polymer (2,3)

Polymers have the unique ability to be hard or glassy at room temperature but upon heating will soften and eventually flow. That property is termed the glass transition temperature,T_g, which is defined as the temperature or narrow range of temperatures below which an amorphous polymer is in a glassy state, and above which it is rubbery. Such a property is considered a second-order transition (2). The T_m is the first-order transition and is characterized as the "melt point" or flow temperature. These characteristics are attributed to long chains, measured as molecular weight (grams/mole), ranging from 10,000 to 10 million. With such high molecular weights the long chains interact with each other to varying degrees of random entanglement and crystalline structure, respectfully named amorphous or semi-crystalline states. Amorphous polymers are transparent while semi-crystalline polymers are opaque.

Increasing transparency involves reducing the crystalline structures in the polymer. This is done using a non-regular chain structure which does not permit chain packing. However, lack of crystallinity weakens the polymer and must be compensated by increasing the strength of the actual chain. Stiff aromatic rings provide the necessary strength compensation as well as contributing better thermal resistance.

Considering these facts, the starting point of the project is the base monomer selection of tetrachlorohydroquinone (TCHQ). This chlorinated aromatic monomer should give high temperature resistance, transparency and perhaps even flame resistance. Two types of polymerization techniques were used to form different linkages with the second monomer and are listed in Table 1.

Table 1

Type 1 Polymer	Ester Linkage	Monomer 1	Monomer 2
1-1	yes	TCHQ	Succinyl Chloride
1-2	yes	TCHQ	Adipyl Chloride
1-3	yes	TCHQ	Camphoryl Chloride
Type 2 Polymer	Carbonate Linkage		
2-1	yes	TCHQ	Tri-phosgene
2-2	maybe	TCHQ	Diethyl carbonate

EXPERIMENTAL

A. Type 1 Polymer Experimental

The following procedure description is analogous to all of the type 1 polymers. The molar ratios of the monomers is kept near 1:1. This close ratio is to ensure high molecular weight and good conversion.

.3560 g of TCHQ (.3560/247.89=.001435 mol)
.2250 g of succinyl chloride (.2250/154.98=.001458 mol)
.2350 ml of pyridine (.2350*1.050/84.14=.002932 mol)
15-20 ml of either methylene chloride or toluene

The TCHQ, pyridine, and solvent are added to a three neck reactor. A rubber septum is placed in the center neck with the nitrogen flowing through the other necks to keep the system oxygen free. The reactor is lowered into an ice bath for temperature control. A magnetic stir-bar keeps the solution well mixed. The weighed acid chloride is drawn up into a syringe and injected through the rubber septum. After injection, the reaction proceeds for 10-20 minutes. The reaction is complete when polymer granules are suspended in the clear solvent.

Acetone and water are used to rinse and collect the granule polymer in a Hirsh funnel. The collected polymer is dried on a watch glass in an oven at 120° C for one hour. The polymer is then transferred to a vial for storage.

The other type 1 polymers are made in the same fashion except substituting the different acid chloride.

B. Type 2 Polymers Experimental

The following procedure is analogous to the type 2 polymers.

.5178 g of TCHQ (.5178/247.98=.002088 mol)
.1900 g of triphosgene (.1900/298.50=.0006365 mol)
.28 ml of triethyl amine(.28*.726/101.9=.001995 mol)
25 ml of trichlorobenzene
50 ml of water

The glassware setup is identical to the type 1 polymerizations, with the exception of the ice bath. The system is purged with nitrogen as before. The solution of TCHQ and triphosgene dissolved in trichlorobenzene solvent is added. The water is added as the second phase above the organic layer. The reactants are stirred quickly with a magnetic stir-bar, as the temperature is kept at ambient conditions. The triethyl amine is added via syringe through the rubber septum.

After an 8 hour reaction time, 200 ml of distilled water are added, precipitating the polymer. The solution is filtered in a Hirsh funnel and collected polymer dried in a 120° C oven for one day.

71

DISCUSSION OF REACTIONS

A. Type 1 Polymers (2, 3, 4)

All of the acid chlorides were purified by distillation under vacuum. The TCHQ and toluene were used as received from Eastman Chemical. The pyridine was dried using a standard KOH reflux/distillation procedure and stored over molecular sieves.

The toluene and pyridine together dissolved the TCHQ. The pyridine is used in the reaction as an acid scavenger and catalyst, but before the reaction starts it dissociate the hydrogen from the slightly acidic -OH functionality of the TCHQ. As the acid chloride is injected to the system the pyridine abandons the solubilized hydrogen from the TCHQ to liberate the condensation product, HCl. Now the nucleophile, TCHQ$^-$, can attack the waiting monomer by an S_N2 reaction to form the polyester functionality and the chain grows as the reaction ensues. Figure 1 and 2 show the reaction for 1-1 and 1-2 polymers.

Tetrachlorohydroquinone Adipyl chloride

Polymer 1-2

Tetrachlorohydroquinone Succinyl chloride

Polymer 1-1
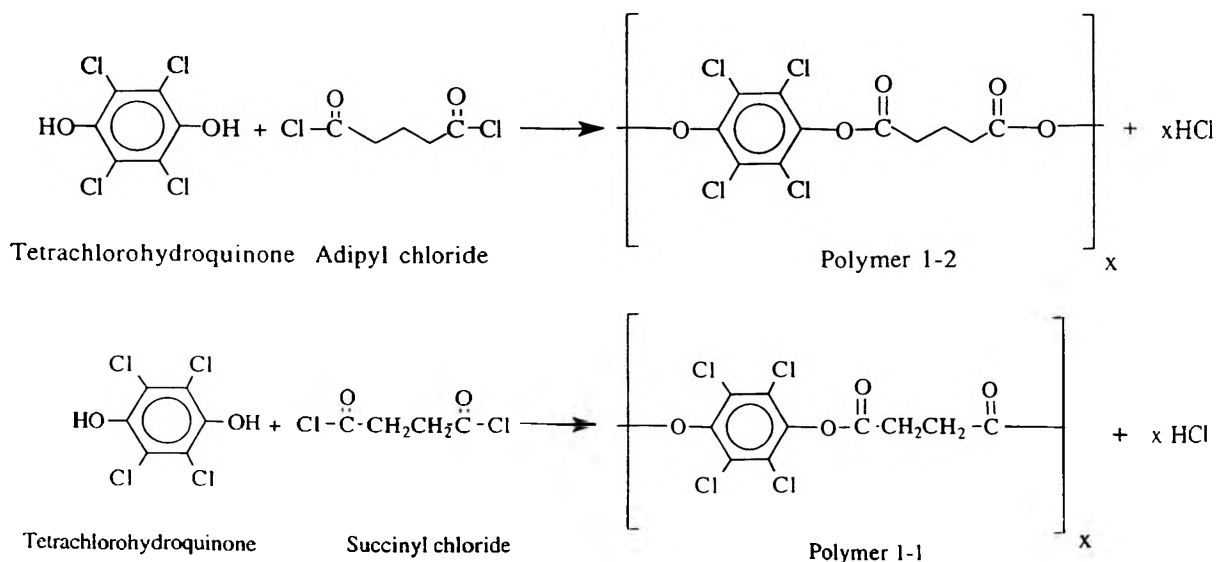
Figures 1 and 2

At first, the acid chloride monomer was added drop by drop and later just added in whole but this addition rate made little difference in the quality of product. The end point of the reaction was denoted by the suspension of polymer granules in the final clear, yellow tinted solution of solvent. The pH of the solvent was found to be highly acidic, also indicating the correct reaction occurred. Finally, the acetone rinse was 5-10% water which terminates the reaction.

The first attempts at this polymerization involved silver nitrate which was used to push the equilibrium to completeness by the formation of the precipitate silver chloride. Unfortunately, this salt became trapped in the polymer matrix and colored the sample a dark gray. Once this additive was removed from the reaction the resulting polymer was a white powder. The silver

nitrate was not used for any of the characterized polymers.

Solubility of all the type 1 polymers was basically the same, insoluble. A number of solvents were tried, each at room temperature and at the boiling temperature. Using the solubility guideline of "like dissolves like", good solvents for this polymer should be some of the usual polyester solvents which include polar groups. Unfortunately, nonsolvents include: water, acetone, various alcohols, N,N dimethyl pyrolidone (NMP), ortho-chlorophenol, ethyl ether, toluene, hexane, chloroform, methylene chloride, DMSO, and acetic acid. Toluene did the best job as it dissolved some of the lower molecular weight polymer but even this would not form a film upon evaporation. The fact that it is not even swollen by any solvent leads to the conclusion of a high degree of crosslinking, or chain to chain interaction. The chlorines attached to the benzene ring are deactivating but still must have enough electronegativity to interact with the polyester groups which would impart a dipole-dipole type of crosslinking

Since an acceptable solvent was not found, characterization was difficult. Techniques like NMR, which would help define the structure, are not possible. GPC (gel permeation chromatography) could not be used to give the molecular weight of the polymer.

The camphoryl monomer, for the type 1-3 polymer, was not readily available. Its synthesis was attempted by reacting thionyl chloride ($SOCl_2$) with camphoric acid under reduced pressure and heat, the monomer formed in low concentration. The separation of the monomer from the thionyl chloride was not satisfactory, resulting in polymer 1-3 being very dark and uncharacterizable. Figure 3 shows the possible reaction.

Tetrachloro hydroquinone   Camphoryl chloride   Polymer 1-3
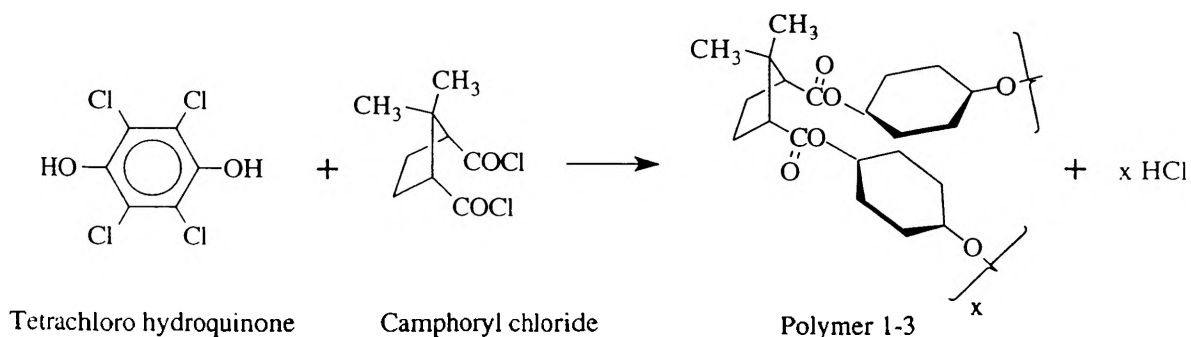
Figure 3

B. Type 2 polymer (3, 5, 6)

The reaction for the type 2 polymers is called interfacial polymerization. This polymerization technique uses two separate phases of solvents, each one containing different components of the reaction. Stirring the mixture causes the surface area of the interphase to increase. This interface is where the polymerization occurs because the reactants are close enough to react, so the higher the surface area the faster the reaction rate. Also this type of polymerization can produce very high molecular weights because the viscosity and thermal exchange are good, the drawback is long reaction times (~8 hours).

73

In this system, the lower layer of trichlorobenzene contained the TCHQ and triphosgene. The initiator, triethyl amine, was added via syringe to the upper aqueous layer. As the mixture was stirred, the evolution of gaseous HCl indicated the reaction was working as shown in Figure 4.

Tetrachlorohydroquinone   Triphosgene   Polymer 2-1
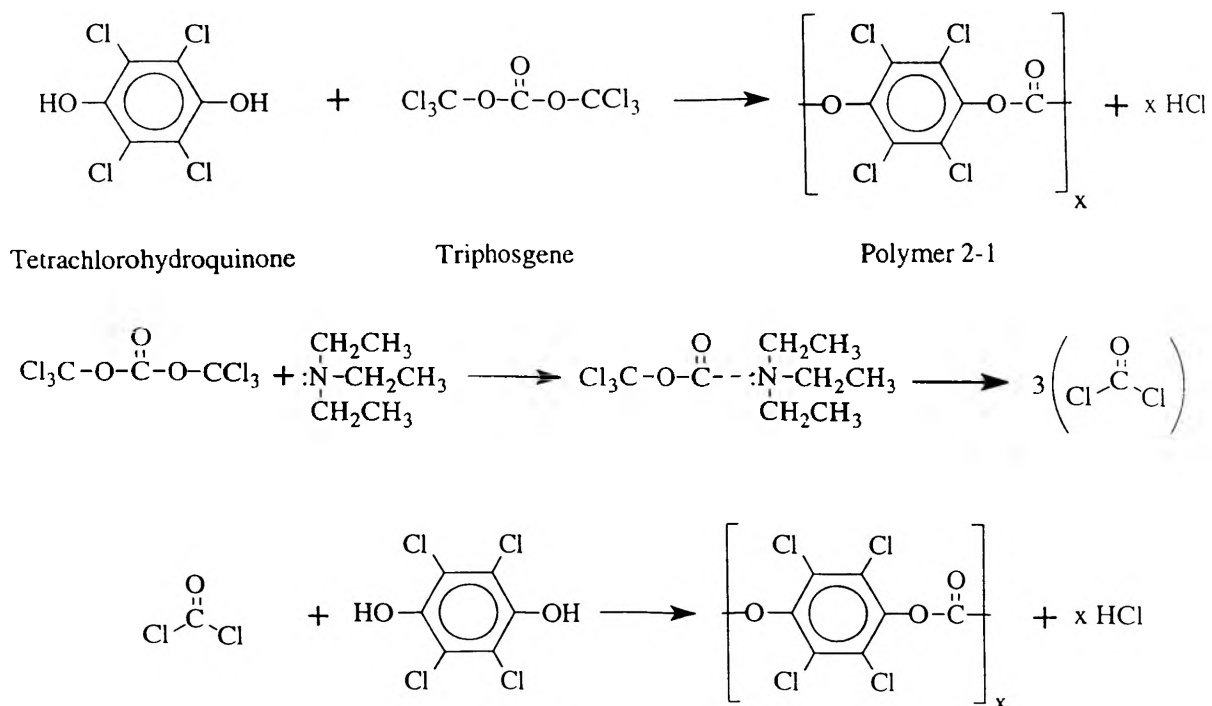
Figure 4

Phosgene has been a standard reactant in the formation of many commercial polycarbonates but is not widely used today because it is very toxic. Triphosgene, however, is a stable solid of phosgene that does not have the dangers of its gaseous counterpart. The triphosgene chemistry is not very well understood partly because it is relatively new product. But a possible schematic for its reaction is demonstrated in Figure 5. Once attacked by the triethyl amine, a weak base, the chemical produces phosgene into the solution because the amine breaks the triphosgene into the three phosgene molecules which are attacked by the TCHQ nucleophile to release HCl as the by-product. The interesting thing about this reaction is that once the phosgene reacts it forms an ester group with the TCHQ and another TCHQ is needed to react on the other side of the carbonyl replacing the chlorine and forming a carbonate linkage.

The polycarbonate linkage usually makes an optically clear polymer because the C-O-C ether linkages are very strong but allow rotation about the bond, resulting in a strong, clear amorphous polymer. The type 2-1 polymer was clear but had a brown tint. The tint is thought to be an impurity, and recrystallization attempts have so far failed at removing the colorant. At room temperature the polymer is very brittle but softens easily upon heating. The type 2-1 polymer is soluble in common polar organic solvents like acetone, ethyl and methyl alcohols and THF. Fortunately it is insoluble in water.

74

RESULTS:

A. Type 1 Polymers (4)

The type 1-1 and 1-2 polymers were characterized by a Fourier Transform Infrared Spectrophotometer. A potassium bromide pellet was made by crushing the salt with a small amount of polymer. The spectra are shown in Figures 5 and 6. The spectra of each polymer gives indication of no aromatic hydrogens but does indicate a small -OH vibration in the 3600-3300 cm^{-1} range, this is possibly from TCHQ's phenol vibration as an end group. The carbonyl peaks characteristic of ester linkages are very strong at 1780 cm^{-1} for the C=O and 1100 cm^{-1} for the C-O-C bond. These resonance frequencies are higher than normal aliphatic ester vibrations because of the electron withdrawing aromatic attached to the ester oxygen. Carbon-hydrogen bonds are apparent, but impossible to determine how many C-H bonds are present between the two samples. So the difference between the 1-1 and 1-2 polymer spectra is minimal except in the trailing fingerprint below 750 cm^{-1}.

Figure numbers 7 and 8 for the 1-1 and 1-2 polymers, respectively, are the differential scanning calorimeter (DSC) results. The temperature range over which the sample was subjected did not show a Tg but did show a decomposition temperature. The decomposition for 1-1 is 380° C and 1-2 is 371° C. This decomposition temperature is characteristic of a crosslinked polymer, similar thermoset polymers do not have Tg or Tm because the covalently bonded crosslinks. It is speculated that type 1-1 and 1-2 polymers have strong chain to chain interaction between the ester and aromatic chlorines.

The Tg could be below the initial temperature, 40° C, of the DSC scans. However, if that were the case the Tm would be observed. After the temperature application, the sample was investigated to reveal a black crunchy residue confirming decomposition.

B. Type 2 Polymer (4)

The type 2 polymer was also investigated with a Fourier Transform Infrared Spectrophotometer. A small sample was dissolved in acetone and formed a film on an IR transparent NaCl plate. Figure 9 is the IR spectra of the sample. Peaks were indicative of a carbonate functionality, with the carbonyl peak at the proper 1800-1750 cm^{-1} range. The aromatic ether groups of the carbonate linkage is apparent as the broad peak covering the range of 1300-1100 cm^{-1}. Unfortunately, the film must have had some of the dissolving solvent, acetone and ethanol, trapped in it because of the C-H resonance at the characteristic 2990 cm^{-1} mark. The acetone would also show up in the carbonyl peak along with the carbonate linkage, explaining the large size of that absorption. Heating the salt plate under vacuum would remove the leftover acetone and its effects.

The DSC scan of the polymer, Figure 10, indicates a tentative Tg of 42° C. This is uncharacteristically low for an aromatic polycarbonate. One possible explanation is the solvent that was found by the IR, is still present, lowering the Tg. Also if the sample had a low molecular weight the Tg would lower. The solvent was thought to be removed by heating the sample to 140° C for 1 hour on a watchglass, in which the polymer had bubbles on the surface, indicating the evaporating solvents, and that it was past the Tg temperature.
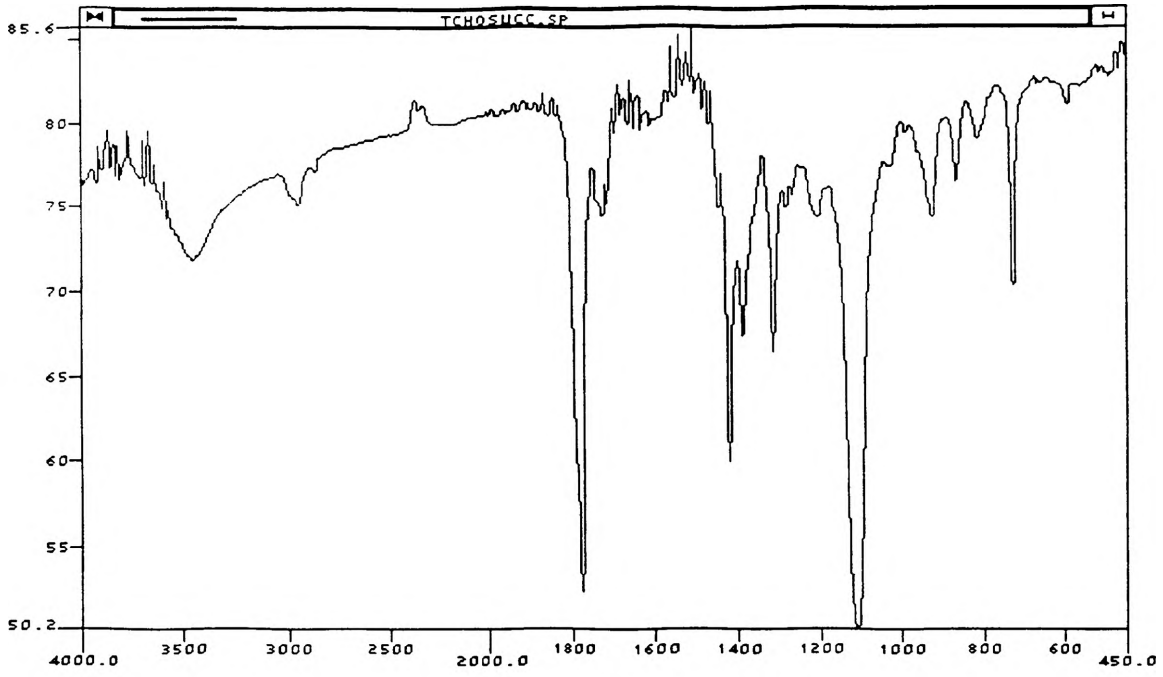
Figure 5

Figure 7   76

Figure 6

ADIPIC

WT: 5.00 mg

SCAN RATE: 10.00 deg/min

MAX: 371.05

PEAK FROM: 361.1
        TO: 385.84
ONSET: 361.1
CAL/GRAM: 22.8

ENDO>

MCAL/SEC

TEMPERATURE (C)

DSC

Figure 8   77

Figure 9

PETCPK

WT: 0.00 mg

SCAN RATE: 20.00 deg/min

T/G FROM: 30.59
TO: 428.07
ONSET: 397.25
MIDPOINT: 377.93
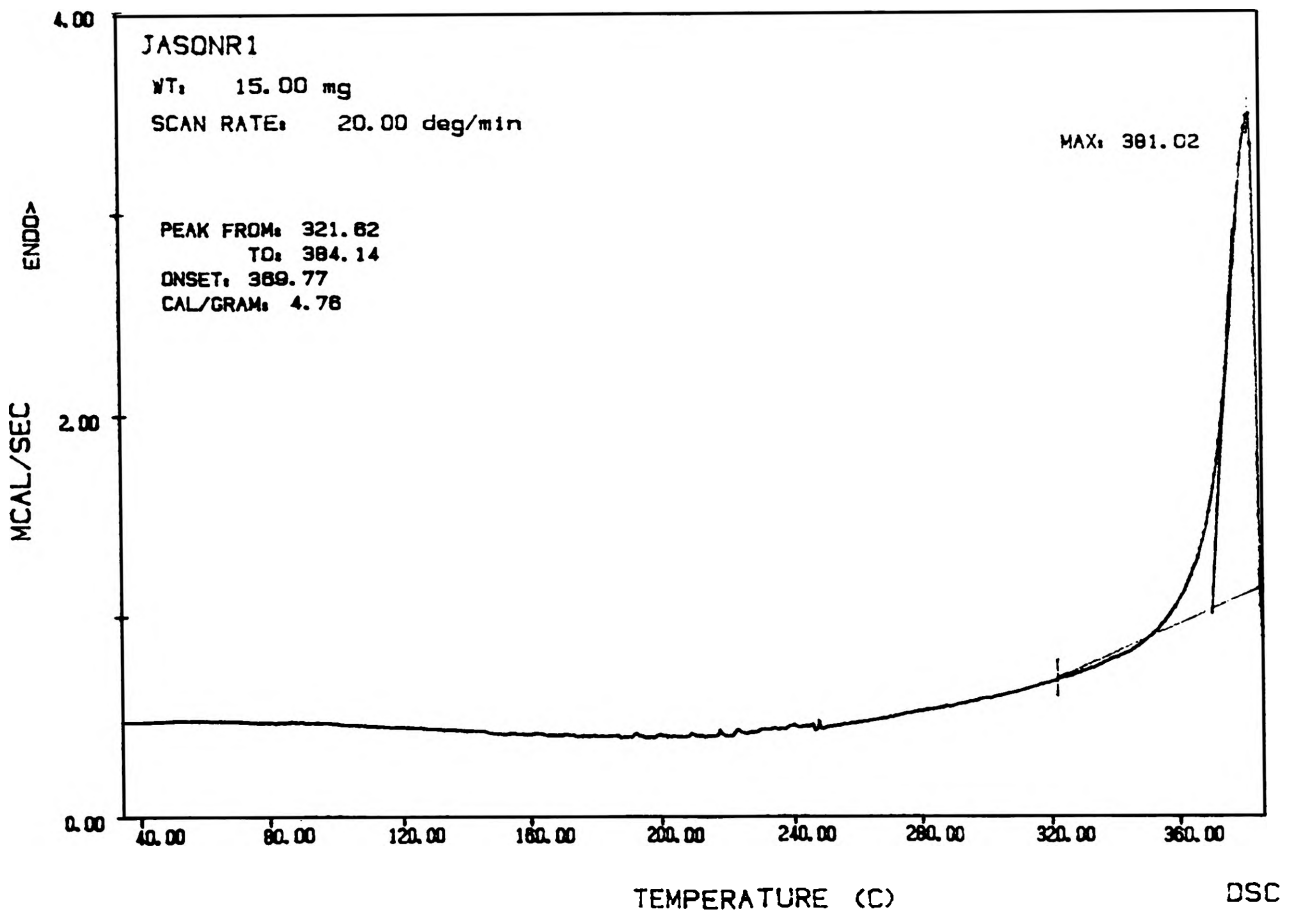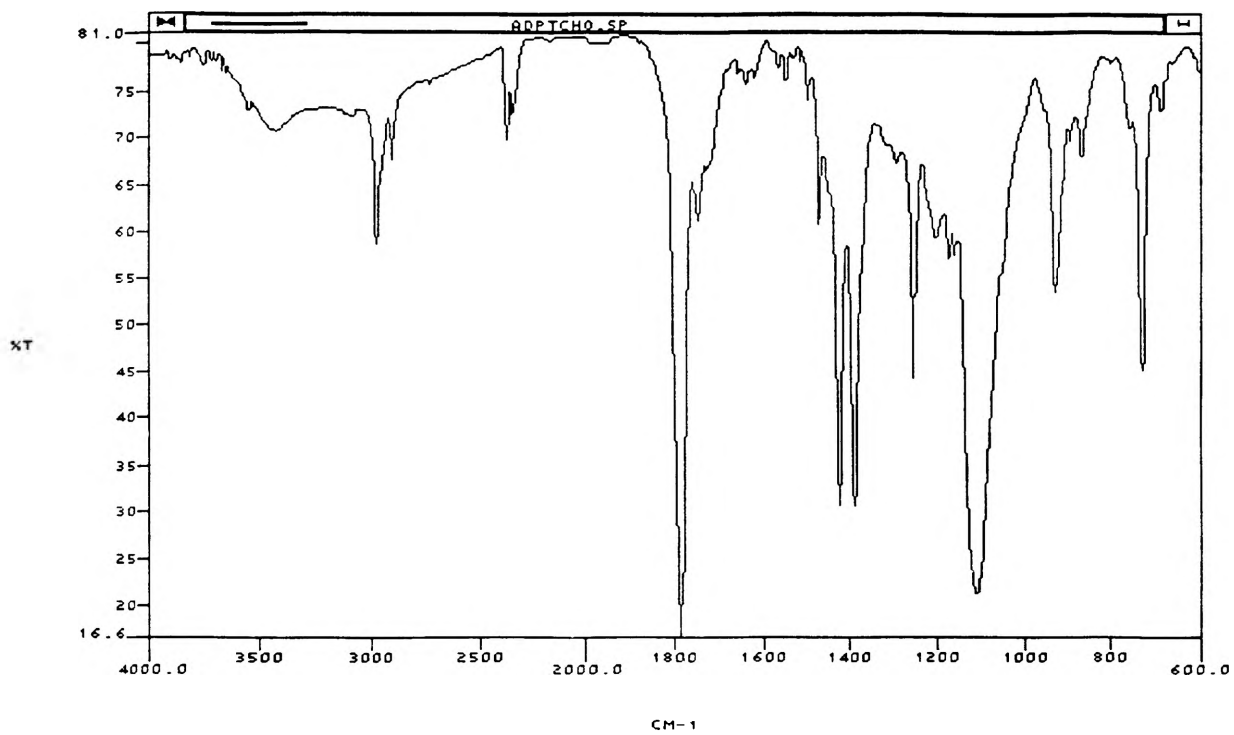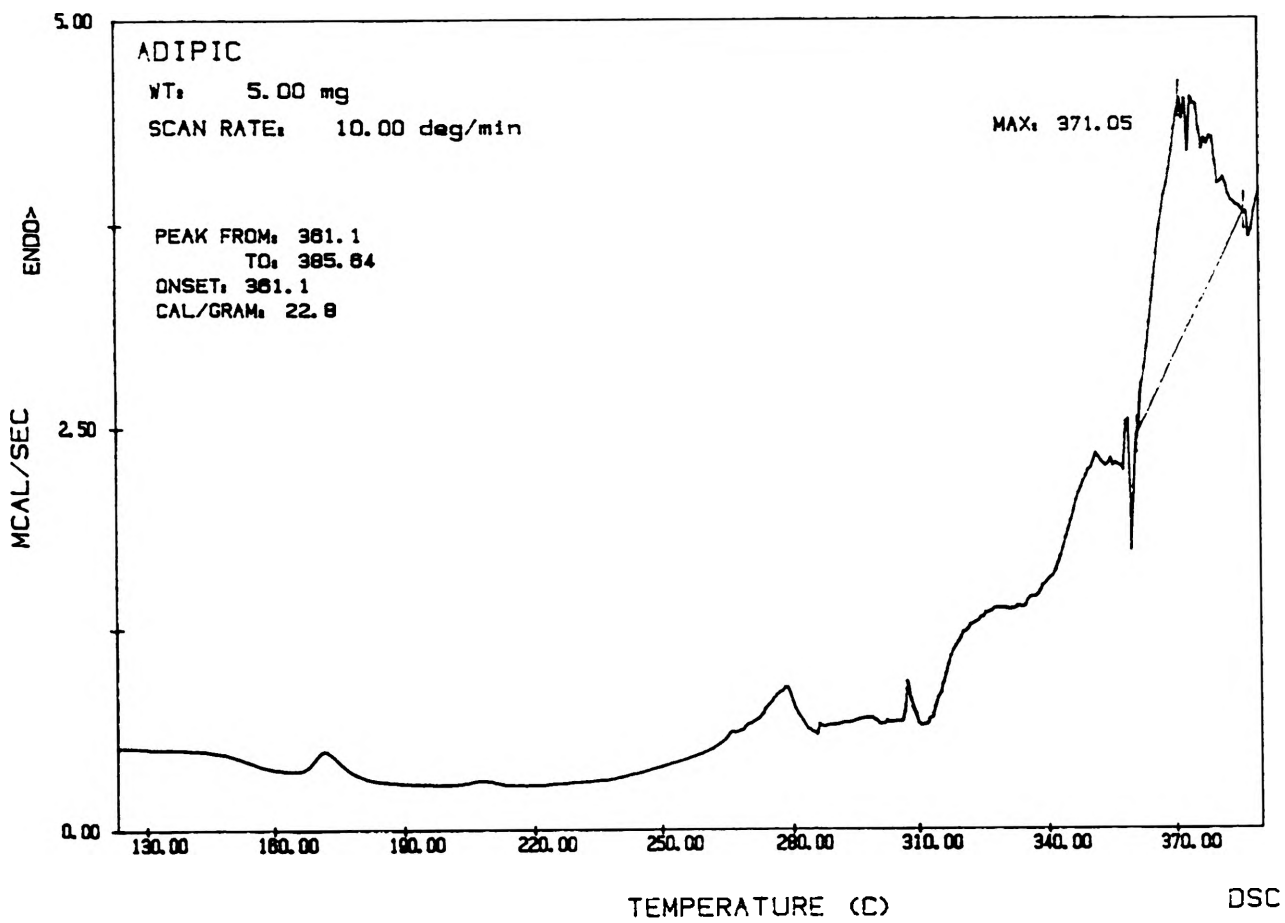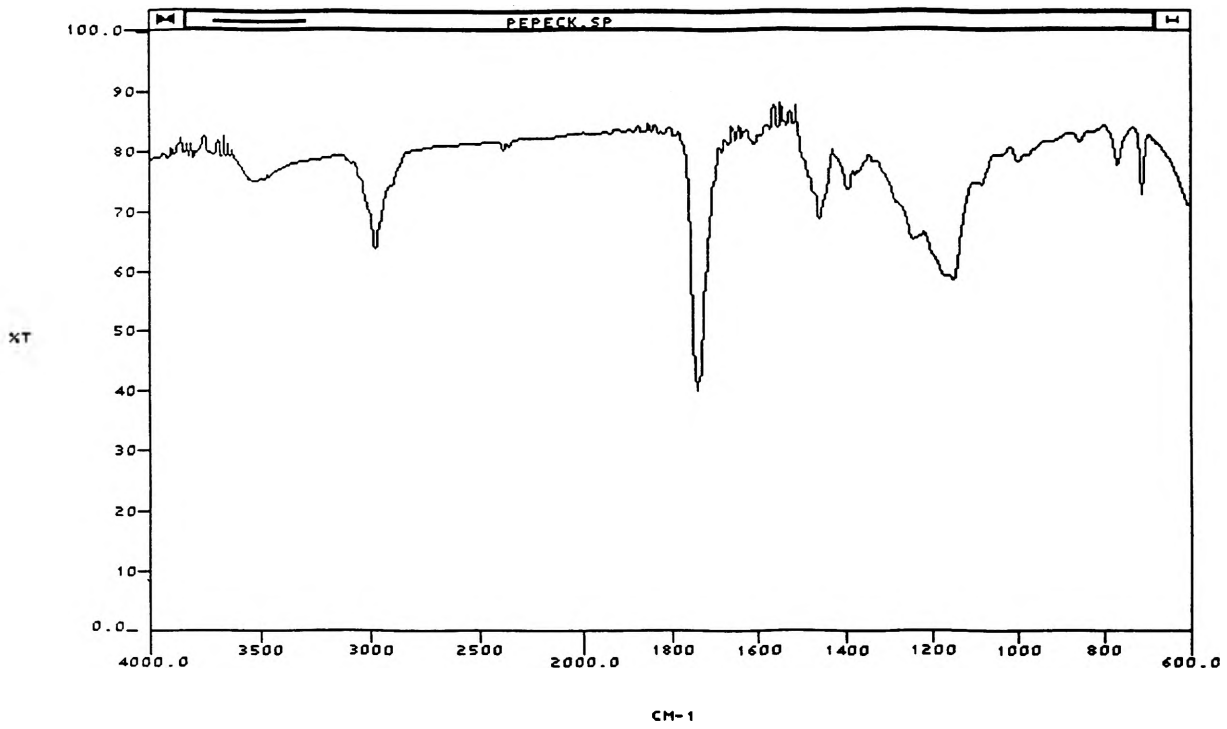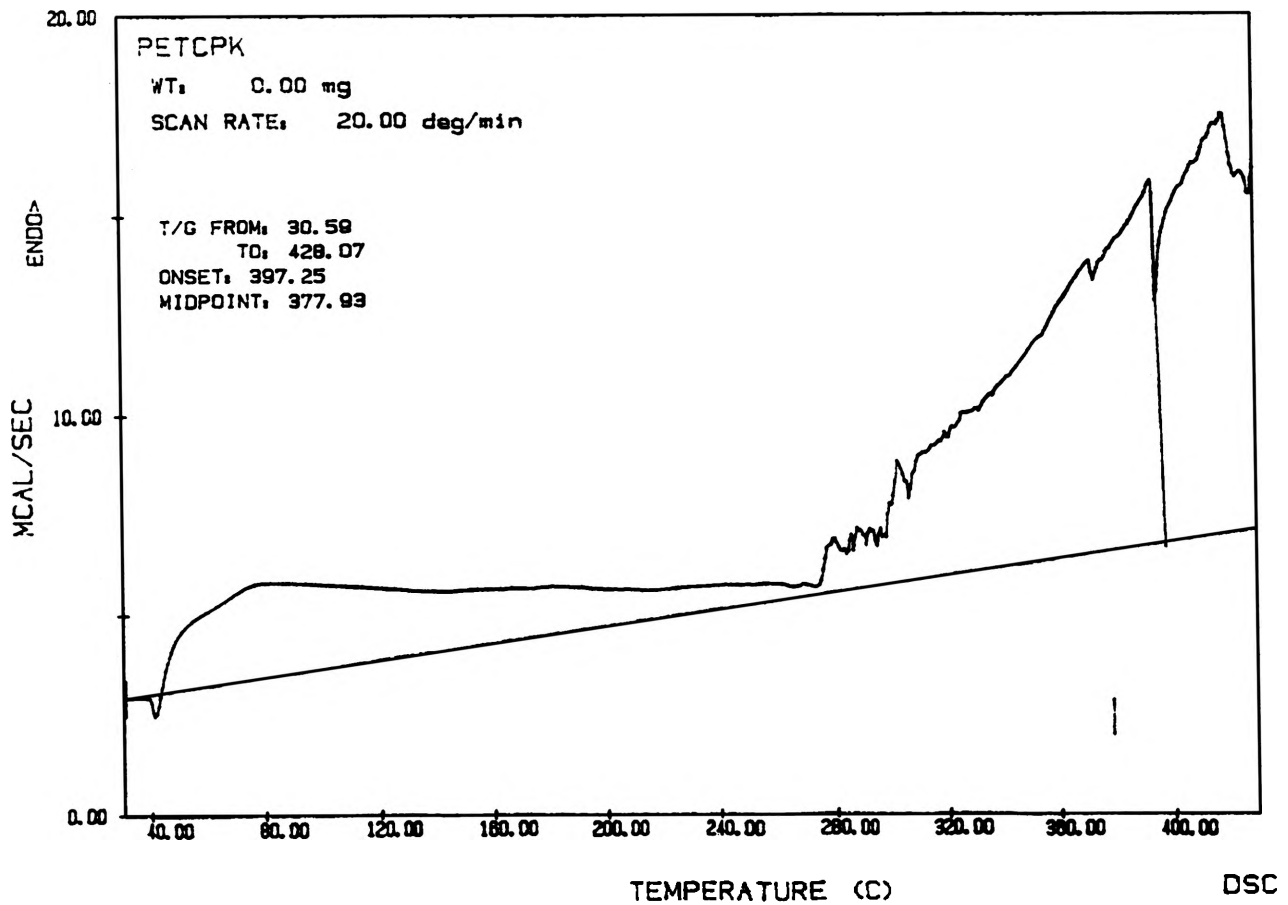
TEMPERATURE (C)   DSC

Figure 10   78

The DSC graph shows a possible Tm at 280° C, but at this point the sample is either degrading or the baseline is shifting due to poor calibration of the instrument at higher temperatures. Consequently, the transitions reported are skeptical at best.

Since the type 2 polymer did not have solubility problems like the type 1's, NMR and GPC studies are currently under investigation.

DISCUSSION OF FUTURE WORK:

As with most aromatic containing polymers, especially halogenated ones, one major concern is brittleness. To compensate for this problem the co-monomer is usually a "plasticizer", a chemical that adds flexibility and solubility to the polymer. In type 1 polymers, the attempt to add flexibility is the chain length separating the stiff aromatic ring. Type 1-1 has a very short chain between the rings, four carbons, and consequently is very stiff and difficult to dissolve. Although the 1-2 polymer has a lengthened plasticizer, 6 carbons, there was no noticeable effect. Type 1-3 used the camphoric acid monomer derivative which should have imparted a three-dimensional character. Which in theory would have reduced chain-to-chain interaction and given low Tg, soluble polymer. However, monomer impurities did not permit the reaction to correctly proceed. Consequently, a longer chain separating the aromatics or some type of functionality on the plasticizer is needed. Currently proposed monomers are 12-18 carbon chain acid chlorides.

The type 2 polymer is still under structural investigation by NMR and GPC. This polymer exhibited good characteristics in temperature resistance, transparency, and chemical resistance.

Other studies on this system appear promising. Diethyl carbonate is being investigated as a potential substitute for the more dangerous triphosgene, but the few attempts at its incorporation have not proved fruitful. Further investigation is necessary before it can be ruled out.

CONCLUSION:

Using the base monomer of tetrachlorohydroquinone (TCHQ), chosen on the basis of basic polymer principals, three different polymers were developed. Each of these polymers achieved different aspects of the desired goal of a new high temperature, transparent, chemically resistant polymer.

Characterization of the type 1 polymers indicated the correct functional linkage of a polyester. The temperature resistance of these polyesters is uncharacteristically high with the 1-1 and 1-2 polymers possessing excellent temperature resistance in excess of 350° C. The type 1 polymers are so chemically resistant, processing them into transparent films is difficult.

The major success of the project was the synthesis of polymer 2-1. Using interfacial polymerization techniques, an aromatic polycarbonate was formed from the monomers of triphosgene and TCHQ. The polymer is transparent with the exception of removable impurities. It has a good Tg and withstood up to 300° C of heat. The 2-1 polymer also demonstrates good

79

chemical resistance.

This project is considered a success because the developed polymers show the attainment of the desired goals. The TCHQ polycarbonate shows excellent characteristics of a polymer that very well could be a commercially important polymer. The reaction's fast rate and room temperature reaction also make the system industrially viable. Currently, this polymer could be used as a composite substrate. With further investigation, this polymer system could be adapted for application in windshields and high speed air transports.

ACKNOWLEDGEMENTS:

REFERENCES:

1.   Transparent Composites of Poly(chlorotrifluoroethylene) Reinforced with Fluorophosphate Glass Fibers, W. L. Dechent, D. E. Day, J. O. Stoffer, PMSE, Vol 68, 26 (1993)

2.   Preparative Polymerization for Polycarbonates: A Simultaneous Reaction-Precipitation Technique, S. K. Sikdar, J. App. Poly. Sci., Vol 28, 587-593 (1983)

3.   Interfacial Polycarbonate Reactions. Defining the Critical Process Parameters, Jen-Tau Gu and Chun-Shan Wang, J. App. Poly. Sci., Vol 44, 849-857, (1992)

4.   Fundamental Principals of Polymeric Materials, S. L. Rosen, J. Wiley and Sons, 2nd e (1993)

5.   Polymer Chemistry, an Introduction, M. P. Stevens, Oxford Univ. Press, 2nd ed. (1990)

6.   Fundamentals of Organic Chemistry, T. W. Gram Solomons, J. Wiley and Sons, 3rd e (1990)

E-mail and Writing

Karlynn D. Herman, English Dept.

ABSTRACT

This project was conducted to determine the effects of e-mail, used in class assignments, on student writing. Essays from two English 20 classes, one using e-mail and one not using e-mail, were examined at intervals over the course of one semester and graded holistically to determine improvement in student writing. These essays were also graded by computer to objectively measure writing improvement using the Grammatik program. Surveys were administered to the two classes at the beginning and end of the semester to gauge the students' confidence with and interest in writing. These same surveys were also administered to an upper-level, writing-intensive economics class at the beginning and end of the semester. Results showed that students' writing improved markedly over the course of the semester in the class using e-mail compared to the class not using e-mail. The students using e-mail were also more confident in their ability to write at the end of the semester than the students who did not use e-mail.

EXPERIMENT SETUP

This project was designed to compare the writing of students in two freshman English (English 20) classes over the course of one semester. In order to accomplish this, the two classes needed to be as similar as possible, thus eliminating all possible variables other than the presence or absence of e-mail in the curriculum.

The two sections finally chosen, section C and section Q, had only a few differences between them: section C was slightly larger than section Q (22 students compared to 18) and section C was a day class, while section Q was a night class. Therefore, section C met three times a week for one hour per meeting, while section Q met one time a week for three hours. Other than these differences, the classes were kept the same—they followed the same syllabus, received the same choice of essay topics for each essay, and were taught by the same professor.

Students in section C were required to obtain e-mail accounts and write e-mail responses to both in-class discussions and to each other. The class was registered on

a listserver so that their responses were delivered to all the other students in the class. These e-mail responses counted as a portion of their class grade, and ranged from simple inquiries about grammar or the effectiveness of a particular sentence or paragraph to debates over paper topics. For example, at one point in the semester the class debated back and forth about gays in the military in response to a student's decision to use that subject as the topic of one of his papers. Section Q, on the other hand, was not exposed to e-mail as a part of their class curriculum in any way.

To measure students' writing, then, three of their essays were collected over the course of the semester (Essays 2, 4, and 6). These three essays were chosen because they were evenly spaced apart--essay 2 was written about one month after the semester started, essay four about a month and a half after that (about halfway through the semester) and essay six about a month after that (a few weeks before finals). These essays were evaluated by computer using Grammatik for Word Perfect, and were also graded holistically by a group of student readers.

Surveys which measured the students' confidence in their ability to write were administered to the two English 20 classes. The same surveys were also given to a writing-intensive Economics course using e-mail within the curriculum, to see if the presence of e-mail affected students similarly in two different classes. These surveys were filled out by the students at the beginning and end of the semester to gauge the change in their feelings about their writing over the course of the semester.

RESULTS

Grammatik scores

Essays in both classes were first graded by computer, using Grammatik for Word Perfect, in an effort to remove the subjective human element from essay scoring. Readability of the essays was graded according to three different formulas, the Flesch Reading Ease score, Gunning's Fog Index, and the Flesch-Kincaid Grade Level. The first of these formulas, the Flesch Reading Ease score, was determined by the equation:

1.015 (average sentence length) + .846 (number of syllables per 100 words) = Total

206.835 - Total = Flesch Reading Ease score

(1)

This score appears as a value on a scale of 1-100, with a lower number representing a more difficult reading level. Using this scale, scores can be interpreted in the following way:

90-100 = Very Easy (4th grade reading level)
80-90 = Easy (5th grade reading level)
70-80 = Fairly Easy (6th grade reading level)
60-70 = Standard (7th-8th grade reading level)
50-60 = Fairly difficult (Early high school)
30-50 = Difficult (Late high school to college)
0-30 = Very Difficult (College level and up).

The second readability score, Gunning's Fog Index, was determined according to the following equation:

average words per sentence + number of words three syllables or more = Total

$$\text{Total} \times .4 = \text{Gunning's Fog Index}$$

(2)

In this case, a higher score is equivalent to more difficult work.

The third measure of readability was the Flesch-Kincaid Grade Level. It was determined using this formula:

[.39 x average number of words per sentence + 11.8 x average number of syllables per word] - 15.59 = Flesch-Kincaid Grade Level.

(3)

The ideal Flesch-Kincaid Grade Level score is one that falls between 6th and 10th grade.

Because all three of these formulas are based on ratios that measure sentence length and syllables per word, they evaluate only a small portion of the elements that constitute effective writing. All three formulas ignore such factors as audience, complexity of subject matter, syntax, and clarity. Their ideal is not a first year college level, but rather a junior high level. Consequently, the results of their evaluations were spotty and inconsistent, in some cases showing greater overall improvement in section C and, in other cases, showing more improvement in section Q. For this reason, their results proved of little use in the project's comparison.

Holistic scores

Holistic scoring was performed by a group of student volunteer readers, primarily English majors. Names were removed from the essays, and they were printed in identical fonts with the same spacing and formatting cues in each essay. Readers

were paired up and the group read sample essays comparable to the English 20 students' essays. In this way, they learned general criteria for grading and were "calibrated" to score in a similar manner. They then were given a group of twelve student essays—essays 2, 4, and 6 from four different students. This procedure ensured that the same group of readers evaluated all three student essays using the same criteria. Readers were asked to read through each essay only once and then to give it a score from 1 (low) to 6 (high). This score was based on content and clarity of writing and, to a very small degree, on grammar and mechanics. Each essay was read twice (once by each member of the pair), and if their scores differed by more than one number, the essay was given to a third reader for scoring.
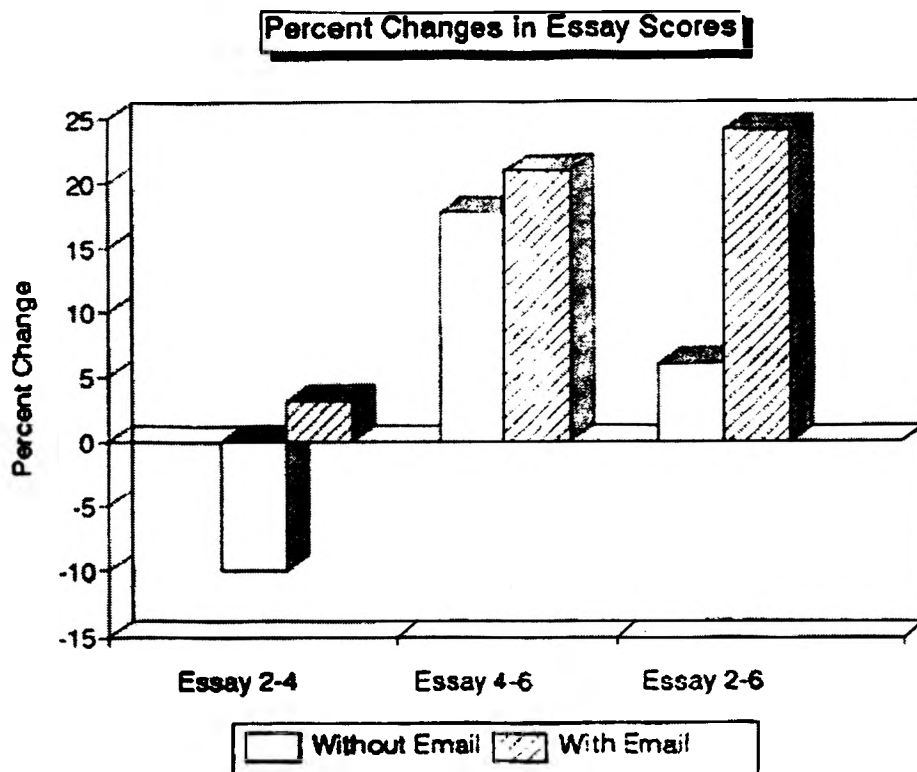
Figure 1. Percent Changes in Essay Scores

Holistic scoring of students' essays showed a considerable difference between the writing improvement of section C and section Q (see figure 1). For section C, the mean between the scores of essay 2 and 4 increased from 3.416 to 3.524, while in section Q the mean was reduced from 4.167 to 3.750. Between essays 4 and 6, section C's mean increased from 3.524 to 4.239, while section Q's mean score rose from 3.750 to 4.417. Table I displays the mean scores and standard deviations for essays 2, 4, and 6 in sections C and Q. From this data, improvement in section C's scores compared to those of section Q becomes more obvious.

TABLE I. MEANS AND STANDARD DEVIATIONS FOR ESSAY SCORES IN ENGLISH 20 SECTIONS C AND Q

| | SECTION C | | SECTION Q | |
	Mean	Standard deviation	Mean	Standard deviation
Essay 2	3.4164	.81566	4.1667	1.36626
Essay 4	3.5236	.94245	3.7500	.61237
Essay 6	4.2386	1.04148	4.4167	.49160

A Chi square test (a statistical test used to show the relationship between a set of factors which could affect one another) was performed on the improvement in essay scores between the two classes. Results of this test showed the correlation between e-mail and writing to be significant, meaning that improvement in writing was directly linked to the presence of e-mail.

Survey Index

Surveys were administered to both classes at the beginning and end of the semester. Students were asked five questions regarding their enjoyment of and confidence with writing. Because the surveys had to be administered with teacher evaluations, they were left anonymous, and only an overall class evaluation can be made regarding their results.

An index of "Comfort with Writing" ratings was prepared comparing the English 20 class using e-mail (section C), the Economics class using e-mail, and the English 20 class not using e-mail (section Q). This index was determined by dividing the mean response value for survey two by the mean response value for survey one, and then multiplying by 100. The results of this index are shown in Figure 2.

Interestingly enough, for **question 1, "How much do you enjoy writing?,"** the class not using e-mail improved more than the classes using e-mail. Perhaps section Q's increased improvement in writing enjoyment over section C was due to the fact that section C did more writing (e-mail assignments plus essays), and thus had more time to "get tired of writing" than did section Q.

For **question 2, "How comfortable do you feel writing?,"** the score of English 20, section C improved over that of section Q. However, the economics class felt less comfortable writing at the end of the semester; probably resulting in part from the fact that the economics class, while writing intensive, did not center around writing instruction.

Question 3 was "How confident do you feel in your ability to find good word ideas and perceptions?" Both of the classes using e-mail showed a much greater improvement in this area than the class without e-mail; the economics class improved by a slight margin over the English class. The improvement of the e-mail classes indicates that work with e-mail allows students to feel more confident in their ability to analyze and explain concepts, perhaps because of the consistent feedback they receive from their peers.

Question 4, "How confident do you feel in your ability to generate lots of words fairly quickly and freely on a topic of interest to you?," showed almost no difference in improvement between English 20 sections C and Q. The economics class showed improvement over both classes. These results are explainable because the students associated the words "fairly quickly and freely" with the process of freewriting. All of section C's e-mail assignments were geared toward producing reflective responses, more in the essay style than the freewriting style. Students had to think about their writing and prepare it before sending it off. Since both sections did the same amount of freewriting in class, then, it would make sense that their confidence in this area would improve equally. The economics class, on the other hand, was not given assignments over e-mail which would be evaluated as a part of their class grade. Their primary use of e-mail was to pose questions about concepts or assignments to the professor or to classmates. Thus, their e-mail experience would be closer to freewriting, and would bring about their improvement in scores for this particular question.
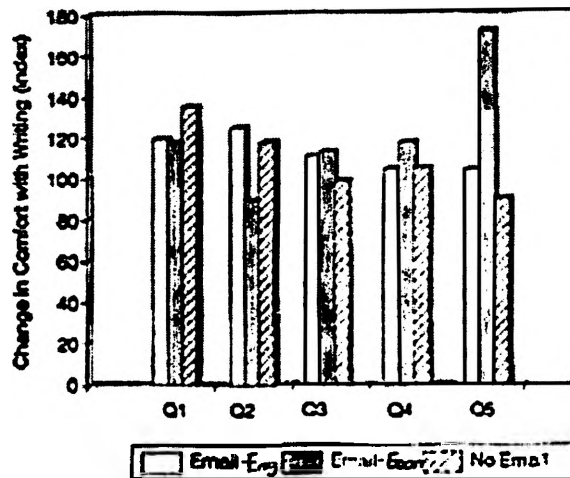
Question 1: How much do you enjoy writing?
Question 2: How comfortable do you feel writing?
Question 3: How confident do you feel in your ability to find good word ideas and perceptions?
Question 4: How confident do you feel in your ability to generate lots of words fairly quickly and freely on a topic of interest to you?
Question 5: How confident do you feel in your ability to generate lots of words fairly quickly and freely on a topic not of interest to you (perhaps an assigned topic)?

Figure 2. Index of "Comfort With Writing" ratings

Question 5 was "How confident do you feel in your ability to generate lots of words fairly quickly and freely on a topic not of interest to you (perhaps an assigned topic)?" The response of the economics class to this question showed marked improvement over both of the English 20 classes--probably because their writing experience in class involved primarily assigned topics and very few personally chosen topics. Section C improved more than section Q, again by a fairly large margin. This is also probably a reflection of the fact that the e-mail responses were over assigned topics, and thus section C was exposed more to this kind of writing than section Q.

Survey Correlation Analysis

Two additional questions were added to the surveys for section C of the English 20 class to judge their confidence with e-mail at the beginning and end of the semester. These two questions were:

> •How comfortable do you feel using e-mail to send personal messages to friends and professors?
> •How comfortable do you feel using e-mail to send messages which the whole class will read?

The same questions were added to the survey administered to the economics class, only the first question was broken up into "How comfortable do you feel using e-mail to send personal messages to friends?" and "How comfortable do you feel using e-mail to send messages to professors?," since the class was not registered on a listserver, and thus their e-mail responses were not sent to both peers and professors simultaneously.

A correlation analysis was then run between all of the questions in the surveys, to see how well the responses correlated with one another. In this analysis, correlation values range between +1 and -1. A value of +1 signifies perfect correlation between the two responses (if the value of one goes up, the value of the other goes up by exactly the same amount). A value of -1 shows perfect opposition between the two responses (if the value of one goes up, the value of the other will go down by exactly the same amount). Table 2 shows correlation test values for the surveys in all three classes.

Most questions in the first survey given to section C showed almost perfect correlation, with values ranging between .82 and .94. The second survey showed similar results, with correlation values ranging between .80 and .97. In section Q, the questions were also in almost perfect correlation, with values ranging from .84 to .94 in the first survey, and from .70 to .94 in the second survey. These close positive correlations indicate that, as students become more confident in one area of their writing, they will become more confident in other areas of their writing as

well. It also indicates that (for section C) student confidence with writing improves as their confidence using e-mail improves.

In the economics class, the first survey again produced a high correlation between all the questions, with values ranging from .80 to .95. However, in the second survey, correlation values changed drastically, in several cases becoming negative values. This change, while apparent everywhere, was most dramatic in the questions dealing with confidence in generating words freely on topics of interest or topics not of interest to the student. An explanation for the inconsistent correlation results in the economics class may lie in the focus of the professor on her students' writing. She taught students to write as concisely as possible, staying strictly to their assigned topic, and keeping responses below one page in length. This focus, while valid, does not lend to "generating words freely"-- instead, students must consider carefully what they write through each step of the writing process. The difference in focus of the two professors was thus reflected quite dramatically through the students' survey responses.

TABLE II. RESULTS OF CORRELATION ANALYSIS
*Each number in these tables is a correlation value between the question number of its row and column. For example, a number (like .900) in column 1, row 2 is a value for the correlation between question one and question two.

Section C--Survey 1

	1	2	3	4	5	6
2	.918	*				
3	.882	.889	*			
4	.900	.851	.866	*		
5	.856	.888	.864	.827	*	
6	.928	.924	.899	.907	.945	*
7	.889	.904	.822	.908	.885	.901

Section C--Survey 2

	1	2	3	4	5	6
2	.922	*				
3	.810	.769	*			
4	.900	.831	.852	*		
5	.807	.802	.973	.848	*	
6	.811	.765	.941	.894	.940	*
7	.891	.882	.883	.956	.885	.923

Section Q--Survey 1

	1	2	3	4
2	.947	*		
3	.928	.889	*	
4	.870	.904	.852	*
5	.911	.910	.700	.859

Section Q--Survey 2

	1	2	3	4
2	.925	*		
3	.844	.942	*	
4	.924	.905	.852	*
5	.864	.911	.701	.859

Economics--Survey 1

	1	2	3	4	5	6	7
2	.810	*					
3	.908	.877	*				
4	.858	.872	.861	*			
5	.834	.800	.873	.818	*		
6	.888	.875	.900	.898	.879	*	
7	.869	.867	.881	.913	.878	.950	*
8	.903	.865	.872	.890	.872	.958	.955

Economics--Survey 2

	1	2	3	4	5	6	7
2	.475	*					
3	.055	.143	*				
4	.037	.074	.002	*			
5	.056	-.169	.020	.072	*		
6	.386	.139	.008	-.033	.070	*	
7	.405	.014	.069	-.114	.256	.410	*
8	.368	-.050	.062	.027	.306	.430	.715

ANALYSIS

This project demonstrated two important things about the use of e-mail within the classroom to enhance student writing. First, e-mail does have a significant effect on student writing. Second, the focus of the professor in the classroom also has a significant effect on how e-mail affects student writing.

The holistic scoring of student essays in two different composition classes, one using e-mail and one not using e-mail, showed that e-mail did cause student writing to

improve over the course of the semester. Probably a large part of this improvement results directly from increased written contact of students both with their professor and with their peers. Students communicating by e-mail received feedback on paper topics and ideas from the entire class, while students without e-mail were likely to get ideas and revisions only from a few select classmates or from their friends. E-mail gave students a forum outside of the classroom with which they could express their ideas and quickly get responses from 21 other classmates. This added communication also gave students exposure to new ideas and new writing styles as they read the responses of their peers to writing assignments over e-mail. In a class without e-mail, copying the responses of all the students in the class to each writing assignment throughout the semester would be time-consuming and result in an unreasonable paper load for everyone. But with e-mail, student responses are quickly and easily transmitted to everyone in the class. Thus, students receive more feedback from their peers and increased exposure to writing--both good and bad.

The differing correlation results between surveys in the English and economics classes using e-mail shows that the professor's focus on writing within the course also plays a significant role in student writing development. Students learn to feel more confident with different styles of writing depending on what they are exposed to in the classroom. The use of e-mail makes the effect of the professor on student writing and confidence even more pronounced.

In conclusion, then, it is important to note that electronic mail can be an incredible asset to students as they learn to write in the classroom. Hopefully, students who have learned to use e-mail within the classroom to augment the writing process will take these skills with them into their next writing classes, gaining even more from the availability of increased contact with other students and different ideas. Also, they may be more likely to get in touch with students and professors outside of their writing courses, benefiting from the use of e-mail not just in writing but across their entire curriculum. However, instructors play a large role in the way e-mail affects their students, and they should be aware of this when planning an e-mail based curriculum for their classrooms.

ACKNOWLEDGMENTS

THE FEASIBILITY OF USING PIEZOELECTRIC FLAP ACTUATION
IN THE ACTIVE CONTROL OF FLUTTER

Aaron Laws
Department of Aerospace Engineering

INTRODUCTION

Wing flutter is one of the most important and dangerous phenomenon faced by aircraft structural design engineers. Flutter is a self exciting aeroelastic phenomenon in which portions of an aircraft structure begin to oscillate with exponentially growing amplitudes, produced by the changing aerodynamic forces and moments brought about by the deformation of the structure. There exists a characteristic flight speed, known as the flutter speed, where the structure exhibits sustained harmonic motion, ie. zero damping. Below this velocity, the vibration of the structure due to a perturbation will decrease exponentially, while above this velocity, the vibration will increase exponentially, eventually leading to catastrophic failure.

One method in controlling the effects of flutter is to use control surfaces, such as trailing edge flaps, to provide forces and moments which oppose the motion of the oscillating structure. The ability to provide a suitable flap control system is a major issue in the study of active flutter control. This investigation analyzes the feasibility of using a piezoelectric ceramic to provide the control power in a flap actuation system. There are numerous reasons piezoelectric ceramics would be effective in a flutter control system. The most significant is the fact that piezoelectric ceramics have very quick response times, greatly simplifying the transfer of the control law signals to the actual control surface. Also, the piezoelectric ceramic is a solid state mechanism, minimizing the number of moving parts and increasing the efficiency of the flap control system.

Two key parameters are necessary to perform a flutter analysis and determine the maximum deflection and force needed from the piezoelectric ceramic. The first parameter is the flutter velocity, Vf, which can be obtained by performing an eigenvalue analysis and finding the flight velocity at which one mode of vibration exhibits sustained harmonic motion. Once the flutter velocity has been calculated, a frequency response of wing to a flap actuator input of $1°$ at .95Vf will give the force necessary to sustain the motion of the system just below the flutter speed. From piezoelectric theory, it will then be determined whether an appropriately sized piezoceramic can produce the deflections and forces necessary to produce the above results. Finally, results from a concurrent study on active flutter control will be used to demonstrate the effects of active flutter control on a wing experiencing actual flutter.

The following analysis was performed using properties from an existing wind tunnel model designed and built for flutter analysis. All values for mass, spring stiffnesses, etc. were taken directly from this model, as well as the important dimensions of the model and the aerodynamic coefficients are listed in the Nomenclature section. The piezoelectric ceramic used in this analysis was Lead Zirconium Titanate (PZT). The values describing the properties of PZT are also given in the Nomenclature section.

MODEL DEFINITION

The first step in any analysis involving the vibration of a structure is to determine the equations of motion. A simplified schematic used in this evaluation is sketched in Figure 1. This system possesses 3 degrees of freedom: x (plunge),
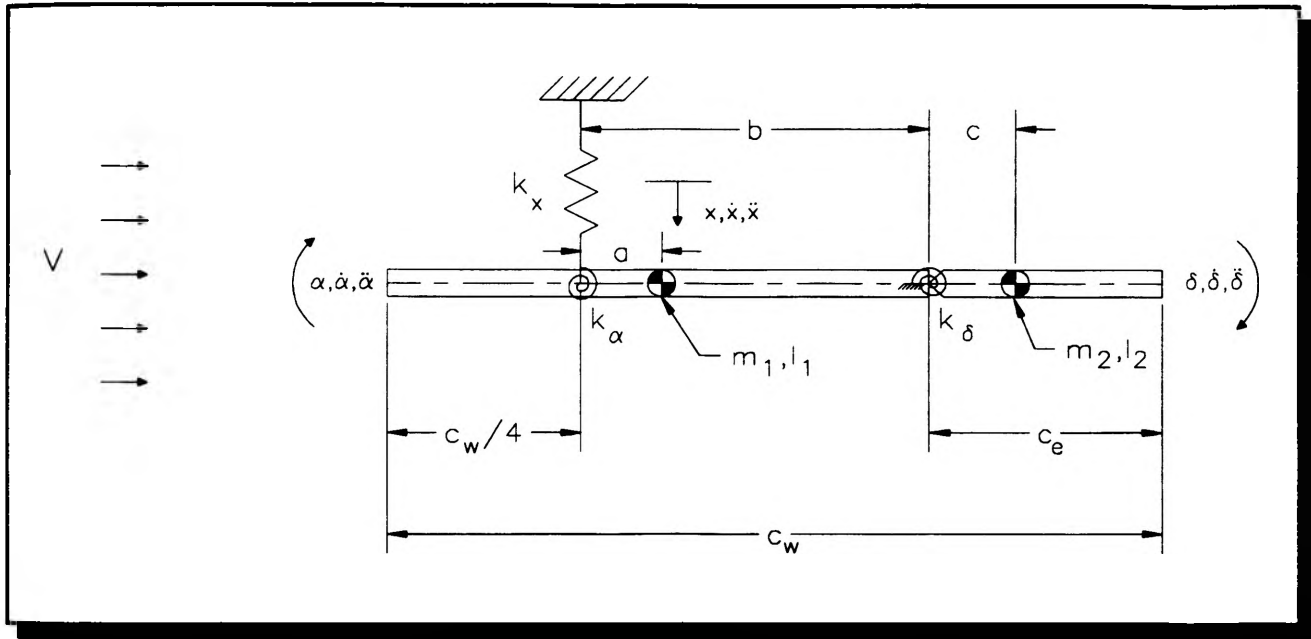
Figure 1
Schematic of wind tunnel model

α (pitch), and δ (flap rotation). A linear spring, k_x, constrains the motion in plunge, and two torsional springs, k_α and k_δ constrain the motion in pitch and flap rotation, respectively. The mass and mass moment of inertia of the main wing body are denoted m_1 and I_1, respectively; the mass and the mass moment of inertia of the flap is denoted m_2 and I_2, respectively.

The flap is actuated through the deflection of a set of piezoelectric ceramics connected to the flap hinge by a steal wire. This setup is shown in Figure 2. Since the steel wire has a finite stiffness and the flap possesses a finite mass moment of inertia, there will be a difference between the actual flap deflection, δ, and the "commanded" or "static" flap deflection, δ_c. Using Newton's Second Law, including the effects of aerodynamics, the equations of motion for this system are given below:
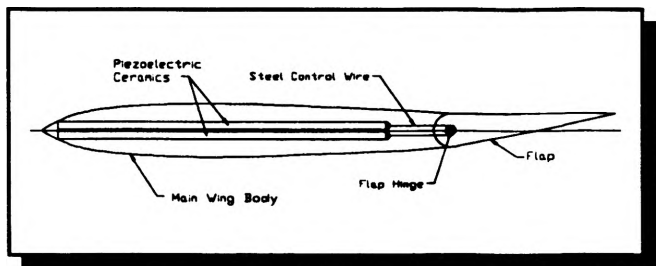
Figure 2 Actuation Setup

93

$$[M]\ddot{X} + [C]\dot{X} + [K]X = F(t) \qquad (1)$$

where

$$X(t) = \begin{Bmatrix} x(t) \\ \alpha(t) \\ \delta(t) \end{Bmatrix} , \quad [M] = \begin{bmatrix} (m_1+m_2) & (m_1a+m_2(b+c)) & (m_2c) \\ (m_1a+m_2(b+c)) & (I_1+m_1a^2+I_2+m_2(b+c)^2) & (I_2+m_2c(b+c)) \\ (m_2c) & (I_2+m_2c(b+c)) & (I_2+m_2c^2) \end{bmatrix} ,$$

$$[C] = \begin{bmatrix} \left(\dfrac{q_\infty S_1 C_{L_\alpha}}{V}+2\zeta\sqrt{k_x m_1}\right) & 0 & 0 \\ 0 & 2\zeta\sqrt{k_\alpha I_1} & 0 \\ \dfrac{q_\infty S_2 c_e C_{H_\alpha}}{V} & 0 & 2\zeta\sqrt{k_\delta I_2} \end{bmatrix} , \quad [K] = \begin{bmatrix} k_x & q_\infty S_1 C_{L_\alpha} & q_\infty S_1 C_{L_\delta} \\ 0 & k_\alpha & -q_\infty S_1 c_w C_{M_\delta} \\ 0 & -q_\infty S_2 c_e C_{H_\alpha} & k_\delta-q_\infty S_2 c_e C_{H_\delta} \end{bmatrix} ,$$

and

$$F(t) = \begin{Bmatrix} 0 \\ 0 \\ k_\delta\delta_c(t) \end{Bmatrix} .$$

In order to determine the flutter speed, it is necessary to solve the homogeneous form of equation (1) for the eigenvalues of the system. The standard method for solving such a system is to assume a solution of the form

$$X(t) = \begin{Bmatrix} x_0\, e^{\lambda t} \\ \alpha_0\, e^{\lambda t} \\ \delta_0\, e^{\lambda t} \end{Bmatrix} \qquad (2)$$

where x_0, α_0, and δ_0 are the amplitudes of plunge, pitch, and flap deflection, respectively, λ is an eigenvalue of the system, and t is time. The eigenvalues are found by substituting equation (2) into equation (1), setting the determinant equal to zero, and solving the resulting characteristic equation for λ. A detailed explanation is provided in Reference 2.

In general, the eigenvalues will be complex, the real part signifying the amount of damping in a particular mode, and the imaginary part signifying the frequency of oscillation. Since the elements of the matrices contain components which are dependent on velocity, it is obvious that the eigenvalues will vary with velocity as well. Plots of the eigenvalues of this system as functions of velocity are given in Figures 3a, 3b, and 3c.

Notice in Figure 3a, the real part of the eigenvalue is initially relatively constant and negative until around 37 ft/s, where it suddenly becomes increasingly negative. Figure 3b is similar, where the real part is relatively constant and negative, but then suddenly becomes increasingly positive, and eventually crosses the zero line at 37 ft/s. This velocity corresponds to the flutter velocity, where one mode of vibration experiences sustained harmonic motion (zero damping). Also notice that the frequencies of the first and second modes (x and α) begin to coalesce. This is a common characteristic of flutter: two degrees of freedom become coupled, characterized by the merging of two frequencies, resulting in two exponentially varying oscillations with the same frequency, one exponentially growing, the other exponentially decaying. The exponentially growing oscillation eventually dominates and results in the ultimate destruction of the wing.

DETERMINATION OF ACTUATOR FORCE

In order to determine the amount of force required to control the flap near the flutter speed, the frequency response of the flap was calculated at a velocity 95% of the flutter velocity. A frequency response is a plot of the amplitude of a degree of freedom to the inputs of the forcing function, in this case the control deflection δc. The force from the piezoelectric can then be calculated using the equation

$$F_{piezo} = k_\delta (\delta_c - \delta) \tag{3}$$
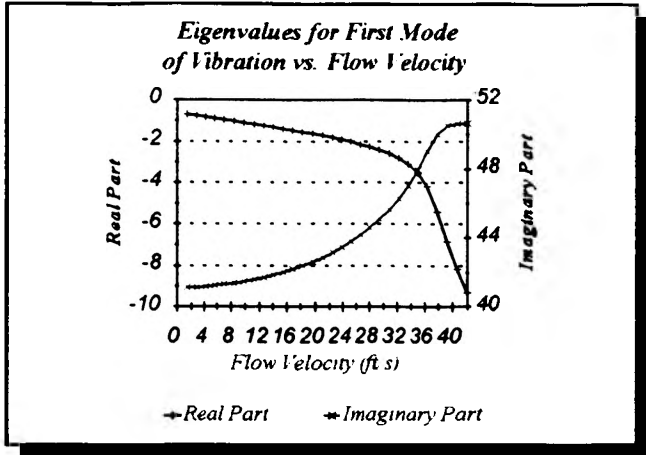
Figure 3a
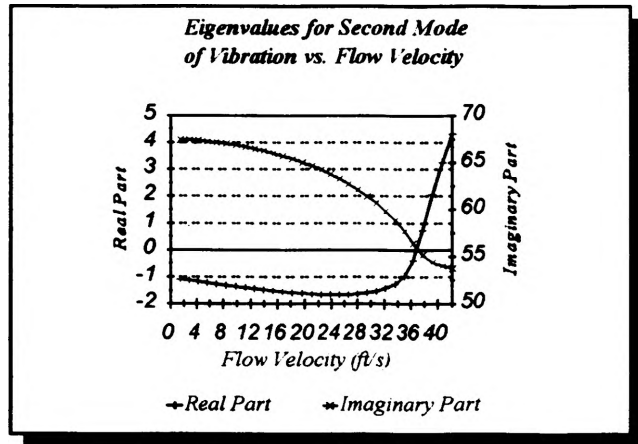
Figure 3b

Figure 3c

95
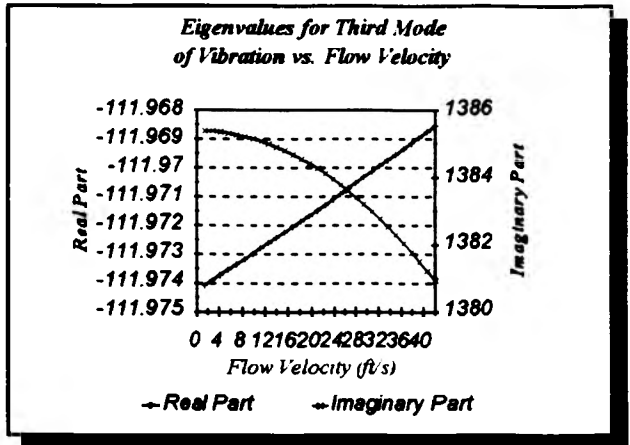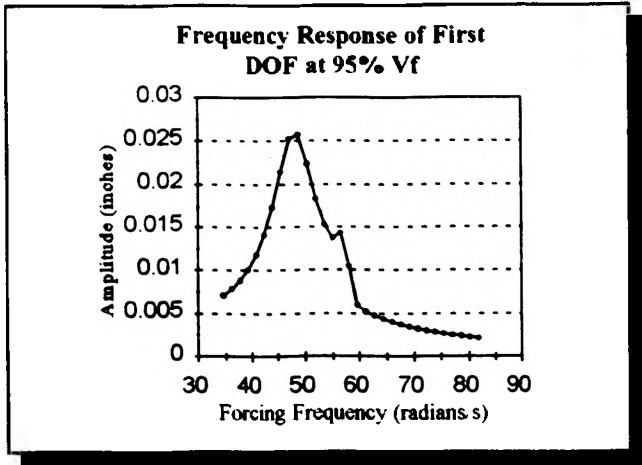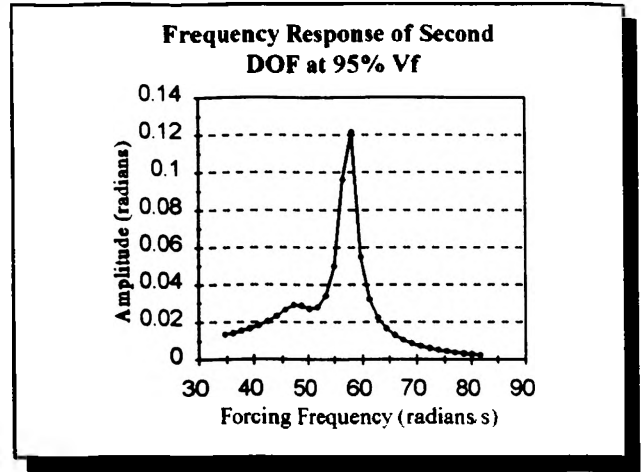
Figure 4a

Figure 4b
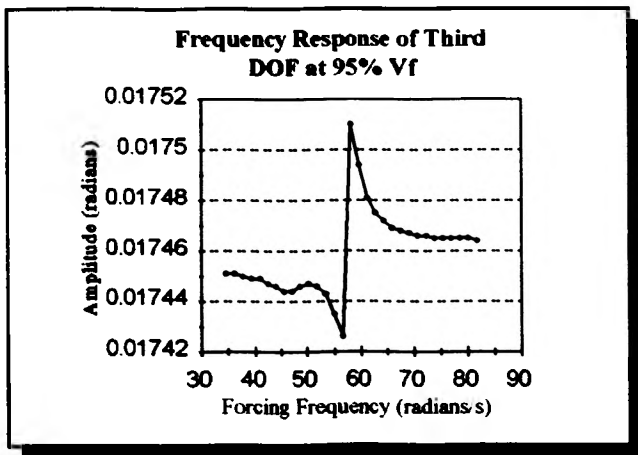
Figure 4c
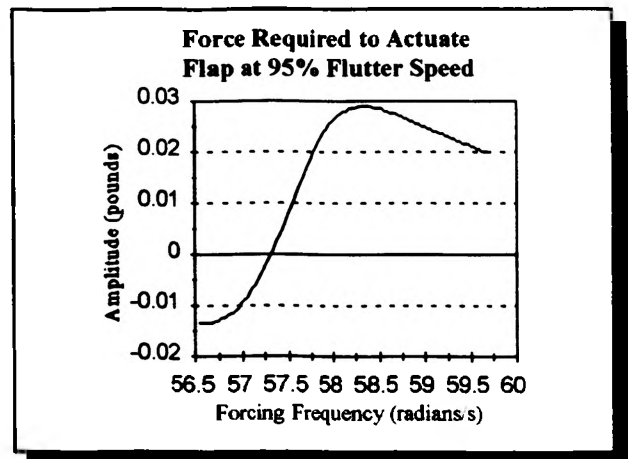
Figure 4d

Figures 4a, 4b, and 4c show the frequency response, at 95% flutter velocity, of plunge, pitch, and flap deflection due to a 1° control deflection, δ_c. Figure 4d shows the resulting force required according to equation (4).

Compared to Figures 4a and 4b, Figure 4c indicates that very small flap deflections are required to produce relatively large responses in plunge and pitch. From Figure 4d, the maximum force required per degree of flap control deflection is almost 0.03 lbf. It must now be determined whether a piezoelectric ceramic appropriately sized for the wind tunnel model is capable of providing adequate displacements and forces to duplicate these results.

DEFLECTION PROPERTIES OF PZT

Piezoelectric ceramics, due to the polarization of the crystal lattice, are able to deflect under the influence of an electric field. A typical piezoelectric specimen is shown in Figure 5. A voltage applied between the two conductive strips forms an electric field through the ceramic. The smaller the distance between the conductive strips, the higher the
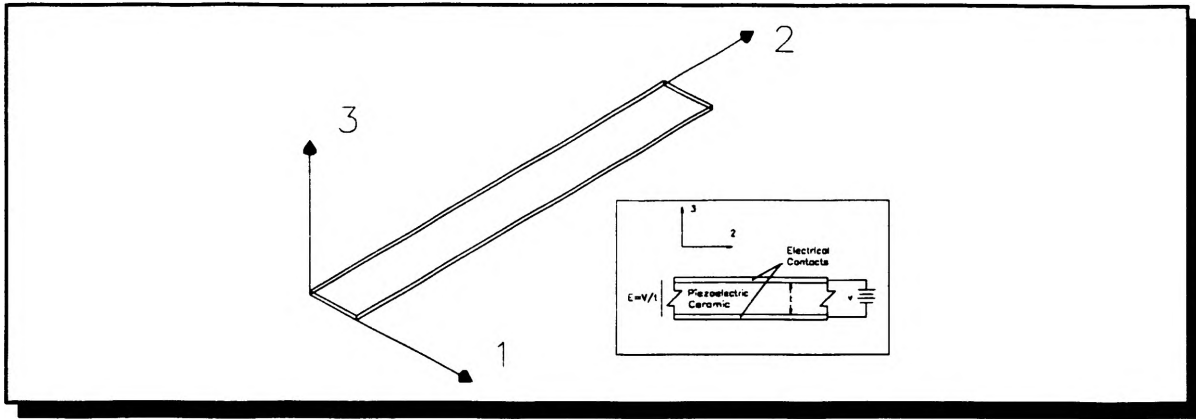
Figure 5 Typical Piezoelectric Ceramic

field for a given voltage. **Nye**[3] showed that the strain tensor, $[\epsilon]$, of a piezoelectric ceramic due to an electric field can be represented by the set of matrix equations below:

$$
[e] = \begin{bmatrix} e_{11} & e_{12} & e_{13} \\ e_{21} & e_{22} & e_{23} \\ e_{31} & e_{32} & e_{33} \end{bmatrix} = \begin{bmatrix} e_1 & \dfrac{e_6}{2} & \dfrac{e_5}{2} \\ \dfrac{e_6}{2} & e_2 & \dfrac{e_4}{2} \\ \dfrac{e_5}{2} & e_{32} & e_3 \end{bmatrix} \text{, where } \begin{Bmatrix} e_1 \\ e_2 \\ e_3 \\ e_4 \\ e_5 \\ e_6 \end{Bmatrix} = transpose \quad \begin{bmatrix} d_{11} & d_{12} & d_{13} & d_{14} & d_{15} & d_{16} \\ d_{21} & d_{22} & d_{23} & d_{24} & d_{25} & d_{26} \\ d_{31} & d_{32} & d_{33} & d_{34} & d_{35} & d_{36} \end{bmatrix} \cdot \begin{Bmatrix} E_1 \\ E_2 \\ E_3 \end{Bmatrix} \quad (4)
$$

The coefficients in the [d] matrix are known as *piezoelectric moduli*, and relate the strain to the electric field strength, $\{E\}$. The deflection in the piezoelectric ceramic can then be determined by using the equation:

$$
\begin{Bmatrix} \Delta L_1 \\ \Delta L_2 \\ \Delta L_3 \end{Bmatrix} = \begin{bmatrix} e_{11} & e_{12} & e_{13} \\ e_{21} & e_{22} & e_{23} \\ e_{31} & e_{32} & e_{33} \end{bmatrix} \begin{Bmatrix} L_1 \\ L_2 \\ L_3 \end{Bmatrix} \quad (5)
$$

where ΔL_i is the deflection in direction i, and L_i is the static length in direction i (refer to Figure 5).

It can be shown that the deflection of the piezoelectric ceramic, $\Delta L2$, is related to the command flap deflection, δc, and the radius of the flap hinge, $r\,h$, by the expression

$$
\Delta L_2 = (r_h)\,(\delta_c) \\
(\delta_c - radians) \quad (6)
$$

From this equation, using $r\,h = .125$ inch from the wind tunnel model, the piezoelectric ceramic deflection per degree of flap command deflection becomes

$$
\Delta L_2 = (.125\ inch)\left(\frac{1° \cdot \pi}{180}\right) = .00218 inch.
$$

97

Typically, the maximum strain achievable with a piezoelectric ceramic is .001 in/in, after which the polarization begins to break down. For PZT, this limiting strain will occur in the 3 direction (the direction of polarization), because the electric field is applied in the '3' direction as well. Utilizing equation (4), with values for the [d] matrix corresponding to PZT, the maximum strain in the '2' direction, the direction used for actuation, was .000421 in/in. Hence, for this particular configuration, the piezoelectric ceramic would have to be approximately 5.2 inches long for each degree of command flap deflection. Although this length is rather long, it is still within the dimensions of the wing, and does not detract from it's feasibility. In fact, results from a concurrent study being conducted by I. Danda Roy and W. Eversman at UMR show that large flap deflections are not necessary to quickly and efficiently control flutter. Danda Roy and Eversman are developing an adaptive control scheme to actively control flutter through the use of trailing edge flaps. Shown in Figure 6 is the time response of the plunge degree of freedom during flutter. At t=8 seconds, the adaptive control scheme is activated, and within 6 seconds, the flutter has been eliminated. The flap control deflections were on the order of 2 degrees, demonstrating that active flutter control through the use of trailing edge flaps is extremely efficient, and within the capabilities of piezoelectric ceramics.
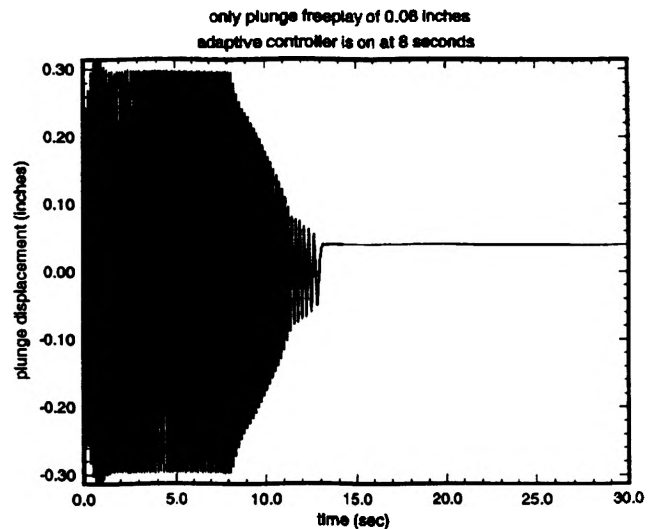
Figure 6 Effects of Active Flutter Suppression

FORCE PROPERTIES OF PZT

The next criterion which needs to be satisfied is the force requirement. The force produced by the piezoelectric ceramic can be calculated utilizing Hooke's law:

$$F_{piezo} = \sigma_2 A = E \, e_2 A \qquad (7)$$

where σ_2 is the stress in the ceramic, A is the cross sectional area, and E is the modulus of elasticity of PZT. Using Equation (7) and assuming a cross sectional area of .2 inch^2, a size suitable for mounting to the wing, the force produced in the '2' direction at the limiting strain condition becomes

$$F_{piezo} = \sigma_2 A = E\, e_2 A = (40 \times 10^6\ \frac{lbf}{inch^2})\ (.000421)\ (.2\ inch^2) = 3368\ lbf$$

The force required to deflect the PZT alone is many time greater than the force necessary to provide a command flap deflection near the flutter speed. In other words, the force from the flap is negligible compared to the force the PZT must produce to undergo an appreciable strain. Clearly the force needed to control the flap is well within the capabilities of an appropriately sized piezoelectric ceramic.

CONCLUSION

The purpose of this investigation was to determine whether using piezoelectric ceramics to control trailing edge flaps on wind tunnel flutter models is a viable option. Although this study focused on applying a piezoelectric ceramic actuator to a particular wing configuration, under a certain set of circumstances, it should be clear that the results presented in this paper can be extrapolated to a multitude of configurations. The limitations on the amount of deflection obtainable from a piezoelectric ceramic can be offset by the relatively large forces available, opening the possibility of utilizing a mechanical multiplier to increase the flap deflection, while retaining sufficient actuation force. The high response time of piezoelectric ceramics should make their use ideal in research, simplifying the transfer of signals between the active control scheme and the control surface. Piezoelectric ceramics are a very viable method of providing flap actuation for wind tunnel flutter models, and possibly for actual aircraft as well.

NOMENCLATURE

m_1 = mass of main wing body = $.345614 \times 10^{-2}$ slugs

m_2 = mass of flap = $.066227 \times 10^{-3}$ slugs

I_1 = mass moment of inertia of main wing body = 141.7971×10^{-6} slug ft^2

I_2 = mass moment of inertia of flap = 20.3546×10^{-6} slug ft^2

k_x = spring constant in plunge = 77.99468 lb/ft

k_α = spring constant in pitch = 2.15601 ft·lb/rad

k_δ = spring constant in flap deflection = 493.8073 ft·lb/rad

ζ = viscous damping factor = .02

c_w = wing chord length = .58333 ft

c_e = flap length = .175 ft

a = distance from elastic axis to main wing body center of gravity = 12.802×10^{-3} ft

b = distance from elastic axis to flap hinge = .2604955 ft

c = distance from flap hinge to flap center of gravity = .049071 ft

S_1 = wing planform area = 1.167 ft^2

S_2 = flap planform area = .35 ft^2

V = air flow velocity (variable)

q = air dynamic pressure = $1/2\, \rho V^2$

ρ = air density = .0023769 slug/ft^3 (sea level)

$C_{L\alpha}$ = change in wing lift coefficient due to pitch angle = 3.81277/rad

$C_{L\delta}$ = change in wing lift coefficient due to flap deflection angle = 2.66966/rad

$C_{H\alpha}$ = change in flap hinge moment due angle of attack = -.152899/rad

$C_{H\delta}$ = change in flap hinge moment due to flap deflection angle = -.120742/rad

$C_{M\delta}$ = change in wing moment due to flap deflection = -1.102944/rad

PZT Piezoelectric Moduli (Volts/Meter)

$d_{15} = d_{2} = .494 \times 10^{-9}$

$d_{31} = d_{32} = -.935 \times 10^{-10}$

$d_{33} = .233 \times 10^{-9}$

The rest are zero.

PZT Elastic Modulus

E = 40×10^6 psi

REFERENCES

1) Bisplinghoff, R., Ashley,H. Halfman, R, "Aeroelasticity", Addison-Wesley Publishing Co. Inc., Cambridge, Mass., 1955, pp. 527-545.

2) James, M., Smith, G., Wolford, J., Whaley, P., "Vibration of Mechanical and Structural Systems", Harper & Row, New York, 1989, pp. 270-480.

3) Nye, J., "Physical Properties of Crystals; Their Representations by Tensors and Matrices", Oxford University Press, 1985, pp. 111-125.

4) Fink, R., Principal Investigator, "USAF Stability and Control DATCOM", 1974, Chapter 6.

5) Hellwege, K., Editor, "Numerical Data and Functional Relationships in Science and Technology: Landholdt & Bornstein", Springer-Verlag, 1981, Volume 16, Group III, p. 123.

6) Kingery, W., "Introduction to Ceramics", Wiley, NY, 1976, p. 777.

ACKNOWLEDGEMENTS

DETERMINATION OF FLOW QUALITY AND BOUNDARY LAYER THICKNESS IN VARIABLE DENSITY WIND TUNNEL

By Marshall Philips
Aerospace Engineering Department

ABSTRACT

The purpose of this paper is to measure the velocity profile in the test section of the Variable Density Wind Tunnel (VDWT). The hot wire anemometer is chosen to measure the velocity profile because of its accuracy and its ability to be moved relatively close to the upper and lower surfaces of the wind tunnel. Special attention is paid to the uniformity of flow velocity in the free stream and whether it varies with position in the tunnel. The measurements were taken at two different stations, two different temperatures, and three different speeds.

Results indicate that the velocity profiles are adequate, having small boundary layers and uniform flow in the free stream, for all conditions tested with the exception of the combination of high temperatures and low velocity. At these conditions the flow in the free stream becomes nonuniform making it less desirable for use in futher experiments.

The cause of this phenomenon is unknown; however, it could be due to small temperature gradients in the flow. Nonuniform flow temperature may cause density gradients and thus a slight amount of swirling in the flow. This swirling would introduce non-axial velocity components that could become significant at low velocities. Recommendations include further testing at higher temperatures, installing anti-turbulence screens, or avoid doing experiments under the unfavorable conditions altogether.

1. INTRODUCTION

The purpose of this paper is to determine the effect of changing flow temperature and flow speed on the quality of air flow in the test section of the UMR Variable Density Wind Tunnel (VDWT). Flow quality is defined as flow that has a relatively small upper and lower boundary layer and constant velocity across the free stream. Obtaining this data is critical because it is part of a larger project that will determine the effect of flow density changes on the accuracy of various common anemometers.

The flow quality was determined by measuring the velocity profile of the flow. The velocity

103

profiles in the test section of the VDWT were measured by using a hot wire anemometer and traversing the hot wire across the height of the test section. The hot wire was chosen because of its accuracy and its ability to be moved relatively close to the upper and lower surface of the wind tunnel.

This paper will begin by first giving a quick background on the principle research project, which is determining the effect of flow density variations on various anemometers. Next a brief description of the hot wire anemometer and its function will be presented so that its advantages and disadvantages can be understood. A section will then be devoted to describing the wind tunnel test facility. The experimental setup and procedure will then be given, and finally the velocity profiles in the test section will be presented and discussed.

2. PRINCIPLE RESEARCH PROJECT AND SCOPE OF THIS EFFORT

The Rotating Vane Anemometer (RVA), Deflecting Vane Anemometer (DVA), and Electronic Vane Anemometer (EVA) are common devices used to measure air flow velocity in a variety of situations. Despite their widespread use, the accuracy of these devices may suffer from density variations in the flow field, caused by changes in temperature, pressure, and humidity. These variations may result in significant errors in the reported velocity of the device [1]. The goal of this research will be to determine which, if any, of these changes in condition will effect the anemometers, and to develop factors that will correct for these effects.

In order to achieve this goal, the devices are tested while varying one of the three variables, temperature, pressure, or humidity, and holding the remaining two variables at standard conditions. For example, temperature may be varied from 50° - 250° F, in 50° increments, while pressure and humidity are held at 14.7 psi and .0077 lbv/lba respectively. At each temperature a simple calibration experiment can be run that would compare the reported velocity of the anemometer with the actual velocity of the flow at a range of flow speeds. In this way, the effect of temperature upon the performance of the listed anemometers can be determined. Similar experiments can be performed to determine the effect of pressure and humidity.

Such devices as the RVA, and EVA are large instruments that take up a significant amount of the cross-sectional area of the test section. It is important that the flow be uniform and nonturbulent across the areas occupied by the anemometers. Any interference due to boundary layer or disturbances upstream could easily effect the results of the experiment. For this reason, the velocity profile in the test section is measured to verify that the flow is sufficiently uniform and that there is no interference from the boundary layer.

3. BACKGROUND ON THE HOT WIRE ANEMOMETER

The main advantages of the hot wire anemometer, and the reasons it was chosen for this project, are its accuracy, and its ability to be moved close to the upper and lower surfaces of the wind tunnel. The accuracy of the instrument is beneficial when measuring turbulent flow because the device responds quickly and accurately to small variations in flow velocity. This is most useful when mesuring velocities inside the boundary layer of a flow. In addition, it is beneficial because of the compact size of the device (the wire itself is only a micron in diameter) and it may be moved as close as six one hundredths of an inch to the upper and lower surfaces of the test section.

104

The principle of the hot wire anemometer is based on heat transfer. Heat transfer states that a moving fluid will extract a certain amount of heat from a cylinder depending on the relative temperatures of the fluid and the cylinder, and the velocity of the fluid. For these calculations, the thermodynamic properties of the fluid such as viscosity, thermal conductivity, and specific heat must be known. Assuming that the temperature at which the cylinder is maintained is constant, the velocity of the fluid is then a function of how much energy is put into the cylinder to maintain its temperature. For further details on the theory of the hot wire, refer to reference [1]

The output of the hot wire anemometer is in the form of the number of Volts that must be applied across the wire to maintain its temperature. Heat in the wire is actually generated by the resistance of the wire to current flowing through it. The following equation relates the Volts input to the actual velocity of the flow.

$$E^2 = A^2 + B\ V^n$$

where E is in Volts, V is the velocity of the flow in fpm (feet per minute), A is the voltage of the hot wire at zero velocity, and B and n are calibration constants that must be determined. The equation can be rewritten in the form:

$$\ln(E^2 - A^2) = \ln(B) + n\ \ln(V)$$

This represents the equation of a line with n being the slope and ln(B) being the intercept along the y-axis. The constants B, and n can now be determined from a graphical plot of the data [1]. A sample graph is shown in Figure 1. Here n and B have been determined to be .45458 and .01 respectively.

T = 70F - 18" from inlet
n = .45458 - B = .01
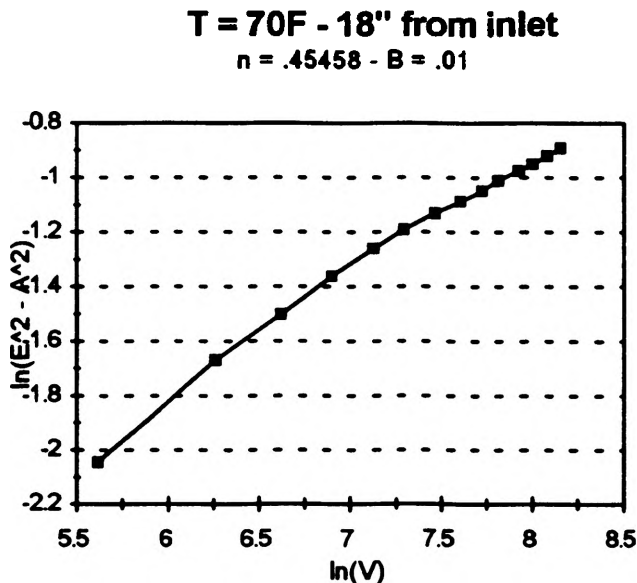
Figure 1. Calibration Curve for Hot Wire

The data for this graph was taken at 70°F, 18 in. from the entrance to the test section. Once the constants B and n have been determined, the velocity of the flow can be calculated from the output voltage. Each time new conditions are encountered, the hot wire should be calibrated and new values for B and n must be calculated.

4. TEST FACILITY

The test facility is a low speed, closed circuit, single return wind tunnel, with a velocity range of 0 - 40 ft/sec. The test section of the tunnel is 36" long and has a cross-section of 10" on a side. The side and top of the test section have been designed with a removable plexiglass window through which the test section can be viewed and equipment and sensors can be installed [2].

The tunnel is equipped with heating coils as well as a refrigeration unit, and can accommodate temperatures from 40 - 250 °F. A thermocouple in the rear of the test section senses the temperature of the flow and can activate or deactivate the heating coils as necessary to maintain the desired temperature. If the desired temperature happens to be below room temperature, then the refrigeration unit can be manually set at a level that will hold the temperature of the tunnel constant. The tunnel is also fully insulated, which helps prevent heat transfer and allows for greater sustainable temperature differences between the tunnel and ambient conditions [2].

The tunnel is pressure sealed and can be pressurized up to 20 psia or vacuum pumped as low as 5 psia. A pressure sensor monitors the pressure inside the tunnel which must be maintained manually by either injecting or bleeding air as necessary [2].
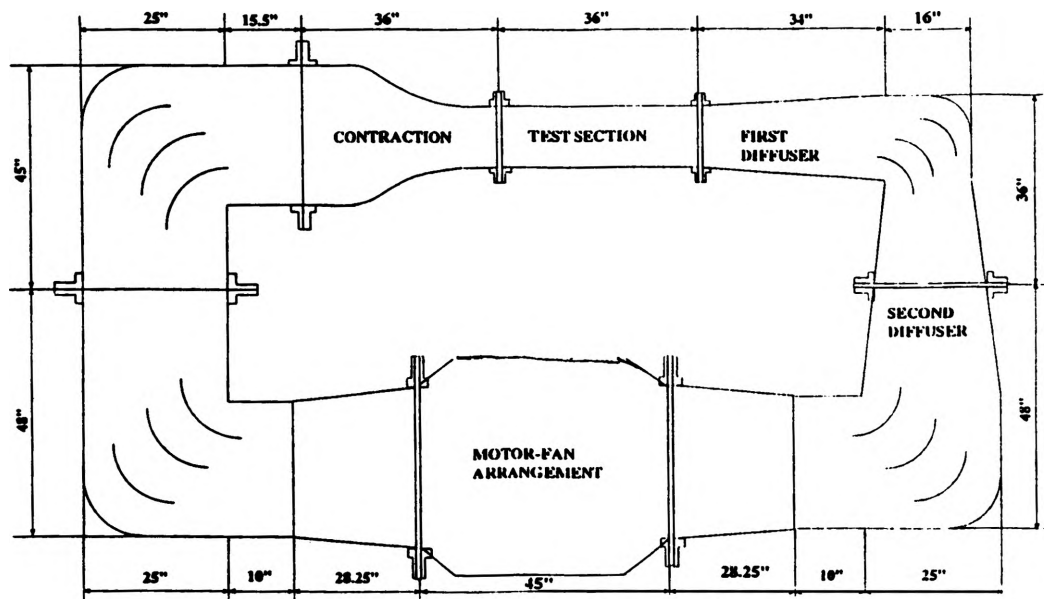
Figure 2: Diagram of VDWT

The humidity level of the tunnel can be controlled via manual injection through a range of .003 - .012 lbv/lba. Humidity is injected by using a hot plate to generate steam from a water bath, the steam is then fed to the tunnel. Humidity is removed by cooling the tunnel and allowing the water vapor to condense on the refrigeration coils. The condensation can then be drained from the tunnel and the tunnel can be reheated to the desired temperature [2].

Extensive arrangements have been made to ensure nonturbulent flow in the test section. A honeycomb structure is installed to reduce any lateral flow disturbances. Furthermore, a set of 86° turning vanes were incorporated at each corner of the wind tunnel [2]. The maximum measured turbulence level in the 1000-3000 fpm range is an acceptably low 0.5% [3].

The general layout of the wind tunnel is shown in Figure 2. As can be seen, the tunnel incorporates two diffusers which serve to slow the flow and increase the efficiency of the motor-fan arrangement. The contraction section immediately preceding the test section is designed with a 6.25 inlet to outlet area ratio. The test section itself has a 10" x 10" cross-section and is 36" long. Two transparent windows are incorporated on the top and front sides of the test section to provide viewing areas [2].

5. EXPERIMENTAL SETUP

The experimental setup consists of a hot wire anemometer, pitot static tube, thermometer, pressure sensor, and humidity sensor. These instruments are all mounted in the test section of the VDWT, as shown in Figure 3. An item in Figure 3 labeled in a box indicates that the output of that
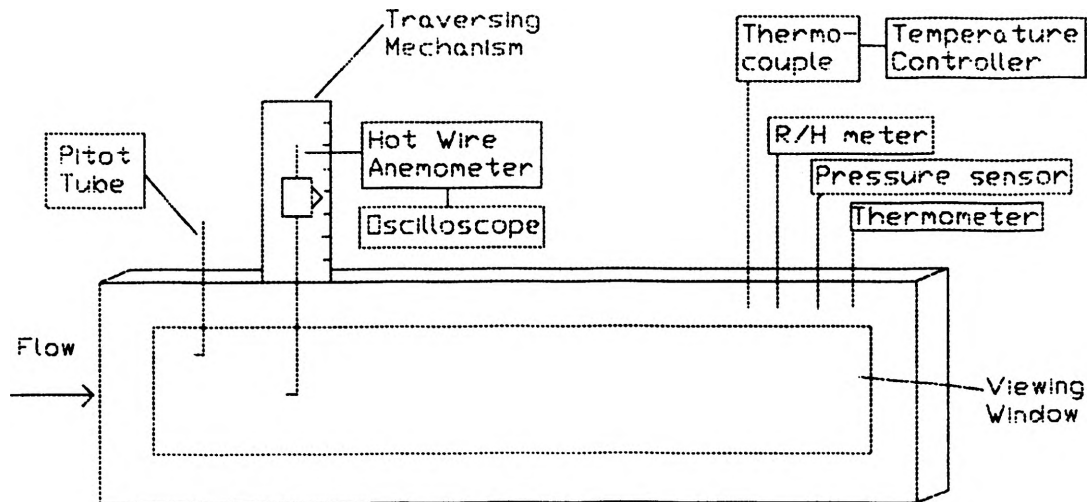
Figure 3. Side View of VDWT Test Section

instrument is continuously displayed to the experimenter.

The hot wire anemometer is mounted approximately 12" from the entrance to the test section along with a pitot static tube. They are each mounted in the same cross-sectional plane in order to prevent disturbances downstream of one instrument from effecting the readings of the other. The speed registered by each instrument is displayed digitally on the workstation. An oscilloscope is included to give the experimenter visual data on the output of the hot wire anemometer.

The hot wire is mounted on a ruled traversing mechanism which allows the hot wire to be raised or lowered to any position in the wind tunnel from the lower surface to the upper surface. The ruler markings along the traversing mechanism allow the exact height of the hot wire to be measured.

As mentioned earlier, the temperature of the wind tunnel can be maintained at any level via a thermocouple which can switch on or switch off the heating coils, as necessary. In addition to the thermocouple, a thermometer is mounted in the tunnel for independent confirmation of the temperature. A pressure sensor is also mounted in the tunnel to provide a reading of the pressure in the test section. The humidity is measured via a humidity sensor and is displayed digitally on the workstation. All temperature, pressure, and humidity sensors are mounted downstream of the anemometers, approximately 5 - 10 in. from the exit of the wind tunnel.

6. EXPERIMENTAL PROCEDURE

The hot wire anemometer is initially calibrated at station 1 (12" from inlet) and at a temperature of 70°F. The procedure followed is then similar to the one described in section 3. of the report. The calibration, however, is important only if the final data is presented in terms of the velocity measured by the hot wire. It is more convenient to present the results in terms of the voltage applied to the hot wire since this is the value that is actually recorded during the experiment. What these results will yield is a series of plots that are qualitatively correct, but give no information on the actual velocity measured. This is acceptable because a qualitative analysis is being applied, and the actual reported velocity is not important.

After the calibration is performed, the hot wire is lowered as close as possible to the bottom surface of the wind tunnel where the voltage of the hot wire is recorded. The hot wire is then raised by an increment of 0.025 in where the new output is recorded and the hot wire is raised again by the same increment. This procedure is repeated until the experimenter feels that the hot wire has left the boundary layer, at which time the increment by which the hot wire is raised is changed to 0.1 in. The procedure continues until the experimenter is absolutely sure the hot wire has reached the free stream, at which time the increment becomes 1 in.

The procedure is repeated in reverse when the experimenter feels that the hot wire is nearing the boundary layer on the upper surface of the wind tunnel. The experimentor will begin raising the hot wire in 0.1 in. increments again, and then when the boundary layer is just about to be entered the increments will switch to 0.025 in.

In this manner, the velocity profile of the wind tunnel can be measured. The procedure above, including the calibration, is repeated for two locations in the test section, station 1 (12" from inlet), and station 2 (18" from inlet). At each station, the profile is measured for two temperatures (70°F, and 100°F), and three flow speeds (500 fpm, 1500 fpm, and 3500 fpm).

7. RESULTS AND DISCUSSION

The results consist of 12 graphs displaying velocity profiles taken at various stations, temperatures, and speeds. Graphs taken at 70°F will be referred to in Figure 4. and graphs taken at 100°F will be referred to in Figure 5. The results will be discussed using two of the graphs as examples.

The first graph, which displays a typical velocity profile, is constructed from data taken at station 1 (12" from inlet), 70°F, and 500 fpm, see Figure 4. The boundary layer at the bottom surface of the test section is under 0.5 in. At the top of the tunnel, a slight acceleration in the flow can be seen just before the boundary layer is reached. This acceleration is typical of the velocity profiles taken at station 1. It does not represent a serious change in velocity. In fact the difference is only .001 Volts or .245% greater than free stream velocity. This velocity profile exhibits an acceptably small boundary layer along with uniform flow in the free stream. The profile is quite satisfactory resul tand is characteristic of most of the measurements taken.

Unfortunately not all the velocity profiles were as good as the first one. The next example demonstrates some of the problems encountered with the profiles. This graph was taken from data at station 2 (18" from inlet), 100°F, and 500 fpm, see Figure 5. As can be seen, the velocity in the free stream does not remain constant throughout the height of the tunnel. There is a change of 0.0093 volts from the free stream value to that at the apex of the dent in the graph. This represents a velocity change of 1.96% from the free stream velocity. This effect was exhibited in a number of graphs, specifically those at 100° and either 500 or 1500 fpm. The trend disappeared at velocities of 3500 fpm.

The cause of the velocity drop is unknown however, it seems to be confined to high temperatures and low speeds. One possible explanation of this phenomenon is that when the flow is heated the temperature does not get distributed in a completely uniform matter. This would cause density variations in the flow and the flow could begin circulating to relieve the variations. This circulation, called swirl, would introduce small components of velocity that are not in the axial direction. At low speeds, these non-axial velocity components could become noticeable, and result in a nonuniform velocity profile in the free stream.

Even though the effect represents less than a 2% actual change in velocity, this change may be significant in conducting the research described earlier. Since the RVA and EVA are large instruments, the velocity would not be constant across their height.

The cause of this problem is not completely understood, therefore, it is difficult to recommend a solution. However, more testing at higher temperatures, installing anti-turbulence screens in the tunnel, and avoiding low speed and high temperature conditions during testing may a prudent recommendation.

STATION 1

Flow Velocity 500 fpm
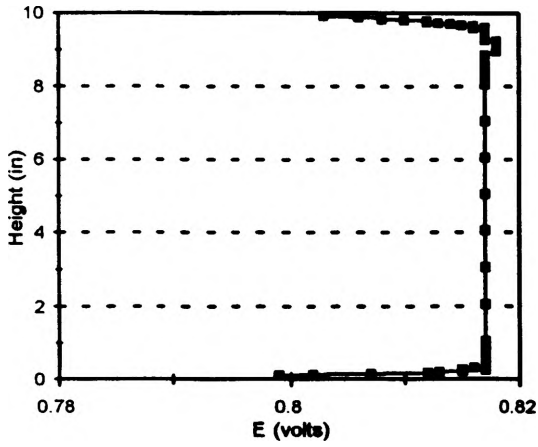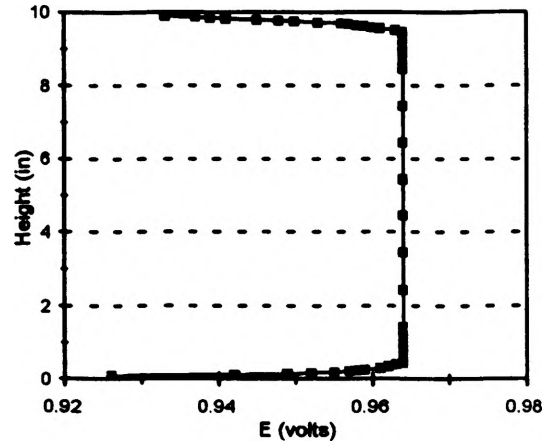
Flow Velocity 1500 fpm

Flow Velocity 3500 fpm
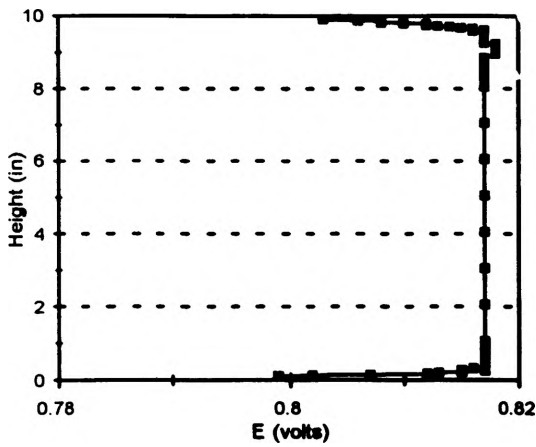
STATION 2

Flow Velocity 500 fpm
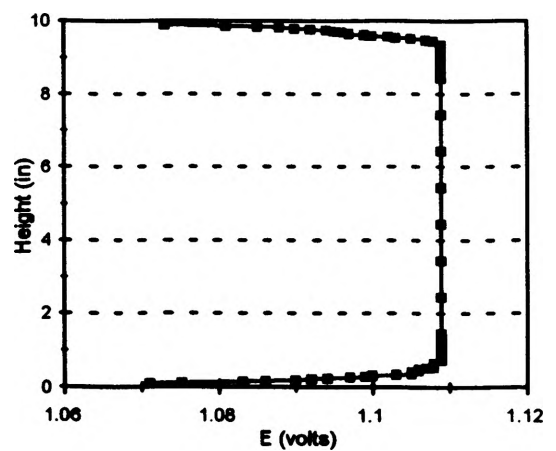
Flow Velocity 1500 fpm
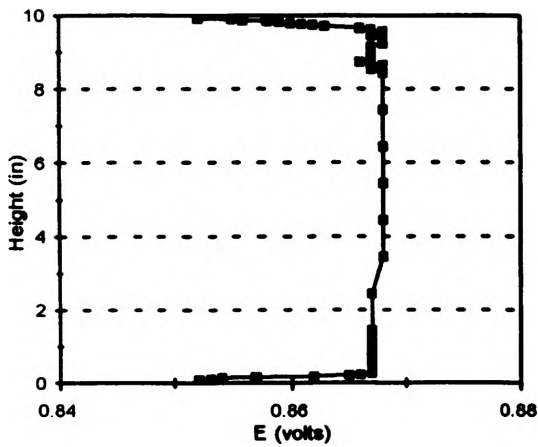
Flow Velocity 3500 fpm
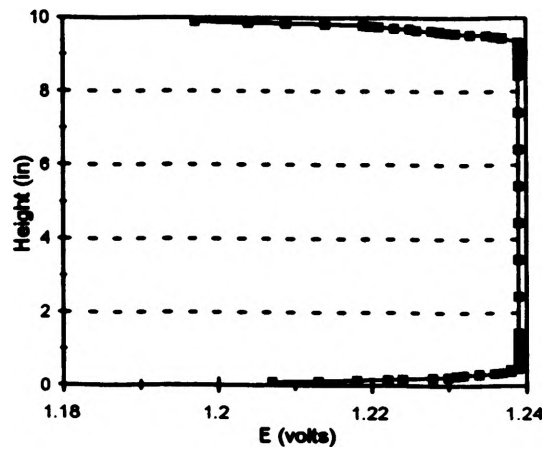
Figure 4. Velocity Profiles in the VDWT Test Section at T = 70°

STATION 1

Flow Velocity 500 fpm
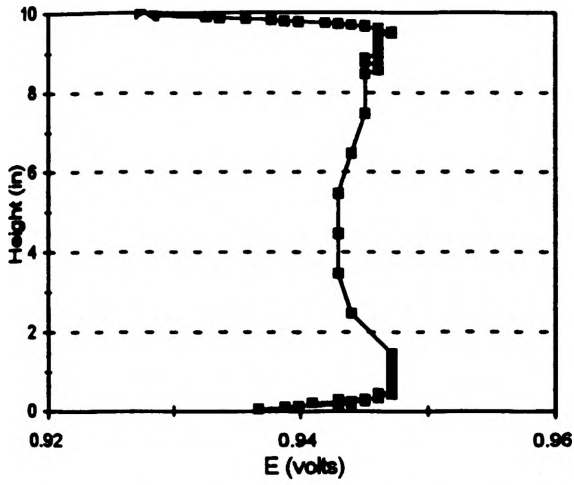
Flow Velocity 1500 fpm
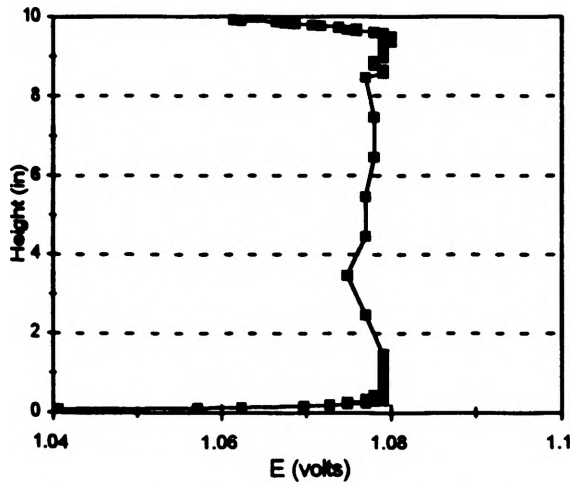
Flow Velocity 3500 fpm
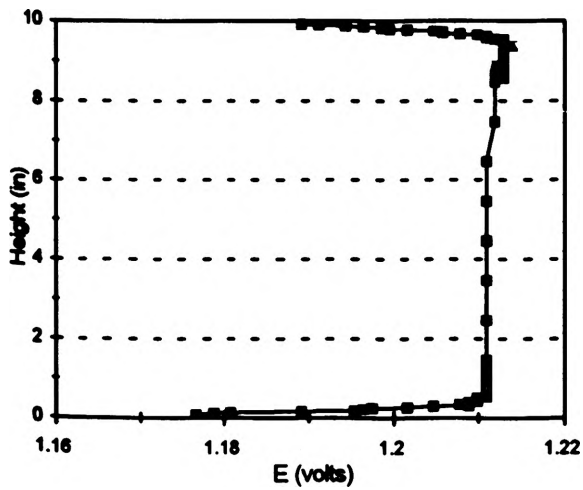
STATION 2

Flow Velocity 500 fpm
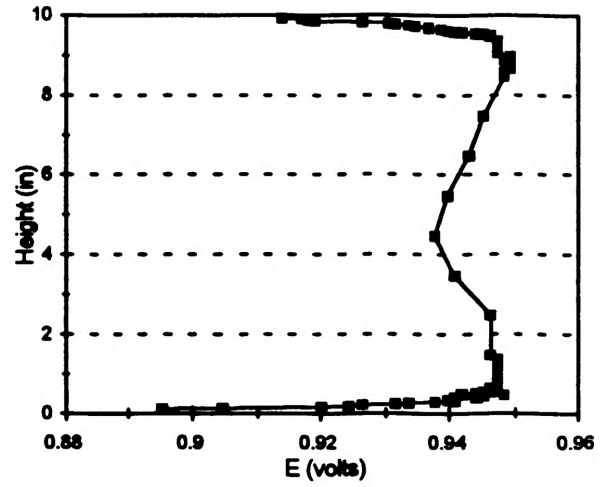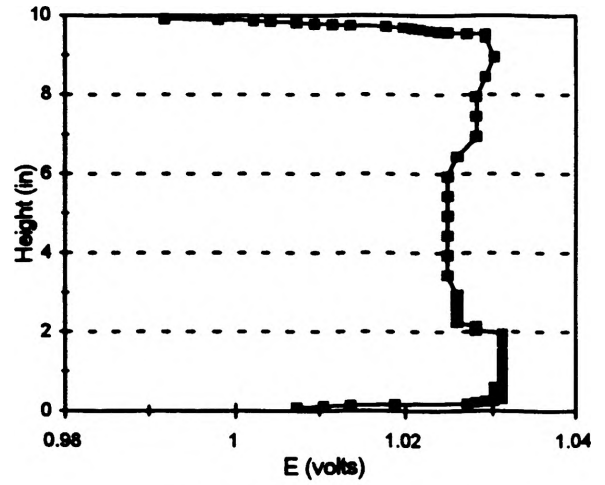
Flow Velocity 1500

Flow Velocity 3500 fpm
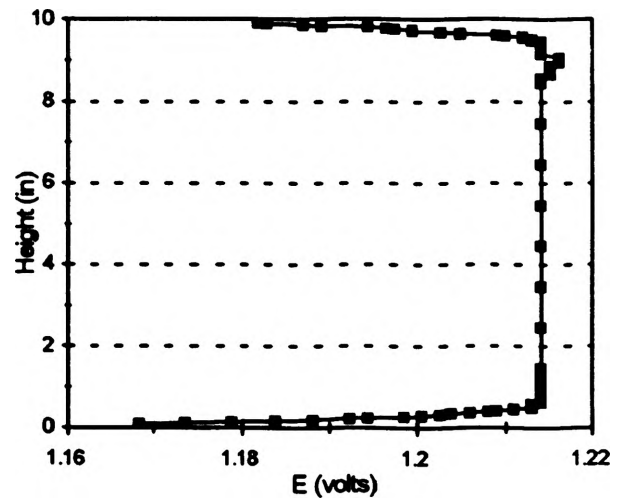
Figure 5. Velocity Profiles in the VDWT Test Section at T = 100°

111

8. CONCLUSION

The primary goal of this paper was to determine the flow quality in the test section of the UMR Variable Density Wind Tunnel under different temperatures and velocities. The need to verify the flow quality arose out of a larger research project concerning density effects on the performance of various common anemometers. Flow quality is defined as a velocity profile having relatively small upper and lower boundary layers, and smooth flow through the free stream.

Results from this experiment indicate that the flow is of adequate quality under all conditions checked, except for the combination of high temperature and slow speed flow. When these conditions are encountered the flow in the free stream of the test section tends to be non-constant and less appropriate for use in conducting further experiments.

Possible causes of this problem include the possibility that the temperature of the flow has not become constant by the time it reaches the test section. If this were the case there could be density gradients in the flow which would cause the flow to circulate and swirl. At low flow speeds, this swirl could introduce a significant velocity component in a non-axial direction causing the flow to be nonuniform in the free stream. This is only a possible explanatior it has not been proven and other explanations may certainly exist.

To overcome this problem, it is recommended that further tests be conducted at even higher temperatures including 150°, 200°, and 250°. This will help to better understand the problem. If the problem persists at the higher temperatures then installing some anti-turbulence screens to reduce longitudinal flow disturbance may be in order. Another possibility is simply to avoid experimental conditions at low speeds and high temperatures. This may be a viable alternative since it apparently does not take long before increasing the flow speed will smooth out the irregularities.

112

10. REFERENCES

[1] George, R., Sauer, Jr., H.J., Finaish, F., Howell, R.H. 1994. Predicting the Temperature, Humidity, Pressure, and/or Density Effects on Velocity Instrumentation. *ASHRAE Transactions* 3763 (RP-698).

[2] Pattabiraman, Shivaram, 1994. Development of a Variable Density Close Return Wind Tunnel And Density Corrections for Velocity Measurements Taken By Vane Anemometers. Presented to the Faculty of the Graduate School of the University of Missouri-Rolla.

[3] Department of Mechanical and Aerospace Engineering and Engineering Mechanics. Brief Description of the Variable Density Wind Tunnel. University of Missouri-Rolla.

Development of a Recycled Glass Corrosion Inhibitor for Surface Coatings and Concrete Applications

Theresa Pierce

Department of Chemistry

ABSTRACT

This research was performed to study the possibility of attaching a metal corrosion inhibitor to recycled glass powder. Such a material would be useful as a corrosion inhibitor component for metal substrate coatings. The major experiments performed were first to produce a metal corrosion inhibitor (Irgacor 153)/silane coupling agent (3-(chloropropyl)trimethoxysilane) adduct and secondly to attach this corrosion inhibitor/silane adduct onto the surface of glass. To test feasibility, qualitative corrosion tests were performed using steel wool as the corroding metal and a number of product samples.

INTRODUCTION

American uses for glass encompass a large variety of everday items ranging from soda bottles and dinnerware to windows and building materials. Over 5400 tons of total glass are wasted each year just in the Ozark region of Missouri alone [1]. One can imagine how great this amount is for the rest of the country. Therefore the need to recycle glass products and create environmentally friendly ones has become a critical concern in today's chemical research.

Another critical technology being researched today involves nontoxic processes that protect metal infrastructures from chemical corrosion. The constant weathering of steel road bridges, oil pipelines, and rebar in concrete give rise to their slow deterioration. Within the coatings industry, efforts to resolve this type of corrosion destruction through the use of a polymer-based coating represent a significant challenge for technological development.

The objective of this investigation applies to developing metal corrosion inhibitor technologies to create a state-of-the-art material relevant in corrosion resistant coatings. Using recycled clear glass to make a fine powder and the

115

commercial liquid organic corrosion inhibitor Irgacor 153, this study attempts to develop a covalently bonded glass corrosion inhibitor. This new anti-corrosive powder could then potentially serve as an effective metal substrate corrosion repressor coating for decaying metal structures.

RESEARCH APPROACH

The commercial liquid organic corrosion inhibitor, Irgacor 153, has been proven to reduce the permeability of coatings to water and ions and to improve the ability of the coating to wet the substrate [2]. It can be incorporated into primer, direct-to-metal and clear coatings with minimal impact on color, gloss, and transparency [2]. With this kind of versatility, a Friedel-Crafts alkylation was performed on this commercial inhibitor with a glass coupling agent, 3-(chloropropyl) trimethoxysilane, to give a corrosion/silane adduct [3, 4]. This Friedel-Crafts mechanism begins with the formation of a carbocation which proceeds to electrophilically substitute an aromatic hydrogen with an R group [4]. The resultant covalently bonded corrosion/silane material was then reacted with recycled clear glass, binding the adduct to the glass surface through an elimination of methanol [4].

Mechanism:
  Reaction #1:

  Reaction #2:

Figure 3 – polymer NMR
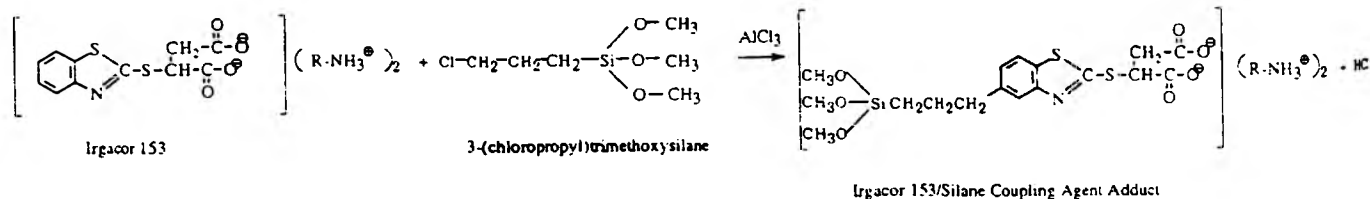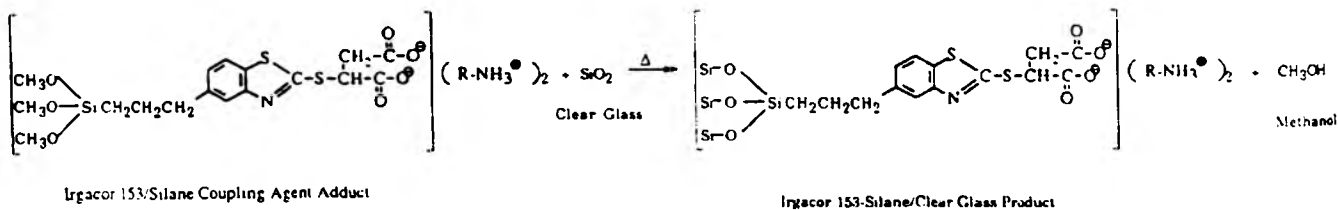
Obs Freq	99.601900(		ppm	
SW +/-	600.0	#	Start	Stop
FREQU	1200.0	1	8.30	7.96
FILTER		2	7.81	6.95
OBFRQ	99.55	3	5.77	5.47
OBSET	51.9000	4	5.13	4.89
IRMOD	NON	5	2.18	2.09
IRSET	51.50			
No. Scans	32			
No. Points	4096			
Last Delay	1.00e+00			
Line Brdng	0.00			
Nucleus	H1			
Sequence	single H1			
Filename	Tim-3/7/9			
Acq. Time	3.41e+00			

File created:
Monday, March 7, 1994
10:52 AM
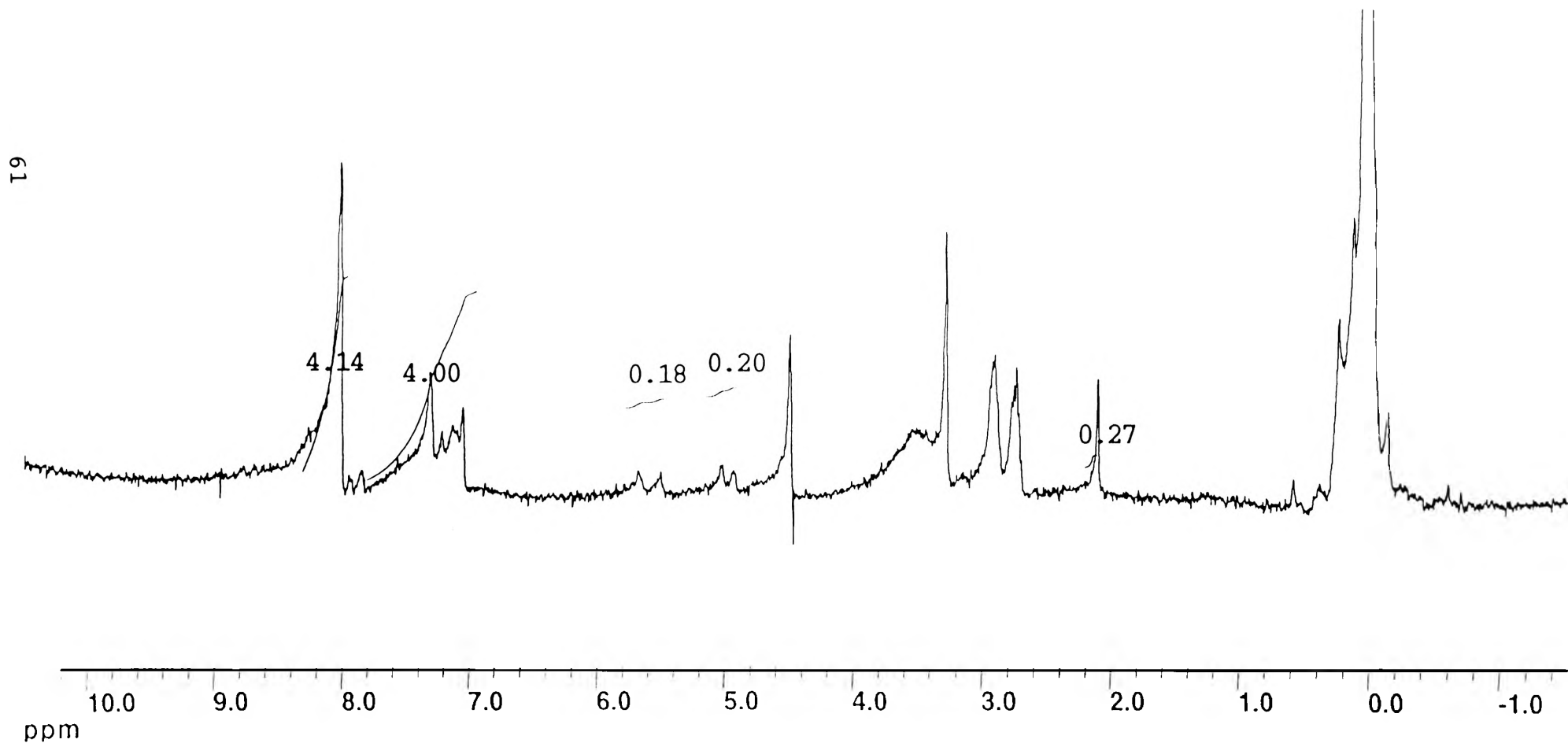
EXPERIMENTAL PROCEDURES

Glass Powder Generation:

(1.) First, obtained some grinded clear recycled glass from the MO-SCI company. The most commonly used grinding methods include the hammer mill and the fluid-energy mill [5].

    (a.) Hammer Mill- Consists mainly of rotating hammers in a chamber with a grinding plate and a screen. The screen size and the hammer/grinding plate liner control the size of the powder [5]. See Figure 1 below.

    (b.) Fluid-Energy Mill- This process uses high-velocity gas streams which cause particles to collide with the mill structure and each other [5]. See Figure 2 below.
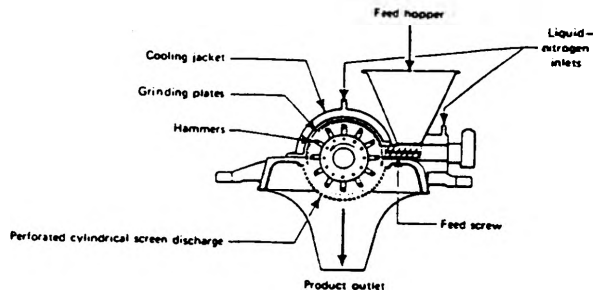
Figure 1: Hammer Mill [5]
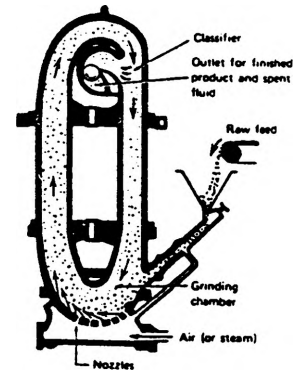
Figure 2: Fluid-energy Mill

(2.) Most powders produced by the above methods vary in particle size and shape so one must perform a powder classification on them. There are two prominant types of this classification: screening and air classification [5]. Screening uses a vibrating screen of desired mesh size while air classification utilizes centrifugal force to separate particles [5]. See Figures 3 and 4 below.
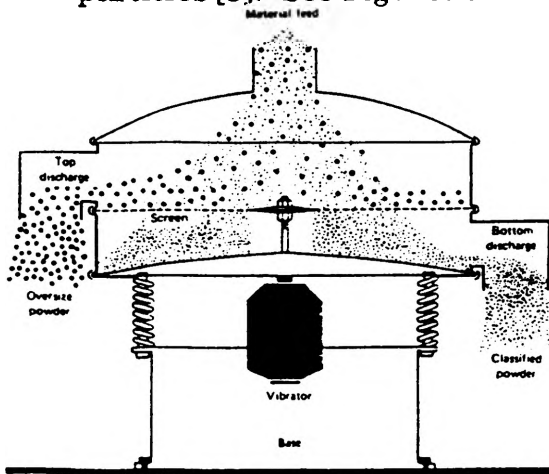
Figure 3: Vibrating Screen [5]
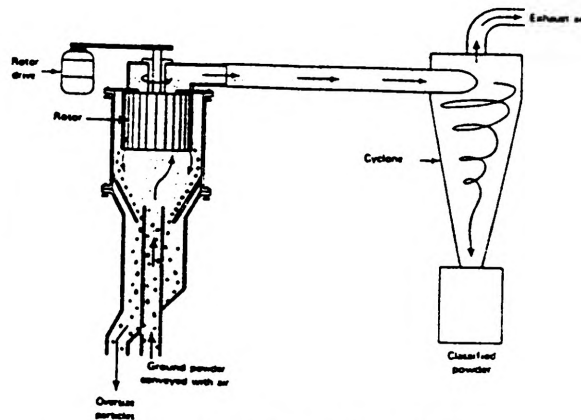
Figure 4: Air Classifier [5]

117

Irgacor 153 Inhibitor/Silane Coupling Agent Adduct Preparation:
   (1.) To a 250 ml round bottom flask mixed 60 ml of chlorobenzene, 5.0 g of the
        Irgacor 153 commercial corrosion inhibitor, 3.0 g of 3-(chloropropyl)
        trimethoxysilane, and 2.0 g of aluminum chloride (catalyst).
   (2.) Then added a magnetic spin bar, attached a water-jacketed reflux
        condenser, and refluxed for about 4 hours with stirring.
        Observation: A light yellow precipitate formed.
   (3.) Vacuum filtered this precipitate/AlCl$_3$ solid.
   (4.) Next, 60 ml of pure alcohol was added to the precipitate/AlCl$_3$ solid to
        dissolve the AlCl$_3$.
   (5.) Vacuum filtered the remaining organic precipitate. Let it dry in a 53°C
        oven.
   (6.) Recrystallized this precipitate by the following method:
        a.) In a 25 ml beaker placed 0.5 g of the dried organic precipitate, 10 ml
            of DMF, and a magnetic spin bar.
        b.) Set this on a hot plate and brought this to a boil.
        c.) Gravity filtered thsi with fluted filter paper.
        d.) To the filtered solution 40 ml of ethyl ether was added.
        e.) Let this sit for a couple days to let the ether evaporate off. A gooey
            brown precipitate was left.
        f.) Placed this in a labeled vial via methanol.
   (8.) Performed NMR's on the 3-(chloropropyl)trimethoxysilane (Fig. 5), Irgacor
        153 (Fig. 6, Let all of the solvents evaporate off of this beforehand.), and
        the gooey brown precipitate obtained above. (Fig. 7, This should be the
        Irgacor 153/Silane coupling agent adduct.) Performed an FTIR on the
        Irgacor 153/Silane coupling agent adduct. (Fig. 8)

Comparison of Results:
        Comparing the aforementioned NMR spectra shown in Figures 5, 6, and 7, one
can see that it looks as if the adduct's NMR is a combination of the beginning
reactants' NMR's. Figure 5 shows a large peak for chlorobenzene at δ3.5-3.8, and a
small multiplet at approximately δ0.6-0.8 and δ1.6-2.0. Figure 7 also possesses
similar peaks in these areas. Furthermore, Figure 6 reveals a large peak at δ2.1, a
medium peak at δ 0.9 and δ1.3, and a small peak at δ8.0. Figure 7 also retains many
of these peaks. The peak at δ8.0 for Figures 6 and 7 demonstrates the existance of
the aromatic ring in both the Irgacor 153 and the adduct. Peaks at δ2.1 represent
CH$_2$-C=O and CH-C=O protons while those at δ0.5-1.8 reveal C-CH$_2$-C protons. The
peaks located in the range of δ3.5-3.8 demonstrate the CH$_2$Cl protons. Therefore,
this proves the formation of the Irgacor 153/Silane coupling agent adduct.

Irgacor 153-Silane/Glass Product Preparation:
   1:10 Ratio Reaction:
        (1.) In a 125 ml round bottom flask mixed 1.0 g of Irgacor 153/silane adduct,
             10.0 g of recycled clear glass powder, 10 drops of H$_2$SO$_4$, and 50 ml of
             chlorobenzene.

(2.) Then added a magnetic spin bar and attached a water-jacketed reflux condenser.

(3.) Refluxed this for 24 hours with stirring. Then proceeded to heat this mixture for one hour at the boiling temperature.

Observation: Noticed the formation of broken rounded fragments of glass in the flask.

(4.) Vacuum filtered off the reaction solvent (chlorobenzene) and washed the product with two 50 ml portions of pure chlorobenzene. Combined the reaction solvent and washings and saved.

(5.) Performed FTIR's on the pure recycled clear glass (Fig. 9), and the 1:10 Irgacor 153-silane/glass product (Fig. 10). Regular IR's were performed on the combined chlorobenzene 1:10 solvent portions (Fig.13), and the pure chlorobenzene (Fig. 12).

1:1 Ratio Reaction:

(1.) Repeated steps # 1-4 in the above 1:10 ratio procedure except this time only 1.0 g of recycled clear glass was added instead of 10.0 g.

(2.) After heating for approximately a half an hour, the mixture changed from a yellow to a dark brown.

(3.) Placed approximately 20 ml of the combined chlorobenzene solvent portions (brown color) in a small beaker and set it on top of the oven for 24 hours to evaporate off the solvent. A black residue remained.

(4.) Performed FTIR's on the 1:1 Irgacor 153-silane/glass product (Fig. 11) and the remaining black residue in step 3 above (Fig. 16). Regular IR's were performed on the combined chlorobenzene 1:1 solvent portions (Fig. 14) and the original commercial Irgacor 153 (Fig. 15).

Comparison of Results:

Comparing Figures 9, 10, and 11 proves that the glass underwent a change in the reaction. The large peak at about 1100 cm^{-1} appears in all three spectra, but the one in Figure 10 seems to have broadened some. Also, two small peaks appear between 1300-1700 cm^{-1} in Figure 9, but Figure 10 shows only one peak. When Figures 9 and 11 are compared, similar observations can be seen. Relating Figures 12, 13, and 14 reveals that none of the Irgacor/silane adduct was left in either of the two combined chlorobenzenesolvent collections. All three of these IR's are almost exactly the same. When comparing Figures 12, 13, and 14 with Figure 15, one sees that there are not any similarities. Finally, comparing similarities between Figures 8 and 16 demonstrates that some of the Irgacor 153/silane adduct remained in the 1:1 combined solvent portion after the reaction. This accounts for the brown color of the 1:1 combined chlorobenzene reaction/washing solvent. Perhaps one on the reasons this did not show up on the IR of the 1:1 chlorobenzene solvent portion is due to the large dilution of the left-over Irgacor 153/silane adduct with chlorobenzene. The above comparisons help to confirm the feasibility of the Irgacor 153-silane/glass product's formation.

Irgacor 153-Silane/Glass Application Testing:

Trial #1:

(1.) Rolled 4 small balls of steel wool and dipped each in regular mineral water.

(2.) The first one was set out on a watchglass with just water.

(3.) The second one was then dipped in mixture of the 2.0 ml of Irgacor 153 and 20 ml of chlorobenzene.

(4.) The third one was coated in the 1:10 ratio reaction powder product.

(5.) The fourth one was coated in the 1:1 ratio reaction powder product.

(6.) Left these out for approximately 5 days to allow corrosion.

Trial #2:

(1.) Redid steps #2-6 in trial one, but this time the steel wool was left in strands instead of balls.

(2.) Added another test strand making a total of 5 test strands. This fifth test strand was dipped in mineral water and then coated with just the recycled clear glass.

Comparison of Results:

For trial one, the 1:10 ratio corrosion inhibitor-silane/glass product seemed to rust more than the 1:1 ratio product. The 1:10 product also seemed to have a darker orange corrosion rust than the 1:1 powder. Upon examination of the centers of the steel wool test balls, hardly any corrosion occurred. The ball that was dipped in the Irgacor 153/chlorobenzene mixture showed no signs of corrsion at all. This at least shows that the Irgacor 153 works well in its liquid form.

The second trial was performed on strands of steel wool instead of balls because of the inability of corrosion to occur inside them. Again, the 1:10 ratio product corroded more than the the 1:1 product. It's corrosion rust also retained the dark, brighter orange color. The Irgacor 153/chlorobenzene strand did not show corrsion while the recycled glass strand showed small traces at the junctions where the strands crossed.

Although each product, 1:10 and 1:1, continued to show corrosion, the appearance of less corrosion on the 1:1 product proves that more of the Irgacor 153/ silane adduct was attached to the glass surface and helped to halt corrosion more.

CONCLUSIONS

It is apparent that a metal surface corrosion inhibitor can be covalently bound to glass surfaces, and that in the qualitative corrosion test applications, one can observe some discernment of the relative effectiveness of the 1:10 versus the 1:1 ratio loading of the Irgacor 153 corrosion inhibitor. One of the major limitations concerns the number of available silicon sites on the glass surface. The corrosion inhibitor attaches to these sites. If there are only a few available sites, then the percentage of the total glass surface covered becomes quite low causing the inhibitor's ability to halt corrosion to decrease.

Subsequent application studies would require testing the effectiveness of glasses with a higher number of silicon sites. This would increase the percentage of glass surface coverage and therefore improve the inhibitor's corrosion resistance. Another suggestion for use in future tests would be to try a number of different commercial corrosion inhibitors. Other inhibitors may have greater reactivities with the silane coupling agent or the glass' surface. For the qualitative corrosion tests, steel panels would be better to use. They provide a larger surface area to observe and can be easily coated with the testing material. Some tests involving various types of water, such as mineral water and salt water, would give one a better idea of how well an inhibitor's corrosion resistance is in areas near the sea as well as inland. A final suggestion is to vary the ratios of inhibitor to glass. Only two were performed in this experiment, but several more would be benefitial to the overall results.

This corrosion inhibitor/glass product could be used in surface coatings for many industrial and construction purposes. Oil pipelines, steel road bridges, and steel rebar in concrete, could be coated with a corrosion inhibitor/glass containing coating to prevent their constant weathering and slow destruction. Uses in actual concrete manufacturing are possible by mixing this new type of corrosion inhibiting coating in with the components of concrete to produce a product that keeps uncoated steel rebar from corroding.

Overall, this research experiment proves the feasibility of covalently bonding a corrosion inhibitor to the surface of glass. Hopefully this idea will be researched further and eventually proven to be a valuable asset to the coatings industry.
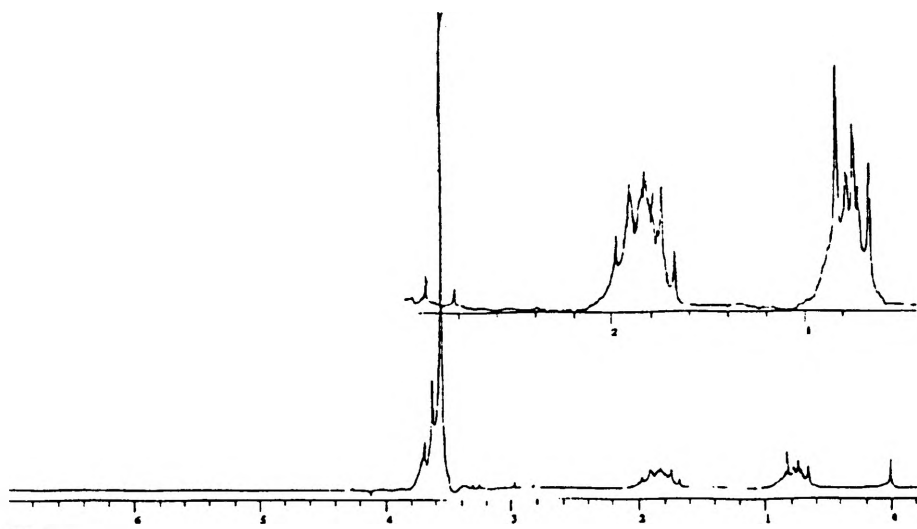
Figure 5: NMR of 3-(chloropropyl)trimethoxysilane
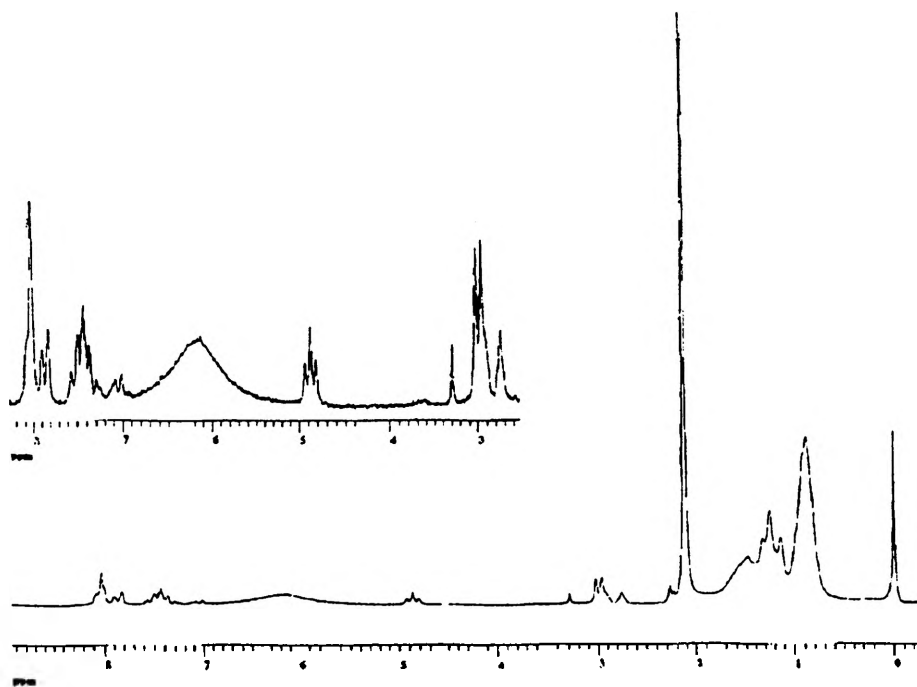
Figure 6: NMR of Irgacor 153 [(2-benzothiazolylthio)-succinic acid amine salt]
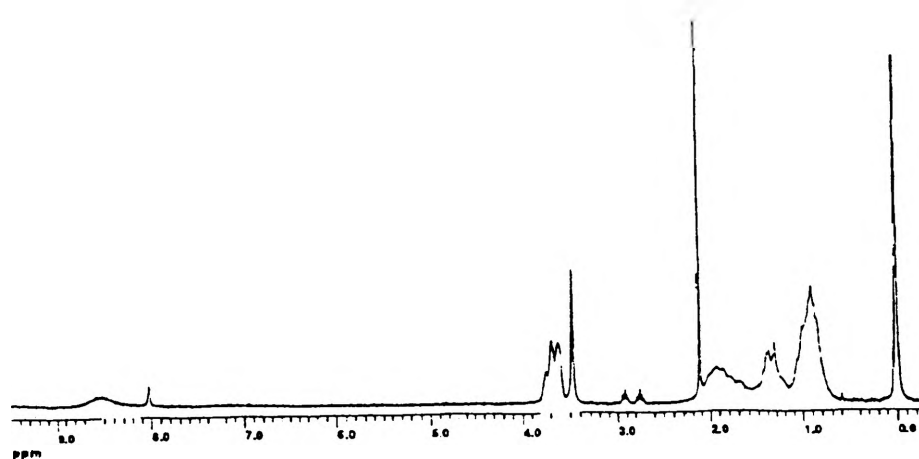
Figure 7: NMR of Irgacor 153/Silane Coupling Agent adduct
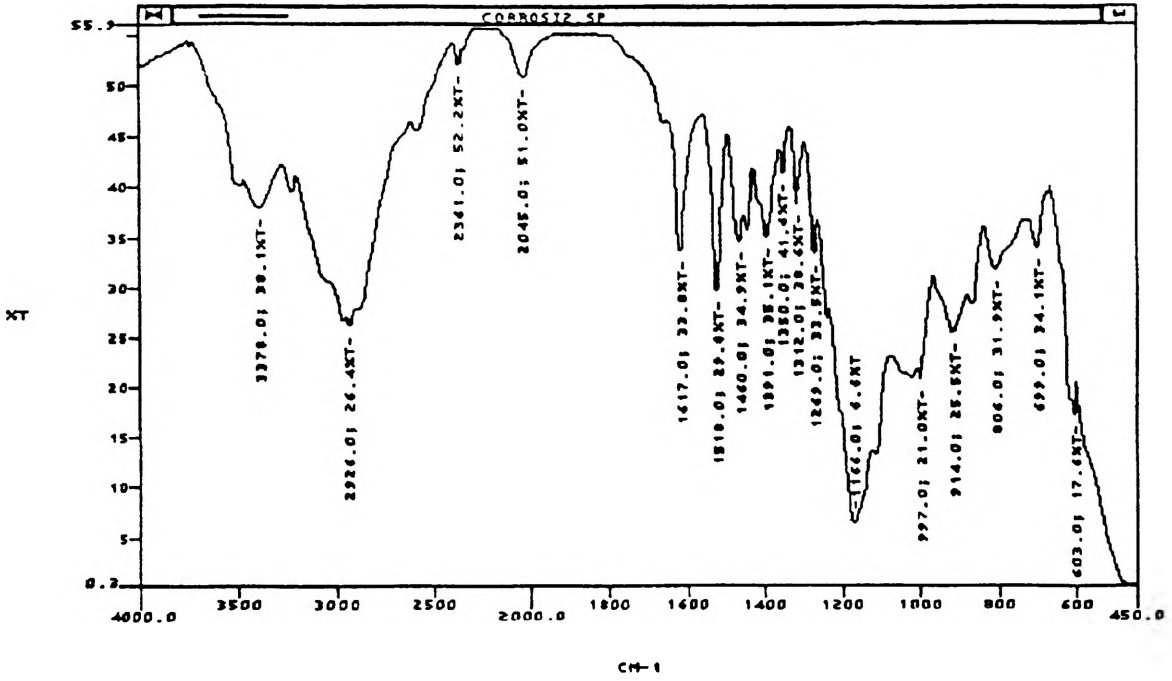
Figure 8: FTIR of Irgacor 153/Silane Coupling Agent adduct
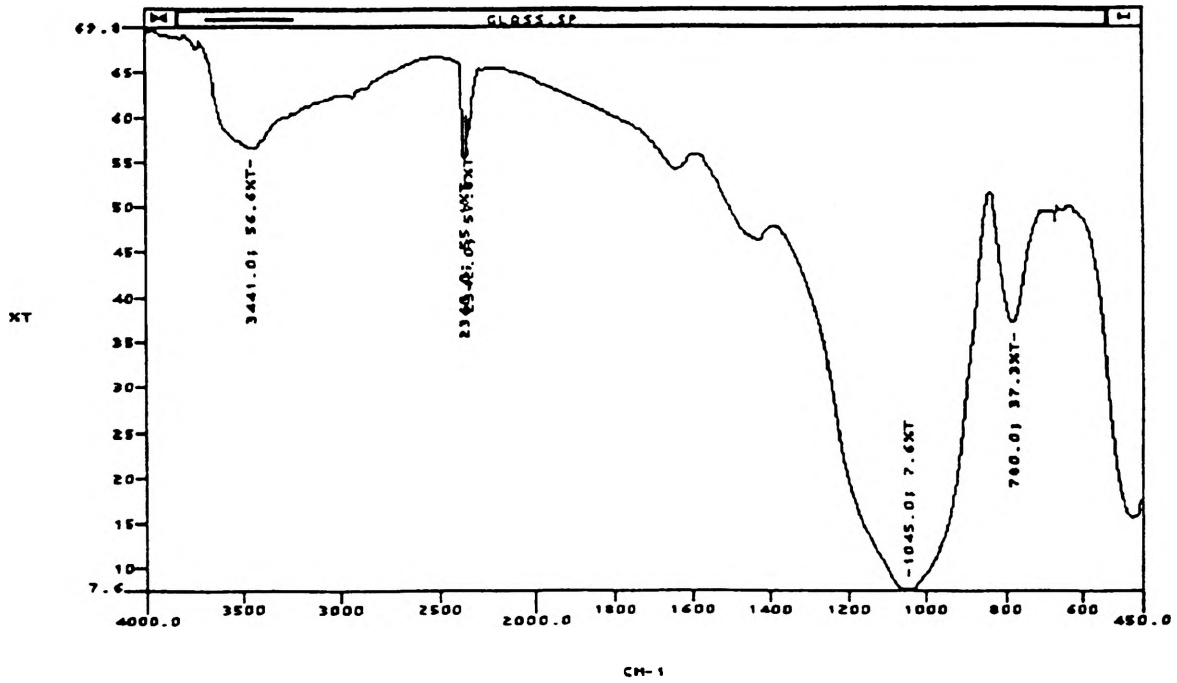
Figure 9: FTIR of the Recycled Clear Glass Powder

123
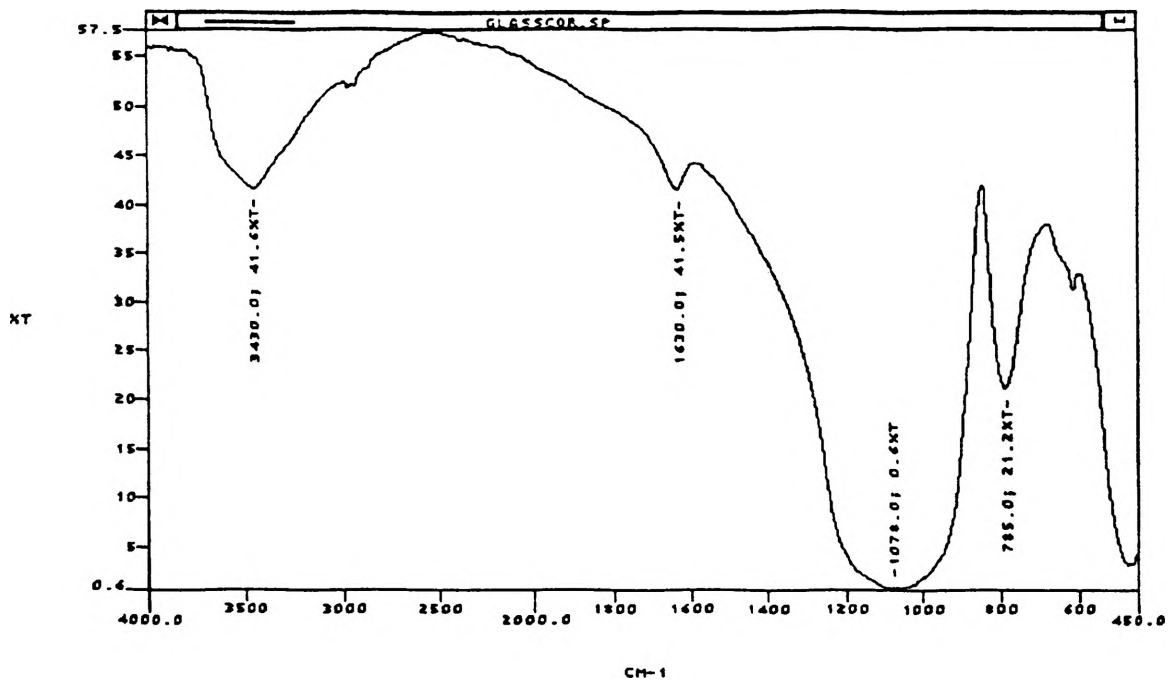
Figure 10: FTIR of the 1:10 ratio Irgacor 153-Silane Adduct/Recycled Clear Glass
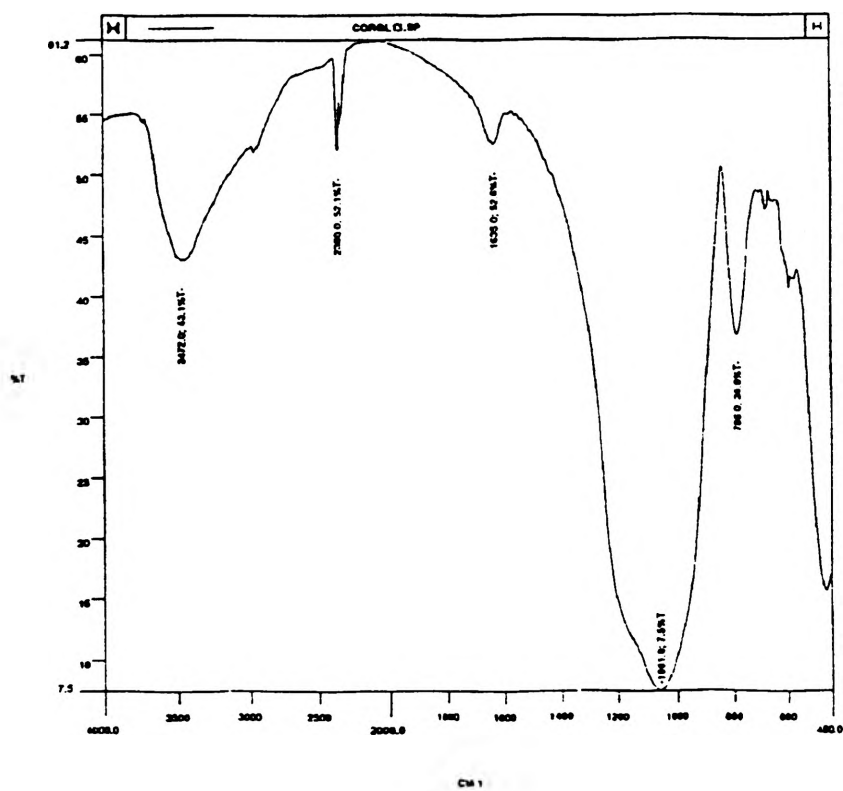
Figure 11: FTIR of the 1:1 ratio Irgacor 153-Silane Adduct/Recycled Clear Glass

124
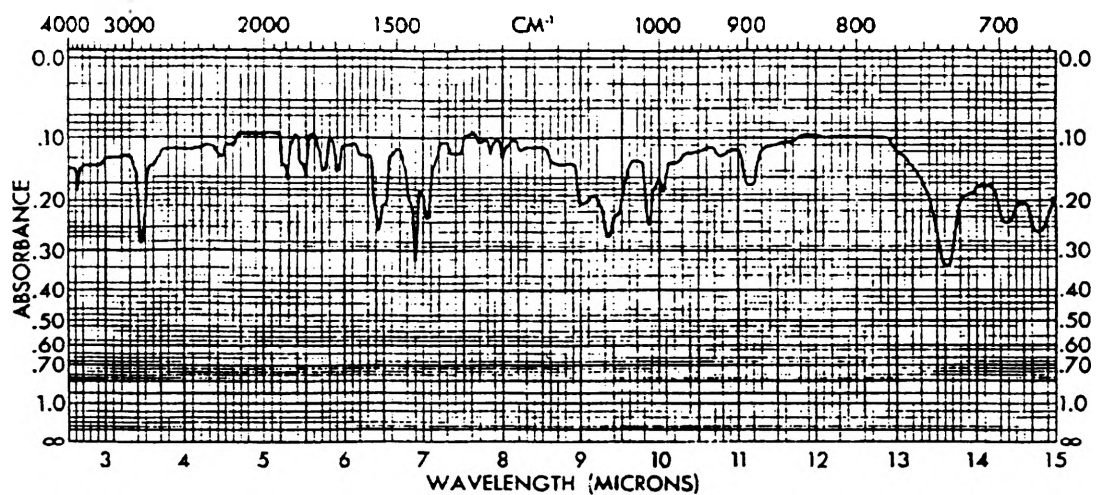
Figure 12: IR of Pure Chlorobenzene
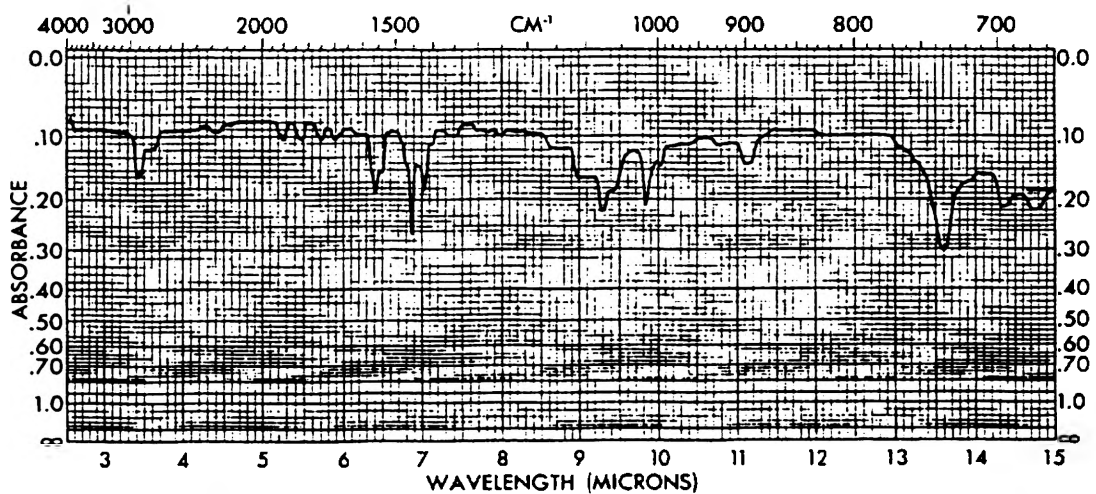
Figure 13: IR of the 1:10 ratio chlorobenzene solvent after the reaction
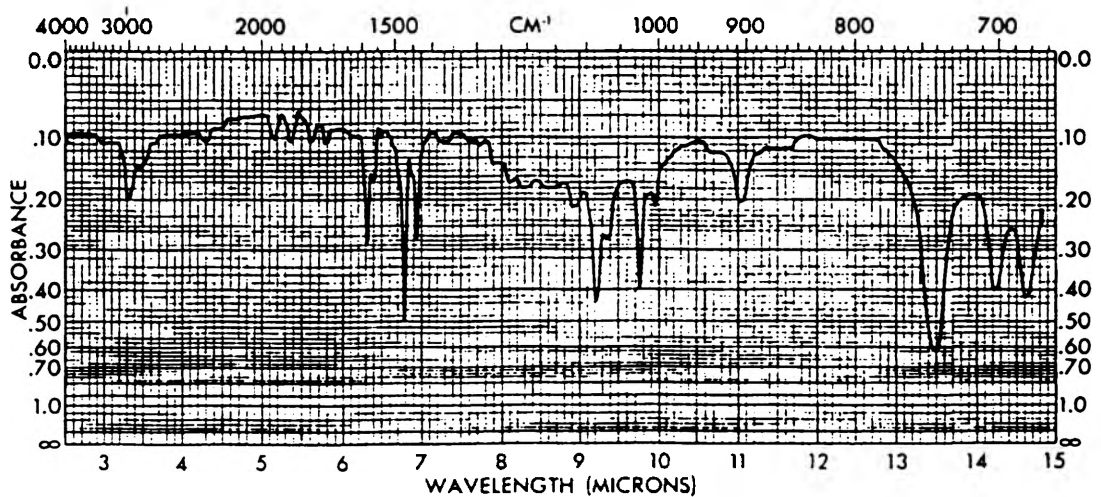
Figure 14: IR of the 1:1 ratio chlorobenzene solvent after the reaction

125
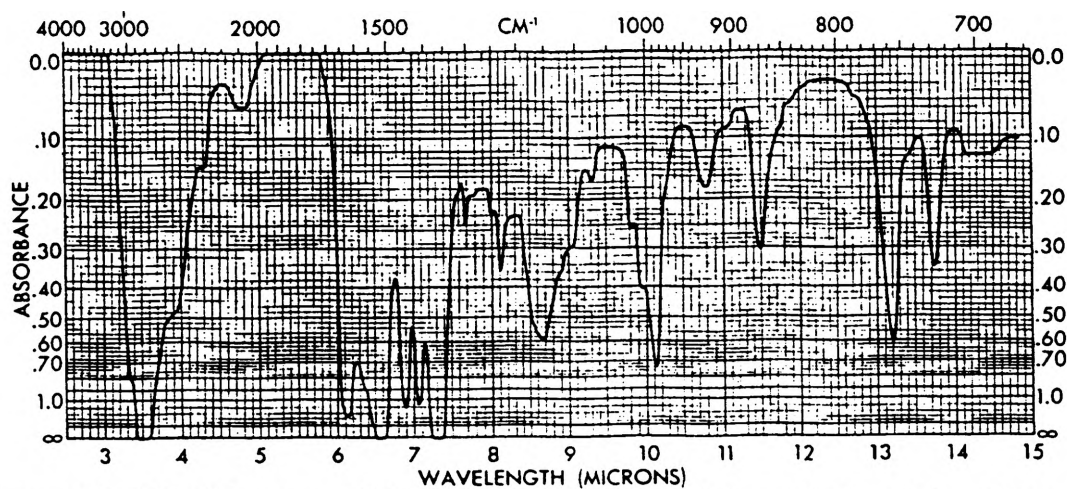
Figure 15: IR of Irgacor 153 [(2-benzothiazolylthio)-succinic acid amine salt]
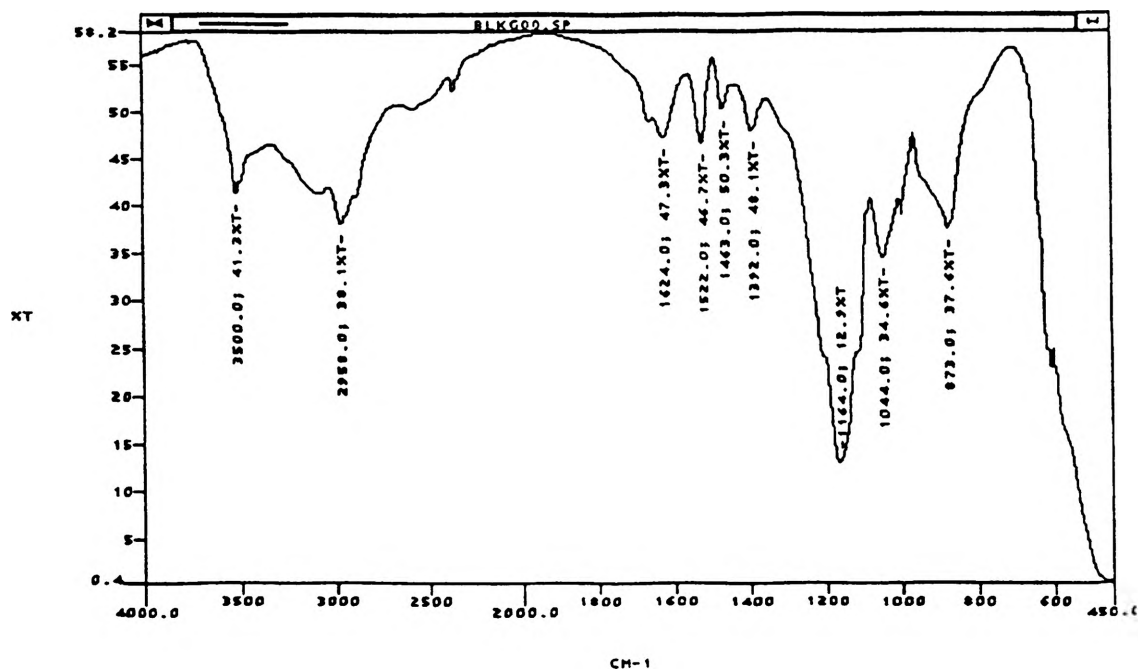
Figure 16: FTIR of Remaining Residue of 1:1 Ratio Reaction after Evaporation of Chlorobenene

126

REFERENCES

1.) "Impact of Waste Glass in Ozark Rivers Solid Waste Management District". MO Division of Natural Resources Report. 1992.

2.) "Corrosion Inhibitors". Additive for Coatings Product Brochure. Ciba-Geigy Corp. 1983. P. 18-25.

3.) "Selected Friedel-Crafts Reactions. I. Boron Halide Catalyzed haloalkylation of Benzene and Alkylbenzenes with Fluouohaloalkanes". Olah, George A., Kuhn, Stephen J. Journal of Organic Chemistry. Vol. 29. July-Sept. 1964. p.2317.

4.) Fundementals of Organic Chemistry. T.W. Graham Solomon's. 3rd Ed. John Wiley & Sons, New York: 1990. p. 487-488.

5.) "Powder Coatings". Surface Coatings. Paul, Swaraj. John Wiley & Sons, New York: 1985. p. 661-666.

ACKNOWLEDGEMENTS

VERIFICATION OF THE ISOLATION OF THE CHALCONE ISOMERASE GENE FROM *GLYCINE MAX*

L. D. Polk

Life Sciences Department

ABSTRACT

In this paper we report the verified isolation of the gene encoding the flavonoid-biosynthetic enzyme chalcone flavonone isomerase (CHI) from *Glycine max* as well as the procedures used to generate the results. We began by electroeluting an 865 base pair (bp) *Hind*III fragment from pCHI1. We then restricted the pDR10 plasmid with *Hind*III. In order to test for homology, we hybridized the pDR10 fragment with nick translated pCHI1 fragment as a probe. For a second electrophoresis experiment, we cut pDR10 with *Eco*RI and *Hind*III. We also restricted several different pDR10 plasmids with a variety of deletions. After performing a Southern blot on the second restriction, we were able to determine that the homology for the CHI gene lies in a 1983 bp segment between the multicloning *Hind*III site and *Pst*I site of the insert.

INTRODUCTION

The chalcone flavonone isomerase gene is involved in the production of metabolic intermediates known as flavonones. Flavonones are responsible for a variety of biological activities including functions during pollination and seed dispersal, flower coloration, legume nodulation and protection from harmful doses of ultraviolet radiation and white light [1, 2, 3]. This particular gene encodes chalcone flavonone isomerase (CHI), an enzyme necessary for the interconversion of naringenin chalcone and naringenin, which is in turn converted into flavonoids, anthocyanins, and isoflavonoids (**Figure 1**) [2]. Flavonoids and anthocyanins are highly UV-absorbent and protect the plant DNA from the mutagenic effects of sunlight. One particular group of isoflavanoids, phytoalexins, play key roles in plant pathogen protection [2, 4].
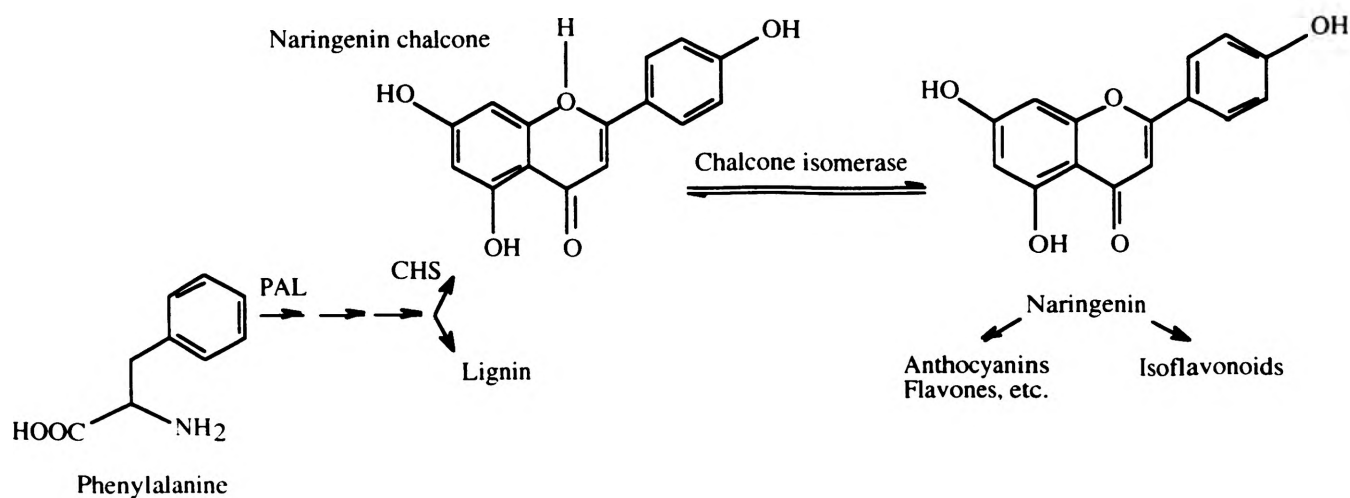
Figure. 1. Metabolic Role of CHI Gene in Phenylpropanoid Biosynthesis.

Previously. a soybean leaf genomic library in lambda Charon 35 was screened using the nick translated pCHI1 (*Phaseolus* CHI clone) plasmid without isolation of the insert cDNA away from other vector sequences. DNA was isolated from several positive recombinant phages. and Southern blots of restricted DNA were performed under similar conditions (entire vector as probe). The location of the putative soybean CHI was narrowed to a 3.9 kilobase (kb) *Hind*III fragment on the phage insert. This fragment was subsequently subcloned into pUC119 for nucleotide sequence determination and designated pDR10 (**Figure 2**). The purpose of the experiments reported here was to verify that the hybridization between the soybean DNA and pCHI1 was the result of homology to the *Phaseolus* gene-containing insert and not vector sequences.
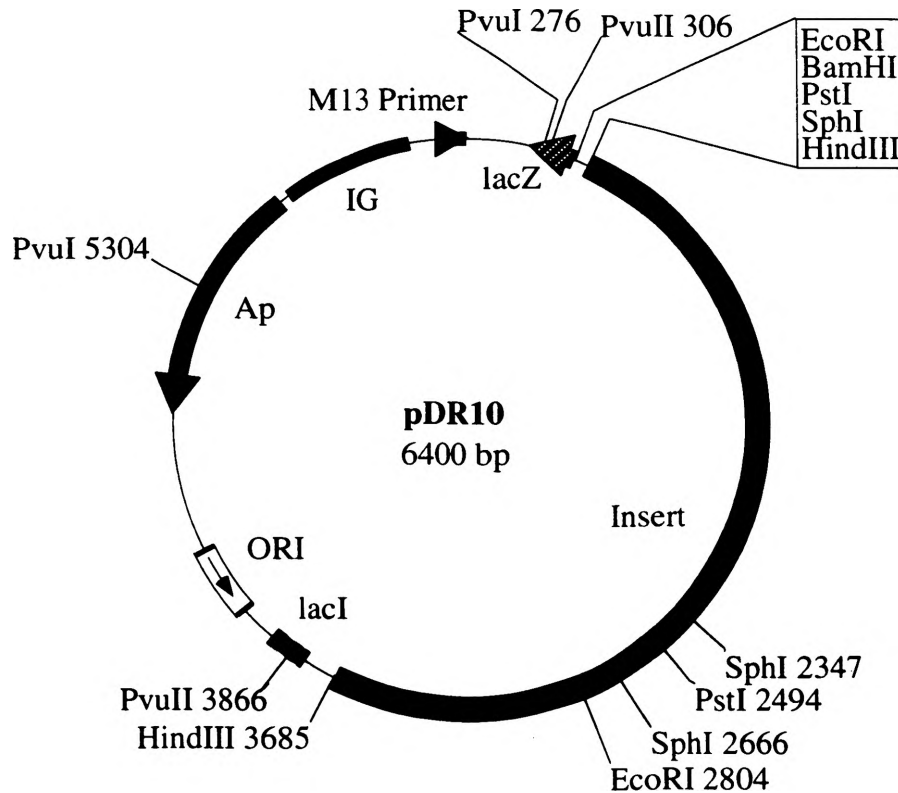
Figure. 2. Diagram of pDR10 Plasmid Showing Subcloned Insert.

RESULTS AND DISCUSSION

Results

Through our endeavors, we were able to produce two Southern blots identifying the location of the CHI gene on a 1983 base pair (bp) fragment located between the *Hind*III and *Pst*I sites of the inserted fragment of the pDR10 plasmid (**Figure 3**).

Methods of Determination

We digested the plasmid (pDR10) with *Hind*III restriction endonuclease, obtaining two fragments of approximately the same size: one containing approximately 3238 bp (soybean insert) and the other containing approximately 3121 bp (vector) (**Figure 4a, Lane 2**).

130
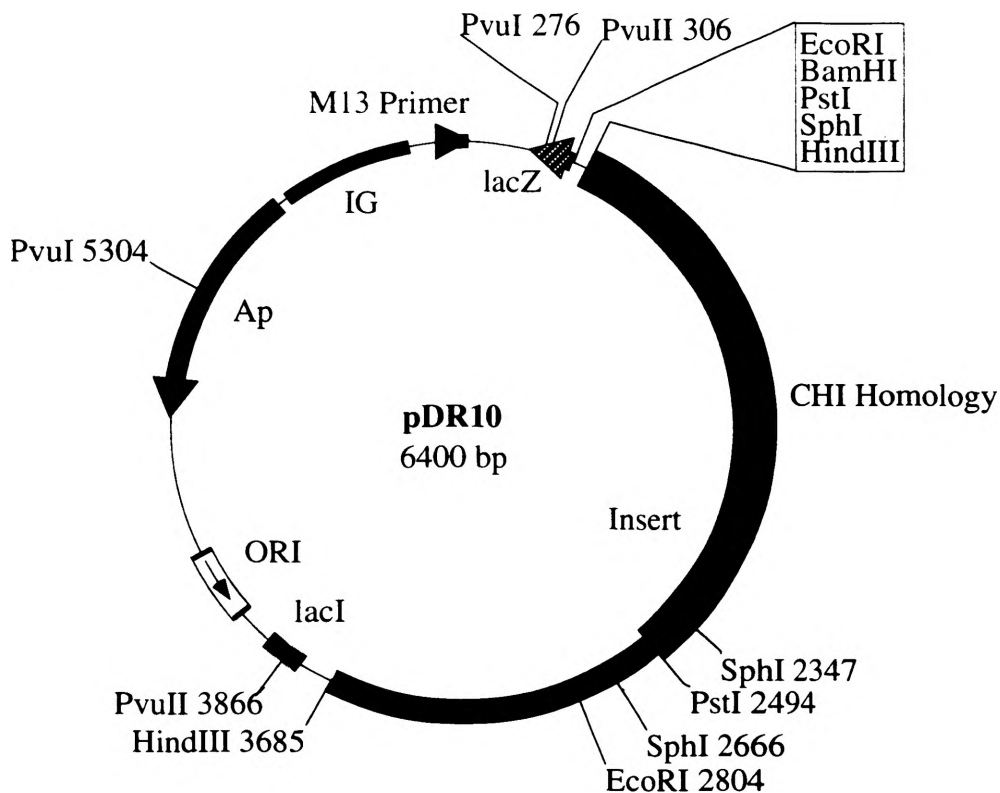
Figure. 3. Diagram of pDR10 Plasmid Showing Region of Homology.

On the Southern blot (**Figure 4b, Lane 2**), we were unable to identify the portion of the plasmid containing the gene because the similar size of the fragments caused them to run in close proximity on the gel. It is apparent from Figure 4b, lane 2 that only one band is hybridizing but without an appropriate control, we could not conclude that it was the band corresponding to the insert and not the vector. We then generated the second restriction, using the pDR10 plasmid digested with *Hind*III and *Eco*RI restriction endonucleases, producing three separate digestion fragments of distinctly different sizes: one containing approximately 3162 bp, a second composed of 2307 bp, and the third containing 931 bp (**Figure 5a, Lane 3**). On the second Southern blot we were able to clearly identify that the 2307 bp fragment (**Figure 5b, Lane 3**) contained the CHI homology.

Conclusions

The restricted DNA fragment that indicated homology lies between the larger and smaller bands allowing us to deduce the approximate location of the gene on the 2307 bp fragment. Another lane on the same gel, shows a *Hind*III/*Pst*I digestion of a plasmid that has the 1991 bp *Pst*I fragment removed. The observation that no hybridization occurred in this lane indicates that the area containing the CHI gene is a 1983 bp segment located in the region between the *Hind*III area of the multicloning site and the *Pst*I site on the inserted fragment (**Figure 3**).

Problems to be Addressed

There are, however, several different things we are unable to decipher from our results. We do not know if the entire gene is included on the 1983 bp strand. The pCHI1 fragment used as a probe is only composed of 86 % of the
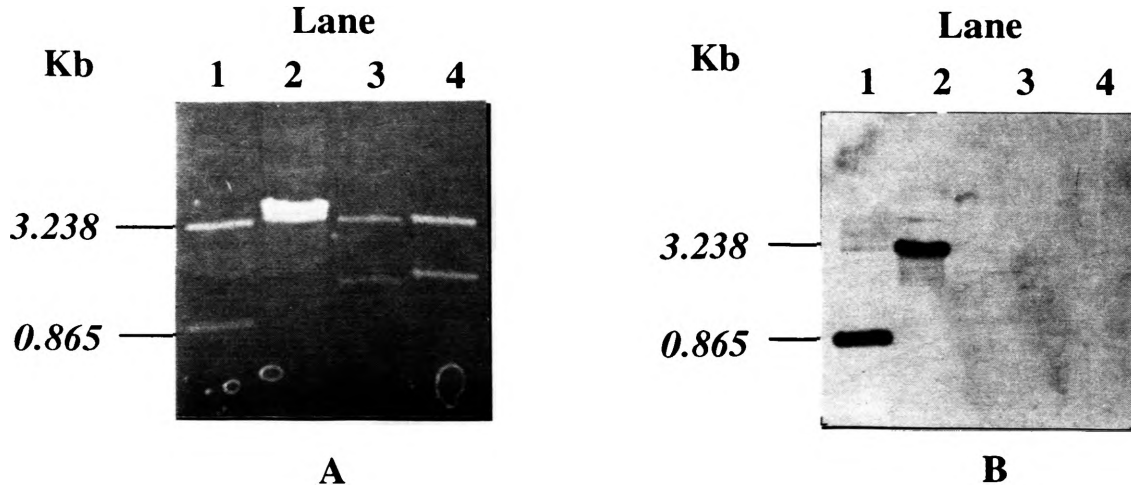
Figure. 4. **Diagram of Electrophoresis Gel (A) and Corresponding Southern Blot (B).**
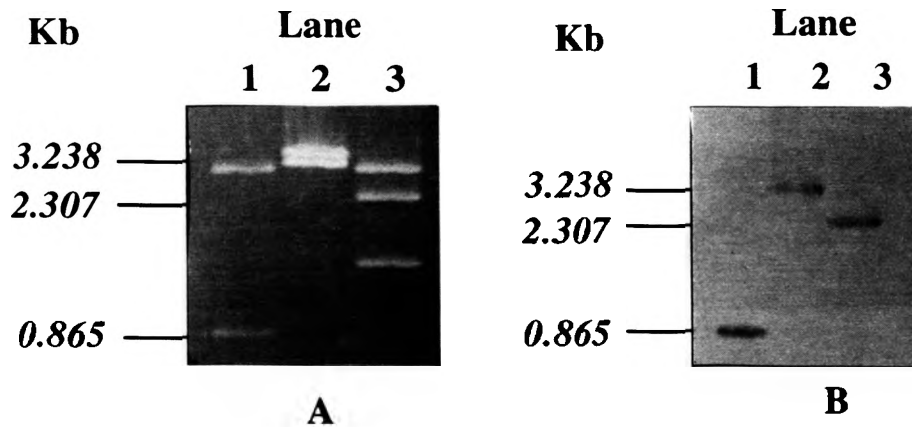
Figure. 5. **Diagram of Electrophoresis Gel (A) and Corresponding Southern Blot (B).**

entire CHI gene [4]. This means that there is 14 % of the gene that we are unable to account for. We are also unable to determine if any of the segment we have isolated includes one or more introns. In *Petunia hybrida*, two separate CHI genes have been isolated: CHI-A and CHI-B. The *P. hybrida* non-allelic CHI genes contain zero and three introns respectively [2]. In *Phaseolus vulgaris*, however, there exists a single CHI gene [2]. If the *G. max* CHI gene demonstrates similarity between the CHI-A of *P. hybrida*, the segment we isolated only contains coding sequences. Likewise, if the *G. max* CHI gene demonstrates similar structure to the CHI-B gene of *P. hybrida*, we have isolated a sequence containing at least one intron and quite possibly three. Since the pCHI1 fragment used as a probe was isolated from *P. vulgaris* and considerable homology was indicated by our experiments, we believe that the *G. max* CHI gene demonstrates several similarities to the CHI gene of *P. vulgaris*.

In order to answer these questions, we are currently working to sequence this gene in its entirety.

MATERIALS AND METHODS

Restriction Endonuclease Digestion and Agarose Gel Electrophoresis

Plasmids (pDR10) were digested with *Eco*RI. *Hin*dIII, *Pst*I, and *Sph*I and pCHI1 plasmids with *Eco*RI in a water incubator at 37 °C for twenty-four hours.

We then loaded the digestions into a 0.7 % agarose gel and applied 150 volts of current for one hour. The gels were then removed from the electrophoresis apparatus, stained using ethidium bromide, and photographed. as seen in figures 4a and 5a.

DNA Probe Preparation

Nick Translation Labeling

We mixed 1 μL of DNA, 6 μL of distilled water, 2 μL of 10X Buffer, 4 μL of dG/dA/dC mix (2 μL of each), 5 μL of biotin-11-dUTP, and 2 μL of Pol I/DNase I mix. We mixed it well by vortexing and incubated it at 15 °C in a water bath. After one hour, we removed the tube from the incubator, added 5 μL of stop buffer and mixed. We then added 75 μL of TNE (Tris-NaCl-EDTA). This mixture was loaded on top of the equilibrated spin column and centrifuged for five minutes at high speed.

Probe Purification by Exclusion Chromatography

We placed a small amount of glass wool into the bottom of 1 mL tuberculin syringe, forcing it to the bottom with the plunger. We then filled the syringe with G-50 Sephadex beads and placed it into a 15 mL Corex tube. At this time, we centrifuged the tube and syringe at high speed for five minutes. We repeated the previous two steps until the packed column reached the 1 mL mark on the syringe. We then loaded 100 mL of TNE on top of the packed column and centrifuged it for five minutes at high speed. We repeated this step a second time. We then placed a decapped Eppendorf tube into the bottom of a clean Corex tube and placed the syringe in the tube, with the bottom of the syringe inside the Eppendorf tube.

Southern Blotting

Transfer

Gels were treated for thirty minutes with 250 mL of 1.5 M NaCl/0.5 M NaOH with one change of solution after fifteen minutes. They were then soaked in 250 mL of 1.5 M NaCl/0.5 M Tris (pH 7.4) for thirty minutes with one change of buffer after fifteen minutes. The gels were then soaked in 6X SSC (0.9 M NaCl/90 mM Sodium Citrate) for fifteen minutes just prior to beginning the transfer procedure. We fabricated a wick (16 cm x 30 cm) from 3MM Whatman filter paper. We then cut three gel sized pieces (7 cm x 8 cm) of 3MM Whatman filter paper and one from nitrocellulose paper. We also cut approximately 7.5 cm of single fold paper towels. The wick was placed on the transfer apparatus and prewet with 6X SSC. The gel was placed, face (well side) down, on the wick. We prewet the nitrocellulose paper in distilled water then in 6X SSC. The nitrocellulose paper was then placed on top of gel ensuring that no air bubbles were trapped underneath. The three pieces of Whatman filter paper were prewet in 6X SSC and placed on nitrocellulose/gel stack. The stack was completed with 7.5 cm of paper towels. A small weight was added to ensure uniform transfer. Plastic wrap was placed over the exposed areas of the Whatman filter paper wick. After twenty-four hours, we disassembled the apparatus and blotted the nitrocellulose with 3MM Whatman filter paper. We then baked the nitrocellulose in an incubator at 80 °C for twenty-four hours.

Prehybridization

We prewet the baked filter in 6X SSC. The filter was then placed into a sealable bag and 10 mL of prehybridization buffer (50 mg Dry Milk/6 mL 20X SSC [3 M NaCl/0.3 M Sodium Citrate]/6 mL distilled water/8 mL Formamide) was added. We removed the trapped air in the bag, sealed it and prehybridized in a 37 °C water bath for twenty-four hours.

Hybridization

We added the nick translated probe DNA to 5 mL of hybridization buffer. We then denatured the probe DNA at 65 °C for ten minutes and quick cooled in ice/water. We removed the prehybridization buffer from the bag, added hybridization buffer, removed trapped air, and sealed. We then incubated the bag in a water bath for twenty-four hours at 37 °C.

Removing Excess Probe

We removed the hybridization buffer and washed the nitrocellulose three separate times in 100 mL of Primary Wash Buffer (2X SSC/0.1% Sarcosyl) for ten minutes each at room temperature with gentle tilting. We washed the filter with three separate treatments of 100 mL of Secondary Wash Buffer (0.1X SSC/0.1% Sarcosyl) for ten minutes each at room temperature with gentle tilting. We then washed the blot in 60 mL of Blocking Buffer (90 µL Tween 20/90 mL Conjugate Buffer) for two hours.

Binding of AP Conjugate

We rinsed the filters in 2X SSC. We then washed the filters in 30 mL of Blocking Buffer three separate times for five minutes each. Next, we incubated the filters in 10 mL of Conjugate Buffer/AVIDx-AP (0.2 g I-Block/0.02 g Sodium Azide/10 mL of 10X PBS/10 µL AVIDx-AP in 100 mL of distilled water) for thirty minutes with gentle tilting. The filters were then washed in 30 mL of Blocking Buffer for five minutes. We then washed the filters in 50 mL of Wash Buffer (0.072 g Sodium Azide/24 mL 10X PBS/0.72 mL Tween 20 in 240 mL of distilled water) four separate times for five minutes each. The filters were then incubated in 20 mL of Assay Buffer, pH 10 (0.025 g $MgCl_2$/0.025 Sodium Azide/1.2 mL DEA in 125 mL of distilled water) two separate times for two minutes each. They were then incubated in 20 mL of Assay Buffer/1 mL Sapphire mixture for thirty minutes with gentle tilting. We washed the filters in 30 mL Assay Buffer two separate times for five minutes each. We then added 50 µL of AMPPD to 5 mL of Assay buffer and incubated the filter in the mix for five minutes.

Chemiluminescent Detection

We drained the solution from the filter. We then placed the filter between two pieces of plastic wrap. The filter was exposed to X-ray film for five minutes in a light-tight cassette. We then developed the autoradiograph using standard procedures. The autoradiographs were then converted into photographs as can be seen in figures 4b and 5b.

REFERENCES

1. Bednar R. A. and Hadcock J. R. (1988). Purification and characterization of chalcone isomerase from soybeans. Journal of Biological Chemistry 263, 9582-9588.

2. van Tunen A. J., Koes R. E., Spelt C. E., van der Krol A. R., Stuitje A. R. and Mol J. N. M. (1988). Cloning of the two chalcone flavanone isomerase genes from Petunia hybrida: coordinate, light-regulated and differential expression of flavonoid genes. EMBO Journal 7, 1257-1263.

3. Frank R. L and Vodkin, L. O. (1991). Sequence and structure of phenylalanine ammonia-lyase gene from Glycine max. Journal of DNA Sequencing and Mapping 1, 335-346.

4. Mehdy M. C. and Lamb C. J. (1987). Chalcone isomerase cDNA cloning and mRNA induction by fungal elicitor, wounding and infection. EMBO Journal 6, 1527-1533.

SPOROMORPHS AND PALYNOLOGICAL INTERPRETATIONS OF LOWER OLIGOCENE STRATA FROM THE EASTERN GULF COAST, U.S.A.

L.M. Reeves
Department of Geology and Geophysics

ABSTRACT

The Vicksburg Group in the eastern Gulf Coast of the United States belongs to one of the most complete and continuous Paleogene strata in the world. Previous studies in this region have neglected the rich palynomorph assemblages of the Lower Oligocene units of the Vicksburg Group. Four samples from Wayne County Mississippi were analyzed for palynological information on the Vicksburg Group. The initial objective of the study was to understand the principles of palynology and the basis for sporomorph identification. A minimum of 300 specimens were counted per slide to determine the distribution of sporomorphs in the sediments. Two hundred and twelve different species of sporomorphs have been identified. The proportion of nonmarine palynomorphs (sporomorphs and fungal remains) relative to marine palynomorphs (dinoflagellates, acritarchs, and microforaminiferal test linings) were also determined in order to evaluate the influence of sea-level fluctuations in the area. The basal unit of the Vicksburg Group (Forest Hill Sand), previously interpreted as deposits of a highstand systems tract, is dominated by nonmarine palynomorphs. This deposit has a high species diversity dominated by Quercoidites. Carya. Mominites. Siltaria. Cupressacites. and Cupuliferoipollenites. Higher units (Mint Spring Marl and Marianna Limestone), considered part of a transgressive system tract, have fewer sporomorph species and are dominated by marine palynomorphs. The assemblage is very rich in two taxodiaceous conifer pollen species resembling Sequoia. Fluctuations in sea-level and sediment supply play a major role in the number of sporomorph taxa recovered from the lithostratigraphic units of the Vicksburg Group. The concentration of the two Sequoia type pollen species can be used to identify transgressive deposition (in particular the Mint Spring Marl and Marianna Limestone) near the Mississippi-Alabama boarder. The prominence of certain pollen taxa (Quercus. Sequoia. Taxodium. Castanea. and Cyrilla) suggest warm, temperate climatic conditions. The climate was, however, cooler than the relatively warm conditions of the Early and Middle Eocene.

INTRODUCTION

The eastern Gulf Coast of the United States (Figure 1) has one of the most continuous exposures of Late Paleogene marine and marginal marine sections in the world. These strata have been part of many extensive biostratigraphic, sequence stratigraphic, and paleogeographic studies using mainly macrofossils and microfossils other than palynomorphs [1,2,3]. Sporomorph biostratigraphy of the Late Paleogene has mostly been neglected in the Gulf Coast, although several studies have been completed by Frederiksen, [4,5], Traverse, [6], Scull *et al.*, [7], and Owens *et al.*, [8]. These biostratigraphic studies of fossil dispersed spores and pollen grains focused mainly on the Jackson Group (Late Eocene) and the Red Bluff and Forest Hill Sand Formations of the Vicksburg Group (Early Oligocene) (Figure 2).

This study presents the initial results of a regional study whose main thrust is the identification and distribution of sporomorphs in all the lithostratigraphic units of the Vicksburg Group. Samples from Wayne County, Mississippi (0.4km NE of Bucatunna Creek) were analyzed for palynological information on the Vicksburg Group. Two hundred and twelve different types of sporomorphs have been identified. The proportion of nonmarine palynomorphs (sporomorphs and fungal remains), relative to marine palynomorphs (dinoflagellates and

acritarchs) has also been determined in order to evaluate the influence of sea-level fluctuations in the area. The sequence stratigraphic framework and terminologies used are those of Pasley & Hazel, [9], Gregory & Hart, [10], and Tew & Mancini, [2].

The study provides the first available sporomorph data for the Mint Springs and Marianna Limestone Formations of Mississippi. The specific objectives of this study were two-fold: 1) to understand the principles of palynology and the basis for sporomorph identification, and 2) to use identified sporomorphs and relative frequencies of marine palynomorphs in the Vicksburg sediments to infer (a) paleoecology of the strata, (b) influence of sea level fluctuation, and (c) paleoclimatic conditions during the Early Oligocene.

Geologic Background

The Lower Oligocene (Rupelian) Vicksburg Group in Mississippi includes the following formations, in ascending order, the Red Bluff Clay, the Forest Hill Sand, the Mint Spring Marl, the Marianna Limestone, the Glendon Limestone, the Byram, and the Bucatunna Clay. (Figure 2). The Red Bluff Clay and Forest Hill Sand are facies equivalent strata that grade into one another laterally and vertically. In Alabama, the Bumpnose Limestone is seen and is also considered to be facies equivalent to the Red Bluff and Forest Hill [2]. As can be seen from Figure 2, all the formations interfinger across the Mississippi-Alabama boarder.

At the Wayne County locality samples from the Forest Hill Sand, Mint Spring, and Marianna Limestone were studied. The Forest Hill Sand was

Figure 1. Location map of studied sections.
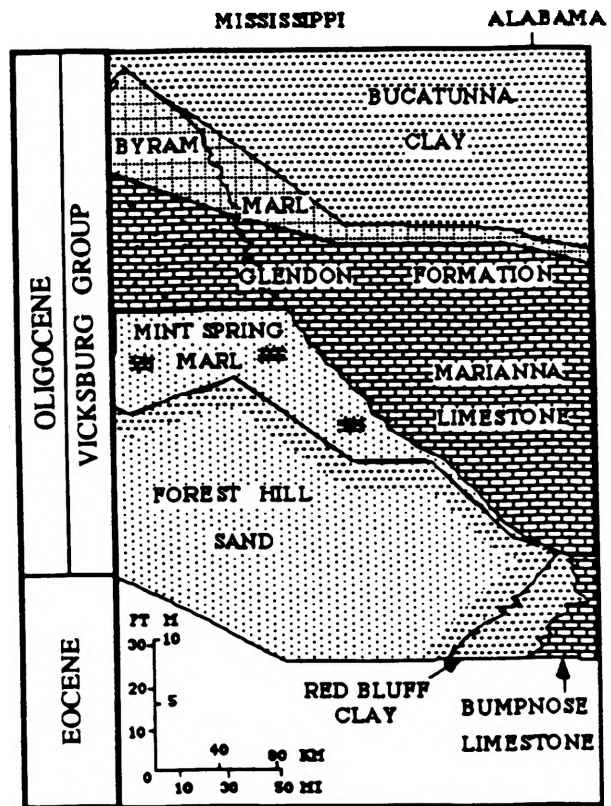
Figure 2. Stratigraphic diagram showing distribution of lithologies and thicknesses of Vicksburg units (modified from Hazel *et al.*, [1]).

136

named by Cooke, [11]. In general, it is a nonmarine to nearshore marine, dark, very fine- to fine-grained sand, silt, and laminated carbonaceous clay with lignite beds near the top and bottom unit [12]. The formation is 100 feet thick in central and western Mississippi and thins to the east [13].

The Forest Hill Sand is disconformably overlain by the Mint Spring Formation. The Mint Spring, also named by Cooke, [11], consists primarily of dark gray, argillaceous to arenaceous, fossiliferous, glauconitic marl [14]. In Wayne County the thickness of the Mint Spring ranges from 1 foot to 17 feet.

The Mint Spring is vertically and laterally gradational into the limestone facies of the Marianna Limestone. The Marianna Limestone, named by Matson and Clapp, [15], is a soft porous, light-gray to white limestone characterized by foraminifera.

METHODS

Samples from Wayne County, Mississippi (0.4km NE of Bucatunna Creek) (Figure 1) were analyzed for palynological information on the Vicksburg Group. At the Wayne County locality the Forest Hill Sand, Mint Spring Marl, and Marianna Limestone were sampled. The samples were collected by the U.S. Geological Survey, and processed by digesting unwanted mineral matter in 32% hydrochloric and 60% hydrofluoric acids, followed by a five-minute oxidation in 35% nitric acid, and concentration with zinc chloride (specific gravity 1.9). The residues were sieved through 10μm nylon meshes before permanent mounts were made.

A minimum of 300 specimens were counted from each slide examined. After counting approximately 300 specimens, the slide was scanned to establish the presence of any rare species. All work was done using transmitted light microscopy on the Nikon optiphot-2 polarizing microscope. Minor work has also been done using scanning electron microscopy. SEM work will become important at the end of the study when new species are described. The specimens illustrated in Plate 1 were photographed at an ASA setting of 100 with Kodak T-MAX 100 film. Photographs were taken with a Nikon UFX-II camera mounted on a Nikon Optiphot-2 polarizing microscope.

Palynological Principles & Basis for Sporomorph Identification

Palynology is the study of organic-walled microfossils; their dispersal and distribution in sedimentary rocks. The bulk of palynology consist of fossilized spores and pollen (sporomorphs); other palynomorphs include dinoflagellates, acritarchs, scolecodonts, and chitinozans (Traverse, [16] Fig. 1.1, p. 23). These microfossils range in size from 5-500μm and are composed of very resistant organic materials such as sporopollenin and chiten. This study focused mainly on the identification of sporomorph species present in the sediments; other palynomorphs were recognized, but were used only for interpretation purposes. We are able to study fossilized spores and pollen because of their following characteristics.

1. Spores and pollen are found everywhere in Silurian to Recent sediments.
2. Spores and pollen are often more abundant than other fossils found in the rock.
3. Spores and pollen walls (exines) have a greater resistance to degradation than most other plant parts, thus facilitating their survival as fossils.
4. Spores and pollen have a complex morphology that allows them to be distinguished and categorized.

137

The underlying assumptions of palynology are the same as those in other areas of paleontology: a trust in the present as being indicative of the past, and a belief that fossils are elements of a continuum of once-living organisms whose succession was shaped by evolution.

A fossil spore or pollen grain is basically a hollow, tough, variously ornamented, and grooved ball, from which the contents (inner wall layers and protoplasm) have been removed through biodegradation. As a fossil the ball is usually squashed flat (like a pancake) and variously contorted [16]. The identification of spores and pollen is dependent on the features mentioned above. The grooved portions of the ball are referred to as apertures; they are attributed to the openings or thinnings in the sporomorph wall used in germination or to accommodate size changes due to humidity. There are basically two types of apertures for pollen grains: colpi (furrows) (Plate 1. fig. 15-21) and pores (pits) (Plate 1. fig. 12-14). In spores the aperture is referred to as the laesura. The form, position, and number of the apertures is the main key used in classification. The various ornaments on the ball called sculpture, are modifications in the sporomorph exine wall. They could be scabrate (Plate 1. fig. 15), psilate (Plate 1. fig. 8), baculate (Plate 1. fig. 5,6), or reticulate (Plate 1. fig. 7) among others. The size, shape, and general structure of the ball refer to the basic morphology of the sporomorph, these properties are not always reliable and must be used with caution in sporomorph identification.

RESULTS

Various intervals in the Vicksburg sediments of Wayne County are marked by fluctuations in sporomorph distribution and in relative frequencies between marine and nonmarine palynomorphs (Figure 3). Fourteen taxa dominated the assemblage at this locality. Nonmarine palynomorphs constitute 99% to 99.6% of the palynomorph assemblages in the Forest Hill Sand, the fluvio-deltaic highstand deposit of the Tejas A Gulf Coast (TAGC)-4.3 sequence. The dominant sporomorphs (>3%) are: Sequoiapollenites lapillipites, Sequoiapollenites sp. 1, Momipites corvloides, Carya simplex, Cupuliferoidaepollenites cf. C. selectus, Quercoidites microhenrici, Quercoidites inamoenus, Siltaria cf. S. scabriextima, Siltaria abouziarovae, and Cupuliferoipollenites spp.

The Mint Spring Marl, which is the lower transgressive deposit of the TAGC 4.4 sequence, shows a decrease in the number of sporomorph taxa. Nonmarine palynomorphs constitute only 30.6% of the palynomorph assemblages in the Mint Spring. The nonmarine palynomorphs are dominated by two pollen species Sequoiapollenites lapillipites and Sequoiapollenites sp. 1 which constitute more than 60% of the nonmarine assemblage. The Mint Spring Marl is clearly dominated by marine palynomorphs (Figure 3).

The two Sequoia type pollen species constitute up to 70% of the nonmarine sporomorphs in the Marianna Limestone, also considered to be in the transgressive deposit of the TAGC 4.4 sequence, but again the unit is dominated by marine palynomorphs (>70%). The number of taxa and total numbers of sporomorphs, however, are fewer in the Marianna Limestone than in the underlying Mint Spring Marl (Figure 3).
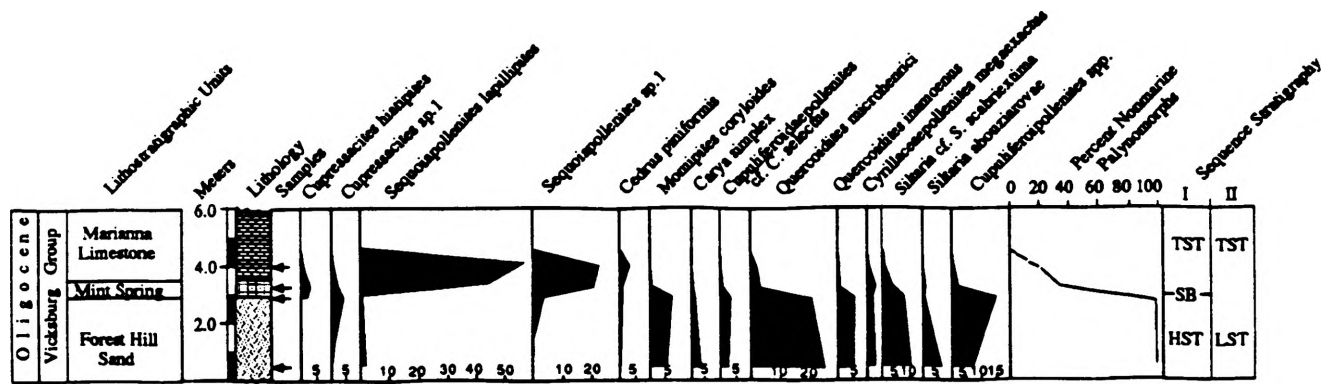
Figure 3. Percent values for dominant sporomorphs, and for total nonmarine palynomorphs in the Wayne County locality. Sequence stratigraphic interpretations I and II are those of Tew and Mancini (1992) and Pasley and Hazel (in review); HST=highstand systems tract; TST=transgressive systems tract; LST=lowstand systems tract; SB=sequence boundary; C.S.=condensed section (modified from Oboh and Reeves in review).
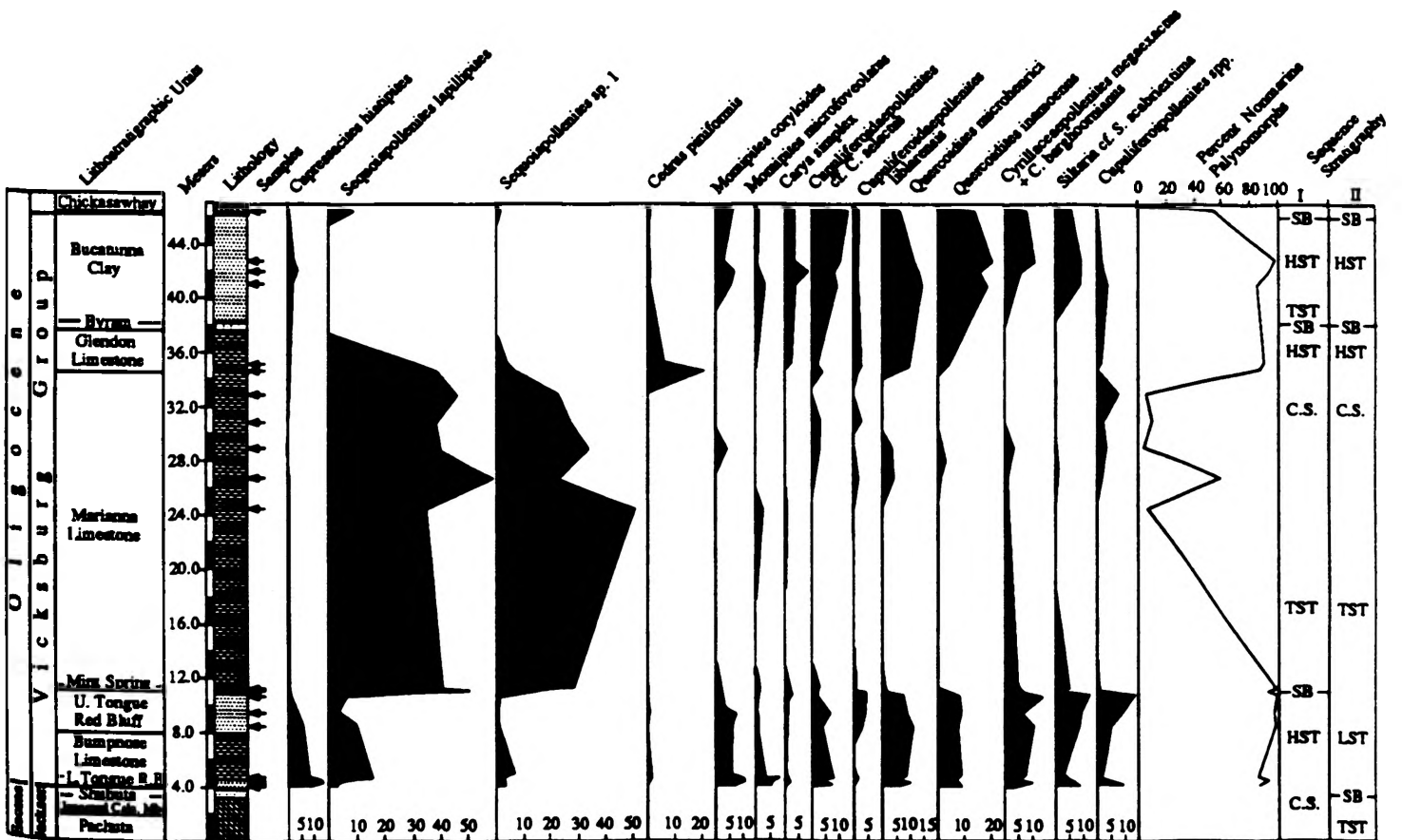
Figure 4. Percent values for dominant sporomorphs, and for total nonmarine palynomorphs in the St. Stephens Quarry. Sequence stratigraphic interpretations I and II are those of Tew and Mancini (1992) and Pasley and Hazel (in review); HST=highstand systems tract; TST=transgressive systems tract; LST=lowstand systems tract; SB=sequence boundary; C.S.=condensed section (modified from Oboh and Reeves in review).

DISCUSSION

The main parameters that had a significant effect on the vegetation record in the eastern Gulf Cost were sea-level fluctuations and climate (see discussion below). During a rise in sea-level terrestrial palynomorphs were at a minimum in the samples; during sea-level highstand and progradation their relative frequencies increased (Figure 3). These fluctuations record a change in sea-level and do not necessarily reflect a change in the vegetation of the area.

TABLE I. Dominant taxa (>3%) of the Vicksburg assemblage.

Taxa	Botanical Affinity
Cicatricosisporites dorogensis	Schizaeaceae (Anemia or Mohria)
Cupressacites hiatipites + Cupressacites sp. 1	Taxodiaceae (Taxodium, Glyptostrobus)
Sequoiapollenites lapillipites + Sequoiapollenites sp. 1	Taxodiaceae (Sequoia, Metasequoia, or Cryptomeria)
Cedrus piniformis	Cedrus
Picea grandivescipites	Picea
Momopites coryloides + M. microfoveolatus	Juglandacae (Alfaroa, Oreomunnea)
Carya simplex	Juglandaceae (Carya)
Ulmipollenites thompsonianus	Ulmaceae (Planer, Zelkova)
Parsonidites conspicuus	Apocynaceae, Balanophoraceae
Cupuliferoidaepollenites liblarensis + cf. C. selectus	Probably Fagaceae
Quercoidites microhenrici + Q. inamoenus	Fagaceae (Quercus or extinct genus Dryophyllum)
Cyrillaceaepollenites megaexactus + C. barghoornianus	Cyrillaceaaea (Cyrilla)
Siltaria cf. S. scabriextima	Possibly Anacardaceae (Rhus)
Cupuliferoipollenites spp.	Fagaceae (Castanea, possibly extinct genus Dryphyllum)

The dominant taxa (>3%) in the Vicksburg assemblage are attributed to the extant genera and families listed on Table I. The palynofloral assemblage is dominated by pollen of Juglandaceae, Fagaceae, Taxodiaceae and Cyrillaceae families. Minor elements include palynomorphs related to Pinus, Abies, Tilia, Ilex, Pterocarva, Platanus, Fraxinus, Sphagnum, Lygodium, Pteris, Podacarpus, Muriophyllum, Amanoa, Nyssa, Alnus, Ephedra, Gramineae, and Juglans. In generally, fungal remains (spores, hyphae and mycellia), bryophyte and pteridophyte spores are less common than angiosperm and gymnosperm pollen. The most common spores are Cicatricosisporites dorogensis, Laevigatorsporites haardti, and Lygodiumsporites adriennis. The sporomorph assemblage is warm temperate in composition and contains mixed mesophytic elements. Sequoia type pollen and Quercus are the most prominent elements in this assemblage

Sequoia dominates the transgressive deposits of the Mint Spring Marl and Marianna Limestone [17]. The concentration of Sequoia is possibly a result of abundant production on land at that time, and their easy dispersal into offshore environments represented by these sediments. If further work on other localities in Mississippi and Alabama reveals that this concentration is indeed unique to the two lithostratigraphic units, then Sequoiapollenites lapillipites and Sequoiapollenites sp. 1 can be used as markers for the Mint Spring Marl and Marianna Limestone across the entire eastern Gulf Coast.

The Middle Eocene to Early Oligocene experienced major changes in global climate. Evidence of climatic deterioration (from plant megafossils and sporomorphs) during the Late Eocene and Early Oligocene have been documented by Wolfe, [18], Wolfe & Poore, [19], Norris, [20], and Frederiksen, [21,22]. A change in the flora and vegetation began late in Jacksonian time and apparently was completed before the beginning of Vicksburgian time. The flora changes show a rise in the relative frequency of an oak-like pollen species (Quercoidites) and a concentration of angiosperm taxon last appearance leading to a decrease in the total taxon diversity. All this evidence points to a rapidly cooling climate at the end of the Eocene. Sporomorph assemblages from Wayne County, Mississippi show a continuation of this cooler climate into the Lower Oligocene.

Quercus pollen, as discussed above, has been used to infer a cool and perhaps dry temperate climate condition in the Gulf Coast, relative to the Early and Middle Eocene, which were quite warm [22]. Since Quercus is seen as a prominent component of the sediments studied, the cooler climatic conditions of the late Eocene have continued into the Lower Oligocene of Mississippi. However, grass pollen, Ephedra, Abies, and other pollen which typify dry conditions [23] are insignificant in the Vicksburg assemblages,

Observation from the Wayne County locality are confirmed by similar results from the St. Stephen's Quarry locality in southwestern Alabama looked at by advisor Dr. Francisca Oboh (Figure 4). Differences in the domination of marine sporomorphs in the Mint Spring Marl of Mississippi (69.4%) compared to only about 10% in Alabama is a result of transgression from the western part of the study area towards the east. Consequently, the Mint Spring is thicker in Mississippi, while the section in Alabama where nonmarine palynomorphs dominate the assemblage are thinner and represent a more marginal facies.

The sequence stratigraphy of the area has recently been revised by Pasley and Hazel, [24]. Using regional stratigraphic relationships and graphic correlation of biostratigraphic data, they identified the Eocene-Oligocene boundary as the sequence boundary between the Shubata Clay and the Bumpnose Limestone/Red Bluff Clay. Pasley and Hazel have also interpreted the Bumpnose Limestone/Red Bluff Clay and Forest Hill as lowstand systems tracts and the base of the Mint Spring as a transgressive boundary, rather than a sequence boundary (Figure 3). These new interpretations disagree with earlier work done on the section by Loutit et al., [25], Tew and Mancini, [2], and others. Results of the Wayne County locality support the new sequence stratigraphy of the area, since fluctuations in the relative frequencies between nonmarine and marine palynomorphs appear to be similar for most sections of a lowstand and highstand systems tract (Gregory & Hart, [10], Fig. 14).

CONCLUSIONS

1.) The number of sporomorph taxa from the lithostratigraphic units of the Vicksburg Group can be related to fluctuations in sea-level and climate.

2.) The concentration of the two Sequoia type pollen species can be used to identify transgressive deposits (in particular, the Mint Spring Marl and Marianna Limestone) in southwestern Alabama and southeastern Mississippi.

141

3.) Palynology. used with other stratigraphic criteria, can be a useful sequence stratigraphic tool.

4.) Results from the Wayne County locality are confirmed by similar results from the St. Stephen's Quarry in southwestern Alabama.

ACKNOWLEDGMENTS

REFERENCES

1. Hazel,J.E., Mumma,M.D., and Huff,W.J., 1980, Ostrocode biostratigraphy of the Lower Oligocene (Vicksburgian) of Mississippi and Alabama: Transactions of the Gulf Coast Association of Geological Societies, v. 30, p. 361-401.

2. Tew, B.H., & Mancini, E.A., 1992, An integrated lithostratigraphic, biostratigraphic, and sequence stratigraphic approach to paleogeographic reconstruction: Examples from the Upper Eocene and Lower Oligocene of Alabama and Mississippi. Transactions of the Gulf Coast Association of Geological Societies, v. 42, p. 735-756.

3. Miller,K.G., Thompson,P.R., and Kent,D.V., 1993, Integrated Late Eocene-Oligocene stratigraphy of the Alabama Coastal Plain: correlation of hiatuses and stratal surface of glacioeustatic lowerings. Paleoceanography, 8:313-331.

4. Frederiksen,N.O., 1980a, Sporomorphs from the Jackson Group (Upper Eocene) and adjacent strata of Mississippi and western Alabama: U.S. Geological Survey Professional Paper, v. 1084, 75p.

5. Frederiksen,N.O., 1988, Sporomorph biostratigraphy, floral changes, and paleoclimatology, Eocene and earliest Oligocene of the eastern Gulf Coast: U.S. Geological Survey Professional Paper, v. 1448, 68p.

6. Traverse,A., 1955, Pollen analysis of the Brandon lignite of VT: U.S. Bureau of Mines Report of Investigations, v. 5151, 107p.

7. Scull,B.J., Felix,C.J., McCalab,S.B. and Shaw,W.G., 1966, The interdiscipline approach to paleoenvironmental interpretations: Transactions of the Gulf Coast Association of Geological Societies, v. 16, p. 81-117.

8. Owens,J.P., Bybell,L.M., Ager,T.A., Sugarman,P., Paulachok,G. and Gonzalez,V.M., 1988, Stratigraphy of the sediments in a 945-foot hole near Mays Landing in the southeast New Jersey coastal plain: U.S. Geological Survey Professional Paper, v. 1484, 39p.

9. Pasley,M.A. and Hazel,J.E., 1990, Use of organic petrology and graphic correlation of biostratigraphic data in sequence stratigraphic interpretations: examples from The Eocene-Oligocene boundary section, St. Stephen's Quarry, Alabama: Transactions of the Gulf Coast Association of Geological Societies, v. 40, p. 661-683.

10. Gregory,W.A. & Hart,G.F., 1992, Towards a predictive model for the palynologic response to sea-level changes: PALAIOS, v. 7, p. 3-33.

11. Cooke,C.W., 1918, Correlation of the deposits of Jackson and Vicksburg ages in Mississippi and Alabama: Journal of the Washington Academy of Science, v.8, p. 186-198.

12. MacNeil,F.S., 1944, Oligocene stratigraphy of southeastern United States: American Association of Petroleum Geologist Bulletin, v.28,p. 1313-1354.

13. Copeland,C.W., and Deboo,P.B., 1967, Summary of the upper Paleogene and lower Neogene stratigraphy of Alabama, in Jones, D.E. editor, Geology of the Coastal Plain of Alabama: Geological Society of America, 80th Annual Meeting, New Orleans, Louisiana, Alabama Geological Society Guidebook 5b, University, Alabama, p. 44-46.

14. May,J.H., 1974, Wayne County geology and mineral resources: Mississippi Biological, Economic, and Topographical Survey Bulletin 117, p. 13-184.

15. Matson,G.C. and Clapp,F.G., 1909, a preliminary report on the geology of Florida with special reference to the stratigraphy: Florida Geological Survey, 2nd Annual Report, p. 25-173.

16. Traverse, A., 1988, Paleopalynology, Allen & Unwin Inc. 600p.

17. Oboh,F.E. and Reeves,L.M., In review, Correlation between Sequoia type pollen and Lower Oligocene transgressive deposits in the eastern Gulf Coast: Submitted to PALAIOS.

18. Wolfe,J.A., 1978, A paleobotanical interpretation of Tertiay climates in the Northern Hemisphere: American Scientist, v. 66, p. 694-703.

19. Wolfe, J.A. and Poore, R.Z., 1982, Tertiary marine and nonmarine climatic trends. In: Climate in Earth History, National Academy Press, Washington D.C., p. 154-158.

20. Norris,G., 1982, Spore-pollen evidence for early Oligocene high-latitude cool climatic episode in northern Canada: Nature, v. 297, p. 387-389.

21. Frederiksen,N.O., 1980b, Mid-Tertiary climate of southeastern United States: the sporomorph evidence; Journal of Paleontology, v. 54, p. 728-739.

22. Frederiksen,N.O., 1991, Pulses of Middle Eocene to earliest Oligocene climatic deterioration in southern California and the Gulf Coast: PALAIOS, v. 6,p. 564-571.

23. Medus,J. and Pairis,J.L., 1990, Reworked pollen assemblages and the Eocene-Oligocene boundary in the Paleogene of the western external French Alps: palaeogeography, Palaeoclimatology, Palaeoecology, 81: 59-78.

24. Pasley,M.A. and Hazel,J.E., In review, Revised sequence stratigraphic interpretation of the Eocene-Oligocene boundary interval, Mississippi and Alabama, Gulf Coast Basin, U.S.A.: Submitted to Journal of Sedimentary Petrology.

25. Loutit,T.S., Vail,P.R., and Baum,G.R., 1988, Condensed sections: The key to age determinations & correlation of continental margin sequences. In, Wilgus, Hastings, Kendall, Posamentier, Ross, & Van Wagoner, Sea-level changes: an integrated approach. SEPM Special Publications No. 42, p. 184-213.

Plate 1

All figures x1000 unless otherwise indicated.

1 Sequoiapollenites lapillinites, R2092C(1), 13.3/108.3.
2 Sequoiapollenites sp.1, R2092C(1), 12.8/117.6.
3 Cupressacites hiatipites, R2096B(1), 5.9/101.3.
4 Cupressacites sp. 1, R2096E, 14.6/112.5.
5-6 ?Baculate sp., R2096B(1), 9.7/110.4 x400.
7 Liliacidites tritus, R2096B(1), 21.2/125.0.
8 Laevigatosporites haardti, R2096B(1), 15.4/101.6.
9 Cicatricosisporites dorogensis, R2096B(1), 10.0/117.4 x400.
10 Polypodiisporited favus, R2096B(1), 10.5/112.1 x400.
11 Cedrus penifuravis, R2092C(1), 11.5/106.8.

12 Carya simplex, R2092A, 9.3/113.9 x400.
13 Momipites coryloides, R2096B(1), 16.5/100.4.
14 Juglanspollenites infrabaculatus, S2043M(BB), 23.2/124.5.
15 Quercoidites inamoenus, R2092A, 21.2/113.7.
16 Quercoidites microhenrici, R2096B(1), 20.6/101/8.
17 Cupuliferoipooenites spp., R2096B(1), 21.4/101.7.
18 Siltaria abouziarovae, R2092B(1), 18.3/101.0.
19 Siltaria Cf. S. scabriextima, R2070AM(1), 18.1/117.9.
20 Cyrillaceiopollenites megaexactus, S2043M(BB), 23.4/127.4.
21 Illex infissa, R2096B(1), 22.0/101.8.
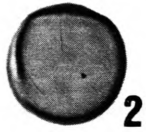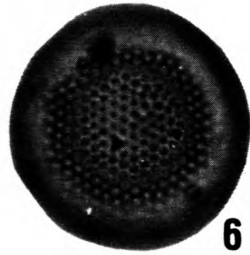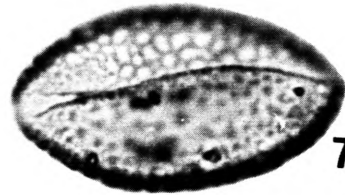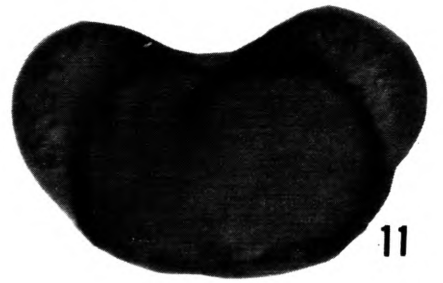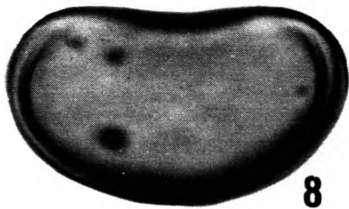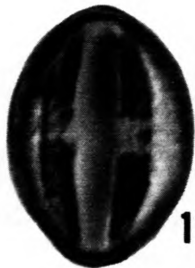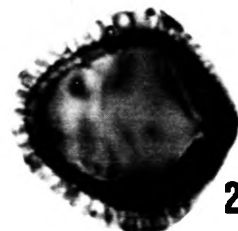
DEVELOPMENT OF A LAUNCH SYSTEM
FOR PERFORMANCE STUDIES OF SMALL AIRCRAFT MODELS

James J. Schneider

Department of Mechanical and Aerospace Engineering
and Engineering Mechanics
University of Missouri-Rolla
Rolla, Missouri   65401

ABSTRACT

This paper presents a design of a launching system that can be employed for performance studies on small aircraft models. Further the article describes a design and development of an aircraft model for use with the system. Initial analysis and testing of the system using the designed aircraft model will be presented.

1. INTRODUCTION

Aircraft design process has progressed to the point where much of the preliminary plan of a new system can be accomplished by theoretical procedures and the use of Computational Fluid Dynamics(CFD). However, it is still necessary to verify mathematical models by conducting tests on physical models.

The purpose of the research was to develop low cost systems and aircraft models to verify theoretical designs. Included in the investigation was the design of the launching system and the development of model aircraft to be used with the launching system. The initial aircraft was an available commercial kit model, powered by a rubber motor, modified as required to operate using the designed launching system. Research has been conducted, and is continuing, to validate theoretical flight performance of the modified model using the designed launching system.

2. LAUNCHING SYSTEM

The purpose of the launching system is to accelerate a small aircraft model to a certain velocity and hence generate the required lift. This system consists of a guidance track, a model carrier, a carrier return mechanism, a retention device, and an arresting setup. Some of the main components of the system are shown in Figure 1. This section presents a brief description of these components and discusses the system performance and use.

2.1 Description of System Components

The launching system is constructed of 8 foot long wood sections. The sections are joined together to form a total track length of 32 feet. Motion on this track is guided by use of 1

145

inch aluminum angle held in place by toggle clamps. To reduce
friction between the carrier and the track, two strips of ultra
high molecular weight polyethylene held in place by the aluminum
angles were employed for the carrier to run on.
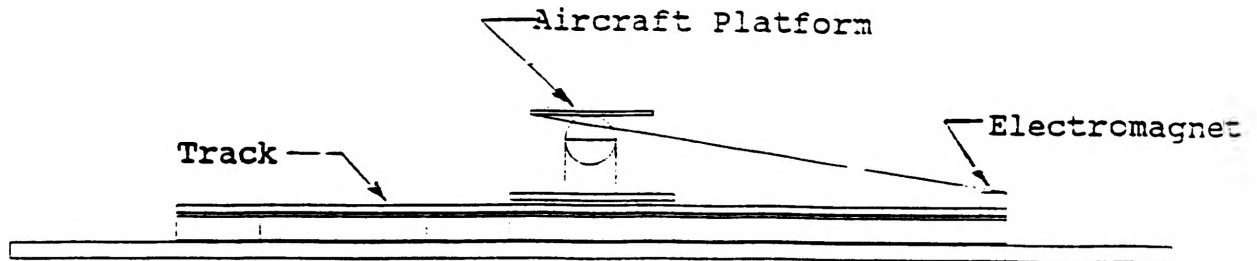
Figure 1   Launching System

To carry a given model and accelerate it to the liftoff
velocity, a cart was designed to travel on the track on one inch
rubber wheels. The top of the carrier is constructed from
plexiglass to serve as a platform on which a model can be mounted
and launched. This platform can be rotated to vary the incident
angle for the model during launch. The aircraft model is held
onto the platform by use of a 1/8 inch wood pin which also holds
the rubber motor powered propeller. The pin is removed from the
cart by means of a predetermined length of a string attached to
the pin.   The length of the string from the release point to the
electromagnet is the distance required to bring the test carrier
cart velocity up to the takeoff velocity of the test-model.

The carrier return mechanism consists of a winch and rope.
The rope is extended and attached to a handle on the carrier by
use of a hook. At the release point the carrier is retained in
place by the use of an electromagnet. This electromagnet is
powered by a 400 ma AC-DC converter. Power is supplied to the
carrier by 5/16 inch diameter latex tubing placed under the
running surface. To absorb the kinetic energy of the carrier a
system of pillows was employed to safely stop the cart at the end
of test runs.

2.2 Performance of the Test-Model Carrier

To determine the position and velocity of the test model
carrier as a function of time, experimental measurements of the
launching force as a function of the model carrier position were
acquired. The force needed to produce such acceleration is
supplied to the cart by mean of a 10.33 foot long stand latex
tubing with 5/16" diameter. The spring constant for the latex

146

tubing was determined by measuring the force required to stretch two 10.33 foot lengths a total distance of 30 feet with measurements Taken every foot. Data taken for the tests is presented in Table I.

Table I   TEST DATA FOR FORCE VS DISPLACEMENT OF LATEX TUBING

Stretched Length feet	Elongation Factor	Elongation Factor^2	Elongation Factor^3	Test Load Data Two Strands lbs				Avg Load 2 Strands lbs	Avg Load per Stran lbs	Measured Force per Strand-N	Curve Fit Force per Strand-N
10.33	1.00	1.00	1.00	0.00	0.00	0.00	0.00	0.00	0.00	0.00	0.00
11.00	1.06	1.13	1.21	1.50	1.20	1.40	1.40	1.40	0.70	3.11	4.06
12.00	1.16	1.35	1.57	3.50	5.10	5.30	4.60	4.63	2.31	10.29	9.21
13.00	1.26	1.58	1.99	5.40	6.30	7.10	6.40	6.30	3.15	14.01	13.80
14.00	1.35	1.84	2.49	7.20	8.60	9.90	9.70	9.43	4.21	18.74	17.90
15.00	1.45	2.11	3.06	9.70	10.20	10.30	10.00	9.80	4.90	21.80	21.53
16.00	1.55	2.40	3.71	10.00	11.40	11.90	11.10	11.03	5.51	24.52	24.76
17.00	1.55	2.71	4.45	11.30	12.20	12.90	12.10	12.23	6.14	27.30	27.54
18.00	1.74	3.03	5.23	12.50	13.40	13.90	13.50	13.33	6.58	29.54	30.20
19.00	1.84	3.35	6.22	14.00	14.40	15.10	14.50	14.53	7.25	32.31	32.50
20.00	1.94	3.75	7.25	15.00	15.50	16.00	15.60	15.53	7.75	34.53	34.58
21.00	2.03	4.13	8.39	15.30	16.50	16.90	16.40	16.35	9.18	36.36	36.50
22.00	2.13	4.53	9.65	16.50	17.50	17.40	17.20	17.18	8.59	38.20	38.30
23.00	2.23	4.95	11.03	17.20	18.00	18.30	18.10	17.90	8.95	39.81	40.04
24.00	2.32	5.39	12.53	18.30	19.10	18.70	19.10	18.80	9.40	41.81	41.75
25.00	2.42	5.85	14.16	18.90	19.70	20.00	19.90	19.63	9.81	43.65	43.48
26.00	2.52	6.33	15.93	19.90	20.90	20.60	20.90	20.60	10.30	45.82	45.30
27.00	2.61	6.83	17.84	20.90	21.70	21.30	21.70	21.38	10.69	47.54	47.23
28.00	2.71	7.34	19.90	21.70	22.50	22.10	22.60	22.23	11.11	49.43	49.34
29.00	2.81	7.88	22.10	22.70	23.50	23.20	23.50	23.23	11.91	51.95	51.66
30.00	2.90	8.43	24.47	23.90	23.90	24.50	24.60	24.20	12.10	53.82	54.26

Notes

1 Unstretched Length = 10.33 Feet

2 Elongation Factor = Stretched Length/Unstretched Length

From the data, the equation of spring force vs displacement was determined, by multiple regression using the software package "Math-Cad":

$$F = -102.70 + 154.42 \times E - 60.28 \times E^2 + 8.86 \times E^3 \quad \dots\dots\dots\dots\dots (1)$$

Using this equation, the force as a function of carrier position, can be determined as shown in Figure 2.
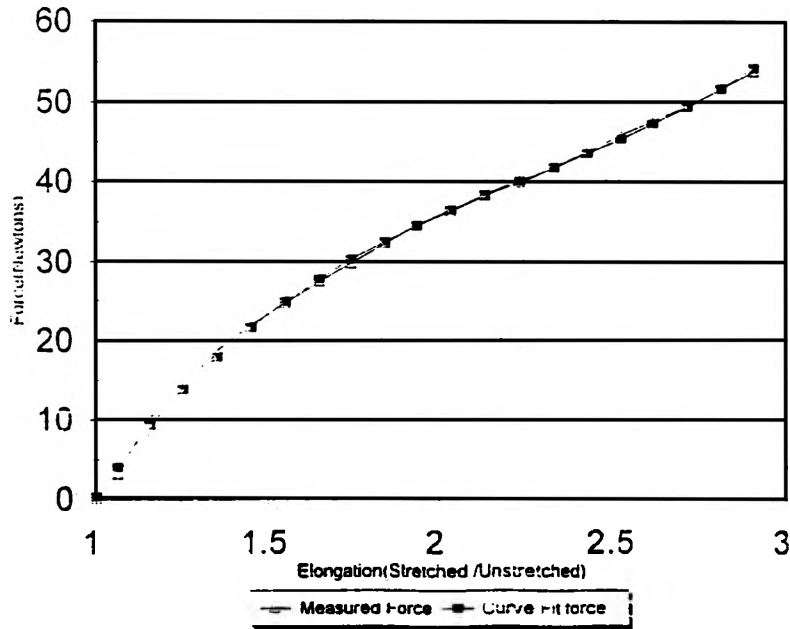
Figure 2 Force vs Displacement of Latex Tubing

This force function was utilized as a source to predict the position and velocity of the test-model carrier, and hence the model performance, during the ground run. To accomplish this objective, the equations[1] that governs the carrier motions were integrated numerically, utilizing the fourth order Runge-Kutta method.

$$F=M \times a \dots\dots\dots\dots\dots\dots\dots\dots\dots\dots\dots\dots\dots (2)$$

$$F_x = \frac{W}{g} \times \frac{dV}{dt} \dots\dots\dots\dots\dots\dots\dots\dots\dots\dots\dots (3)$$

$$T\cos\theta - D - \mu\,(W - L - T\sin\theta_T) = \frac{W}{g} \times V \times \frac{dV}{ds} \dots\dots\dots\dots\dots\dots (4)$$

Sample results of position and velocity of the test model carrier with respect to time are presented in Figures 3a and 3b. The developed computer program can be utilized to conduct parametric studies on the performance of the carrier and examine the dependance of its position and velocity with the initial launching force.

148

a) Position   b) Velocity
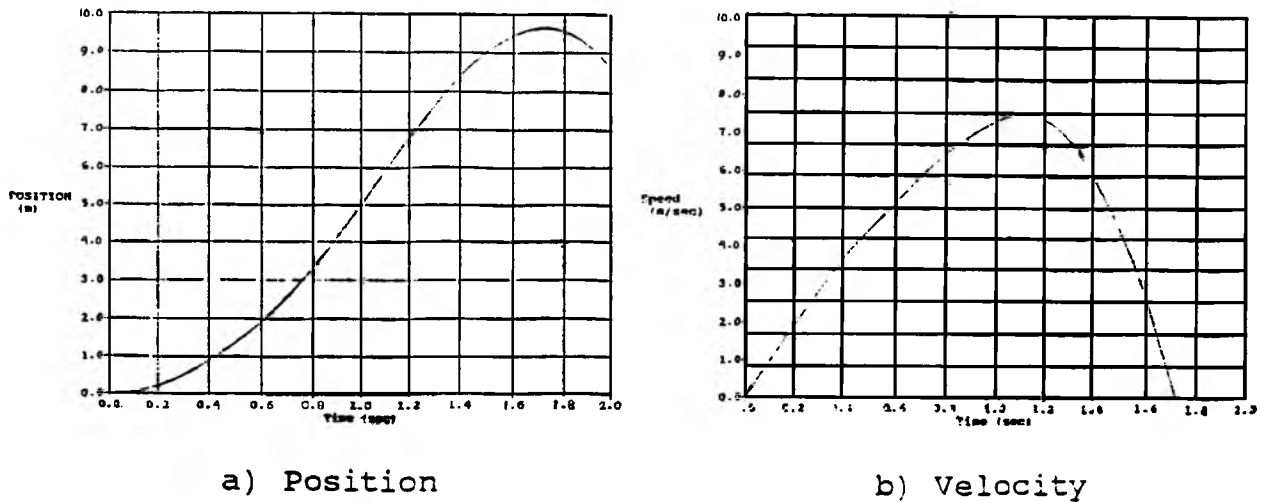
Figure 3   Test-Model Carrier Performance as a Function of Time

2.3 System Operation and Use

The launching system is operated by position the test-model carrier at the launch station, holding it in place by powering the electromagnet and arranging the arresting system. Once the carrier is held in position, the aircraft model is attached to the cart by means of an 1/8" pin. The launching of the carrier is initiated by un-powering the electromagnet which will set the cart holding the model in motion. At the determined point the, the pin holding the aircraft onto the model carrier is pulled out by the string attached to the electromagnet, allowing the model to fly free. The cart continues on to be safely stopped by the arresting setup.

3. AIRCRAFT MODEL SELECTED

The model aircraft that has been tested with the system is a modified version of the rubber powered "Sig Cub"[2] produced by the Sig Manufacturing Co., Inc. of Montezuman, Iowa. The plans for the Sig Cub are provided in Figure 4.

149
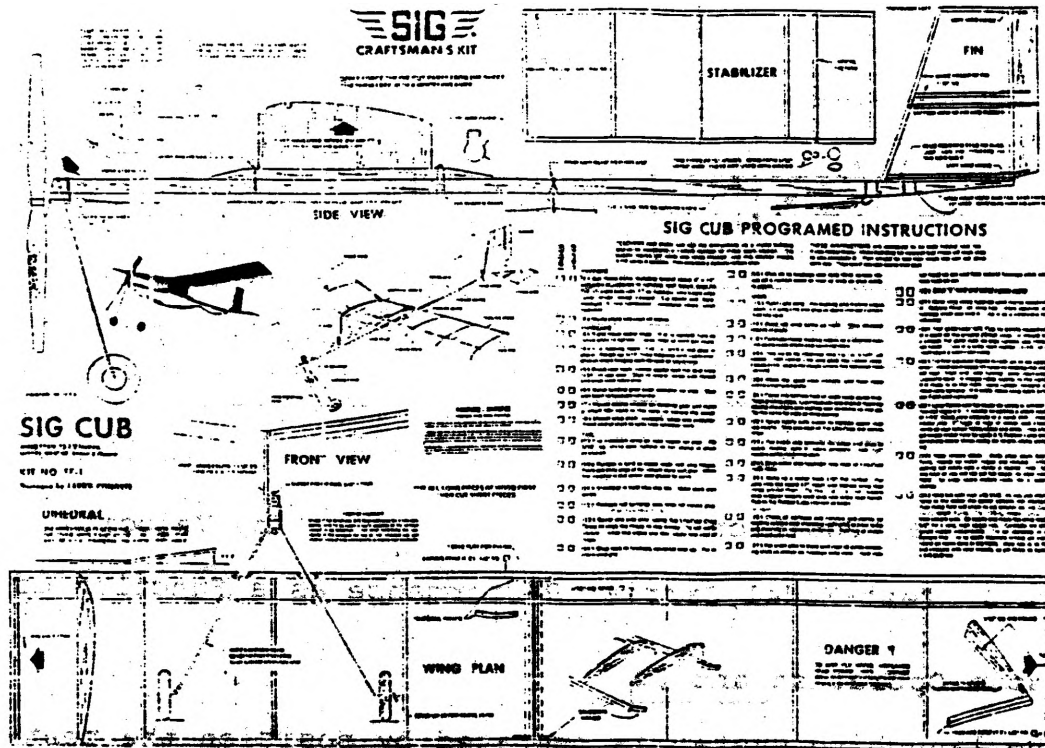
Figure 4   Plans of a Select Aircraft Model(Sig Cub)

Modifications of this model were necessary to make it compatible with the carrier and to enhance the strength of some components. Changes required to make the model compatible with the carrier included moving the rubber motor from the bottom of the fuselage to the side, deleting the landing gear and attaching a block to mount the model on the carrier. Modifications introduced to increase strength include increasing the size of the horizontal and vertical stabilizers and using bass wood instead of balsa for the stick fuselage. An example of design parameters for this model is presented in Table II.

TABLE II DESIGN PARAMETERS FOR THE SELECTED MODEL

ITEM	DESCRIPTION
Wing 　　Area 　　Length 　　Dihedral Angle 　　$C_{L\alpha}$	0.06 square meters 0.60 meters 16.0 degrees 0.074 per degree
Horizontal Stabilizer 　　Area 　　Length 　　$C_{L\alpha}$	0.02 square meters 0.20 meters 0.065 per degree
Vertical Stabilizer 　　Vertical Stabilizer 　　Length 　　$C_{L\alpha}$	0.01 square meters 0.10 meters 0.055 per degree
Weight	0.06 kg

4. ANALYSIS AND PRELIMINARY TESTING

Testing is now underway to determine the determine the required displacement of the carrier cart for liftoff, the position and velocity of the model with respect to time after lift-off and compare these results with theoretical calculations. Parameters that are being varied include weight of the model, incident angle of the model carrier cart and power supplied to the aircraft rubber motor (number of winds of the motor).

4.1 Calculation of Liftoff Distance and Speed

To achieve lift-off the model must be accelerated to at least the stall velocity where enough lift is generated to support the aircraft in flight. The stall velocity required for the aircraft can be written as[3]:

$$V_{stall} = \sqrt{2 \times W / \rho \times S \times C_l} \dots \dots \dots \dots \dots \dots \dots \dots \dots \dots (5)$$

For a margin of safety it is generally recommended that the actual velocity at lift-off be 1.2 times the stall speed. From a review of the airfoil sections presented in "The Comprehensive Reference Guide to Airfoil Sections for Light Aircraft"[4], it was determined that the airfoil referenced as 620, shown in Figure 5, was close enough to the airfoil used on the selected model. The lift slope of this airfoil, $C_{l\alpha}$ was determined to be 0.074.

The required travel of the carrier for to achieve liftoff velocity is found as follows. From the selected weight of the model, and the coefficient of lift from Figure 5, for the chosen

151

angle of attack at lift-off, the required velocity at lift-off is
determined from the above equation. Using the graph of model-
carrier velocity vs time, the required time to reach lift-off
velocity is determined. Then using Figure 3a the carriers
position is read for the required lift-off velocity. A length of
string is measured corresponding to this position. As the model
carrier cart passes this point the pin is pulled out by the
string, attached to the electromagnet, allowing the aircraft to
fly free.
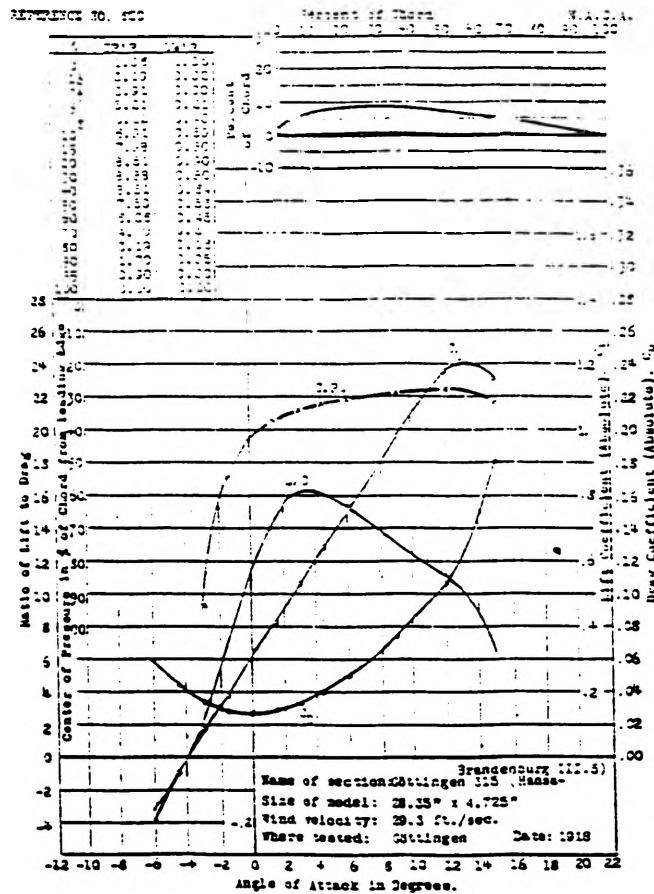
Figure 5   Lift and Drag for the Selected Airfoil Profile

Testing has been started to compare the actual position and
velocity of the model after lift-off with theoretical
predictions. Preliminary results have been achieved concerning
the physical position and velocity of the model at any given
time. The theoretical position of the aircraft with respect to
time is dependent on the thrust produced by the rubber powered
propeller. Although an approximate value of the propeller thrust
has been determined, the value is not accurate enough for
comparison purposes.

152

5. CONCLUSIONS AND OUTLOOK

The system was developed that has the capability of accelerating the designed test-model carrier with predictable energy transfers. Using the predictable energy transfer it is possible to determine the velocity and displacement of the cart as functions of time. The lift-off velocity of the model aircraft is found by using the lift slope of the plane in conjunction with the weight and proposed angle of attack of the wing. With the known required liftoff velocity of the model it is possible to determine the point on the track where the model should be released. After liftoff the position and velocity of the model can be determined theoretically and compared with actual test results.

Future work concerns the design of a pusher canard arrangement for use with the system.

NOMENCLATURE

a = acceleration
C_l = coefficient of lift
$C_{L\alpha}$ = lift slope
D = drag
E = elongation factor
F = force
g = acceleration due to gravity
L = lift
M = mass
s = ground distance
T = thrust
V = airspeed, velocity
W = weight
μ = coefficient of friction
ρ = density

ACKNOWLEDGMENTS

REFERENCES

1. Kohlman, D.L., "Introduction to V/STOL Airplanes", Iowa State University Press, Ames, Iowa, 1989

2. "Plans to the Sig-Cub Kit No. FF-1", Sig Manufacturing Company, Montezuman, Iowa

3. Shevell, R.S., "Fundamentals of Flight", Prentice-Hall Inc., Englewood Cliffs, NJ, 1989

4. "Comprehensive Reference Guide to Airfoil Sections for Light Aircraft", Aviation Publications, Appleton, WI, 1982

DESIGN, CONSTRUCTION, CALIBRATION AND APPLICATIONS OF AN APPARATUS WHICH CONDUCTS THE LARGE MISSILE IMPACT TEST

Mr. John Schroeder, Civil Engineering Department

Abstract

Prior to Hurricane Andrew (August 1992), the South Florida Building Code maintained provisions for the design of building openings based on wind pressure only. Hurricane Andrew provided evidence of other failure modes, including windborne debris and internal pressure. Following the hurricane, several changes were made to building codes in South Florida. One addition requires building openings to resist windborne debris. A missile impact test incorporated into recently accepted Dade and Broward Counties editions of the South Florida Building Code states a window, door, or external protection device shall resist a prescribed number of impacts from a nine pound 2x4 timber accelerated to 50 ft/sec. The design, construction and calibration of an apparatus to conduct this test, as well as its current applications are presented in this report.

INTRODUCTION

The report begins with a brief overview of recent developments in the building codes in South Florida as a result of Hurricane Andrew. It then details the large missile impact test incorporated in these new code provisions. Design criteria used in the development of the apparatus to conduct the missile impact test are stated along with descriptions of the general design and construction processes. Velocity versus pressure curves for the apparatus and external checks of the missile timing system are reported. Recommendations for improvements in accuracy and operating efficiency are made throughout, and a summary of the objectives accomplished is provided.

BACKGROUND

Hurricane Andrew has become the most researched storm in several years. Although meteorologists and engineers disagree on the exact wind speed generated by the storm, the storm contained winds of at least 110-125 MPH. [1] Many people considered the South Florida Building Code [2], at the time Hurricane Andrew roared into Dade County, completely adequate with its design wind speed of 120 MPH. This was the highest design wind speed in the nation. With the devastation well researched and documented [3], the design wind speed was proven not to be the only important feature of the building code and several deficiencies were highlighted.

The code contained no requirements for internal pressure, or impacts from windborne debris. Consequently, many buildings remained structurally sound (no members ruptured), but received severe damage on the interior of the building because the building envelope failed allowing wind and rain to enter. As the winds increased, they began to pick up surrounding materials and subjected the structures not only to intense pressures, but also to a barrage of windborne debris. These missiles included everything from 2x4s to trash cans. The most destruction resulted from roofing tiles and roof gravel. As the buildings were impacted by debris, windows, doors and shutter systems began to fail, creating internal pressure. This, effectively doubled the pressure on some other building components, and promoted further failures.

To avoid similar situations in the future, Dade and Broward counties in South Florida have taken two important steps. The first was adoption of ASCE 7-88 [4], the national standard for loads on buildings which contains provisions for internal pressure. The other major step was to adopt provisions requiring building openings to resist missile impacts, thus assuring the integrity of the building

envelope.

In the new codes in Dade and Broward counties [5,6], a "large" missile impact test along with cyclic pressure loadings are used to determine if particular building products can be used in the lower thirty feet of a structure, where large windborne debris is prevalent. A "small" impact test is used to test building materials utilized above thirty feet. The codes maintain the following large missile specifications:

1. The large missile is to be a 2x4 piece of graded lumber.
2. It must be without knots within 12 in. of the impact end.
3. It is to maintain a weight of 9.0-9.5 lb including the sabot.[1]
4. It shall have a normal impact with a specimen.
5. It is to be accelerated to a speed of at least 50 ft/sec using an air cannon.

The codes also detail the test apparatus:

1. The cannon is to use compressed air to accelerate the missile.
2. It is to be comprised of a compressed air supply, pressure release valve, pressure gauge, barrel, supporting frame, and a timing system.
3. The barrel and frame are to facilitate the aiming of the missile at the desired locations.
4. The timing device is to measure the speed of the 2x4 after exiting the barrel using photoelectric sensors and an electronic clock operating at a frequency of no less than 10 kHz.

Three specimens are to be provided for testing. They are to receive a prescribed number of impacts in specified areas, and then subjected to cyclic pressure loadings. If two of the three specimens tested resist the large missile impacts and the cyclic pressure loadings without forming a crack longer than 5 in. or an opening more than 3 in. in diameter, the product has passed the code and may be certified. For example, a window is to receive two impacts from the 2x4 missile; one within a five in. radius circle located at the center of the specimen, and the other within a similar circle centered in a corner a distance of 6 in. from the supporting members. After the specimen is impacted twice, it is then subjected to cyclic pressure loadings.

DESIGN CRITERIA

At the time of design, specific criteria governing the cannon as stated above were not in place. Therefore, the design was based on a similar existing cannons, and ideas for further improvement. The following design criteria were established to facilitate fabrication of a properly functioning test apparatus:

1. The cannon must accelerate a 2x4 missile weighing 9.0-9.5 lb to the required velocity of 50 ft/sec, and accommodate possible increases in the required velocity due to future changes in building codes.
2. The apparatus must facilitate the aiming of the 2x4 missile to ensure the accurate impact of the missile against a test specimen; impact heights range from approximately 10 in. to 6 ft above the ground.
3. The cannon must be constructed within economic constraints.
4. The cannon must employ a device to accurately time the missile's velocity upon exit from the barrel.

---

[1]A sabot is a plug attached to the trailing edge of the missile which conforms to the basic dimensions of the cannon barrel. It gives the compressed air a larger area to contact and accelerate the missile.

DESIGN AND CONSTRUCTION

Compressed air was chosen as the energy source to accelerate the missile to the required velocity. It was easy to acquire, provided for a safe acceleration within a barrel, and provided a simple means to adjust the resulting missile velocity by regulating the amount of pressure. Another option, a mechanical arm utilizing a spring system was considered, but concerns about the accuracy of the impact, safety, and timing instrument implementation deemed this option incompatible for the situation. Use of compressed air requires a storage tank of large enough volume to provide for proper acceleration of the missile. The necessary containment was estimated. In this calculation, a particular tank size and barrel configuration was assumed and the pressure required to accelerate the missile to the required velocity was found. The calculations were completed using the basic definition of pressure, the ideal gas law, and assuming a twenty percent decrease in available pressure for acceleration due to losses of the air around the sabot and through the pipes and valve. Other assumptions included the amount of friction and air drag present. The results indicated a tank volume of 30 gallons would provide the required air to yield 50 ft/sec with as little as 5 psi pressure.

To provide for possible increases in required missile velocity, variations in missile weights, and adaptations in the barrel configuration, a tank of 50 gallons or more was thought to be necessary. An out-of-service 60 gallon compressed air tank was available for no charge and promptly used. The tank contained two 2 in. diameter outlets on its face; this was in contrast to a single 4 in. diameter outlet considered in design calculations. However, with a 60 gallon tank and the low amount of pressure estimated to be required, the losses involved in the expansion from 2 in. outlets to a 4 in. barrel were relatively insubstantial. The use of the existing 2 in. holes also avoided the expense of creating a 4 in. outlet.

The barrel was chosen to be 4 in. diameter PVC pipe. Other considerations included a sizable rectangular barrel made from aluminum which would have provided a much larger sabot area for the compressed air to accelerate the projectile. This approach would have required a more extensive supporting frame, and a more complicated expansion from 2 in. outlets to a rectangular barrel. These requirements made this option impractical.

With the barrel selected, the transition from the 2 in. outlets to the 4 in. barrel was designed. It consisted of inserting two 2 in. male adapters into the outlets, which were then connected to 2 in. unions. The unions were connected to a 2x4 reducer, thus providing the necessary diameter. The reducers were connected to 90° bends which brought the two sides together into a 4 in. tee. The tee then exited into a female adapter connected to a 4 in. (quarter turn fully open) ball valve. The ball valve was connected to the barrel using a 4 in. steel nipple. This piping network is shown in Figure 1.

PVC schedule 40 pressure fittings were used at all locations with exception to the steel nipple. Schedule 40 PVC provides for pressure capabilities over 200 psi. The pressure fittings contributed a slightly deeper socket and gluing area, thus incorporating additional safety. The steel nipple was used to accommodate the moment present from the weight of the barrel. The 2 in. unions provided for construction ease and the ability to remove the piping from the tank.

The 4 in. (quarter turn fully open) ball valve was chosen in part due to the simplicity of operation. A 4 in. butterfly valve was also considered. The butterfly valve would have provided for a "quicker and cleaner" opening, yielding a better impulse of air. Along with the butterfly valve, a solenoid trigger system was considered; all of these components would increase the accuracy and efficiency of the system. Because of the relative ease of manually controlling a ball valve, these options were not chosen.

The compressed air tank was connected to shop air using a 1/2 in. stop valve. The line enters the tank through a pressure regulator which provides a means of controlling the pressure. A 30 psi pressure gauge was obtained with 0.5 psi increments for accuracy in reading the tank pressure. It was manufactured with a 0.5% error and was chosen to provide repeatable tank pressures. A relief valve set to approximately 20 psi was also included for safety.

157
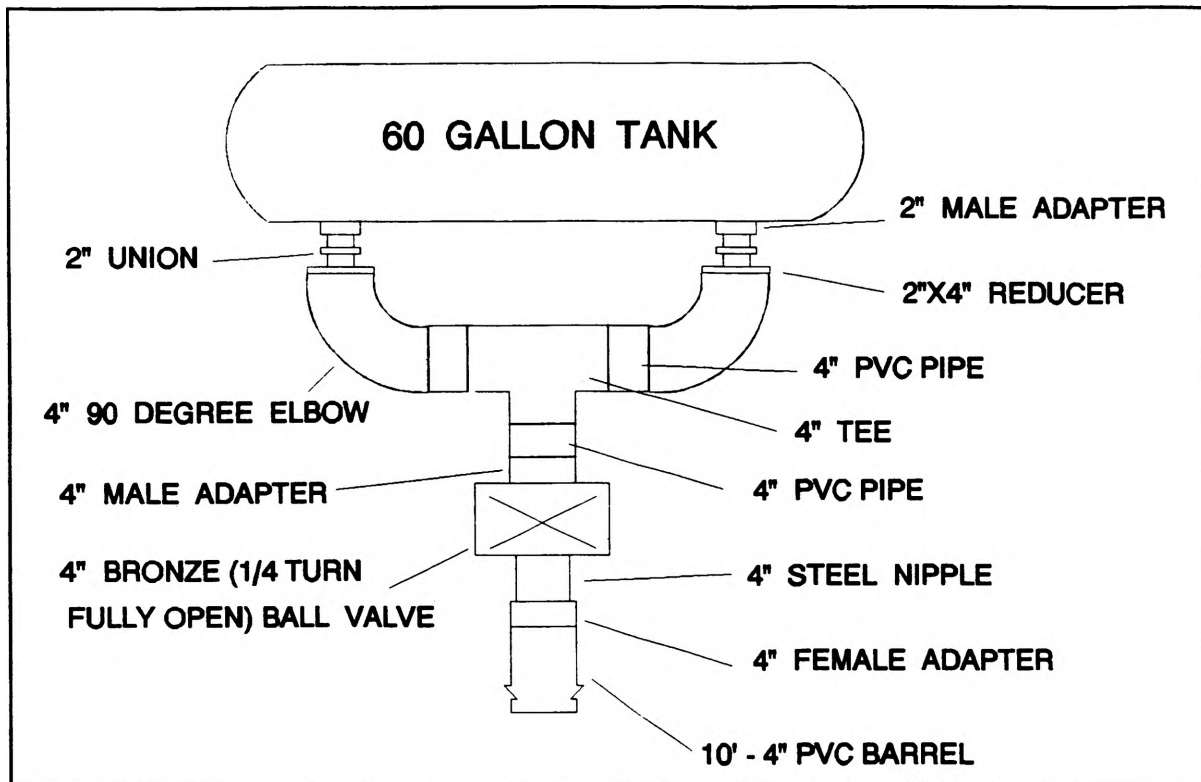
Figure 1. Piping Network

At this stage, the design of a frame was considered. The frame needed to support the vertical loads of the apparatus and the horizontal load due to the "kick"; it also must be maneuverable in all directions. The "kick" was estimated to be a maximum of approximately 300 lb, assuming a constant acceleration of a 9.5 lb missile in a 10 foot long barrel to a speed of 100 ft/sec. The value of 100 ft/sec was used as a worst case scenario. The vertical load was also very small; it was estimated to be less than 500 lb. In order to accomplish maneuverability, the frame was designed to allow the hand forklift already present in the research laboratory to raise and lower the apparatus.

The frame was designed and constructed of 3" steel channel. It supported the air tank and piping system up to the barrel. The majority of the weight was due to the air tank. However, the valve was estimated to weigh approximately 50 lb, and required support to avoid stresses in the PVC connections to the tank. The horizontal "kick" force is transferred to the frame through bolts connecting the air tank and a 4 in. U-bolt tightly fastened around the valve. The frame is raised 4 in. off the ground to allow the forklift to slide underneath. Four swivel casters were also provided to accommodate movement of the apparatus around the lab.

The timer consists of a two sensor array within a diffuser. The 4 in. PVC barrel exits into a 6"x4" reducer and then into the 6 in. diffuser made from PVC pipe as shown in Figure 2. The diffuser's basic function is to allow the compressed air to exit around the sabot and out through the slots provided to avoid acceleration of the missile during the timing process. The timer uses a two sensor array activated by the reoccurrence of light. The sensors are separated by a distance of one foot. As the trailing edge of the missile passes the upstream sensor, an electronic clock, operating at 100 kHz, is started. The missile continues to exit, passing the second sensor; this stops the electronic clock. The digital readout displays a number which corresponds to the electronic clock reading. The inverse of this number is multiplied by 100000 and the velocity of the missile in ft/sec is obtained.

158
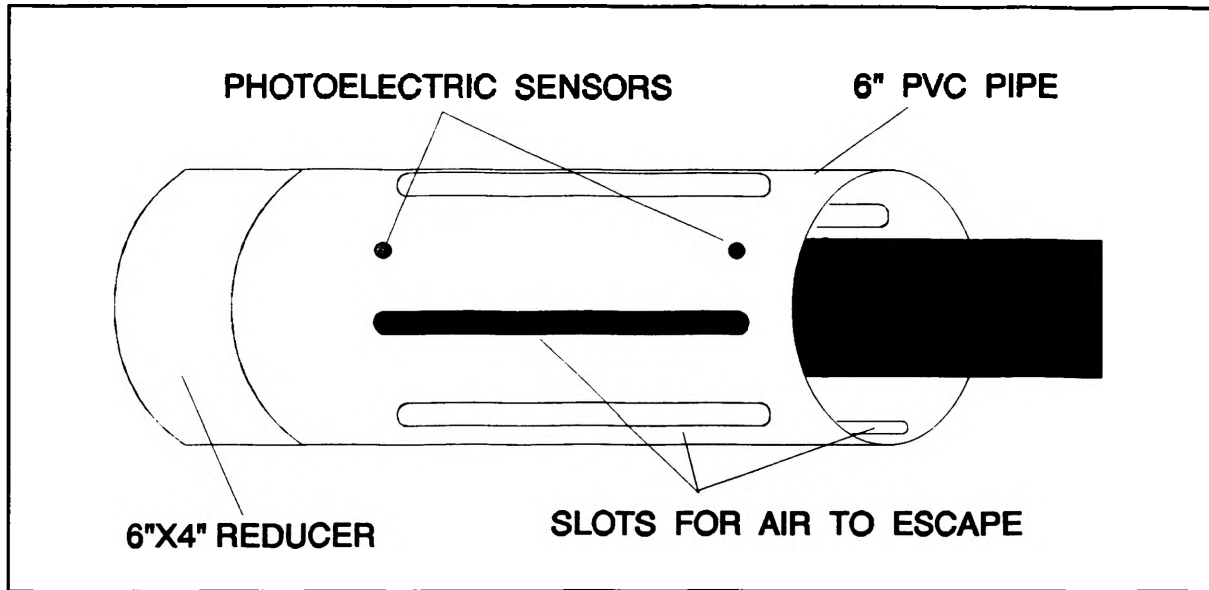
Figure 2. Timer/Diffuser

VELOCITY VERSUS PRESSURE CURVES

The results of the design and construction phase of the project produced an apparatus, as shown in Figure 3, which satisfied the design criteria. Continuing to ready the apparatus for research required the development of velocity versus pressure curves. This task was completed by firing the cannon more than 190 times over a range of pressures and recording the resulting velocities. Procedures and results follow.

Figure 3. Large Missile Impact Apparatus

159

A backstop, as shown in Figure 4, was constructed to absorb the missile impacts during the calibration process. It consisted of about 1.5 ft of compressed cardboard turned on a 90° angle. Under the vertical cardboard was a 1 in. horizontal layer of cardboard, and an oak wood skid. The backstop proved rather poor in its original form. The 2x4 traveled between the vertical cardboard, through a seam, and impacted the horizontal cardboard and the wood skid. Carpeting was later added to alleviate this problem. Although serving its purpose, the backstop deteriorated quickly.
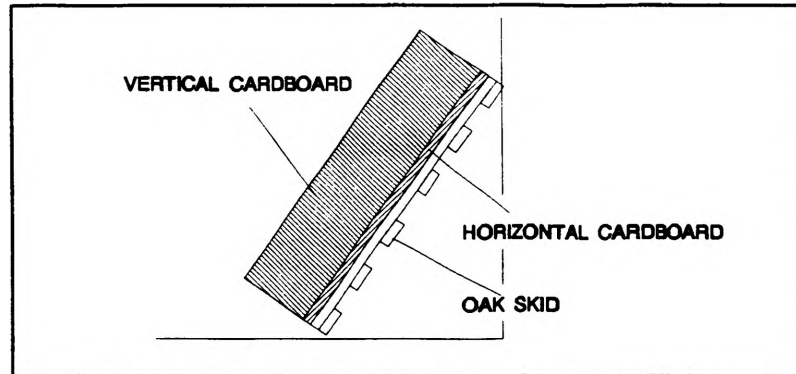
Figure 4. Backstop

The cannon was set-up, and aligned with the backstop. The timer was attached and the air tank was pressurized to a desired level. The cannon was fired, and the timer readout and pressure were recorded. A sample of the data collected is shown in graphical form in Figure 5. Several factors affected the velocity of the 2x4, these included:

1. Manual operation of the ball valve
2. Size and stability of the sabot
3. Weight of the missile
4. Condition of the barrel interior

The obvious variable was the manual operation of the ball valve. When the operator opened the valve as quickly as possible during each firing, the overall effect on the missile velocity was not substantially apparent. With the amount of data collected for individual sabot and 2x4 combinations, there was little deviation within the various sets of data. This result indicated that the effect of manual valve operation was insignificant. However, when the operator opened the valve "slower", deviation from the expected missile velocity became apparent. The valve would release part of the air before it was completely open. This reduced the remaining pressure in the tank without providing for substantial acceleration of the missile. When the valve finally reached the open position, the tank no longer had the required pressure to accelerate the missile to the expected velocity.

The size and stability of the sabot used proved to be a critical variable. Five different sabots were tested throughout 194 shots. They varied in composition from woods; namely plywood, oak and fir; and also included aluminum. Three different types of sabot attachment configurations were used ranging from a simple nail to supporting angles. A final configuration submerged the 2x4 into an aluminum sabot. All configurations are shown in Figure 6.

The plywood and fir sabots deteriorated quickly as they fell to the floor after the missile impacted the backstop. The plywood sabot developed chips along its edge making data repeatability unlikely. The fir sabot cracked after falling to the floor a few times. The oak sabots did not deteriorate in the same manner, but the attachment configuration to the 2x4 proved to be an important factor in the consistency of the results. When the sabots were connected with one common nail the stability of the sabot was deficient and the resulting data showed a wider deviation from the best fit line. When two small angles were used along with the nail, the results were more consistent. The oak sabots split after repeated impacts to the floor.
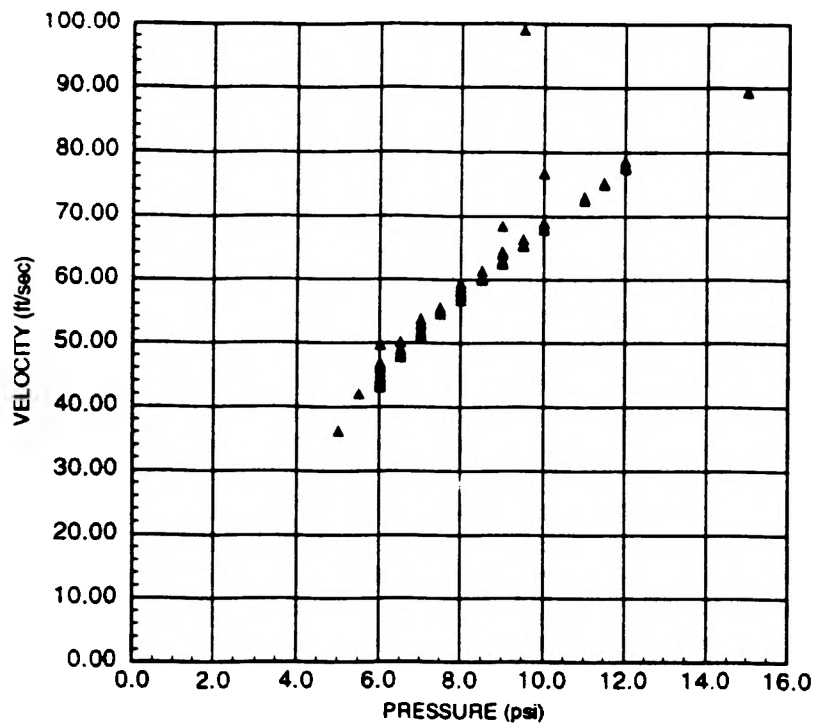
Figure 5. Velocity versus Pressure Curve-Aluminum Sabot

The final sabot was aluminum and the attachment configuration submerged the 2x4 into the sabot. As expected, the aluminum sabot held up superbly and did not loosen throughout the 102 shots performed with it. There was a high degree of consistency in the data as exhibited by a correlation coefficient of 0.95 for the logarithmic best fit line. However, a few shots developed a higher velocity than expected. The anticipated reason is because the sabot was milled to a slightly smaller diameter than the wooden sabots. This process reduced the amount of available contact area for the air. This effect was indicated in the overall data as the aluminum sabot yielded slightly lower velocities for all pressures than the larger wooden sabots. However, the difference in diameter also created enough room for the sabot to get "caught" in the downstream impulse of air and effectively "float", reducing the friction and increasing the velocity. This occurred about 3% of the time. The results are shown in Figure 5.
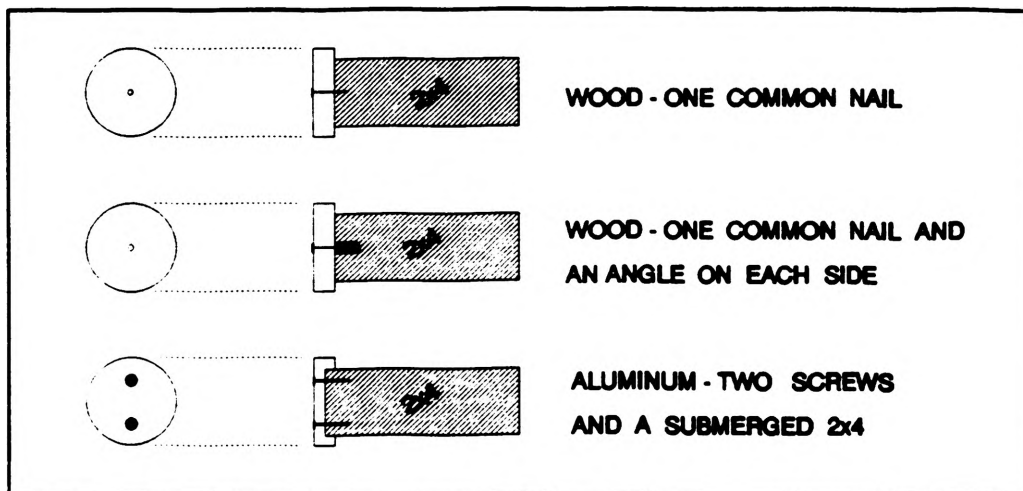
Figure 6. Sabot Attachment Configurations

161

The operator may choose the sabot type for a particular research project, and only a small amount of data is needed to obtain a velocity versus pressure curve for a desired pressure region. In the case of the codes implemented in South Florida the desired velocity of the 2x4 is 50 ft/sec and the required pressure is approximately 6.5 psi depending on the exact sabot used. Recommendations include an aluminum or plastic sabot with a secure attachment configuration and a diameter close to that of the barrel. A cushion placed on the floor will soften the sabot's fall.

The differing missile weights are also a variable. Again, the amount of deviation developed as a the result of a 0.5 lb change in the overall weight was not readily apparent. A final variable in the velocity versus pressure curve was the condition of the barrel. Throughout the 194 shots the same 4 in. PVC barrel was used; its condition deteriorated. The inside of the pipe became scratched, and its surface was no longer smooth. Although this obviously had some effect on the results, no systematic decline in the velocities for a given pressure were observed. Thus, the effect is minor and can be neglected for any research conducted without firing several hundred shots.

EXTERNAL ACCURACY CHECKS

The timer determines the velocity of the final foot of the missile as it exits the barrel. This procedure is important due to the magnitude of acceleration applied to the 2x4 while it is in the barrel. Two external checks on timer accuracy were performed. One was completed by dropping a short length of 2x4 through the timer from a known height and then comparing the timer reading and corresponding object velocity to that given by basic physics. This check was not without flaws. The object was dropped through a 4 in. PVC pipe to ensure proper entry into the timer, and during the descent the 2x4 grazed the sides of the PVC pipe providing friction and effectively slowing the object. This minor amount of contact was neglected and this process was used to calibrate the timer.

The second check completed on the timer utilized a video camera. The cannon was set up in its usual manner and the timer secured to the end of the barrel. The video camera was set up perpendicular to the end of the timer. A 1"x2" piece of wood approximately six feet long was obtained and lines were drawn on it at one foot increments. This piece of wood was attached to the outside of the timer and extended through mid-air. The set-up is shown in Figure 7.
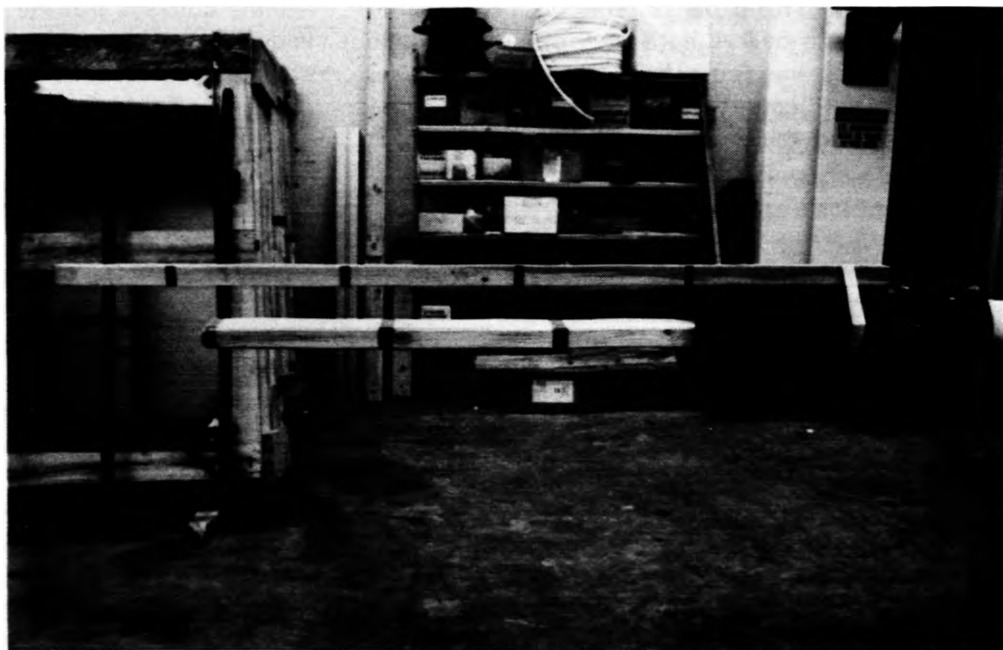
Figure 7. Calibration Set-up

162

The cannon was fired several times while the camera recorded each shot and the corresponding timer reading. The video tape was played back using a frame-by-frame VCR and the end of the missile was observed as it passed the markings on the piece of wood attached to the timer. With the knowledge of the exposure length for each frame of the tape being 0.0333 seconds (or 30 frames per second film speed) and the distance traveled in one frame observed, the approximate velocity of the missile was determined. This velocity was compared to the timer's velocity.

The results indicate the timer is adequate. In general when the trailing edge of the missile was easily viewed using the frame-by-frame VCR, the deviation between the timer velocity and the calculated velocity was less than 2 ft/sec. However, in several shots the approximate position of the trailing edge of the 2x4 was indeterminable. This was due to a "blurring" effect the missile created as it traveled during the exposure length.

CURRENT APPLICATIONS

The cannon is currently being used to provide research data for the American Plywood Association. Various grades, widths, and spans of plywood to be used as external protection devices, or shutters, are tested in accordance with the Dade and Broward counties editions of the South Florida Building Code. The plywood panels are attached to a wooden frame shown in Figure 8 using common 8d nails spaced 6 in. on center. The cannon is used to impact the panels in the center and 6 in. from each edge with a 9.0-9.5 lb 2x4 accelerated to a velocity of 50 ft/sec. Each impact is recorded using a video and still camera, and a written damage log is completed. The exact velocity, weight, and length of the missile are recorded. Penetration is noted, along with dynamic deflection, if applicable.
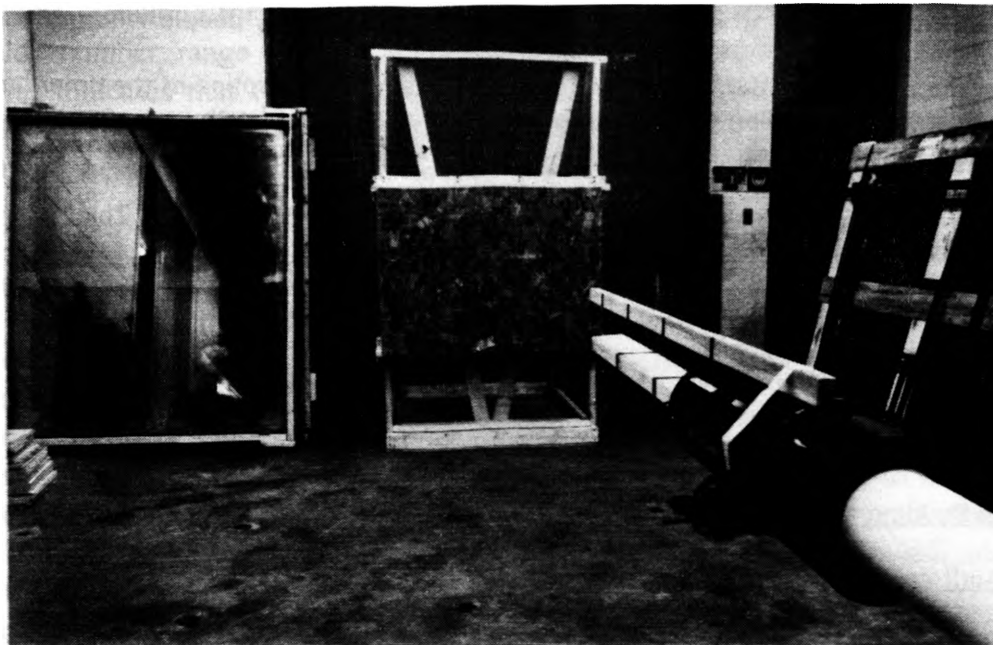
Figure 8. Plywood Backstop

With the first set of tests completed, 5/8 in. Douglas Fir plywood in a 4 foot width and a 4 foot span was able to withstand the center impact, but full penetration occurred when it was impacted in the corner. The 3/4 in. Douglas Fir plywood in a 4 foot width and 5 foot span was able to withstand the center impact, and also resisted the corner impact at times. To date, none of the panels of smaller thickness have been able to resist penetration.

The width and span are important parameters affecting the behavior of the panel. The same

163

panels passing with large widths and spans have failed with shorter widths and spans. This indicates the ability of the panel to absorb the energy of the missile by deflection is critical.

SUMMARY

Building code changes implemented in South Florida require building openings to resist windborne debris, thus preserving the integrity of the building envelope and avoiding the development of internal pressure. Along with these changes, the challenge of product certification is created. One part of the certification process involves a "large" missile impact test which consists of accelerating a 2x4 missile to 50 ft/sec and impacting a test specimen in the appropriate locations.

To accomplish this task, a 60 gallon compressed air tank was acquired. Using existing 2 in. diameter outlets on its face, the tank discharges compressed air through a network of piping which exits through a 4 in. ball valve down a 4 in. PVC barrel. A sabot is used behind the 2x4 to facilitate the required acceleration. Many types of sabots may be used, but the size and stability of the sabot affect the discharge velocity of the missile. The operator should choose the sabot carefully and conduct several calibration shots before beginning a research project to obtain the pressure required to produce the desired velocity. The timer uses a two sensor array within a 6 in. PVC diffuser, and is triggered by the reoccurrence of light. This procedure has proven to effectively time the last foot of the missile as it exits the barrel. The cannon is currently being used to research the ability of different grades, widths and spans of plywood, used in shutter systems, to resist penetration.

Acknowledgements

REFERENCES

Reinhold, Vickery, and Powell, Wind Speeds In Hurricane Andrew: Myths and Reality, Hot Topics Session, American Concrete Institute, Annual Convention, San Juan, Puerto Rico, October 26, 1992.

South Florida Building Code, Dade County Edition, Metropolitan Dade County, Miami, Florida, (1992).

Hurricane Andrew - Preliminary Observations of WERC Post-Disaster Team, Wind Engineering Research Council, Inc, College Station, Texas, September 1, 1992.

Minimum Design Loads for Buildings and Other Structures, ANSI/ASCE 7-88, American Society of Civil Engineers, Approved Nov. 27, 1990.

South Florida Building Code, Dade County Edition, Metropolitan Dade County, Miami, Florida, Adopted Dec. 14, 1993.

South Florida Building Code, Broward County Edition, Broward County, Ft. Lauderdale, Florida, Adopted Feb. 10, 1994.

THE EFFECT OF SPATIAL VARIATION OF THE TURBULENT PRANDTL NUMBER AND CALCULATION METHODS FOR HEAT TRANSFER IN HIGH MACH NUMBER FLOWS

Thomas W. Scott[*]
Aerospace Engineering Dept.
University of Missouri —Rolla
Rolla, MO

ABSTRACT

The effect of using various spatial distributions of the turbulent Prandtl number on the predicted surface heat transfer in the numerical simulation of Mach 4 flat plate flow is studied. The spatial distribution of the turbulent Prandtl number is shown to have a small effect on surface heat transfer, hence suggesting that the standard assumption of a constant turbulent Prandtl number is acceptable for high Mach number boundary layer type flows. In addition, a wall-cell control volume technique for computing heat transfer shows superior predictive capacity across the Reynolds number range when compared to the conventional calculation of surface heat transfer. This indicates that typical levels of refinement now used can be considerably relaxed when calculating heat transfer, with substantial savings in computing resources as well as allowing more accurate assessment of hypersonic vehicle heating loads.

INTRODUCTION

The ongoing development of both airframes and hypersonic propulsion systems (see Figure 1) for high Mach number flight vehicles requires the accurate assessment of vehicle structural cooling requirements. Heat transfer to both external and internal surfaces due to the high stagnation temperatures associated with high Mach numbers has been a difficult quantity to predict and/or measure either experimentally or numerically. The purpose of this work is to examine the effect of varying the ratio of turbulent diffusion of momentum to turbulent diffusion of heat (i.e. the turbulent Prandtl number) on the heat transfer received by a relatively simple geometry in a Mach 4 airflow. Also investigated is the utility of using a wall-cell oriented energy balance in turbulent flow instead of the more conventional temperature gradient approach. Such a formulation has been shown to yield close agreement with data correlations for coarse CFD grids for laminar flows.

Currently, the standard model for numerical heat transfer in high speed flows is based on a constant turbulent Prandtl number, although published work demonstrates considerable spatial dependence of this quantity. Several models for this spatial distribution are available but, unfortunately, show conflicting trends. Blom [1] presents a decreasing variation of the turbulent Prandtl number near the wall in flat plate flow (see Figure 2). It is important to note that Blom's results have been frequently reprinted without reference to the very low flow velocities used in his study (≤ 10.1 m/s). Other studies at somewhat higher speeds (Wassel and Catton [2] and

---

[*] undergraduate research assistant

Simpson [3]) tend to conflict with Blom's results (see Figure 3). With new experimentation methods now being developed, more accurate measurements should soon be available at higher Mach numbers, thus allowing direct correlations between CFD and experiments. This paper compares heat transfer results obtained using several spatial published variations of the turbulent Prandtl number distribution.
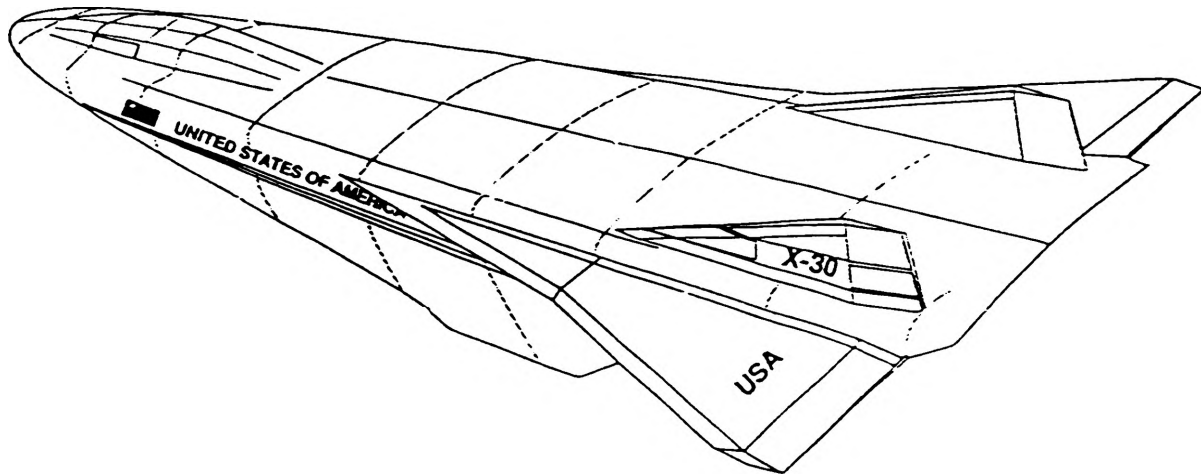
Figure. 1. Conceptual Hypersonic Vehicle Configuration
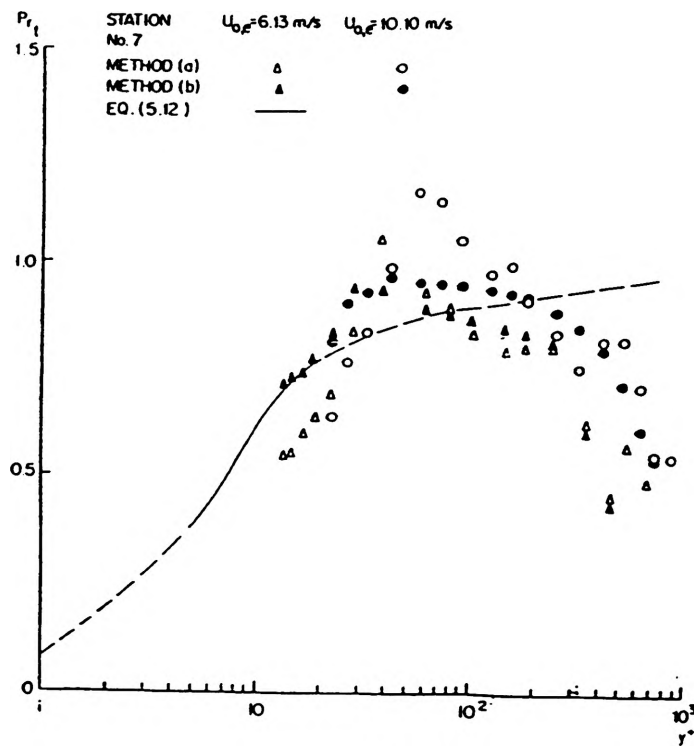
Figure. 2. Blom's Variation of Turbulent Prandtl Number

166
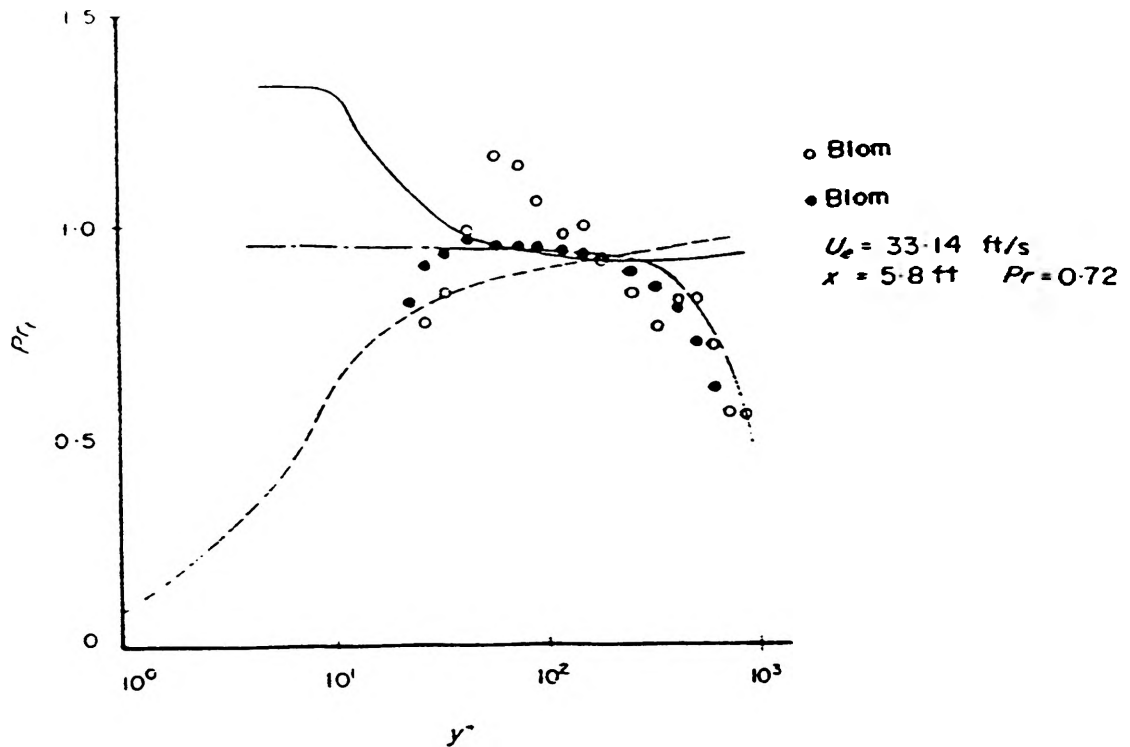
Figure. 3. Spatial Variations of Pr_t Postulated by Wassel and Catton Compared to Blom's Data.

DESCRIPTION OF CODE DOMAIN AND MODIFICATION

Flow Field

A two dimensional isothermal flat plate flow field is simulated numerically by defining a grid with 110 vertical nodes (normal to the plate surface) with a height of 4 cm and a unit width of 1 cm. In order to obtain Reynolds numbers high enough for comparison to van Driest heat transfer correlation, the axial length used in the analysis is approximately 0.5 meters. Inflow Mach number, freestream temperature, plate temperature, and pressure are 4, 964.2 K, 300 K, and 43992.37 Pa, respectively. The laminar Prandtl number is 0.72 for this flow.

Modification of PNS code 'ESCAPE'

The LARC PNS (marching) code 'ESCAPE' is modified to calculate the turbulent Prandtl number based on formulas which are functions of eddy diffusivity of momentum, kinetic viscosity, density, temperature, and the laminar Prandtl number. Eddy diffusivity (or turbulent viscosity) is calculated using the Baldwin-Lomax algebraic model. Constants in the turbulent Prandtl number formulations are modified to match freestream flow conditions ($Pr_t=0.8$ for M=4). Originally the code used a data statement and a constant turbulent Prandtl number. Modifications were performed to allow increases and decreases in the turbulent Prandtl number distribution in the near wall region while maintaining a constant value in the freestream. Many formulations for the turbulent Prandtl number, such as equation (1), Wassel and Catton [2], are valid only in the near wall region or in a decreasing velocity gradient (i.e. approaching the wall) and cannot be used in the entire flow region.

167

$$U = \frac{un}{\sqrt{\dfrac{\mu \cdot \dfrac{d}{dz} un}{\rho}}}$$

$$Pr_t = \frac{\exp(K \cdot U) - 1 - K \cdot U - \dfrac{(K \cdot U)^2}{2} - \dfrac{(K \cdot U)^3}{6} - \dfrac{(K \cdot U)^3}{24}}{\exp(K \cdot U) - 1 - K \cdot U - \dfrac{(K \cdot U)^2}{2} - \dfrac{(K \cdot U)^3}{6}} \qquad K = 0.4 \qquad (1)$$

Wassel and Catton [2] present another formulation that develops an adequate Prandtl number variation throughout the flow field. Originally this formula was written for a decreasing turbulent Prandtl number, equation (2), but, by inversion and defining new constants, can equally well model the decreasing case, equation (3). Due to the extreme experimental uncertainty of the actual magnitude and distribution of the turbulent Prandtl number there is no reason the original formulation should be considered more or less accurate than the altered formulation.

decreasing
$$Pr_t = \frac{C_3}{C_1 \cdot Pr} \cdot \frac{1 - \exp\left[-\dfrac{C_4}{\left(\dfrac{\varepsilon_M}{\nu}\right)}\right]}{1 - \exp\left[-\dfrac{C_2}{Pr \cdot \left(\dfrac{\varepsilon_M}{\nu}\right)}\right]} \qquad (2)$$

$C_1 = 0.21 \quad C_2 = 5.25$

$C_3 = 0.217687 \quad C_4 = 5.0$

increasing
$$Pr_t = \frac{C_3}{C_1 \cdot Pr} \cdot \frac{1 - \exp\left[-\dfrac{C_2}{Pr \cdot \left(\dfrac{\varepsilon_M}{\nu}\right)}\right]}{1 - \exp\left[-\dfrac{C_4}{\left(\dfrac{\varepsilon_M}{\nu}\right)}\right]} \qquad (3)$$

$C_1 = 0.21 \quad C_2 = 5.25$

$C_3 = 0.06401 \quad C_4 = 5.0$

The boundary layer formulation developed in this work is a function of temperature, density, and viscosity and is valid throughout the flow field. It is derived to observe the effect of a boundary layer variation of the turbulent Prandtl number. Equation (4) shows the formulation used to increase the mean turbulent Prandtl number in the boundary layer. All attempts to decrease the turbulent Prandtl number using flow properties caused code failure. Therefore, a nonvariable spatial distribution for the first eight nodes was encoded to raise and lower the turbulent Prandtl number in the near wall region.

increasing
$$Pr_t = 9782.177 \sqrt{\frac{\mu \cdot \rho}{T}} \qquad (4)$$

Heat Transfer Calculation

Overall, thermal conductivity in 'ESCAPE' is related to the turbulent Prandtl number by equation (5).

$$k_1 = Cp \cdot \left(\frac{\mu_{laminar}}{Pr} + \frac{\mu_{turbulent}}{Pr_t} \right) \qquad\qquad k = k_1 + Cp \cdot \frac{\mu_{turbulent}}{Pr_t} \qquad\qquad (5)$$

Based on the energy and momentum equations, a theoretical expression which yields the wall heat transfer with more generality than the basic (classic) formulation of $-k\frac{dT}{dz})_{wall}$ can be derived. Hence equation (6), derived by Hill and Peterson [4], was modified for the CFD control volume adjacent to the wall (see Figure 4).

$$\rho \cdot un \cdot \frac{d}{dx}\left(h + \frac{un^2 + wn^2}{2} \right) \cdot dy \cdot dz + \rho \cdot zn \cdot \frac{d}{dz}\left(h + \frac{un^2 + wn^2}{2} \right) \cdot dx \cdot dy = \frac{d}{dz}\left(k \cdot \frac{d}{dz}T \right) \cdot dy \cdot dx + \frac{d}{dz}\left(\tau_x \cdot un \right) \cdot dx \cdot dy \quad (6)$$
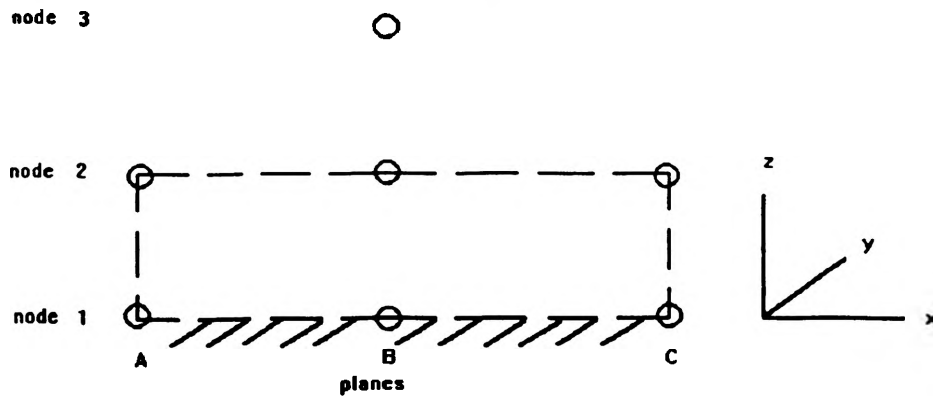
Figure . 4. Energy Balance Control Volume.

In such a formulation there exist numerous choices in defining the gradients. A study was performed to examine which were the most feasible. The results showed that the velocities at the sides of the control volume are best modeled by averaging the velocities at nodes 2 and 1, at planes A and C. Flow through the top of the control volume can be evaluated at node 2, plane B. The heat transfer though the top of the control volume is modeled using the gradient between nodes 3 and 2, plane B and the thermal conductivity at node 2. Due to the no-slip constraint, the shear stress work term at the wall is zero. At the top of the control surface, the gradient for the shear stress work term is taken between nodes 3 and 2, plane B (as in the heat transfer calculation) and the viscosity and velocity are taken from node 2.

For the classic approach, $q_w = k\frac{dT}{dz})_{wall}$, the temperature gradient is taken between nodes 1 and 2 and the thermal conductivity at node 1 is used. The value obtained for thermal conductivity was verified from Schetz [5].

The heat transfer coefficient, C_{hc}, is calculated from equation (7):

$$C_{he} = \frac{q_w}{\rho_{\infty} \cdot Un_{\infty} \cdot C_p \left(T_{aw} - T_w\right)} \quad \text{where} \quad T_{aw} = T_{\infty} + \frac{Pr^{\frac{1}{3}} \cdot Un^2}{2 \cdot C_p} \tag{7}$$

where the wall temperature is 300 K and the inflow conditions are used as the freestream conditions. The quantity $Pr^{\frac{1}{3}}$ represents the recovery factor.

RESULTS AND DISCUSSION

Several distributions of the turbulent Prandtl number are used in the analysis (see Figure 5). B.L. designates the variation tied to the boundary layer. The designation 'up' or 'down' refers to the overall trend in the B.L distribution as well as the trend between the last two nodes of Wassel and Catton's formulation (prt). Unfortunately, the B.L. variation is not as parabolic at high Reynolds numbers as originally desired, however, at low Reynolds numbers (i.e. near the leading edge) the variation is parabolic. Wassel and Catton's formulation has a discontinuity at the wall which provides the desired large turbulent Prandtl number variation. The final step to the wall reverses a longer slight trend in the opposite direction; the effect may be a partial cancellation of the specified variation. For the nonvariable (N.V.) spatial distributions encoded the maximum and minimum turbulent Prandtl number values are 1.3 and 0.4, respectively.
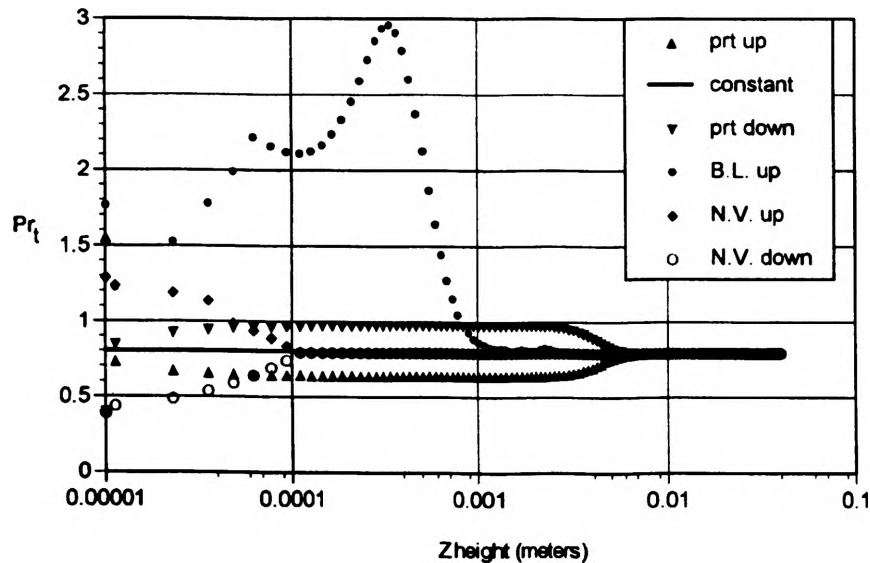
Figure. 5. Turbulent Prandtl Number Variation.

Comparing the classic and energy balance heat transfer formulations for a constant turbulent Prandtl number (see Figure 6), one notes that the energy balance predicts a much larger heat transfer at low Reynolds numbers, which corresponds to the leading edge of the flat plate. The PNS code has inaccuracies near the leading edge, therefore, the results in this region for both formulations are questionable. Examining the heat transfer at higher Reynolds numbers, the two formulations are seen to converge at a Reynolds number of approximately 4.4 million.

170
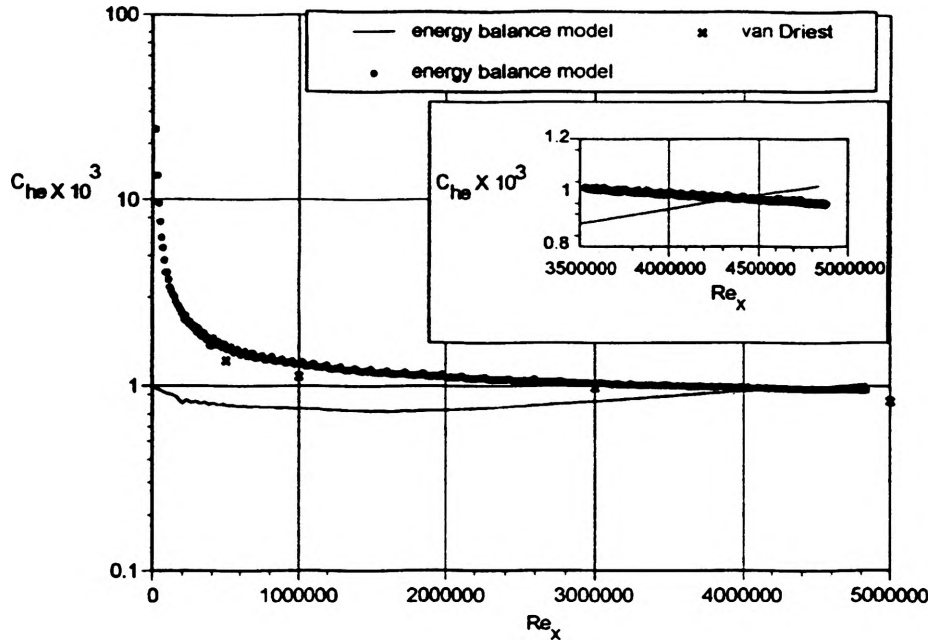
Figure. 6. Comparison of Classic and Energy Balance Heat Transfer Formulations for a Constant Turbulent Prandtl Number

Comparing these results to the experimental correlations of van Driest [6] (see Figure 7) the energy balance formulation is seen to have a much closer correlation than the classic approach across the Reynolds number range. Extrapolating the results of the classic approach seems to show a continued deviation from theory, even at high Reynolds numbers.
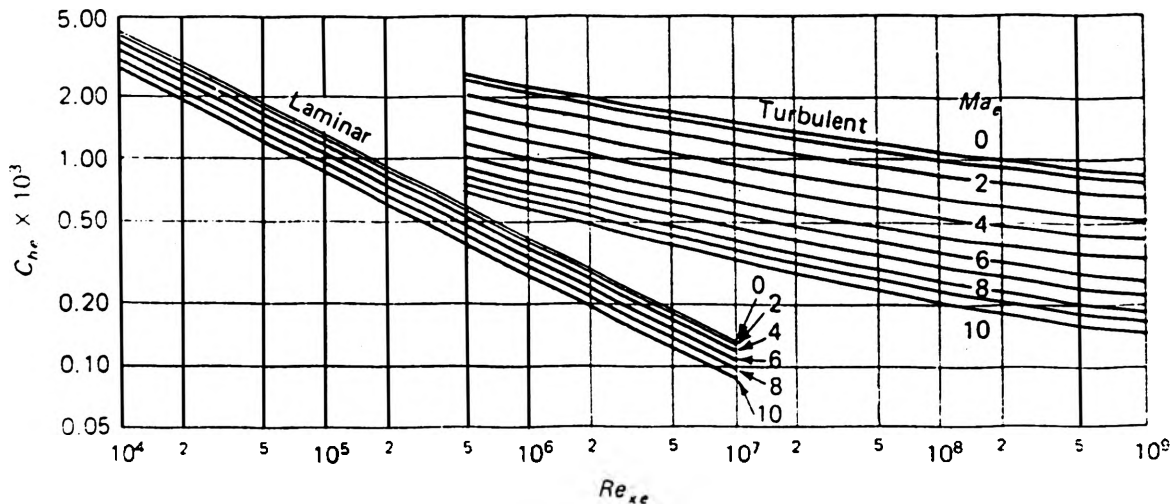
Figure. 7. Theoretical Local-Wall Heat Flux Coefficients on an Isothermal Flat Plate at High Mach Numbers.

Variation of the heat transfer coefficient for Wassel and Catton's formulation, equations (2) and (3), of the turbulent Prandtl number in the low Reynolds number region is very small compared to the overall rise in the heat transfer coefficient. The heat transfer coefficient at high

171

Reynolds numbers (see Figure 6) indicates slight variations across the range. The similarity of the results is possibly due to the wall discontinuity used to obtain the large turbulent Prandtl number gradient opposing a slight trend that develops earlier in the opposing direction (see Figure 5) producing the equivalent of a constant turbulent Prandtl number.
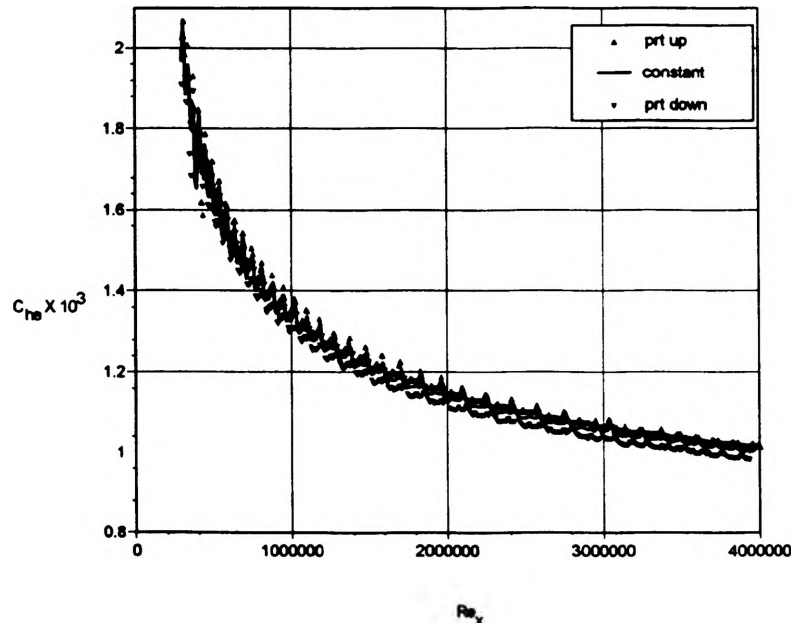
Figure. 8. High Reynolds Number Variation of C_{he} with Pr_t.

The boundary layer formulation and the nonvariable spatial variations are compared to the constant turbulent Prandtl number case (see Figure 9). Using a large spatial distribution of the turbulent Prandtl number causes the heat transfer coefficient to deviate from van Driest correlations regardless of the direction of the variance.
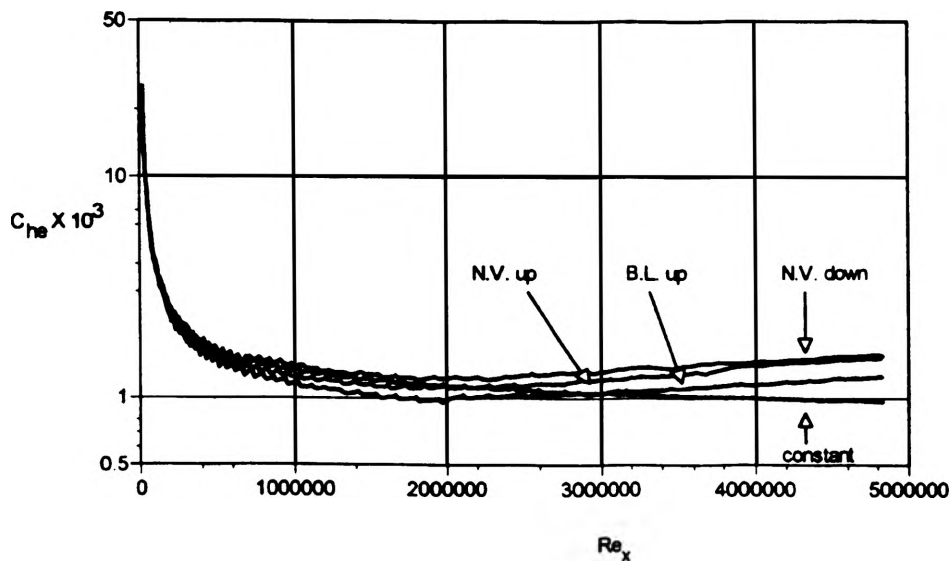
Figure. 9. Examination of Boundary Layer Pr_t Variations.

CONCLUSIONS

Although no conclusive data is available on the actual variation of the turbulent Prandtl number in high speed flows, numerical analysis can be used to evaluate the degree of influence of Prandtl number variation on heat transfer to surfaces. Enforcing large turbulent Prandtl number variations in the boundary layer produces heat transfer results inconsistent with data correlations. Formulations proposed by Wassel and Catton have deviations in heat transfer which are small enough to be considered negligible. Therefore, assuming a constant turbulent Prandtl number, as is currently done, reduces computational time with little effect on the computed heat transfer. For heat transfer calculation with simple geometries the turbulent Prandtl number spatial variation is shown to be insignificant, as long as a reasonable freestream value of the turbulent Prandtl number is selected. Note that this conclusion may be significantly different for more complex three-dimensional flow fields with vorticity and shocks. It is also recommended, based on this work, that a cell control volume approach be used to accurately calculate heat transfer when using CFD grids rather than the conventional wall temperature gradient method.

Acknowledgments

NOMENCLATURE

C_{hc} .... heat transfer coefficient
Cp.. specific heat
h .... enthalpy
k .... thermal conductivity
Pr .... Prandtl number
Pr_t .... turbulent Prandtl number (Schmidt number)
un .... horizontal velocity component
T_{aw} .... adiabatic wall temperature
T .... temperature
T_w .... isothermal wall temperature
wn .... vertical velocity component
ε_m .... eddy diffusivity of momentum $\frac{\mu}{\rho}$
μ .... viscosity
v .... kinetic viscosity $\frac{\mu_{laminar}}{\rho}$
ρ .... density
τ_x .... shear stress

REFERENCES

[1] Blom, Johannes. "An Experimental Determination of the Turbulent Prandtl Number in a Developing Temperature Boundary Layer." Dissertation. Techische Hodeschool Te Eindoven

[2] Wassel, A. T. and Catton, Ivan. "Calculation of Turbulent Boundary Layers Over Flat Plates with Different Phenomenological Theories of Turbulence and Variable Turbulent Prandtl Number." *International Journal of Heat Transfer*, Vol. 16, pp. 1547-1563, 1973.

[3] Simpson, R.L., D.G. Whitten and R.J. Moffet, "An Experimental Study of the Turbulent Prandtl Number of Air with Injection and Suction." *International Journal of Heat Mass Transfer*, Vol. 13, pp. 125-144, 1970.

[4] Hill, Phillip and Carl Peterson. . *Mechanics and Thermodynamics of Propulsion*. Reading: Addison Wesley Publishing Company Inc., 1992. pp. 124-127.

[5] Schetz, Joseph A. *Foundations of Boundary Layer Theory for Momentum, Heat, and Mass Transfer*. Englewood Cliffs: Prentice-Hall Inc., 1984. p 283.

[6] White, Frank M. *Viscous Fluid Flow*. New York: McGraw-Hill Inc., 1974. p 640.

Solar Spectroscopy using 50 Meters of Fiber Optic Cable and CCD Camera

Christopher P. Smith

Department of Physics, University of Missouri - Rolla

ABSTRACT

Measurements of the variation of the Ca II K line profile using very modest equipment is discussed. The equipment used included a Spex 0.75 meter spectrometer, a Santa Barbara Instrument Group 16 bit ST-6 Charge Coupled Device (CCD) camera, fiber optic cable, and a 10-inch Cassegrain telescope. Observations were made in both regions of little or no solar activity as well as in regions of high solar activity (sunspots). A roughly 8% increase in Ca II K emission was observed over a sunspot. The combination of the unique observing apparatus and the intensity resolution of the CCD camera was essential for the success of the experiment.

TABLE OF FIGURES AND TABLES

TABLE OF CONTENTS

I. INTRODUCTION

It has long been known that the Ca II K line of the Sun and other stars exhibits a self-reversal (this phenomena will be discussed more fully below), in the one angstrom core of the line, which varies with time and solar activity.[1] Since the measurements of Wilson and Bappu, there has been a considerable amount of research conducted on the K line. It has been seen that the K line emission intensity does in fact vary with the solar activity cycle.[2,3] It has also been seen that there is a local variability of the K line, which has been attributed to local areas of activity, i.e., sunspots.[2,3] The focus of the experiment is to attempt to detect the variability of the self-reversed core using the Santa Barbara Instrument Group (SBIG) ST-6 CCD camera and other very modest equipment.

For our study, we obtained four major pieces of apparatus, a 0.75 meter spectrometer, a spool of fiber optic cable, a 10-inch telescope, and the ST-6 CCD camera with all necessary hardware. In addition, the mount to attach the CCD camera to the spectrometer and the mount to hold the fiber optic cable to the telescope were designed and built in the Physics Department. We also designed a lens system to more effectively couple the output light from the fiber optic cable to the spectrometer. A complete listing of all the equipment used can be found on page 6.

Once the entire apparatus was assembled, we began our survey of the solar spectrum in the vicinity of the Ca II K line approximately 3934 Å. After competing with the typical cloudy Missouri winter and spring, we finally observed sunspots on the solar disk and were able to observe the K line emission. The intensity of the K line emission was found to vary over the several sunspots that were observed. The largest increase in the emission intensity was found

to be approximately 8%.

II. Equipment List

Item	Company	Model #
Fiber Optic Cable	Beiden	220001
Cassegrain 10-inch telescope	Celestron	217
Double convex lens	Edmund Scientific	32879
70 X 35 mm EFL		
Telescope-fiber optic mount	Physics machine shop	---
CCD spectrometer mount	Physics machine shop	---
Aspheric lens	Rolyn Optics	17.1015
12 X 8.5 mm EFL		
CCD camera	Santa Barbara Instruments Group	ST-6 OPTO-HD
3/4 meter spectrometer	Spex	1500
IBM 286 compatible computer	Zenith	---

III. BACKGROUND

Before beginning the discussion of the Ca II K line variation, a clarification on the notation used in this discussion is appropriate. The K designation of the Ca II line arose when Fraunhofer first studied solar spectra. Fraunhofer designated several of the absorption lines of the solar spectra, in the order in which they appeared, by letters of the alphabet. [The K notation should not be confused with the K electron subshell of an atom. It is merely an old spectroscopic notation and nothing more.]

A. Description of the Solar Chromosphere[4,5,6]

The solar chromosphere is the inner most layer of the solar atmosphere directly above the photosphere and is only a few thousand kilometers high. The photosphere is the "surface" of the sun, or more appropriately, the region of the sun which is seen with the naked eye. Sunspots reside on, and solar flares, prominences, etc. erupt from, the photosphere. From this point of view, the chromosphere could be said to be analogous to the earth's atmosphere. Since the chromosphere is directly above the photosphere, chromospheric effects are very difficult to detect in normal daylight. However, the chromosphere has emission lines, unique to it, in the blue and ultraviolet wavelengths. With the unique lines, we can make direct observations of the chromosphere during the day.

The spectrum of the chromosphere shows strong hydrogen Balmer lines (transitions from the $n=2$ state) and also from Fe II, Chr II, Si II, and others. All of these lines are seen as emission lines because they are observed as an optically thin layer of hot gas against a background of cooler interstellar matter. The spectral lines attributed to the chromosphere are lines which are formed in layer with a T_{eff} up to about 15,000 K. This raises an interesting

question: How can the photosphere, with a T_{eff} of about 6,000 K, heat the chromosphere to temperatures far greater? Unfortunately, there is not an all encompassing theory of how the chromosphere is heated to these temperatures. However, the strength of the K line emission is an indicator of the amount of extra energy which is being transferred to the chromosphere. A few of the theories which describe where this extra energy comes from will be reviewed, but, due to their length, will not be covered in depth.

One way of heating the chromosphere is Joule heating. This arises from changing magnetic fields causing electric current to flow through the chromosphere. Since the chromosphere is composed of ions, there are a sufficient number of electrons to develop a current. As we well know from basic physics, if a current flows through a medium with a certain resistivity, the medium will be heated due to collisions between the electrons and the molecules of the medium. However, the chromosphere is a rather low density medium, thus there are relatively few collisions. This fact allows us to conclude that Joule heating alone will not contribute significantly to chromospheric heating.

A second heating method to consider is by heat conduction In this process, particles from higher layers of the atmosphere, with their correspondingly higher velocities might migrate into the lower cooler layers and, through collisions, transfer their kinetic energy to the lower layer. The converse of this also occurs for particles from the lower layers. A third form of heating is by acoustic or magnetohydrodynamic waves. These waves are formed by the large turbulent velocities in the solar granulation of the photosphere. As these waves travel upwards from the photosphere, they steepen into shock waves upon entering the chromosphere. These shock waves are then damped and their energy transferred as heat into the surrounding material.

It is not known which method is actually heating the chromosphere.

B. What is Self-Reversal?

To begin, we need to consider how an absorption line is formed. In our case we have a large amount of ground state calcium in the lower regions of the chromosphere capable of absorbing any radiation with a wavelength of 3914 Å. So, the Ca II K line from the lower regions of the chromosphere will appear as a dark, although not devoid of light, band in the spectra profile. In order to get the emission line of the self-reversed K line we must have calcium which has been excited to its first excited state. This excited calcium is known to be in regions of the chromosphere known as plages (analogous to clouds in the earth's atmosphere) which form above regions of high solar activity. So, what we expect our spectra of a self-reversed absorption line to appear as an absorption line with a small emission peak in the core of the line.

The conditions which are necessary for the self-reversal of an absorption line show why the phenomena can be used as a measure of non-radiative heat transfer processes within the solar chromosphere. Since the lower chromosphere absorbs the radiation needed to excite the high layers, there must be another mechanism at work. One of the reasons this phenomena is very prominent around areas of high solar activity is that there is an increased amount of non-radiative heat transfer processes associated with the increased activity, e.g., the increase in magnetic flux into a sunspot or the motion of ionized matter during a solar eruption. Since the sunspots have a longer lifetime and are far easier to detect in normal daylight we have chosen to concentrate on sunspots.

182

IV. EQUIPMENT

The research which served as our model was performed at Sacramento Peak National Observatory. The most notable pieces of equipment used in the research was the heliostat used to track the sun as well as the 13.8 meter spectrometer available in the solar observatory. Lacking these components a new system was developed and assembled here on the University of Missouri - Rolla campus. The final design for the apparatus, seen schematically in Figure 1 below, was a modified version described by Ratcliff et al[7]. What follows is a detailed description of the equipment used along with the reasons for choosing these various components.

1. Celestron Telescope

The telescope used was a 10-inch Cassegrain with a 135 inch focal length. The telescope served dual purposes, first, it served as our solar tracking system. We did not have ready access to a heliostat and the time necessary for construction of one was impracticle. The telescope also served as our light collection and focusing device. The image projected by the telescope had a diameter of approximately two inches, making the images of sunspots approximately 225 μm. The telescope was located in the back yard (south side) of the Physics Building.

2. Fiber Optic Cable

In order to transmit the light collected by the telescope to the second floor of the Physics Building, where the spectrometer was located, we used approximately 50 m of fiber optic cable donated to us by Dr. Watkins of the Electrical Engineering Department. The fiber was a standard glass, multi-mode fiber. This fiber was chosen on the basis of its availability as well as its throughput. We found the output of the 50 m length was on the order of approximately 200 mW, a sufficient amount to expose the CCD camera.
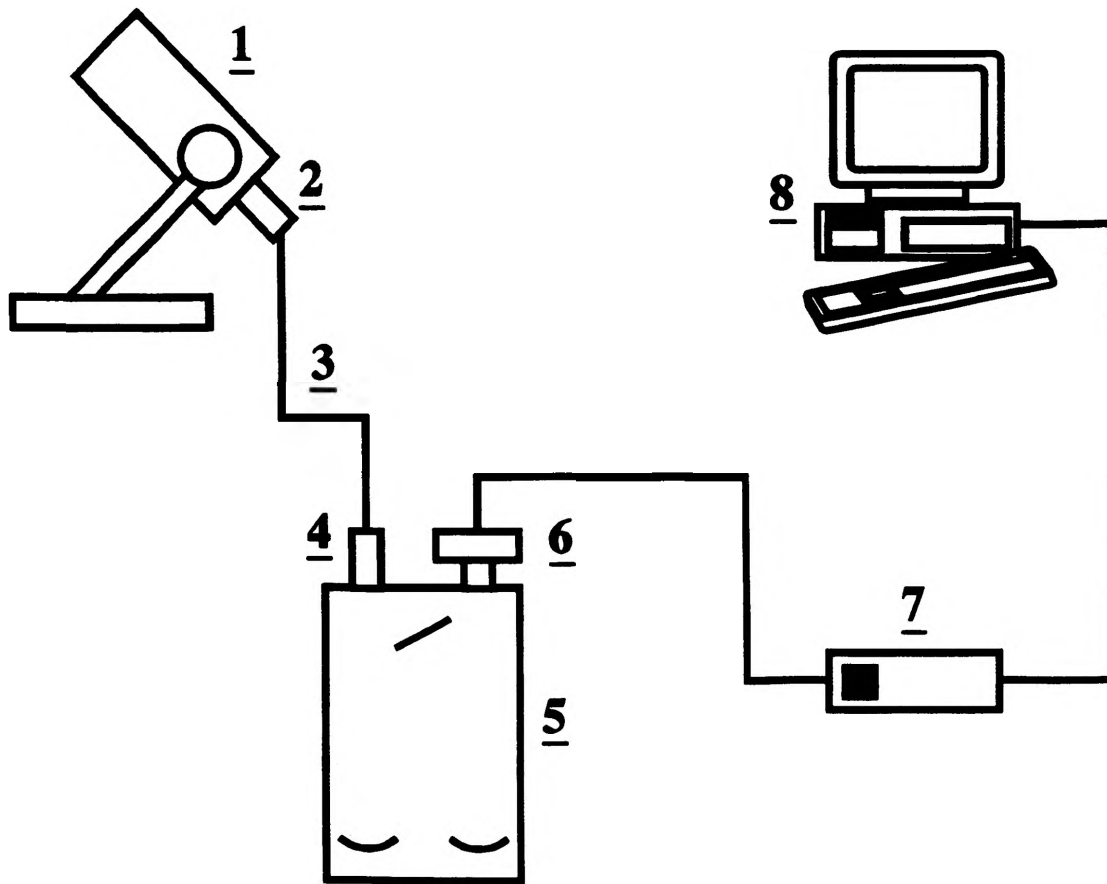
Figure 1. Schematic of apparatus setup; (1) 10 inch-telescope in south yard of Physics Building (ground level); (2) Telescope - fiber optic cable mount; (3) 50 meters of fiber optic cable; (4) Fiber optic cable to spectrometer lens coupling system; (5) Spex 3/4 meter spectrometer (second floor Physics Building); (6) SBIG ST-6 CCD camera as detection device; (7) CCD - IBM compatible computer interpreter; (8) IBM 286 compatible computer.

3. Spex 0.75 m Spectrometer

This spectrometer, owned by the Advanced Physics Laboratory, was also chosen on the basis of its availability. The spectrometer employs a diffraction grating with a ruling of 1200 lines/mm with a variable entrance slit with a width span from 5 to 1500 μm. Its position remained fixed on the second floor of the Physics Building in the Fuller Reading Room throughout the experiment. In order to more efficiently couple the output of the fiber optic cable to the spectrometer a lens system was designed and constructed. By using the lens system the amount of scattered light within the spectrometer itself was reduced while at the same time decreasing the exposure time necessary to capture an image on the CCD.

Calibration of the spectrometer was straight forward. We had available a mercury discharge lamp which provided a reliable source of spectral lines. By referencing the CRC Handbook of Chemistry and Physics we used five different emission lines characteristic of Hg which ranged from 4000 Å up to 9000 Å to insure that the spectrometer was accurate at most wavelengths. We found that the spectrometer was at most off by 2 Å from the accepted value of the Hg lines.

4. Santa Barbara Instruments Group (SBIG) ST-6 CCD camera

The Department of Physics purchased the SBIG ST-6 CCD camera during the summer of 1992. Prior to this experiment the camera was used primarily for astronomical observations. There were several factors which led to the use of the CCD camera as the detection device for this experiment. Foremost was the intensity resolution attainable by the camera. The ST-6 model is a 16-bit camera, which means it is capable of detecting 2^{16} distinct intensities. This large number of distinct intensities gives the CCD an intensity resolution of approximately

0.002%. Since the self-reversal in the K line is a relatively small deviation we felt the excellent intensity resolution of the CCD would improve the chances of detecting the phenomena. Another factor was the linearity of response the camera offered. The response of the camera is virtually constant at about 0.5 from 3800 Å up to 9000 Å.

The camera replaced the exit slit of the spectrometer. In our configuration the spectrometer was used as a monochromator rather than as a scanning spectrometer. The reason for this is that the CCD is capable of capturing roughly $\pm$ 47 Å from the spectrometer setting.

The physical dimensions of the CCD are 242 by 375 "pixels" each measuring 23 by 27 μm, which gives an overall array size of 6.5 by 8.6 mm. The CCD is connected to an IBM compatible 286 computer by an interpreter. The interpreter is used to store multiple images used in conjunction with astronomical photometry, not used in this experiment. The computer is used to control the temperature of the CCD chip and for general control of the camera. Images from the camera are downloaded to the computer and stored on disk in a standard format. By capturing an image of the K line we found we also saw the Ca II H line on the same image. From the known separation of these two lines we were able to determine that each pixel on the array corresponded to approximately 0.25 Å in the spectra.

5. LinePro Image Reduction Software

Unfortunately, there is no software available on the market which will upload an image created by the ST-6 and turn the image into a line profile. This was circumvented by the development and writing of software by the author to create the desired line profiles. The profiles of the spectra are created by taking the arithmetic average of the pixel intensity for each column of pixels. The final profile is then exported in a number of formats as ASCII data to

be read into various other data analysis programs. The disadvantage of simply taking the arithmetic average intensity is that the camera must be precisely aligned such that each column of pixels is parallel with the spectral lines. This was mainly accomplished by taking an image of the standard Hg source a adjusting the camera until the emission line was as vertical as possible.

V. OBSERVATIONS

Once the apparatus assembly was completed, spectra images were taken for regions of the quiet sun and for regions of solar plages (indicated by regions of sunspot activity). Images were taken on 22 April and 27 April 1993. The data included images of the quiet sun and one sunspot. Data was only taken on this day due to constraints imposed by time and weather. As it was necessary to see the image of the solar disk in order to target sunspots for imaging it was possible to collect data only on days in which direct sunlight as well as sunspots on the solar disk was available. 22 April and 27 April 1993 were the only days on which acceptable conditions occurred following the completion of the observing apparatus.

Data were collected in the following manner: The telescope was directed at the sun and focused to provide an image. The end of the fiber optic cable was moved to a central part of the solar disk image. The spectrometer was set for the wavelength of the Ca II K line, 3934 Å. The spectrometer entrance slit was set at 23 μm, the setting for the maximum spectral resolution. The CCD camera software program was started and the camera was cooled to -25 C below ambient room temperature to reduce noise. The exposure time was set and an image was taken. Image exposure times for the data presented here were in the one-half to two second range.

The ST-6 CCD camera software next processed the image and stored it as a binary file.

This file consists of a two kilobyte (2048 bytes) header followed by the pixel reading stored sequentially by rows. The resulting byte file was further processed by the program LinePro. The image file was read in (by rows) one pixel at a time. An arithmetic average of pixel intensity was computed for each column. This was to provide an intensity profile for the spectra recorded by the camera. A sample of a spectra image and the profile calculated from the image can be seen in Figures 2 (a) and 2 (b) respectively. Observations were made on the two occasions noted above, and the results are summarized below in Table 1. The observations made consist of spectra images made of a quiet area of the sun and a plage area, indicated by the existence of a sunspot. All of the images were taken with the spectrometer set on the wavelength of the Ca II K line. The Ca II K absorption line is the large white band in the central region of the image (the image is printed as a negative for clarity). The large whit band to the right is the Ca II H line, which we are not concerned with-the focus of the project was on the K line. The identity of these two lines is certain, as testing indicated that the spectrometer used in this experiment was reasonably well calibrated, and it is known that these two absorption lines are far larger than any other absorption lines in this region of the solar spectra, enabling their easy identification.

Table 1. K line intensity relative to continuum.

Observation	Area Type	Continuum Int.	K-line Int.	Relative Int.
4_27_93.2	Sunspot #1	86.66	75.65	0.87
4_27_93.7	Sunspot #2	84.16	73.23	0.87
4_27_93.9	Quiet Sun	95.94	71.42	0.74
4_22_93.6	Quiet Sun	278.90	104.92	0.37
4_22_93.4	Sunspot	217.07	112.91	0.52
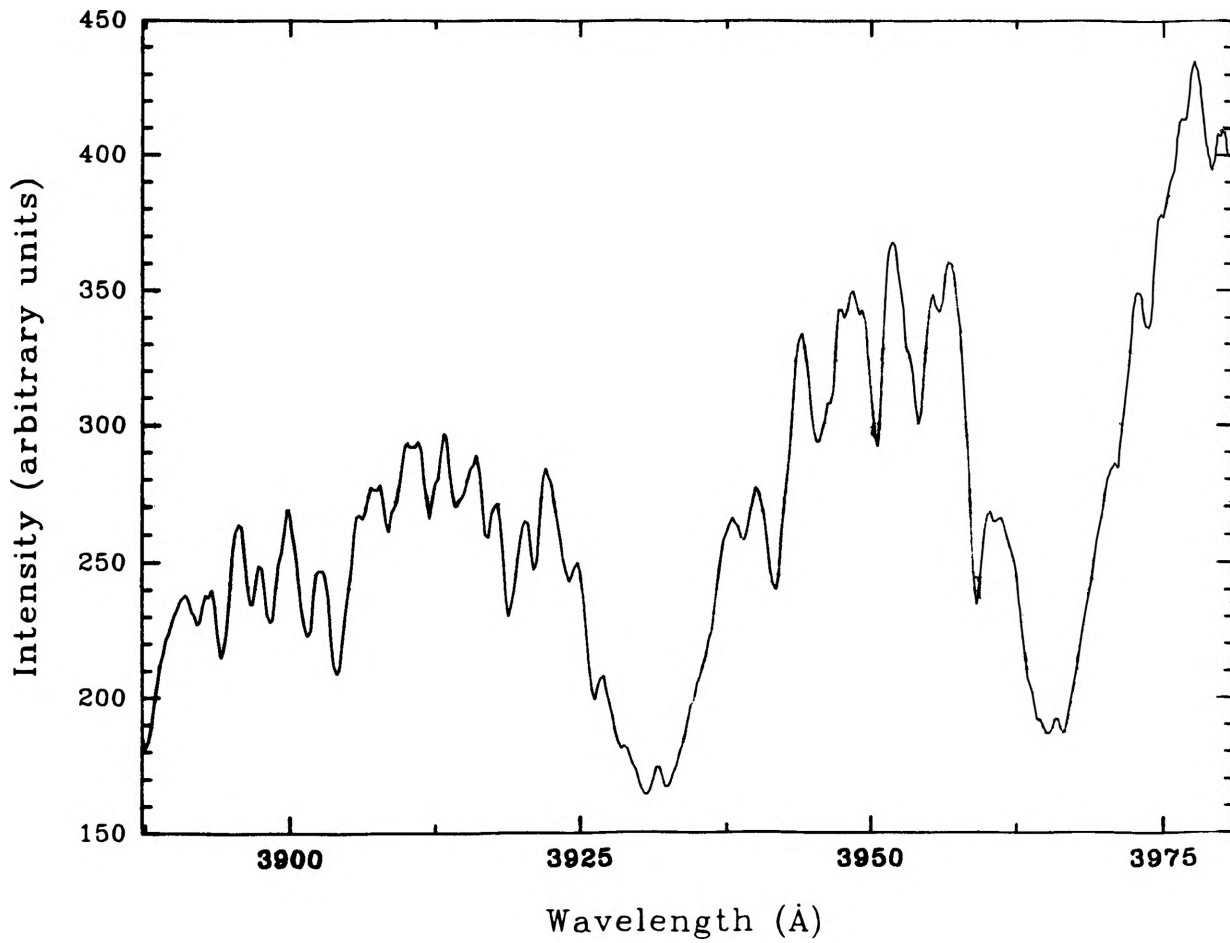
Figure 2. (a) (Top) CCD recorded image spectra of run 4_22_93.4 (sunspot). (b) (Bottom) Line profile generated from (a).

Figures 3 and 4 are profiles of a quiet sun region and a plage region. The plainly evident "bump" in the bottom of the absorption line of the plage spectra, being absent from the quiet sun spectra, clearly shows a difference in the K line in quiet and plage regions of the sun an indicates the self-reversal we were looking for. This "bump" indicates that the absorption line has reversed itself at the core to become an emission line. Figure 5 is a profile with the self-reversed K line with a line drawn to estimate the continuum. This is only a rough guess, as the determination of the actual continuum is very difficult. This rough estimate of the local continuum was arrived at by assuming the two most prominent peaks to lie on the continuum. The position for these two peaks (column number) was established for each spectra, and a line calculated for the two peaks. This line was then used to establish a "best guess" for the position of the continuum above the center of the K line. These are the values recorded for spectra in the third column of Table I. The minimum intensity value of the profile or the local maximum at the center of the K line are recorded in column four, according to whether the spectra was taken over the quiet sun or over a plage. The K line intensity is divided by the continuum intensity to give the relative intensity, the K line fraction of the continuum. In order to give some estimate of the percent intensity of the continuum of the quiet sun and plage regions, a continuum baseline is needed for the calculations. The baseline was also arrived at by a crude approximation, taking the quite sun K line intensity to be approximately five percent continuum[1]. When this is used to provide an estimate of the baseline, the percent of the continuum of the plage and quiet sun intensity can be calculated, and this is summarized in Table II below.

Table II. K line as percent of continuum.

Observation	Base (est.)	Continuum	K line Intensity	% Continuum
4_27_93.2	63	87	76	54
4_27_93.7	61	84	73	52
4_27_93.9	70	96	71	5
4_22_93.6	96	279	105	5
4_22_93.4	75	217	113	27
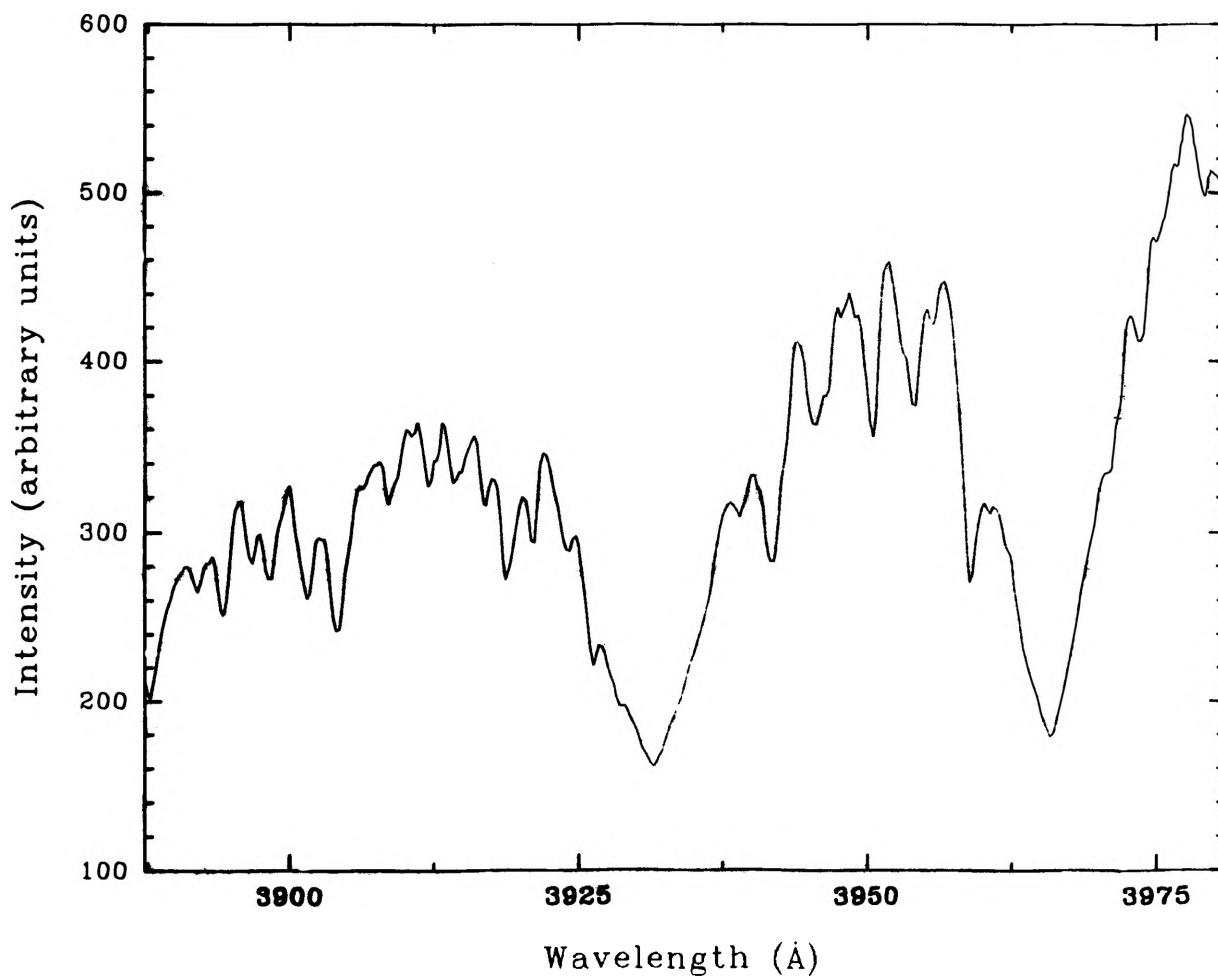
Figure 3. Line profile of recorded spectra from run 4_22_93.6 (quiet region).
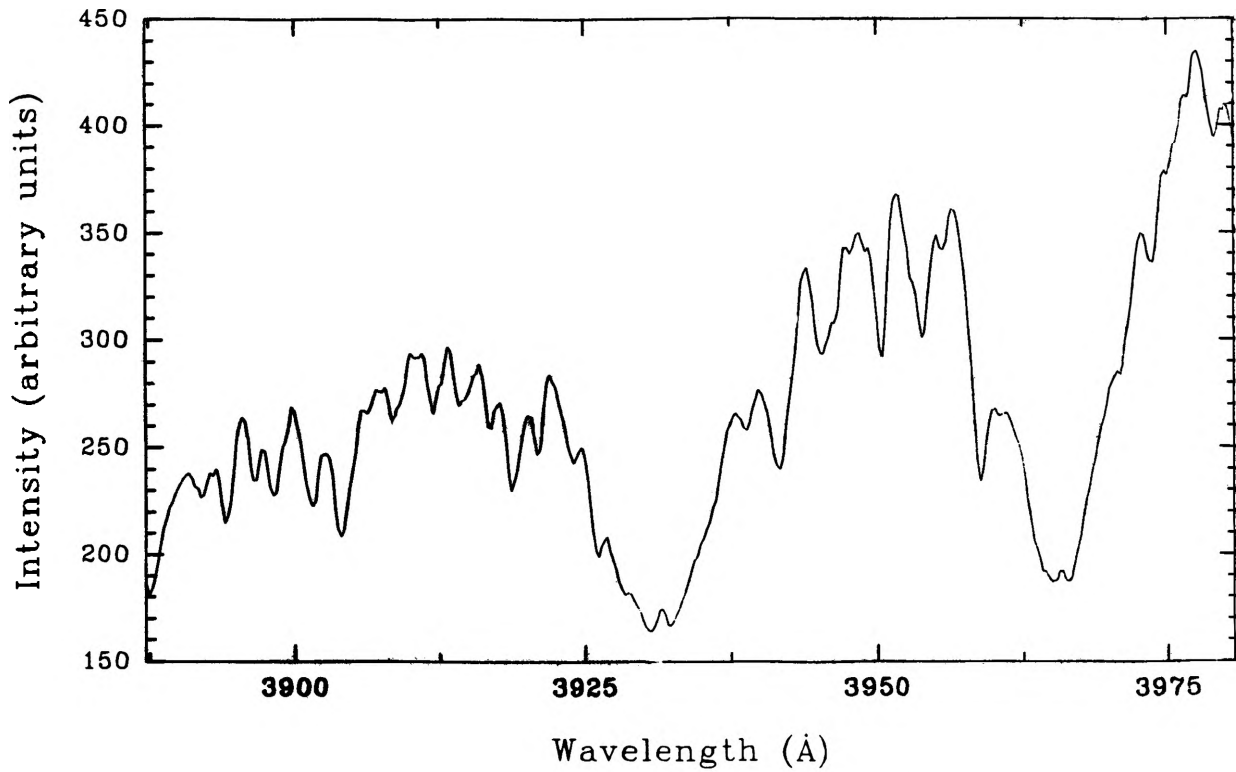
Figure 4. Line profile of recorded spectra from run 4_22_93.4 (sunspot).
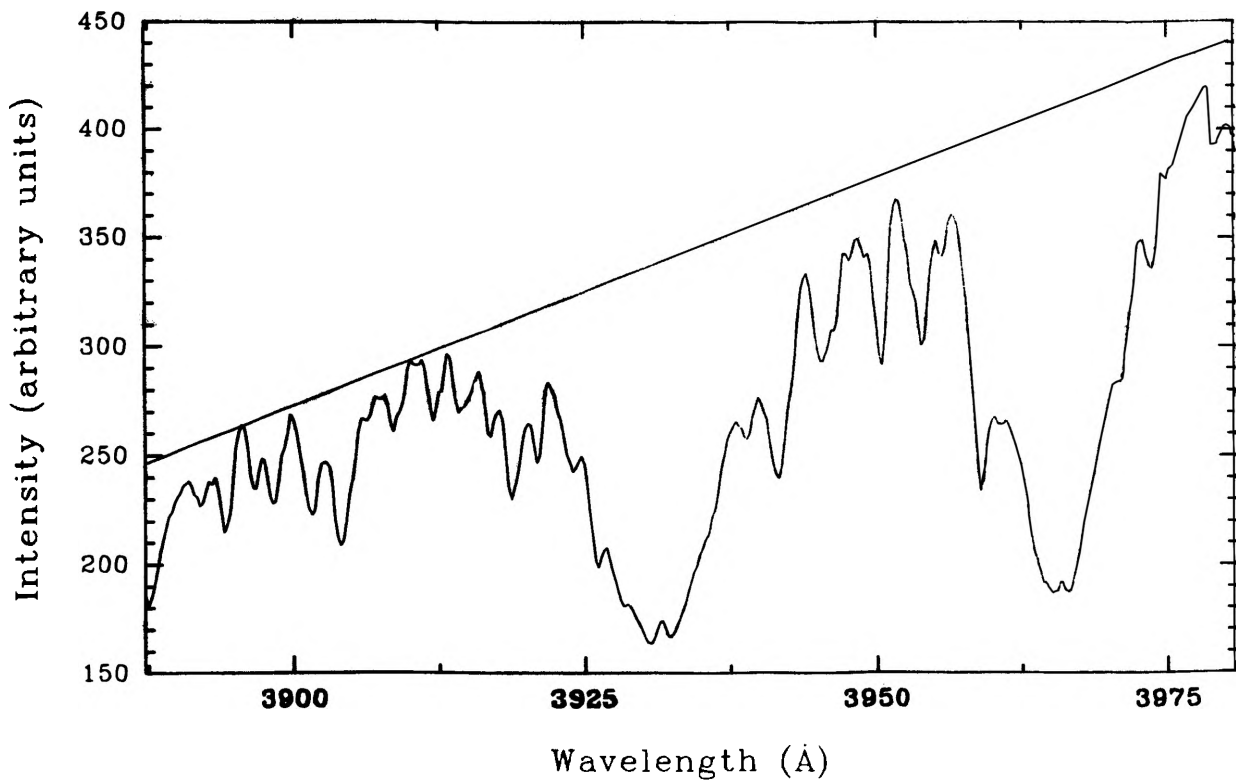
Figure 5. Line profile of recorded spectra with estimated continuum line drawn in.

VI. CONCLUSIONS

This project has demonstrated the feasibility of using the CCD camera, the 10-inch telescope, and the Advance Physics Laboratory's spectrometer together as a system for performing spectral analysis on objects accessible to the telescope. The results obtained clearly indicate that the Ca II K line intensity varies with the region on the sun's surface. The observations show that the K absorption line is only an absorption line in areas of the sun's surface not occupied by solar activity in the form of solar plages. With these plage regions, however, it is clear that the absorption line reverses itself at the core and becomes an emission line.

VII. ACKNOWLEDGEMENTS

VIII. References

1. O. C. Wilson and M. K. V. Bappu, *H and K Emission in Late-Type Stars: Dependence of Line Width on Luminosity and Related Topics*, Astrophys. J. **125**, 661-683 (1957).

2. O. R. White and W. Livingston, *Solar Luminosity Variation. II. Behavior of Calcium H and K at Solar Minimum and the Onset of Cycle 21*, Astrophys. J. **226**, 679-686 (1978).

3. O. R. White and W. C. Livingston, *Solar Luminosity Variation. III. Calcium K Variation from Solar Minimum to Maximum in Cycle 21*, Astrophys. J. **249**, 798-816 (1981).

4. E. Bohm-Vitense, *Introduction to Stellar Astrophysics, Volume 2: Stellar Atmospheres* (Cambridge University Press, Great Britain, 1989), p. 29-38 and 190-208.

5. P. Foukal, *Solar Astrophysics* (Wiley-Interscience, New York, 1990), p. 289-309.

6. H. Zirin, *Astrophysics of the Sun* (Cambridge University Press, Cambridge, 1988). p. 155-216.

7. S. J. Ratcliff, D. K. Noss, J. S. Dunham, E. B. Anthony, J. H. Cooley, and A. Alvarez, *High-Resolution Solar Spectroscopy in the Undergraduate Physics Laboratory*, Am. J. Phys. **60** (7) (1992).

INTERACTIVE MULTIMEDIA APPLICATIONS FOR THE CORRELATIONS OF PETROLEUM FLUIDS PROPERTIES

1994 OURE
Herman Smith III
Petroleum Engineering Department
University of Missouri-Rolla

Abstract

Interactive Multimedia Applications for the Correlations of Petroleum Fluids Properties is a truly interactive and multimedia computer application designed to better help students taking the class "The Properties of Petroleum Fluids", Petroleum Engineering 141. This computer program incorporates error and information voice messages, control over three different computer applications (HyperCard 2.2, Mathcad V3.1, and DeskPaint™ V3.2), three-dimensional multi-coloration, pop-up graphics, directional buttons, object/label-oriented programming, and floating palettes. This creates one computer application to calculate petroleum properties versus the use of multiple, often crowded graphs.

INTRODUCTION

"Multimedia authoring programs are software tools that enable users to "branch" or link text with video, audio, graphics, animations, or other digital data to create multimedia presentations or products" [1]. Many computer applications claim to be *interactive* and *multimedia*. These types of programs have existed in the past, but because the applications use "buttons" does not necessarily make them interactive and just because the applications exist on computer does not necessarily make them multimedia. *Interactive Multimedia Applications for the Correlations of Petroleum Fluids Properties* is a truly interactive and multimedia application designed to better help students taking the class "The Properties of Petroleum Fluids", Petroleum Engineering 141. Interactive capabilities allow the user to fully understand the step-by-step process of inputting information and receiving back new information from the application as quickly as possible through the use of user-friendly programming. "They help students think about thinking" [1]. *Interactive Multimedia Applications for the Correlations of Petroleum Fluids Properties* incorporates error and information voice messages, control over three different computer applications, three-dimensional multi-coloration, pop-

up graphics, directional buttons, object/label-oriented programming, and floating palettes.

The computer-generated correlations are for the physical properties of oil, gas, and formation brine, such as: density, compressibility, viscosity, and formation volume factor. The need for such an application of calculations exists due to the petroleum industry's reliance on the use of multiple, often crowded graphs for the determination of many of these values. Graphical estimation creates three problems: (i) a student spends a disproportionate amount of time estimating the correct answer between pre-defined lines, (ii) the incorrect answer ruins the remaining calculated answers because of its inclusion, and (iii) when faced to prove the final answer, the student must argue the estimation of a possible "incorrect" reading. *Interactive Multimedia Applications for the Correlations of Petroleum Fluids Properties* allow both the student and the professor the opportunity to "check" their work with the exact same equations that initially produced the graphs to be read, with the ease and quickness of the computer application. This allows the professor to concentrate on teaching and the student on learning.

DERIVATION OF THE CORRELATIONS

Many of the equations that were used in this application for the oil and gas are published in Appendix B of *The Properties of Petroleum Fluids*, the textbook used for Petroleum Engineering 141 [2]. While, the empirical correlations for the relative compressibility of brine, relative formation volume factor of brine, and relative density of brine were conceived during the formulation of this research project. All three procedures for the properties of relative compressibility, relative formation volume factor, and relative density are based on one basic method of correlating relative values for brine versus pure water, an empirical ratio.

Method Used to Derive Correlations: Brine

Data for each property is collected, made into relative values, and fit with appropriate correlating equations for reservoir brine. Keeping pressure and salinity constant, data is correlated with respect to temperature by second degree polynomials of the form:

$$X + Y*T + Z*T^2.$$

Since, X, Y, and Z are functions of salinity and pressure, then for each of the three properties (Pr):

$$Pr = X(S,p) + Y(S,p)T + Z(S,p)T^2. \tag{1}$$

With a fixed salinity (S_1) and pressure (p_1), X_1, Y_1, and Z_1 can be found. Varying salinity n times, X_1---X_n, Y_1---Y_n, and Z_1---Z_n can then be found using Eq. 1. X_1---X_n can be fitted with a polynomial of the form:

$$X_n = A_1 + A_2S + A_3S^2 \qquad (2)$$

similarly for Y,

$$Y_n = A_4 + A_5S + A_6S^2 \qquad (3)$$

and for Z,

$$Z_n = A_7 + A_8S + A_9S^2. \qquad (4)$$

The combined result for a fixed pressure is now of the form:

$$Pr = A_1 + A_2S + A_3S^2 + (A_4 + A_5S + A_6S^2)T + (A_7 + A_8S + A_9S^2)T^2. \qquad (5)$$

Changing the pressure and repeating Eqs. 2, 3, and 4, new values of $X_{(p2)}$, $Y_{(p2)}$, and $Z_{(p2)}$ can now be found. Varying pressure m times (m must equal n), X_1---X_m, Y_1---Y_m, and Z_1---Z_m can then be found using Eq. 1. Last step, fitting $X_{p=1}$---$X_{p=m}$, $Y_{p=1}$---$Y_{p=m}$, and $Z_{p=1}$---$Z_{p=m}$ with a straight line equation of the form:

$$D = R + pQ. \qquad (6)$$

will give the complete equations for the three properties of relative compressibility, relative formation volume factor, and relative density for brine versus pure water ratios.

$$C_r = (A_1 + A_2S + A_3S^2) - 10^{-4}(A_4 + A_5 + A_6S^2)T - 10^{-6}(A_7 + A_8S + ...$$
$$A_9S^2)T^2 + 10^{-8}(A_{10} + A_{11}S + A_{12}S^2)T^3(A_{13} + pA_{14}) \qquad (7)$$

$$B_{wr} = (A_1 + A_2S + A_3S^2) - (A_4 + A_5S + A_6S^2)T - (10^{-7})T^2 + p1.41 \cdot 10^{-7} \qquad (8)$$

$$\rho_r = (A_1 + A_2S + A_3S^2 + pA_4) - (A_5 + A_6S + A_7S^2 + pA_8)T + ...$$
$$(A_9 + A_{10}S)T^2 \qquad (9)$$

where S = salinity in weight percent
   T = temperature in °F
   p = pressure in psia.

CREATION OF THE APPLICATION

The creation of the *Interactive Multimedia Applications for the Correlations of Petroleum Fluids Properties* is done with the integration of three computer applications: HyperCard 2.2, Mathcad V3.1, and DeskPaint™ V3.2. These three

applications are linked together to form a single application that uses each one's best qualities of user-friendliness, computation, and graphics.

The Ultimate Erector Set: HyperCard 2.2
The combination of being both interactive and multimedia starts with HyperCard [3]. This authoring program can be extended to control others by writing values to files, launching them, and reading back their written values. HyperCard is a simple authoring program assembled through the use of stacks of cards or screens, linking buttons and icons to following cards, and the ability to script a message for each button/icon. Card icons enable you to navigate within screens. Each card or screen leads to the next by the depression of a button or icon with the "pointing hand". A button is designated to be a "rounded" rectangle within the card. Within each card, there exists a number of options to continue: flipping back and forth to particular screens, showing the graph specific to the calculation, entering values, receiving information on what to do next, and calculating the result.

Once the application is opened, the first card is immediately shown with a large button of "Begin?" printed within it, automatically inferring a button/icon linking program (Figure. 1.). An "info" button within the top corner of every card is for informing the user on how to continue with a voice message, "Touch the 'Begin?' button to continue." A pop-up floating palette, for every card, is for displaying the option of showing the graph specific to the card. If no graph exists for that specific card, an error message is voiced, "This card doesn't have a graph," and no graph is shown.

Figure. 1. "Begin?" Card

When the "Begin?" button is selected by depressing the mouse, a command or script is sent throughout the stack of cards and the program reacts accordingly, "On mouseUp, visual effect dissolve fast, go to card id 3678, end mouseUp." This scripts says: when the mouse is depressed and let go, clear the screen quickly, show the next card numbered 3678, end of message. After the "Begin?" button is

touched, a menu of options to calculate petroleum fluids properties is displayed giving all the choices of the properties that can be calculated (Figure. 2.).
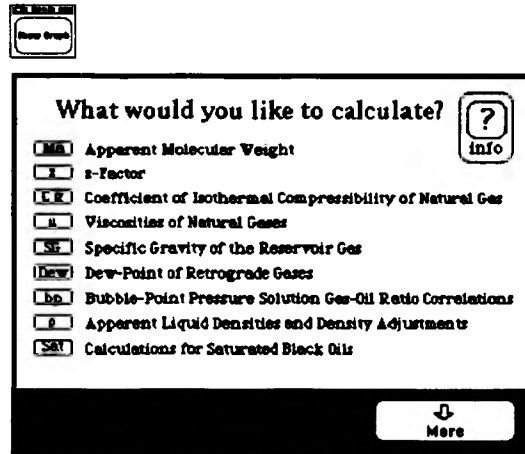
Figure. 2. "More" Card

Within the "More" card, one has a number of decisions to make on which button will serve best. Depressing the "info" button, again, will explain each of these buttons or by selecting the "More" button, a new card will appear with even more choices of different calculations. The "info" button's script, "On mouseUp, playTitleInfo, end mouseUp," is a generic command. Within each screen, there are hidden fields of text in the background of the card that store a file for most of the buttons used (Figure. 3). HyperCard can take user input into data fields and control that data or file. Inside of the background field "TitleInfoSound", exists the name of a different audio file to be played for each card. When this button is pressed, the audiotaped "info" message is played.
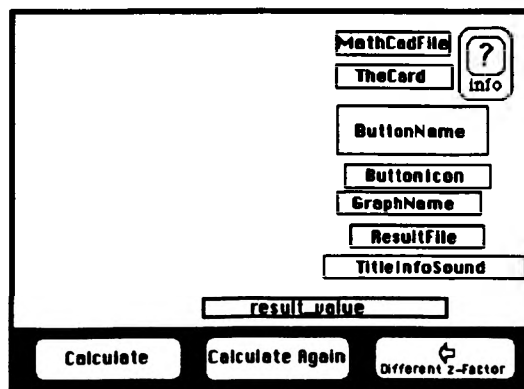
Figure. 3. Background Card

The background field "ButtonName" gives the title to the "More" button by having entered the text "More" within it. The background field "ButtonIcon" decides which type of icon id number to be used within the "More" button. Is the

199

arrow up, down, to the right, or the left? can be determined by a different number each time a new card is drawn.

Picking the "z" button on the "More" card for calculating z-Factors activates the script, "On mouseUp, go to card id 3867, end mouseUp," yielding Figure. 4. Selecting the "Psuedocritical" button, the calculation screen for psuedocritical properties of known compositions arises (Figure. 5.). The "Psuedocritical" card is a card for inputting values that can control Mathcad and DeskPaint. Two new buttons "Calculate" and "Calculate Again" arise within the bottom portion of the card (also, notice that the floating palette "Roam" still pops up with each new card).
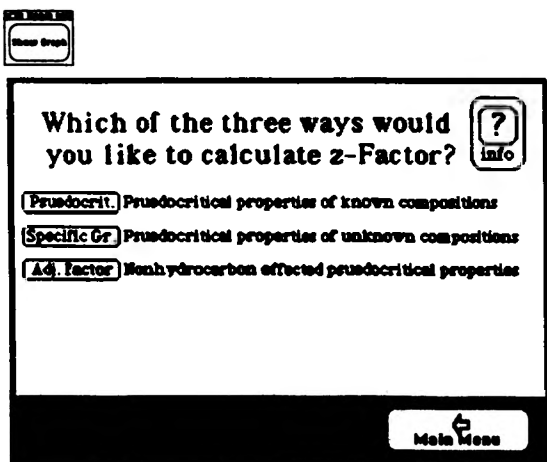
Figure. 4. "z-Factor" Card
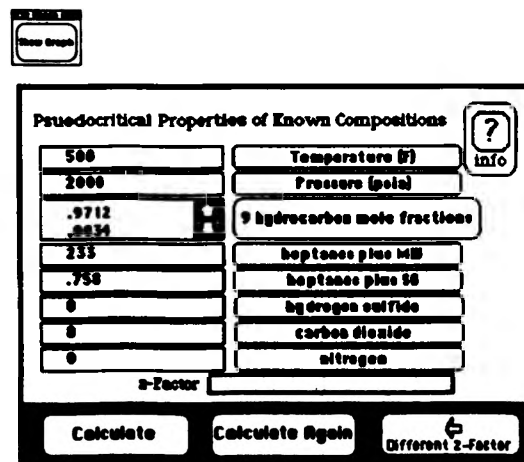
Figure. 5. "Psuedocritical" Card

To input a temperature value, press the "Temperature (F)" button and a small inputting screen pops up, waiting for the value to be entered, "on mouseUp, ask the short name of me & ':', put it into card field 'Value1', end mouseUp," (Figure. 6.). Typing "500" into the slot and pressing the "OK" button, the field next to the "Temperature (F)" button shows the value "500" (Figure. 5.). Doing this for each corresponding button of data, the values needed to calculate z-Factor are entered. The "9 hydrocarbon mole fractions" button is a dummy button without a script because the values must be entered through its respective scrolling text field. The program will not be able to compute unless there are 9 decimal values entered in the "9 hydrocarbon mole fractions" field.
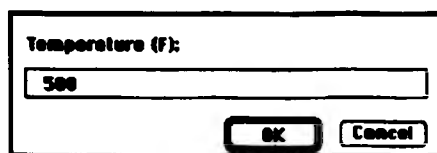
Figure. 6. Value Input Screen

200

Showing the Old Way of Doing Things: DeskPaint™ V3.2

The "old way of doing things" includes a calculator and a graph. While today, a computer is sufficient, for it includes both the calculator, the graph, and everything else needed to find answers. DeskPaint is an easy drawing application that can read in scanned pictures, either black and white or color, and be able to improve on that scanned material or draw its own. Graphs that would have been used to calculate different petroleum properties are scanned and re-opened as PICT files into DeskPaint. These graph images have been increased or reduced in size in order to maximize their readability once HyperCard launches it.
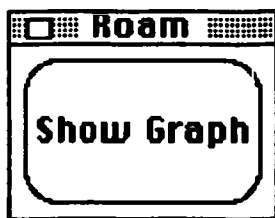
Figure.7. Floating Palette
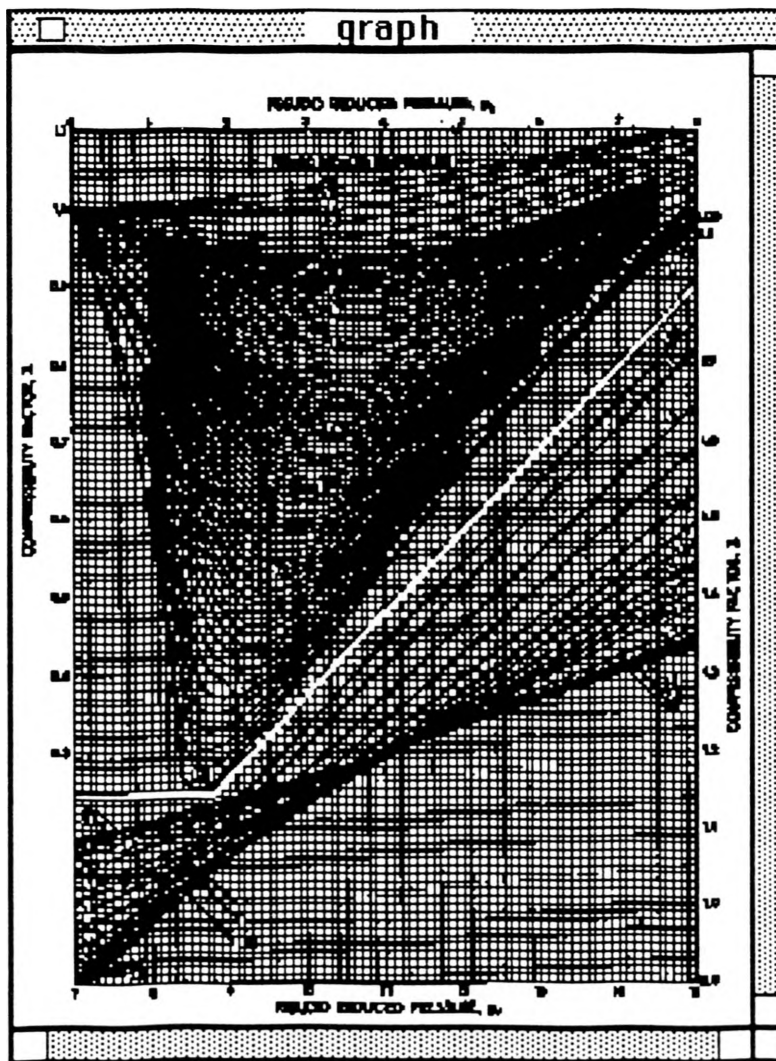
Figure. 8. z-Factor Graph

HyperCard has a special feature called the floating palette (Figure. 7.). This palette "floats" from card to card, waiting for its usage. The floating palette can either be closed or moved to avoid obstructing the view of the current card and without disturbing the active card. Once the floating palette "Show Graph" button is selected, and the background field "GraphName" is entered with a

201

specific graph name, DeskPaint is launched, only displaying the graph itself within a closeable and scrollable pop-up graphic window (Figure. 8.).

The Computational Engine: Mathcad V3.1
After every value is entered, the "Calculate" button is depressed. HyperCard writes a file for each value, which Mathcad can read, and launches (opens) the corresponding background field "MathCadFile" name with Mathcad V3.1. The Mathcad file program reads the value entered in each value file, inputs them into pre-defined equations or correlations, calculates a result, and writes back a result value file which HyperCard can read to input into the "result_value" field (Figure. 3.).

The unfortunate thing about this system is that Mathcad is non-scriptable. Mathcad actually cannot be controlled by an outside program, although Mathematica can. So, the real challenge for this program was to create an interactive system that originally was not designed to be, due to Mathcad's inability to be scripted. HyperCard can open just about any Macintosh application with HyperTalk including Mathcad, but unfortunately, that is just as far as the control of HyperTalk gets. So, by creating a file system, HyperCard opens the particular Mathcad program, writes values to a shared file with Mathcad, which reads the values, and writes its own back to the file. The only time the user needs to use a command outside of the application itself, is to select the Finder icon to go back to HyperCard and see the result!

Mathcad's true beauty is that it works in a way that a student can pick up very quickly because the equation editor is easy and intuitive [4]. Mathcad lets the student concentrate on solving problems and finding the correct answer to compare with a graph estimation. "The resulting equations look exactly as [one would] expect to find in any physics or mathematics book," [5]. In fact, many of the graphs are created with the same equations used within this application so there are no differences in petroleum property limits and percent error for these properties!

Taking a look at one of the z-Factor calculations, inputting equations is the same as writing them down on a piece of paper (Figure. 9.). The Mathcad example very simply shows how to generate a graph of one's own with the right equation. This particular program automatically reads values, inputs them into equations, and generates both the graph of a particular psuedocritical temperature (T_{pr}) and the z-Factor at a specific pseudocritical pressure (P_{pr}). During the life of a producing well, the temperature and the psuedocritical temperature basically remain the same as the pressure and pseudocritical pressure drop dramatically. This particular graph can historically represent the life of this well, continuously representing z-Factors, with respect to pressure, graphically and in numeric form. A particular z-Factor graph for a particular well, this is the new way of doing things.

202

$$TF \ = READ(\,value1\,) \quad p \ = READ(\,value2\,) \quad \gamma_g \ = READ(\,value3\,)$$

$$TF = 250 \qquad\qquad p = 50 \qquad\qquad \gamma_g = 0.577 \quad \rho_{pr1}(z) \ = .27 \cdot \left(\dfrac{p_{pr1}(p)}{z \cdot T_{pr1}(T)} \right)$$

$$T_{pr1}(T) = 2.051 \qquad p_{pr1}(p) \ = \dfrac{p}{p_{pc\gamma}} \qquad p_{pr1}(p) = 0.074$$

$$Z_1(z) \ = \left[\mathrm{root} \left[\begin{array}{l} -z + 1 + \left(.3265 - \dfrac{1.07}{T_{pr1}(T)} - \dfrac{.5339}{T_{pr1}(T)^3} + \dfrac{.01569}{T_{pr1}(T)^4} - \dfrac{.05165}{T_{pr1}(T)^5} \right) \cdot \rho_{pr1}(z) \ldots, z \\[2mm] + \left(.5475 - \dfrac{.7361}{T_{pr1}(T)} + \dfrac{.1844}{T_{pr1}(T)^2} \right) \cdot \rho_{pr1}(z)^2 \ldots \\[2mm] + (-.1056) \cdot \left(\dfrac{-.7361}{T_{pr1}(T)} + \dfrac{.1844}{T_{pr1}(T)^2} \right) \cdot \rho_{pr1}(z)^5 \ldots \\[2mm] + .6134 \cdot \left(1 + .721 \cdot \rho_{pr1}(z)^2 \right) \cdot \left(\dfrac{\rho_{pr1}(z)^2}{T_{pr1}(T)^3} \right) \cdot (2.7183)^{-.721 \cdot \rho_{pr1}(z)^2} \end{array} \right] \right]$$

$$Z_1(z) = 0.998 \qquad result \ = Z_1(z) \qquad WRITE(\,result\_value1\,) \ = result$$

Figure. 9. Mathcad Example

SUMMARY

Interactive Multimedia Applications for the Correlations of Petroleum Fluids Properties has been implemented. Briefly, the necessary steps to perform the calculations are: (i) enter values within HyperCard screen, (ii) depress the "Calculate" button to open Mathcad, (iii) scroll down the Mathcad program until the user sees the result, and (iv) use the "Finder" icon to go back to Hypercard to see the result, the user may print out both the Hypercard screen and Mathcad program to keep or to turn in with the rest of the work. *Interactive Multimedia Applications for the Correlations of Petroleum Fluids Properties* is an exemplary application program that can only lead to greater things in education. "In the future, multimedia will be a standard form of communication in education," [4]. Not forgetting about industry, the petroleum industry is in need of such authoring programs that can very simply teach and train a possible engineer a certain task, on site, while performing the task. A program very similiar to *Interactive Multimedia Applications for the Correlations of Petroleum Fluids Properties* can help an engineer make those tough decisions on site, as well. *Interactive Multimedia Applications for the Correlations of Petroleum Fluids Properties* is a <u>complete</u> success!

Acknowledgments

REFERENCES

[1]   D'Ignazio, F.: "Getting a Jump on the Future: Everything you'll ever need to know about multimedia authoring tools," *Electronic Learning* (November/December 1992) 28-31.

[2]   McCain, W.D.: *The Properties of Petroleum Fluids, Second Edition,* PennWell Publishing Company, Tulsa, OK (1990).

[3]   Beekman, G.: "Insights on HyperCard 2: Tips to make working with HyperCard a little less mysterious and a little more fun," *MACWORLD* (Sept. 1991) 297-300.

[4]   Seiter, C.: "Numerical and Symbolic Computation: Mathcad 3.1," *MACWORLD* (June 1993) 154.

[5]   Ga Côté, R.: "Mathcad: Better than Paper," *BYTE's Essential Guide to Windows* (Spring 1993) 115-117.

DEVELOPMENT OF A BILL OF MATERIALS FROM THE PDXI DATA MODELS

B. A. Stanford
Department of Chemical Engineering

ABSTRACT

The research on the development of a bill of materials has resulted in the construction of a portion of the working data model, as designed in theory by the Process Data Exchange Institute (PDXI). The theoretical object model can be found in *The PDXI Data Models* [1]. It was necessary to develop this working data model in order to be able to produce the bill of materials. The bill of materials was created with the help of the software package Paradox for Windows (version 4.0).

INTRODUCTION

The bill of materials research was performed for the Process Data Exchange Institute, a group of thirty companies in the computer, chemical, oil, and manufacturing industries. The PDXI team at the University of Missouri-Rolla has developed an interface between the AutoCAD program and the Paradox database that lets information such as equipment size and performance parameters be changed automatically in the database when it is changed in AutoCAD. The next logical program to develop is one that will automatically place an order for new or replacement parts when an engineer changes his schematic in AutoCAD. Thus, the research of the generation of bills of materials was performed.

PROJECT RESULTS

To accomplish the task of producing a bill of materials, the software program Paradox for Windows (version 4.0) was chosen because of its form designing capabilities and its inexpensive price. A working data model was programed into the database. The model is based upon the object model created by PDXI [1]. However, due to its enormous size, only selected portions of the Planning Level Model [1] and the other equipment models [1] were developed into a working data model. Some revisions to the PDXI object model were also necessary to include manufacturer information for the equipment.

Once the working data model had been completed, research began on the creation the bill of materials. With the help of the *Paradox for Windows User's Guide* [2] and an example provided by Dr. Neil Book [3] , a sample form (Fig. 1) was produced. The sample form describes the parts necessary to order from the manufacturer (Beckman Piping) if a section of pipe containing an orifice meter at Angeline's Los Angeles plant is to be replaced.

At this time, the program will perform a query for a piece of process equipment and retrieve the manufacturer and all parts indicated to be replaced

205

However, research is continuing on the integration of this program with the aforementioned AutoCAD- Paradox link developed by PDXI.

DISCUSSION

Research is still continuing in this area. Besides the previously mentioned research into the compatability of this program with the AutoCAD- Paradox link, research into the expansion of the object model continues. Work continues on the working data model as well. There is additional research being performed on various other applications associated with the working data model.

Angeline, Inc.

605 W. Alemeda Dr.

Los Angeles,   CA   94321

Beckman Piping, Inc.

811 Pine

Westchester,   VT   10233

03/23/94

Bill of Materials

Quantity	Description
1	1/2" Oriface Meter
2	5" Diameter Flanges
1	50 ft. Section Sched. 40 Steel Piping

Figure 1. Sample Bill of Materials

ACKNOWLEDGEMENTS

REFERENCES

Process Data Exchange Institute, The PDXI Data Models, Phase I Final Draft, American   Institute of Chemical Engineers, New York, 1993.

Borland International, Inc., Paradox for Windows User's Guide, version 4.0, Borland   International, Inc., Scotts Valley, CA, 1992.

Book, Dr. Neil L., Personal Communication, 1993-94.

PRELIMINARY EFFORTS TOWARDS THE ANALYSIS OF UNSTEADY PRESSURE MEASUREMENTS AROUND WING MODELS IN TRANSONIC FLOW

Stephen Witherspoon*
Department of Mechanical and Aerospace Engineering and Engineering Mechanics
University Of Missouri-Rolla, Rolla, Missouri 65401

ABSTRACT

A computer code was developed to implement methods of analyzing unsteady pressure measurements acquired from a wing model immersed in transonic flow. The code uses the fast Fourier Transform to identify phase changes and magnitudes of dominant frequencies over time in the unsteady pressure coefficients. The transformed data, as well as the raw data, are graphed and the results explained in detail identifying features depicted in the graphs. Also, the code performs some simple statistical calculations and smoothes the data to remove insignificant noise in the signal, if desired.

INTRODUCTION

Transonic flow refers to a flow speed that is subsonic, but that may become supersonic when it passes over a given body. As the speed of a flow over a wing, for example, approaches the speed of sound, the acceleration of this flow caused by the camber of the wing can generate supersonic speeds on the wing surface even though the free stream Mach number (M_∞) is subsonic. The free stream flow speed at which the flow becomes supersonic at some point along the body is referred to as the critical Mach number (M_{cr}) (Fig. 1.a.). When wings and other such bodies are immersed in transonic flow, certain unsteady phenomena can be observed. For instance, the formation of supersonic flow regions or "bubbles" on the wing surface may be seen as sketched in Figure 1.b. Inside the bubble, the flow is supersonic while outside the bubble, the flow is still subsonic. The bubble size grows as the free stream velocity approaches Mach 1. The supersonic flow inside the bubble decelerates due to friction and if the deceleration is not a smooth one, a shock forms at the bubble's downstream boundary. The ensuing steep pressure gradient causes the flow to become separated from the wing, and this separation

---

* Honor student

destroys the lift at that point and causes high drag (Fig. 1.c.). This Mach number is known as the Mach number at which the drag diverges or becomes large ($M_{drag-divergence}$). Since supersonic flow can develop from subsonic flow wherever sufficient camber is encountered, the lower surface of the wing can have the same problems of shocks, separation and drag as experienced by the upper surface. These complex flow features
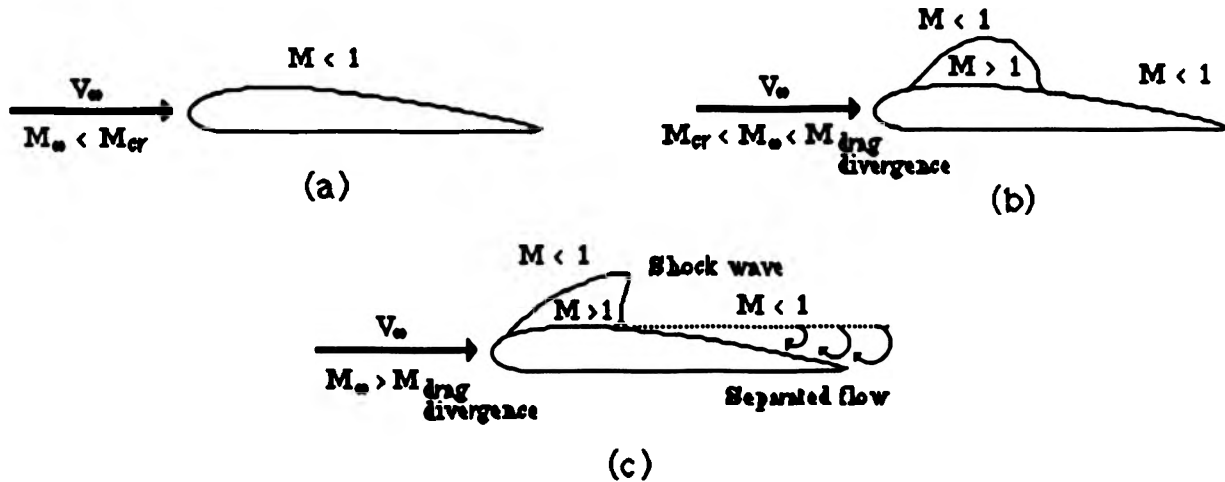
Figure. 1.   Phenomena caused by increasing flow Mach number.

are further complicated by the elastic nature of the wing model's structure. When conditions are right, shocks can alternate between upper and lower wing surfaces and the wing is said to flutter. This can obviously have catastrophic effects on the wing and structures to which it is attached, therefore, the prediction of the location and knowledge of the triggering mechanisms of these flow features is of great importance.

The investigation performed here consisted of analyzing unsteady pressure coefficients, collected from pressure transducers mounted in the wing model, in an attempt to study the various flow features. This was accomplished by developing a program that uses spectral analysis, among other things, to identify such features as flow separation, transition, and reattachment as well as shock waves along the wing surface. The data used for analysis is realistic, i.e. it is actual wind tunnel data where the flow is unsteady, viscous, compressible, and may have shock waves and massive flow separation. This kind of analysis can be used to validate CFD codes that attempt to predict flow features from mathematical formulations.

EXPERIMENTAL PROCEDURE

All the data used in this study was recorded from a benchmark model developed at the NASA Langley Research Center and tested in the NASA Langley Transonic Dynamics Tunnel (TDT) [ref. 1]. The model

210

consisted of a rectangular planform, half-span wing with an NACA 0012 airfoil cross-section attached to a pitch and plunge apparatus (PAPA). The apparatus allowed the model to move in the pitching (rotational) and plunging (translational) directions. The wing was separated from the apparatus by a splitter plate so that the flow would be undisturbed by struts and gauges. Pertinent instrumentation on this model consisted of 40 pressure transducers at each of two span locations, 60 and 95 percent of the wing span. At each location, the transducer ports were distributed over the upper and lower wing surfaces as shown in Figure 2. The concentration of transducers over the upper surface of the wing was greater, and since the wing was symmetrical, only data for transducers from the upper surface was analyzed.
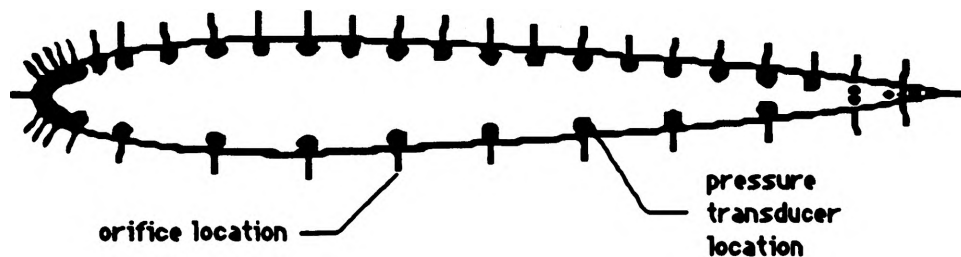
Figure. 2. Location of pressure transducers on wing model cross section.

METHOD OF ANALYSIS

As mentioned before, the data that was analyzed was in the form of non-dimensional pressure coefficients (Cp). Pressure coefficients are defined as being functions of free stream pressure (P_∞) and Mach number (M_∞), local pressure (p), and the ratio of specific heats (γ) as in equation 1.

$$C_p = \frac{2}{\gamma M_\infty^2}\left[\frac{p}{P_\infty} - 1\right]$$ (1).

The sign of Cp, then, would indicate whether the local pressure was higher or lower than the free stream pressure. If Cp were negative, there would be suction at that point on the airfoil surface. It is precisely these negative Cp values that are responsible for creating lift. The plots that are shown later are plots of negative Cp as a function of position (x) along the chord (c) of the wing, denoted (x/c).

With this in mind, simple statistical features of the data, such as the mean, variance, skew, and kurtosis were calculated for a given pressure coefficient versus time series. Smoothing of the data, to eliminate unwanted high frequency oscillations of the data (noise), was made possible by using the fast Fourier Transform (FFT) to low pass filter the

raw signal. The FFT was also employed in performing spectral analysis on the data. The computer program was designed to isolate the data of an individual transducer from a data set containing data for 40 transducers and to then evaluate the FFT of this data. The resulting data set contained a set of complex numbers symmetrical about the zero frequency. The half of the complex numbers that were on the negative frequency side were meaningless, but from the other half, the magnitude and phase could be calculated. The complex numbers produced by the FFT were split into real and imaginary portions and placed in consecutive data elements. Magnitude was then found by calculating the square root of the sum of the squares of two consecutive elements. The phase was simply the arc tangent of the two consecutive data elements. Some conditioning of the phase was done to reduce erroneous results of dividing two very small numbers. This division was necessary because the phase angle is equal to the arc tangent of the quotient of the imaginary over real portions of a given complex number.

RESULTS

The pressure coefficient data is highly unsteady at some points, as can be seen from Figure 3, a sample of Cp versus time plot for several transducers at M=0.882. Therefore the plots in Figure 4 are plots of the time-averaged pressure coefficient. These pressure coefficient plots (Fig. 4) for the given airfoil cross-section have the typical convex region
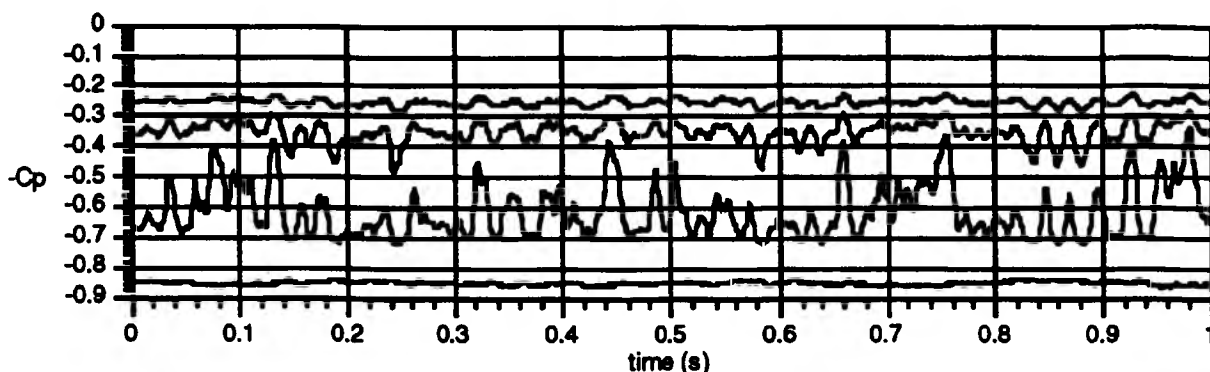
Figure. 3. Unsteady pressure coefficient measurements at M=0.882

indicating a low pressure area that is due to the flow acceleration over the airfoil camber. These plots, however, contain pressure variations that are not typical. Parts (a) and (b) of Figure 4 show a suction peak near the leading edge, at 0.075c, that does not follow the general trend of the rest of the pressure coefficients. Parts (c)-(e) of Figure 4 exhibit large convex regions with steep trailing edge boundaries. These sharp increases in pressure may indicate shocks.

212

Figure 4 presents the pressure coefficient plots in order of increasing Mach number in order to better visualize the appearance and progression of flow features. Part (a), at M=0.512, shows a fairly smooth Cp profile with the exception of a suction peak at x=0.075c. The smoothness of the profile indicates that there are no shocks over the airfoil. The nature of the suction peak is not fully understood at this point, but it is thought to be some sort of bubble in which separation, transition, and reattachment of the flow occurs. The pressure recorded by the transducer within the

(a)

(b)

(c)

(d)

(e)
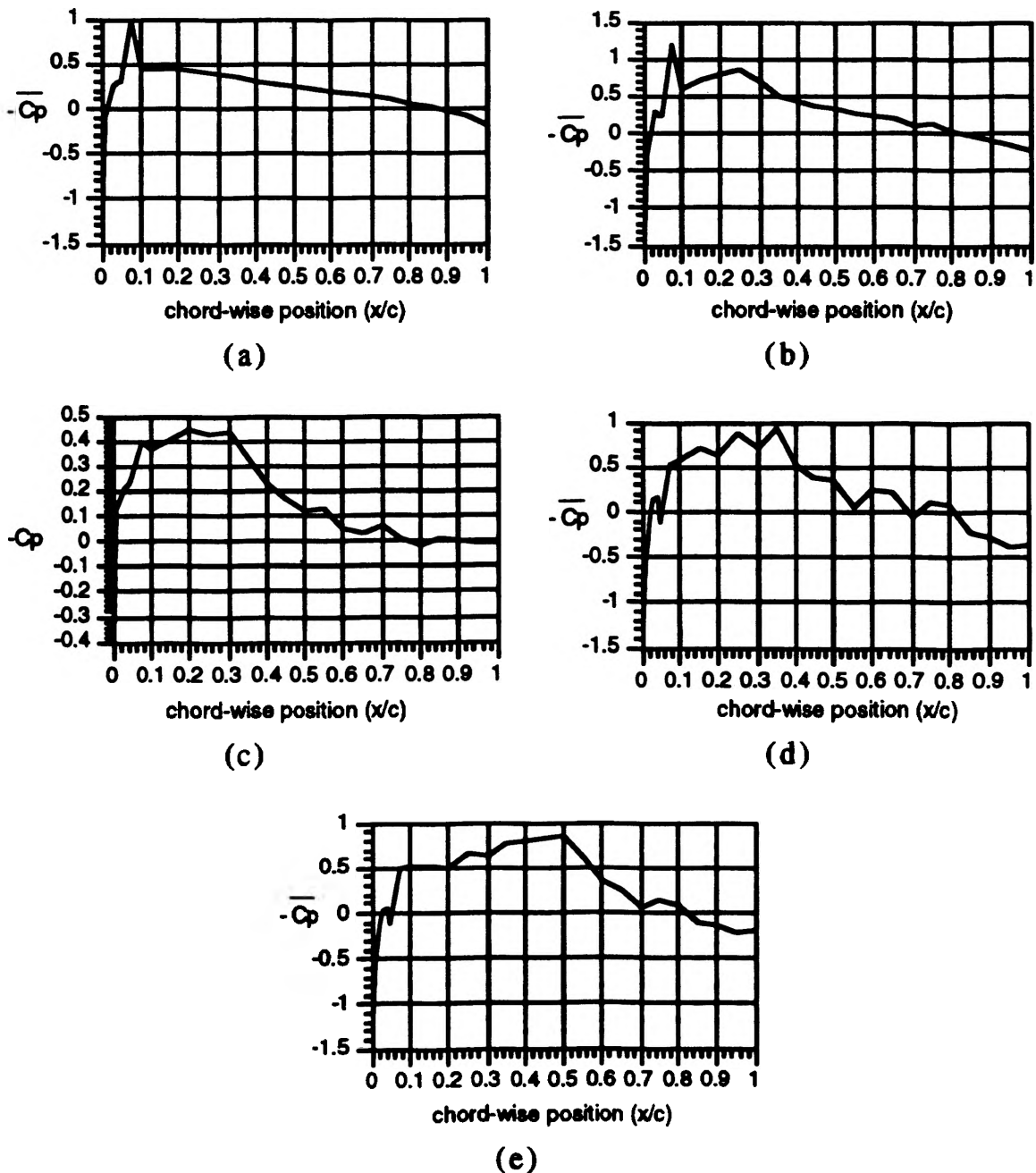
Figure. 4. Mean pressure coefficients (Cp$_{bar}$) versus chord-wise position (x/c). (a). M=0.512; (b). M=0.774; (c) M=0.780; (d) M=0.824; (e) M=0.882.

bubble is quite low when compared to the free stream pressure and thus shows up as a peak in pressure coefficients. It is possible, even at Mach numbers of 0.512 and lower, for supersonic flow to be present in this bubble causing the suction peak [ref. 2]. As the Mach number is increased to M=0.774, (b), the suction peak is still present, but another bulge has appeared. This bulge between x=0.1c to x=0.35c may be a supersonic bubble as described before and sketched in Figure 1. The trailing edge of this bubble may not be steep enough at this point to be a shock. A smaller rise in Cp values occurs around x=0.75c. This may be the beginnings of a smaller supersonic bubble. Once the Mach number has increased to M=0.780, the leading edge suction peak and supersonic bubble have merged to form a large region of low pressure. The downstream boundary of this bubble indicates that a shock is present. There also seems to be a series of two smaller bubbles and weak shocks at x=0.55c and x=0.7c after the main bubble and shock. For a Mach number of 0.824, the flow is very complex and highly unsteady. Part (d) of Figure 4 shows an oscillation at x=0.05c and then the large supersonic bubble starting at about x=0.075c. The large bubble contains what could be multiple weak shocks at x=0.15c and x=0.25c and then a large shock at
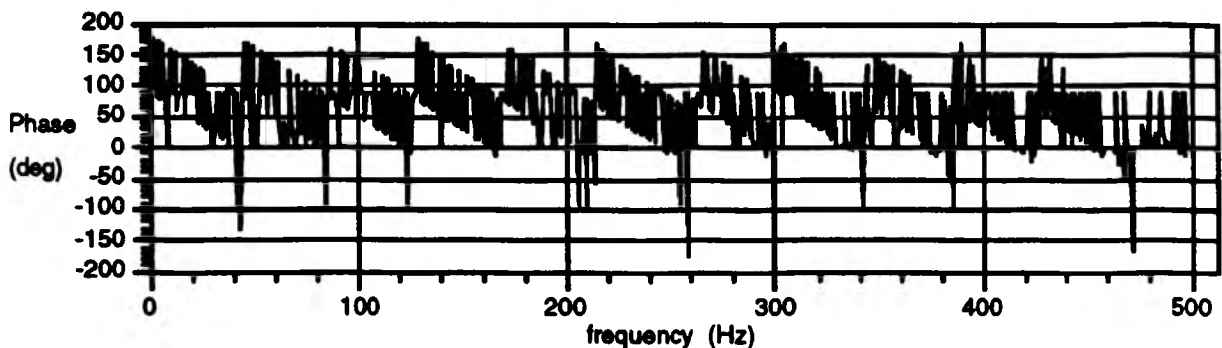
Figure. 5. Phase for M=0.882.
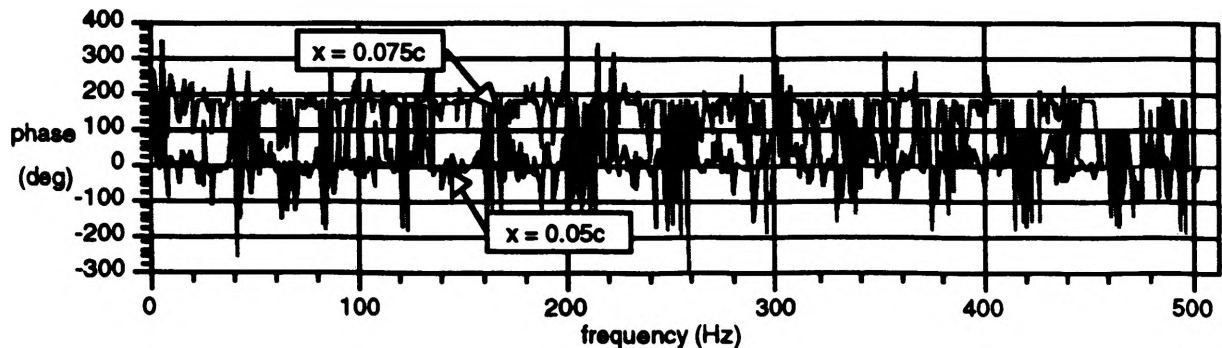
Figure. 6. Phase difference at M=0.882.

x=0.35c evidenced by a large drop in Cp. The flow after this contains even more weak shocks at x=0.65c and x=0.8c as the flow attempts to accelerate again. By the time a Mach number of 0.882 is reached, part (e), the supersonic bubble is well developed and occupies a large portion of the airfoil surface from x=0.075c to x=0.5c. Perhaps one weak shock occurs within the bubble at x=0.25c, but otherwise, the bubble is fairly uniform, unlike the case at M=0.824. At x=0.5c, the drop in Cp values indicates the presence of a strong shock, and only one weak shock follows at x=0.8c.

When phase information from the FFT for a given transducer was plotted, the resulting graph was quite periodic (fig 5). This information was somewhat confusing in terms of its value in describing flow features and activity. In order to discern any patterns that might be present in the flow, phase differences were calculated instead. This difference was the value of the phase at the leading edge transducer minus the value of the phase at a given transducer. These differences were calculated and plotted for several transducers at each of several flow speeds. The lines shown in some of the phase difference graphs are actually third degree polynomial curves that best fit the data. This was done so that the average phase could be better visualized. From these figures, one can clearly see when there is a shift in phase somewhere between various pressure transducer locations. Figure 6 shows the actual data for the highest Mach number case, M=0.882. As is evident from the graph there is considerable oscillation around the mean value of a given series. For this reason, subsequent plots are shown as best fit curves. Even so, the trends can be seen from Figure 6 and the phase shift is obvious. The phase shift in this figure occurs between x=0.05c and x=0.075c. Figure 7, however, shows that this shift occurs much earlier on the airfoil surface. For a Mach
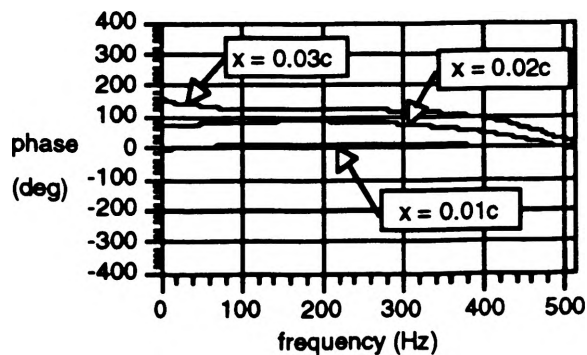
Figure. 7. Phase difference at M=0.824.
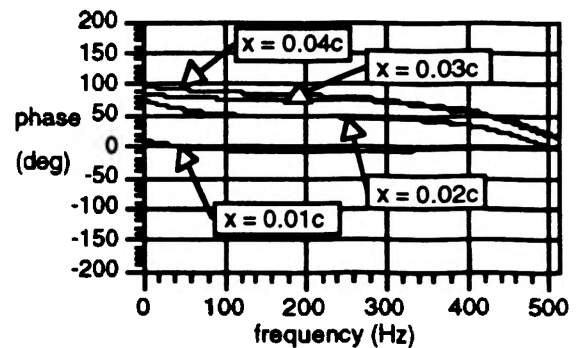
Figure. 8. Phase difference at M=0.512.

number of 0.824, the shift occurs between x=0.01c and x=0.02c, as can be observed from the figure. The shifting is caught in stages as evidenced by

the fact that at x=0.02c the phase shifts a little more before stabilizing at x=0.03c.

The same trend can be seen in Figure 8, which is for a much slower speed of M=0.512. The shift again begins right after x=0.01c and finally stabilizes at about x=0.03c. This behavior of early phase shifting is characteristic of all the flow speeds analyzed between 0.512 and 0.824.

The meaning of a 180° shift in phase is that the value of the signal before transformation has changed sign. The phase shift makes sense, then, when one observes the graphs of the pressure coefficient versus chord-wise position (fig. 4). In parts (a) through (c) of Figure 4 the positive pressure coefficient goes negative quickly, whereas in parts (d) and (e), the transition is further back along the airfoil surface. This corresponds to the phase shift not occurring at M=0.882 until x=0.05c to x=0.075c.

The magnitude, in arbitrary units, versus frequency series can also be obtained from the FFT and plotted. Figure 9 shows a sample of these results for M=0.824. At positions x=0.01c and x=0.02c, there was a spike at a frequency of about 4.5 Hz. This low frequency corresponded to the pitching and plunging motions of the wing. The wing model's angle of attack changed due to the pitching motion, and the velocity vector of the free stream relative to the wing changed due to the plunging motion of the wing. These variations with time corresponded to variations in the pressure coefficients. Figure 10 shows the variation
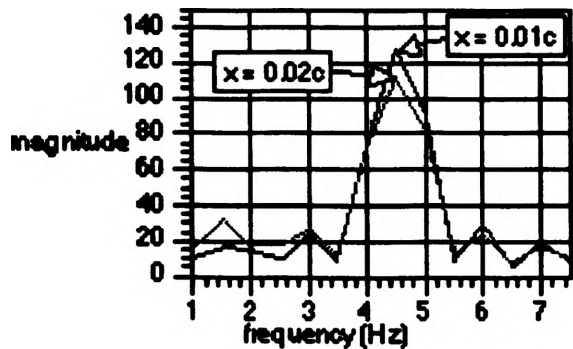
Figure. 9. Magnitude versus frequency versus at M=0.824.
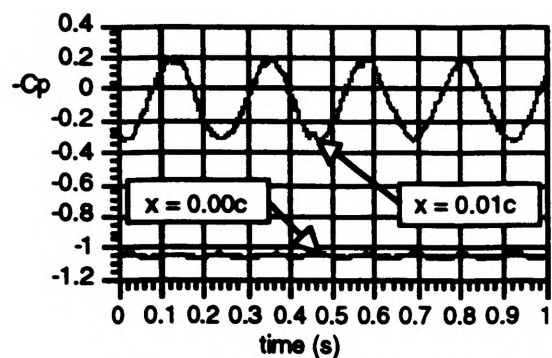
Figure. 10. Pressure coefficient time at M=0.512.

with time of the pressure coefficients for two pressure transducers located at x=0.00c (leading edge of the wing) and x=0.01c. The frequency of 4.5 Hz for x=0.01c seen in Figure 9 is clearly seen in Figure 9 where the sinusoidal wave repeats itself about 4.5 times over the sampling period of one second.

CONCLUSIONS

During the course of this research effort, several computer routines were developed to analyze unsteady flow measurements around an aeroelastic wing model in transonic flows. Preliminary results indicate that the FFT could be a useful tool for the analysis of transient flow measurements. By observation of the raw data as well as the FFT of this data, it is possible to determine the basic structures in complex flows. Structures such as transition bubbles, supersonic bubbles, and shock waves can be identified as well as the dominant flutter frequencies and phase shifts.

Further research is necessary to determine more precise meanings of the phase information gathered by the FFT, in particular, it's periodic nature. Comparisons between data from the two span-wise positions as well as between data from upper and lower wing surfaces might also lead to new knowledge of flow developments. Sequences of graphs over a time interval could aid in discovering patterns in the flow not seen previously from a frozen instant in time.

The overall research experience has been multifaceted in its educational value to me. I have become familiar with workstations, the UNIX operating system, the C programming language, the Fast Fourier Transform, and naturally the problem of unsteady flow over an airfoil. The opportunity to be involved in a project related to my major field of study has given me motivation and helped to keep my interest in the aerospace engineering profession. The repercussions of what I have learned through this project will be felt for a long time.

ACKNOWLEDGMENTS

REFERENCES

1. Rivera, J. A., Jr.; Dansberry, B. E.; Bennett, R. M.; Durham, M. H.; Silva, W. A., "NACA 0012 Benchmark Model Experimental Flutter Results with Unsteady Pressure Distributions", AIAA paper No. 92-2396, April, 1992.

2. Chandrashekhara, M. S.; Carr, L. W.; Wilder, M. C., "Interferometric Investigations of Compressible Dynamic Stall over a Transiently Pitching Airfoil", AIAA Journal, Vol. 32, No. 3, March 1994, pp 586-

593.

3. Brigham, E. O., "The Fast Fourier Transform", Prentice-Hall, Inc., 1974.

4. Bennett, Robert M.; Dansberry, Bryan E.; Farmer, Moses G.; Eckstrom, Clinton V.; Seidel, David A.; and Riviera, José A., Jr., "Transonic Shock-Induced Dynamics of a Flexible Wing with a Thick Airfoil", Journal of Aircraft, Vol. 30, No. 1, Jan.-Feb. 1993, pp 112-118.

5. Stack, J. P.; Mangalam, S. M.; and Berry, S. A., "A Unique Measurement Technique to Study Laminar-Separation Bubble Characteristics on an Airfoil", AIAA paper No 87-1271, June, 1987.

6. Johnson, C. B.; Carraway, D. L.; Stainback, P. C.; and Fancher, M. F., "A Transition Detection Study Using a Cryogenic Hot Film System in the Langley 0.3-Meter Transonic Cryogenic Tunnel", AIAA paper No 87-0049, January 1987.

7. Owen, F. K., "Transition Experiments on a Flat Plate at Subsonic and Supersonic Speeds", AIAA Journal, Vol. 8, No. 3, March 1970, pp 518-523.

HIGH-PRESSURE WATERJET TECHNOLOGY: A REVIEW AND DESIGN OF HIGH-PRESSURE HYBRID DRILLBITS

Zainal Adnan, Azmi
Department of Petroleum Engineering

ABSTRACT

The petroleum industry has seen many technological advances since oil was first discovered in the 19th century. Some of the current technological advances in the industry include cuttings transport, drillbit design, logging, and horizontal and directional drilling. Currently, research projects are being done at UMR to find ways to further reduce drilling costs and develop new technology that could improve the drilling effectiveness. One such project is the development of high-pressure waterjet / hybrid bits to replace the conventional mechanical drillbits. In this design, the advantages of waterjet penetration are combined with those of mechanical teeth cutting action.

At UMR, the project is under the overall direction of Dr. David A. Summers, a well-known researcher on the high-pressure waterjet technology, and Dr. A.W. Iyoho, an expert in the drilling technology. Preliminary results show that there are many advantages to high-pressure waterjet bits compared to conventional bits. Therefore, it is possible that the high-pressure waterjet technology could someday be used commercially in the mining and petroleum industries once the design is perfected.

This paper discusses advantages and problems related to the high-pressure waterjet/ hybrid bit technology and proposes a design to address the problems. The designs were developed in partial fulfillment of an advanced drilling course (PE314) taught by Dr. Iyoho.

INTRODUCTION

Studies have shown that rocks could be eroded or cut by water when subject to a high pressure. However, since there is some difficulty associated with supplying the amount of energy needed for the process, another alternative, which is the high-pressure waterjet / hybrid bit was developed.

This alternative design, which combines the advantages of waterjet penetration and that of mechanical teeth cutting action, might be more feasible. Studies have also shown that the high-pressure waterjet / hybrid has potential in reducing drilling costs and improving drilling effectiveness.

ADVANTAGES

There are many advantages found on the high-pressure waterjet bits compared to conventional bits. Some of the advantages include programmed borehole roughness, higher penetration rate, longer bit life, and a tighter turning radius. These advantages can be applied in slim-hole drilling and high-angle, horizontal drilling.

Programmed Roughness

Using the high-pressure waterjet, a programmed roughness of the borehole wall could be achieved [1]. The roughness of the borehole is important to provide a strong contact between the casing and the borehole wall during cementing. If the borehole wall is too smooth, the cement will not be able to hold the casing and this would cause the casing to slip.

The roughness of the borehole wall could be programmed by controlling the incremental distance advanced by the drill for each revolution of the drillhead [1]. If the incremental distance advanced by the drill per revolution is too large, the borehole wall would be relatively smooth and vice-versa.

Higher Turning Radius

The high-pressure waterjet / hybrid bit also allows a tighter turning radius. In a study done at UMR, it was found that a horizontal well could be drilled with a turning radius on the order of 1 ft. Because of this advantage, the high-pressure waterjet / hybrid bit could be used in drilling multiple overshoots from one vertical well and in drilling with coiled tubing.

Longer bit life and higher penetration rate

The high-pressure water-jet / hybrid bit is also more durable compared to conventional bits. On a study by CERCHAR in France, it was found that using the same thrust, the penetration rate of a bit-assisted by a jet with two diamond inserts was higher than that of a conventional bit with two inserts [2]. This is shown in figure 1.
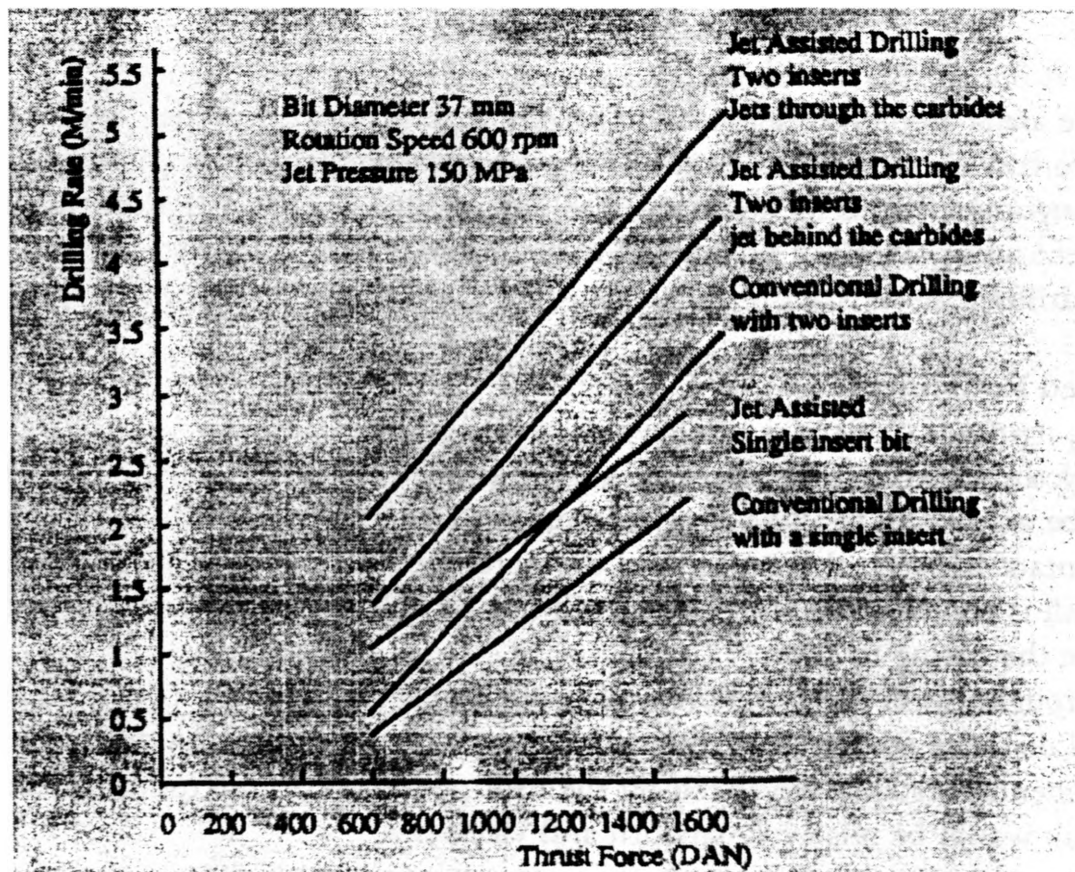
Figure 1: Study of Relative Performance of Differently Designed Waterjet Assisted Mechanical Bits by CERCHAR in France.

In studying the advantage on bit life, it was found that the waterjet-assisted bit has a longer life than the conventional bit. The study showed that at a drilling rate of 1 meter per minute, a waterjet bit with two 0.4 mm nozzles could penetrate up to about 26 meters while the conventional bit could only penetrate up to about 6 meters [1]. This is shown in figure 2.
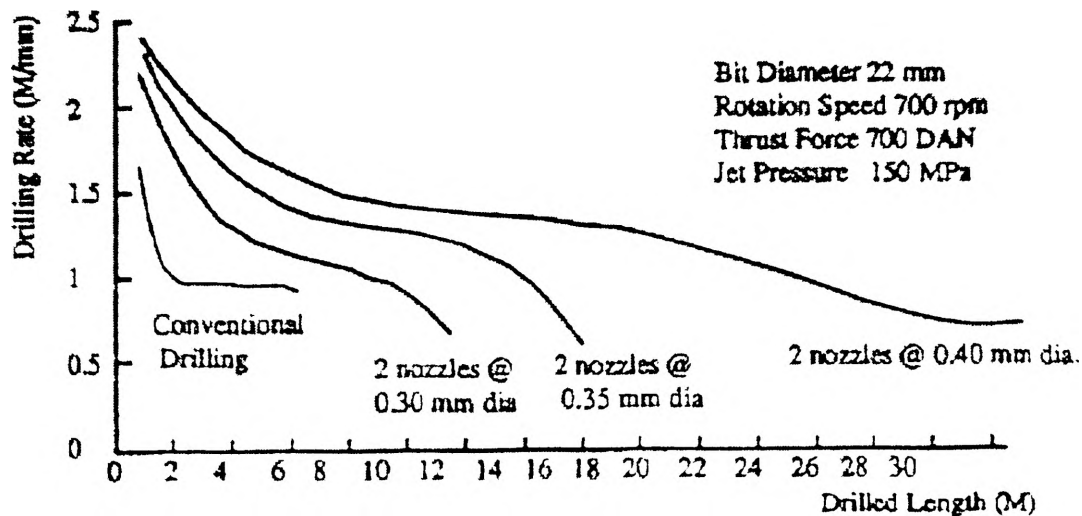
Figure 2: Effect of Differently Designed Waterjet Assisted Mechanical Bits on Bit Life

Economical

The high-pressure water-jet / hybrid bit is not only better in performance to the conventional bit, it is also more economical. The high-pressure waterjet / hybrid bit has potential in reducing drilling cost associated with drilling deeper wells. This is because high-pressure waterjet / hybrid bit has a longer life and higher penetration rate compared to conventional bit. In drilling a well, time is money. If the bit has a higher penetration rate and a longer life, the time needed to change the bit can be reduced, thus reducing the drilling time and saving money

In a comparison made on the cost of using a jet-assisted bit and a conventional bit, it was found that the jet-assisted bit is cheaper than the conventional bit. The data taken at the Somerset Mine of U.S. Steel demonstrated this in the table 1 on the next page.

TABLE 1: APPROXIMATE COMPARISON OF CONVENTIONAL AND WATERJET ASSISTED DRILLING COST USING RESIN BOLTING.

Item	Conventional	Jet Assisted
Machine Cost	$70,000	$110,000
Drilling Rate (M./min.)	0.75	2.4
Bolting Cycle (min.)	5.0	3.2
Bit Reconditioning Cost	$6.00	$40.00
Bit Life (M. drilled)	6	112.5
Drill Rod Cost	$28.00	$110.00
Drill Rod Life (M. Drilled)	180	1,500
DRILLING COST ($/M.)	$1.17	$0.43

Note: The basis of the comparison can be summarized as: installing bolts through a combined sandstone and shale roof, with the bolts being installed to a depth of 1.8 meters. With conventional drilling the drill is plugged approximately once every third hole, and bits are changed after each hole. The data is taken from observations at the Somerset Mine of U.S. Steel.

PROBLEMS

Although the high-pressure water-jet bit was better than the conventional bit, some problems existed in the tests and studies done. One problem is in determining the angle of the nozzles and the rate of advance of the bit. These must be designed so that the drillhead is not obstructed by protruding rock ledges created when the rate of advance of the bit is too slow. This is shown in figure 3.
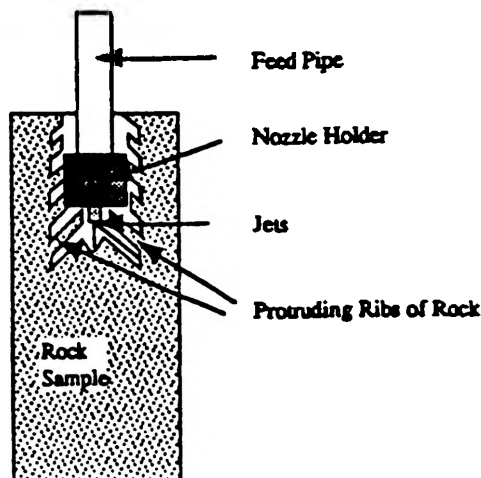
Figure 3: Protruding rock ledges preventing the drillhead
from advancing.

Another problem exists when using the high-pressure waterjet / hybrid bit with coiled tubing. Since the drill string does not rotate, swirling around the drillstring is reduced. This would cause an increase in particle settling and soon causes dune formation along the annulus. The dune would ultimately fill the hole and cause a stuck pipe [3].

DESIGNS

All the designs presented here are of the rotating drillhead type. The nozzles are made of ceramic instead of ordinary steel so that the nozzles would last longer. Steel nozzles might wear off quicker when the material is subjected to the high pressure of the water passing through and if some abrasives are added to assist the cutting power of the jet.

The drillheads are fitted with collars to counter the problem of the drillhead from being prevented from passing through the hole by the protruding rock ledges [1]. The collars would function to break the rock ledges on contact.

To solve the problem of particle settling, angled retrojets could be installed along the drillstring. These retrojets would cause the fluid in the annulus to swirl around the drillstring to the surface and reduce the possibility of particle settling. Drilling muds could also be run through these retrojets to help in transporting the cuttings to the surface.

Adding steel shots to the jet stream is also recommended in the design to aid in cutting through hard rocks such as basalt. The effectiveness of this method has been proven by researchers at UMR [1].

Design 1

This design has two nozzles that are inwardly pointing toward one another. However, the nozzles are positioned at an angle so that the path of the jets does not interfere one another. The inner nozzle functions to cut the bohehole wall on the outer diameter large enough so that the drillhead could pass through. The outer nozzle functions to cut the rock on the inner diameter to clear the path directly in front of the bit body. This would eliminate the possibility of the bit being prevented from advancing.

The two nozzles are located almost directly opposite one another so that the force exerted by the waterjet coming through the nozzle would be balanced. This is to ensure that the drillhead would cut in a straight direction and not be strayed off-course.

TOP VIEW

CROSS-SECTION VIEW

Waterjet Pipe

Retrojet

Rotating Bit

Collars

Diamond Insert
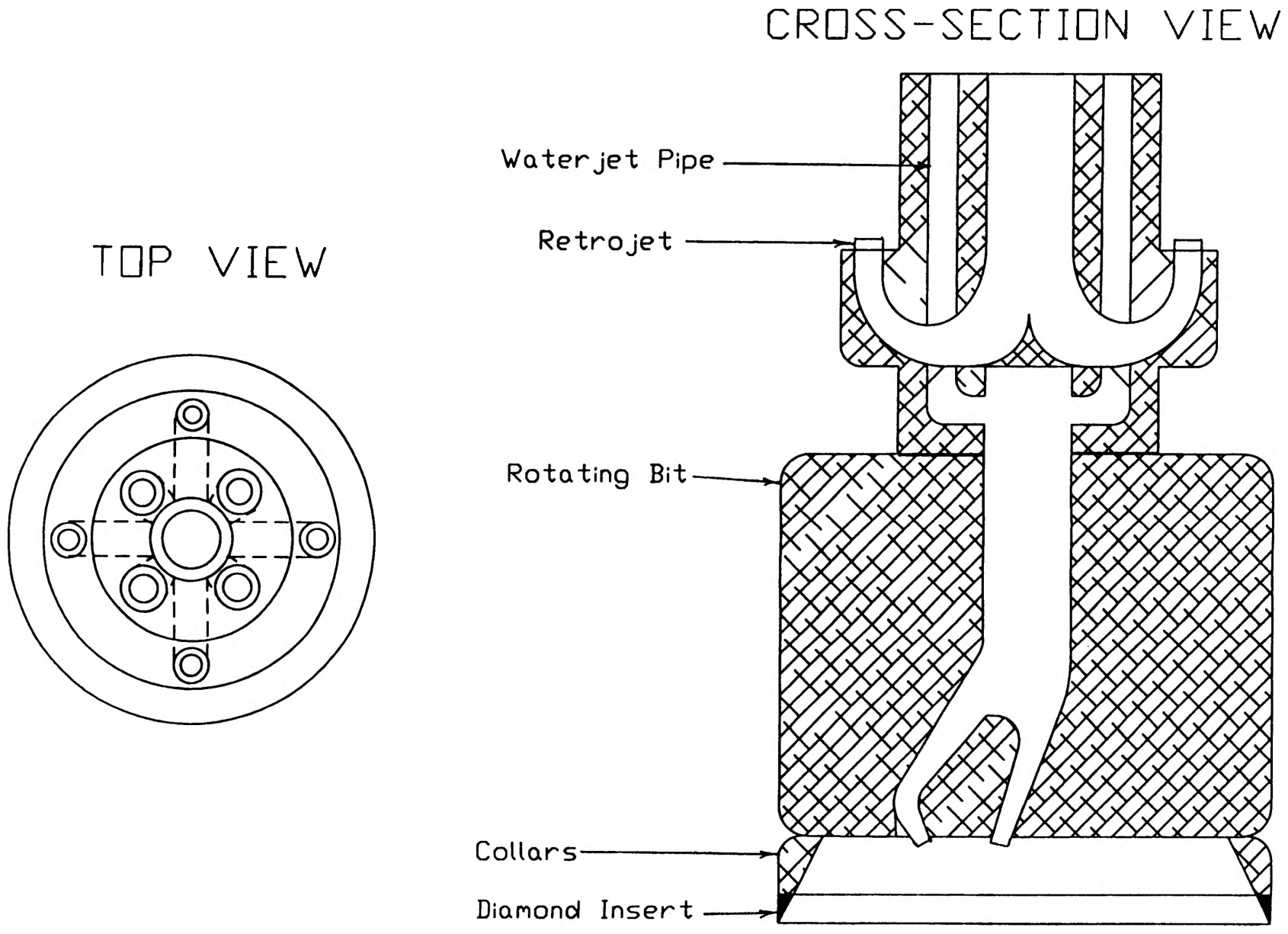
Figure 4: Cross-sectional and Top View of Design 1

ANGLED RETROJETS
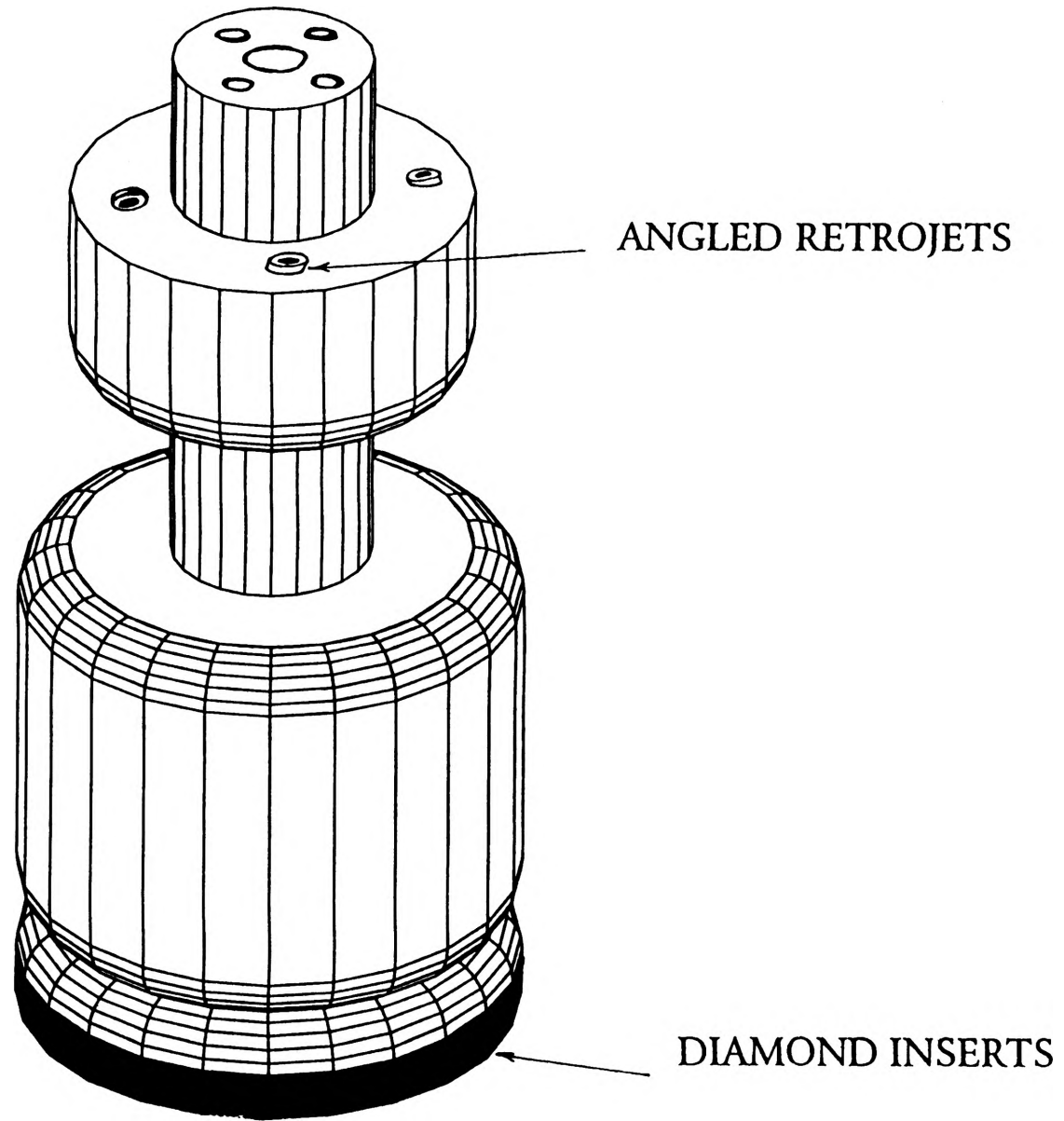
DIAMOND INSERTS

Figure 5: 3-D View of Design 1 Showing Retrojets.
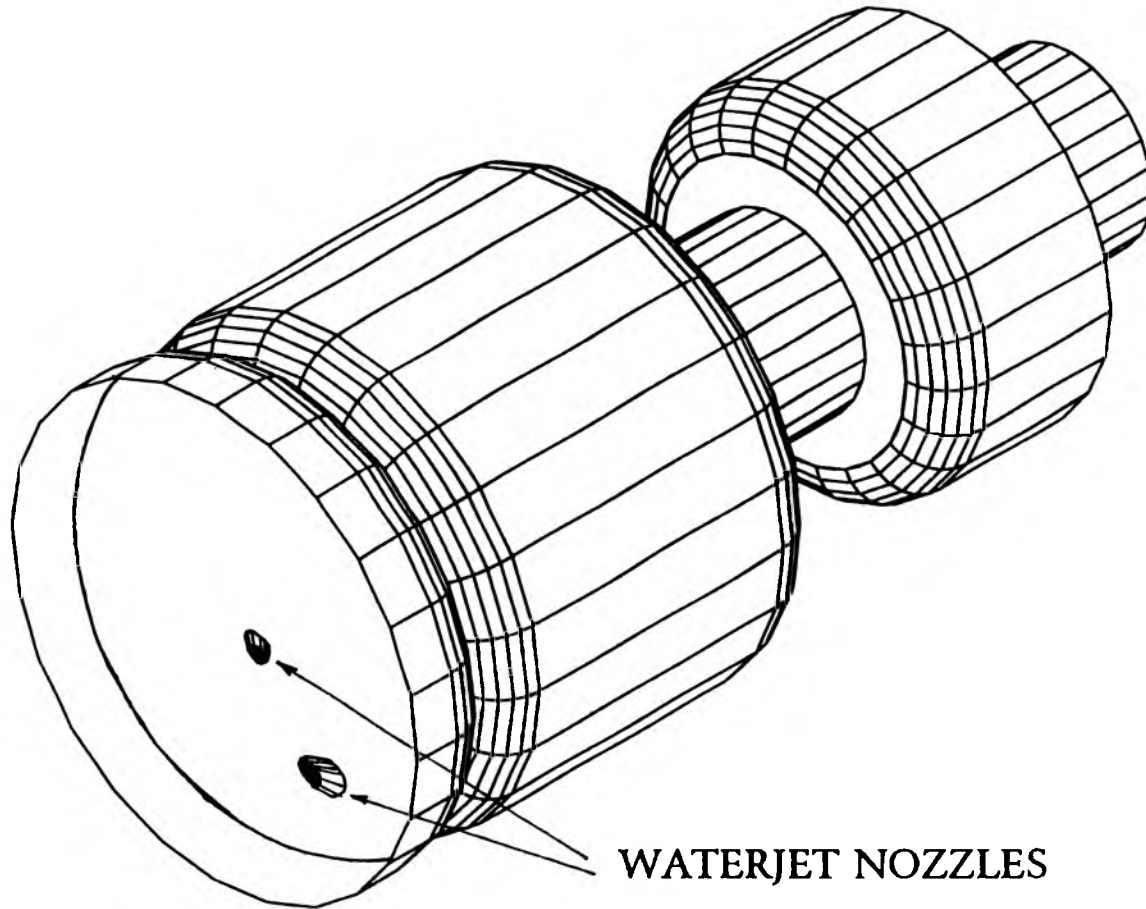
WATERJET NOZZLES

Figure 6: 3-D View of Design 1 Showing Waterjet Nozzles

Design 2

This design has one nozzle located in the center of the bit body and a row of diamond or PDC inserts attached to a mechanical cutter. The nozzle is aimed toward the outer diameter of the borehole and functions to cut the rock such that a core would be developed in the inner diameter of the borehole. The core would then be broken into smaller fragments by the PDC or diamond cutter.

Another way to prevent protruding rock ledges from obstructing the drillhead from advancing is by making sure that the drill does not advance faster than the width of the waterjet cutting zone on each rotation [1]. This means that the speed of rotation of the drillhead and the rate of advancement of the drillhead should be controlled.

TOP VIEW

3-D VIEW

SIDE VIEW

DIAMOND INSERT

Figure 7: Design 2
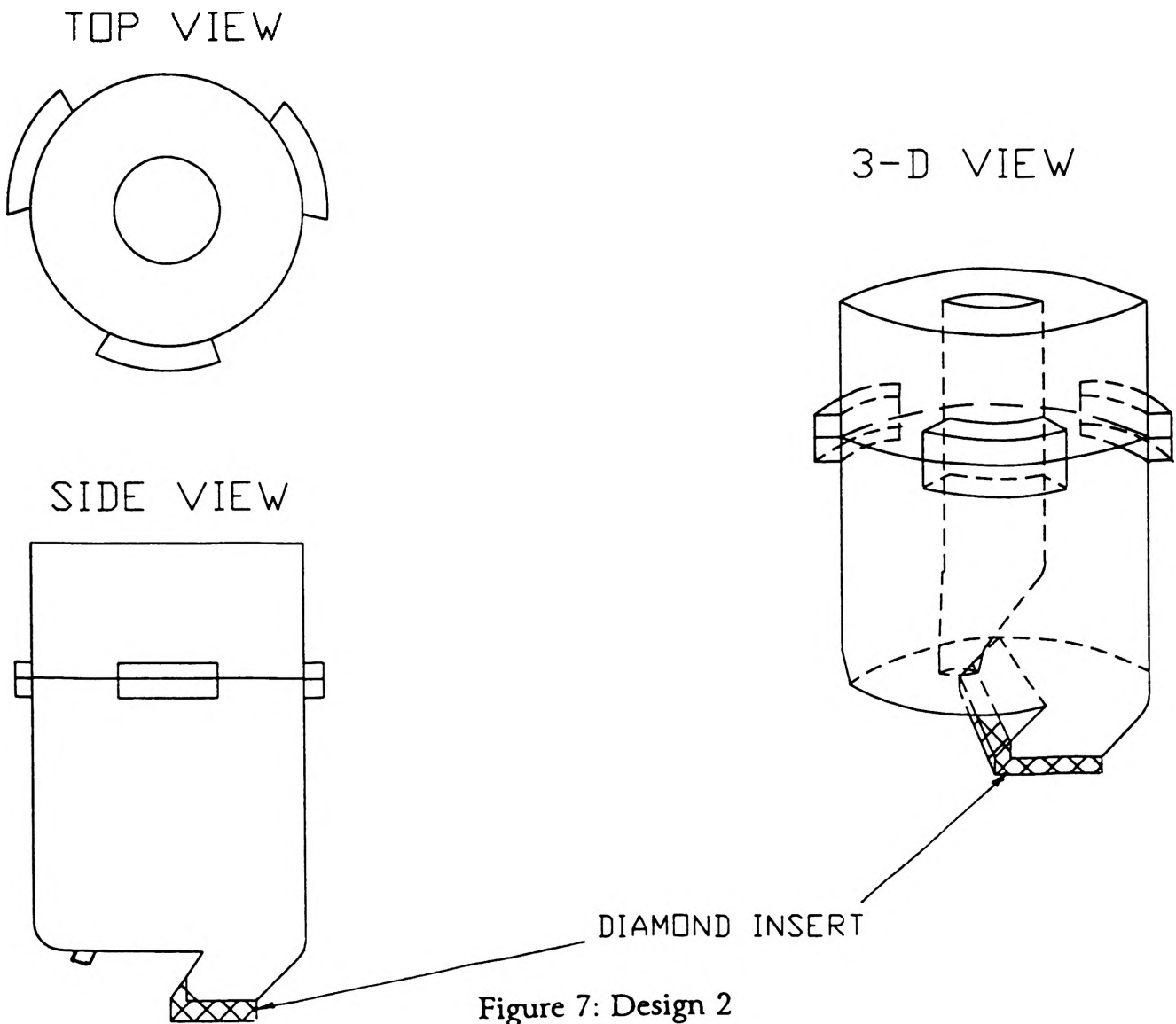
CONCLUSION

The development of the new design and technology of the high-pressure water-jet is very important in the mining and petroleum industry because of the many advantages that it could bring. With these advantages, marginal production zones could also be developed due to the reduced cost of drilling and this would increase the resource base available. Based on the many advantages of the new technology, it is possible that the high-pressure waterjet / hybrid bit would someday be used in the mining and petroleum industry to replace conventional methods.

ACKNOWLEDGMENTS

REFERENCES

1.   Iyoho, A.W., Summers, D.A., Galecki, G., "Petroleum Applications of Emerging High-Pressure Waterjet Technology," 68th Annual Technical Conference and Exhibition of SPE, SPE 26347, October 1993.

2.   Lefin Y. & Hurel A. "Rotary Drilling assisted by Waterjets and other recent developments of high pressure waterjets for the cutting of rocks in France," paper H3, Proc 7th ISJCT, BHRA, June 1984, Ottawa, Canada, pp. 439-454.

3.   Summers, D.A., "The Development of High-Pressure Waterjet for Drilling Purposes," Paper II-3, Proc Int Symp Water Jet Tech, Tokyo, Japan, Dec., 1984.

UMR OURE PAPERS

EVALUATION OF THE EDGE STRENGTH OF ARCHITECTURAL GLASS

Kevin L. Alexander, Department of Civil Engineering

ABSTRACT

A mechanical device to test the edge strength of glass was developed in a previous study and was to be modified for more accurate results in this study. The mechanical apparatus allows for a load to be applied and directed along one diagonal of a glass beam making the other diagonal the neutral axis. This allows only one edge to be in tension where the failure is desired.

This study evaluated the scored edge lines and the other edge lines of annealed glass which was cut by an experienced glass cutter with a steel scoring wheel, and a carbide scoring wheel. The failure loads were recorded for four test series of 30 samples each. The first two series were performed to determine the scored edge strength of the glass specimen. The third series tested the other edge of both the steel and carbide cut glass. Finally, one series of tests was administered to determine the combined effects of the scored edge line and the other edge line of carbide cut glass. The scored edge line was on the order of 50 percent weaker than the other edge line and the steel cut glass exhibited 25 percent less strength than the carbide cut glass.

INTRODUCTION

The edge strength of an architectural glass window is an important property in the design of glass. Care must be taken not to overlook the importance of thermal and mechanical loads which can cause failure or cracking at the glass edges. In the case of mechanical forces such as wind pressure, surface strength or edge strength can be deterministic of failure and in the case of thermal stresses, edge strength is always deterministic of failure [1]. Glass, from its chemical composition is a very stiff and brittle material, and like most brittle material tension is the predominant

mode of failure. Glass strength is dependent on the glass surface exhibiting tensile stresses. Larger surfaces under tensile stresses increase the probability of premature failure according to the weakest-link theory. The larger the surface, the more flaws and weak spots which predetermine the initial failure locations. This sensitivity to surface conditions means that strength is not an intrinsic property of glass, and that the strength depends strongly on the history of treatment, handling of surface [2].

The handling of the surface and edges when cutting glass can determine how a glass lite will respond to loadings. Cutting a glass window to size requires a careful scoring of one surface followed by breaking the lite along the scored line (see Figure 1).
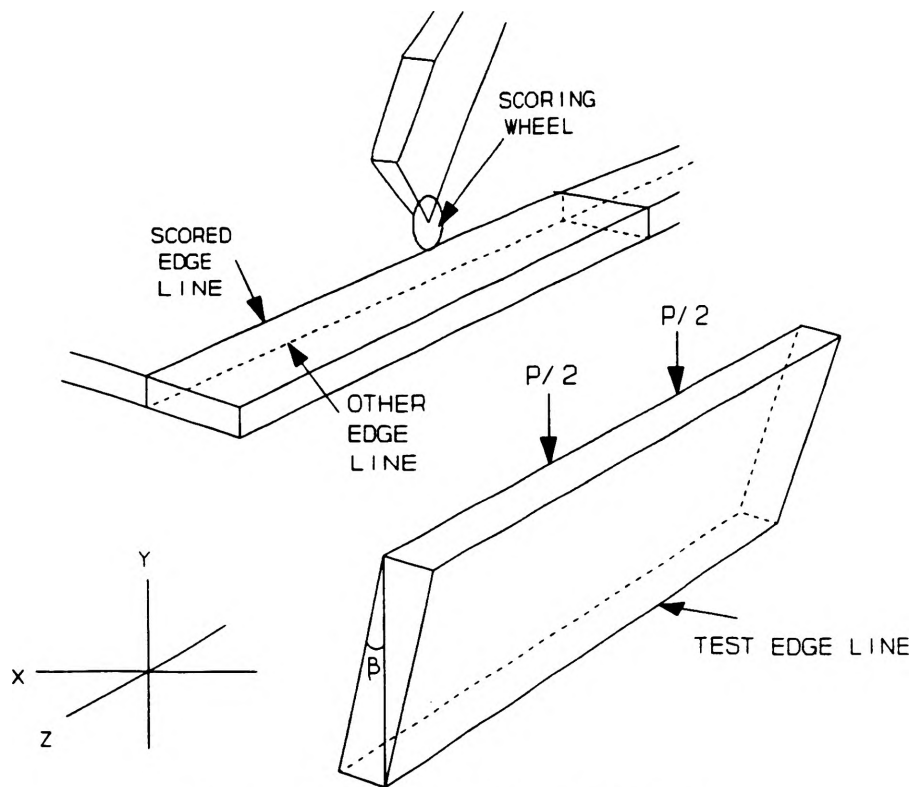
FIGURE 1. Edge Definitions

Scoring the glass when cutting damages the glass surface and induces flaws along that edge. A glass window will then have a weak scored edge and a relatively strong unscored edge called the "other edge."

This research focused on the evaluation of the edge strength

236

of window glass. The test of both the scored edge line and the other edge line of annealed glass specimens constituted the experimental program of this investigation. The test was to model the thermal and mechanical edge stresses that are observed during the normal use of a glass unit. Thermal stresses are created by a temperature gradient generated by the interior of the glass being heated by the sun and the edges of the glass being kept cool by the frame of the window. If the temperature gradient is large enough, the expansion of the interior of the glass can force the outside edge into tension therefore inducing failure and cracking at the edges. In the case of mechanically induced stresses, the wind causes the window to deflect in or out putting the edges and one of the surfaces in tension. This tension, if large enough, can cause failure.

The following report identifies the research plan and theory, describes the testing apparatus, presents some preliminary results, identifies errors, and gives insight into the test. The report also includes some recommendations for future work.

RESEARCH PLAN

The research plan was to perform edge strength tests on glass lites for the scored edge and the other edge when cut with a steel wheel cutter and a carbide wheel cutter (see TABLE I).

TABLE I: Testing Outline

Test specimen size: Beam of 6.00" span, 1.00" deep, and
                        0.125" wide
Type Of Glass: Annealed glass
No. of Specimen Tested: 30 per series
Test Parameters: *Type of Scoring Wheel, Steel vs. Carbide
                     *Test Edge, Scored edge in tension while
                        other edge exhibits nil stresses, other
                        edge in tension while the scored edge
                        exhibits nil stresses, and both edges in
                        tension simultaneously
Series of Tests:
             I. Steel Scoring Wheel - Scored Edge Line
            II. Carbide Scoring Wheel - Scored Edge Line
           III. Other Edge Line
            IV. Carbide Scoring Wheel - Combined Edge Line
Loading Rate: 100 lbs. per minute

Test Concept

This study incorporated the theory of unsymmetrical bending of rectangular beams [3]. The loads were applied along the diagonal of a rectangular glass specimen. This placed the edge line where the force was applied into compression and placed the opposite edge line in tension. This allowed the other diagonal of the rectangular cross section to become the neutral axis.

In order to provide pure bending in the test region, a four point loading was applied (i.e. two supports, and two applied loads). This test arrangement was chosen over the three point loading system, in order to test a larger area of the edge line.

Machine Description

The testing facility used in this project was based on a modification of an existing facility used in a previous study. The new facility consisted of the glass testing bed, the loading angle and ball bearing, a hydraulic cylinder and jack, a hydraulic control valve, a 2000 lb. load cell, a load conditioner, and an X-Y plotter. This system was the same as the previous system, however changes were made to the glass testing apparatus and to the way the loads were applied.
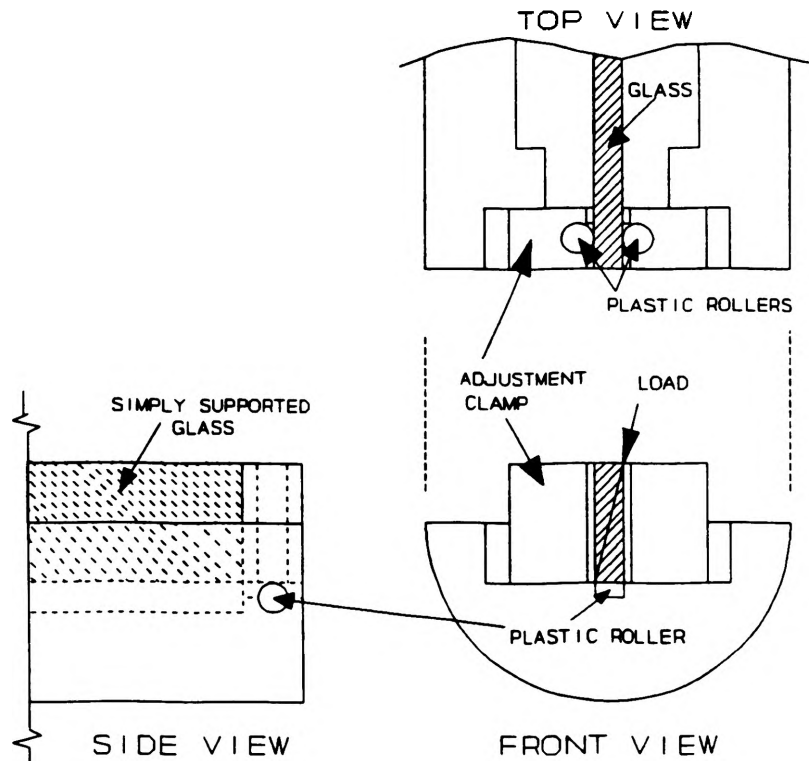
FIGURE 2. Glass Test Bed End Conditions (Three Views)

238

The loading angle, ball bearing, and loading bar arrangement were added to more accurately direct the load through the diagonal of the glass and to prevent some of the error that existed in the previous study.

The glass testing bed was the first piece of equipment to be evaluated and changed in order to better model the desired bending conditions. The first change that developed from the previous machine was that the entire depth of the glass was to be enclosed at the boundary conditions rather than being allowed to rest halfway into the cylinder of the test bed. The previous arrangement introduced additional bending stresses in the third direction due to the glass being cantilevered along its depth. The desired stress was to be introduced in the direction which was parallel to the edge of the glass which constitutes the Z-direction, however the cantilevered glass was introducing stress in the Y-direction which is along the depth of the cross section.

The second change dealt with the end conditions. The previous machine modeled the end conditions as fixed-fixed in one direction and pinned-pinned in the other direction. This arrangement complicated the stress distribution and placed both bottom edges in tension. Therefore, boundary conditions were created which would allow for both the X and Y-directions to be modeled as pinned connections. This was done by using Nylon 101 dowel rods in the ends to act as rollers (see Figure 2). The Nylon 101 was used since it did not cold flow like Teflon under the loading. The plastic also helped to distribute the loads in order to keep from having shear failure caused by point loads at the end conditions. With the end conditions modeled as pinned-pinned connections, the following two dimensional stress equation could be used to solve for the stress:

$$\sigma = \frac{M_x C_y}{I_x} + \frac{M_y C_x}{I_y} \qquad (1)$$

where:

M_x = Moment about the X-axis created by the failure load component in the Y-direction due to the beta (β) angle of the glass

M_y = Moment about the Y-axis created by the failure load

component in the X-direction due to the beta (ß)
angle of the glass

I_x = Moment of inertia about the X-axis
I_y = Moment of inertia about the Y-axis
C_x', C_y = Distance from centroidal axis to point of stress
observation

The moments about the X and Y-axis can be identified with the following equations:

$$M_x = \frac{P \cdot \cos(\beta) \cdot L}{6}$$
(2)

and:

$$M_y = \frac{P \cdot \sin(\beta) \cdot L}{6}$$
(3)

where:

P = Failure load
ß = Angle glass is rotated to direct vertical force
through the diagonal of the glass beam
L = Beam span (5.5 inches)

The third change to the glass test bed made it easier to align the glass parallel with the Z-axis and to secure it in the machine (see Figure 2). End clamps were designed to adjust the end conditions from one side of the testing apparatus making the test preparation much easier and more accurate. Previously, shims were used to make the end connections fit correctly. The shims created problems in the alignment of the glass in the Z-direction.
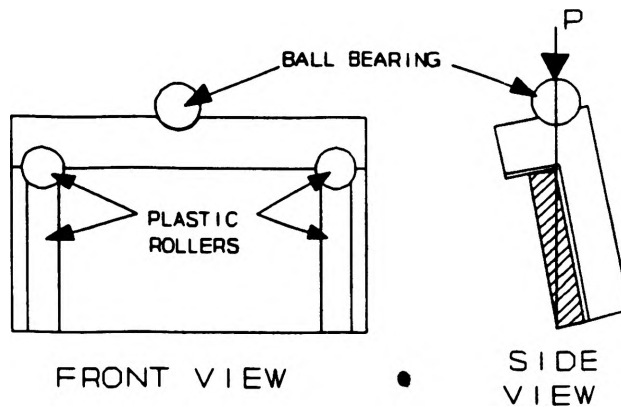
FIGURE 3. Loading Angle And Ball Bearing

Allowing the rollers to be adjusted from one side removed the risk of the glass not being aligned parallel with the Z-axis which could create unnecessary stresses.

After developing the glass testing device, the glass loading angle had to be developed. The mechanism had to apply a two point load, each located a third of the span from the support, which would provide the assumed perfect bending between the two loads (see Figure 3).
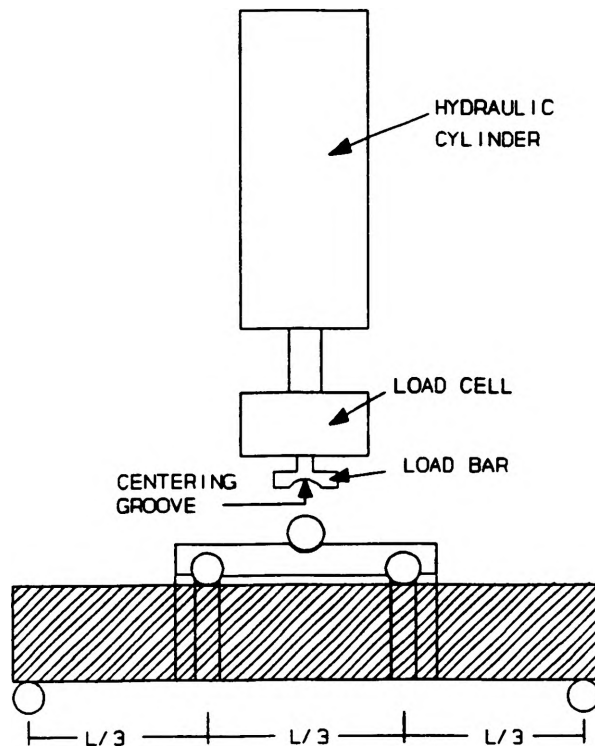
FIGURE 4. Loading Arrangement

The force was to be applied to the loading angle using the hydraulic cylinder and the load bar. The loading bar was designed with a groove for the ball bearing to adjust to the different angles created by different thicknesses of glass (see Figure 4). The groove in the load bar also assisted in centering the loading angle on the glass specimen, therefore, placing the forces a third of the span away from the supports. This decreased any errors associated with measuring the center as in the previous study.

Error Identification

Throughout the development of the testing apparatus, the

objective was to create a machine which would decrease the amount of errors. The observed errors which could not be overcome were errors in the precision of the instrument, which were identified as errors in the angles, and errors in the bending moments.

The first errors were introduced by differences in the beta (ß) angles which are associated with the cutting and manufacturing of the glass. This introduced error since the beta (ß) angle for each specimen was different depending on the dimensions. Another error associated with the beta (ß) angle, was the error introduced by the loading angle being designed for glass of 0.125 inch by 1.00 inch. Each of the errors can be identified with the following equation:

$$e=\cos(\triangle\beta)+\frac{h^2-t^2}{2ht}\cdot\sin(\triangle\beta)-1 \qquad (4)$$

where:
    e = Error
    h = Height of glass specimen
    t = Thickness of glass specimen
    ∆ß = Angle difference between the actual and the theoretical beta angle

This equation was developed to determine the error introduced in the failure stress by incorrect angles. For example this relationship gives an error in the stress of 2.289 percent for an angle difference of 00°20'00 (0.3333°) relative to the theoretical beta (ß) angle.

The errors in the angle also introduced a small amount of torsion into the glass. This torsion created some shear stress in the glass. The shear stress could be calculated by using relationships developed from torsion in reinforced concrete [4]. For an angle difference of 00°20'00" (0.3333°) relative to the theoretical angle and for a failure load of 125 lbs. the shear stress was calculated to be 77.25 psi.

There was also error introduced in the bending moments by the loading angle not being exactly centered between the supports. For example if the loading angle is off center by a difference of 0.1 inch the error in the moment is calculated to be 1.62 percent. This error as well as the angle errors could be considered

242

insignificant if care was taken during the procedure.

Test Procedure

All of the glass specimen were placed in the testing device and were loaded through the loading angle and ball bearing. The load rate was kept constant at 100 lbs. per minute for all of the specimens. This load rate was applied manually using the hydraulic jack and by using an X-Y plotter with time on the X-axis and load on the Y-axis. When the specimen would fail the peak load could be determined from the plots, and could be read from the display of the load conditioner.

From the recorded failure loads, the bending moments were calculated using Equations 2 and 3. After finding the bending moments, the failure stresses were calculated using Equation 1.

Test Results

Failure loads and failure stresses for annealed glass specimens cut with a steel scoring wheel and a carbide scoring wheel were calculated using Equation 1 in conjunction with Equations 2 and 3. The average failure loads and failure stresses are reported in Tables II-V.

TABLE II. STEEL SCORING WHEEL - SCORED EDGE LINE

Average Failure Load:	114.5 lbs.
Standard Deviation for Load:	12.1 lbs.
Average Failure Stress:	10286 psi
Standard Deviation for Stress:	1117.8 psi
Coefficient of Variation for Load and Stress:	10.9 %

TABLE III. CARBIDE SCORING WHEEL - SCORED EDGE LINE

Average Failure Load:	154.3 lbs.
Standard Deviation for Load:	28.2 lbs.
Average Failure Stress:	13900 psi
Standard Deviation for Stress:	2553 psi
Coefficient of Variation for Load and Stress:	18.4 %

TABLE IV. STEEL AND CARBIDE SCORING WHEEL - OTHER EDGE LINE

Average Failure Load:	276.3 lbs.
Standard Deviation for Load:	62.9 lbs.
Average Failure Stress:	24858 psi
Standard Deviation for Stress:	5492.2 psi
Coefficient of Variation for Load and Stress:	22.1 %

TABLE V.   CARBIDE SCORING WHEEL - COMBINED EDGE LINES

Average Failure Load:	224 lbs.
Standard Deviation for Load:	25.5 lbs.
Average Failure Stress:	9723 psi
Standard Deviation for Stress:	1054.6 psi
Coefficient of Variation for Load and Stress:	10.8 %

From the results, the scored edge line for the steel cut glass was 25 percent weaker than the scored edge line of the carbide cut glass. During the test, there was a noticeable difference in the glass edges cut with the steel wheel and the carbide wheel. The steel cut glass had rougher edges than the carbide cut glass. In comparing the results, the coefficient of variation for the steel scored edge line was less than that of the carbide cut glass. It is inherent that by introducing more edge flaws with the steel scoring wheel the probability of failure was increased and the strength was thereby decreased.

In comparing the scored edge line to the other edge line, the other edge line was 58 percent stronger for the steel cut glass and 44 percent stronger for the carbide cut glass. When the combined edge strength was tested, the break stress dropped to below the edge strength of the scored edge. This drop can be attributed to the increased area under tensile stresses increasing the probability of failure and decreasing the strength of the glass.

From the results it was noticed that the break stresses were significantly higher in comparison to most handbook values. Typical strength values for annealed glass are 8000 psi and 22 percent for the coefficient of variation [5]. Checks were made on the testing apparatus calibration and on the glass surface stresses to determine possible sources of error. To date, there is no explanation as to why the reported values are so much greater than the book values.

CONCLUSIONS AND RECOMMENDATIONS

This research focused on the determination of the edge strength of annealed glass cut with two different scoring tools. The research proved that the strength of glass edges is determined

by the conditions of the edge after cutting. The research showed that the edge strength of the scored edge is approximately 50 percent of the other edge.

With the machine already designed, it is recommended that further research be done in the area of glass edge strength testing. Testing should be performed further on annealed glass to determine the reasons for the high failure stresses. When the reasons are determined, it is recommended that tests be performed on heat strengthened glass and fully tempered glass. There is much to be learned from the strength of glass in engineering design.

ACKNOWLEDGEMENTS

REFERENCES

[1]   Pantelides, C.P., Sallee, G.P., Minor, J.E. (1991), "The Edge Strength of Window Glass By Mechanical Test," Technical Report, University of Missouri-Rolla, Rolla, MO 65401, 8 pp.

[2]   Bansal, Narottam P., Doremus, R.H. (1986), Handbook Of Glass Properties, Materials Engineering Dept., Rensselaer Polytechnic Institute, Troy, New York, Academic Press Inc., Orlando Florida.

[3]   Boresi, A.P., Sidebottom, O.M., (1984), Advanced Mechanics of Materials, 4th Ed., John Wiley & Sons, Inc., New York, N.Y.

[4]   Hsu, Thomas T.C. (1984), Torsion Of Reinforced Concrete, Van Nostrand Reinhold Company, Inc., New York, NY.

[5]   McLellan, G.W., Shand, E.B., (1984), Glass Engineering Handbook, 3rd Ed., McGraw-Hill Book Company, New York, NY.

The Reduction of Dielectric Constant By Shaped Porosity

Weiping Cai

Advisor: D.M. Mattox

OURE, UMR

May, 1994

Abstract:

In multi-layer circuits, the reduction of the dielectric constant in substrate materials is becoming increasingly important, as the heat emission of the circuits increases with an increasing number of layers. One way to achieve a lower dielectric constant is to create porosity in the material. In this project, two types of substrate samples were made with coin-shaped porosity. One had holes of 8.0mm in diameter, and the other had holes of 2.5mm in diameter. The total vacuum area was 250mm^2, or 7.7% of the total area, in either case. It was hoped to discover a relationship between aspect ratio and the effectiveness of dielectric constant reduction. But due to problems with measurements and sample size, trends were not clear, although it could be tentatively stated that the smaller porosity gave less reduction.

Introduction:

The manipulation of a material's dielectric constant through the mixing of different materials has been a subject of research for a long time. For the multi-layer substrate application, a low dielectric constant is desired as a way of increasing thermal conductivity. The effectiveness of mixing porosity with material on dielectric constant reduction was studied in this project, as well as the impact aspect ratio has on the reduction.

Procedure:

1. Punch out 7 circles (diameter=64.4mm) of the dielectric tape using a cutter and a hydraulic press.

2. Punch out circles (diameter=8.0mm or diameter=2.5mm) in a regular,

radially distributed pattern on 3 of these circles using brass tubings.

3. The 7 layers of tape are stacked together, alternating the ones with holes and the

ones without, and are laminated at 70°C and 1000psi for 7min.

4. The laminated tape is placed on a piece of alumina substrate, which is already dusted

with a layer of alumina powder, for heat treatment.

5. The heating cycle: 10°C/min to 350°C for 1.5 hr of burnout, 10°C/min to 850°C for

15min of sintering, 10°C/min cooling rate to room temperature.

6. Aluminum foil is glued on the sintered tape using vaseline gel.

7. Capacitance measurements are made at frequencies from 75kHz to 12MHz.

Data Analysis:

The following formula was used to find the dielectric constant:

$$K = (t)(C)/(A)(e_o),$$

where K=dielectric constant,

t=thickness of the substrate,

C=Capacitance,

A=area of the substrate,

e_o=permittivity of free space.

The results of the calculations, as well as the collected data, are presented in Table 1. Seven

layers of solid tape were sintered in a stack to serve as a standard. Its dielectric constant

was found to be 6.2. Out of the six samples with the 8.0mm holes, two had dielectric

constants in the range of 4.8 to 4.9, and three had dielectric constants in the range of 7.5 to

8.0. The remaining sample had a short and gave a dielectric constant of 0. One of the 2.5mm samples had a dielectric constant of 4.9, and the other had a dielectric constant of 2.4. All the dielectric constants reported above were taken at 75kHz.

Three of the 8.0mm samples had an increase in dielectric constant, implying either the solid sample gave too low a reading or these measurements were wrong. An actual increase in dielectric constant is ruled out because that violates physical laws. Although the data for the other 8.0mm samples showed a decrease in dielectric constant, within a fairly tight range, it cannot be interpreted as factual either since it was observed in a minority number of cases. A similar problem exists in analyzing the 2.5mm data. Although both showed a reduction, the small sample size makes it impossible to judge the accuracy of the measurement. And the problem is made worse by the spread in the data.

A number of factors could have contributed to errors in the measurements. First of all, very small holes and cracks might have appeared during sintering due to poor thermoexpansion characteristics or poor sintering techniques. Two, the bond between the layers in a substrate might not have been tight. Three, aluminum foil might not be the best contact to use. Lastly, any warping of the tape caused by sintering would have thrown off the capacitance measurements.

Conclusion:

This project was unsuccessful in determining the effect of porosity on dielectric constant and also the aspect ratio effect. The problems were in the small sample size and in poor sample making techniques. Four more 2.5mm samples were made, but because an available furnace could not be found within a few days, the already laminated samples

disintegrated. Many more samples would need to be made before any meaningful conclusion can be drawn.

References:

1. Mitoff, S.P. "Properties Calculation for Heterogeneous Systems," Advances in Materials Research, Vol 3, Herbert Herman (editor), Interscience Publishers, New York, 1968.

2. Polder D. and Van Santen J.H. "The Effective Permeability of Mixtures of Solids," Physica XII, No 5, North-Holland, August 1946.

TABLE 1. CAPACITANCE MEASUREMENTS AND DIELECTRIC CONSTANT CALCULATIONS

SAMPLE TYPE	FREQUENCY (HZ)	THICKNESS (MM)	CAPACITANCE (F)	D	DIELECTRIC
LARGE	75000	1.21	1.35043E-10	0.002496	7.50
	150000	1.21	1.34919E-10	0.002367	7.49
	500000	1.21	1.34723E-10	0.002565	7.48
	750000	1.21	1.34667E-10	0.002694	7.48
	1000000	1.21	1.34651E-10	0.002787	7.47
	2000000	1.21	1.34749E-10	0.003473	7.48
	4000000	1.21	1.35496E-10	0.005637	7.52
	8000000	1.21	1.36238E-10	0.042928	7.56
	10000000	1.21	1.37111E-10	0.055731	7.61
	12000000	1.21	1.38044E-10	0.068833	7.66
SMALL	75000	1.2	8.85813E-11	0.003333	4.88
	150000	1.2	8.84925E-11	0.003757	4.87
	500000	1.2	8.8311E-11	0.006813	4.86
	750000	1.2	8.82638E-11	0.008778	4.86
	1000000	1.2	8.82276E-11	0.01072	4.86
	2000000	1.2	8.81887E-11	0.018119	4.86
	4000000	1.2	8.84669E-11	0.032695	4.87
	8000000	1.2	8.8651E-11	0.103837	4.88
	10000000	1.2	8.69593E-11	0.133058	4.79
	12000000	1.2	8.68228E-11	0.146305	4.78
LARGE	75000	1.16	8.96401E-11	0.002294	4.77
	150000	1.16	8.95752E-11	0.001969	4.77
	500000	1.16	8.94637E-11	0.001962	4.76
	750000	1.16	8.94467E-11	0.002001	4.76
	1000000	1.16	8.94406E-11	0.002078	4.76
	2000000	1.16	8.94773E-11	0.00251	4.76
	4000000	1.16	8.9816E-11	0.003364	4.78
	8000000	1.16	8.9917E-11	0.035067	4.79
	10000000	1.16	9.03505E-11	0.044312	4.81
	12000000	1.16	9.08531E-11	0.054061	4.84
SOLID	75000	0.96	1.41783E-10	0.003255	6.24
	150000	0.96	1.41644E-10	0.002753	6.24
	500000	0.96	1.41416E-10	0.002674	6.23
	750000	0.96	1.41361E-10	0.002701	6.23
	1000000	0.96	1.41338E-10	0.002777	6.23
	2000000	0.96	1.41414E-10	0.00327	6.23
	4000000	0.96	1.42061E-10	0.004645	6.26
	8000000	0.96	1.42655E-10	0.037736	6.28
	10000000	0.96	1.43695E-10	0.047874	6.33
	12000000	0.96	1.44908E-10	0.058679	6.38

SAMPLE TYPE	FREQUENCY (HZ)	THICKNESS (MM)	CAPACITANCE (F)	D	DIELECTRIC
SMALL	75000	0.96	5.4473E-11	0.020274	2.40
	150000	0.96	5.43104E-11	0.028381	2.39
	500000	0.96	5.35966E-11	0.06245	2.36
	750000	0.96	5.31919E-11	0.087121	2.34
	1000000	0.96	5.27742E-11	0.109514	2.32
	2000000	0.96	5.07176E-11	0.192738	2.23
	4000000	0.96	4.57819E-11	0.342836	2.02
	8000000	0.96	3.45779E-11	0.632443	1.52
	10000000	0.96	3.01983E-11	0.748172	1.33
	12000000	0.96	2.65758E-11	0.850501	1.17
LARGE	75000	1.75	1.43961E-16	-2.21383	0.00
	150000	1.75	-3.18544E-16	-1.90225	-0.00
	500000	1.75	-8.5475E-17	-19.9073	-0.00
	750000	1.75	-5.4769E-17	-46.4402	-0.00
	1000000	1.75	-1.55561E-16	-21.4519	-0.00
	2000000	1.75	-2.18363E-16	-31.6686	-0.00
	4000000	1.75	-1.54358E-15	-8.87215	-0.00
	8000000	1.75	3.19878E-15	-9.43421	0.00
	10000000	1.75	2.73562E-15	-12.8204	0.00
	12000000	1.75	-6.40647E-18	-6380.92	-0.00
LARGE	75000	1.25	1.33654E-10	0.002477	7.66
	150000	1.25	1.33532E-10	0.002307	7.66
	500000	1.25	1.33336E-10	0.002421	7.65
	750000	1.25	1.33296E-10	0.002481	7.64
	1000000	1.25	1.33269E-10	0.002575	7.64
	2000000	1.25	1.3337E-10	0.003129	7.65
	4000000	1.25	1.34058E-10	0.005	7.69
	8000000	1.25	1.34531E-10	0.040632	7.72
	10000000	1.25	1.35298E-10	0.051739	7.76
	12000000	1.25	1.36192E-10	0.063001	7.81
LARGE	75000	1.3	1.34095E-10	0.003483	8.00
	150000	1.3	1.33954E-10	0.003972	7.99
	500000	1.3	1.33664E-10	0.006751	7.97
	750000	1.3	1.33569E-10	0.008636	7.97
	1000000	1.3	1.33507E-10	0.010386	7.96
	2000000	1.3	1.33439E-10	0.017361	7.96
	4000000	1.3	1.33568E-10	0.034738	7.97
	8000000	1.3	1.33183E-10	0.095064	7.94
	10000000	1.3	1.3358E-10	0.118905	7.97
	12000000	1.3	1.34039E-10	0.143581	7.99

SAMPLE TYPE	FREQUENCY (HZ)	THICKNESS (MM)	CAPACITANC (F)	D	DIELECTRIC
LARGE	75000	1.53	6.96384E-11	0.033625	4.89
	150000	1.53	6.91342E-11	0.047725	4.85
	500000	1.53	6.71676E-11	0.108184	4.71
	750000	1.53	6.57265E-11	0.149249	4.61
	1000000	1.53	6.43896E-11	0.187057	4.52
	2000000	1.53	5.84458E-11	0.325301	4.10
	4000000	1.53	4.63824E-11	0.560263	3.26
	8000000	1.53	2.8626E-11	0.945817	2.01
	10000000	1.53	2.3674E-11	1.07496	1.66
	12000000	1.53	2.019E-11	1.17355	1.42

Automation of Process Data Management

Stephen C. Chadwick
Chemical Engineering Department

Abstract:

The project goal is to create an automated system for managing data that describes a chemical process. The data is both graphical, such as piping and instrumentation diagrams, and numerical, such as pipe schedule and diameter. AutoLisp and C++ programs were developed and tested to simplify the creation of the automated system.

Introduction:

The automated system is envisioned as follows: a computer user, most likely an engineer, will be at a PC. The engineer will decide the part of the process that needs to be modified. Perhaps the flow into a reactor should be increased or decreased or the pressure in a line should be changed or the piping in the plant should be rerouted. The engineer will make the graphical and numerical changes in AutoCad (version 12.0). AutoCad will communicate the numerical changes to Paradox, which is the attached data base, and the changes will update throughout the plant data. Essentially, this will allow plant configuration and parameters to be changed from a graphic user interface (GUI). This procedure is extremely beneficial because the piping and instrument diagrams (P&ID's) will always be current which is required by regulations set forth by the Occupational Safety and Health Administration (OSHA) and the Environmental Protection Agency (EPA). There will be fewer chances for transcription errors because both graphical and numerical data are updated using a single data management system. The automated data management system will eliminate transcription errors, save time, and make current drawings with correct plant parameters commonly available. Essentially, all changes will be registered in the computer and easily accessible to other personnel in the plant.

Background:

The C++ language is particularly valuable because it follows the object oriented paradigm and its flexibility. Object orientation is important to this project because of the way it handles classes through the use of structure. Because of these characteristics it is a useful tool when modeling plants. The following is an example of how C++ could be used to model pumps in a plant.

There is a class, a class of pumps. All of these pumps are in some way similar to each other. For example, they are used to move materials from one location to another and are rated

by power requirements. The pumps have many common traits; these traits are grouped together into a superclass. However, there are various types of pumps (for example, centrifugal and positive displacement) that have different characteristics. These types of pumps would be subclasses (or children) of the superclass (or parent). In the object oriented paradigm, common characteristics of the superclass are inherited by each of its subclasses. All instances of a subclasses belong to the superclass. It is because of the inheritance of plant characteristics that object orientation is used.

Since C++ can handle these systems so well, a method was designed to interface with Paradox tables. This is possible based on the Paradox engine. This engine acts as an interpreter between C++ and Paradox. Essentially, programs can be written to search the Paradox tables and extract the desired data from the data base tables and place the information into the appropriate class structure of C++. It would also be possible to retrieve the data from Paradox, manipulate it in C++ and then return it back to Paradox. The data could also be manipulated and sent to different plant controllers, such as a distributed control system (DCS). The automated data management system has these capabilities.

Auto Lisp is the programming language of AutoCad. As the name indicates, Auto Lisp is designed to handle lists. These lists could range from plant sites down to the types of pumps to be used. The interface between AutoCad and Paradox is handled through Auto Lisp commands.

Project:

An Auto Lisp program was developed that would read strings from a computer text file based on a ordinal number given from a user input. (A listing of the source code for this program can be found in the attachments). The program works as follows: the computer user is asked by the program to input a number. The number specifies a line number in the text file where a string composed of substrings delimited by spaces resides. A sample file can be found in the attachments. Once the ordinal number is entered, the string in the file is printed at the bottom of the screen.

Also, a C++ program was developed that checks an Auto Lisp program. Auto Lisp counts parentheses as a first check. A C++ program was developed that reads an Auto Lisp program, counts the number of parentheses missing, and indicates whether or not a right or left parenthesis should be added. The program simplifies Auto Lisp program development because there is no compilation time under AutoCad, and the error analysis that is given by the program is much more detailed and easily understood by the user. (The source code can be found in the attachments).

The C++ source code for the Auto Lisp retrieve program is also included. The C++ retrieve function works in the same manner as the Auto Lisp function, but it is independent of any program platform. With the growing use of C++, due to the power and flexibility of the language, it is important whenever possible, to write the corresponding C++ code. Notice how much more compact the C++ code is when compared to the Auto Lisp code.

Applications:

At the end of an AutoCad session, the variables either created and/or used during the session cannot be saved if they exceed five in number. However, these variables can be written to an ASCII text file. The Auto Lisp retrieve program allows Auto Lisp variables to be stored in an ASCII text file and to be retrieved while working in an AutoCad session. The variables in the text file can be stored and retrieved in a subsequent session, as well. A text file called *names.txt* was populated with first, middle, and last names. The names in the data file represent any type of variable data created while working in an AutoCad session. The purpose of the retrieve function is to read the middle name on a specified line based on user input. This was chosen because retrieving the middle name involves characters before and after the desired substring, and these characters have to be taken into account. Often data in a system is surrounded by characters that are not needed. As long as the format of the data is known, the program can take into account potentially unwanted characters. This type of retrieve function is essential when working with large amounts of data, such as the automated data management system.

Acknowledgments:

At this time I would like to thank Dr. Book for all of his help and insight. Without his guidance I don't think that what I have accomplished would have been possible, and the knowledge that I have gained from this experience would never have been found. I would also like to thank Mr. Khandekar who was a fountain of information and helped me work out many bugs in my source codes, and also answered countless questions at all hours of the day with great enthusiasm.

Auto Lisp Program: Retrieving The Middle Name

```
(defun retrieve ()
        (setq refname "names.txt")
        (setq fil (findfile refname))
        (if fil
                (setq refname fil)
                (princ
                (strcat "\nPlease load the file "refname"."))
        )
(setq num (getint "Enter a number:"))
(setq f (open "names.txt" "r"))
(setq cnt 0)
(princ num)
(princ "\n")
  (while (< cnt num)
        (progn
                (princ num )
                (princ "\n")
```

```lisp
            (princ cnt)
            (princ "\n")
            (setq d (read-line f))
            (princ d )
            (princ "\n")
            (setq cnt (+ cnt 1))
        )
  )
(setq a (read-line f))
(setq b (read-char f))
(princ "\n")
  ( while (/= b 32)
          (princ b)
          (setq b (read-char f))
  )
(princ"\n")
(setq mid " ")
(setq middle " ")
(setq b (read-char f))
  (while (/= b 32)
      (princ b)
      (princ mid)
      (setq middle (strcat mid (chr b)))
      (setq mid middle)
      (setq b (read-char f))
  )
(princ "\n")
(princ middle)
)
```

C++ Program: Function For Parentheses Check

```cpp
//count.cpp
#include <fstream.h>
#include <conio.h>
#include <process.h>
void main(int argc, char* argv[])
        {
                if(argc != 2)
                  {
                    cerr<<"\nFormat: count filename.ext";
                    exit(-1);
                  }
                ifstream infile;
```

258

```
            infile.open ( argv[1] );
            if (!infile)
              {
                cerr<<"\nCan't open  "<<argv[1];
                cout<<"\nPlease re-enter the command and filename.ext"<<endl;
                exit(-1);
              }
            int cnt1=0,cnt2=0;
            char ch;
            while (infile)
              {
                infile.get(ch);
                if( ch = = ' ( ' ) cnt1++;
                if( ch = = ' ) ' ) cnt2++;
              }
            clrscr();
            cout<<"\nThere are  "<<cnt1<<"  ( parenthesis"<<endl;
            cout<<"There are  "<<cnt2<<"  ) parenthesis"<<endl;
            if(cnt1-cnt2 = = 0) cout<<"good job";
            else cout<<"Please try matching your ()'s again."<<endl;
      }
```

C++ Program: Retrieving The Middle Name

```
//This is C++ retrieve function (same as Autolisp's function, but in C++)
#include <fstream.h>
#include <conio.h>
#include <stdio.h>
void main()
{
        int a=0;
        char ch;
        int counter=0;
        const int max=80;
        char buffer[max];
    clrscr();
    printf("This will retrieve the middle name");
    printf("\nEnter the line number of the name ");
    cin>>a;
    int b=a-1;
    ifstream infile("names.txt");
    while (infile && !(counter==b) )
        {
        infile.getline(buffer,max);
```

```
        counter++;
        }
while(ch != ' ')
        {
        infile.get(ch);
        }
infile.get(ch);
cout<<"\nThe middle name of choice "<<a<<" is ";
cout<<ch;
while(ch != ' ')
        {
        infile.get(ch);
        cout<<ch;
        }
    cout<<endl;
}
```

Names file:

David Michael Chadwick
Michael Ross Chadwick
Stephen Christian Chadwick
Mara Pageen Chadwick
Mary Francis Chadwick
Fred Stephen Chadwick

Designing a New Programming Methodology for Optimizing Array Accesses in Complex Scientific Problems

Larry Coffin

Computer Science Department

Many problems of interest to scientists and engineers, such as fluid flow and stress analysis, require the solution of complex PDEs. Often the solution requires discretizing the physical domain into a mesh or grid then stepping from a given initial state towards some final state using small incremental time steps. Grid sizes can reach several thousand to hundreds of thousands of elements and the number of time steps required to solve the problem can vary from several thousand to tens of thousands or more. Traditional programming techniques are unable to take advantage of the non-random grid access patterns and generally result in array accesses that are computationally expensive. Our research has produced a method of programming based on the method of Psi Calculus (Mullin, 1988) that results in faster access times -- producing programs that run significantly faster than programs written in a traditional style.

INTRODUCTION

Many real world problems on which scientists and engineers spend much time and computational resources often require the solution of complex partial differential equations, or PDEs. Many problems, such as air flow around an airplane wing or the stress analysis of a bridge strut, are modeled on a computer in order to try to understand them in more detail than is possible by studying a real system. Other problems, such as air and fuel mixture and combustion in a hypersonic jet engine can not be studied in the real world and must be modeled on a computer. The solution to these problems often requires discretizing the physical domain by use of a mesh or grid then stepping through time from some initial state in order to reach some final state or just to study the changes in the system over time. Grid sizes can easily exceed several hundred thousand elements -- the larger the grid size, the more accurate the solution. The number of time steps can vary from several thousand to tens of thousands or more -- smaller

261

time steps can also increase the accuracy of the solution over a given time span or can provide a better simulation of a dynamic system. Both grid size and the number of time steps are limited by the amount of memory and CPU time available. A typical problem with grid sizes of over 300,000 elements and 20,000 time steps can take from 15 to 20 hours of CPU time on a Cray YMP (Riggins, 1992). These problems are extremely important and their solution can greatly benefit the advancement of science. However, these problems are also so restricted by lack of memory and time limitations that any improvement in computational efficiency can greatly extend the capability of computers to solve larger an more accurate problems.

GOALS

Our work was based on several goals: first, we wanted to familiarize ourselves with PDEs. Second, we wanted to develop a programming technique which would speed up programs which rely on the solution of complex PDEs by means of an explicit iterative solution. And thirdly, we wanted to create a technique by which programs based on an arbitrary number of dimensions can be solved.

We decided to focus on the PDE for heat flow or heat transport because it is a simple problem involving one component, heat. The PDE can be solved with an iterative technique similar to more complex PDEs and can also be solved directly, allowing us to compare answers and check the validity of our technique.

BASIC C PROGRAMMING LANGUAGE SYNTAX

First, for those unfamiliar with the C programming language, some of the syntax as used in the paper:

• Arrays of size N elements are accessed with an index from 0 to N-1.

• Multi-dimensional arrays are stored in row-major format rather than in column-major format (as in Fortran). See Figure 1.

Figure 1: Storage in memory of array elements in a row-major format.
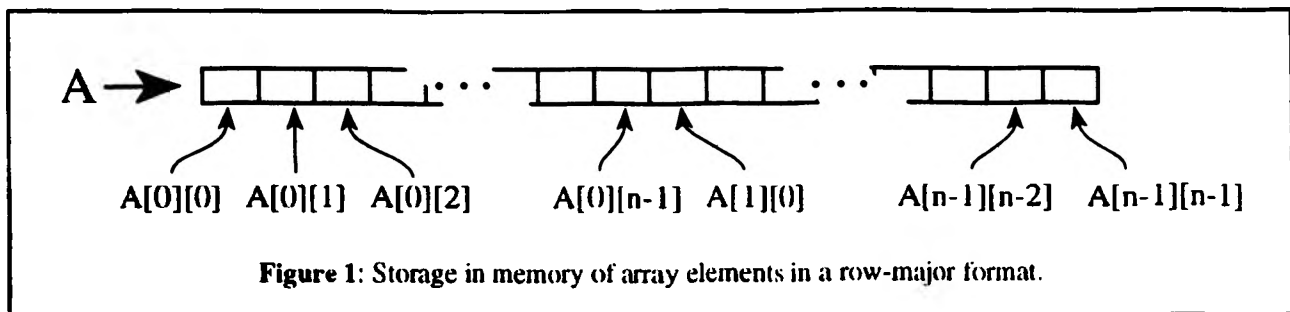
• C provides address storage and manipulation via pointers and pointer arithmetic. If "ptr" is a

pointer to (address of) an element in memory, "ptr + 3" is a pointer to the third element beyond "ptr". Note that "ptr + 3" involves an implicit multiplication by the size of an element so that if the value of "ptr" is 1000 and the size of an element is six bytes, then the value of "ptr + 3" is 1000 + 6*3 = 1018, not 1003.

• The value of the element that a pointer points to can be found by the dereferencing operator. In C this is a prefixed asterisk -- "*ptr" is the value of the element pointed to by "ptr". Likewise "*(ptr + 3)" is the value of the third element beyond "ptr".

• In C, arrays can be accessed in two ways -- by index or by offset via the use of pointer arithmetic. Writing "A[5]" is the same as "*(A + 5)" -- the name of an array is taken to be a pointer to the beginning (the first element) of the array in memory.

• For loops (DO loops in Fortran) are written as:

```
for (Initial; Test; Modify) {
        Body
}
```

which can be thought of as:

```
do Initial statement
while Test is true
        do Body statement(s)
        do Modify statement
end of while loop
```

• "=" is the assignment operator.

GENERAL PROBLEM

We initially decided to focus on PDEs because the solution to these problems often requires the use of extremely large multi-dimensional arrays. In a computer system, memory exists only in the form of a linear array of bytes. Therefore, in order to handle multi-dimensional arrays, the compiler must supply some sort of function that maps the multi-dimensional array to the linear array of physical memory. For arrays of a single dimension, the mapping is straightforward -- the address of an element can be computed by

$$address = start + index * size \text{ of an element in bytes.} \qquad (1)$$

263

For example, given an array of N elements whose size is four bytes and a starting address of 1000, to find the 63rd element (index = 62 if index goes from 0 to N-1) we use:

$$address = 1000 + 62*4 = 1248. \tag{2}$$

For a two dimensional M by N array and elements of size S bytes, the formula for finding an element indexed by i and j becomes:

$$address = start + S*(i*N + j). \tag{3}$$

This can be extended to an N dimensional array with dimensions $D_0 x D_1 x D_2 x...x D_{n-1}$ with elements of size S. For an element indexed by $I_0, I_1, I_2,...,I_{n-1}$ the formula becomes:

$$address = start + S*(I_0*(D_1*D_2*...*D_{n-1}) + I_1*(D_2*D_3*...*D_{n-1}) \tag{4}$$
$$+ ... + I_{n-3}*(D_{n-2}*D_{n-1}) + I_{n-2}*D_{n-1} + I_{n-1}).$$

Even if the product terms $P_0 = (D_1*D_2*...*D_{n-1}), P_1 = (D_2*D_3*...*D_{n-1}), ... P_{n-2} = D_{n-1}, P_{n-1} = 1$ are precalculated, the formula will be:

$$address = start + S*(I_0*P_0 + I_1*P_1 + ... + I_{n-2}*P_{n-2} + I_{n-1}). \tag{5}$$

This still involves N multiplications and N additions to find a single element! So as the number of dimensions increases, the cost of randomly accessing any element becomes large.

Often though, elements are not accessed randomly. Consider for example the initialization of a linear array:

```
for (i = 0; i < N; i = i+1){
        array[i] = 1;
}
```

All elements are accessed in an increasing fashion. Rather than calculating the address of each element from the starting address and its index, we know that the next element that we want to access is located S bytes beyond the current element. The formula thus becomes:

$$address of next element = current address + S. \tag{6}$$

This formula works for arrays of any dimension as long as the elements are accessed in the order in which

they are stored (i.e. in a row-major order language, the "column" index increases faster than the "row" index). Most optimizing compilers will automatically convert:

```
for (i = 0; i < M; i = i+1) {
        for (j = 0; j < N; j = j+1){
                array[i][j] = 1;
        }
}
```

to:

```
end = array + M*N;        (The address of the first byte beyond the end of the array)
for (ptr = array; ptr < end; ptr = ptr+1){
        *ptr = 1;
}
```

This involves only two multiplications, M*N+1 additions and M*N comparisons vs. 2*M*N multiplications, 3*M*N + M additions and M*N + M comparisons.

However, as loops become more complex, compilers are less able to able extract the non-randomness and reduce them to more efficient loops. For example, consider the main loop as found in the solution to the 3D heat transfer PDE:

```
for (i = 1; i < L-1; i = i+1){
    for (j = 1; j < M-1; j = j+1){
        for (k = 1; k < N-1; k = k+1){
            uprime[i][j][k] = u[i][j][k]
                + λ*C*(u[i-1][j][k] + u[i+1][j][k] + u[i][j-1][k] + u[i][j+1][k]
                        + u[i][j][k-1] + u[i][j][k+1] - 6*u[i][j][k]);
        }
    }
}
```

There are two problems in trying to optimize this, first all the elements are not accessed. All elements whose i, j, or k index equals zero or where i = L-1, j = M-1, or k = N-1 are skipped. These are the boundary elements -- the elements that lie on the boundary of the physical domain. The second problem is that at each iteration multiple elements are accessed whose addresses are based on increments or decrements to the indexes i, j, and k (i±1, j±1, k±1). These extra elements are based on what is termed a "mask". These elements are the "neighbors" of the central element (index = i, j, k). Figure 2 shows masks for 1, 2 and

265

3D problems.

Figure 2: Neighboring points from mask patterns for 1, 2, and 3 dimensional problems.
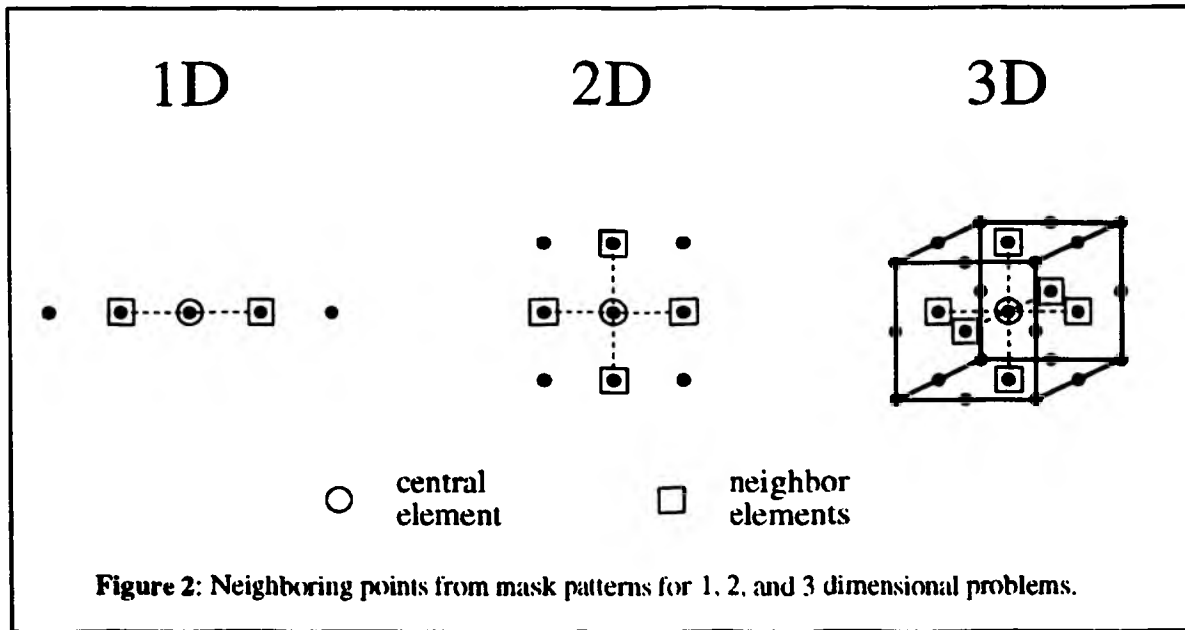
In trying to design a programming methodology for optimizing these types of array accesses, we decided that we could break the problem down into two parts: finding the address of the central element, then once we have found this, finding the addresses of its neighbors.

To reduce the computations necessary to access the non-boundary elements, a second array was created that contained the offsets from the start of the array of the non-boundary elements which are calculated once at the start of the program. Thus the algorithm for accessing all the central elements becomes:

```
for (i = 0; i < (L-2)*(M-2)*(N-2); i = i+1)(
        *(uprime + offset[i]) = *(u + offset[i]) ...;
)
```

In order to access the central element's neighbors we looked at the extra elements we wanted to access. If we take the six elements from the previous 3D example: u[i±1][j][k], u[i][j±1][k], u[i][j][k±1] and the central element: u[i][j][k] and convert these indexed representations to the corresponding addresses using offsets we get:

$$u[i][j][k] \quad = u + i*M*N + j*N + k \qquad\qquad\qquad = c$$
$$u[i±1][j][k] = u + (i±1)*M*N + j*N + k = u + i*M*N + j*N + k ± M*N = c ± M*N \quad (7)$$
$$u[i][j±1][k] = u + i*M*N + (j±1)*N + k = u + i*M*N + j*N + k ± N \quad = c ± N$$
$$u[i][j][k±1] = u + i*M*N + j*N + (k±1) = u + i*M*N + j*N + k ± 1 \quad = c ± 1$$

These differences are equal to the number of elements in the sub-array for the dimension whose index

266

is modified. So for the neighbor in the yth dimension, i.e. $I_y \pm 1$, the two elements can be found by $c \pm P_y$. So once we have the address of the central element, it only requires a single addition or subtraction to get any of its neighbors. The previous example can be rewritten as:

```
for (i = 0; i < (L-2)*(M-2)*(N-2); i = i+1){
        new = uprime + offset[i];
        old = u + offset[i];
        *new = *old + λ*C*( *(old-P[0]) + *(old+P[0]) + *(old-P[1]) + *(old+P[1])
                        + *(old-P[2]) + *(old+P[2]) - 6*(*old));
}
```

The final aspect of the problem that we looked at was the problem of handling an arbitrary number of dimensions. By writing programs that can handle an arbitrary number of dimensions, time can be saved by eliminating the need to modify the program if the number of needed dimensions changes. We looked at the solution equations to the heat transfer PDE for 1, 2 and 3 dimensions (see equations number eight) and from them we designed and derived a generic program for a dimension independent equation using the Psi Calculus (Mullin, 1988):

$$1D \rightarrow u'_i = u_i + \lambda C(u_{i-1} + u_{i+1} - 2u_i)$$
$$2D \rightarrow u'_{i,j} = u_{i,j} + \lambda C(u_{i-1,j} + u_{i+1,j} + u_{i,j-1} + u_{i,j+1} - 4u_{i,j}) \tag{8}$$
$$3D \rightarrow u'_{i,j,k} = u_{i,j,k} + \lambda C(u_{i-1,j,k} + u_{i+1,j,k} + u_{i,j-1,k} + u_{i,j+1,k} + u_{i,j,k-1} + u_{i,j,k+1} - 6u_{i,j,k})$$

If we use n to mean the number of dimensions and d_1, d_2, and d_3 to indicate subscripts for dimensions 1, 2, and 3 such that, in 3D, $u_{i+1,j,k} \equiv u_{d_1+1}$ these equations can be rewritten as:

$$1D \rightarrow n = 1, u' = u + \lambda C(u_{d_1-1} + u_{d_1+1}$$
$$- 2nu)$$

$$2D \rightarrow n = 2, u' = u + \lambda C(u_{d_1-1} + u_{d_1+1}$$
$$+ u_{d_2-1} + u_{d_2+1} \tag{9}$$
$$- 2nu)$$

$$3D \rightarrow n = 3, u' = u + \lambda C(u_{d_1-1} + u_{d_1+1}$$
$$+ u_{d_2-1} + u_{d_2+1}$$
$$+ u_{d_3-1} + u_{d_3+1}$$
$$- 2nu)$$

In general we get:

$$u' = u + \lambda C(\Sigma^n_{q=1}(u_{d_q-1} + u_{d_q+1}) - 2nu)$$ (10)

Note that the address of $u_{d_q\pm1}$ = address of $u \pm P_{q-1}$.

The final algorithm thus becomes:

```
num_elem = 1;  (The number of non-boundry elements)
for (q = 0; q < num_dim; q = q+1){
        num_elem = num_elem * (D[q] - 2);
}
m2n = -2*num_elem;
lambda_C = lambda*C;
```

(time step loop) {

```
        for (i = 0; i < num_elem; i = i+1){
                off = offset[i]
                old = u + off;
                new = uprime + off;
                *new = m2n*(*old);
                for (q = 0; q < num_dim; q = q+1){
                        p = P[q];
                        *new = *new + ( *(old-p) + *(old+p));
                }
                *new = (*new)*lambda_C + *old;
        }
}
```

Since num_elem, m2n, and lambda_C are calculated only once, at each time step we do (3*num_dim+2)*num_elem fetches, (6*num_dim+5)*num_elem additions, (num_dim+1)*num_elem compares, (3*num_dim+5)*num_elem multiplies, and num_elem stores.

RESULTS

Several programs were written: three with the traditional method of array indexing for 1, 2, and 3 dimensional problems and one with the new method. For the program written with the new technique, the number of dimensions, the size and of the grid, as well as the number of time steps to iterate over were read in from an input file. For the other programs, these values were hard coded into the program. The

programs were run on NeXT workstations and the programs reported the CPU time they took to run. The resulting times were (in seconds):

1D

Size	Traditional	New
40	3.69	7.04
80	5.50	9.84
120	7.24	14.03
160	9.27	22.78

2D

Size	Traditional	New
40x40	23.27	25.02
80x80	128.69	107.09
120x120	425.81	243.45
160x160	535.80	447.55

3D

Size	Traditional	New
20x20x20	61.64	25.20
30x30x30	283.54	96.38
40x40x40	575.24	239.69
50x50x50	1417.76	475.00

As can be seen from the times, the traditional method was better for 1D problems, but the new method was, for the larger arrays, significantly faster for 2D problems and for all size arrays, much faster for 3D problems.

Of course, keeping an array of offset values uses up memory that could be used elsewhere. Assuming that we use long integers (0 to $2^{32}-1$) to store offset values we will be using four bytes for each element of the main array (not counting boundary elements, but for an upper bound we can assume the 1 to 1 ratio of offset elements to grid elements). The solution to the problem requires that we have two main arrays u and u' to hold the current values and the values for the next time step. So, as in the case of the heat transfer problem that we worked with, if we are storing a single floating point value (also four bytes) in each element, the addition of the offset array will increase the memory usage by approximately 50% of the original, necessary memory usage. If, however, we store more information in each element, and typical PDEs (as in combustion/reaction problems) often store from three to nine or more values, requiring 12 to 36 bytes for single precision values or 24 to 72 bytes for double precision values. The extra memory required for the offset array will be from $4/24 = 17\%$ (3 values, single precision) to $4/144 =$

3% (9 values, double precision) or less of the necessary memory. For complex problems, the memory increase will be very small and more than offset by the increase in speed of the overall program.

ACKNOWLEDGMENTS

REFERENCES

Mullin, L. R., "A Mathematics of Arrays", Ph.D. dissertation, Syracuse University, Syracuse, NY, 1988.

Riggins, D., et. al., "Modeling of Supersonic Combustor Flows Using Parallel Computing", *Computing Systems in Engineering*, Vol. 3, Nos 1-4, pp. 217-229, 1992.

THE AFFECTS OF BUTYL ACETATE AND ACETONE ON PLEXIGLASS

Tracy E. Downs
Department of Chemical Engineering

ABSTRACT

The actions that solvents take on polymers was the focus of the summer 1993 research. There were two goals: one was to measure the distances between the cracks that formed in the plexiglass and two was to determine the time of arrival of the cracks. Two solvents, butyl acetate and acetone were used to generate data on polymethyl methacrylate (PMMA/Plexiglass).

The measurement of the time of arrival of a crack was another goal. This quantity is related to the growth of the fractures. This was difficult since only a localized portion of the plexiglass sample could be viewed.

INTRODUCTION

It has been observed that engineering apparatus such as distillation columns cannot be designed using polymeric materials as they are always in contact with organic liquids. In the presence of organic liquids they crack easily. This is called environmental stress cracking.

Researchers have suggested various mechanisms and theories which have been reviewed by E.H. Andrews in The Physics of Glassy Polymers [1]. These mechanisms are often conflicting and are not reliable. If a mechanism is to be used, it should be able to predict two things: 1) how cracks are distributed, i.e., the gap between adjacent cracks and 2) the rate at which the cracks appear.

When polymers are contacted with a solvent fractures form. The gap size, the distance between the cracks, is related to what is called the perturbation wavelength.

The distances between and the sizes of the cracks were among our interests in the research.

EXPERIMENTAL

The procedure used for research was essentially the same as that developed by Matt Griscom, an undergraduate student who had worked on the project earlier [2]. He studied the size of the cracks themselves. With a few alterations, the procedure was as follows:

271

1) A 1/2" (approximate) square of plexiglass was machined to create a 1/4"(approximate) groove in the plexiglass. This is shown in Figure 1. Myrlen Troutt, Supervisor of Technical Labs, did the machining.

2) A piece of wax was placed on the grooved surface covering it entirely. It was observed that the wax was easier to work with if softened between the fingertips first. The wax must cover the surface to prevent solvent from contacting horizontal surfaces.

3) The wax was trimmed away at an angle using a utility knife. This allows vertical contact and keeps the horizontal surfaces covered. This is shown in Figure 2.

4) A small drop of solvent, butyl acetate or acetone, was placed on the diagonal surface of the wax and allowed to sit approximately 45 minutes. The orientation of the wax allows the solvent to rest against the vertical surface of the polymer and it also protects the horizontal surfaces from exposure. Thus, viewed from the top, we have two halves: one half is dry PMMA and the other half is acetone. This is shown in Figure 3.

5) With the microscope set at 10X power the slides were observed. The microscope was equiped with a graduated eyepiece thus allowing easy measurement of the distances between the cracks.

6) Distances, in mm, between cracks were noted and the data collected. The form of the cracks and the arrangement in general are shown in Figure 4.

RESULTS

Two solvents were used: butyl acetate and acetone. The butyl acetate was used for most of the data because it showed better results than the acetone. The butyl acetate produced fewer cracks but they were longer in length. The acetone produced large quantities of small cracks. Also, if there was a long contact time large pockets would dissolve out of the plexiglass sample.

Table 1 shows the data that were collected. The first column shows the length of the distances between cracks, r mm. The second column shows the number of cracks less than r mm. Column three shows the smoothed data. The slope is calculated in column four using the smoothed data and attributed to an average value of r. The butyl acetate data is listed first then the acetone data.

In Figure 5, the distribution of gap sizes is shown for the butyl acetate solvent. Figure 5 shows the cumulative gap size distribution of gaps less than a certain dimension. All butyl acetate data was taken at approximately 45 minutes of reaction time. In Figure 6, the derivative was taken of the data to show

272

which gap size were most preferred. A maximum occurs at approximately 0.3 mm. This means that the most cracks are closer to one another by less than 0.5 mm. Another small maximum is located at about 2.75 mm.

Figures 7 and 8 show the acetone data that was collected. These samples were allowed to react for about 24 hours. Figure 7 again shows the cumulative distribution and Figure 8 the maxima. Once again the maximum occurs at an r less than 0.3 mm.

In conclusion, the data that was collected consistently showed that the majority of the gap sizes are of small r values.

ACKNOWLEDGMENTS

REFERENCES

Haward, R.N. ed. The Physics of Glassy Polymers. Applied
      Science Publishers, Ltd., 1973. Pgs. 394-451.

Griscom, Matt. The Effects of Acetone and Butyl Acetate on
      Plexiglass. 1993
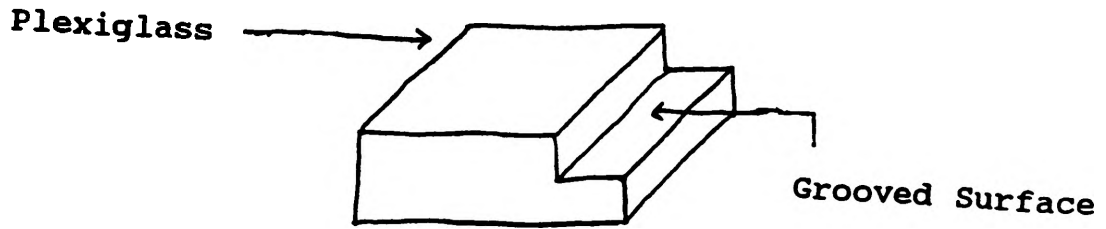
Figure 1. Schematic of machined polymer
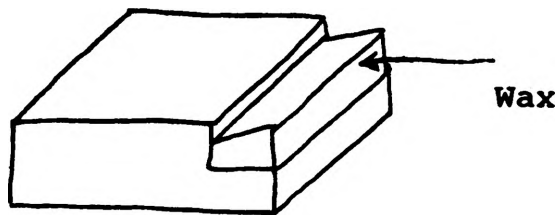
Figure 2. Placement of wax
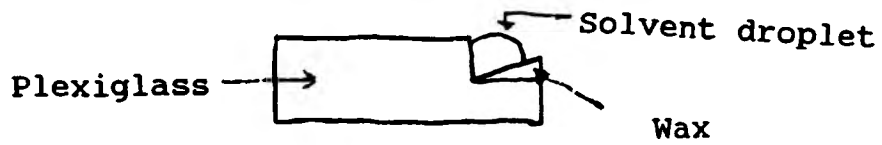
Figure 3. Orientation of solvent droplet on polymer and wax
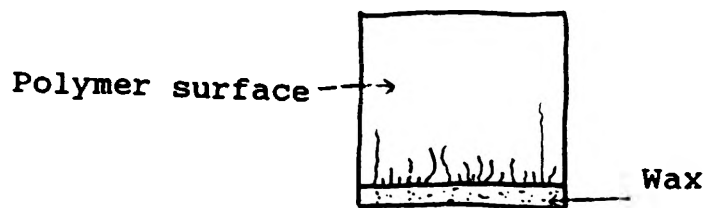
Figure 4. Form of the cracks and general arrangement

Table 1

Butyl Acetate Data

x r mm	y number	y' number	slope	r mm corrected
0	0	0	0	0
0.3	24	23	98.6	0.267
0.5	45	49.3	94	0.533
0.8	79	70	85.4	0.767
1	86	92	68.6	1.033
1.3	111	104.3	49.4	1.267
1.5	116	116.7	38.8	1.533
1.8	123	123.7	30	1.767
2	132	131.7	26.6	2.033
2.3	140	138	21.2	2.267
2.5	142	142.3	18.6	2.533
2.8	145	147.3	20	2.767
3	155	152.3	18	3.033
3.3	157	156.3	11.4	3.267
3.5	157	158	8	3.533
3.8	160	159.3	6.6	3.767
4	161	161.3	7.4	4.033
4.3	164	163	6	4.267
4.5	164	164.3	3.4	4.533
4.8	165	164.7	2.8	4.767
5	165	165	0	5.033

Acetone Data

x r mm	y number	y' number	slope	r mm corrected
0	0	0	0	0
0.3	11	10	93.2	0.267
0.5	19	23.3	43.64	0.533
0.8	40	34	26.53	0.767
1	43	44.7	15.24	1.033
1.3	51	50	10.4	1.267
1.5	56	57.7	9.03	1.533
1.8	66	64	7.43	1.767
2	70	70.7	5.37	2.033
2.3	76	75	4.27	2.267
2.5	81	80.3	3.65	2.533
2.8	84	84.3	2.91	2.767
3	88	86.3	2.52	3.033
3.3	93	92	1.97	3.267
3.5	95	94.7	1.32	3.533
3.8	96	96.7	1.23	3.767
4	99	99.3	1.38	4.033
4.3	103	102.3	1.41	4.267
4.5	105	105.3	1.1	4.533
4.8	106	107.3	0.842	4.767
5	109	109.3	0.673	5.033
5.3	111	110.7	0.514	5.267
5.5	112	112	0.36	5.533
5.8	113	112.7	0.174	5.767
6	113	113	0.0496	6.033
6.3	113	113	0.16	6.267
6.5	113	114	0.305	6.533
6.8	116	115	0.296	6.767
7	116	116	0.184	7.033
7.3	116	116.3	0.097	7.267
7.5	117	116.7	0.093	7.533
7.8	117	117	0.129	7.767
8	117	117.7	0.161	8.033
8.3	119	118.3	0	8.267

275
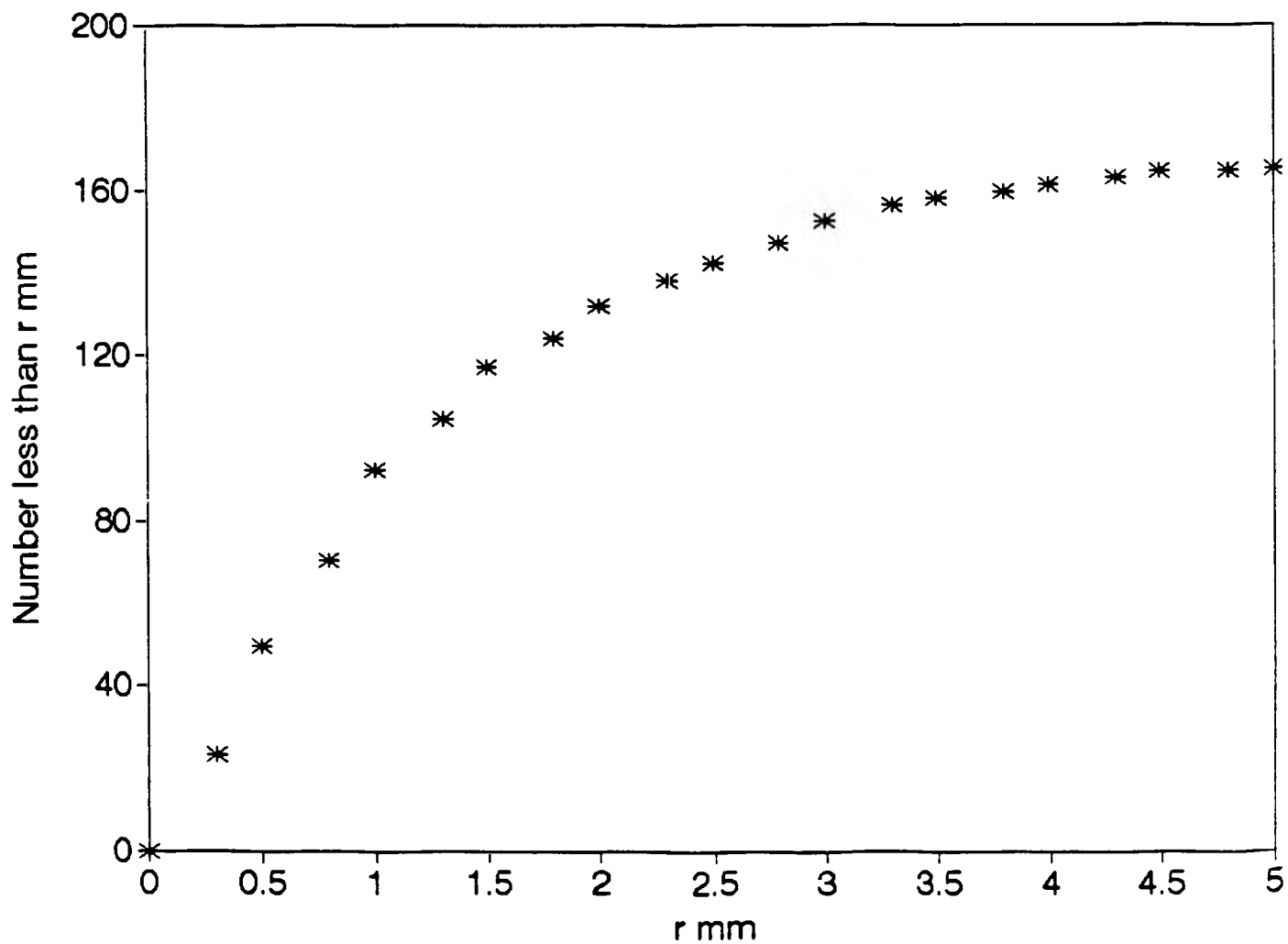
Figure 5. Cumulative gap size distribution for butyl acetate. Shows the number of adjacent cracks that occur below a gap of r mm
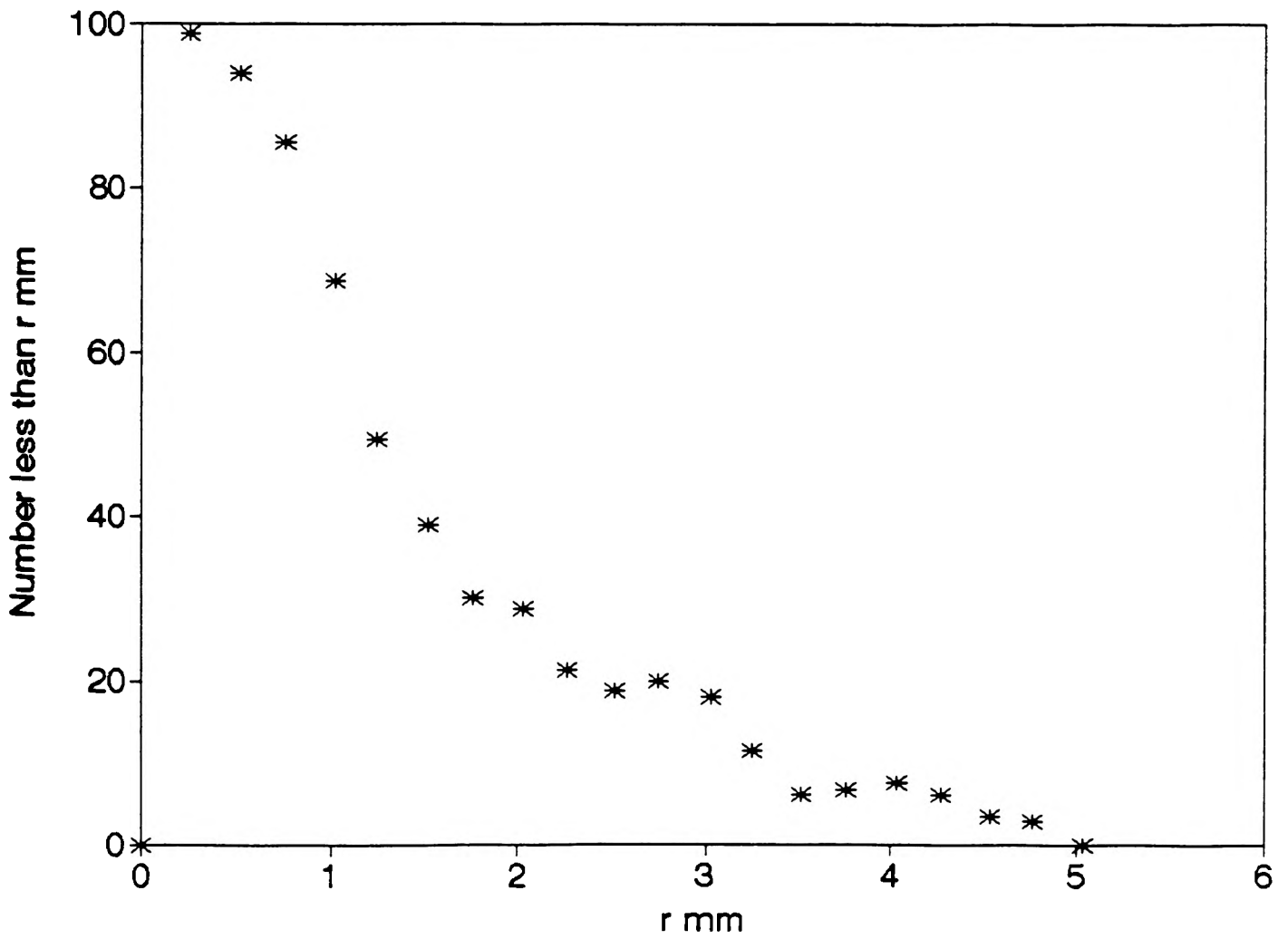
Figure 6. Derivative of Figure 5. Shows the frequency distribution of adjacent cracks with a gap of r mm
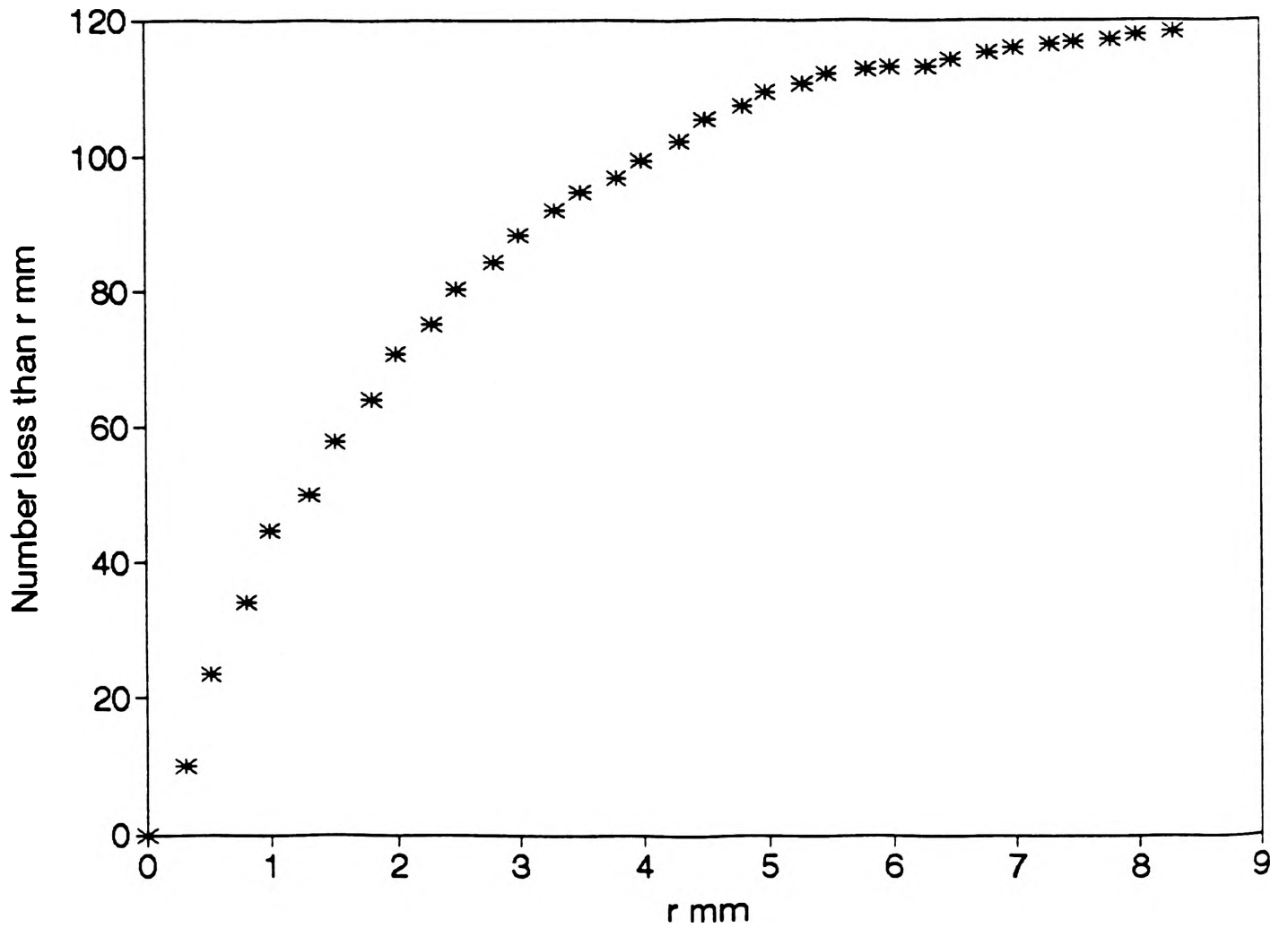
Figure 7. Cumulative gap size distribution for acetone. Shows the number of adjacent cracks that occur below a gap of r mm
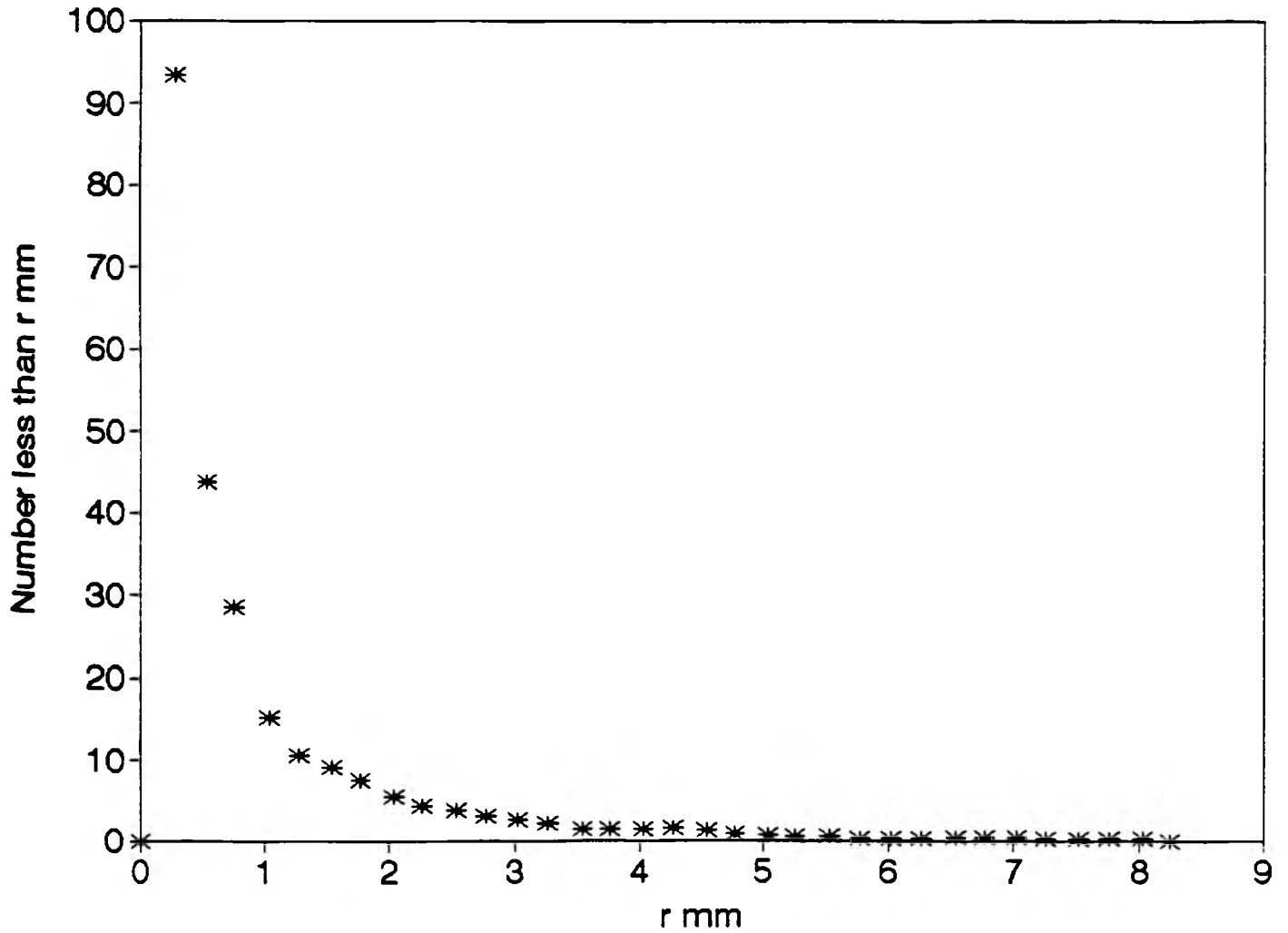
Figure 8. Derivative of Figure 7. Shows the frequency distribution of adjacent cracks with a gap of r mm

AUTOMATION OF THE ELECTROSTATIC AEROSOL CLASSIFIER AND THE CONTINUOUS FLOW CLOUD DIFFUSION CHAMBER

DARON W. DRYER
DEPARTMENT OF MECHANICAL ENGINEERING

ABSTRACT

Analyzing cloud condensation nuclei through the use of a Continuous Flow Thermal Diffusion Cloud Chamber (CFD) and an Electrostatic Aerosol Classifier (EAC) can be very time consuming. An alternative to manually monitoring these devices is to automate the equipment, thus freeing personnel for other research as well increasing CCN data collection.

Automation of the EAC will be carried out by digital command through the use of a Quick Basic program. This program will be run from an IBM personal computer outfitted with a digital input/output board.

RS-485 Standard will also be incorporated into the Quick Basic program in order to control the CFD.

INTRODUCTION

This investigation involves automation of two instruments used in aerosol research. Aerosol here means liquid or solid particles suspended in air. The first instrument is called an electrostatic aerosol classifier (EAC). In the EAC, particles carrying one or more electrical charges are passed through an annular region between two cylindrical electrodes which provide an electrical field. At the exit end of the EAC, air passes through a slit in the inner electrode, and this air will contain only particles in a narrow range of electrical mobility. The EAC acts like a filter which passes only particles of a specific mobility. The inlet aerosol is exposed to a device to give the particles an equilibrium distribution of electrical charges, which results in the situation that the aerosol at the outlet of the EAC contains mostly singly charged particles in a narrow size range. Automation of the EAC consists of using a computer to control the voltage of the center electrode. The voltage is supplied by a Bertan model 205C power supply, which is equipped for external control of the output high voltage. The voltage is to be changed in steps, so that with a suitable particle counter at the output of the EAC, the size distribution of the aerosol at the inlet of the EAC can be measured.

The second aerosol instrumentation to be automated is a continuous flow diffusion chamber (CFD). This device exposes an aerosol to a supersaturation, defined as the excess of the relative humidity above 100%. Water drops grow in the CFD on some of the particles, and these drops are counted downstream of the CFD. The supersaturation of the CFD is controlled

by changing the temperature of one part of the CFD, a part called the hot plate. The typical use of the CFD would be to vary this hot plate temperature in steps, in order to record the number of particles as a function of supersaturation. Thus to automate the CFD, a computer is to be used to control the CFD temperature. In this particular case the computer needs to send a set point signal to an Omega model CN6070A controller.

COMPUTER AND SOFTWARE

An IBM compatible computer is used, with DOS 3.3 as the operating system. The programming is done in Quick Basic, version 4.5. For the EAC automation, an I/O board was employed (National Instruments model PC-DIO-96). For the CFD automation a communications port was accessed in the Quick Basic program. Commands were then issued using the RS-232 electrical standard (which Quick Basic requires). A piece of hardware that converts from RS-232 to RS-485 was also employed because the temperature controller requires RS-485, and because eventually more devices will need to be controlled, and RS-485 allows multiple devices to be controlled by one communications port.

PROCEDURE

Controlling the Electrostatic Aerosol Classifier (EAC)

The voltage supply for the Electrostatic Aerosol Classifier is produced by a BERTAN Model 205c high power supply. This instrument can be controlled through 16 bits of digital input. To automate this device, a National Instruments PC-DIO-96 digital I/O board was employed. The PC-DIO-96 was installed in an IBM compatible personal computer. It contains 96 bits of digital input and output, which are arranged into 12 ports containing 8 bits apiece. These ports are labeled as APA, APB, APC, BPA, BPB, BPC, CPA, CPB, CPC, DPA, DPB, and DPC or 0 through 11 for digital I/O functions. Since the voltage supply only requires 16 bits of input, these can be represented by lines 2 through 17 of a standard cable with line 2 being the most significant bit. Only ports APA, APB, and APC were used for cable connection; APA and APB were used for output; and port APC was used for control purposes. Figure 1 illustrates the relationship of the lines from the voltage source to their pin positions in the DIO-96 connector.

Using NI-DAQ Software

The National Instruments package also contained NI-DAQ software that was essential for the use of the I/O board. This software contained a set of functions that could be incorporated into the Quick Basic program through the use of "quick libraries". Once called up with the Quick Basic program through a batch file, these functions made the output of data to the voltage source possible. In order to employ these functions into a program the programmer must type commands in the syntax listed in the NI-DAQ Function Manual along with the information needed for the function to complete its task. When the function has completed its work it will then send back an integer status code revealing whether or not the operation was successful. Figure 2 shows syntax for utilizing NI-DAQ functions and demonstrates how a block of code used to send digital output would appear, as well as giving an explanation for each step.

282
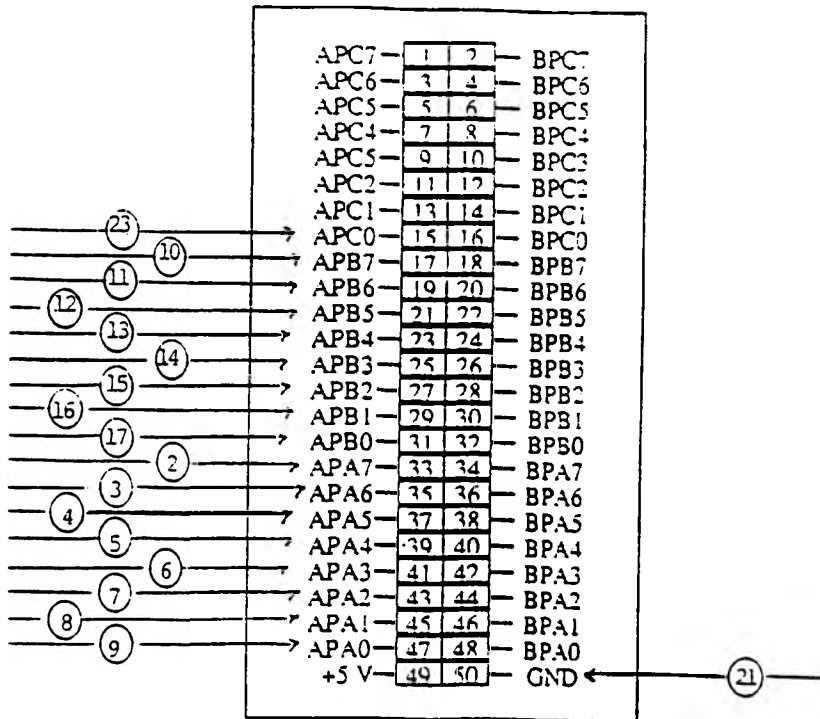
Figure 1. Assembly Connector Pinout for PC-DIO-96 Connector

STATUS% = DIG.OUT.PORT(BOARD,PORT,PATTERN)

Writes digital data to the specified port.

BOARD = Integer, represents the I/O board slot or I.D. number.

PORT = Inteter, represents the digital I/O port number.

PATTERN = Integer, represents the 8-bit digital command.

PRINT STATUS%

Prints the integer status code.

Figure 2. Syntax for Utilizing NI-DAQ Functions

283

Special Programming Considerations for EAC

Due to equipment requirements, grouping together of ports (treating two 8 bit ports as one 16 bit port) was not possible. This presented a problem that needed to be solved before the writing of Quick Basic could begin. The problem was due to the fact that two 8 bit ports had to be used to send output to an apparatus that required 16 bits. For example, if the user wanted to bring the voltage device to full power the digital command that the device must receive is: $2^0+2^1+\ldots\ldots+2^{14}+2^{15}$ or 65535. Each port can only hold a number of: $2^0+2^1+\ldots+2^7$ (255), any more will over load that port. Therefore, when we enter a command, "255" can be placed in the least significant port, APB, because it contains the lower 8 bits, but "65280" cannot be input in the most significant port, APA, because like APB it is just an 8 bit port.

In order to rectify this inconvenience a method had to be devised to transform the desired digital command into two separate numbers acceptable to the two eight bit ports, yet keeping the same positive logic. The algorithm produced achieved this through three steps.

First, it sorted the initial digital command, given the variable name DIG&, in order to determine the values that must be output through each port. A one dimensional array "Port" was created to store the values that would be held in the most significant port APA. Then each of these values were compared to the digital command by a FOR...NEXT loop until the largest possible value that could be stored in APA was found. It and the remainder were then stored as two variables, TOTAL& and NUM, respectively. It should be noted that the first element in the array "Port" would ideally be 2^{15} or 32768, but in order to keep the array single precision, it was entered as 32767. The algorithm described is shown below.

```
K = 14
PORT(1) = 32767
FOR I = 2 TO 8
PORT(I) = 2^K
K = K - 1
NEXT I
TOTAL& = 0
FOR I = 1 TO 8
IF PORT(I) + TOTAL& < = DIG& THEN
TOTAL& = TOTAL& + PORT(I)
ELSE TOTAL& = TOTAL&
ENDIF
NEXT I
NUM = DIG& - TOTAL&
```

Second, the value to be input into the most significant port APA had to be modified for the eight bit port. This was achieved by calculating to what power two was raised, subtracting eight from this number, raising two to this new value, and storing it as the new variable to be placed in port APA. This portion of the program is as follows.

$$N1 = (LOG(TOTAL\&))/(LOG(2))$$

284

$$N2 = N1 - 8$$
$$NEWTOT = 2^\wedge N2$$

The last step consists of outputting these variables, both NEWTOT and NUM, to their respective ports.

EXAMPLE:

Consider a case in which the digital command 300 would be entered. The largest value that could be stored in port APA would be 2^8 or 256. By taking the natural logarithm of this number and dividing it by the natural logarithm or two, the program finds to what value two was raised.

$$\ln(256)/\ln(2) = 8 \qquad\qquad 1).$$

By subtracting eight from that number, then raising two to that new value, a digital command is found that can be placed in port APA.

$$2^{(8-8)} = 2^0 = 1 \qquad\qquad 2).$$

Notice, as Figure 3 suggests, that the value "one" places a positive logic in the first bit of the port APA. This is the same location it would have been had 256 been placed in the upper half of a 16 bit port.

LINE NUMBER	17	16	15	14	13	12	11	10	9	8	7	6	5	4	3	2
BINARY NUMBER	2^0	2^1	2^2	2^3	2^4	2^5	2^6	2^7	2^8	2^9	2^{10}	2^{11}	2^{12}	2^{13}	2^{14}	2^{15}
POSITIVE LOGIC			+1	+1		+1			+1							

16 BIT PORT WITH DIGITAL COMMAND OF 300 ENTERED.

APB

LINE NUMBER	17	16	15	14	13	12	11	10
BINARY NUM.	2^0	2^1	2^2	2^3	2^4	2^5	2^6	2^7
POSITIVE LOGIC			+1	+1		+1		

APA

LINE NUMBER	9	8	7	6	5	4	3	2
BINARY NUM.	2^8	2^9	2^{10}	2^{11}	2^{12}	2^{13}	2^{14}	2^{15}
POSITIVE LOGIC	+1							

8 BIT PORTS APA AND APB. DIGITAL COMMAND OF 1 ENTERED INTO APA AND COMMAND OF 44 ENTERED INTO APB.

Figure 3. Port Comparison

Automating the Temperature Controller for the CFD

The water temperature for the hot plate of the CFD is controlled by an OMEGA CN6070A series temperature controller. Unlike the voltage source for the EAC, the temperature controller employs RS-485 serial programming. Unfortunately, Quick Basic would usually only be able to program through the use of RS-232, but by using an Omega RS-232 to RS-485 converter it was possible to communicate with the CN6070A successfully. RS-232 and RS-485 are electrical standards that are published by the Electronic Industries Association (EIA). These two electrical standards provide specifications that dictate voltage ranges for data and control signals in order to insures proper transmission. RS-485 differs from the RS-232 do to the fact that the RS-485 interface allows multiple devices to be connected to the same communications port.

Programming the CN6070A

A communications port had to first be opened in order for the computer to communicate with the temperature controller. The CN6070A responds to ASCII 7 bit code with one start bit, one stop bit, and odd parity. This information had to follow the OPEN "COM1" statement in order to successfully open communications with the CN6070A. A helpful example of this process can be found on pp. 133-134 of the text Programming in Quick Basic by Microsoft Corp.

Next came the task of programming using the syntax required by the CN6070A. The commands required to control the CN6070A are very rigid in regard to the positioning of the characters. Therefore, if an exact syntax was not followed the CN6070A would not respond. The command that must be sent is in the form of a string. This string consists of a start mark, controller number, command letter, parameter number, and parameter to be changed, as well as its units if needed. The start mark consists of a symbol used to inform the temperature controller where the command string begins; for this case it was a "#". The controller number indicates the number assigned to the CN6070A by the operator's manual; this number was 05. The command letter informed the CN6070A of what kind of task it was to perform. The parameter to be changed in this case was temperature, with its units of Celsius. Figure 4 gives a clearer example of how this string command must appear, as well as showing the CN6070A's response. Further information can be found on pages 15-16 and 27-33 in the CN6070A's operator's manual.

Special Programming Considerations For CFD

Future plans for the automation of this system consist of incorporating equipment that count CCN particles produced by the CFD. In order to determine when the particle counter should begin counting CCN particles, the Quick Basic program had to wait until the newly set temperature stabilized. This was accomplished by executing a programmed temperature check every 2 seconds until the set temperature matched the actual temperature of the water. When communicating with the CN6070A it had to be kept in mind that the Quick Basic program not only had to send commands to the CN6070A, but it had to wait for the CN6070A to send responses back. Quick Basic is so fast that it would check its input port before the CN6070A

6.3.2   To modify a parameter (but not enter into memory)

Enter: *   05   M   1   —   0125   F   (CR)
Start Mark _____| | | | |
Controller Number _____| | | |
Modify "M" _____| | |
Parameter Number to be changed _____| |
Space or Minus _____|
New Value (4 Digits) _____
F. C. or space (whichever applies) _____
Carriage Return _____

            Controller Response:

                                          (LF)   *05C1   0125F   (CR)   (LF)
                                                       |
            "C" Temporary Change confirmed. _____|

The set point (Parameter 1) for controller 05 has now been temporarily
changed to 125 F. If power is removed the previously "Entered" value
will appear.

NOTE: For the RTD models an extra character must be added to accommodate

Example:
    ENTER: *05M1-0125_F (CR)   For range 26C
    ENTER: *05M1-125 0 F (CR)   For range 22F
    ENTER: *05M4-0125__ (CR)   For Parameters
                        |
                      Space

Figure 4. Example of a CN6070A String Command

had a chance to respond. Therefore, when the temperature check algorithm was run the Quick
Basic program would always read a "0" for the actual water temperature because no data was
yet present. This resulted in the particle counter never starting its count. To avoid this problem
a two second pause was incorporated into the code before the section that checked the modem.
This two second timer allowed the CN6070A proper time to respond.

Another aspect of this type of programming that deserves to be noted is the transition
from integer to string and string to integer that occurred often with the variables. As stated
earlier, the CN6070A's syntax required string commands, and sent string responses. In order
to transform these variables back and forth into something Quick Basic utilizes, the "VAR" and
the "STR$" functions became very valuable. The "LTRIM" statement was also used in order
to trim the space that Quick Basic inserts in front of all numbers. This was essential in meeting
the CN6070A syntax.

RESULTS

The Quick Basic programs have performed exceptionally well. Through the use of the PC-DIO-96 I/O board and the NI-DAQ software, the Quick Basic program can currently control the Electrostatic Aerosol Classifier's voltage supply with less than one percent error in most cases. The only instance in which the error is greater is if a command of less than five volts is input. This can be attributed to the resolution of 16 bit control and should be of no consequence to the future experiments. The only aspect of this portion of the project remaining is to put a step function into the Quick Basic code that will systematically step the voltage by the square root of two. This can be done during the final phase of combining all of the Quick Basic programs.

The Omega temperature controller responds to its' inputs flawlessly. When given a starting and ending temperature, the program will cause the CN6070A to set to the beginning temperature. It will then check the actual temperature every 2 seconds until it is within 0.2 degrees of the set point. At this time it will pause waiting for the counting process to complete, then step to the next temperature.

CONCLUSIONS

Although the process of collecting experimental data is usually a very time consuming and labor intensive process, through this venture it is shown that automation can be an effective alternative. The use of the PC-DIO-96 I/O board, Quick Basic, RS-485, and other programming techniques, successfully controlled the Electrostatic Aerosol Classifier as well as the temperature controller for the Continuous Flow Cloud Diffusion Chamber. Future studies are required, however. A method to collect and retrieve the data produced by the EAC and the CFD is needed in order to render the system completely automated. This can be accomplished with just a few hours of simple programming and should be of no hinderance to the overall goal of producing a completely automated system.

ACKNOWLEDGMENTS

BIBLIOGRAPHY

Alofs, Darryl J., "Performance of a Dual-Range Cloud Nucleus Counter," Journal of Applied Meteorology 17 (Sept. 1978): 1286-1296.

Microsoft Corporation. Microsoft Quick Basic, Programming in Basic Version 4.5 for IBM Personal Computers and Compatibles. Microsoft Corporation, 1988.

National Instruments Corporation. NI-DAQ Software Reference Manual for DOS/Windows/Lab Windows Version 4.3. National Instruments Corporation, March 1992.

National Instruments Corporation. NI-DAQ Function Reference Manual for DOS/Windows/Lab Windows Version 4.3. National Instruments Corporation, August 1992.

National Instruments Corporation. PC-DIO-96 User Manual. National Instruments Corporation, June 1992.

FIXED SITE FACILITATED TRANSPORT OF OXYGEN AND NITROGEN THROUGH PLASMA POLYMER FILMS

Chad Dunnegan
Chemical Engineering

ABSTRACT

A method of preparing plasma polymer films, in which metal chelate molecules are incorporated, is briefly outlined. The chemical reactivity of metal chelate molecules is preserved so that they may "facilitate" the transport of oxygen molecules through the membrane. The method for testing permeability of the films is presented and results are analyzed with respect to the dual mode sorption model, applied to fixed site facilitated transport.

INTRODUCTION

In the present study, low vapor pressure metal chelates were sublimed into a plasma and codeposited on to the substrates. The metal chelates are capable of reversibly binding oxygen, but not nitrogen, thereby highly promoting permselective transport of oxygen through metal chelate containing plasma polymer films. This highly promoting permselective transport is described as Fixed Site Facilitated Transport (FSFT).

The use of gas transport through membranes for the purpose of separation is appealing because of its efficiency from an energy standpoint. Separation of gas mixtures by permeation is based on differences in the diffusion coefficients of the gases. High selectivity, high flux, and good stability are potential advantages of the use of plasma polymer membranes capable of fixed site facilitated transport of one gas in a mixture.

This project focuses on a specific part of a larger research project being investigated by Dr. Nicholas Morosoff and Youngson Choe. The purpose of this project is to gain an understanding of the parameters involved in trying to reach a high permselectivity (O2/N2) through a plasma polymer film and to gain some relevant lab experience.

DIFFUSION, PERMEABILITY, AND PERMSELECTIVITY

Before description of the experiment occurs, some discussion of the physical phenomena involved in the study is in order. It has long been established that between gas mixtures with varying

relative concentrations of a particular species, a process results which tends to equalize their compositions. This process is called diffusion and, according to the solution-diffusion model, can be divided into four parts. These are: (1) sorption of the compound on to the surface, (2) solubilization of the permeant into the material, (3) diffusion of the permeant within the material to the opposite surface, and (4) release of the permeant from the sorbing material.

Both diffusion and solubility characteristics of the permeant in a material are incorporated in a measure of the permeant's permeability in that material. It has been shown that gases dissolving in rubber follow Henry's and Fick's law of diffusion:

$$C = k_D p \tag{1}$$

$$J = -D \frac{\Delta C}{\Delta x} \tag{2}$$

where C is the concentration of gas in the polymer in cm^3 gas (at STP)/cm^3 of polymer, k_D is the solubility constant or Henry's law constant in cm^3 gas (at STP)/(cm^3 of polymer * cm Hg), p is the partial pressure of gas in cm Hg, and D is Fick's diffusion coefficient in cm^3/second. ΔC is the permeant concentration change
across a thickness Δx.

Fixed gases (gases above their critical temperature) diffusing through rubbery polymers present fairly simple behavior [1]. For such a system the permeability is defined as:

$$J = \frac{P \Delta p}{l} \tag{3}$$

where P is the steady state permeability expressed in cm^3(STP)cm/(sec*cm^2*cm Hg), Δp is the pressure difference across the membrane, l is the thickness of the membrane, and

$$P = k_D D \tag{4}$$

where k_D is the adsorption coefficient (for sorption of the gas in the membrane), and D is Fick's diffusion coefficient. The above unit of permeability multiplied by 10^{-10} is currently referred to as the 'barrer' and is a common unit of permeability. These three constants can be obtained by measuring the permeation rate through an initially degassed membrane.

Permselectivity (or separation factor) has been widely used to characterize gas transport through membranes. The ideal selectivity between the permeants is expressed as the ratio of the two pure gas permeabilities in a membrane.

$$\alpha = \frac{P_A}{P_B} \qquad\qquad (5)$$

A good gas separation should have both a high permeability and a high selectivity. Evidence has been provided that the most important parameter is the diffusion coefficient [2]. It has also been noted [3] that there is an inverse relationship between O_2/N_2 permselectivity and O_2 permeability. This results in an O_2/N_2 permselectivity ceiling of 9-10 for organic polymers.

CONVENTIONAL FSFT VS. PLASMA POLYMER FSFT

Improvements in the separation of O_2 from O_2/N_2 mixtures have been made by incorporating oxygen carriers into conventional polymer membranes. It has been shown that the use of immobilized synthetic transition metal chelates improve O_2/N_2 separation through permselective membranes [4]. O_2 binds to the metal complexes on one side of the membrane. O_2-transition metal complexes diffuse through the membrane to the lower O_2 concentration. Finally, O_2 dissociates from the complex and evaporates from the membrane surface. This dual mode sorption model, it has been established, is indicated by a pressure dependence of the transport behavior. This pressure dependance is due to Langmuir mode by which sorption occurs. Henry's mode of transport through the matrix is pressure independent. These two postulates explain why such membranes are most effective at low pressures.

Conventional polymer FSFT membranes suffer from short lifetime problems due to diffusion of metal chelate complexes in the polymer matrices, and subsequent dimerization of the metal chelates. Plasma polymers have been introduced to overcome this obstacle in the hope of inhibiting this diffusion, thus preventing the dimerization, by means of increasing the degree of crosslinking of polymer structures.

APPARATUS AND TESTING

Plasma polymers were deposited onto Al_2O_3 membranes (Anodisc). The membrane pore size was 200 A. Anodisc was used as a supporting substrate to withstand the high pressure gradient across the membrane since the plasma polymer films are extremely thin (800 - 2000 A) and very brittle. The membranes were spin-coated with a two component silicone potting compound (RTV-615), vinylmethylpolysiloxane(VMPSiO), d=0.98 g/cm^3, General Electric Silicones Inc.). Each membrane was weighed before and after application of the coatings. Membranes were spun at 7200 rpm for 4 minutes, then cured in an oven at 75 C for 15 hours. A cross

section of the composite filter is shown below:

Figure 1: A diagram of the substrate for permeability measurement.
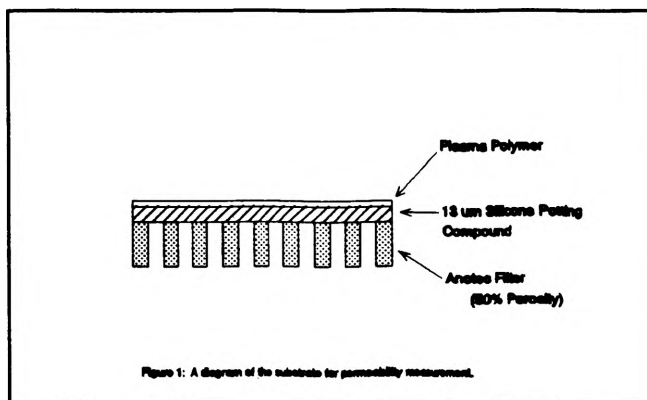
Permeation studies were performed using trans-2-butene plasma polymer films to determine the separation abilities of the polymer prior to metal complex incorporation. Trans-2-butene plasma polymer films were deposited onto VMPSiO coated substrates. Complete coverage is obtained at a mass thickness of 9.5 ug/cm^2.

Permeability measurements were accomplished using the equipment schematically shown in Figure 2.
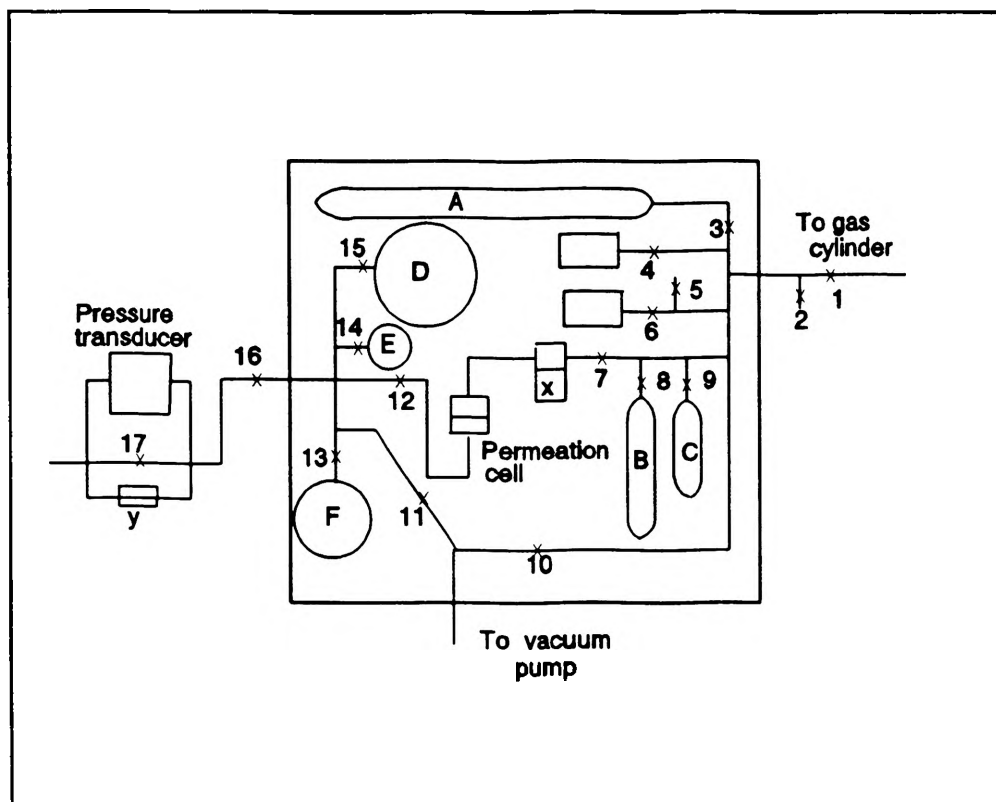
Figure 2:   Permeability Measurement Apparatus

The upstream side consists of three feeding gas reservoirs connected via valves to the gas cylinder; the pressure was monitored by two Heise Baratrons (a range of 0-1000 Torr and 0-1000 Torr) on a personal computer by A/D board and a Data Acquisition and Control System which was purchased from Strawberry Tree Computers, Inc. (Sunnyvale, CA). The downstream side has three receiving reservoirs and the pressure was monitored by a Heise Baratron that had a full range of 10 torr and sensitivity of +/- 0.001 Torr. The permeation cell used was a Millipore high pressure stainless steel 47 mm disc filter holder. The permeation cell consisted of a two part stainless steel housing, a perforated metal insert, and a porous metal support disk. The metal insert was placed inside the bottom half (low pressure side) of the cell and the porous metal support was placed on top of the insert. The membrane sample was set on top of the support disk. A lightly greased Silastic gasket sealed the membrane in the cell. Both sides were evacuated for 12 hours and filled with oxygen or nitrogen. Computer collection of pressure measurements on the low pressure side was then initiated, with pressure being recorded every 2 seconds for nitrogen or oxygen by a Data Acquisition and Control Program (Analog Connection ACJR™-12-8, Strawberry Tree Computers Inc., Sunnyvale, CA).

Permeation for the composite film was then calculated by the following equation:

$$P = \left(\frac{p_1}{t} \right) \frac{VL}{60ATp} \left(\frac{273}{76} \right) \tag{6}$$

where P is the composite permeability in $cm^3(STP)cm/(sec\ cm^3\ cm$ Hg), p_1/t is the slope of the low side pressure versus time graph in torr/minute, V is the volume of the low pressure side in mL, T is the temperature in Kelvin, A is the surface area of the membrane in cm^2, L is the composite thickness in cm, and p is the pressure of the high pressure side gas in torr. To obtain the permeability of the plasma polymer layer alone, the following equation was applied

$$\frac{L}{P} = \frac{L_1}{P_1} + \frac{L_2}{P_2} \tag{7}$$

For the composite, the ideal selectivity is defined as:

$$\alpha = \frac{P(O_2)}{P(N_2)} \tag{8}$$

and for the plasma polymer, the ideal selectivity is defined as: where L is the composite thickness in cm, P is the composite permeability in barrers, L_1 is the plasma polymer layer thickness

295

$$\alpha_1 = \frac{P_1(O_2)}{P_1(N_2)}$$

(9)

in cm, L_2 is the VMPSiO coating layer thickness in cm, P_1 is the plasma polymer permeability in barrers, P_2 is the VMSiO coating layer permeability in barrer. All of the variables except P_1 were obtained experimentally or by direct measurement.

RESULTS

The ideal O_2/N_2 selectivity of VMSiO/trans-2-butene composite is plotted versus thickness of plasma polymer film in Figure 3. The maximum ideal O_2/N_2 selectivity is obtained at a thickness of 9.5 ug/cm^2. The ideal O_2/N_2 selectivity gradually decreases with increasing mass thickness of plasma polymer films. At 10 ug/cm^2 thickness of plasma polymer films, the average ideal O_2/N_2 selectivity is 3.8.
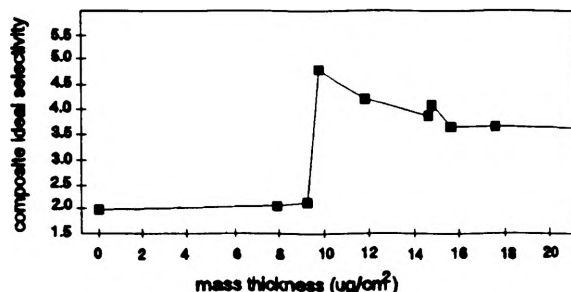
Figure 3: Selectivity vs. thickness (no chelate)

These results may be compared with those obtained by Choe for CoTPP/trans-2-butene plasma polymers. These films were deposited onto VMPSiO/Al$_2$O$_3$ substrates, and successfully deposited with loadings up to 50%. The ideal O_2/N_2 selectivity of CoTPP/trans-2-butene plasma polymer film (or composite) is plotted versus mass thickness of the polymer film in figure 4. Complete coverage is obtained at a mass thickness of 8.5 ug/cm^3. The ideal O_2/N_2 selectivity of composite decreases with increasing mass thickness of the plasma polymer film, dropping from 8.8 to 6.3 as mass thickness increases from 8.5 to 17.5 ug/cm^3.
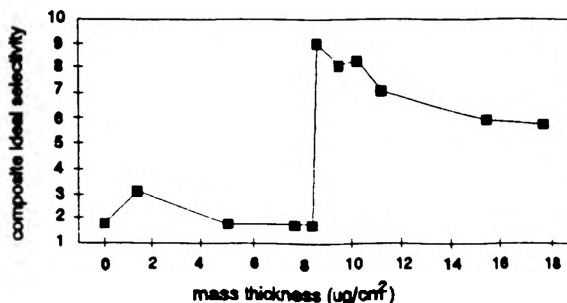
Figure 4: Selectivity vs. thickness (containing chelate)

296

Also shown in figure 5 are the time lags obtained for several 2% loaded plasma polymer films.
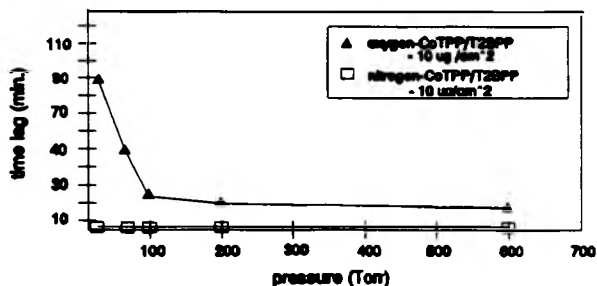
Figure 5: Time Lag vs. Pressure

Only for the combination of CoTPP and O_2 are pressure dependant time lags obtained. This is evidence of fixed site facilitated transport through CoTPP loaded film.

Trans-2-butene plasma polymer films containing CoTPP have ideal selectivities which are higher than trans-2-butene plasma polymers without the metal chelate. The ideal selectivity of CoTPP plasma has been shown to increase with increased film loading, up to 5% CoTPP in plasma polymer, for films of the same mass thickness (10-11 ug/cm^3), as expected for fixed site facilitated transport. This is caused both by a decrease in nitrogen permeability and an increase in oxygen permeability. The permeability of nitrogen decreases as the concentration of the metal complex increases.

These phenomena can be explained by an increase in "tortuosity" with increasing CoTPP concentration. Large molecules such as CoTPP in the polymer matrix lengthen the path which solute molecules travel, resulting in smaller apparent diffusion coefficients. This effect is combatted in the case of oxygen, up to an optimum of about 5% loading, by the reversible bonding, and its facilitating effects, that occurs between oxygen and CoTPP.

For films with greater than 5% loading, the ideal O_2/N_2 selectivity of CoTPP/trans-2-butene plasma polymer film decreased with increasing % loading of CoTPP.

The dual mode sorption model, modified based on Barrer's four type diffusion model[5], is very important to explain the behavior described above.

$$J_A = - [D_{HH} + D_{DH} + D_{DH} (\frac{C_A}{C_T}) + D_A (\frac{C_{AO}}{C_{ABO}}) + D_{OH} (\frac{C_{AO}}{C_{ABO}}) C_B] \frac{dC_{AB}}{dx} \qquad (10)$$

As the % loading of the metal chelate increases, the solute flux of the O_2 increases, but beyond the optimum % loading the solute flux begins to decrease.

297

Above about 20% loading, a different effect is introduced. Solubility tests of CoTPP loaded films indicate a lack of crosslinking, since the deposition rate is too high to build up enough crosslinks within the films. In these higher loaded films, N_2 permeability is higher than that of lower loaded films, resulting in decreasing ideal selectivities of composites with higher loading percents.

ACKNOWLEDGEMENTS

REFERENCES

[1]   Stannett, V.T., Koros, W. J., Paul, D.R., Lonsdale, H. K., and Baker, R.W. (1979). "Recent Advances in Membrane Science and Technology" in Advances in Polymer Science (Fortschritte der Hoch Polym. - Forschung) 32, 69.

[2]   Lee, W.M. (1980). Polym. Eng. and Sci. 20, 65.

[3]   Delaney, M.S., Redy, D., and Wessling, R.A. (1990). J. Membr. Sci. 49, 15.

[4]   Choe, Youngson (1994). "Fixed Site Facilitated Transport in Co-Chelate Containing Plasma Polymer Films", UMR Doctoral Dissertation.

[5]   Choe, Youngson (1994). "Fixed Site Facilitated Transport in Co-Chelate Containing Plasma Polymer Films", UMR Doctoral Dissertation.

AN ASSESSMENT OF THE "AN/EX" STRUCTURAL ENGINEERING TEACHING LABORATORY

Gregory E. Effland

Department of Civil Engineering

ABSTRACT

An innovation in teaching structural analysis, the "AN/EX" Structural Model Laboratory, has been implemented into the civil engineering curriculum at UMR. The purpose of the AN/EX innovation is to give the students a "hands-on" lab in structural engineering that will help correct some of the deficiencies currently found in engineering design education. In an effort to determine the effectiveness of the "AN/EX" Laboratory at correcting some of the education deficiencies, a rigorous, semester long assessment was conducted. This assessment included an attitude assessment and an ability assessment. The methods and results of both assessments are provided in this report.

INTRODUCTION

Over the past few years, many engineering disciplines have discussed the need for innovations in the engineering curriculum. Practicing engineers and professors alike have been suggesting that the methods for teaching design need to be reformed [1]. Many articles have been published that discuss what and how engineering students should be taught [2,3,4,5,6]. Most of the articles imply that the current trends in education tend to provide the students with the skills necessary to understand the theory, but not with the skills that are necessary for the application of that theory. At the University of Missouri-Rolla (UMR), the "AN/EX Structural Model Laboratory," an innovation in teaching structural analysis, has been implemented into the civil engineering curriculum to help solve some of the deficiencies in engineering design education [7].

ENGINEERING DESIGN EDUCATION

"Industry needs, and will continue to need better designers [8]." In the words of John Dixon, Mechanical Engineering Professor at the University of Massachusetts, "Engineering design education is not successful; ... Industry continues to be dissatisfied with the design education of engineering students [9]." Even ABET annual reports show design deficiencies have been prominent [10]. Many different methods for fixing deficiencies in engineering education have been tried. Each of these methods works best in a specific environment that is dependent on what is being taught and what deficiencies are trying to be corrected. Independent of the method used for

correcting education deficiencies, the main emphasis should be on providing the best education possible to the design engineers of tomorrow.

TEACHING STRUCTURAL ANALYSIS AT UMR USING "AN/EX"

The AN/EX facility consists of four basic components. These components include:
1. **Computer**
2. **Test Bed**, which provides an environment for the students to perform physical experiments.
3. **M-STRUDL**, a professional-level structural analysis software package [11].
4. **Specially designed AN/EX software**, which helps teach M-STRUDL, runs an analysis through M-STRUDL, handles data acquisition tasks required by students when performing experiments, and provides graphs and tables correlating the computer analysis to the physical experiment.

The main goal of AN/EX is to solve as many of the deficiencies in engineering design education as possible. Some of the key skills required in engineering design education, that AN/EX is intended to provide, include:
1. **Computer Skills.** With the increasing use of computers in the engineering process, it is clear that engineering students must be prepared in the use of computers [12].
2. **Judgment Skills.** With the increasing use of commercial software packages in engineering, it is becoming even more important that the engineers can make rational judgments about the validity of the computer output.
3. **Nontechnical Skills.** Skills such as writing, speaking, and organization are included in this group. Education of these skills better prepares engineers to adjust for and understand changing conditions that will affect "technology development in the global marketplace of the future [13]."
4. **Synthesis/Design Skills.** With the numerous variations and special considerations included in each project in industry, it is apparent how just knowing the theory behind the solution is not always sufficient. The ability to synthesize or create solutions to unique problems is critical for design engineers. Synthesis involves the use of parts of many techniques to solve a single problem.

OBJECTIVE OF ASSESSMENT

To determine if AN/EX corrected any deficiencies in engineering design education, a semester long, rigorous assessment of the impact of AN/EX on the abilities and attitudes of civil engineering undergraduates in an introductory structural analysis course at UMR was completed.

"AN/EX" ASSESSMENT

Assessment Methodology

To determine the impact of AN/EX in the introductory structural analysis class, a rigorous, semester long assessment was completed. This assessment consisted of an ability assessment and an attitude assessment. The assessment was applied to a sixty student class. First the class was randomly divided into two groups, equal in prior academic performance. The only difference between the two groups in this course was the lab session that they attended.

Group A performed a semester long open ended design project that required the use of the AN/EX Laboratory. Group A was divided into working teams of 3-4 students. Their design project consisted of the design, construction, testing, and presentation of a balsa wood tower.

Group B attended weekly "guided" problem sessions. Each week, students from Group B were randomly chosen to present homework solutions on the chalkboard during their problem session. The students were graded in terms of technical merit (i.e., accuracy) and presentation quality (i.e., explanation and response to questions). For both groups their "lab" counted towards 20% of their final grade. The assessment methodology is graphically presented in figure 1 on the next page.

Attitude Assessment Methodology

The attitude assessment consisted of two questionnaires, one, immediately after dividing the class into two lab groups and the other at the end of the semester. These two questionnaires were used to evaluate the student attitudes towards the class, the lab groups, etc. The first questionnaire consisted of seven questions regarding such topics as structural engineering, graduate school, feelings about their assigned lab group, etc. The second questionnaire consisted of the original seven questions and an additional three questions regarding the lab. Figure 2 illustrates the questions on the two questionnaires.

Ability Assessment Methodology

Both Lab Group A and B took the same exams throughout the semester. These exams consisted of 80% classical structural analysis and M-STRUDL problems along with 20% nontraditional "synthesis" problems. The nontraditional, synthesis oriented problems had multiple constraints and a single solution. To solve these problems, the students had to draw upon knowledge from prerequisite coursework, such as statics and mechanics of materials. These problems required an overall understanding of structural analysis concepts instead of a direct step-by-step solution method. Figure 3 shows the synthesis problems from the second and third exam.

After the semester was completed, the exam scores were compiled and statistically analyzed. The exam scores were analyzed in the following categories:
1. Overall Grade
2. M-STRUDL portion of the overall grade
3. Classical structural analysis portion of the overall grade
4. Synthesis portion of the overall grade

Each group's exam statistics were analyzed to determine the mean, standard deviation and coefficient of variation. The normal distributions of these statistics were converted to a standardized normal distribution. Then, based on a level of significance of 1 percent and the null hypothesis that the two groups were equal (B=A), the statistics were evaluated by means of a two-tailed probability test to determine if there was a statistically significant difference between the two groups.

301

```
                    ┌──────────────────┐
                    │   60 Junior Level │
                    │  Civil Engineering│
                    │     Students      │
                    └──────────────────┘
```

Group A
30 AN/EX Lab Participants

Attitude Survey
Have students complete attitude survey regarding course, laboratories, etc. at beginning of semester

Group B
30 Problem Session Participants

Divide students randomly into two laboratory groups

Student Teams (3-4 members) perform experiments and participate in design competition using AN/EX facility

Randomly selected individuals work homework problems on the chalkboard

Both Groups take the same exams containing analysis, synthesis, and M-STRUDL problems throughout the semester

Attitude Survey
Have students complete attitude survey regarding course, laboratories, etc. at end of semester

Ability Results
Compare Groups A and B to determine if there is a significant statistical difference between the two groups.

Compile **Attitude** and **Ability** data for both groups and perform statistical analyses

Figure 1. Assessment of AN/EX in an Introductory Structural Analysis Course.

302

CE-218 STRUCTURAL ANALYSIS
Student Opinion Questionnaire

Note: This questionnaire is anonymous and will have absolutely NO effect on your course grade. Your thoughtful responses will be appreciated.

Group:

_____ Design project using ANEX (Group A)

_____ Problem Solving Sessions (Group B)

Your Current Overall GPA: _____/4.0

Your Average Grade in Statics
and Mechanics of Materials: _____/4.0

1. I plan to emphasize structural engineering in my BSCE degree.
2. I plan to go to graduate school and specialize in structural engineering.
3. I am satisfied with the laboratory group to which I have been randomly assigned.
4. My current feeling is that the design project using ANEX is a good emphasis for the laboratory portion of this course.
5. My current feeling is that problem solving sessions are a good emphasis for the laboratory portion of this course.
6. Learning how to use a structural analysis software package such as M-STRUDL is a valuable part of my engineering education.
7. I am comfortable with engineering problems that require trial-and-error procedures and judgment calls in order to solve.

Questions added to second questionnaire

8. The laboratory component of this course had a positive influence on my attitude toward structural engineering.
9. The laboratory component of this course had a positive influence on my ability to solve structural engineering problems.
10. Using the ANEX Lab to perform hands-on experiments would help me to learn structural engineering.

Note: The questions were rated between 0 and 4 by the students, with 0 representing *Strongly Disagree* and 4 representing *Strongly Agree*.

Figure 2. Attitude Questionnaires

Exam 2.

An 18-ft (216 in.) long simply supported beam is to be designed to carry a uniformly distributed load of 4 k/ft, which include the weight of the beam. The beam material has the following properties: compressive and tensile normal allowable stresses of 4 ksi, shear allowable stress of 1.5 ksi, elastic modulus of 4,000 ksi, and shear modulus of 1,600 ksi. The beam is to have a rectangular cross section of width b and height h. Using the above material properties and loading, estimate b and h in order to satisfy the following:

(1) the total weight of the beam is minimum,
(2) the midspan deflection due to shear and bending $(\Delta_V + \Delta_M)$ is minimum,
(3) the ratio of shear deflection to bending moment deflection (Δ_V/Δ_M) at midspan is not to exceed 1.5%,
(4) and none of the allowable stresses are exceeded.

Note that:
(i) the shape factor of a rectangular cross section used for the computation of shear deflection is k = 1.2,
(ii) the internal normal stresses in a beam due to bending moments are $\sigma = \dfrac{My}{I}$
(iii) and the internal shear stresses in a beam due to shear forces are $\tau = \dfrac{VQ}{Ib}$


```
          4.3 k/ft (0.3333 k/in.)
```

18 ft (216 in.)
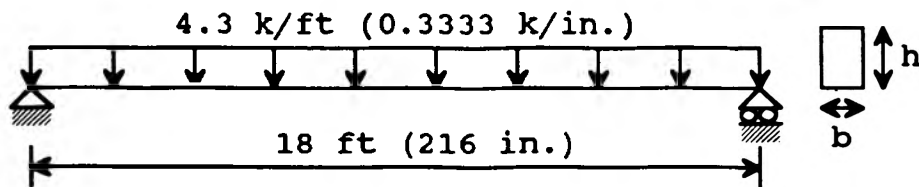
Exam 3.

A 10 ft (120 in.) long cantilever beam is to be designed to carry a uniformly distributed load of 48 k/ft, which includes the weight of the beam. The beam material has the following properties: tensile normal allowable stress of 2.5 ksi, compressive normal allowable stress of 5 ksi, shear allowable stress of 0.5 ksi, and elastic modulus of 3,000 ksi. In order to minimize the volume of construction material, the beam is to be designed to have two different rectangular cross sections, of width b and height h, along its length.

(1) Using the above material properties and loading, estimate the values for b and h and the location of the cross section transition.
(2) Given the beam design in part (a), compute the maximum deflection due to bending effects only using the virtual work method.

Note that:
(i) the internal normal stresses in a beam due to bending moments are $\sigma = \dfrac{My}{I}$
(ii) the internal shear stresses in a beam due to shear forces are $\tau = \dfrac{VQ}{Ib}$

Figure 3. Synthesis Problems Used in Introductory Structural Analysis Class.

Results of Assessment

Ability Assessment Results

From the statistical analysis, the groups were determined to be statistically equivalent in all exam categories *except the synthesis problems*. The results of the two-tailed test are presented in table I.

TABLE I. ABILITY ASSESSMENT RESULTS

Exam	Category	z value	Significance (Yes/No)
Exam 2	Overall	-0.26	NO
	M-STRUDL Problems	-1.24	NO
	Analysis Problems	0.855	NO
	Synthesis Problems	-2.6	YES
Exam 3	Overall	-0.807	NO
	Analysis Problems	1.13	NO
	Synthesis Problems	-3.54	YES

Note: A absolute value of z greater than 2.576 was required to show a 1 percent level of significance. All z values in this table assume Group B = Group A. Negative Values represent that Group A did better in those categories.

Attitude Assessment Results

The results of the attitude assessment are shown in Table II.

TABLE II. ATTITUDE ASSESSMENT RESULTS

Question	z from First Questionnaire	Significance (Yes/No)	z from Second Questionnaire	Significance (Yes/No)
1	-1.23	NO	0.81	NO
2	-1.74	NO	-0.217	NO
3	-0.788	NO	-1.2	NO
4	1.24	NO	-2.05	NO
5	2.13	NO	3.61	YES
6	3.03	YES	1.23	NO
7	-0.9	NO	-2.47	NO
8	N/A	N/A	-5.14	YES
9	N/A	N/A	-0.09	NO
10	N/A	N/A	-0.14	NO

Note: A absolute value of z greater than 2.576 was required to show a 1 percent level of significance. All z values in this table assume Group B = Group A. Negative Values represent that Group A rated those questions better.

CONCLUSIONS

The statistical difference between the exam score for the synthesis problems showed that the AN/EX Laboratory did indeed make an impact on the learning of the design process in the introductory structural analysis class. Due to the larger z value of the exam 3 synthesis problem (3.54 as compared to 2.6), it could easily be inferred that the amount of the exposure to AN/EX is directly proportional to the increase of knowledge in the design process. According to the attitude results, Group A felt stronger than Group B about the laboratory having a positive influence on their attitudes toward structural engineering. The AN/EX Lab improved student performance in the area of synthesis/design problems.

ACKNOWLEDGMENTS

REFERENCES

[1] J. C. Liebman, "Designing the Design Engineer," *Journal of Professional Issues in Engineering*, July, 1989.

[2] J. S. Russell and B. G. McCullouch, "Civil Engineering Education: Case Study Approach," *Journal of Professional Issues in Engineering*, April, 1990.

[3] P. Tarricone, "Education at a Crossroads," *Civil Engineering / ASCE*, Oct., 1990.

[4] D. W. Gentry, "Educating Engineers for the Next Century," Proceedings -- 1990 SPE Annual Technical Conference and Exhibition, New Orleans, LA, Sept. 23-26, 1990.

[5] R. B. Corotis and R. H. Scanlan, "Future of Civil Engineering Profession and Role of Education," *Journal of Professional Issues in Engineering*, April, 1989.

[6] J. R. Dixon, "Engineering Design Science: New Goals for Engineering Education," *Mechanical Engineering*, March, 1991.

[7] R. A. Behr and D. S. Vollenweider, *ANEX Laboratory Manual*, Department of Civil Engineering, University of Missouri-Rolla, Rolla, MO 65401; 1992.

[8] L. M. Nicolai, "Designing a Better Engineer," *Aerospace America*, April, 1992.

[9] J. R. Dixon, "Engineering Design Science: The State of Education," *Mechanical Engineering*, Feb., 1991.

[10] J. B. Jones, "Design at the Frontiers of Engineering Education," Proceedings -- 1991 Frontiers in Education Conference.

[11] *User's Manual for M-STRUDL and CAST Utility*, Computer Aided Structural Technology, Inc., P.O. Box 7326, Fremont, CA 94537-7326; 1986.

[12] K. H. Law, W. J. Rasdorf, M. Karamouz, and O. Y. Abudayyeh, "Computing in Civil Engineering Curricula: Needs and Issues," *Journal of Professional Issues in Engineering*, April, 1990.

[13] R. W. Eck, "Developing a Civil Engineer for the 21st Century," *Journal of Professional Issues in Engineering*, April, 1990.

Image Processing Techniques and Implementations in Software for use with a CCD Camera

Clarence Franklin, Jr.
Department of Computer Science, University of Missouri-Rolla
Rolla, Missouri 65401

ABSTRACT

The concept of image processing is used whenever there is a reference to digital images. By random and natural errors introduced into the image during collection and transmission, the images are distorted. Image processing techniques are used to eliminate these error before viewing of the images. For this experiment, the images provided by the ST-6 CCD Camera System will be used in the development and implementation of image processing techniques into a software package.

INTRODUCTION

Digital images have become a fact of everyday life. They are used in a wide range of applications, spanning the range from satellite images to digitized photographs to spectroscopy profiles and beyond. During the process of collecting and transmitting, natural and random errors are introduced into these images. For instance, noise can be introduced into the image when it is transmitted, through the air or over a line, to some receiver. Another instance could be overexposure of the image during the time when the image is collected (too much light was on the object whose image was being taken or too much light entered the camera). These errors, which are often unavoidable, can distort the image. A means to correct these errors is then needed; this is the purpose of digital image processing.

EQUIPMENT

The choice of images to be processed for this experiment are supplied by the Model ST-6 Professional CCD Imaging Camera [1]. This choice is partly attributed to the wide range of applications this camera can be used to perform. The camera, since it can take long exposures (several hours in length), is ideal for taking astronomical images (since long exposures are needed to capture faint light from distant stars), yet can take a profile of a light sample supplied via optical cable (which is unlike a traditional image). Also, CCD (charge-coupled device) technology is commonly used in light weight home video cameras, so the techniques used to process ST-6's digital images can be used to process other digital images as well.

To understand how the images are collected for processing, a brief explanation of the ST-6 system is warranted. The ST-6 Camera consists of a camera head, a CPU (central processing unit) box, a

wall transformer and necessary cables & software. The camera head contains the CCD, the thermoelectric cooler and Analog-to-Digital (A/D) converter. During an exposure, the CCD, which is an array of optical detectors, converts incoming photons into electrons and stores the charge until later. Each element, called a pixel, does this operation individually, thus obtaining the digital image information. Later, the readout electronics use the 16 bit Analog-to-Digital converter to convert the stored charge into a digital number from 0 to 65535 and transmits the number to the CPU, which is the display, analysis and storage device for the images. If the photographer wishes to view the image at a later time, the image can be saved as a special "image" file which the software recognizes at the later date.

The choice of programming language to write the software to process the stored images in was Borland C++ [2]. Borland C++ is very versatile and supports many of the graphics functions needed for image display and processing. Also, the dual MS-DOS/Windows package, that was purchased for this experiment, allows for programming in a MS-DOS environment and a Windows based environment.

DIGITAL IMAGE STORAGE AND PROCESSING TECHNIQUES

I. Tagged Image File Format (TIFF) [3]

The file format chosen to store image files for this experiment was the Tagged Image File Format (file extension .TIF). This choice was made due to the several advantages of this file structure. Many graphics file formats follow a standard structure of placing a fixed-length header (which contains important information about the image) at the beginning of the file, followed by a fixed-length image data area. This approach makes the file very inflexible. If any changes are made to the data contained in the file, the whole file must be reprocessed and rewritten to a new file. A TIFF file takes a different approach which can be seen by examining the file structure.

First, a single 8 byte header appears at the beginning of the file (not a 2K or larger header). This header contains 3 pieces of information: 1) the type of machine the file was made with (Intel or Motorola), 2) the version number of the file format and 3) the pointer to the first image file directory (IFD). The image file directory contains all of the information about the image not found in the pixel data (such as, imagewidth, imagelength, Xresolution, etc ...) and pointers to the pixel data. Each entry in the IFD is 12 bytes in length (except for the 1st entry which contains the number of entries in the IFD) and contains a tag & pointer/data. If the data that the tag refers can be placed in the 12 bytes accompanying the tag, the data is placed in the directory entry; otherwise, the data is placed elsewhere in the file and a pointer to the data is placed in the directory entry. A list of tags that can be used in the IFD is offered in [Table 1]. At the end of the

IFD, is one more entry that points to the next IFD (the entry is zero if there if not another IFD in the file).

The flexibility of this file format allows for a dynamic pixel data space, a dynamic "header information" space and multiple images per file. Plus, if any changes are made to the file, only the information that is updated is changed in the file (restructuring of the whole file is not necessary). Barring the added complexity of this file format to software design, the TIFF file structure is ideal for image storage and processing.

II. Conversion of ST-6 Files to TIFF Files

The TIFF file structure may be ideal for image storage, unfortunately the ST-6 CCD Camera saves its files in its own format (file extension .ST6). The files are in a fixed format with a 2K header and a fixed pixel data space. A sample of the header of a ST-6 image file is offered in [Figure 1]. To be able to use the information in the ST-6 image files with our software, they must first be converted to TIFF image files. This can be done easily by taking out of the ST-6 header only the information needed and placing it in the new TIFF file using tags. Then the pixel data is transferred from the ST-6 file over to the new TIFF file according to the TIFF data format. After these steps are performed, the old ST-6 file can be discarded and all of the image processing can be performed on the new TIFF file. This conversion is necessary to prevent extra code from being added to the original software package. Instead, file conversion code can be introduced externally.

III. Gray-Scale Modification [4]

Gray-scale modification is a simple and effective way of modifying an image's dynamic range or contrast. For instance, if an image has been taken with too much light in the background, gray-scale modification can increase the shadowy regions of the image, giving the image more clarity. The technique is described below:

$$n_x = input\ intensity \qquad n_y = output\ intensity$$

These values can be related to each other through the transformation:

$$n_y = T[n_x]$$

Given all of the input intensities and the output intensities, a histogram of the image can be produced. The histogram function, denoted below, represents the number of pixels that have a specific intensity as a function of the intensity variable n_x :

$$p(n_x)$$

Due to the simplistic nature of the transformation, it is possible that the operator viewing the image could choose a new transformation by looking at the processed image and the histogram of the image. Or, the operator could use the following automatic transformation to modify the image's gray-scale:

$$p_d(n_y)$$

Represents the desired histogram of the output image (a given set of values), which normally has a maximum around the middle of the dynamic range and decays as the intensity increases or decreases.

$p'(n_x)$, $p_d'(n_y)$ represent cumulative histograms given by:

$$p'(n_x) = \sum_{k=0}^{n_x} p(k) = p'(n_x-1) + p(n_x)$$

$$p_d'(n_y) = \sum_{k=0}^{n_y} p_d(k) = p_d'(n_y-1) + p_d(n_y)$$

Then we can find n_x and n_y for:

$$n_y = T[n_x]$$

Such that:

$$p_d'(n_y) \quad , \quad p'(n_x)$$

are closest together.

IV. Median Filtering [5]

Median filtering is a nonlinear process useful in reducing impulsive or salt-and-pepper noise. It is also useful in preserving edges in an image while reducing random noise. The technique is described below:

0	0	0
0	X	0
0	0	0

A window slides across the image. In each window, is contained X = the pixel to be processed and 0 = the surrounding pixels. In each window position, the surrounding pixels are averaged together and replace the pixel that is being

processed. Then the window moves on to the next position, unit the whole image has been covered.

This type of filtering has an advantage over other types of filtering, such as low pass filtering and high pass filtering. Median filtering will smooth the image, removing the noise, but will preserve discontinuities in a step function and can smooth a few pixels whose values differ from their surroundings without affecting the other pixels. Thus, the median filter eliminates the blurred effect of low and high pass filtering.

V. Thresholding [6]

Thresholding is a type of contrast manipulation, however unlike the previous techniques, it is not designed to enhance the image contrast. Instead, thresholding divides an image into segments by a single gray level threshold. For instance, if an image that contained dark areas and light areas, thresholding would darken the pixels that fell below the threshold value and lighten the pixels that fell above the threshold value. This techniques sharpens specific areas of an image and removes the extraneous areas at the same time.

VI. Other Image Processing Techniques

Other image processing techniques that were considered to be included in this software package were:
1. Color Enhancement [7]: adding color to a black and white image to enhance the present detail of the image.
2. Registration [8]: the overlaying of multiple images and having the frames line up correctly with each other.
3. RGB Color Images: allowing input of three images (1 Red, 1 Blue and 1 Green), registering the images into one picture and based on this information produce a color image.
4. Maximum Entropy [9]: using a probability distribution function that has the maximum entropy allowed by the present information in the image, to recover the information that is missing from the image.

CONCLUSION

Multitudes of image processing techniques have been discovered and more are on the way with the creation of new imaging techniques. Not all techniques work for all images. For instance, a low pass filter will remove the low noise from an image, but if the image clarity is sufficient before the filter is applied, the filter will blur the image instead of enhancing the image. So, careful consideration has to be used to determine which techniques should be used for a particular application.

I would like to conclude by stating that my research participation in this experiment has been more of a learning experience, than that of producing a product. I have learned

several image processing techniques over the period of this experiment. However, I compounded the task of learning a new language (Borland C++), experimenting with the special functions of the language, picking up some of its finer aspects, learning image processing techniques and implementing those techniques in a new language. The task proved to be too much to do in the time period I had allotted myself. Although, a foundation of doing further research in this area has been made, of which I plan to continue and extend.

With the continuing integration of computers into the mainstream of our everyday lives, new techniques in image processing are becoming more and more valuable. Research in this area should be continued.

ACKNOWLEDGEMENTS

REFERENCES

1.   *Model ST-6 Professional CCD Imaging Camera*, operations manual, Santa Barbara Instrument Group, No Date Provided.

2.   *Borland C++*, computer software, Borland International, Inc., 1992.

3.   Alfred Poor, "Lab Notes: Looking at the TIFF Specification From the Inside" *PC Magazine* 17 December 1991: 371-376..

4.   J. S. Lim, ed. M. P. Ekstrom, "Image Enhancement", *Digital Image Processing Techniques* (Academic Press, Ontario, Fl., 1984), pp. 5 - 11.

5.   J. S. Lim, ed. M. P. Ekstrom, "Image Enhancement", *Digital Image Processing Techniques* (Academic Press, Ontario, Fl., 1984), pp. 25 - 31.

6.   R. A. Schowengerdt, *Techniques for Image Processing and Classification in Remote Sensing*, (Academic Press, Ontario, Fl., 1983), pp. 68-71.

7.   J. G. Moik, Digital Processing of Remotely Sensed Images, (N.A.S.A., Washington, DC, 1980), pp. 141-158.

8.   J. G. Moik, Digital Processing of Remotely Sensed Images, (N.A.S.A., Washington, DC, 1980), pp. 187-198.

9.   R. M. Haralick, et al., ed. H. Stark, "The Principle of Maximum Entropy in Image Recovery", *Image Recovery: Theory and Application*, (Academic Press, Ontario, Fl., 1987), pp. 157-193.

Tag (decimal)	Hexidecimal	Tag Name
254	FE	NewSubfileType
255	FF	SubfileType
256	100	ImageWidth
257	101	ImageLength
258	102	BitsPerSample
259	103	Compression
262	106	PhotometricInterpretation
263	107	Tresholding
264	108	CellWidth
265	109	CellLength
266	10A	FillOrder
269	10D	DocumentName
270	10E	ImageDescription
271	10F	Make
272	110	Model
273	111	StripOffsets
274	112	Orientation
277	115	SamplesPerPixel
278	116	RowsPerStrip
279	117	StripByteCounts
280	118	MinSampleValue
281	119	MaxSampleValue
282	11A	XResolution
283	11B	YResolution
284	11C	PlanarConfiguration
285	11D	PageName
286	11E	XPosition
287	11F	YPosition
288	121	FreeOffsets

Table 1. Tagged Image File Format (possible tags for IFD entries)

314

Tag (decimal)	Hexidecimal	Tag Name
289	121	FreeByteCounts
290	122	GrayResponseUnit
291	123	GrayResponseCurve
292	124	Group3Options
293	125	Group4Options
296	128	ResolutionUnit
297	129	PageNumber
301	12D	ColorResponseCurves
305	131	Software
306	132	DateTime
315	13B	Artist
316	13C	HostComputer
317	13D	Predictor
318	13E	WhitePoint
319	13F	PrimaryChromaticities
320	140	ColorMap

Table 1. Tagged Image File Format (possible tags for IFD entries)
(continued)

```
ST-6 Compressed Image or ST-6 Image
File_version = 2
Data_version = 1
Exposure = xxx
Focal_length = xx.xxx
Aperture = xx.xxx
Response_factor = xx.xxx
Note = xxxxxxxx
Background = xxx
Range = xxx
Height = xxx
Width = xxx
Date = xx/xx/xx
Time = xx:xx:xx
Exposure_state = xx
Temperature = xx.xx
Number_of_exposures = xx
Each_exposure = xx
History = xxxxxx
Observer = xxxxxxxx
End
```

Figure 1.   Header format of a ST-6 image file.

316

SKIN EFFECTS DUE TO PERFORATIONS- A STUDY OF ANALYSIS TECHNIQUES

Jon Michael Gibbs
Petroleum Engineering

ABSTRACT

Until 1991, two methods could be used to evaluate the skin effect due to perforations, the Brons and Marting Method and the Harris Method. Due to the simplicity of the technique, the Brons and Marting Method has been the preferred method of use in the petroleum industry. However, with the recent development of a third technique to evaluate the skin effect due to perforations, the need has arisen to evaluate each of these techniques to determine which method is the most accurate under given conditions. This paper reviews and compares each of the three methods for evaluating the perforations skin. Recommendations concerning the use of these methods have also been made by the author.

INTRODUCTION

In petroleum engineering, engineers are not able to see the environment which they study, the reservoir. Subsequently, they must be able to obtain sufficient information about the reservoir to analyze its performance and to predict its future production under various modes of operation [1]. Much of this information can be determined from a pressure transient test.

Transient pressure testing techniques, or well testing, include pressure buildup, drawdown, injectivity, falloff, and interference. These techniques all consist of generating and measuring pressure verses time at reservoir depth. The most useful information obtained from a transient pressure test includes the permeability, average reservoir pressure, and the relative amount of skin damage or skin improvement [2].

DEFINING THE SKIN EFFECT

At or near the wellbore, the ability of the reservoir fluids to flow into and through the wellbore may be altered due to a change in the near wellbore permeability or by any flow restrictions below the pressure measuring device. This phenomena is called the skin effect. The change in permeability near the wellbore may be reduced due to mud caking, cement problems, clay dispersion, partial completion, paraffin buildup, or plugged perforations. It also may be increased resulting by acidizing or fracturing a well. Flow restrictions which may contribute to the skin effect include downhole chokes or downhole pumps, to name a couple. The sign convention for the skin factor is as follows: a positive indicates wellbore damage and a negative skin indicates wellbore improvement. Since the change in permeability is close to the wellbore, its effect may be accounted for as an additional pressure drop caused by the presence of the 'skin'. A schematic of the skin effect is shown in Figure 1: Skin Effect. Following along the pressure profile curve, note the additional pressure drop encountered within the skin, or zone of damage. To overcome the additional pressure loss, the wellbore pressure must be drawn down an additional amount equal to the Δp_{skin} in order to receive the same amount of fluids from the reservoir as if the skin were not present.

The skin factor is determined from a transient pressure analysis. The transient pressure analysis will yield the total skin factor. As equation (1) shows, the total skin factor is a combination of several individual skins. Some of these individual skins are the skin due to perforations, skin due to partial penetration, skin due to slant hole, skin due to turbulence, skin due to fractures, and the skin due to equipment.

317

$$S_{total} = S_{actual} + S_{perfs} + S_{pen} + S_{slant} + S_{turb} + S_{frac} + S_{equip} \quad\text{......................................(1)}$$

The individual skin effects must be determined to evaluate the actual skin factor (as shown in equation (1)) from the total skin factor, as wellbore remedial treatments should be designed based on the actual skin factor.

Little research has been conducted concerning the skin due to perforations, S_{perfs}. This effect is created when a well is completed with casing and perforated. The perforations are small holes in the casing which limit the flow into the wellbore (as compared to an open hole completion). Until recently, only two techniques existed to evaluate the skin due to perforations.

Figure 1: Skin Effect
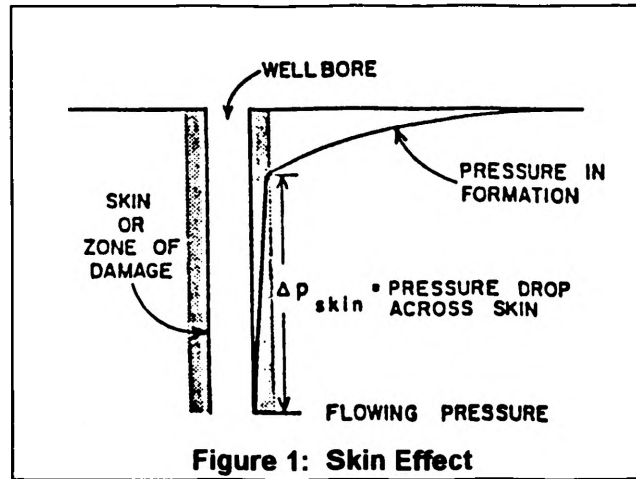
EVALUATION TECHNIQUES

Currently, there are three techniques to evaluate the skin due to perforations, Brons and Marting Method, Harris Method, and Karakas and Tariq Method. The following section addresses each of the three method for evaluating the skin due to perforations. A detailed evaluation of the Karakas and Tariq method is included since little research has been conducted on this technique.

Brons and Marting Method:
The first technique to determine the skin due to perforations was developed by F. Brons and V.E. Marting in 1960 [3]. However, their technique was not originally developed to evaluate the skin due to perforations, but rather is an extension of the skin due to partial completion and partial penetration. Figure 2: Brons and Marting Technique, represents the development of their skin due to perforations.

Figure 2A shows the situation where a well only partially penetrates the formation. Skin effects would be present in this situation since the reservoir fluids in the lower portion of the reservoir will not flow as readily into the wellbore as the reservoir fluids horizontal to the perforated penetrated portions of the reservoir. Figure 2B shows a well producing from only the central portion of a productive reservoir. A skin effect will also be present in this situation since reservoir fluids from the upper and lower portions of the producing interval must flow vertically to enter the wellbore as opposed to the horizontal flow in the portions adjacent to the completed interval. Figure 2C is Brons and Marting's 'model' for the skin due to perforations. It is a combination of the situations presented in 2A and 2B. In Figure 2C, the entire reservoir has been penetrated and completed. However, a skin effect due to perforations will still be present since all portions of the reservoir do not have equal access to the wellbore (i.e. the flow is not entirely horizontal in all areas). Also note that their model assumes an open disk, or 360° of perforations as opposed to individual shots for perforations.

318

Figure 2: Brons and Marting Technique

(A)   (B)   (C)
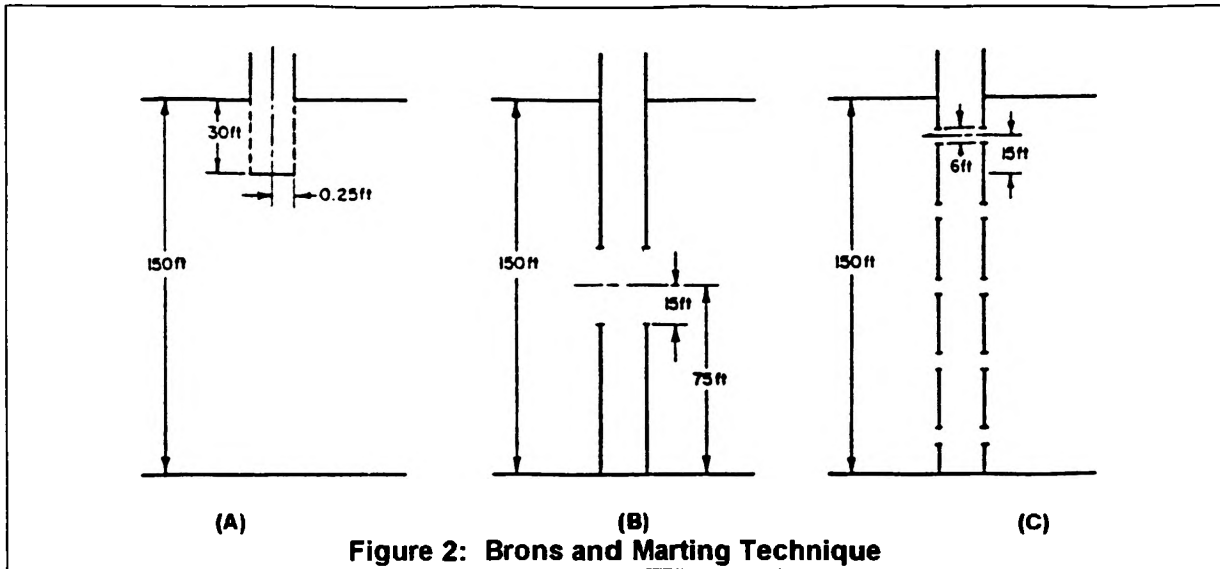
Figure 3: Brons and Marting Skin Factor for Perforations, is the graph which is used in their technique to evaluate the skin due to perforations (it can also be used to evaluate partial penetration and partial completion skins).

Figure 3: Brons and Marting Skin Factor for Perforations
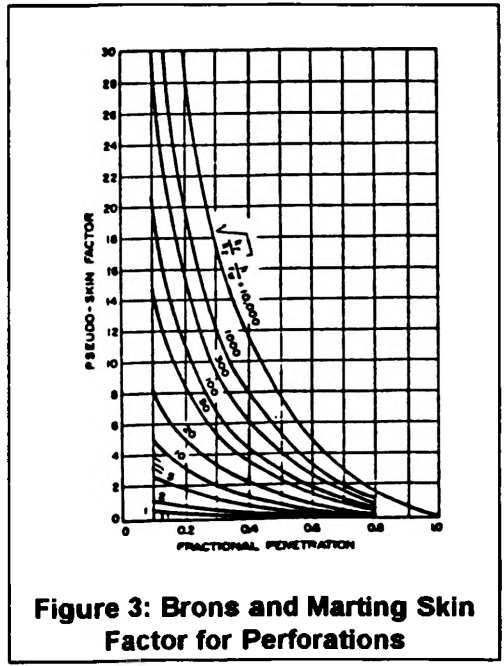
The plot indicates a pseudoskin factor as a function of the fractional penetration, which for all possible cases is defined as the ratio of the open interval(s) to the total interval.

$$f_p = \frac{h'}{h} \quad \text{...(2)}$$

where:
f_p = fractional penetration
h' = interval open to flow (ft)
h = total net pay (ft)

The plot is also a function of the term

319

$$\sqrt{k_r/k_z}(\frac{h}{r_w}) \quad \dots\dots\dots\dots\dots\dots\dots\dots\dots\dots\dots(3)$$

where:

k_r = radial permeability (md)
k_z = vertical permeability (md)
r_w = wellbore radius (ft)
h = for perforated intervals use one-half of the distance between
    perforations (ft)

Therefore, to evaluate the skin due to perforations by Brons and Marting's technique, calculate the fractional penetration (equation 2) and the term in equation (3), enter the plot shown in Figure 3 and read the pseudoskin, which in this case is the skin due to perforations.

The Harris Method:

The second technique to determine the skin due to perforations was introduced in 1966 by M.H. Harris [4]. Unlike the Brons and Marting technique, Harris' technique was specifically designed to evaluate the skin due to perforations. Figure 4: Harris Model is an illustration of the model for the Harris technique. Harris' model assumes an asymmetrical perforation design, or multiple perforation shots within a given plane. Once again, this type of perforating does not depict current perforation techniques.

Harris defines three dimensionless variables and 'm', the number of perforations per plane, which are used to evaluate his skin due to perforations.
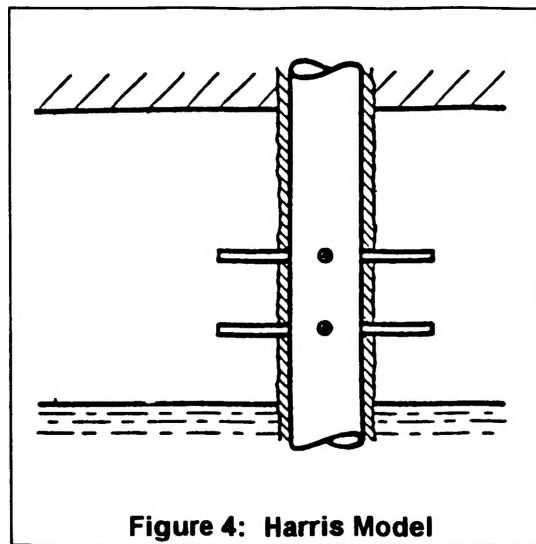
Figure 4: Harris Model

$$d_D = \frac{d}{r_w}\sqrt{k_r/k_z} \quad \dots\dots\dots\dots\dots\dots\dots\dots\dots\dots(4)$$

$$a_D = \frac{a}{r_w} \quad \dots\dots\dots\dots\dots\dots\dots\dots\dots\dots\dots\dots(5)$$

$$h_D = \frac{h}{r_w}\sqrt{k_z/k_r} \quad \dots\dots\dots\dots\dots\dots\dots\dots\dots(6)$$

320

$$m = \frac{360}{\theta_z} \quad \text{...(7)}$$

where

d = perforation diameter (inches) r_w = wellbore radius (inches)

k_r = radial permeability (md) k_z = vertical permeability (md)

h = vertical perforation spacing (inches)   m = no. of perforations per plane

θ_z = angular dimension (phasing, degrees)

a = perforation on notch penetration beyond cement sheath (inches)

To determine the skin effect, several plots, similar to that shown in Figure 5: Example Harris s_{perf} Plot, have been generated which apply to various values of 'm' and the three dimensionless variables. For example, the graph in Figure 5 would apply to a well with an h_D between 4 and 100 (the actual h_D is interpolated), four shots per plane (m), an a_D between zero and 9, and a d_D of 0.1666. To determine the skin due to perforations the dimensionless skin from the coordinate axis must be adjusted by the term in parenthesis. Thus, if a dimensionless skin effect of 10 was read from the plot, the skin due to perforations would be 10 - 4, or 6.

Figure 5: Example Harris S_{perfs} Plot
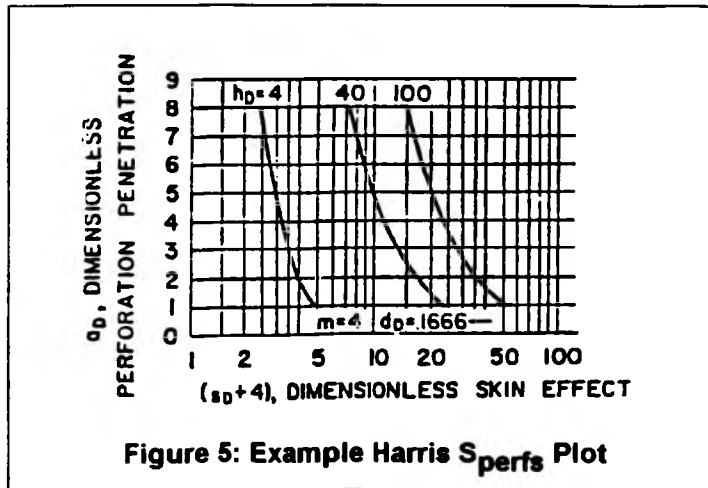
Karakas and Tariq Method:

In 1991, Metin Karakas and S.M. Tariq developed a technique through the use of a finite element method to evaluate the skin due to perforations [5]. A diagram of the model for their technique is presented in Figure 6: Karakas & Tariq Model. Several downhole parameters, phase angle, perforation diameter, perforation spacing, perforation diameter, crushed zone diameter, damaged zone diameter, and open hole diameter comprise their model.

In Karakas and Tariq's technique, the skin due to perforations is the sum of several 'mini-skins', consisting of wellbore, vertical, and horizontal skin values. In equation form:

$$s_{perfs} = s_{wellbore} + s_v + s_h \quad \text{..........................(8)}$$

The parameters shown in Figure 6 contribute to the above mini-skins. Three dimensionless terms have been introduced to evaluate each mini-skin: dimensionless perforation spacing,

$$h_D = (h / L_p)\sqrt{k_h / k_v} \quad \text{.................................(9)}$$

dimensionless perforation radius,

$$r_{pD} = (r_p / 2_h)(1 + \sqrt{k_v / k_h}) \quad \text{.....................(10)}$$

321

and dimensionless well radius,

$$r_{wD} = r_w/(L_p + r_w) \dots\dots\dots\dots\dots (11)$$

where.

h = spacing between perforations (inches)
L_p = length of perforations (in.)
k_h = horizontal permeability (md)
k_v = vertical permeability (md)
r_p = perforation radius (inches)
r_w = wellbore radius (inches)
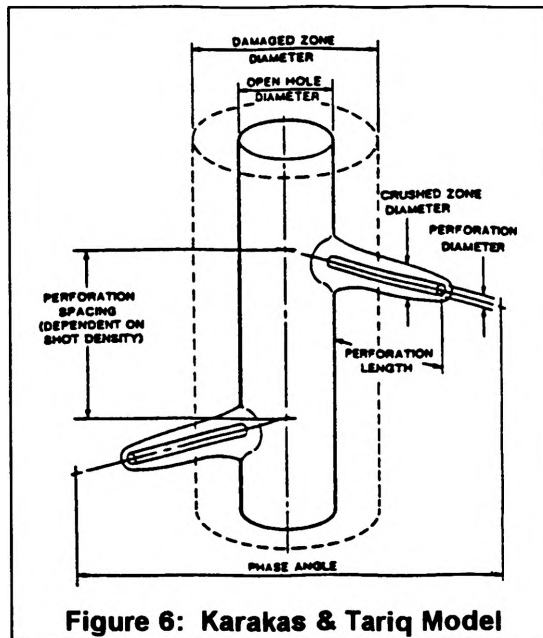
Figure 6: Karakas & Tariq Model

The mini-skins are defined individually as the wellbore mini-skin, s_{wb}:

$$s_{wb} = c_1(\theta)\exp[c_2(\theta)r_{wD}] \dots\dots\dots (12)$$

for $0.30 \leq r_{wD} \leq 0.90$, where c1 and c2 are given in Table I: Variable c1 & c2 in Eq. (12).

Table I: Variable c_1 & c_2 in Eqn. 12

Phasing (degrees)	c_1	c_2
0(360)	1.6X10-1	2.675
180	2.6X10-2	4.532
120	6.6X10-3	5.320
90	1.9X10-3	6.155
60	3.0X10-4	7.509
45	4.6X10-5	8.791

The last term in equation (8) is the horizontal mini-skin, s_h:

$$s_h = \ln(r_w/r_{we}) \dots\dots\dots\dots\dots (13)$$

322

where r_{we} is the effective well radius and is given by:

$$r_{we}(\theta) = \begin{cases} 1/4 Lp & \text{if } \theta = 0 \\ \alpha_\theta(r_w + L_p) & \text{otherwise} \end{cases} \quad \dots\dots(14)$$

and the variable alpha can be determined form Table II: α_θ Determination. The vertical mini-skin, s_v is

$$s_v = 10^a h_D^{b-1} r_{pD}^{b} \dots\dots(15)$$

where

$$a = a_1 \log_{10}(r_{pD}) + a_2 \dots\dots(16)$$

and $b = b_1 r_{pD} + b_2$ ....(17)

Table II: α_θ Determination	
Phasing (degrees)	$r_{we}/(r_w + L_p)$
0(360)	0.250
180	0.500
120	0.648
90	0.726
60	0.813
45	0.860

The coefficients in equations (16) and (17) are listed in Table III: Vertical Skin Correlation Coefficients.

Karakas and Tariq also provide an equation for a crushed zone mini-skin. However, since the permeability in the crushed zone must be known, and since it is difficult to obtain this data without extensive laboratory testing, the crushed zone mini-skin has not been included in this paper.

The equations which Karakas and Tariq have developed were verified by comparing their outcomes with those obtained through actual, finite-element simulations. (For further discussion concerning these results, see reference 5).

Table III: Vertical Skin Correlation Coefficients				
Phasing (degrees)	a_1	a_2	b_1	b_2
0(360)	-2.091	.0453	5.1313	1.8672
180	-2.025	.0943	3.0373	1.8115
120	-2.018	.0634	1.6136	1.7770
90	-1.905	.1038	1.5674	1.6935
60	-1.898	.1023	1.3654	1.6490
45	-1.788	.2398	1.1915	1.6392

NOTE: Values good for $h_D \leq 10$ and $r_{pD} \geq 0.01$

ANALYZING THE KARAKAS AND TARIQ METHOD

To evaluate Karakas and Tariq's technique for determining the skin due to perforations, a FORTRAN computer program was developed. The program is a direct application of equations (8) through (17).

323

Several values for each of the five parameters in the model where chosen to evaluate the skin due to perforations by the Karakas and Tariq Technique. Table IV: FORTRAN Program Variables contains the values of each parameter evaluated in the program. The skin due to perforations was determined for every combination of the variables shown in Table IV, resulting in 540 runs with the program.

Table IV: FORTRAN Program Variables

r_w: 2", 3", 4"
L_p: 1", 3", 6", 9"
Phasing: 0°, 45°, 90°, 120°, 180°
k_v/k_h: 0.01, .1, 1.0
h: 12", 4", 2" (1 spf, 3 spf, 6 spf)

Since constants for several phasing values were calculated (see Tables I, II, III) by Karakas and Tariq, the effect of phasing on the skin due to perforations was studied.

The two cases shown in Table V: Phasing and Wellbore Effects on Perforation Skin, show the relationship between the perforation skin and phasing. First consider the 2" wellbore radius in Case I. Throughout the range of phasing, the skin due to perforations only changes from a minimum of 1.61 at 90°, to a maximum of 1.86 at 45°. The difference in the skin due to perforations over the phasing range is 0.25, a very small change. Similar trends are shown for the 3" and 4" wellbore radius in Case I. Examining Case II, the same trends are present. For example, the skin due to perforations only changes from 5.47 to 6.37 for the 2" wellbore: a change in skin of only 0.9. For Case II, as in Case I, the skin due to perforations varies very little over practical phasing values.

Table V not only shows the relationship between phasing and the perforations skin, but also the effect of wellbore radius on perforations skin. Consider Case I with a phasing of 45°. The perforation skin changes from 1.86 at an r_w = 2" to 2.22 at an r_w = 4", a difference of less then 0.50. The trend is also present for each phasing angle in both Case I and Case II.

Table V: Phasing and Wellbore Radius Effects on Perforation Skin

Case I:

k_v/k_h = 1.0
Perf. Length (L_p) = 3 inches
3 shots per foot (h=4")

Phasing

	45°	90°	120°	180°
rw = 2"	1.86	1.61	1.77	1.71
rw = 3"	2.08	1.85	2.03	2.02
rw = 4"	2.22	2.01	2.21	2.25

Case II:

k_v/k_h = 0.01
Perf. Length (L_p) = 3"
3 Shots per foot (h = 4")

Phasing

	45°	90°	120°	180°
r_w = 2"	5.67	5.47	6.37	6.28
r_w = 3"	5.89	5.71	6.63	6.59
r_w = 4"	6.03	5.87	6.81	6.82

There are several relationships which can now be developed for the skin due to perforations. First, as the k_v/k_h ratio decreases, the reservoir becomes more stratified, and the skin due to perforations increases (Case I average S_{perfs} of 2.0, Case II average S_{perfs} of 5.4). As the reservoir becomes more stratified, vertical flow in the reservoir

is reduced which results in more damage in the near wellbore area, or a higher perforation skin. Secondly, for practical wellbore radii (2" to 4"), the perforation skin for a given phasing will change very little. Finally, the skin due to perforations will not significantly change over practical values of phasing, as shown in Table V. The phasing effect is important because we may not know the phasing of the well, and, as these results suggest, a best estimate for the phasing can be made which will still result in a reasonable estimation of the skin due to perforations.

REVIEW OF TECHNIQUES

Before a comparison is conducted between the three techniques for evaluating the skin due to perforations, a brief review of each technique will be discussed to highlight the important information from each method. The first technique was developed in 1960 by Brons and Marting. Their technique was not originally designed to determine the skin due to perforations, but rather is an extension of partial penetration and partial completion of a well. Brons and Marting's model also assumes an open plane, or disk, for perforations (see Figure 2).

The second technique was presented in 1966 by Harris. Although his technique was developed specifically to determine the skin due to perforations, the technique had limited computer and mathematical technology at the time of its development. Harris' model used multiple shots in a plane for perforations (see Figure 4), a technique which is no longer employed in well completions.

The final technique to evaluate the skin due to perforations was developed in 1991 by Karakas and Tariq. Their technique is the most recent since 1966 and it considers several downhole parameters. It is based on current computer and mathematical technology and it reflects current perforations methods, individual shots spiraling down the casing (see Figure 6).

COMPARISON OF TECHNIQUES

The three techniques to determine the skin due to perforations have been compared to determine the relevancy and similarities between the methods. The techniques have been compared in Table VI Comparison of Techniques. Several important conclusions can be drawn from Table VI. First, the skin due to perforations by Brons and Marting are significantly lower, indicating less damage, than those by Harris and Karakas and Tariq. Brons and Marting assume an open disk for perforations thereby allowing more fluid into the wellbore, or less flow restriction. This assumption will result in a lower skin due to perforations. The perforation skin values by Harris's technique are somewhat in-between those of Brons and Marting and Karakas and Tariq. This

Table VI: Comparison of Techniques

Wellbore Conditions:
$k_v/k_h = 1.0$
3 spf (h = 4")
Perf. Length $(L_p) = 3"$

r_w	Brons & Marting s_{perfs}	Harris s_{perfs}	Karakas & Tariq s_{perfs}
2"	0.1	0.7	1.77
3"	0.1	2.0	2.03
4"	0.1	2.0	2.21

somewhat in-between those of Brons and Marting and Karakas and Tariq. This trend occurs because Harris' model assumes multiple perforation shots within a plane. The multiple shots will allow more fluid into the wellbore than Karakas and Tariq's method, but less than Brons and Marting's method thus resulting in skin due to perforations values between Brons and Marting's and Karakas and Tariq's. Table VI also shows that the skin due to perforations by Brons and Marting is constant for the given wellbore conditions. Under these conditions, the skin due to perforations must be determined from the lower left hand side of Figure 3. In this area, the curves are close

together and therefore it is difficult to differentiate between the curves. Another trend present in Table VI is that the wellbore radius greatly affects the skin due to perforations by Harris' technique, as the perforation skin more than doubles when changing from a 2" to 3" wellbore radius. Finally, the values for perforation skin by Karakas and Tariq's method are most representative of the actual skin due to perforations because their model reflects current perforation techniques.

CONCLUSIONS

This paper presents and discusses the three techniques presently available to evaluate the skin due to perforations. The first technique by Brons and Marting will yield optimistic values for the perforation skin due to their perforations model. The model assumes an open disk for perforations which consequently allows significantly more fluid into the wellbore than by conventional perforating methods. The second technique evaluated is by Harris. Values for his skin due to perforations will be less optimistic than Brons and Marting, but his definition of phasing is not practical today. Harris' model assumes multiple perforation shots within a plane which, as noted previously, does not reflect current perforating techniques. The method developed by Karakas and Tariq will yield the most representative values for the skin due to perforations for several reasons: the model considers several downhole criteria (see Figure 4), uses modern mathematical and computer technology, and the model reflects current perforation methods. It should also be noted that although Karakas and Tariq's method considers the perforation diameter, the perforation diameter within the range of 0.5" to 0.75" has little or no effect on the skin due to perforations. This observation is noted by Karakas and Tariq and, therefore, the perforation diameter in their model has been fixed at 0.5" for all calculations presented in this paper.

The significance of wellbore radius and phasing is small with respect to the skin due to perforations for practical wellbores ($r_w = 2"-4"$, $L_p > 3"$). The effect of the phasing is extremely important since the phasing of a well may not be known. These results suggest that a 'best guess' estimation of the phasing will result in reasonable estimations of the skin due to perforations.

RECOMMENDATIONS

Based on the research of this paper, the author would like to make the following recommendations. The method by Karakas and Tariq should be used to determine the skin due to perforations for the following reasons:

- the method considers many downhole criteria
- the method uses modern mathematical and computer technology
- the method is the most accurate representation of current perforating practices

During the 540 runs made with the FORTRAN program, the technique by Karakas and Tariq failed under the following conditions:

(1) low perforation length
(2) low wellbore radius
(3) low k_v/k_h (highly stratified reservoir)

The technique fails because one or more of the dimensionless parameters (equations (9), (10) or (11)) do not fall within the range specified by Karakas and Tariq (see Table III and equation (12)). The specific reason for the dimensionless term ranges, whether limits of the model or the limit of their calculations, is not given in their paper.

However, when Karakas and Tariq's technique does fail, Brons and Marting's technique should be used to evaluate the skin due to perforations. As a reservoir becomes more stratified, vertical flow is reduced and the downhole conditions approach the model presented by Brons and Marting, several individual reservoirs each producing through one set of perforations. It is not suggested that Harris' method be used due to the difficulty of converting conventional perforation definitions to those presented by his technique. The conversion must be performed to determine the dimensionless terms (see equations (4), (5), and (6)).

Results from the FORTRAN program also indicate that for a homogeneous reservoirs, $k_v/k_h = 1$, and reasonable perforation parameters, $L_p > 3"$, $r_w = 2"$ to $4"$, the skin due to perforations will be less than or equal to 2. The significance of this observation is that if a situation arises where a quick estimation of the actual skin factor must be made, a value of 2 can be used for the perforation skin. The estimation of the actual skin will therefore be a worst case scenario value.

Eliminating the skin due to perforations would obviously result in increased production, flow into the wellbore is increased. However, the only way to significantly decrease the skin due to perforations is to increase the perforation length. Perforation length is analogous to fracture length: the longer the fracture, the more fluid that will flow into the wellbore.

Although Karakas and Tariq's technique appears to be the best method to determine the skin due to perforations, it would be nice to prove their technique with a physical laboratory method or an actual well. However, while reviewing the literature for this paper, no references could be found either attempting to prove or disprove the techniques by Brons and Marting and Harris, and these techniques have been in existence for over thirty years.

ACKNOWLEDGMENTS

REFERENCES

1. Earlougher, Jr.. "Advances in Well Test Analysis", Monograph Vol. 5 of the Henry L. Doherty Series, pages 1-19, 1977.
2. Koederitz, L.F.. "Notes on Well Test Analysis," pages 25-45, 1991.
3. Brons, F. and V.E. Marting: "The Effect of Restricted Fluid Entry on Well Productivity," Trans., AIME 222, pages 172-174, 1961.
4. Harris, M.H.: "The Effect of Perforating on Well Productivity," Trans., AIME 237, pages 518-528, 1966.
5. Karakas, Metin and S.M. Tariq: "Semianalytical Productivity Models for Perforated Completions," Trans., AIME, 291, Section II pages 73-82, 1991.

327

IMPROVED TECHNIQUES FOR MANUFACTURING LAYERED LAMINATE COMPOSITE MATERIALS

Michael D. Grabber

Department of Mechanical and Aerospace Engineering and Engineering Mechanics

ABSTRACT

An increasingly important class of engineering materials are known as fiber reinforced composite materials. They offer outstanding mechanical properties, unique flexibility in design, and ease of fabrication. Because of this, fiber reinforced composites are being found more and more in such diverse applications as aircraft, space vehicles, automobiles, sporting goods, and appliances.

The main objective of this research project was to develop a procedure for which high quality composite plates could be manufactured. The procedure needed to be able to accommodate materials of various thicknesses as well as various sizes. We also wanted the procedure to be versatile enough to allow us to be able to manufacture Smart Materials. Smart Materials are a class of composites which are able to continuously monitor and even manipulate their structural characteristics. Methods for constructing these materials involves embedding sensors and actuators within the composite itself.

INTRODUCTION

In order to reach the above described objectives, we first had to learn how to use the Dake 75 ton hydraulic laboratory press. The Dake model #44-806 hydraulic press, shown in Figure 1, consists of an upper and lower platen which measures 19 inches square. The platens are heated via electrical resistance heating elements and are cooled by passing water through the water channel system which is embedded within the platens. The temperature of the upper and lower platens are controlled with a 180 Series Single Relay Output Controller. The desired platen temperature of the upper and lower plates can be input into the controller as the set point. The temperature of the platens can then be easily read from the LED display. The required force on the sample can be calculated from the desired pressure and the cross-sectional area of the sample to be fabricated. This force is obtained by pushing on the pump handle located on the right hand side of the press. This force, displayed in tons, can be read off the gauge located in the upper right hand corner of the press.
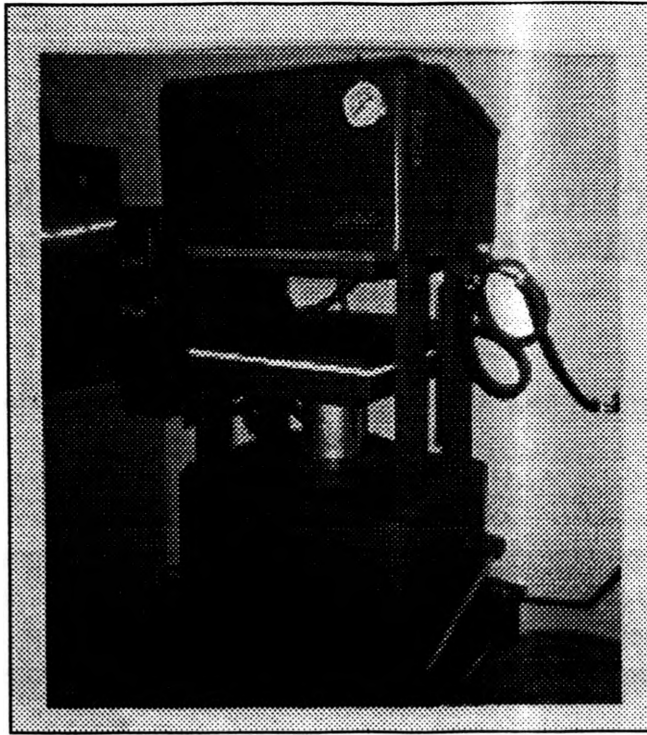
Figure 1

THE LAY-UP PROCEDURE

For this research project, the composite materials we used were preimpreginated fiber-reinforced plastics, otherwise known as prepregs. The prepregs we used, come in a roll that is 12 inches wide and is approximately 140 feet long. The material must be stored in the freezer, as it cures at room temperature.

The first step in the lay-up procedure consists of cleaning the work area and all the utensils with acetone to remove any contaminates that might be present. We are now ready to cut the prepreg to the desired dimensions. Prior to handling the prepreg however, we must put on rubber surgical gloves in order to protect the material from us, as the oils in our hands will contaminate the material and cause a delamination in the final product. As each piece is cut, it is placed back into the freezer in an effort to keep it as cold as possible. After all the pieces are cut, the are placed together in the proper orientation and the paper backings are removed. This layered laminate is now ready for the curing process.

Most of the samples we manufactured were symmetric cross-ply laminates. Symmetric means that they are symmetric with respect to the central axis of the material. Cross-ply indicates that each subsequent layer has a fiber orientation which is rotated 90 degrees from that of the previous layer. Figure 2 shows the fiber orientation for an 8 layer symmetric cross-ply laminate.
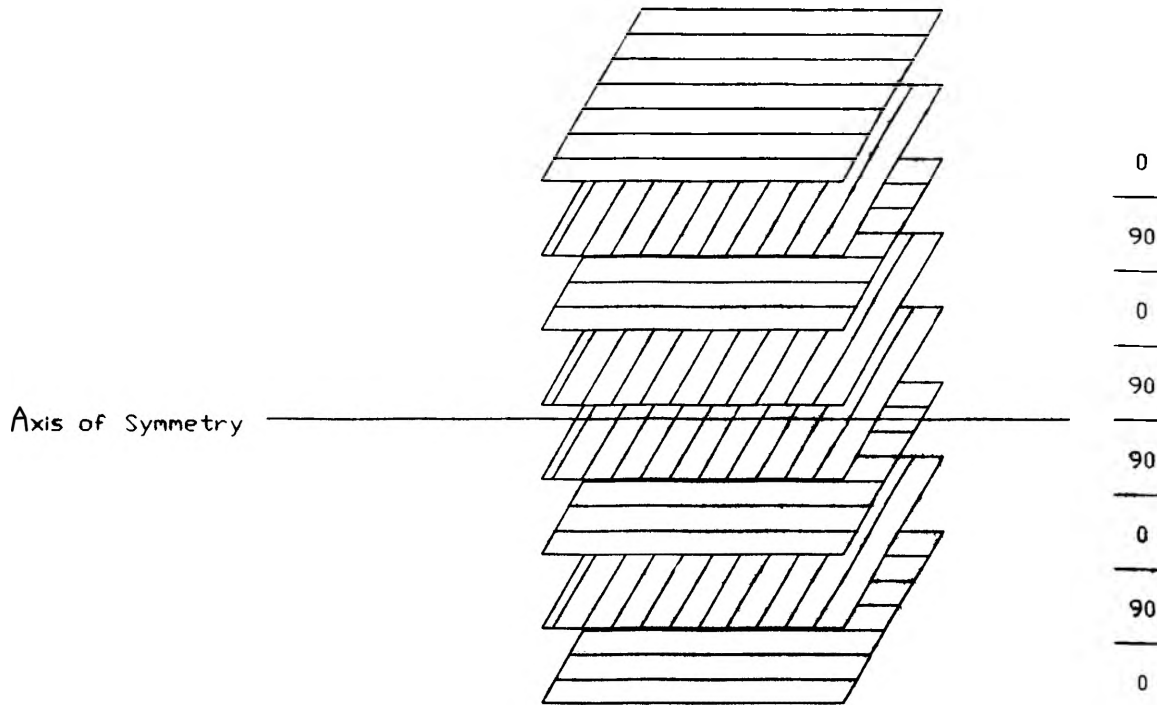
Figure 2

THE CONVENTIONAL METHOD

The conventional method of composite fabrication consists of placing the sample between two flat aluminum plates. The first step in this procedure is to sandblast the aluminum plates. This step is necessary to remove any contaminates such as old matrix which might have been left from previous samples. Next the plates were cleaned with acetone to remove any residual impurities. the surfaces of the two plates were then sprayed with Chemlease 40. Chemlease 40 is a chemical releasing agent which is used to prevent the composite from sticking to the aluminum plates. We applied three coats of Chemlease 40 to the plates, allowing 15 minutes drying time between coats.

Next, two 15 inch square sheets of release fabric were cut. The release fabric is to be placed between the composite sample and the aluminum plates. It's purpose is to allow moisture and air to flow out of the composite during the heating and cooling processes, without letting the matrix flow out. One piece of this fabric is placed on one of the plates. The layered laminate is then placed in the center of the piece of material. Next, a high temperature sealant, frequently referred to as "tacky tape", is placed around the laminate. It is placed at a distance of approximately half the width of the tape away from the laminate in order to allow for expansion of the "tacky tape" during the compression process. The "tacky tape" is used to maintain the dimensions of the sample as well as to keep the matrix material from flowing out of the composite. The other piece of release fabric and the other aluminum plate are placed upon this assembly, respectively. The entire package is then placed into the Dake press to be cured.

331

THE CURING PROCESS

In this research project, we worked exclusively with two different types of materials. The first material was a Glass/Epoxy prepreg manufactured by the 3-M Corporation. The manufacturer supplied curing cycle is shown in Figure 3. The curing cycle requires that the sample be kept at a pressure of 100 Psi. The following equation is used to convert this pressure to the indicated force which is shown on the dial on the press.

$$\text{Force} = \frac{100 \text{ Psi} * (\text{Surface Area in IN}^2)}{2000 \text{ Pounds/Ton}}$$

This force is then applied to the sample. The curing cycle also shows that the sample must be heated from room temperature to 250° F while maintaining a temperature gradient of 2 to 10 degrees per minute. This is done by setting the set point on the 180 Series Single Relay Controllers approximately 40 degrees above room temperature. The temperature of the upper and lower plates are recorded every two minutes as well as the set point. The temperature gradient, on a per minute basis, between the recorded temperature and the previous temperature reading is calculated and recorded as well. This temperature gradient is the most important part of the data, as it tells us whether we are staying within the specified heating or cooling rate. Periodically, we turn the set point up on the relay controllers so that we will continue to increase the temperature of the sample within the specified range. When the set point reaches 235° F, we stop increasing the set point. This is done because of the hysterisis which is inherent in the relay controller. The temperature will overshoot the set point by about 15 or 20 degrees, reach a plateau, and then begin to fall back off. Just as it starts to fall back off, the set point can be turned up to 250° F and the controller will maintain the plates at that temperature. When the sample first reaches a temperature of 250° F, we switch to taking temperature readings every 15 minutes as opposed to every two minutes. This region is what we refer to as the plateau. Here, we maintain the sample at a temperature of 250° F and at a pressure of 100 Psi for a period of 60 minutes. At the end of this plateau, we begin the cooling process. Here, we go back to recording temperatures every two minutes. The set point on the control relays are set to a point below room temperature. Short burst of cooling water are then let into the cooling channels of the press, watching to make sure we stay within the cooling gradient of 2 to 10 degrees per minute. We continue cooling the sample until it reaches a temperature that is below 150° F. At this point, the pressure is released and the sample can be removed from the press. The now complete sample is marked to indicate the sample number and the date which it was manufactured. A copy of the data collected from one of the Glass/Epoxy samples is shown in Figure 4.

Cure Cycle for Glass/Epoxy

Figure 3

13" X 13" Plate

Glass/Ep   8 Ply symmetric   22 October 93

Area = 15.25 x 15.25   Tacky tape distance from composite = 5/8"
Pressure = 100 Psi   Tacky tape distance from second tape layer = 1/4"

Force = 11.6 Ton

Time	Top	Bottom	Delta T	Set Point
04:20	81	84	—	110
04:22	88	90	3	110
04:24	94	97	3.5	110
04:26	100	103	3	130
04:28	109	113	5	130
04:30	118	121	4.5	140
04:32	127	130	5	150
04:34	137	140	5	150
04:36	147	149	5	160
04:38	155	158	4	170
04:40	167	169	5.5	180
04:42	176	178	4.5	180
04:44	188	190	6	200
04:46	202	204	7	200
04:48	212	212	5	210
04:50	218	218	3	220
04:52	224	225	3.5	230

Time	Top	Bottom	Delta T	Set Point
04:54	232	234	4.5	240
04:56	240	242	4	240
04:58	247	248	3	240
05:00	254	254	3	240
05:15	250	250	—-	250
05:30	254	254	—-	250
05:45	254	254	—	250
06:00	250	250	—	250
06:02	238	234	7	70
06:04	223	220	7	70
06:06	213	212	4	70
06:08	209	201	5.5	70
06:10	203	183	7	70
06:12	196	180	1.5	70
06:14	173	160	10	70
06:16	151	147	6.5	70

Figure 4

333

The other material used was a Graphite/Epoxy prepreg manufactured by Hercules. The manufacturer supplied curing cycle is shown in Figure 5. The process is very similar to that of the Glass/Epoxy material. The sample is heated from room temperature to 240° F at a temperature gradient of 3 to 5 degrees per minute and a pressure of 90 Psi. The first plateau lasts for 60 minutes. At the end of this plateau, the pressure is increased to 100 Psi and the temperature is increased to 350° F at a temperature gradient of 1 to 5 degrees per minute. The sample is held at this second plateau for 120 minutes. At the end of this second plateau, the sample is cooled off at a rate of 3 to 5 degrees per minute until it reaches 200° F. The pressure is then released and the sample is removed and marked to indicate sample number and manufacture date. A copy of the data collected from one of the graphite samples is shown in Figure 6.

Cure Cycle for Graphite/Epoxy

Time
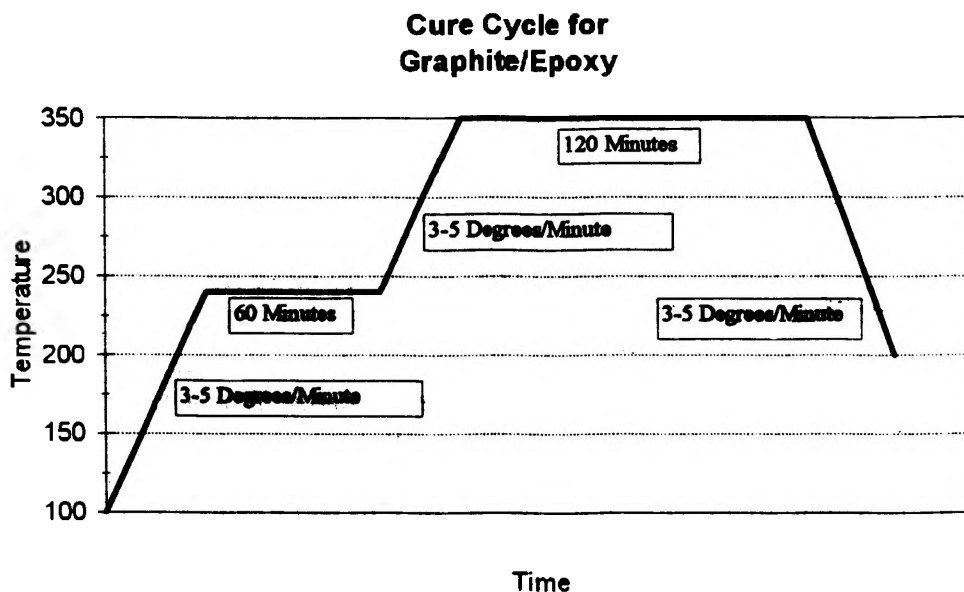
Figure 5

ANALYSIS OF THE CONVENTIONAL METHOD

We made several samples using the conventional method. The first problem that we encountered was keeping the epoxy from flowing past the tacky tape. We solved this problem by placing a second row of tacky tape around the sample. On the first couple of samples that we ran with a double row of tacky tape, the epoxy didn't flow past the tape, but the sample turned out warped, or buckled. We found that as the tacky tape was compressed, since there were two rows, the inner row could only expand towards the sample. This caused the inner row of tape to expand up against the sample and caused compression on the ends of the fibers. This compression induced stresses in the material which in turn caused the sample to buckle. This problem was solved by increasing the distance between the tape and the sample. Using this procedure, the 8 layer and thicker Glass/Epoxy samples turned out fine, as did the 16 layer samples of Graphite/Epoxy. The 8 layer Graphite/Epoxy samples, however, did not cure

12" X 12" Plate

Graphite/Epoxy   16 Ply symmetric   20 January 94

P1 = 90 Psi   Force 1 = 6.5 Ton

P2 = 100 Psi   Force 2 = 7.2 Ton

Time	Top	Bottom	Delta T	Set Point
04:56	76	77	----	100
04:58	77	78	0.5	100
05:00	82	84	3	100
05:02	86	89	2.5	100
05:04	90	93	2	100
05:06	95	97	2	110
05:08	101	102	2.5	110
05:10	106	106	2.5	120
05:12	111	112	3	120
05:14	117	118	3	130
05:16	----	----	----	130
05:18	129	130	3	130
05:20	134	135	2.5	140
05:22	140	142	3.5	150
05:24	146	148	3	150
05:26	153	154	3	160
05:28	160	162	3	160
05:30	165	167	2.5	170
05:32	----	----	----	170
05:34	177	178	3	180
05:36	183	185	4	190
05:38	190	191	3.5	190
05:40	200	200	5	200
05:42	209	209	4.5	200
05:44	212	212	1.5	210
05:46	214	216	2	220
05:48	219	220	2	220
05:50	225	226	3	225
05:52	227	228	1	225
05:54	231	232	2	230
05:56	235	235	1.5	230
05:58	238	238	1.5	230
06:00	240	240	1	230
06:15	240	240	----	240
06:30	241	241	----	240
06:45	241	241	----	240
07:00	241	241	----	240
07:02	243	243	1	260
07:04	249	250	3.5	260

Time	Top	Bottom	Delta T	Set Point
07:06	251	251	1	270
07:08	256	256	2	270
07:10	260	261	2.5	280
07:12	267	267	3	280
07:14	273	275	4	290
07:16	281	283	4	290
07:18	287	288	2.5	300
07:20	294	297	4.5	310
07:22	302	305	4	310
07:24	312	314	4.5	320
07:26	317	319	2.5	320
07:28	325	326	3.5	335
07:30	332	333	3.5	335
07:32	338	340	3.5	335
07:34	344	345	2.5	335
07:50	351	349	----	350
08:05	351	351	----	350
08:20	351	351	----	350
08:35	351	351	----	350
08:50	350	350	----	350
09:05	350	350	----	350
09:20	350	350	----	350
09:35	350	350	----	350
09:37	338	338	6	60
09:39	328	327	5	60
09:41	315	315	6	60
09:43	310	310	2.5	60
09:45	300	298	5	60
09:47	282	280	9	60
09:49	----	----	----	60
09:51	265	263	4.5	60
09:53	245	238	10	60
09:55	233	225	6	60
09:57	231	224	0.5	60
09:59	221	216	5	60
10:01	213	210	3.5	60
10:03	208	200	5	60
10:05	200	187	6.5	60
10:07	180	167	10	60

Figure 6

335

properly. The epoxy cured in the center of the sample, but not around the edges. This led us to believe that the tacky tape would not flatten out enough to allow samples which were 8 layers and thinner to be fabricated. This meant that we had to come up with another fabrication method. We tried using a mold which had been made for a 12" X 12" thermosetting plastic. This allowed the 8 layer sample to cure properly, however it was difficult to remove the finished sample from the mold. Another problem with this mold, is that it is difficult to clean-up and it will only fabricate a 12" X 12" plate. Since the Intelligent Systems Control (ISC) group needed us to make them a 13" X 13", 8 layer Graphite/Epoxy sample for acoustic testing, we needed to come up with another manufacturing technique.

THE NEW MOLD

In order to meet the new project requirements, we designed a new mold. The design sketches for this new mold are shown in Figures 7 thru 10 and the actual finished product is shown in Figures 11 thru 13. The majority of the mold is manufactured from 3/4" plate aluminum. The base of the mold will accommodate up to a 15" X 15" composite. When the mold was manufactured, we had inserts made for a 12" X 12" plate and for a 13" X 13" plate. If a different size composite needs to be manufactured, all that needs to be made is a new set of inserts for the mold. This allows the mold to be adjustable, which makes it highly versatile. Another advantage of this mold is that after it was manufactured, we polished the interior surfaces to a satin finish. We found that when the three coats of Chemlease 40 are applied to a satin finished surface, we obtain a surface which the epoxy will not stick to. This eliminates the need to sandblast the mold. Another advantage is that the inserts are removable. The removable inserts make the removal of the sample from the mold extremely easy. A final advantage is that since the cavity of the mold is exactly the size we need, and since the top of the mold fits so snugly, we do not need to use any tacky tape. This mold gives us an excellent sample that is exactly the specified dimensions.

THE MODIFIED FABRICATION METHOD

The modified fabrication method for composite fabrication consists of placing the layered laminate inside the above described mold. The lay-up procedure for this method is the same as for the conventional method. The first step in this procedure is to clean the mold and inserts with acetone to remove any contaminates which might be present. The surfaces of the mold and the inserts are sprayed with three coats of Chemlease 40, allowing 15 minutes drying time between each coat. Next we cut two sheets of release fabric. One piece is cut 15" X 20" and the other piece is cut the same size as the sample. The 15" X 20" piece is placed into the mold. the inserts are then placed into the bottom of the mold on top of the piece of release fabric. The release fabric will hang out of the mold on two sides. This is to make the insert easier to remove after the composite is cured. The layered laminate is now placed into the mold. Then the last piece of release fabric is placed on top of the layered laminate and then the top of the mold is put on. The entire assembly is then placed into the Dake press to be cured. The curing process is the same as for the conventional method.

336

Top View

1/2'
1'
1/2'
2'
1'-5'
1'
1'-3'
1'-3'
1'-5'

3/4'
1/2'

End View

3/4'
3/4'
3/4'

3/8'
5/16'
7/16'
3/4'

Material is 3/4' Aluminum Plate

Standard 5/16' X 1' Bolt

REV	DATE	DESCRIPTION		APP

MDGI
MICHAEL DWAYNE GRABBER INDUSTRIES

PROJECT TITLE
SMART STRUCTURES

DRAWING TITLE
COMPOSITE MOLD BOTTOM PLATE

CONTRACTOR NAME: PHILIP CHRISSOS

DWG. NO. 001	
PROJECT NO. 005	DESIGN BY: MDG
DATE: 18 NOV 93	DRAWN BY: MDG
CAD FILE NO. PHIL1	APPROVED BY: MDG	REV. 0
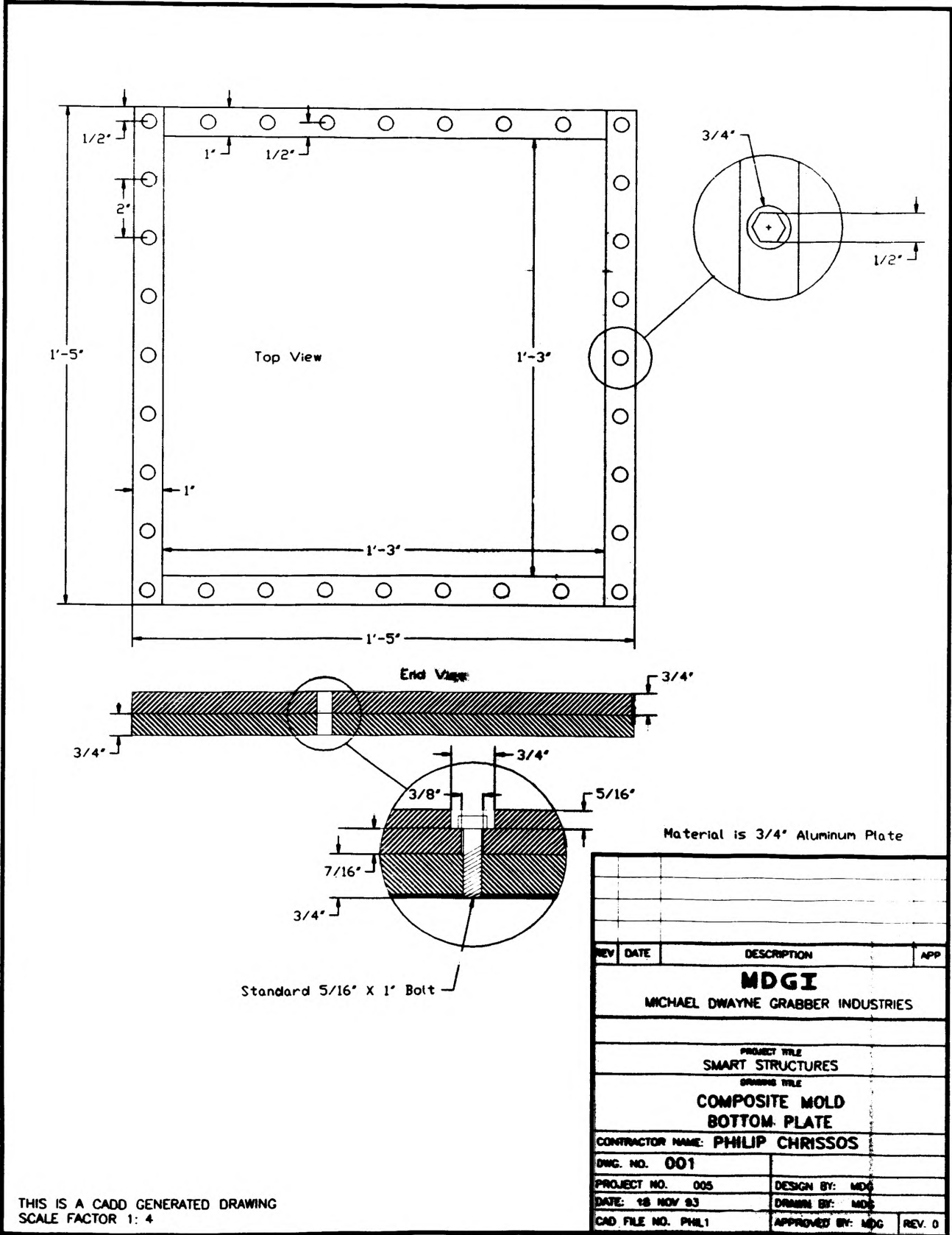
THIS IS A CADD GENERATED DRAWING
SCALE FACTOR 1: 4

Figure 7

4 1/2"

8"

1'-5"

1' 5"

ø5/16"

4 1/2"

Standard Countersink

1/4"
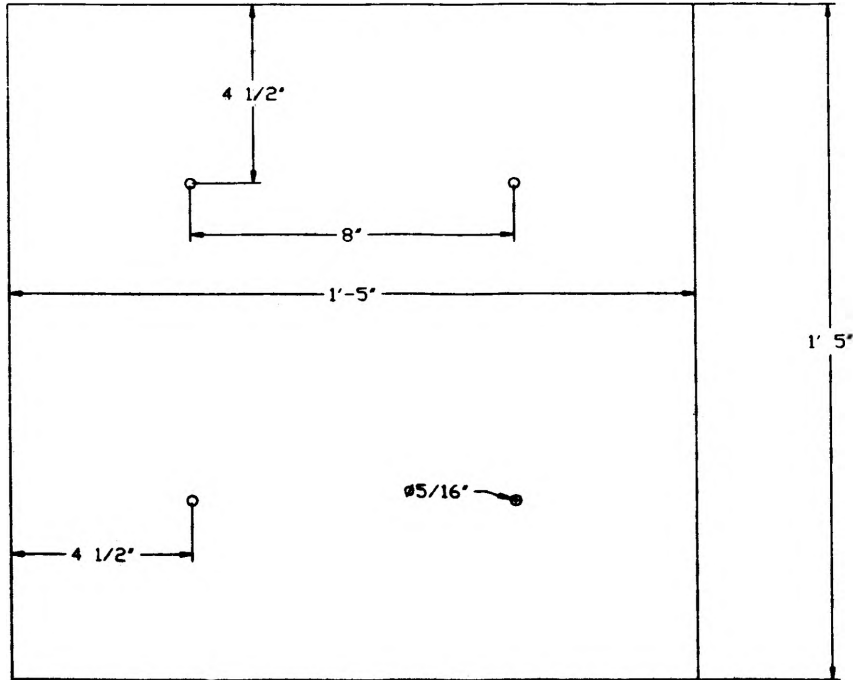
Material is 1/4" Aluminium Plate

1	Jan 94	Changed Size of Screw Holes	MDG
1	Jan 94	Changed Material Thickness	MDG
REV	DATE	DESCRIPTION	APP

MDGI
MICHAEL DWAYNE GRABBER INDUSTRIES

PROJECT TITLE
SMART STRUCTURES

DRAWING TITLE
COMPOSITE MOLD
TOP PLATE

CONTRACTOR NAME: PHILIP CHRISSOS

DWG. NO. 002	
PROJECT NO. 005	DESIGN BY: MDG
DATE: 18 NOV 93	DRAWN BY: MDG
CAD FILE NO. PHIL2	APPROVED BY: MDG REV 0

THIS IS A CADD GENERATED DRAWING
SCALE FACTOR 1: 4

Figure 8
338

Holes drilled and tapped for standard
NC 20 1/4" X 3/4" tapered head screws

Holes drilled and tapped for standard
NC 20 1/4" X 3/4" tapered head screws

Material is 3/4" Aluminum Plate

1	Jan 94	Changed the Size & Type of Mounting Screws	MDG
REV	DATE	DESCRIPTION	APP

MDGI
MICHAEL DWAYNE GRABBER INDUSTRIES

PROJECT TITLE
SMART STRUCTURES

DRAWING TITLE
**COMPOSITE MOLD
TOP INSERTS**

CONTRACTOR NAME: PHILIP CHRISSOS

DWG. NO. 003	
PROJECT NO. 005	DESIGN BY: MDG
DATE: 18 NOV 93	DRAWN BY: MDG
CAD FILE NO. PHIL3	APPROVED BY: MDG	REV 0

THIS IS A CADD GENERATED DRAWING
SCALE FACTOR 1: 4

Figure 9

339

NOTE
Two of each are required.

1'-3"   1'-1"   1'-3"   1'

1"   1"   1 1/2"   1 1/2"

3/4"   3/4"   3/4"   3/4"
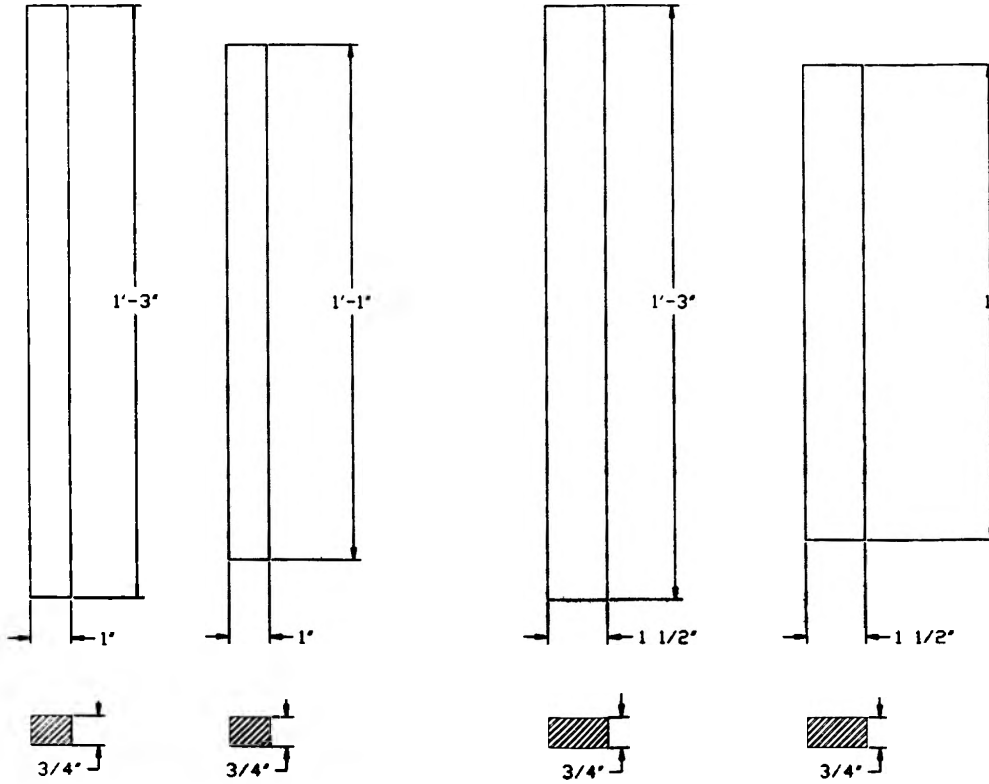
Material is 3/4" Aluminum Plate

REV	DATE	DESCRIPTION	APP

MDGI
MICHAEL DWAYNE GRABBER INDUSTRIES

PROJECT TITLE	
SMART STRUCTURES	
DRAWING TITLE	
COMPOSITE MOLD SPACERS	

CONTRACTOR NAME: PHILIP CHRISSOS	
DWG. NO. 004	
PROJECT NO. 005	DESIGN BY: MDG
DATE: 18 NOV 93	DRAWN BY: MDG
CAD FILE NO. PHIL4	APPROVED BY: MDG	REV 0

THIS IS A CADD GENERATED DRAWING
SCALE FACTOR 1: 4

Figure 10
340

Figure 11

341

Figure 12

342
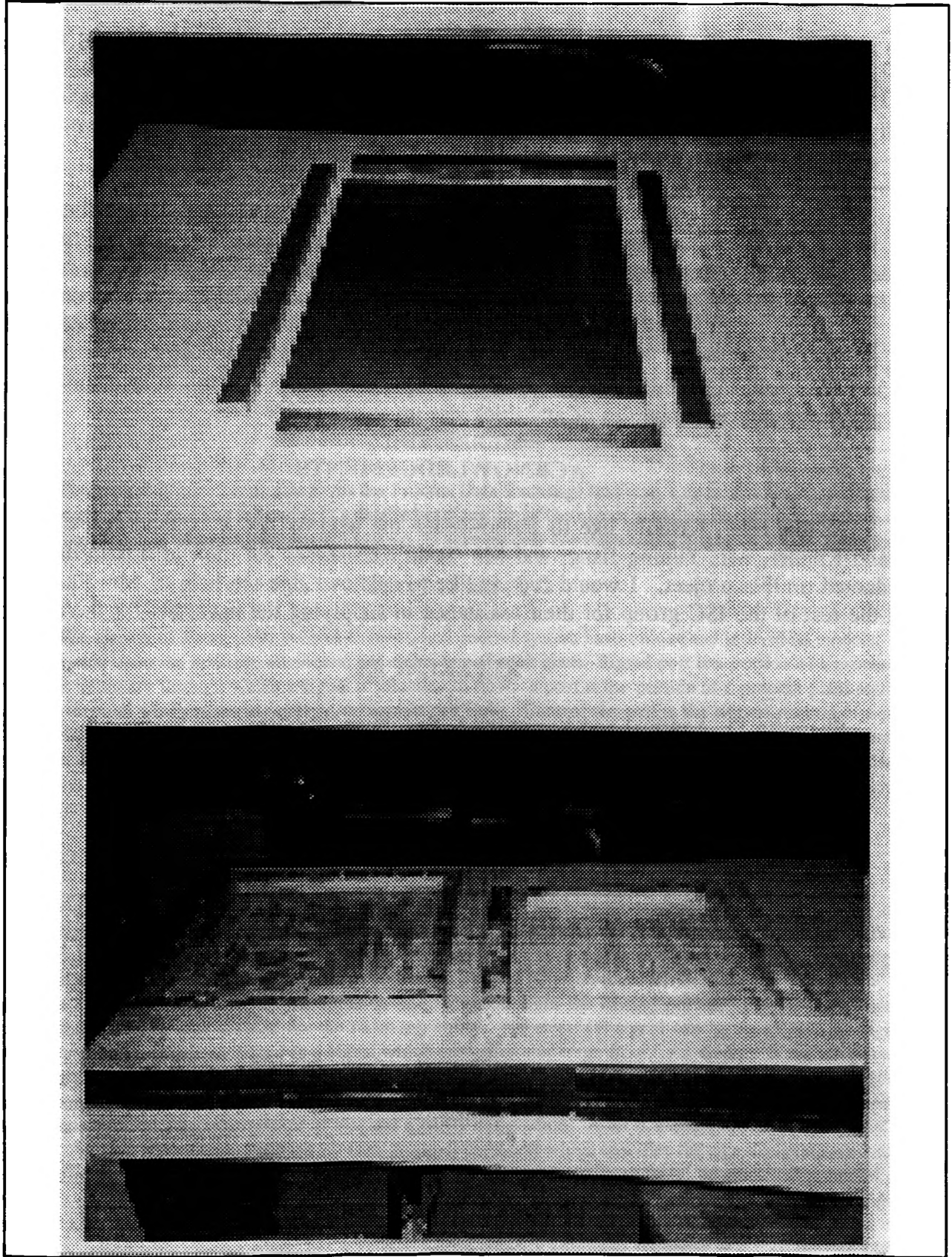
Figure 13

343

VERIFICATION OF THE NEW MOLD IN THE FABRICATION PROCESS

After the mold was manufactured, several composite samples were made in order to verify the effectiveness of the new mold in eliminating the problems encountered with the conventional method. The first two samples made in the new mold were 8 layer, 13" X 13" symmetric cross-ply laminates of Graphite/Epoxy fiber. Both samples turned out excellent. They were held to exactly 13 inches square, they were completely cured, and there was no buckling apparent. The samples were also easy to remove from the mold. Furthermore, because of the combination of the satin finished surfaces and the Chemlease 40, none of the matrix material stuck to the mold. Therefore, sandblasting of the mold is not necessary.

The last sample made in the mold was a 4 layer, 12" X 12" symmetric cross-ply laminate of Graphite/Epoxy fiber. This sample turned out perfect as well. This served to prove that we can use this mold to produce composite samples up to 15 inches square. It also shows that we can produce composite samples of any thickness up to about 3/4".

ACKNOWLEDGEMENTS

REFERENCES

1. Bhagwan D. Agarwal and Lawrence J. Broutman. Analysis and Performance of Fiber Composites. John Wiley and Sons, INC.: New York, 1990; 2nd Edition
2. Operations Manual, Dake Press - Model # 44-806, 1989.

AN EXTENSION OF PDXI DATA MODELS TO INCLUDE PROCESS CONTROL DATA

J. D. Graber   Chemical Engineering Department

ABSTRACT

The results described herein have culminated into the creation of an object model which extends an existing engineering data model to include process control data. The existing data model is described in Volume I of the deliverables for the Process Data Exchange Institute(PDXI) Data File Interchange Format Project. This object model was created using the OMTool* software package on Sun Stations in the Intelligent Systems Center(ISC) of the University of Missouri-Rolla(UMR). It expands on the classes of signal port, control element, and control system.

INTRODUCTION

These models have been created for the Process Data Exchange Institute, a consortium of thirty companies in the process industries. The following is a detailed explanation of the object modelling results for the three classes of signal port, control element, and control system. These models are reflected in figures 1,2 and 3 respectively.

PROJECT RESULTS

The classes of signal port, control element, and control system have unique and individual models. These models expand upon the makeup, attributes, and definition of each class. Signal port is a portion of a process plant equipment boundary through which a signal is intended to flow; a port is the portion of a process plant equipment boundary through which material, energy, or signals can flow. Control element is the wetted portion of a process plant equipment which senses or varies process fluid parameters. Control system is a type of process plant equipment that has as a principle function the generation, transmission, indication, and/or manipulation of signals. Control systems are not intended to be in contact with process material and do not include sensors and actuators(control elements). [Process Data Exchange Institute, 1993]

Signal Port

Signal ports may carry electrical or pneumatic signals. Each of these signals has a transmission method which describes the occurrence of the signal, be it discrete or continuous. Signal purpose, another enumeration of these signal types, may be defined as either measurement(such as a pressure signal for a pressure gauge), or manipulation(such as a pressure signal which actuates a valve). One attribute of these signals is lag time, which represents the time between signal transmission and reception from the exiting port defined for the transmitting entity to the reception port defined for the receiving entity. An electrical signal can be an amperage, digital, or voltage signal. An amperage signal is a signal which embodies amperage flow. An ampere is the unique amount of current which causes a force of 2×10^7 newton(for each meter of length) between two long parallel wires in free space separated by one meter[Considine, 1974]. A digital signal is a signal carrying discrete numerical values which have the attributes of a certain number of bits and a parity designation. A bit is a quantitative unit of digital signal capacity. Parity is a designation carried by each group of eight bits which specifies the sign designation of numbers contained in the eight bits. A voltage signal is a signal which occurs when voltage, an electrical potential caused by a relative build up of electrons, travels through a medium. A voltage signal has a specified range of output, and amperage has a standard range between 3 and 20 mA. Voltage signals may be either alternating or direct current signals. An alternating current signal has a voltage whose polarity alternates regularly at a specific rate known as the cycle time. A direct current voltage signal does not have a polarity alternation, but rather maintains constant polarity.

345

Control Element

A control element has a control type, purpose, and transmission. The control type is an enumerated variable which may be electrochemical, photometric, or chromatographic[Nichols, 1988]. The purpose is a rational for existence and may either be practicality or safety. Transmission specifies the type of signal, be it discrete or continuous. There may be one or many controlled entities for every one or many control elements. A controlled entity is the process fluid which is monitored and/or manipulated by a control element. Control elements include actuators and sensors. An actuator alters process fluid flow for control purposes, while a sensor collects process fluid control data to be compared with a set point. Actuators and sensors specified herein are only those components wetted by the process fluid. This specification is made to avoid confusion with process plumbing system models. A sensor may be a thermometer, or pressure transducer[Benedict, 1977]. A thermometer measures object or fluid temperature at a particular location. A pressure transducer is a device which senses and transmits a pressure signal, utilizing electricity. Also, every pressure transducer may need one or no electrical ports.

Control System

A control system may be specified by a location. A control system may be a signal carrier, readout, or controller. A signal carrier is an entity, usually having two ports, which is a medium of signal transfer. A signal carrier may be a wire, pneumatic tubing, or fiber optic cable. A wire, a signal carrier which is a medium for a particular electrical signal, has a specific capacity. This capacity is the voltage within-which a specific wire can safely and properly operate. Pneumatic tubing, tubing which carries a pressure signal, has a pressure range and signal purpose. This pressure range is the span of pressures within which a pressure signal can be safely carried. Furthermore, the signal purpose may be either pressure reading or actuation. Fiber optic cable is defined as a medium of data transfer which utilizes light signals and photometric sensors. Fiber optic cable has a data capacity, which represents the maximum rate of data transfer which can be realized in the fiber optic cable itself. A readout, a source of data on process control status which may be heard or seen, can be designated by specifying range, type of range, and span[Considine, 1974]. Range is the domain over which a specific readout can measure a process variable's value. Type of range is an enumeration of the readout class which includes measured variables, measured signals, and scales. Span represents the algebraic difference between the upper and lower range values[Andrew, 1974]. A readout may be a strip chart recorder, visual meter, or computer. A strip chart recorder is a device which chronologically records data, usually implementing time as the x-axis and the process variable(data) as the y-axis. A visual meter displays process variable values in a visual manner, but has no recording apparatus. A computer is an electronic device which receives commands and data, performs manipulations, and then generates feedback in the form of an image on a monitor or a printing device. A computer has a mega-hertz(mhz) which represents the processing speed of the central processing unit(CPU), and random access memory(RAM) which can be accessed for data storage and reading or complex manipulations.

DISCUSSION

Unresolved questions about this model include where alarms should fit into the control system model and also whether or not the control system should represent all control devices for a particular controlled variable. The alternative for control system is that it would individually represent single control devices such as the signal generator, comparator and compensator. Moreover, alarms may be considered a type of readout or a unique control system class. Possibly a control system sub-class such as "process safety" could be implemented to include control system alarms. Using a wetted portion to distinguish between control elements and plumbing has been resolved as a good concept. The basic classes and subclasses have been designated, but some expansion is warranted in these items as well as the attributes. Additional control system sub-classes to consider may be signal transducers such as P/I, D/A, A/D, and I/P; signal generators; and controllers such as algorithmic, proportional, proportional-integral, and proportional-integral-derivative. Moreover, the actuator sub-class may be broken into sub-classes such as valves, resistors, and electrical switches. Some attributes to consider adding include length, gauge, insulation material, and insulation thickness for wire; as well as chart speed and paper width for strip chart recorders. I recommend that this document be submitted to a knowledgeable firm for a final evaluation.
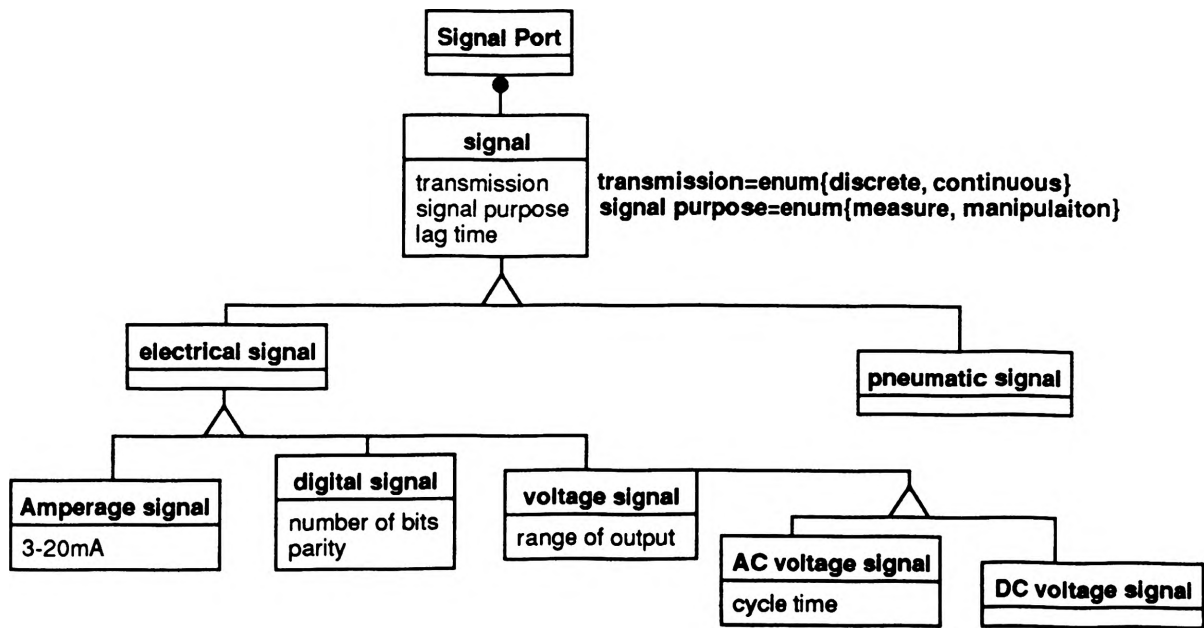
Figure 1. Signal Port Panel
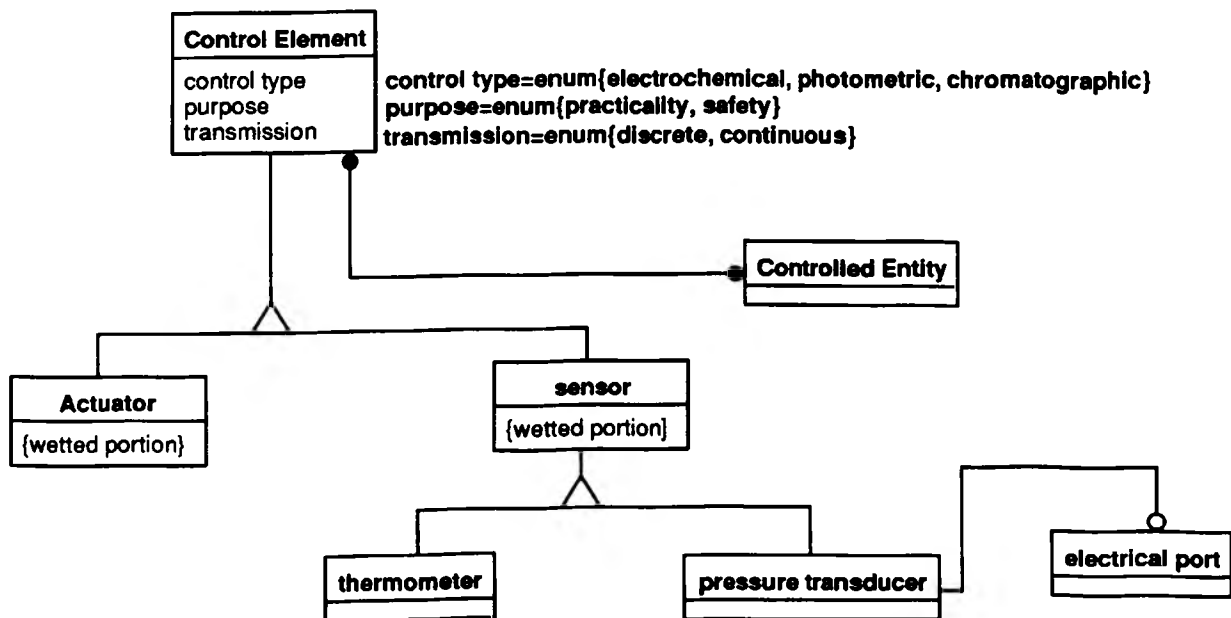
Figure 2. Control Element Panel
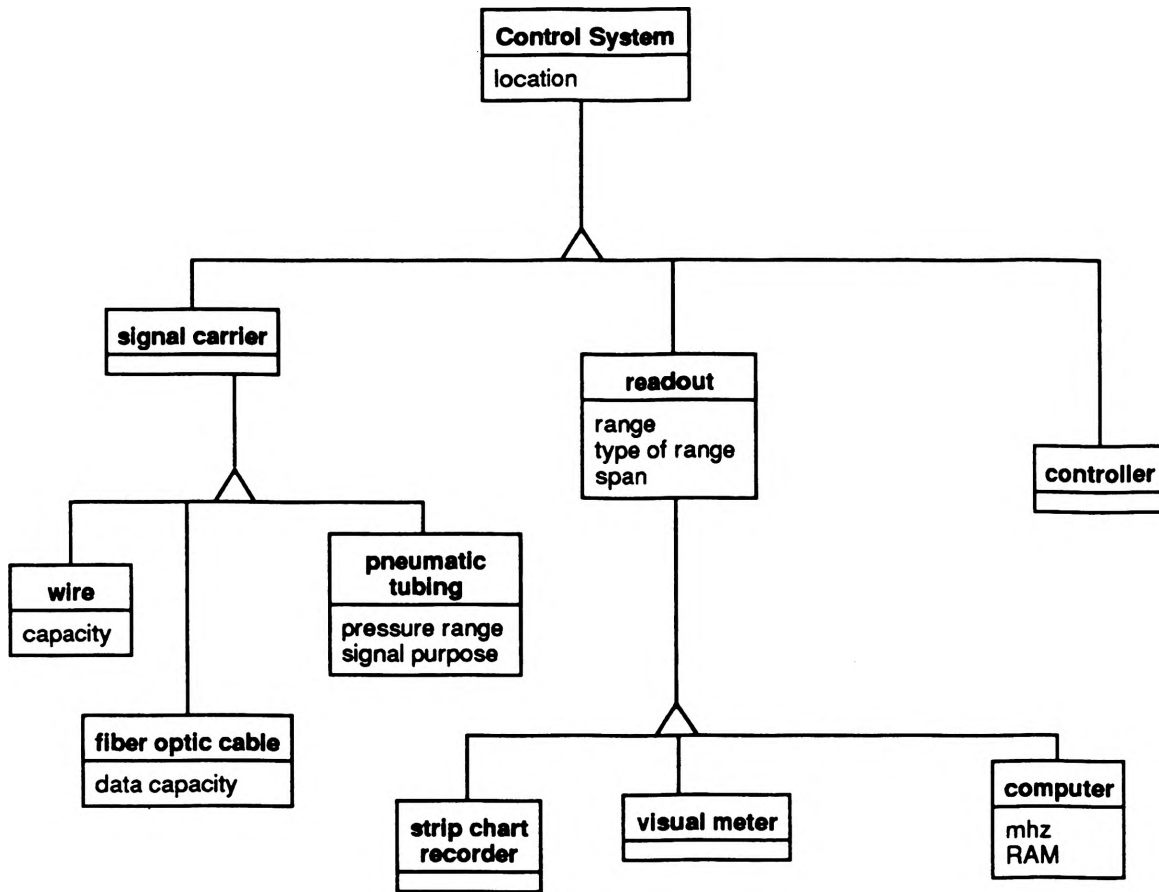
347

Figure 3. Control System Panel

NOMENCLATURE

AC VOLTAGE SIGNAL A voltage signal whose polarity is constantly alternating with a specific cycle time.

AC VOLTAGE SIGNAL.cycle time The time required for one alternation cycle of an AC VOLTAGE signal.

ACTUATOR A wetted control element which alters the process fluid flow for control purposes.

AMPERAGE SIGNAL A signal which constitutes a magnitude of flow of a current.

COMPUTER An electronic device which receives commands and data, performs manipulations, and then generates feedback in the form of an image on a monitor or printer.

COMPUTER.mhz The megahertz of a COMPUTER, representing the processing time of the CPU.

COMPUTER.ram A type of computer memory which can be accessed for data storage and reading or complex manipulations.

CONTROL ELEMENT The wetted portion of a CONTROL SYSTEM which senses or varies process fluid.

CONTROL ELEMENT.control type An Enumerated variable which may be electrochemical, photometric, or chromatographic.

CONTROL ELEMENT.purpose A control element's rational for existence: practicality or safety.

CONTROL ELEMENT.transmission The type of signal which is directly involved with a control element's port. Transmission is an enumerated variable which may be discrete or continuous.

CONTROL SYSTEM A type of process equipment that has as a principle function the generation, transmission, indication, and/or manipulation of signals. Control systems are not intended to be in contact with the process material and do not include sensors and actuators.

CONTROL SYSTEM.location The room or coordinates of a control system within a specified plant site.

CONTROLLED ENTITY The process fluid which is monitored and/or manipulated by a control element.

DC VOLTAGE SIGNAL A voltage signal whose polarity does not change in time.

DIGITAL SIGNAL A signal carrying discrete numerical values contained in bits.

DIGITAL SIGNAL.number of bits A quantitative unit of digital signal capacity.

DIGITAL SIGNAL.parity A signal unique to each numerical byte(8 bits) which gives a sign specification for the bits.

ELECTRICAL PORT A port which carries an electrical potential.

ELECTRICAL SIGNAL A signal which involves the rearrangement of electrons in a conducting media.

FIBER OPTIC CABLE A medium of data transfer which utilizes light signals and photometric sensors.

FIBER OPTIC CABLE.data capacity A maximum rate of data transfer through a fiber optic cable.

PNEUMATIC SIGNAL A signal whose medium of transfer is a pressure differential.

PNEUMATIC TUBING Tubing which carries a pneumatic signal of a specific range and purpose.

PNEUMATIC TUBING.pressure range The rated pressure range over which signals can be safely carried.

PNEUMATIC TUBING.signal purpose Pneumatic Tubing's rational for existence: pressure reading or actuation.

PRESSURE TRANSDUCER A device which senses and transmits a pressure signal utilizing electricity.

READOUT A source of data on process control status which may be heard or seen.

READOUT.range The numerical domain over which a specific readout can measure a process variable's value. This entity is specified by an upper and a lower boundary value.

READOUT.span The algebraic difference between upper and lower boundary values which are specified by the range.

READOUT.type of range An enumerated variable which may be a measured variable(°F), measured signal(mV), or scale(lb/hour).

SENSOR A device which collects process fluid control data to be compared with a given set point.

SIGNAL A message, energy, or force sent along some medium for control purposes.

SIGNAL.lag time The time between signal transmission and signal reception from port to port.

349

SIGNAL.signal purpose The reason for a signal: measure or manipulation.

SIGNAL.transmission The occurrence of a signal: discrete or continuous.

SIGNAL CARRIER An entity usually having two ports which is a medium of signal transmission(ie. wire).

SIGNAL PORT A portion of a process plant equipment boundary through which a signal is intended to flow.

STRIP CHART RECORDER A device which chronologically records data(a graph of data vs. time).

THERMOMETER A device which measures object or fluid temperature at particular location and time.

VISUAL METER A type of readout which can be read visually but has no recording apparatus.

VOLTAGE SIGNAL The electrical potential caused by a relative build up of electrons at a site.

VOLTAGE SIGNAL.range of output the voltage range within which a particular voltage signal functions.

WIRE A signal carrier which is the medium of a particular electrical signal.

WIRE.capacity The voltage within-which a specific wire can safely and properly operate.

ACKNOWLEDGEMENTS

REFERENCES

Andrew, W. G., Applied Instrumentation in the Process Industries, Volume 1 A Survey, Gulf Publishing Company, Houston, 1974.

Benedict, Robert P., Fundamentals of Temperature, Pressure and Flow Measurements, 2nd ed., John Wiley & Sons, New York, 1977.

Nichols, Gary D., On-Line Process Analyzers, Wiley Interscience, New York, 1988.

Considine, Douglas M., Process Instruments and Controls Handbook, 2nd ed., McGraw-Hill Book Company, St. Louis, 1974.

Process Data Exchange Institute, The PDXI Data Models, Phase I Final Draft, American Institute of Chemical Engineers, New York, 1993.

351

THE DEVELOPMENT OF EQUIPMENT SPECIFICATION FORM FROM THE PDXI DATA MODELS

J. M. Juengel
Department of Chemical Engineering
University of Missouri- Rolla

ABSTRACT

The project has culminated in the development of a simplistic working model, based upon the existing data model created by the Process Data Exchange Institute (PDXI). This data model is depicted in Volume 1 of the deliverables for the PDXI Data File Interchange Format Project. The working model, based in part on the Planning Level Model and the Heat Transfer Model [1] of the overall data model, was then used to create an equipment specification form (Fig 1) for a heat exchanger, partially utilizing the standards set forth by the Tubular Exchanger Manufacturers Association (TEMA).

INTRODUCTION

The development of the working data model and the equipment specification forms was accomplished for the Process Data Exchange Institute, a consortium of around thirty companies in the process industries. The ultimate goal of PDXI is to design and fabricate a large data interface amongst many different simulation and process design programs in the form of a database that allows data to be exchanged freely. The development of the equipment specification forms project entails the beginning of the fabrication of this database and an application of it.

A major problem that most companies in the process industries are faced with is the difficulty in manually maintaining equipment specification sheets during periods of frequent equipment replacement. The PDXI team at the University of Missouri- Rolla recently researched and developed a link from the AutoCAD design program to the Paradox database that will update information stored in the database about a piece of process equipment when it is changed in the AutoCAD program. Therefore, it became desirable to create a program that would produce an updated equipment specification sheet when a piece of process equipment is changed in AutoCAD.

PROJECT THEORY

The purpose of this project was to research and develop a method of creating equipment

specification forms from the existing data model created by PDXI. In theory, this can be accomplished by programming a working model into a relational database software program, such as Paradox, D-Base, or Oracle. These databases have the advanced object linking abilities essential for the immense size of the PDXI data model. Many of these databases also have form-generation capabilities that allow the user to program the format of the output and automatically extract the necessary data for this output from the database.

PROJECT RESULTS

The database Paradox for Windows (version 4.0), produced by Borland International, Inc., was utilized to program the working data model. It was chosen for its data modeling abilities, its vast form- generating capabilities, and its inexpensive price. Once the working model was developed on Paradox, research began into the formation of the heat exchanger specification sheet. It was discovered by examining the software user's guide [2] that a form could be generated from a query with a separate data model. Using the TEMA heat exchanger specification sheet found on page 690 of *Chemical Process Equipment* [3] as a guide, the sample specification sheet was constructed (Fig. 1).

The sample form illustrates a specification sheet for a standard shell and tube heat exchanger. The program performs a query on all the flow specifications and critical information in the database for this heat exchanger. The methods developed for the production of this specification sheet can be utilized to create any other desired document.

CONCLUSION

The ramifications of this project on future research are great. The heat exchanger specification sheet is but one application of the working data model that was created in this project. Additional equipment specification forms can be generated for any pieces of equipment located in any given process plant. These can be customized to meet any company's specific guidelines with relative ease.

Also currently under development by the UMR PDXI team is a program that will automatically produce a bill of materials for any piece of process equipment in the database that is to be replaced. This, in conjunction with the aforementioned AutoCAD- Paradox link, is an extremely valuable industrial inventory management tool. Also being examined for future research are additional links from software packages commonly used by industry to the data model. With the creation of additional links, the possibilities for applications of this working data model are limitless.

ACKNOWLEDGMENTS

Special thanks are in order for Dr. Neil L. Book, department of chemical engineering faculty member and faculty advisor for this project, for the contribution of his technical expertise in this field and his provision of the PDXI overall data model. Thanks, too, go to Bryan A. Stanford, fellow chemical engineering student, for his advice on the creation of the working data model. Also, Borland International, Inc. is hereby acknowledged for their provision of the Paradox 4.0 for Windows software and their on- line technical support with this product.

Meister Co.

Louisville   KY

Heat Exchanger Specification Sheet
Performance of One Unit

	Shell Side	Tube Side
Fluid Circulated	Benzene	Water
Temperature In	75.00 F	250.00 F
Temperature Out	135.00 F	215.00 F
Operating Pressure	100.00 PSI	450.00 PSI
Number of Passes / Shell :	1	2
Velocity :	10.00 ft/s	35.00 ft/s
Pressure Drop	35.00 PSI	15.00 PSI
Fouling Resistance :	0.01 s3/ft lb F	0.00 s3/ft lb F

Construction

Tubes No.   25   OD   0.12 ft   Length   20.00 ft

Shell   ID   10.00 ft   OD   10.50 ft

Heat Exchanged :   100.00 BTU/hr

Figure 1- Sample Heat Exchanger Specification Sheet

REFERENCES

1. Process Data Exchange Institute, <u>The PDXI Data Models,</u> Phase I Final Draft, © 1993 American Institute of Chemical Engineers, New York.

2. Borland Int'l, Inc., <u>Paradox for Windows- User's Guide,</u> Version 4.0, ©1992 Borland International, Inc., Scotts Valley, CA.

3. Walas, Stanley M., <u>Chemical Process Equipment,</u> ©1988 Butterworth Publishers, Stoneham, MA.

Fabrication of Composite Laminates with Embedded Pizo-ceramic Sensors and Actuators

Todd Nelson Kelsheimer

Department of Mechanical and Aerospace Engineering and Engineering Mechanics

ABSTRACT

The purpose of the research project is to investigate the methods for embedding pizo-ceramic sensors and actuators in a composite (a fiber reinforced epoxy matrix). The importance of these sensors and actuators is vital in controlling the vibration and excessive strain on a structure causing fatigue or failure. With the control of these instabilities by the actuator, proper performance of the structure is achieved. Most sensors and actuators are surface mounted because (1) The sensor can pick up the greatest strain on the surface of a structure. (2) The actuator can create a stronger moment to counter balance the strain when the actuator is further from the central axis of structure. The surface bonding of sensors and actuators work fine when testing in a lab, but when this technology is tested in the environment, the pizo-ceramics need to be protected from damage. This is why research in embedding sensors and actuators is important. The whole goal of the project is to embed the sensors and actuators as close to the surface of a composite structure as possible. This creates better sensing and dampening of strain and vibration while protecting the pizo-ceramic.

INTRODUCTION

The main goal of this research was to develop and improve upon the methods of producing smart composite structures. Throughout the period of research, small goals had to be obtained before the final goal could be reached (producing a smart structure). One of the very first goals was to learn how to use the Dake heated press. This was achieved by laying up a composite using graphite/epoxy prepreg tape and curing the composite in the press. The cure cycle that was used can be seen in Figure 1, which was provided by Hercules Incorporated. After the heated press was used and found to be in good working order, there were several problems that came about which prompted a new mold to be made. Finally after months of testing, the composite structures were coming out of the heated press in perfect condition. Now that all the kinks were worked out, the smart structure research began. From this research, new improvements were made to some of the older conventional methods of fabricating smart structures. With some of these new ideas or modifications to old

methods, the main goal for the research was completed. Hopefully, from the problems and mistakes that were overcome, future testing for composites and smart structures can be developed with less time and complications.

FABRICATING A CONVENTIONAL COMPOSITE PLATE

When fabricating a composite plate, there are several considerations before placing the composite in the heat press for curing. The configuration of the composite plate is the most important step to be considered from the very beginning. The configuration is the orientation each lamina will have with respect to an arbitrary xy axis. Most composites and smart structures are oriented perpendicular to each other or [0/90]s with the s representing symmetry (i.e. an eight layered plate with [0/90]2s = [0/90/0/90/90/0/90/0]). Another important thing to remember when laying up a composite is not to leave the lamina (the sheet of prepreg tape) out very long because the lamina will start curing at room temperature (this can be seen when the epoxy starts to become very sticky). One of the last things to consider in the fabrication process is the position of the pizo-ceramic sensors and actuators. This will be discussed in detail later.

USING THE DAKE HEATED PRESS

In order to cure a composite plate or a smart structure, the process of high pressure and elevated temperatures are needed. Because the Dake hydraulic press measures in tons, the required pressure found in Figure 1 is converted to tons. To do this, the area of the composite (Ac) is taken in square inches. The required pressure (Pr) is then multiplied by the area of the composite. After this is done, the pounds of pressure is changed into tons by multiplying the pounds of pressure by 1 ton/2000 lbs.. The final equation is (Ac * Pr * 1 ton/2000 lbs.) to find the amount of pressure in tons needed for the curing cycle of the composite. The same process is used for smart structures. Once the pressure is applied, the heating plates on the Dake press are turned on. Then, the temperature gage for the plates are adjusted accordingly to follow the temperature versus time graph represented in Figure 1. As can be seen in Figure 2, the temperature curve for a Graphite/Epoxy follows fairly close to the original. The only problems that need to be considered is the ability to keep both heating plates close to the same temperature. Also, the pressure has a tendency to drop when the epoxy becomes fluid and raises as the composite plate cures.

IMPROVEMENTS IN THE FABRICATION PROCESS

During the first part of research, there were complications. The most important problem was in the curing cycle of the composite. When the composite was being prepared for the heated press, tacky tape was used to keep the epoxy from running out the sides of the composite mold. While twelve ply composites worked really good using the tacky tape, the composite that was less than twelve ply did not cure right on the outer edges. After extensive studying and testing was done on the problem, it was decided that the problem was the inability of the tacky tape to compress to the thickness of the desired ply level. This prompted a new mold to be made where the tacky tape would not be used

358

Cure Cycle for AS4/3501-6 (Gr/Ep)
Tape and Fabric (by Hercules Inc.)
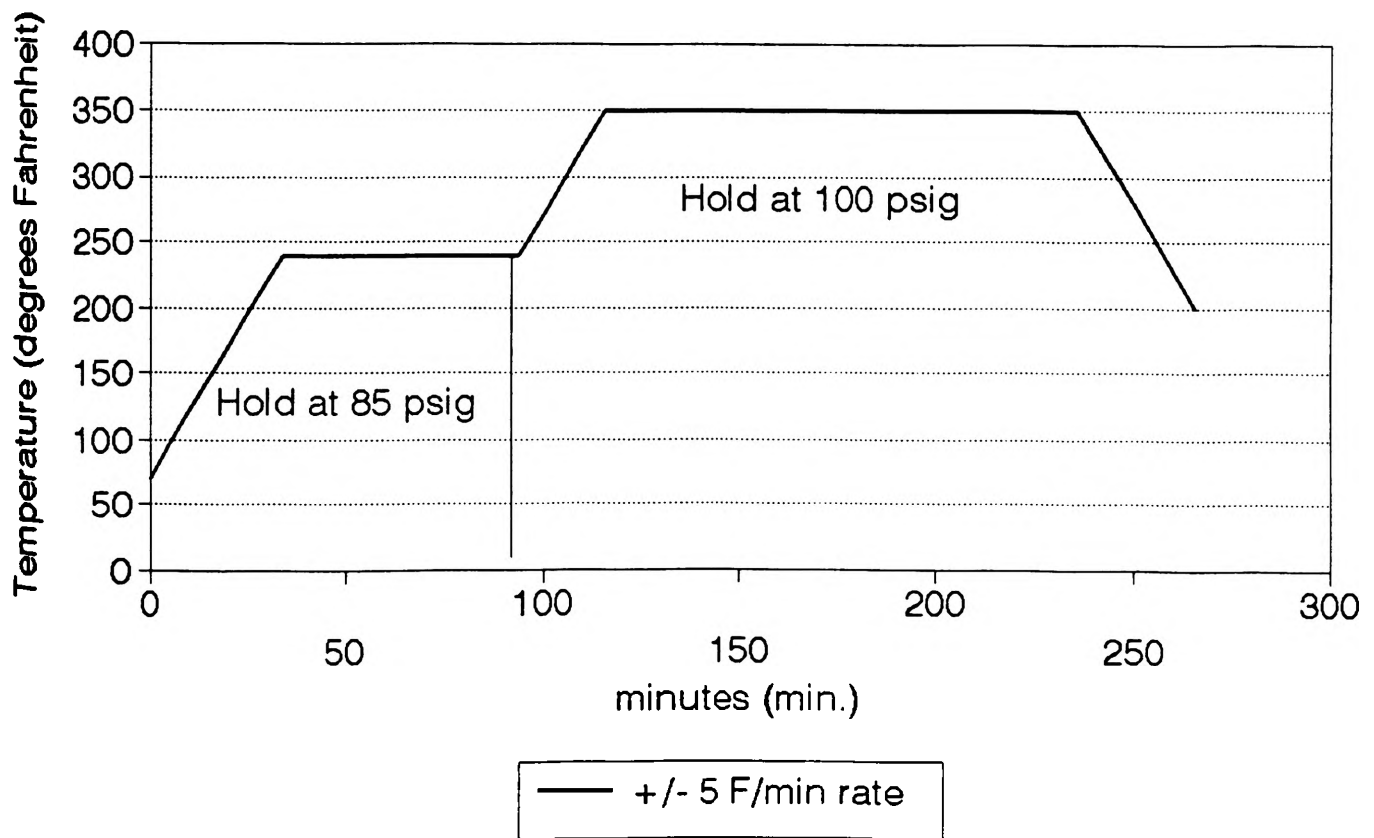
Figure 1: The curing cycle for Graphite/Epoxy from the Hercules Inc.

TABLE I. DATA FROM THE CURING CYCLE OF AS4/3501-6 GRAPHITE/EPOXY

List of date used to plot out Figure #2
Sample #9 Gr/Ep - [0/90]3s 12" * 12" plate
Area of plate = 144 in.^2
for 85 psig = 6.12 tons
for 100psig = 7.2 tons

Time minutes	The plates temperature in the Dake Press			minutes	top	bottom	average
	top	bottom	average				
0	74	74	74	120	266	268	267
2	78	78	78	122	272	274	273
4	82	83	82.5	124	278	280	279
6	88	90	89	126	285	288	286.5
8	94	95	94.5	128	291	293	292
10	100	101	100.5	130	299	300	299.5
12	104	105	104.5	132	307	309	308
14	112	112	112	134	316	317	316.5
16	118	119	118.5	136	324	325	324.5
18	125	126	125.5	138	332	334	333
20	131	132	131.5	140	339	340	339.5
22	139	140	139.5	142	345	345	345
24	149	150	149.5	144	350	350	350
26	157	157	157	159	352	351	352.5
28	167	167	167	174	348	348	348
30	172	173	172.5	189	349	350	349.5
32	180	181	180.5	204	353	353	353
34	188	189	188.5	219	351	352	351.5
36	202	199	203.5	234	350	350	350
38	211	210	211.5	249	350	350	350
40	219	219	219	264	350	350	350
42	223	223	223	266	332	332	332
44	230	231	230.5	268	327	328	327.5
46	234	234	234	270	313	315	314
48	238	239	238.5	272	294	294	294
63	243	242	243.5	274	284	286	285
78	240	240	240	276	271	271	271
93	240	240	240	278	259	260	259.5
108	240	240	240	280	246	250	248
110	240	240	240	282	239	241	240
112	246	248	247	284	234	234	234
114	250	252	251	286	222	220	223
116	254	256	255	288	214	213	214.5
118	260	262	261	290	205	204	205.5

Cure Cycle for AS4/3501-6 Tape & Fabric
Graphite/Epoxy (from HERCULES INC.)
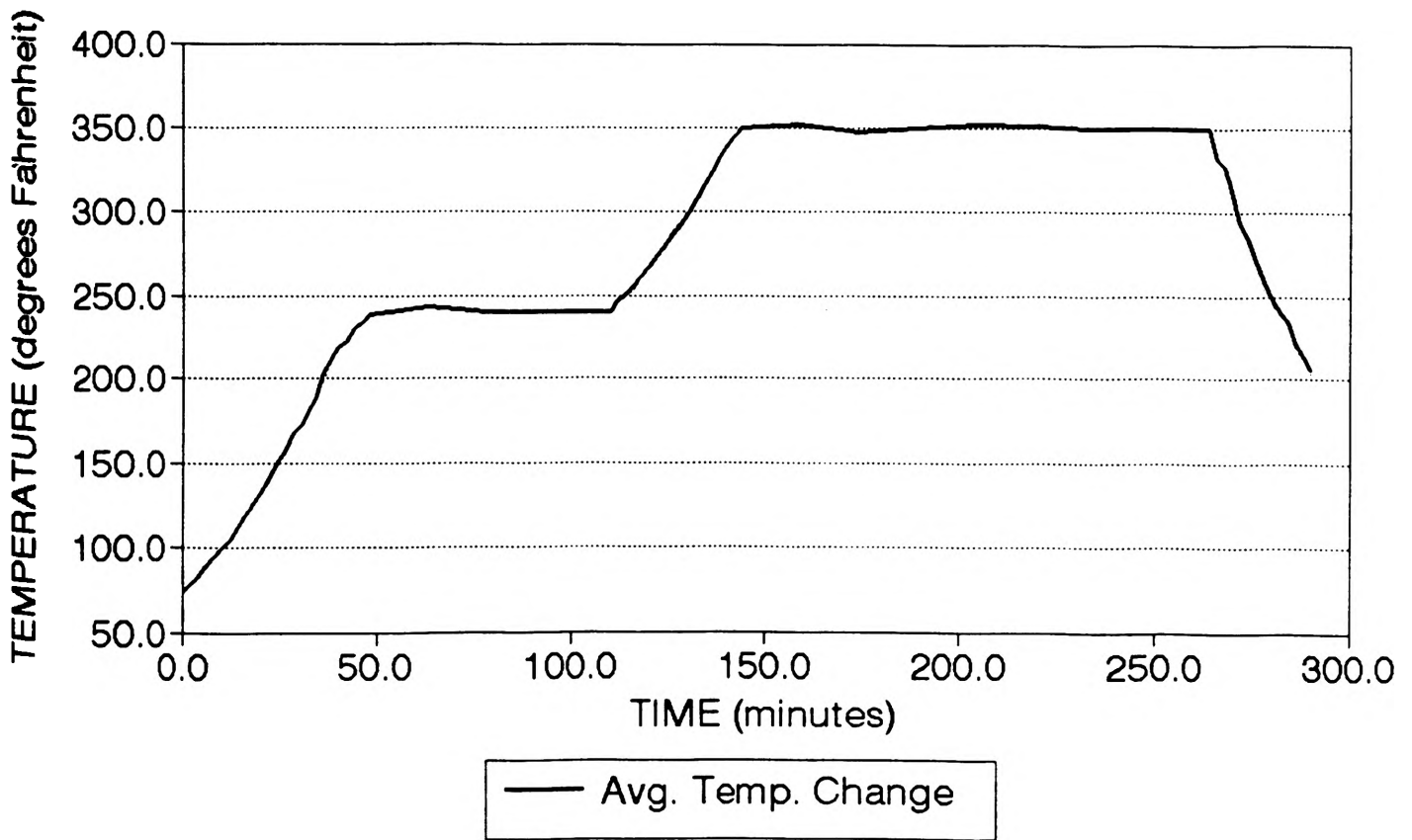
Figure 2: The actual curing cycle done in the lab with the Dake heated press

The mold successfully cured a four ply composite. Also, the mold was designed to make various size composites by adding or removing plates inside the mold.

Another complication that developed during the curing cycle was the temperature variance in the cool down cycle. It was noticed that at the boiling point of water (220 degrees Fahrenheit), the temperature of the top plate would start cooling slower then the bottom plate. The water cooling system for the hot plates seemed to let water flow easier to the bottom plate just below the boiling point. The problem was overcome by allowing the water to remain on all the time at about 210 degrees Fahrenheit while releasing the mold from the compressed state. This allowed the top of the mold to air cool which is very close to the cooling rate of the bottom of the mold. The bottom of the mold was still on the heated plate. At about 150 degrees Fahrenheit, the mold was removed so it could be air cooled. The new compensating process reduced the amount of thermal stress that could be seen in the warping of the composite plate. The new mold and the cooling process helped in producing a near perfect composite plate for testing.

METHODS FOR EMBEDDING PIZO-CERAMIC SENSORS AND ACTUATORS

After the fabrication process for composites was perfected, the attention was turned to the development of a smart structure. The most effective placement of the pizo-ceramic sensors and actuators were on the surface of the structure because it picks up the maximum strain and creates a maximum moment on a structure. For the sensors and actuators to be effective on structures (i.e. airplane wings, stabilizers, and helicopter blades), they should be protected from the harsh environmental conditions. All of the methods that have been researched follow these main ideas.

EMBEDDING PIZO-CERAMICS IN A GLASS/EPOXY

The first smart structure fabricated was a Glass/Epoxy plate with the pizo-ceramic sensors and actuators embedded inside the lamina. Because the Glass/Epoxy plate was nonconducting, the embedded pizo-ceramics can meet all the objectives with no problem. This fabrication process can be seen in Figure 3.

EMBEDDING PIZO-CERAMICS IN A GRAPHITE/EPOXY

The most difficult problem faced in the fabrication of smart structures was the embedding of the pizo-ceramics in a Graphite/Epoxy. Because the Graphite/Epoxy composite was conductive, the embedded pizo-ceramics should be insulated to protect it from short circuiting. Three different method for insulating the pizo-ceramics were developed to help overcome the problem of the pizo-ceramic sensors and actuators from being shorted out.

The first method used for insulating a pizo-ceramic in a Graphite/Epoxy was by using Teflon. Teflon tape was used by wrapping the pizo-ceramic and its leads. Then the inside lamina closest to the surface was cut so the pizo-ceramic could fit inside the lamina (see Figure 4 for the lay up). After the smart structure was cured, the resistance was tested by the leads which were connected to the pizo-ceramics. The resistance, which was tested by a volt meter, was found to be zero. Thus,
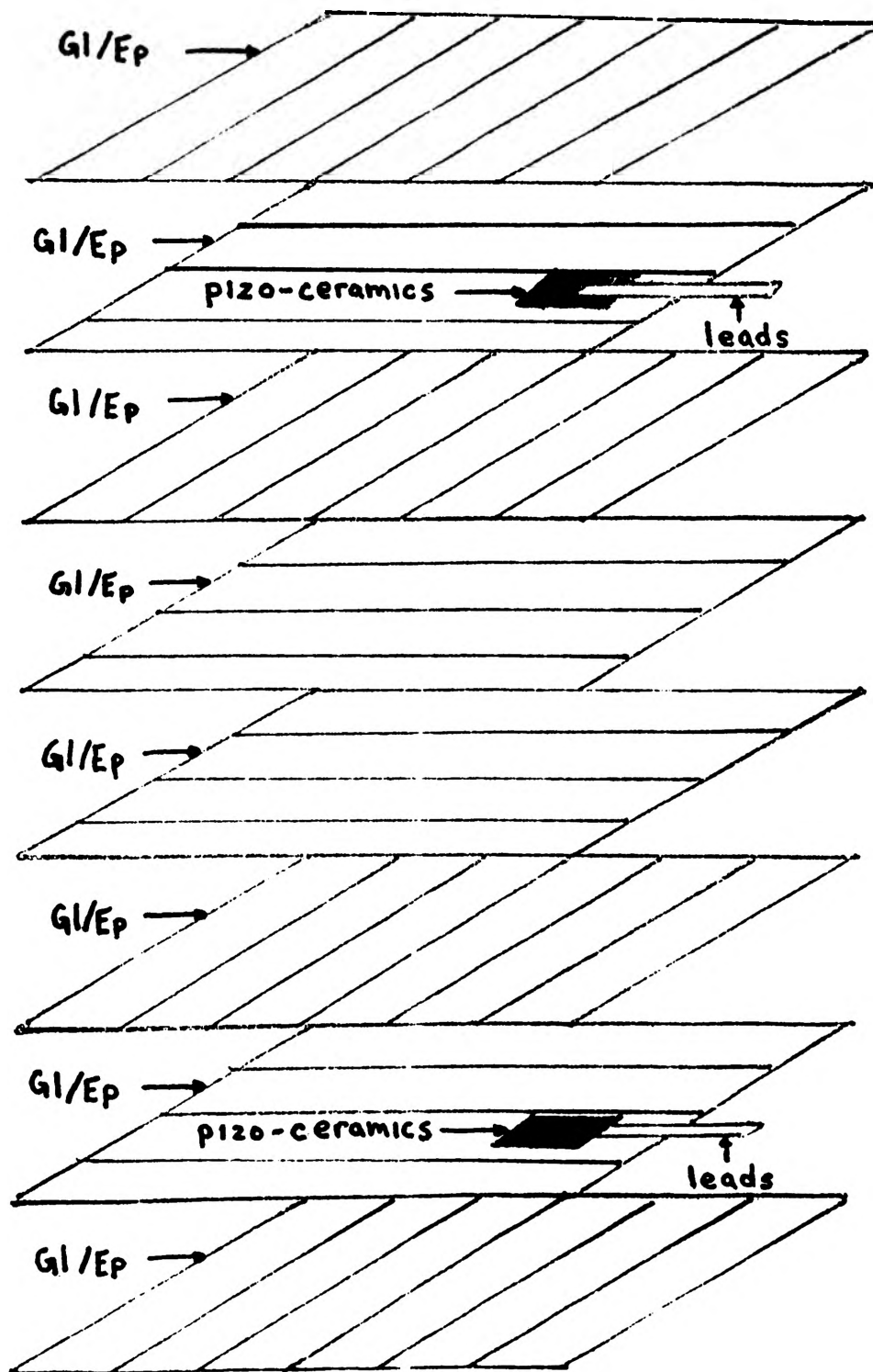
Figure 3: Pizo-ceramics embedded in a Glass/Epoxy (Gl/Ep) matrix
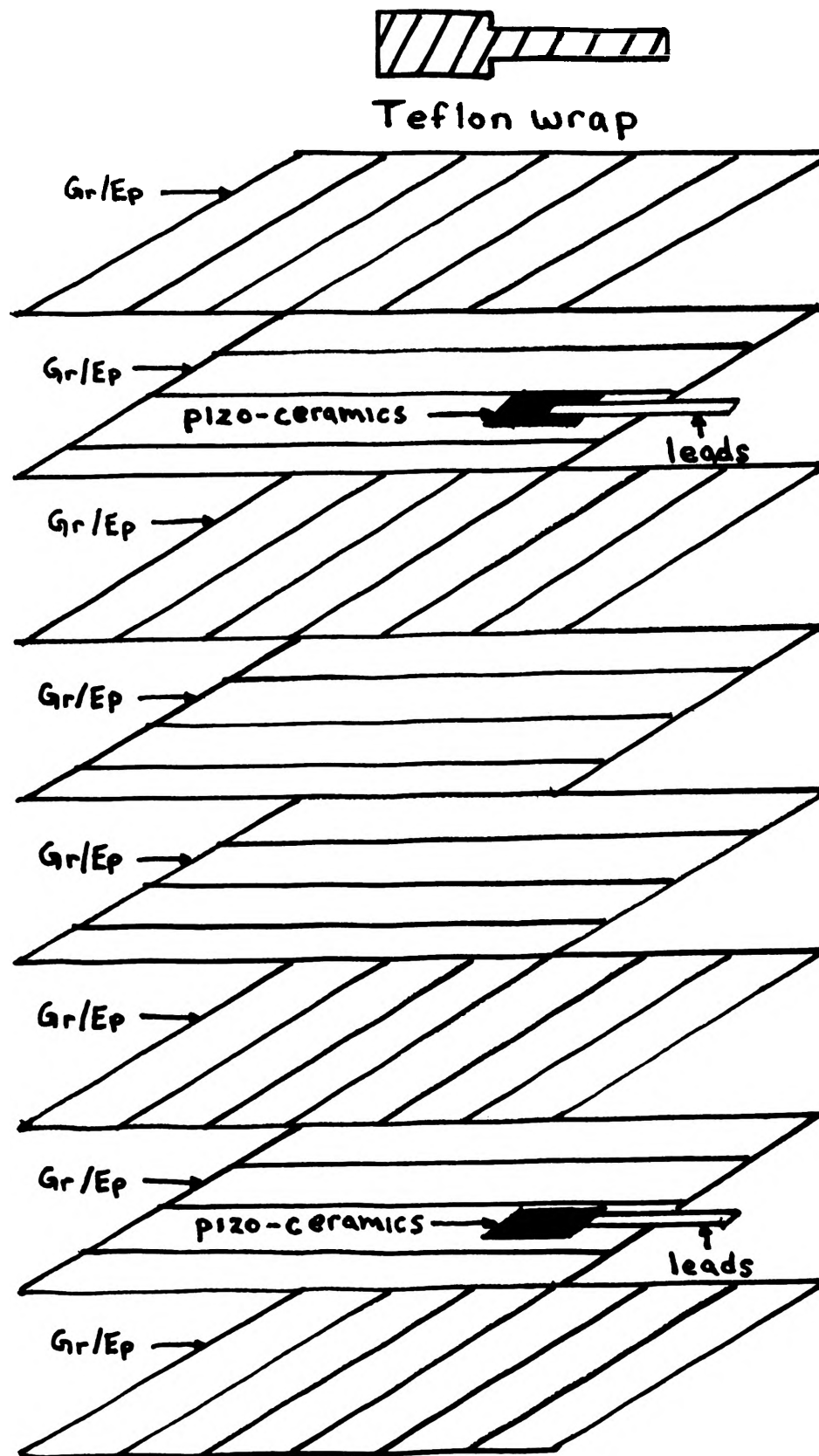
Figure 4: Teflon insulated Pizo-ceramics embedded in a Graphite/Epoxy (Gr/Ep) matrix
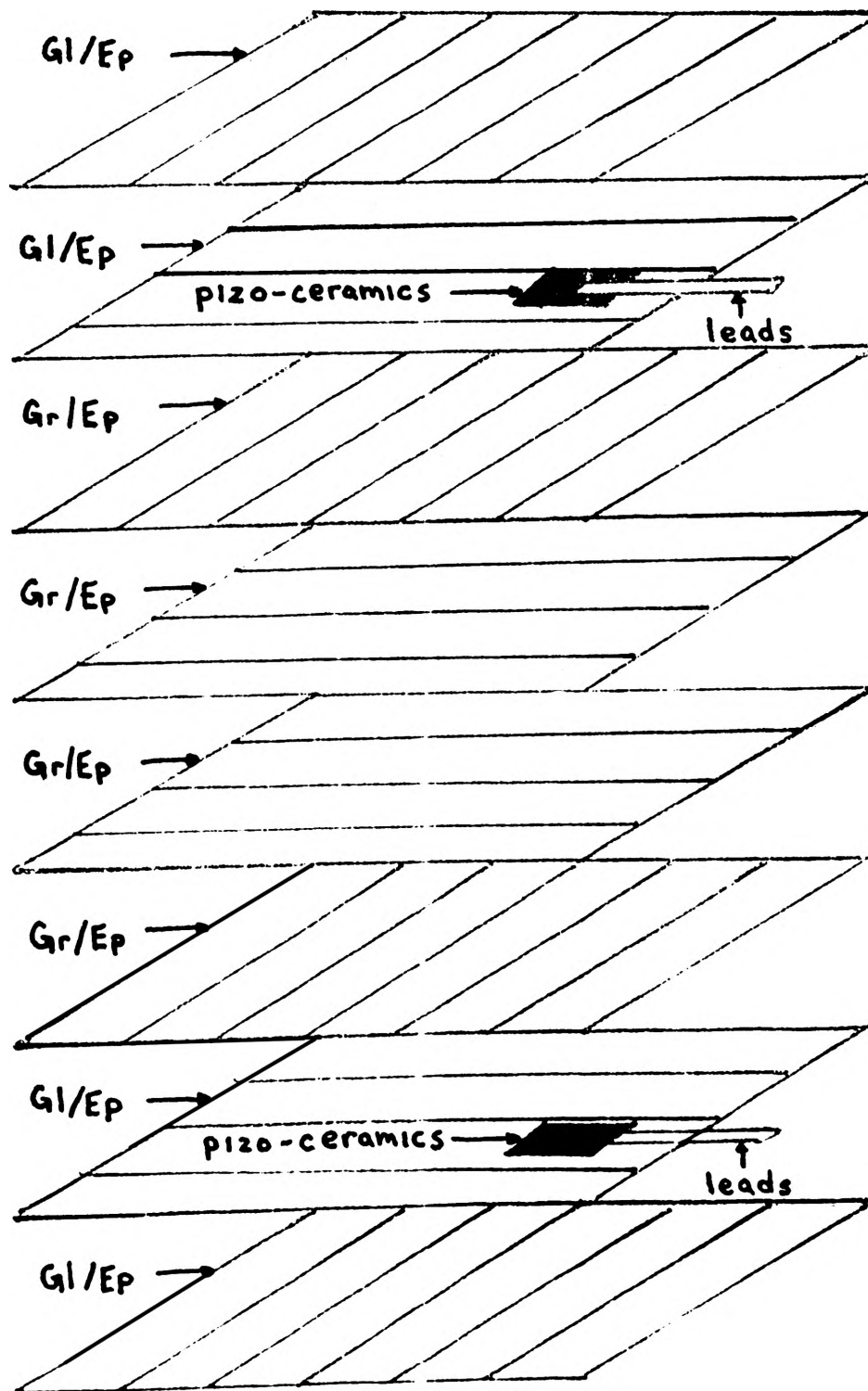
Figure 5: Pizo-ceramics embedded in Glass/Epoxy (Gl/Ep) matrix surrounding a Graphite/Epoxy (Gr/Ep) matrix

the insulator for the pizo-ceramics and their leads worked without any problems from the conductive Graphite/Epoxy structure.

The second method used for insulating the sensors and actuators was the use of polypropylene. This method did not work because the polypropylene had to be heated to 600 F before it would become liquid. Also, the polypropylene liquid was to thick to coat the pizo-ceramics. The last reason the polypropylene did not work was because the high temperature might have caused thermal stresses on the pizo-ceramic. For these reasons, the polypropylene coating of the pizo-ceramics was not used.

The last method for insulation a pizo-ceramic was the use of Glass/Epoxy and Graphite/Epoxy mixed. The Graphite/Epoxy composite was prepared while the pizo-ceramics were being placed between two Glass/Epoxy laminas. After both Glass/Epoxy and Graphite/Epoxy structures were made, the two Glass/Epoxy structures (each structure contained one pizo-ceramic) were placed on opposite sides of the Graphite/Epoxy (see Figure 5). In this way, the pizo-ceramics are protected from the environment and the conductive Graphite/Epoxy matrix.

CONCLUSION

In the end, the new methods developed for fabrication of composites and smart structures will help future research in this area. With this technology, airplanes, helicopters, and automobile are able to preform better and last longer. Also, with the smart structures information on fabrication, fiber optics could be embedded in a composite. A fiber optics grid network could be used to run a diagnostic test on an aircraft to determine damage or the health of its skin.

ACKNOWLEDGMENT

366

Relaxation Technique for the Fitting of Numerical Data

M. J. Lehmann, Physics Department

March 24, 1994

Abstract

Data, in particular that generated through successive computer approximations, may not always follow the smooth curve it is suppose to. Approximations in input data, round off error, and estimations made in the mathematical formulas, are just some of the things that could cause this problem. In any respect, this data must somehow be smoothed or fitted for publication. One way of fitting such data sets is the relaxation method. This method does not rely on the data conforming to a specific mathematical shape, as opposed to other programs that require the data to be fitable by some mathematically generated curve. Instead, the relaxation method uses the values of the points surrounding the current one to determine the new value at that location. This provides a curve independent method for fitting the data.

1 INTRODUCTION

The relaxation method was originally used in determining electrical field distributions. The field was mapped out as a two dimensional grid of estimated potentials. The potentials would then be better approximated by passing the grid through the relaxation process. The idea behind the method was to take a potential U_0 and calculate a new potential based on its value and the values of the four potentials, U_1, U_2, U_3, and U_4, surrounding it. This would be done for every point in the grid, producing a new grid with better approximations for the actual potentials. Then, by repeating the process for each new grid, the error of determining the potential for a given point is reduced.

Taking this idea into one dimensional work simplifies the matter down to only two surrounding potentials, U_2 and U_4, in which to calculate a new U_0 potential. This method can now be applied to xy curves. Defining the potential at each point to be equal to its y value, the method will relax these y values into a smooth curve. It is this process that we hope to apply towards our data curves.

2 THEORY

The calculations start with the two dimensional case as defined in figure (1)[1]. Each

367
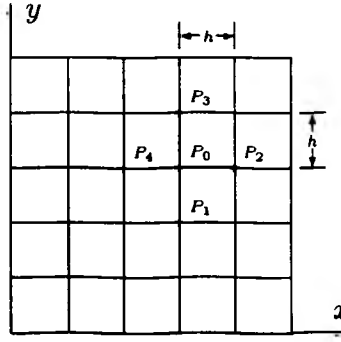
Figure 1: Computational lattice for the relaxation technique

point P_i corresponds to a potential value U_i used in the following U_0-dependent equations given by Paszkowski[1].

$$U_1 = U_0 - \left(\frac{\partial U}{\partial y}\right)_0 h + \frac{1}{2}\left(\frac{\partial^2 U}{\partial y^2}\right)_0 h^2 - \frac{1}{6}\left(\frac{\partial^3 U}{\partial y^3}\right)_0 h^3 + \cdots \tag{1}$$

$$U_2 = U_0 + \left(\frac{\partial U}{\partial x}\right)_0 h + \frac{1}{2}\left(\frac{\partial^2 U}{\partial x^2}\right)_0 h^2 + \frac{1}{6}\left(\frac{\partial^3 U}{\partial x^3}\right)_0 h^3 + \cdots \tag{2}$$

$$U_3 = U_0 + \left(\frac{\partial U}{\partial y}\right)_0 h + \frac{1}{2}\left(\frac{\partial^2 U}{\partial y^2}\right)_0 h^2 + \frac{1}{6}\left(\frac{\partial^3 U}{\partial y^3}\right)_0 h^3 + \cdots \tag{3}$$

$$U_4 = U_0 - \left(\frac{\partial U}{\partial x}\right)_0 h + \frac{1}{2}\left(\frac{\partial^2 U}{\partial x^2}\right)_0 h^2 - \frac{1}{6}\left(\frac{\partial^3 U}{\partial x^3}\right)_0 h^3 + \cdots \tag{4}$$

Each of these equations, when summed together, give us equation (5).

$$\sum_{n=1}^{4} U_n = 4U_0 + \left[\left(\frac{\partial^2 U}{\partial x^2}\right)_0 + \left(\frac{\partial^2 U}{\partial y^2}\right)_0\right] h^2 + \cdots \tag{5}$$

Since it is the one dimensional case needed as a fitting routine, only the U_2 and U_4 potentials are summed together, as follows

$$U_2 + U_4 = 2U_0 + \left(\frac{\partial^2 U}{\partial x^2}\right)_0 h^2 + \cdots \tag{6}$$

so that the terms containing the partial y will drop out. If the "terms of higher order (small value of h) are neglected"[1], equation (6) becomes

$$U_2 + U_4 - 2U_0 - h^2 \nabla^2 U_0 = 0 \tag{7}$$

and when there is "no space charge ($\nabla^2 U_0 = 0$)"[1] then

$$U_2 + U_4 - 2U_0 = 0 \tag{8}$$

"Since values are assumed at the beginning of the calculations, equation (8) may not be satisfied and there may be a residue"[1], where

$$U_2 + U_4 - 2U_0 = R_0 \tag{9}$$

368

If "the value of R_0 is a measure of the deviation from the proper potential at point P_0, U_0 must be changed so that the residue (R_0) vanishes."[1] This correction being

$$\triangle U_0 = \frac{1}{2}R_0 \tag{10}$$

Finally, combining the previous two equations (9) and (10) to get the formula for the change in U_0,

$$\triangle U_0 = \frac{1}{2}[U_2 + U_4 - 2U_0] \tag{11}$$

Then if $U = y$ then for $i = 1$ to n,

$$\triangle y_i = \frac{1}{2}[y_{i+1} + y_{i-1} - 2y_i] \tag{12}$$

where i is the index into the set of points and n is the number of points in that set. The formula in equation (12) provides a starting point for a simple relaxation routine to do curve fitting. To get a better degree of smoothing, just pass each new data set back through the algorithm.

3   RESULTS

The relaxation method was tested on modifications of two plots, a *sin* curve and a $1/x$ curve. Theses curves were modified to test the fitting of distortion on a relatively gentle slope area, a steep slope area, and a sharp peak or arc. Each of these effects can be found in amplitude curves intended to be fitted.

This first plot is a modified $1/x$ curve where a few points were selectively distorted to see if the relaxation method could produce a $1/x$ fit. The original curve is being represented
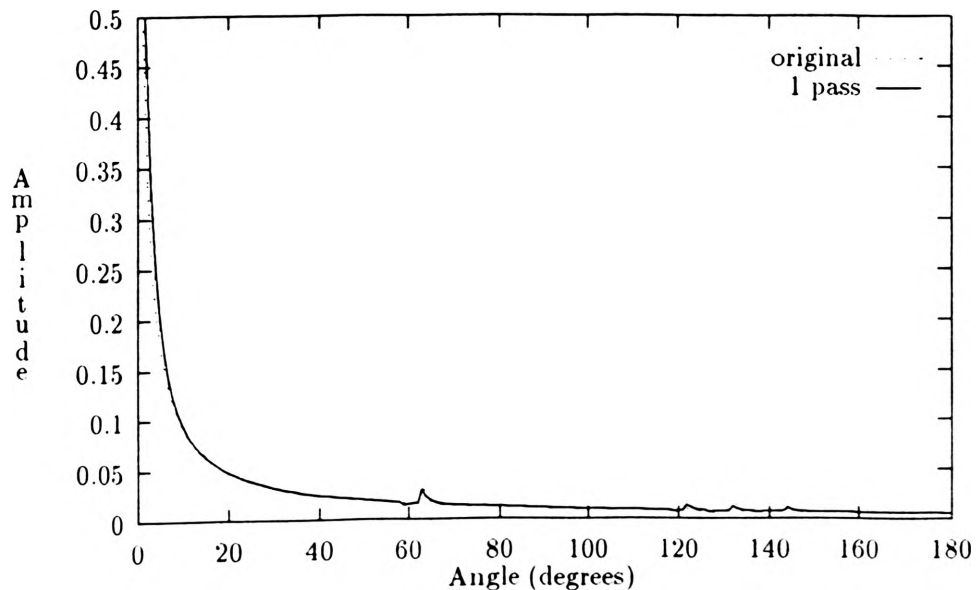
Figure 2: $1/x$ with some points distorted

with a dotted line, and a single pass through this data with the relaxation technique has

369

produced the solid line shown in figure (2). As you can see, the distortion around 60 and 130 degrees has been partially smoothed out by only one pass through the algorithm. By making more passes through this data, these spikes were further relaxed, as shown by the thicker line and thicker dots of figure (3), representing three and five passes respectively.
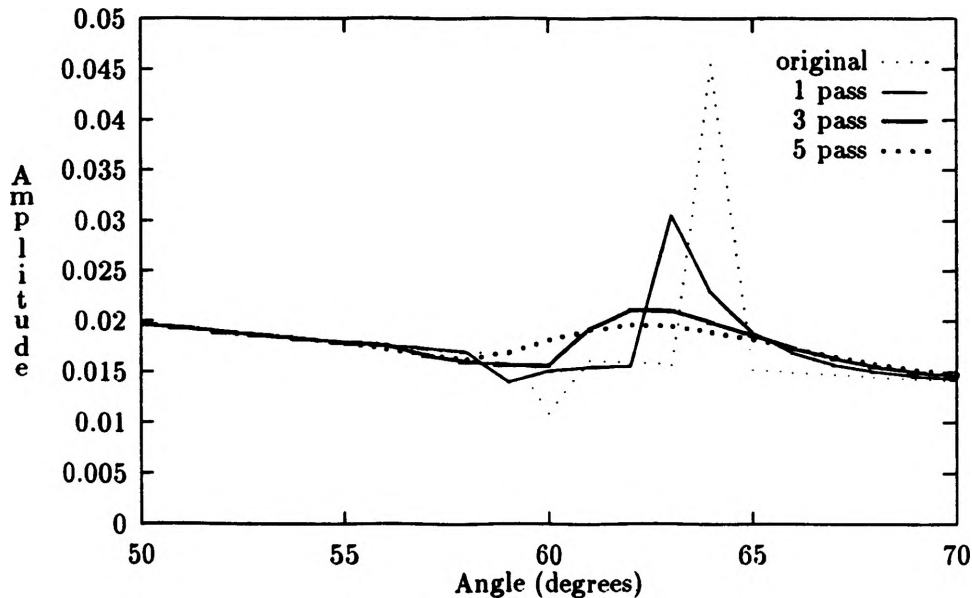
Figure 3: Comparison of multiple relaxation passes on gentle slope

Unfortunately, not all effects were good. Figure (2) shows that the fit for steeper slopes are effected more, producing a shift slightly to the right. With more passes through the algorithm, this effect becomes more exaggerated.

To see how the relaxation method would effect relatively sharp peaks and valleys, a modification of a *sin* curve was chosen. Figure (4) shows this *sin* curve, with distortion in a peak around 60 degrees and distortion in the steep slope area around 130 degrees. Again the original curve is represented with a dotted line, and a single pass through the relation algorithm is represented by the solid line. As you can see, just a single pass has relaxed the data around the peak at 60 degrees, and straightened the steep slope at 130 degrees.

As in figure (2), more passes through the *sin* data has made the distortions virtually disappear in both areas of interest. These two areas are represented in a plot of both arcs in figure (5). Unfortunately with the increase of the number of passes, a shift or decrease in the amplitudes around 60 and 120 degrees can again be seen.

One example of an amplitude curve that must be fitted is shown in figure (6). This plot displays the original data with dots, where the distortion is in the larger angles. It took five passes through the data to produce the smooth line fit. The distorted data has been smoothed, but at the expense of the decrease in amplitude around 30 degrees. This curve follows the same patterns seen with the previous two curves, where the resulting curve is more relaxed, but the steep slope area and sharp peaks experience a shift from the original data.

370
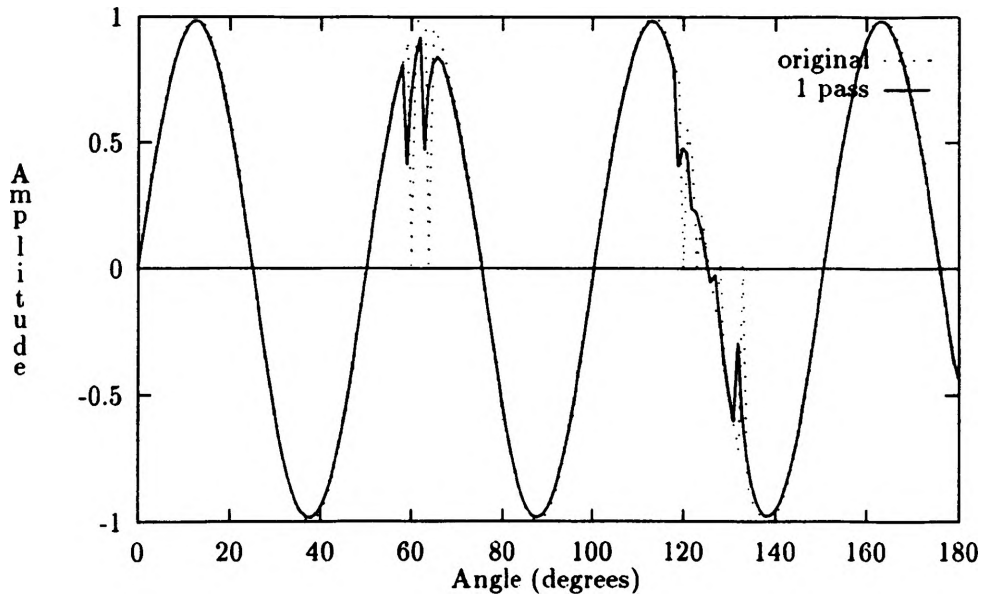
Figure 4: $Sin(x)$ with some points distorted
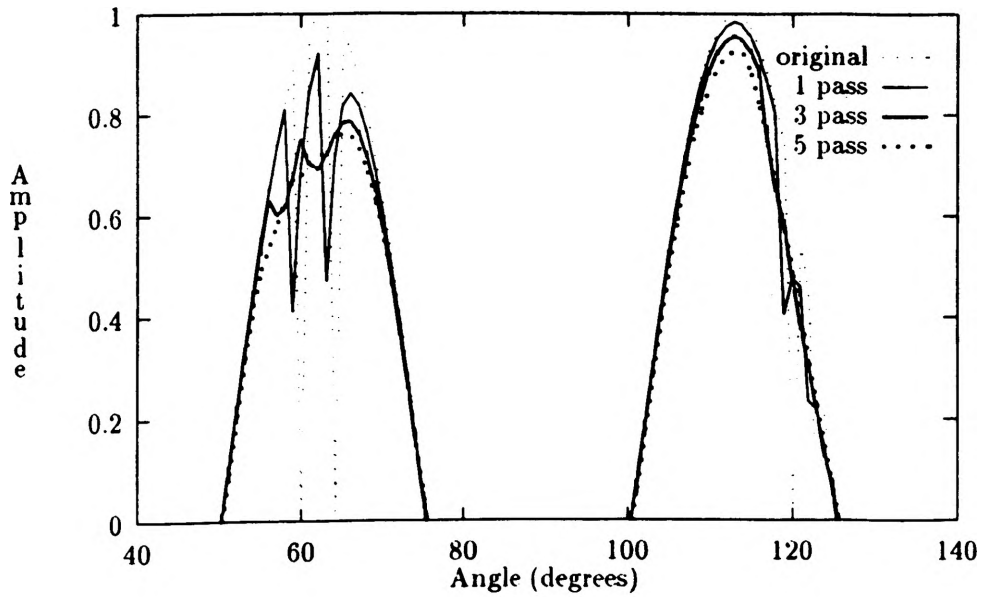
Figure 5: Comparison of multiple relaxation passes on sharp peak
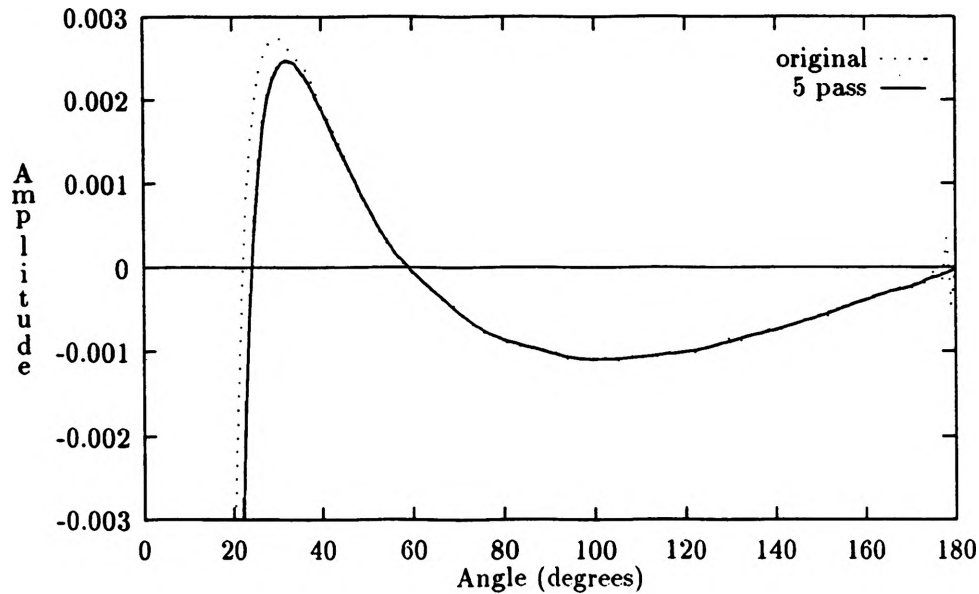
Figure 6: Amplitude curve

4 CONCLUSIONS

Areas of gentle slopes produce great results with very few passes through the algorithm; however, the shifts in the area of steep and rapidly changing slopes is a serious problem. These changes seem to be related to the slope and arc of the curve at a specific point. Several variables must be taken into account to improve this method of fitting. These would include the range on the y axis, the slope of the curve at a point, and the arc of the curve at each point. The y axis range should be considered, because the relation of the axis range to the range of the distortion that needs to be fitted tends to vary among the amplitude curves. The arc and amplitude of the arc could provide vital information on whether the curve area is gentle wiggles to be fitted or a peak to be left alone. Initial studies into a slope dependent factor being used to adjust the Δy from equation (12), has proven to lessen the effects of the amplitude shifting.

Further study is required to produce an algorithm which would work in the general case of curve fitting. Based on the results of the initial studies of a slope dependent factor, it seems possible to produce dampening routines or an intelligent algorithm to make use of the above variables, and lessen the effects to those areas where relaxation is not needed or desired.

5 ACKNOWLEDGEMENTS

372

6   REFERENCES

Paszkowski, Bohdan. *Electron Optics.* Iliffe Books Ltd., Great Britain, 1968, pp. 77-87.

FORCED CONVECTIVE DIFFUSION
AND
INTERPHASE HEAT AND MASS TRANSFER:
COMPUTATIONS OF RADIAL FUNCTIONS, TEMPERATURE AND
CONCENTRATION FIELDS, AND PRESENTATION OF
LOCAL AND AVERAGE NUSSELT AND SHERWOOD NUMBERS

Opportunities for Undergraduate Research Experience Report

X B Reed, Jr.[1], N. Y. Shah[2] A. E. Penn[3] S. Myers[3,4]
Chemical Engineering Department
University of Missouri-Rolla
Rolla, MO 65401

[1]Professor, to whom correspondence should be addressed
[2]Doctoral student
[3]Senior student
[4]OURE student

Abstract

Theoretical calculations have been carried out for forced
convective transport for uniform streaming and uniaxial and
biaxial extensional axisymmetric flows past single spheres.
Homogeneous and heterogeneous chemical reactions, both of first
and of second order have also been or are presently being
treated. Orthogonality and other properties of Legendre
functions have been used, together with introduction of an
eigenfunction expansion, to reduce the mathematical description
from a partial differential equation with variable coefficients,
which is nonlinear for homogeneous second order chemical
reactions, to a system of coupled ordinary differential equations
for the radial modes. The numerical solutions of the latter have
been obtained using the robust, adaptive grid algorithm of
Pereyra and Lentini. Plots of the radial functions for given
Peclet and Damköhler numbers give insight into the role and
interaction of L and of r_∞ (the number of terms necessary for
convergence of the expansion and the finite radius at which the
boundary conditions at infinity are imposed). From the radial
modes, local and average Nusselt and Sherwood numbers, as well as
the temperature and concentration fields, can be obtained. Plots
of radial function families provide new insights that complement
physicochemical understanding gained from isocontour plots of the
temperature and concentration fields. Plots of local interphase
transfer coefficients reflect the behavior of the flux field over
the sphere surface and show how the average coefficients arise.

1. INTRODUCTION

This preliminary report covers a limited set of computations on several novel, potentially significant physicochemical processes while pointing out some computational and presentational limitations.

All but one of the basic elements of the physicochemical processes are hardly novel. We consider steady forced convective diffusion of temperature or of a reactant undergoing a homogeneous or a heterogeneous chemical reaction. The reaction may be first or second order. The geometry is spherical. The domain is the semi-infinite one external to a solid sphere. The convecting velocity field, moreover, is axisymmetric, solenoidal, and satisfies the steady, linearized Navier-Stokes equation and the no-slip condition at the surface of the sphere.

What is novel about this forced convective diffusion-reaction problem is the remaining element, the boundary condition imposed on the velocity field far from the sphere. It is not always the uniform streaming flow of Stokes (1842; see also Lamb, 1932; Happel and Brenner, 1965; Leal, 1992) but includes the low Reynolds number, axisymmetric extensional motion important in the rheology and flow of dispersions and elsewhere (see, e.g., Leal, 1992). This lends an importance to the problem beyond that of being an Re≪1 convective diffusion-reaction class of problems that are axisymmetric yet not the simplest problem of this class. The incorporation of axisymmetric extensional flows into the class of forced convection problems nonetheless enlarges

the class considerably, taking it in fundamentally new directions having significantly different ranges of applications.

The biaxial extensional flow approaches the sphere from the poles at $z = \pm \infty$ and departs in the equatorial latitudes, doing so radially symmetrically in the equatorial plane. The uniaxial extensional flow has the same streamlines as the biaxial one; the direction of the flow is, however, reversed along the same streamlines, approaching the sphere at the equatorial latitudes and departing in the opposite directions, from the poles of the sphere.

For a more complicated yet axisymmetric flow, what are some of the issues which might arise? For a given Peclet number, will the average Sherwood numbers have about the same values for the biaxial and uniaxial flows? Or will the magnitudes of the locally enhanced contributions in the stagnation region(s) of one flow, which correspond roughly to locally reduced contributions in the separation region(s) of the other flow, be significantly different? Or, again phrased oversimplistically, will they be comparable? Or will the area of enhanced (reduced) equatorial interphase mass transfer be greater or less than the area of reduced (enhanced) transfer at the poles for the uniaxial vs. the biaxial flow, whether or not the magnitudes of the fluxes are comparable in those regions.

The study of extensional flows for the forced convective diffusion problem without reaction was initiated by Shah and Reed (1994). For the convective diffusion problem, the passive

additive could be either temperature or concentration (Shah and Reed, 1994). The passive additive field $\theta(r,\theta)$ was obtained as a function of the Peclect number Pe, as were the average and local Nusselt numbers for heat or mass transfer, Nu and $Nu(\theta)$; in chemical engineering, the latter are more commonly called the average and local Sherwood numbers, Sh and $Sh(\theta)$, respectively, if the passive additive is the concentration field $c(r,\theta)$. In the present study, samples of $c(r,\theta)$, Sh, and $Sh(\theta)$ are reported as functions of Pe and of Da_{II} (or Da_I), the second (or first) Damköhler group, which is the chemical rate constant made dimensionless with the diffusive (or convective) time scale. Answers to such questions as were posed above will be answered in the course of this research program.

The effects are already subtle for the convective diffusion problem, and inferences about magnitudes of local fluxes and resultant averages over the sphere surface for convective diffusion-reaction conceivably could follow intuitively from the results for convective diffusion in the absence of homogeneous reactions. Conversely, the qualitative effects of the reaction may not be so trivially inferred from convective diffusion alone. Overall mass transfer coefficients for a given flow, whether biaxial or uniaxial, would be enhanced by reaction and increasingly so by a faster reaction. Yet local effects for biaxial flows could conceivably be affected differently by reaction than those for uniaxial flows.

In Section 2, we sketch the theoretical analysis leading to

the system of ordinary differential equations for the radial

modes for axisymmetric extensional flows convecting a diffusing

chemical species that may undergo a first order (or no) reaction;

from the radial modes, the full concentration field can be

obtained, as can the local and average Sherwood numbers. In

Appendix II, the analogous analysis and results are outlined for

a uniform streaming flow and for a second order reaction.

In Appendix I, a variety of results are presented. The

computational limitations that can arise and the manner in which

different limitations manifest themselves are discussed, both

there and in Section 3, in which the perspective is broader than

the litany of specific cases discussed in Appendix I. Finally,

in Section 4 we stress the importance of the research program

that is under weigh.

2. PHYSICOCHEMICAL BACKGROUND AND THEORETICAL FORMULATION

If by any physicochemical process the concentration of a reactant

is maintained constant at the surface of a solid sphere, and if

the reactant is yielded up to a surrounding fluid where it

undergoes an irreversible first order homogeneous chemical

reaction, as well as forced convective diffusion, then the

reactant concentration satisfies the dimensionless partial

differential equation

$$Pe \; v \cdot \nabla c = \nabla^2 c - Da_{II} c, \quad \text{for } 1 < r < \infty, \tag{1}$$

subject to the boundary conditions

$$c = 1, \quad \text{at} \quad r = 1, \tag{2}$$

$$c \to 0, \quad \text{as} \quad r \to \infty. \tag{3}$$

The axisymmetric extensional velocity field convecting the reactant satisfies the adherence condition at $r = 1$. The boundary condition at infinity is, in <u>circular</u> <u>cylindrical</u> coordinates,

$$(v_\rho, v_z) \to \pm (\rho, -2z), \tag{4}$$

with the plus sign indicating the biaxial flow, the negative sign the uniaxial flow. If further the velocity field is solenoidal and satisfies the linearized Navier-Stokes equation, then it may be expressed in terms of the <u>spherical</u> geometry as

$$v_r = \pm F(r) (1 - 3\cos^2\theta), \tag{5}$$

$$v_\theta = \pm G(r) (3\sin\theta\cos\theta), \tag{6}$$

$$v_\phi = 0, \tag{7}$$

in which

$$F(r) = r - \left(\frac{5}{2}\right) \frac{1}{r^2} + \left(\frac{3}{2}\right) \frac{1}{r^4},$$

$$G(r) = 1 - \frac{1}{r^5},$$

and in which +/- refers throughout to biaxial/uniaxial extensional flow.

The radius a of the sphere has been used as the characteristic length scale, and the strain rate $|E|$ of the flow far from the sphere has been employed to form the characteristic

velocity $|E|a$. The Peclet and the first and second Damköhler

numbers are defined in the usual manner for a first order

reaction, except that in an unusual though not singular manner

the characteristic length is taken to be the radius a __throughout__

(i.e, in the Sherwood numbers Sh and Sh(θ), as well):

$$Pe = |E|a^2/D,$$

$$Da_I = k/|E|,$$

$$Da_{II} = k\ a^2/D = Da_I Pe.$$

The local value of the Sherwood number is the local

dimensionless flux at the surface,

$$Sh(\theta) = -\ \partial c(r,\theta)/\partial r \qquad at \quad r = 1. \tag{8}$$

The average or overall mass flux Sh is then given by

$$Sh = \tfrac{1}{2} \int_{\theta=0}^{\pi} Sh(\theta)\sin\theta\ d\theta \tag{9}$$

The dependent variables $c(r,\theta)$, $Sh(\theta)$, and Sh, are to be

determined in terms of the parameters Pe and Da_{II} (or Da_I). The

second Damköhler group has the advantage that it may be

expressed solely in terms of physicochemical properties (the

chemical rate constant and the molecular diffusivity) and the

radius. All convective effects then reside in the Peclet number.

The eigenfunction expansion

$$c(r,\theta) = \sum_{\ell=0}^{\infty} c_\ell(r) P_\ell(\cos\theta), \tag{10}$$

in which the $P_\ell(\cos\theta)$ are Legendre functions and the radial

functions $c_\ell(r)$ are the unknowns to be determined, is introduced

382

into Equation (1) and boundary conditions (2) and (3), along with (5), (6), and (7). Several properties of the Legendre functions are then used (Shah and Reed, 1994), the last of which is their orthogonality (e.g., Abramowitz and Stegun, 1964). The result of the calculations is an infinite system of coupled ordinary differential equations for the radial functions,

$$
\begin{aligned}
\pm \text{Pe} & \left\{ \left[F(r) \frac{dc_k}{dr} - 3 \left[\frac{(k+1)^2}{(2k+3)} + \frac{k^2}{(2k-1)} \right] \right] \left[F(r) \frac{dc_k}{dr} - kG(r)c_k \right] \right. \\
& - 3 \left[\frac{k(k-1)}{(2k-1)(2k-3)} \right] \left[F(r) \frac{dc_{k-2}}{dr} - (k-2)G(r)c_{k-2} \right] \\
& \left. - 3 \left[\frac{(k+1)(k+2)}{(2k+3)(2k+5)} \right] \left[F(r) \frac{dc_{k+2}}{dr} + (k+3)G(r)c_{k+2} \right] \right\} \\
& = \mathcal{L}_k c_k - \text{Da}_{II} c_k,
\end{aligned}
$$

in which,

$$
\mathcal{L}_k = \frac{1}{r^2} \frac{d}{dr} \left(r^2 \frac{d}{dr} \right) - \frac{k(k+1)}{r^2},
$$

subject to the boundary conditions

$$ c_0 \ (r = 1) = 1, \tag{12a} $$

$$ c_\ell \ (r = 1) = 0, \ \ell \geq 1, \tag{12b} $$

$$ c_\ell \ (r \to \infty) \to 0, \ \ell \geq 0. \tag{13} $$

In these equations, for $\ell < 0$, $c_\ell \equiv 0$.

The velocity field plays the role of a pair of variable coefficients (Equations (5), (6)) in the forced convective

diffusion partial differential equation for $c(r,\theta)$, Equation (1).
If there were no angular velocity component <u>and</u> if the radial
component depended solely upon the radius, then the radial modes
$c_\ell(r)$ would not be coupled to one another. That is, if $\underline{v}$ =
$v_r(r)\underline{i}_r$, then the system, Equations (11), would not be coupled.
Neither is true, so that $v_\theta = v_\theta(r,\theta) \neq 0$ and $v_r = v_r(r,\theta)$ for
different reasons necessitate no small amount of theoretical
calculations in order to arrive at Equations (11), which become
the corresponding equations of Shah and Reed (1994) upon setting
$Da_{II} = 0$. The treatment of second order reactions for uniform
streaming flow and the reduction to the corresponding system of
ordinary differential equations is presented in Appendix II.

Numerical methods would be required in the solution of
Equations (11) because of the variable coefficients in r, even if
they were not coupled. Equations (11), (12), (13) constitute the
boundary value problem which we solve using the adaptive grid
method of Pereyra and Lentini (Pereyra, 1967, 1968, 1975, 1978;
and Lentini and Pereyra, 1974, 1978).

3. COMPUTATIONAL FEATURES

To implement the algorithm, the series must be terminated at
a finite value L (i.e., $c_\ell(r) = 0$, $\ell > L$), and the infinite domain
must be made finite by selecting a finite radius r_∞ (denoted by R
on the figures) at which the boundary conditions (13) are
imposed. L must be large enough that the series (10) has

converged to the desired accuracy. Unfortunately, L cannot be known *a priori* because it must be specified <u>before</u> the $c_\ell(r)$ can be computed. The optimal selection of L depends upon Pe, Da_{II}, r_∞, and the computer available for the computations. Similarly, the optimal selection of r_∞ depends upon Pe and Da_{II} for a given computer.

Generally speaking, for a given computer, as Pe and Da_{II} increase, L must be increased and r_∞ decreased. The tolerance and the initial and the maximum number of mesh points must also be specified, and they play crucial roles which are both subtle and interrelated, not only with one another, but with the parameters of the problem Pe and Da_{II} and with the other major players of the algorithm, L and r_∞.

In earlier research on the forced convective diffusion of a passive additive by a uniform flow (Spears and Reed, 1991; Reed, Spears, and Shah 1994), and for forced convective diffusion by the same flow of a reactant undergoing a first order reaction (Reed, 1994) or a second order reaction (Shah, Kleinman, and Reed, 1994), moderate to high values of Pe and of $Da_{I\ or\ II}$ could be reached on the local IBM 4381, the exception being a relatively mild one for Pe and a much stronger one for Da_I for the second order homogeneous reactions.

In the research described above, for which the convecting velocity is an extensional one, we are limited to much smaller values of Pe and $Da_{I\ or\ II}$ by the IBM 4381.

In this preliminary report we do not attempt to present —

indeed, we do not yet have — extensive results. Instead, we focus on some of the different kinds of difficulties that can arise for the various problems, as well as indicating some typical results (Appendix I).

On the IBM 4381, the maximum number of radial modes L+1 for which computations can be carried out is about 33. More recently, computations have been carried out on the IBM RS 6000 and HP 9000 series, for which significantly higher values of L could be computed. This has enabled us to compute more accurately with more realistic values of r_∞. In particular, for r_∞ too small, the radial functions — and thence most derivative results except occasionally the average Nusselt and Sherwood numbers — can be distorted by the relatively close proximity of r_∞ to $r=1$.

In addition, the radial plots for the first vintage of results are all shown as one plot to a page (with typically 6 radial functions to a plot). This made it difficult to compare different cases, and it made it difficult to get an overview of all of the radial functions for a single case. Our first improvement was to reduce the plot size while putting more plots (6) to a page; this enabled us to present $c_0 - c_L$, for L up to 35, on a single page. With the acquisition by UMR of the NIC (numerically intensive computers, in local terminology) IBM RS 6000 and the HP 9000 workstations, we can reach significantly higher values of L than 35. Because smaller plots cannot be read and more curves to a plot make for "too busy" a plot, rather than

attempting to display all radial plots on a single page, we have

now developed the capability of sequential pages, each with 6

plots to a page.

In Appendix III, radial plots for computations on the HP

9000 for L = 70 are shown for Pe = 10 and r_ω = 100. An r_ω of 100

is a factor of more than two larger that what could have been run

on the IBM 4381 for the same case, yet it is clear from the plots

that the series has converged by L=70. For still larger values

of Pe, values of L of order 100 become necessary, a capability we

have for the plots. But for L very much beyond 100 we encounter

memory limitations on the HP 9000. Thus, although these

computations are CPU intensive, they are not inordinately so, as

measured against our local capabilities. The computations are

above all memory intensive. With the 128 MB of RAM available on

the cluster of IBM RS6000 and HP9000 machines which are used as

campus-wide, multi-user computers, we typically have difficulty

with runs projected to require ~ 100 MB.

4. SIGNIFICANCE OF AND PERSPECTIVES ON THE RESEARCH

There are several features of the past, present, and future

research that are noteworthy.

(i)   For the practicing engineer, but no less for the

         scientist and engineering scientist, the overall

         dimensionless interphase transfer coefficients Nu and

         Sh are of the greatest importance and will be used in

applications, both widely and immediately.

(ii)   But the local Nusselt and Sherwood numbers $Nu(\theta)$, $Sh(\theta)$
         are also of direct utility, as well as being of
         fundamental significance, for the local properties
         $Nu(\theta)$ and $Sh(\theta)$ offer insight into the manner in which
         the macroscopic properties Nu and Sh arise.

(iii)   The temperature and concentration fields $\Theta(r,\theta)$ and
         $c(r,\theta)$ are too often considered to be only a means to
         an end by the practicing engineer, the end being the
         dependence of Nu and Sh, or perhaps $Nu(\theta)$ and $Sh(\theta)$, on
         Pe (and on Da_{II} for reacting systems). Yet $\Theta(r,\theta)$ and
         $c(r,\theta)$ in turn provide insight into the nature of $Nu(\theta)$
         and $Sh(\theta)$, just as they provide insight into Nu and Sh.

An understanding of the character of the passive additive
field and especially its boundary layer(s) and its wake(s)
enables one to develop intuition and to make engineering
estimates of the manner in which and the extent to which, for
instance, chemical reactions affect the concentration field and
thereby enhance mass transfer. In a multiparticle system,
knowledge of the passive additive boundary layers and wakes
enables one to make estimates of the interparticle distance at
which interphase transfer could no longer be assumed to be an
additive property of the individual particles, even in the
absence of meaningful hydrodynamic interactions.

(iv)   Finally, in the same manner in which Fourier modes and
         spectra offer an alternative way of thinking about

fields, so also do radial functions provide a deeper insight into θ(r,θ) and c(r,θ). And the number of coupled modes in a given modal differential equation that arise from different convective, diffusive, or reactive contributions has the same sorts of advantages in offering completely different perspectives that Fourier modes and modal coupling have in wave and other physical and chemical phenomena, right up to the level of complexity of pattern and chaotic behavior.

Overriding all of the above, however, are the <u>completely different classes of flow fields</u> and concomitant <u>new classes of forced convective diffusion</u> and <u>diffusion-reaction problems</u> attacked in this research program.

There are a number of different research directions in this general area which could be pursued. For forced convective diffusion about a solid particle, with or without chemical reaction, in addition to the convective to diffusive effect as measured by the Peclet number Pe, there is the inertial to viscous effect characterized by the Reynolds number Re. Because Pe = Re Sc or RePr, an increase in Re has a profound effect on forced convection. This is true not solely in the sense of increasing Pe parametrically, but in modifying the very nature of the velocity field; with increasing Re the velocity first manifests fore-aft asymmetry of the streamlines, then a clear momentum boundary layer-wake, and eventually a closed, recirculating wake (e.g. Batchelor, 1967). This research

direction, in which Re is increased, has been taken earlier by A. Acrivos, B. T. Chao, D. W. Moore, B. A. Finlayson, and others. The present research is predicated in the first instance on an (r,θ)-separable velocity field, and in the second on the θ-dependence being exactly expressible in terms of a finite number of Legendre functions. The PI's approach does not preclude velocity fields that do not satisfy the linearized Navier-Stokes equations. And although there are <u>approximate</u> solutions to the full Navier-Stokes equations for uniform streaming flow past a solid sphere for Re > 1, there are no such exact solutions.

The PI has elected to limit the present stage of his research program to Re < 1 — physically, to small particles or very viscous fluids — but to consider other flows than the uniform streaming flow, and for the case of a uniform streaming flow to incorporate reactions into the flowing medium or at the surface of the solid sphere.

The PI's overriding concern was thus not to simply extend the range of the values of the parameters for a given class of problems, but to carry the research into entirely new classes of problems, either by dent of new classes of convecting velocities or by dent of incorporating homogeneous second order reactions, rather than just bringing first order ones into the ambit. The classes of problems would also be enlarged to include consideration of heterogeneous reactions, both linear and nonlinear.

390

Solvent Recovery for an Extraction Process

Denise C. Ratcliff

Department of Chemical Engineering

University of Missouri-Rolla

ABSTRACT

The solvent recovery project involves the recovery of a valuable solute, acetic acid, from a spend solvent stream generated in a laboratory extraction experiment. The majority of this project's efforts center on the simulation of a ten-stage distillation column that will recover the acid. These simulation results will then be used to specify the ancillary process equipment needed for this distillation process.

INTRODUCTION

Description

The solvent recovery project represents a small part of the University of Missouri-Rolla Chemical Engineering Department's efforts to develop a zero-waste laboratory. This laboratory, when completed, will perform the multicomponent separation of an acetic acid/ethyl acetate/water system. The completed laboratory will accomplish the zero-waste goal by integrating three mass transfer unit operations - extraction, distillation, and adsorption. Since the separation of acetic acid from water represents the key step in the zero-waste laboratory, we have decided to focus our study on the distillation process used for this separation.

The relative volatility between acetic acid and water, especially at low acid concentrations, is very close to unity (less than 1.2 below acid mole fractions of 0.1). This makes the purification of the water-rich distillate extremely difficult. The presence of an entrainer, such as ethyl acetate, can potentially increase the separation between the acid and water and thus represents an avenue that we will explore in this paper.

Koch Industries, a manufacturer of a variety of mass transfer process equipment, has pledged a ten-stage, bubble-cap column for the acetic acid/water separation so our design is constrained. To achieve our desired goal of recycling both the acid and water, our simulation studies explore process variables, such as feed location, thermodynamic state of the feed, and reflux ratio subject to this ten-stage constraint. These results will aid in the design of ancillary process heat exchange equipment, such as the reboiler and condenser.

Rationale for Project

We have two main motivations for the zero-waste laboratory. The first is simply the cost associated with offering laboratories that use chemicals. The cost to purchase and dispose of chemical solvents continues to escalate without appreciable increases in the university operating budget to offset this cost. The fact that universities are now subject to substantial fines if they violate EPA regulations for the safe storage and disposal of chemicals only exacerbates the problem. Therefore, if the UMR Chemical Engineering Department is to offer meaningful laboratory courses that deal with real chemical systems, they must develop a program that reduces chemical waste.

The second motivation for the zero-waste laboratory centers on the development of educational experience that actively promotes the reduction of chemical waste in the laboratory. Three

approaches could be taken: the first would be a computer-simulated laboratory where the use of any chemicals is totally eliminated; the second would be a laboratory experience where only innocuous chemicals, such as water and air, are used; a third approach would be a laboratory where the chemicals are recycled. The first two alternatives seriously undermine the educational objectives of UMR's Chemical Engineering Department, which seeks to train engineers who can safely design chemical processes and conduct experimental chemical process research and development. Therefore, we have decided to handle both the health and safety issues and educational objectives by developing new laboratory experiments that process our chemical laboratory waste.

APPROACH

The major thrust of this project was the separation of acetic acid and water using a ten equilibrium stage distillation column. Figure I shows the vapor-liquid equilibrium for the acetic acid/water at 1 atm. These data were obtained from a flash calculation performed using the Aspen Plus simulation package and physical properties package SYSOP07D, which uses the UNIFAC liquid activity coefficient model and Hayden-O'Connell method to describe dimerizable acetic acid in the vapor phase. Figure I shows that at increasing dilute acid concentrations the relative volatility between the acid and water approaches unity.
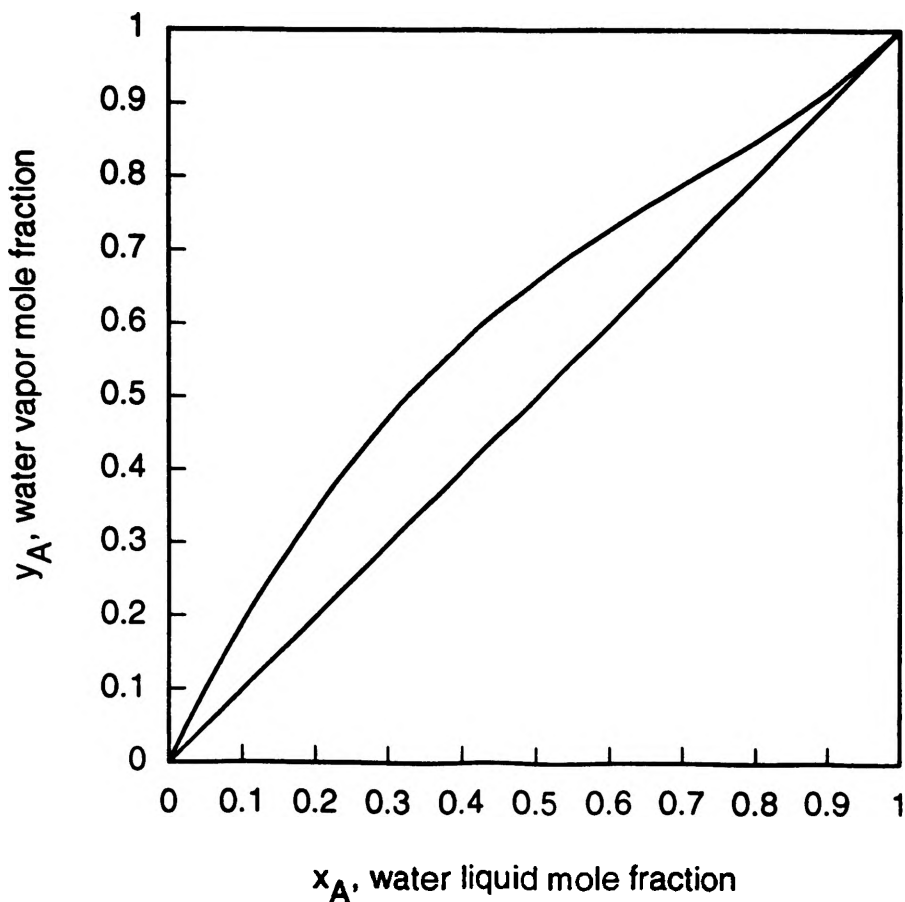
Figure I. Vapor-Liquid Equilibrium for Acetic Acid/Water at 1 atm

Table I shows this relationship more clearly.

Table I. Relative Volatilities Between Acetic Acid and Water at 1 atm as a function liquid water mole fraction. A represents water and B represents the acid.

x_A	α_{AB}
0.0	3.24
0.1	2.09
0.2	2.09
0.3	2.08
0.4	2.02
0.5	1.93
0.6	1.79
0.7	1.60
0.8	1.39
0.9	1.20
1.0	1.31

For the sake of simplicity, we decided to first study the separation of 50/50 mixtures of acetic acid and water and a feed flow rate of 100 lb mol/h. This allows us to establish base cases from we can compare our simulations. Eventually, we will simulate the column using acid mole fractions between 0.15 and 0.05, which more closely represent the waste solvent stream that the extraction process generates.

STUDIES COMPLETED WITH RESULTS

The first case studied involved the separation for a single-feed distillation column. We tested various feed locations to identify the optimum feed location. The optimum feed stage location corresponds to one that gives the highest degree of separation. For the case of 50/50 feed mixture, reflux ratio of four, and bottoms rate of 40 lb mol/h, the optimum feed location is the fourth tray. This case recovered 79 percent of the acid with a bottoms acid mole fraction of 0.9901. The optimum feed location was found to be dependent on the reflux ratio and draw ratio of the distillate and bottoms product. Because of this dependence, we chose a feed stage of four for our base case from which we have made our subsequent comparisons.

The second study tested the effect of an ethyl acetate entrainer at a modest reflux ratio of one. The presence of ethyl acetate dramatically increased the purity of acetic acid as the amount of entrainer mole fraction was increased from 0.0 to 0.2 while maintaining a 50/50 mole ratio of acid to water. We also adjusted the bottoms and distillate product draws to compensate for the increased amount of ethyl acetate. Table II summarizes the effect of the acetate entrainer.

A third case studied the effect of a two-enthalpy feed. Wankat and Kessler [1] suggested that a new method of distillation could increase the separation for a fixed number of stages and constant reflux ratio, especially for 50/50 mixtures. The method should also yield a reduction in energy demand because the reflux ratio can be reduced for the same desired separation as that of the single feed case. We tested the case of a liquid feed at stage five and a vapor feed at stage seven but saw no improvement in separation. As predicted by Wankat and Kessler, we did see a dramatic reduction in the reboiler duty. Table III provides detailed information on the two-enthalpy feed case study.

393

TABLE II. ENTRAINER CASE STUDY

	Feed Type	Feed Stage	Feed Flow (lbmol/hr)	Mole Frac. AA in Feed	Mole Frac. H2O in Feed	Mole Frac. EA in Feed	Distillate Flow (lbmol/hr)	Bottoms Flow (lbmol/hr)	Reflux Ratio	
1	Liquid	5	100	0.5000	0.5000	0.0000	50	50	1	
2	Liquid	5	100	0.4900	0.4900	0.0200	51	49	1	
3	Liquid	5	100	0.4750	0.4750	0.0500	52.5	47.5	1	
4	Liquid	5	100	0.4500	0.4500	0.1000	55	45	1	
5	Liquid	5	100	0.4000	0.4000	0.2000	60	40	1	

	Recovery Acetic Acid	Recovery H2O	Condenser Duty (Btu/hr)	Reboiler Duty (Btu/hr)	Mole Frac. AA in Distillate	Mole Frac. H2O in Distillate	Mole Frac. EA in Distillate	Mole Frac. AA in Bottoms	Mole Frac. H2O in Bottoms	Mole Frac. EA in Bottoms
1	0.7918	0.7918	-1654510	1671760	0.2081	0.7918	0.0000	0.7918	0.2081	0.0000
2	0.7710	0.7710	-1734380	1739960	0.1897	0.7710	0.0392	0.8025	0.1974	0.0000
3	0.7430	0.7716	-1784510	1791370	0.1903	0.7716	0.0381	0.8212	0.1787	0.0000
4	0.6993	0.7720	-1867740	1877130	0.1915	0.7720	0.0364	0.8547	0.1452	0.0000
5	0.6185	0.7685	-2029870	2045870	0.1961	0.7685	0.0333	0.9277	0.0722	0.0000

TABLE III. TWO FEED EFFECTS ON SEPARATION AND ENERGY REQUIREMENTS

	Feed1 Type	Feed1 Stage	Feed1 Flow (lbmol/hr)	Feed2 Type	Feed2 Stage	Feed2 Flow (lbmol/hr)	Mole Frac. A in Feed	Mole Frac. H2O in Feed	Mole Frac. EA in Feed	Distillate Flow (lbmol/hr)	Bottoms Flow (lbmol/hr)	Reflux Ratio
1	Liquid	5	100	—	—	—	0.5000	0.5000	0.0000	50	50	4
2	Liquid	5	100	—	—	—	0.5000	0.5000	0.0000	50	50	2
3	Liquid	5	100	—	—	—	0.5000	0.5000	0.0000	50	50	1
4	Liquid	5	50	Vapor	7	50	0.5000	0.5000	0.0000	50	50	4
5	Liquid	5	50	Vapor	7	50	0.5000	0.5000	0.0000	50	50	2
6	Liquid	5	50	Vapor	7	50	0.5000	0.5000	0.0000	50	50	1

	Recovery Acetic Acid	Recovery H2O	Condenser Duty (Btu/hr)	Reboiler Duty (Btu/hr)	Mole Frac. AA in Distillate	Mole Frac. H2O in Distillate	Mole Frac. E in Distillate	Mole Frac. AA in Bottoms	Mole Frac. H2 in Bottoms	Mole Frac. EA in Bottoms	
1	0.8707	0.8707	-4254080	4282620	0.1292	0.8707	0.0000	0.8707	0.1292	0.0000	
2	0.8389	0.8389	-2524810	2548410	0.1610	0.8389	0.0000	0.8389	0.1610	0.0000	
3	0.7918	0.7918	-1654510	1671760	0.2081	0.7918	0.0000	0.7918	0.2081	0.0000	
4	0.8724	0.8724	-4256790	3557560	0.1275	0.8724	0.0000	0.8724	0.1275	0.0000	
5	0.8345	0.8345	-2520920	1815770	0.1654	0.8345	0.0000	0.8345	0.1654	0.0000	
6	0.7713	0.7713	-1641560	928207	0.2286	0.7713	0.0000	0.7713	0.2286	0.0000	

CONCLUSIONS

Our work is still very preliminary but we can conclude that the presence of an entrainer substantially improves the acid purity. Also we have reduced the reboiler duty by using a two-enthalpy feed. This method does not necessarily reduce that overall energy demand of the distillation process but it does reduce the temperature at which the energy must be supplied.

FUTURE PLANS

In this work, we used the Aspen Plus properties option set SYSOP07D to estimate the vapor-liquid equilibrium (VLE) for the acetic acid/water/ethyl acetate system. We feel that the description of the ternary VLE can be improved by fitting the experimental binary VLE data [2] to the

UNIQUAC liquid activity coefficient model. Other studies we feel warrant further investigation are:

- the effect of the two-enthalpy feed method at lower acetic acid feed concentrations, and

- the effect of entrainer at lower acetic acid feed concentrations

We hope to achieve substantial improvements in the acetic acid purity over what would result from the standard single feed column.

NOMENCLATURE

AA - Acetic Acid
H2O - Water
EA - Ethyl Acetate

ACKNOWLEDGMENTS

REFERENCES

1. Wankat, P.C. and D.P. Kessler, "Two-feed Distillation: Same-Composition Feeds With Different Enthalpies," *Ind. Eng. Chem. Res.*, Vol. 32, No. 12, pp. 3061-3067.

2. Wichterle, I., J. Linek, and E. Hala, *Vapor-Liquid Equilibrium Data Bibliography*, Elsevier, Amsterdam, 1973 (plus three supplements: 1976,1979, 1982).

CCD PHOTOMETRY AT THE UMR OBSERVATORY

Christopher P. Smith

Department of Physics, University of Missouri-Rolla, Rolla, Missouri 65401

ABSTRACT

During the summer of 1993 a number of advances at the University of Missouri-Rolla's observatory have taken place. These advances range from cleaning the mirrors and polar aligning the 16-inch Cassegrain telescope to the acquisition of needed supporting material. A program for observing variable stars, implementing the newly acquired CCDIR image reduction program, searching galaxies for supernova, and the possibility of adding low resolution stellar spectroscopy to our research capabilities will be discussed. This manual will discuss how to implement the new CCDIR program.

INTRODUCTION

The summer of 1993 proved to be a challenging time in which to make astronomical observations. The lack of clear evenings hampered our attempts to make long term studies of celestial objects. However, we were able to make several repairs to our existing facilities and also acquire improved supporting materials.

The completed repairs include the cleaning of the mirrors of the telescope and the just completed polar alignment. The new supporting materials include the purchase of a Celestron C-80 telescope, the construction of a new carrying case for the CCD camera, the purchase of several variable star charts from the AAVSO, and the purchase of the CCD image reduction program CCDIR. These repairs and acquisitions will aid in the progress of future research projects.

For future research projects the new star charts and CCDIR program will be indispensable. The repairs to the telescope have been seen to have lowered our detection limit by almost two magnitudes. We have also

considered the possibility of providing the apparatus necessary to conduct low resolution stellar spectroscopy.

I. SUMMER OBSERVING SETBACKS

With the summer of 1993 came the rains of 1993 ushering in the wettest summer on record. These rains made observing almost impossible due to the lack of clear nights. The beginning of the summer was to be used for myself to become quite familiar with how the telescope and CCD camera operated together. Unfortunately, this process took substantially longer due to the lack of clear nights.

However, in spite of the overcast conditions we were able to carry out several repairs (§ II.) which have improved the quality of our observational data.

II. ADVANCES

The first repair conducted was the cleaning of the primary and secondary mirrors of the 16-inch telescope. With the aid of Dr. John Schmitt and David A. Thilker, the mirrors were painstakingly washed with cotton balls soaked in acetone. It should be noted that this procedure should NOT be done without Dr. Schmitt present. After initially cleaning the mirrors with acetone they were then rinsed with water to remove any further dust that was not removed with the cotton balls. This procedure has decreased the amount of scattering in the collected light. This has resulted in better image quality and has also lowered our detectable limit of stars down to approximately 17th magnitude, an almost two magnitude improvement.

The most recent repair, completed on 29 July 1993, was the polar alignment of the telescope. The procedure followed was that given by Sidgwick[1]. The motivation for this polar alignment was two fold. First, the realignment of the telescope has helped to minimize the tracking error caused by the aging electronics and stepper motors in the tracking system. Second, the declination and hour angle circles have been reset to roughly the correct positions. Having reset these, one can now find the declination and hour angle of an object and then simply adjust the telescope to these coordinates. We have found that the object of interest now usually appears in the field of view of the C-80 finder scope. Prior to this alignment, the declination was off by about two degrees and the hour angle off by several minutes. These discrepancies made locating any object extremely difficult. It would at times take

up to an hour to locate a single object. Now, though, the time required to locate an object has been decreased by about a factor of two.

The acquisition of the Celestron C-80 finder telescope has proved to be invaluable. This telescope has a field of view roughly five times that of the main telescope. With this larger field of view, locating the object of interest has become far easier.

Another problem in locating various objects, i.e., variable stars, has been the lack of adequate star maps. The computer programs that had been used in the past showed stars down to a magnitude of only 9.0. Unfortunately, we cannot limit the magnitude of stars seen to only 9th magnitude. This has made it somewhat difficult to locate some of the fainter objects. Also, many variable stars, at their brightest, are fainter than 9th magnitude. It is these stars that are of the most interest due to the lack of observational data collected from them. To this end we have ordered the Variable Star Atlas and about 125 individual variable star charts from the American Association of Variable Star Observers (AAVSO). The Variable Star Atlas shows stars down to 9th magnitude while the individual charts show stars down to around 11th magnitude. All of these charts will make the locating of the variable stars substantially easier. The programs we have been using do not give any indication of whether a star is a variable or not, so we had to rely on coordinates only obtained from various sources. As noted earlier, until the polar alignment locating an object on coordinates alone, with no star charts of the area, was impossible.

To be able to make serious variable star observations it is necessary to extract the stars magnitude from the CCD image. In order to avoid doing these calculations by hand, the CCDIR Astronomical CCD Image Reduction program was purchased. This program will accept image files in the FITS file format after being processed by conversion program accompanying the CCDIR program. A complete description of how to implement the program can be found in the observer's manual attached to the end of this report.

Two other measures were taken in order to enhance or observational facilities. The first was the construction of a carrying case for the CCD camera. Until recently, the CCD camera was moved to and from the observatory via a cardboard box filled with styrofoam "peanuts." We realized that in time this method of transportation could result in the damage of the camera. With a carrying case donated to us from the Cloud and Aerosol Sciences Laboratory and packing foam from a laser shipping case we have constructed a safe storage case

for the camera and its accessories. This case greatly increases the safety and ease of transporting the CCD to and from the observatory.

Secondly, Dr. Ron Bienik is currently writing a proposal to the National Science Foundation (NSF) for equipmental upgrades to our observatory. Dr. Bienik asked for Mr. Thilker's and my assistance in determining our future equipment needs.

III. FUTURE RESEARCH PROJECTS

For future variable star research, I have included a complete and thorough explanation which can be found in the observational manual attached to the end of this report. The variable star charts described in § II. should be used for locating the stars of interest. Once the observational data has been reduced it can then be forwarded to the AAVSO to be combined with other observers across the nation to obtain an overall record of the star.

Work is currently under way to try and add low resolution stellar spectroscopy to our research capabilities. The apparatus is a modification of that used by Smith, Jefferson, and Tavenner[2]. The addition of this research will serve two purposes. First, it will allow an observer just beginning their career to become acquainted with the method of spectral classification of stars and also an analysis of stellar spectra. Second, there are several variable stars which do not exhibit a variability in magnitudes, rather in several of the spectral lines. Thus, having the necessary equipment to produce and examine stellar spectra, we would be able to also include these stars in a variable star research program.

IV. CONCLUSIONS

Even with the persistent rains of the summer of 1993, a great deal of progress was made in our efforts to update and expand our observational astronomy facilities. The two major repairs, described above, have improved the quality of future images. The acquisition of the various AAVSO star maps will greatly increase the number of faint objects to be included in future studies and will also aid in the task of locating these objects. The purchase of the CCDIR program will aid in the reduction of images gathered. Finally, the observer's manual will provide a complete guide to collection and reduction of data gathered by future researchers.

400

V. ACKNOWLEDGEMENTS

VI. REFERENCES

1. J.B. Sidgwick, *Amateur Astronomer's Handbook* (Dover, New York, 1971) ch. 16.

2. C.P. Smith, S.N. Jefferson, E.L. Tavenner, *Ca II K Variability of the Solar Chromosphere*, Physics 332 Report (unpublished)

OBSERVER'S MANUAL

University of Missouri-Rolla Observatory

August 1993

TABLE OF CONTENTS

1

Introduction

This manual provides the reader with a complete description of variable star observations from arrival at the observatory to performing the data reduction and analysis. It is assumed that the reader knows how to properly operate the 16-inch Cassegrain telescope at the observatory and also has an understanding of sidereal time, declination, right ascension, and the hour angle.[1,2] However, for the inexperienced Charged-Coupled Device (CCD) camera user, detailed discussions are given concerning the proper operation of the CCD camera.[3] Should any problems with any of the equipment in the observatory arise Dr. Schmitt or the chairman of the Physics Department should be contacted as soon as possible. Enjoy your observations!

2

Observing Session[4]

This chapter will guide you through an observing session from the time you arrive at the observatory until the time that you leave. It should be noted that the following procedures will vary in order depending upon the time of your observing session. It is advisable that you read through this entire section before proceeding to the observatory so that you may determine what order certain procedures need to be performed.

2.1 Setting up

After arriving at the observatory, the first thing you need to do is remove as much of the light pollution surrounding the observatory as possible. This is accomplished by turning off the light directly outside the observatory with the covered switch and then calling the UMR Police (ext 4300) and have the lights on the Engineering Research Laboratory (ERL) building turned off. Just tell the police your name, that you are at the observatory, and that you would like to have the lights on ERL turned off. This should be done as soon as you arrive since it may take the police up to an hour at times to have the lights turned off. You will need to plug in the tracking drive on the telescope, the motor for rotating the dome, and the motor for raising and lowering the slit since these should have been unplugged by the last observer. You will then need to remove all of the various covers on the telescopes. These should be placed such that the amount of dust, dirt, and other foreign particles settleing on the portions facing the lenses or mirrors is a minimum. This will help in preventing dust build-ups on the various lenses and mirrors.

Now you can attach the CCD interface to the 16-inch telescope. This is accomplished by first removing the eyepiece holder by unscrewing it from the telescope. Be sure to place this in a safe location so as to avoid damage to it. Next, you can find the mounting screws and requisite allen wrench in the desk drawer. Position the interface such that its eyepiece points toward the smaller (white) finder scope and insert the mounting screws. Care should be exercised when attaching the interface to avoid damage to the interface, CCD camera, main telescope, or finder telescope. Once this is accomplished you may turn on the camera and begin the process of focusing it.

2.2 Turning on and focusing the CCD camera

Before applying power to the camera it is necessary to make sure that all of the connections are secure. Extra care should be exercised in making sure that the cable connecting

405

the CCD camera head and interpreter is secure. **DO NOT CONNECT OR DISCONNECT THIS CABLE FROM THE CAMERA OR INTERPRETER WHILE THE SYSTEM IS TURNED ON, TO DO SO WOULD SEVERELY DAMAGE THE CCD CAMERA HEAD!!**

Once the camera has been turned on you will need to enter into the ST6OPS program by typing ST6OPS at the command line of the directory with the program. You will see an information box appear telling you that the program is establishing a connection with the camera. If the program says that it cannot find the camera make sure that the program is checking the correct COM port. This can be checked or changed by going into the MISC menu and selecting the PC SETUP option. If the COM port is set correctly go to the CAMERA menu and select the ESTABLISH COM LINK... option. If it still will not recognize the camera you will need to refer to the CCD Operating Manual (there should be a copy in the observatory or in the SPS room in the Physics building).

Now, once ST6OPS has found the camera you will need to cool the camera down. This is done by selecting the SETUP option under the CAMERA menu. If the TEMPERATURE REGULATION is OFF set it to ACTIVE. Next, reset the SETPOINT, a good starting value is -20.00. In the lower right corner of the screen you will see a temperature value and a percentage in parentheses. The SETPOINT should be adjusted so that the percentage reads about 90%, this is the optimal operating temperature of the camera. The small white fan, which should be in the green cabinet somewhere, should be used to aid the cooling of the camera (this can be omitted during the winter months). Now that you have cooled the camera down you can now begin to focus the camera.

1.   Adjust the focus ring on the interface such that it lies in the center of its travel range.

2.   There should be three small metal bars used to find a good beginning point in focusing the camera. If you are using the camera on the main telescope find the ones marked "INTERFACE" and "SECONDARY MIRROR". The one marked INTERFACE should be placed such that one end lies on the mounting plate of the interface and the other touches the rectangular section of the interface. Adjust the focus ring so that this bar will fit in between the plate and interface. The one marked SECONDARY MIRROR should be placed so that it lies along the metal shaft of the adjustment knob. Adjust the mirror so that this bar lies completely along this metal shaft.

3.   Using the finder scope, center a moderately faint star (magnitude 8) in the center of the field of view. You will also need to be sure that the tracking system has been turned on. If you do not hear the tracking system flip the switch to the ON position on the telescope. If you still hear noting flip the switch on the hand paddle.

4.   Now, under the CAMERA menu select the FOCUS mode for a series of 2 or 3 second integrations.

5. If no object appears in the image you may need to adjust the position of the star you have chosen.

6. As you watch the images appear on the computer screen, take note of the "peak" value. This number represents the highest pixel value recorded in the field of view. You will want to maximize this number, concentrating as many photons as possible into a small area.

7. In order to increase the peak value, slowly turn the focus ring slightly as the camera downloads an image. The next image downloaded, 2nd to be displayed, will reflect your adjustment. When the peak value of the image is maximized, allowing for fluctuations due to atmospheric instability, you have successfully focused the camera.

Note: If the first image of the star appears in the form of a "*doughnut with spokes*," the camera has not been adequately focused using the measuring bars. Return to step 2 and proceed once again.

Now that you have successfully focused the camera you can now adjust the tracking of the telescope so as to minimize tracking error.

2.3 Adjusting the tracking system

In this section the method of evaluating and adjusting the telescope tracking system will be described. This will have to be done at every observing session since the tracking system response varies with outdoor conditions.

1. Select the full-frame FOCUS mode under the CAMERA menu.

2. Choose a moderately bright star lying near the center of the field of view.

3. If this star appears to drift over time some drive speed adjustments need to be made.

4. In this case, select the PLANET mode from among the FOCUS readout methods.

5. Isolate the direction of needed correction by grossly turning the rate potentiometer (located in the upper-right-hand corner of the paddle) in one direction or the other. *Only* take this action after noting the previous setting of the potentiometer dial.

6. By turning the pot in this manner you should be able to tell whether the original setting of the clock drive needed to be increased or decreased.

7. Return the pot to its original position and adjust accordingly.

8. Use the method of successive approximations in order to make the stars remain fixed. You should plan to watch the star for at least five frames to insure that the response of the drive is sufficient to hold a star in a fixed position.

Now that you have focused the camera and adjusted the tracking you can now begin to locate the objects which you wish to observe.

2.4 Locating the object of interest

1. *Acquire a good star map.* Remember just how sensitive the CCD camera is. An exposure of a few seconds can record stars in the range of 16th magnitude. Most star maps or programs only show stars down to 7th, 8th, or 9th magnitude. The AAVSO variable star finder charts go down to 11th.

2. A good starting place is the telescope's setting circles and the finder scopes.

3. First, identify the right ascension (RA) and declination (DEC) associated with the star, galaxy, nebulae, cluster, or whatever tickles your fancy. This information can be found with most maps, in the current issue of the *Astronomical Almanac*, or even with a program like *The_Sky for Windows*.

4. Next, compute the required hour angle using the INFOLOG astronomical Windows applications. Or for the more adventuresome, HA = RA - LMST[1].

5. Dial up the correct hour angle and declination on the telescope setting circles. A positive hour angle indicates pointing the telescope east, negative hour angles indicate a western direction. With the polar alignment in July 1993, the setting circles are fairly accurate and will get you very close to the desired object.

6. Look for the object in the finder scope. If you find it proceed to center the telescope on the appropriate field of view.

7. If you can't immediately locate the object visually in the finder scope, don't despair. The white finder presents a field of view on the order of more than one degree. This angular width corresponds to over ten CCD frames in each direction.

8. Now is where your star map becomes your most important tool. Identify the current field of view in the finder scope. Recall, the finder presents and inverted image with respect to the star map, north is south and east is west.

9. Based on your knowledge from the map, begin to devise a plan for "starhopping" from star to star to your object of interest. Use the telescope paddle to move the image in the finder. If there are two observers and you feel daring, unlock one telescope axis at a time as you starhop along. When starhopping in either manner, always keep in mind the relative distances between your "landmark" star. In this way, you may easily estimate the necessary magnitude of each successive movement.

10. It is not always humanly possible to see the object of interest in the finder scope. Usually, however, you can spot enough stars (found on your star chart) to "guess" where an object will be found.

11. Throughout the process of starhopping, it is always necessary to place the CCD camera in FOCUS mode using a reasonably long exposure time (5 or 10 seconds). You never know when you'll get lucky and chance upon the object of interest.

Now that you have set everything up, focused the camera, and have found the object you want to observe you can now begin to take data. First, though, a few things need to be said about flat fields, dark frames, and bias frames so that your data set will be complete.

2.5 Dark frames, flat fields, and bias frames

In order to extract meaningful data from the images you record you will need to do some radiometric corrections to the images. This will actually be discussed in some detail in § 3.1. For now, we will discuss the different images needed for this process.

First, we'll start with *light images*. Light images are those images which contain astronomical data. These images are reduced, or analyzed, by means of radiometric correction. These are the images that you will spend the majority of your time collecting.

Next, we come to the *dark frames*. Dark frames are used to remove the thermal background from a light image. The entire dark frame is subtracted from the light image being corrected before application of flat-field correction techniques. Dark frames must be of equal duration with respect to the light image, except with the shutter closed. Equal CCD temperature is also a necessary criterion. Fortunately, the ST6OPS program will automatically take and subtract a dark frame from an exposure. To insure this occurs, when you select the GRAB command under the CAMERA menu make sure that the DARK FRAME option is listed as also. ST6OPS will then take a dark frame of equal duration as the image automatically before taking a light image. As the image is downloaded from the camera the dark frame will be subtracted. Proceeding in this manner reduces the risk of using an inappropriate dark frame. Since the dark frame is taken just prior to the light image the temperature of the camera does not change a great deal between the two frames. Should you find that ST6OPS was not set to automatically take and subtract the dark frame, don't worry, just take a dark frame, by setting the DARK FRAME option to ONLY, as soon after the light image as possible. You can then instruct ST6OPS to subtract the dark frame later.

Now on to *flat-fields*. Flat-fields are used to correct for the systematic response variation

of each pixel on the CCD array. These images, which should be close to the exposure times of the light images, must be recorded while the camera is in focus and viewing a source of uniform illumination. There MUST be a flat-field for every filter that you have either used or plan to use. The two sources of uniform illumination available at the observatory are the twilight sky and also the dome being illuminated by the interior light. A flat-field image is recorded in the same manner as a normal light image. Point the telescope at the darkened (deep blue) twilight sky or the dome. Select the GRAB command under the CAMERA menu. Select the exposure time and set the DARK FRAME option to ALSO. Then proceed to take the image. In the case of using the dome it is necessary to have the dome rotating during the light exposure. By rotating the dome the image of the dome is averaged to remove the obvious non-uniformity of the dome. Once the image has been downloaded it can then be saved for use during radiometric correction.

Finally, we come to *bias frames*. Bias frames represent what the CCD camera would record if it looked at noting for no time. These images record the systematic error introduced by the reset of the analog to digital converter. To record a bias frame, select the GRAB command under the CAMERA menu, set the exposure time to 10 milliseconds, and set DARK FRAME to ONLY. These images are used in the radiometric correction process which will be described in § 3.1.

2.6 Gathering Data

Now that we have discussed the necessary preliminaries, we can now turn our attention to the gathering of data. There are three different types of observing sessions, those from dusk into the night, those from the night into daybreak, and those only during the night. The only affect that the different times of observing have on the data gathering sequence in when and how to obtain your flat fields. The following method will be that of observing from dusk into the night, however, at the end of the procedure the changes for the other two observing sessions will be outlined.

1. You should plan to arrive at the observatory about 30 minutes prior to sunset. Once there proceed with § 2.1 Setting up, § 2.2 Turning on and focusing the CCD camera, and § 2.3 Adjusting the tracking system. Since stars may not yet be visible, you can focus the camera on the most distant earthly object you can find.

2. Now, as the sun sets record a suitable bias frame, as discussed earlier.

3. Now point the telescope at a relatively dark (deep blue) portion of the sky.

4. Proceed to record a flat-field, as described earlier, for each of the five filters (BVRI and the clear plate of glass). Be certain which position the filter wheel is in so that you can incorporate it into the file name. File names such as B_FLAT.ST6, V_FLAT.ST6, etc. are often most effective.

5. After the sky is dark and the stars have finally emerged you should re-focus the camera on a moderately faint star. Also be sure that the tracking has been set correctly to avoid tracking errors.

6. Next, proceed to locate your image using the method described above.

7. Once you have located the image you are now ready to take data. REMEMBER to always obtain an appropriate dark frame for each image.

8. When you are done for the evening make sure to shut everything down, see § 2.7.

If you are observing from the night into dawn the major change is when flat-fields are obtained. Once at the observatory you can set up, focus the camera, adjust the tracking system, and then proceed with step 6 of the above procedure. The flat-fields are obtained in the same manner with the exception that they are taken during the early morning twilight.

If you are only observing during the night then the flat-fields may be taken at any time during the session. In this case the flat-fields are actually called *dome-flats*. The procedure is the same except that the interior of the dome while being lit with the light inside the observatory is used as the source rather than the twilight sky. Remember to have the dome rotating during the light exposure so as to spatially average the interior of the dome. It is still necessary to obtain a unique flat-field for each filter.

2.7 Shutting down

Now that your observing session is complete the only thing left to do is to shut down the observatory. This is almost as important as taking data in that it will help insure that none of the equipment will be damaged until your or someone else's next observing session.

The first thing is to warm the camera back up. Go into the SETUP command under CAMERA and change the SETPOINT to about +10.00. While the camera is warming up you can disconnect it from the telescope and reattach the objective holder. Make sure that you unplug the tracking system. If the tracking system is left running the telescope will eventually crash into the cement pier and seriously damage it. ALWAYS place the dust covers over the mirror and lenses of the various telescopes. Before putting them back on make sure that no rocks, pieces of wood, or anything else has fallen into the portions facing the mirror and lenses. Once the covers are in place you will need to reset the telescope so that it points due north. The large ballast needs to point toward the floor and the main mirror of the telescope should point toward the north star. Once the camera has warmed up you can exit the ST6OPS program and replace the camera to the carrying case. Make sure to unplug the dome and slit motors from the wall sockets. Now before you lock up and leave for the night you will need to call the UMR Police back (4300) and tell them that they can turn the lights back on at the ERL Building. You MUST call and tell them this otherwise the lights will not get turned back on. Finally, just before you get into your car, or whatever you came in, turn the light on just outside the observatory. Now that you have gathered your data and returned home you can now begin to analyze your data.

411

3

Data Reduction

This chapter will discuss the method of radiometric correction and the use of the CCDIR programs. The method of performing differential photometry by hand has been discussed in detail elsewhere[5] and will not be discussed here. Due to the large number of commands used by the CCDRED and CCDPHOT programs, rather than rewrite the Reference Manuals[6], only a brief description of their purposes will be given

3.1 Radiometric Correction

The process of radiometric correction to the CCD images is necessary before using CCDIR or doing differential photometry the old fashioned way. Without these corrections, any calculations would be in error.

The first step is to load the desired image and subtract a dark frame from it. As discussed earlier, this is most easily accomplished by letting ST6OPS take and subtract a dark frame from each image as it is downloaded. If this has not been done, then you will need to enter the UTILITY menu and select the SUBTRACT DARK FRAME option. ST6OPS will ask for the dark frame file name. Remember, the exposure time and camera temperature of the dark image must be the same as the light image being corrected.

Next, the bias frame can be subtracted from the image using the same technique as for subtracting a dark frame. This removes the error introduced by the resetting of the A/D converter.

Now, also under the UTILITY menu, choose the FLAT-FIELD option in order to divide the current image by an appropriate flat-field. The filter type MUST match. If the flat-field is not of the same filter the resulting image will be useless.

To remove the effects of any comic ray events or dead pixels select the REMOVE HOT PIXELS and the REMOVE COOL PIXELS commands. Once all of these corrections have been completed you can now proceed to reduce the image using the CCDIR program.

3.2 CCDIR and supporting programs

3.2.1 FITS File conversion

In order to use the CCDIR program the file format from ST6OPS must be modified to conform to the appropriate FITS file format. The image should be saved in the FITS file format. Next, you will need to run the FITS File Conversion program. For this you will need

to record the header information manually at the telescope. You will then need to create a header file using an ASCII editor (the MS-DOS editor will do just fine). The header should follow the format given below in Table I.

Table I Header File Format[6]

ITEM	COLUMNS	COMMENTS
File name	1 - 30	File name of the image, may include a path
Object ID	33 - 62	Object name etc.
UT hour	65 - 66	UT hour at START of exposure
UT minute	68 - 69	UT minute at START of exposure
UT seconds	71 - 72	UT seconds at START of exposure
Year	75 - 78	4 digit year (e.g. 1993)
UT month	80 - 81	2 digit month (e.g. August = 08)
UT day	83 - 84	2 digit day
Image type	87 - 92	image type (object, bias, flat, dark)
Exposure	95 - 98	exposure in seconds
Filter ID	101 - 106	Filter designation
Right Ascension	109 - 116	Right ascension in format: HH.MMSS
Declination	119 - 126	Declination in format: HH.MMSS
Epoch	129 - 136	Epoch of coordinates (e.g. 1993.5)
Comment	139 - 202	comment field

To execute the program type FITS at the prompt while in the directory where the program is located. The program will prompt you for all other necessary information.

3.2.2 CCDRED and CCDPHOT

CCDRED performs the same radiometric correction operations as ST6OPS does. It will subtract out the dark frame and bias frame and will also divide the image by the appropriate flat-field. However, CCDRED does perform one very important operation that ST6OPS will not, it will extract from the image the instrumental magnitudes of selected objects. For any given image 30 instrumental magnitudes may be extracted. These magnitudes are written to a file which is then passed on to the CCDPHOT program for further manipulation.

CCDPHOT accepts data files created by the EXTRACT command of CCDRED and reduce the data for either differential or all-sky photometry. The DIFF command is used for processing differential photometry. This is similar to the process described by Hall.[5] The EXT1 command is used to calculate the atmospheric extinction coefficients from observations of a single star over a range of air mass. In order to perform this you will need to have multiple observations of the star during the same evening. The EXT2 command determines the atmospheric extinction coefficients from observations of stars whose first color index (i.e. the color index which uses the magnitude filter) is near zero. For the UBV system, this color index would be B - V, because V is the magnitude filter. The EXT3 command determines the atmospheric extinction coefficients from observations of standard stars (of any color) at various air masses, *when the transformation coefficients are known*. These coefficients are obtained by executing the TRAN command. The TRAN command determines the coefficients to the standard photometric system. Finally, the CONV command converts the instrumental magnitudes into standardized magnitudes and colors and writes the information to a file.

From these brief descriptions of what these programs can do, it is easy to see just how valuable they are to anyone doing CCD photometry research. All of the programs described here can be found in the PHYS 11 accounts on the Department of Physics file server. Should you have any problems with these programs you should first consult the reference manuals and if you are still having problems you should then contact Dr. Schmitt.

References

1. D.S. Birney, *Observational Astronomy* (Cambridge, New York, 1991), chs. 1&2.

2. E. Bohm-Vitense, *Introduction to Stellar Astrophysics, Volume 1: Basic Stellar Observations and Data* (Cambridge, New York, 1989), ch. 1.

3. *Model ST-6 Professional CCD Imaging Camera Operating Manual* (Santa Barbara Instrument Group, Santa Barbara).

4. D.A. Thilker, ----------, Physics 390 Report (unpublished).

5. D.S. Hall, *Variable Star Research: An International Perspective; Photoelectric Photometry of Variable Stars* (Cambridge, New York, 1990), pg. 95 - 108.

6. *CCDIR Reference Manuals* (United Software Systems, Arizona, 1993)

Solubility of Red Phosphorous in Lead

Sean E. Walker

Metallurgical Engineering

ABSTRACT

The determination of the solubility of red phosphorus in lead can be used to produce a plot of the solubility with respect to temperature and pressure. The plot is produced with experimental data, activity determination from present thermodynamic data, and compilation of the two sets of data into the semi-regular solution format. A lead-phosphorus solubility diagram is necessary to determine the amount phosphorus that will be absorbed by lead and will remain unreacted in a given process.

INTRODUCTION

A lead-phosphorus solubility plot is needed for two specific processes. The production of lead grids and the removal of copper from lead.

A new method of producing lead grids for maintenance free lead acid batteries involves the introduction of phosphorus into the lead. The addition of phosphorus reduces the antimony content needed for increased strength. Grain refinement is also believed to occur due to the phosphorus. Resistance to cracking is another area the phosphorus could possibly improve. Presently a trial and error estimation of the amount of phosphorus soluble in lead is used for phosphorus addition determinations.

Phosphorus forms a compound with copper. When red phosphorus is placed in molten lead containing copper, the resulting compound of copper and phosphorus forms in the dross. A solubility plot could be used determined to the excess amount of phosphorus needed to exceed the solubility of lead and compound with all of the copper.

THERMODYNAMIC BACKGROUND

The solubility of red phosphorus in lead can be determined by controlling temperature and pressure within the lead-phosphorus system. Since phosphorus has a sublimation temperature of 431°C (704 K) at that temperature the reaction

$$4P_{(s)} \rightarrow P_{4(g)}$$
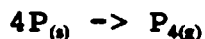
occurs. Formation of phosphorus gas from solid phosphorus produces free energy of:

$$\Delta G° = -RT \ Ln[P_{P4(g)}/(a_{P(s)})^4] \tag{1}$$

In an atmosphere containing no other gases at the sublimation point the partial pressure of phosphorus will be one atmosphere. Therefore, with the free energy data interpolated past the sublimation temperature using the free energy of formation equation for phosphorus at temperatures greater than its boiling point, the activity of solid phosphorus in the lead can be determined.

Experimentally, controlling the temperatures of lead and phosphorus and indirectly the partial pressure of phosphorus, the mole fraction of phosphorus in the lead can be determined. Using the formula

$$a = \gamma*N \Rightarrow a/N = \gamma$$

$$Log(a') - Log(N') = Log(\gamma')$$

$$Log(a') = A^f + B^f/T \tag{2}$$

$$Log(N') = A^s + B^s/T \tag{3}$$

$$Log(\gamma') = (A^f - A^s) + (B^f - B^s)/T$$

$$Log(\gamma') = A + B/T \tag{4}$$

the Logarithm of γ can be determined. From equation 2 the semi-regular solution can be completed as follows:

$$Log(\gamma) = (A + B/T)*(1-N)^2$$

$$\alpha = Log(\gamma)/(1-N)^2 = A' + B'/T \tag{5}$$

The standard graph for the solubility is 2.303 α versus $10^4/T$ as shown in graph A.

EXPERIMENTAL PROCEDURE

A pure lead specimen of approximately 10 grams was place in the tube at position A, while red phosphorus was placed in position B of the quartz tube in figure 1. The two C's denote dimples in the quartz which limited movement of the two specimens and kept the molten lead from flowing thin or mixing with the solid phosphorus. The position marked D was where Ti-Zr is introduced into the system and held in place by steel wool.

A   C   C   B   D
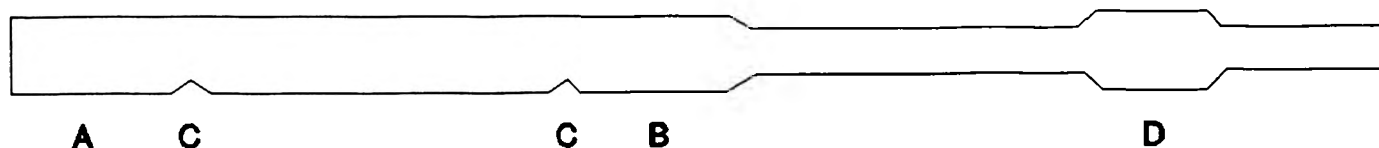
FIGURE 1. Reaction Tube

Once the lead, phosphorus, and titanium were in position the end of the tube nearest the lead was sealed. The narrow end was then hooked to a vacuum pump and the air was removed. Internal pressures of < 10 μatm. were the lowest pressures obtainable. After reaching the lowest pressure attainable the tube was flushed three times with argon gas to remove as much oxygen as possible. The tube was then sealed while in a near vacuum state. Next the titanium-zirconium was heated with a Bunsen burner to remove the remaining oxygen down to a negligible partial pressure. Finally, the tube was sealed near point A on figure 1 so that only the large diameter section with the two samples is left and under a vacuum.

A prepared reaction tube was then placed within a larger tube and into a tube furnace with a three region temperature control. The larger tubes were sealed with rubber stoppers to retain heat. Thermocouples were used for temperature measurements and as a temperature control device. Two thermocouples were placed at positions A, B, and directly between A and B in figure 1. One thermocouple at each position was connected to a power source which controls the heating elements, and the other thermocouple was connected to an electronic temperature readout for data collection. The readout set of thermocouples were placed inside the larger tube and directly on the reaction tube. This produced greater readout accuracy than the furnace control thermocouples which were on the outside of the larger tube.

After heating the lead and phosphorus for 24 hours at the desired temperatures, the reaction tube was removed from the furnace and quenched to retain the phosphorus in that had diffused into the lead at the elevated temperature. Lead and phosphorus samples were then removed from the cooled tube. The used phosphorus was saved for later use.

Lead samples were digested in nitric acid and the solution is analyzed by gas atomization for the phosphorus content. Since concentrations were small gas atomization was one of only a few processes capable of determining the phosphorus content accurately.

The lead digestion began by cutting the lead pieces into 1 gram samples and the actual weight is recorded. The 1 gram samples were then placed into a 150 ml beaker with 50 ml concentrated nitric acid and 50 ml of deionized water. The beaker and contents were then heated just below the boiling point of water. The temperature was sustained until all of the lead was dissolved. Once the lead was dissolved, the beaker was allowed to cool to room

temperature and was diluted to 250 ml in a volumetric flask. The solution was then shaken until equilibrium was obtained. Finally, a sample of the solution was placed in the gas atomizer and the phosphorus concentration in the solution was determined. Using the weight of the sample and the concentration of the lead nitrate solution the atomic percent of phosphorus was determined as follows:

$$F*250/Twt = wt\% \ P$$

$$\text{using 100 g basis} \rightarrow (100*wt\% \ P/100)/GFW \ P = \#P \text{ moles}$$

$$(100*(1-wt\% \ P/100)/GFW \ Pb = \#Pb \text{ moles}$$

$$N_P = \#P \text{ moles}/(\#P \text{ moles} + \#P \text{ moles})$$

EXPERIMENTAL THEORY

At the phosphorus end of the tube the reaction is the same as at the lead end, however, the phosphorus is in contact with an excess amount of solid phosphorus which produces:

$$a_P = 1 \rightarrow \Delta G^\circ = -RT \ Ln[P_{P4(g)}/1]$$

The reaction at the phosphorus end of the tube is the pressure controlling reaction. Therefore the temperature controls the pressure. The temperature of the lead, since the pressure is known and constant due to the phosphorus temperature, can be varied to produce a variation in a_P within the lead. a_P is not 1 within the lead. A solid or liquid phase is not actually present, however, unreacted phosphorus is present within the molten lead. a_P in lead is useful for determination of γ as previously described.

DATA PROCESSING

The data collected from the gas atomizer had several possible errors involved. Specimens that showed greater than average amounts of phosphorus concentrations per temperature can be explained by the following. When the lead was removed from the furnace and quenched the solidified lead was in the shape of a bead with surface area exposed to the phosphorus atmosphere. Most of the time the tube fractured upon quenching and solid phosphorus formed on the lead's surface. Since the concentration of the phosphorus on the surface was much larger than the concentration within the lead, it must was removed. If the molten lead was jostled during the quench, ripples in the lead were solidified, causing removal of phosphorus with a steel brush extremely tough.

420

Specimens that showed less than average phosphorus concentrations can be explained by losses in the nitric acid digestion. The specimens while being digested in the nitric acid did not digest completely or some of the phosphorus was lost as vapor.

While one of the tubes for the 750°C was being sealed some of the phosphorus oxidized. The tube was heated anyway. As shown in the data table, the presence of oxidized phosphorus cut the solubility in half.

RESULTS

From the data collected equation five parameters have been determined:

$$\text{Pressure} = 1 \text{ atm.} \rightarrow 2.303 * \alpha = 1752/T - 1.338 \qquad (6)$$

$$\text{Pressure} = .2 \text{ atm.} \rightarrow 2.303 * \alpha = 1957/T - 1.292 \qquad (7)$$

Equations 6 and 7 are used to plot the Phosphorus Solubility In Lead graph. The standard error in equation 6 is .9% for B and .7% for A. This produces a random error of 1.1%. Only two points are present at .2 atm., therefore error determination is pointless.

NOMENCLATURE

G	free energy
R	gas constant (1.986 cal/mol)
T	temperature Kelvin
N	mole fraction
a	Raoultian activity
γ	activity coefficient
A,B	constants
α	alpha function
F	grams phosphorus per ml solution
wt%	weight percent
GFW	gram formula weight
Twt	total sample weight

421

atm.	atmospheres
Log	logarithm to base 10
Ln	logarithm to base e

Superscripts:

f	fusion
s	saturated solution

ACKNOWLEDGEMENTS

REFERENCES

1. T.R.A.Davey, V.Ramachandran & J.White,"Determination of Activities from Solubility Data in Binary Metallic Systems by Use of Solution Models," p.207-215 in Advances in Extractive Metallurgy, ed. M.J.Jones; Instn. Mining & Metallurgy, London, 1977.

2. Davey T.R.A. "Derivation Of Activities From Metal Solubilities."

DATA TABLE

Sample	wt %P	AVE. %P	pp. P	Temp C	Element
1	0.0563	0.0582	1	431	P
	0.0506			431	Pb
	0.0678				
2	0.0815	0.0857	1	431	P
	0.0982			500	Pb
	0.0775				
3	0.0189	0.0343	0.9	429	P
	0.0497			500	Pb
4	0.1752	0.1366	1	431	P
	0.0644			431	Pb
	0.1701				
5	0.1055	0.0904	1	431	P
	0.0863			550	Pb
	0.0794				
6	0.0638	0.0638	0.2	383	P
	0.0638			600	Pb
7	0.0921	0.0856	1	431	P
	0.0841			600	Pb
	0.0805				
8	0.0302	0.0221	0.2	383	P
	0.0188			500	Pb
	0.0174				
9	0.0854	0.0878	1	431	P
	0.1026			550	Pb
	0.0755				
11	0.8865	0.937	1	435	P
	0.9029			902	Pb
	0.8816				
	0.9529				
	0.9696				
	0.9988				
	0.9681				
	1.4456				

DATA TABLE

12	0.4968	0.734	1	437	P
	0.9511			900	Pb
	0.7290				
	0.7805				
	0.7141				
13	1.5736	1.850	1	434	P
	2.2318		Pb	904	Pb
	1.7450				
	0.5972				
14	1.5053	1.595	>1	441	P
	1.2419			851	Pb
	1.6850				
	1.9474				
15	0.6871	0.687	1	433	P
				800	Pb
16	4.0591	0.637	1	432	P
	0.8573			800	Pb
	0.6498				
	0.4029				
17	0.1697	0.172	1	432	P
*	0.1659			750	Pb
	0.1800				
	0.9800				
	3.6631				
	1.8587				
18	4.8182	0.310	1	433	P
	2.2733			750	Pb
	0.2927				
	0.3163				
	0.3185				
	0.2976				
	0.3083				
	0.3257				

note.

* The phosphorus on this run was partially oxidized.

pp. is partial pressure

AVE. is an average excluding extremely high or low values.

424

Phosphorus Solubility
In Lead
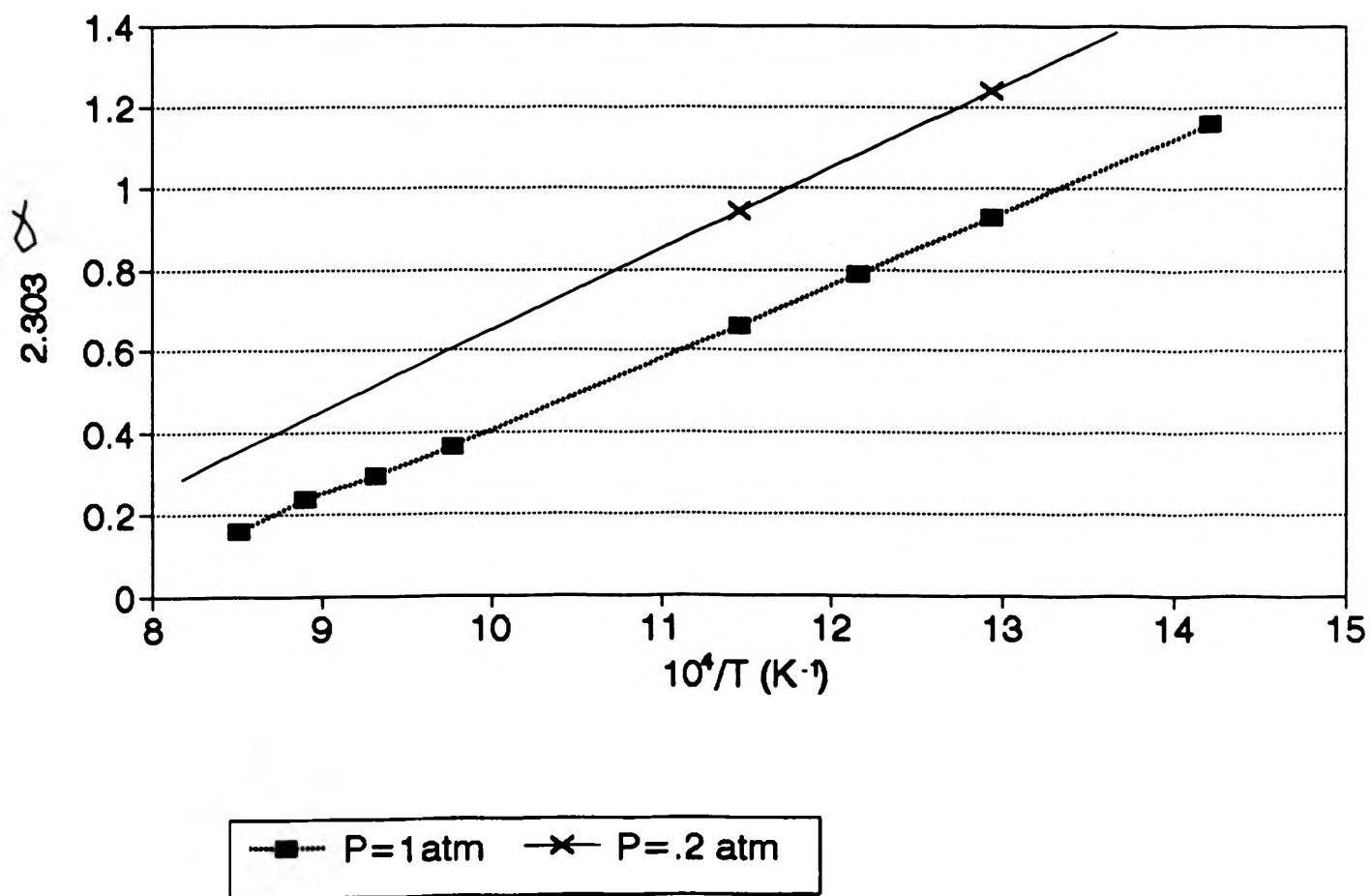
A COMPUTER GRAPHIC TEACHING AID
FOR THE SYNTHESIS OF FOUR-BAR LINKAGES

S. K. Woon
University of Missouri - Rolla
Mechanical & Aerospace Engineering & Engineering Mechanics
Rolla, MO 65401

ABSTRACT

This project involves developing software for the use as a teaching tool in the classroom. The "four-bar linkage mechanism", often used in kinematic movement, is the main subject.

The software provides a working environment to perform a graphical synthesis of a four-bar linkage to move one of the links through three specified positions in the plane. The construction process is facilitated by the built in kinematic intelligence so that the student can quickly and easily visualize the process. The construction lines are dynamically updated as the free parameters in the design are modified. This is particularly beneficial because it allows the student to see the dynamic nature of the solution, as opposed to considering it as a static situation. Once the synthesis task is completed, the four-bar linkage is animated to provide immediate verification of the satisfaction of the original motion specifications.

The software can be run on the Mechanical Engineering Department computer network.

INTRODUCTION

The traditional way of teaching relies heavily on static blackboard and pictures in the text books. Some teaching tools also depend on cardboard modelling, but this method is only good for a simple rotation of motion. Many students have difficulties in visualizing the dynamics of the mechanisms. A computer aided software environment is being developed to provide kinematic intelligence to the simulated blackboard [1]. This computer graphic animation enhances the efficiency and quality of education. Diagrams and graphic pictures can be drawn to precise dimensions, thus eliminating rough sketches often drawn by instructors on the static blackboard. This software supported computer graphic animation will help the students in understanding the motion and movement concepts more easily. This concept is applicable not only in engineering fields, but also in other areas such as in architecture, physic and chemistry.

No one can deny the important role of an instructor in the classroom. However, the author feels that this computer graphic animation will assist the instructors in bringing the point across to the students more effectively; especially on the subjects that demand a high degree of imagination. This powerful teaching method will undoubtedly increase the productivity of the instructors and students. The instructors and students will share the same ideas and visualize the same concept, thus eliminating unnecessary repetition of explanations and demonstrations. Consequently, this can enhance the communication between the two parties.

This computer software is not only designed to teach the concepts in the course, but to increase the students interest in the course as well. This interactive nature can change the way students think and learn. With the help of this computer graphic animation, students will have a strong foundation in introductory kinematics of mechanisms. At the same time, students will improve their overall computer usage skills. This will help students in preparing for their real life environment after they have finished their college education.

The author's project emphasized one aspect of the overall kinematics environment, namely three positions synthesis. Three positions synthesis involves motion generation of four-bar linkages, in which three positions of a line in the plane are specified. It is desired to determine the dimensions of a four-bar linkage configuration to move it to each of those positions [2].

Following is an example on constructing a four-bar linkage using synthesis method:

Refer to figure 1 for the following construction:

1. Draw three design positions. The points are denoted as A1, A2, and A3.
2. Draw a construction line from point A1 to A2 and from A2 to A3 . Then draw a bisector line between point A1 and A2, and also between A2 and A3.
3. Ground pivot (G1) is determined by the intersection of both bisector lines.
4. Connect G1 with A1 and call it R2 (input) link.

Refer to figure 2 for the following construction:

5. Pick any point on the plane and call it B1. The relationship between B1 and A1 must be fixed (rigid). Now use B1 to define the three positions of the link.
6. Draw a construction line from point B1 to B2, and from B2 to B3.
7. Draw a bisector line between B1 and B2, B2 and B3.
8. Draw a ground pivot (G2) point, where it is determined by the intersection of both bisector lines.
9. Connect G2 with B1 and call it R4 (output) link.
10. Connect A1 with B1 and call it R3 (coupler) link (rigid body).

Note the construction lines are lines connecting two given points. Bi-sector lines are lines drawn through the mid-point of construction lines and are perpendicular to the construction lines.
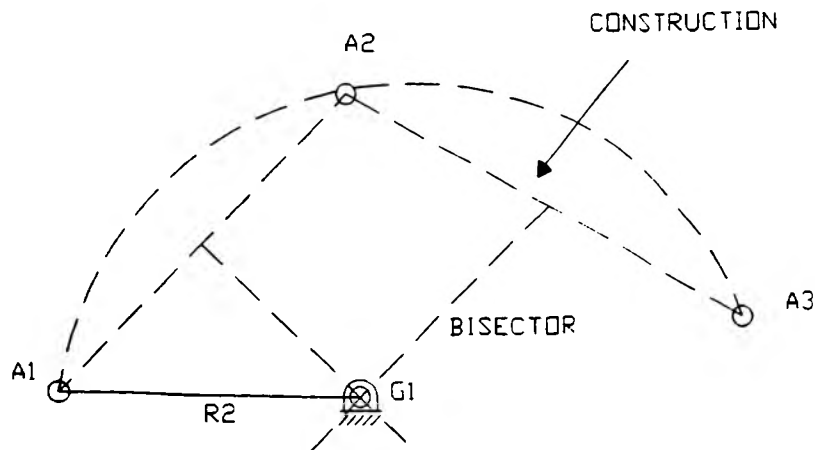
Figure 1. Construction lines, Bi-sector and Ground Pivot.
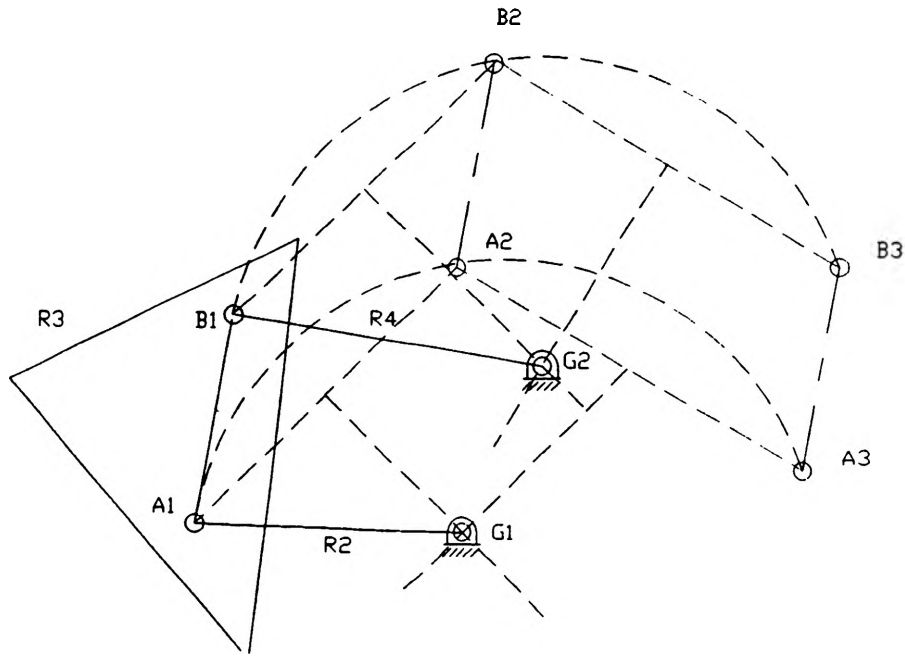
Figure 2. Three positions motion synthesis.

R2 and R4 are very unique links. R2 will rotate from point A1 to A2 and to A3 and vice versa by making an arch with respect to the G1. R4 will rotate from point B1 to B2 and to B3 and vice versa, by making an arch with respect to the G2. The number of free choices for three precision positions is four, (x and y for each moving pivot point). Therefore, the number of free choice for each bar is two (x and y).

The actual four-bar linkage is shown in figure 3. It is important to note that any two points on R3, such as A and B, can define as a rigid body. Points A and B can be anywhere on the rigid body, thus creating an infinity of solutions [2].

The obtained solution is guaranteed to assemble in all three positions, but there is no guarantee that
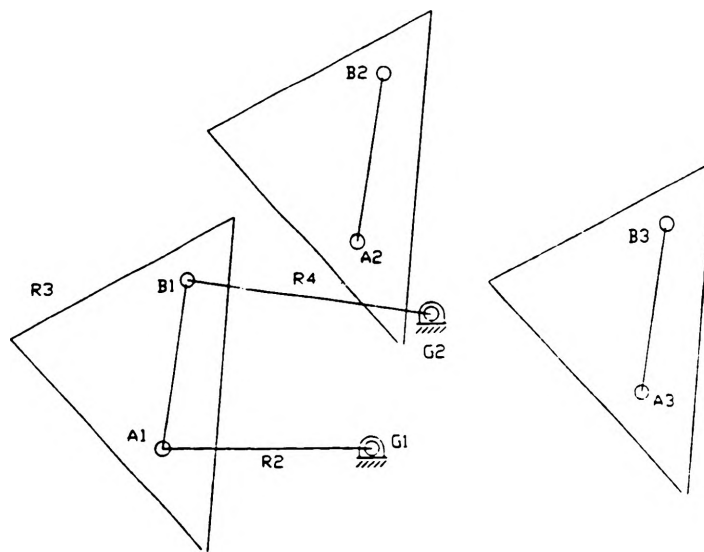
Figure 3. Sample four-bar linkage.

429

the linkages will move between those precision positions. The resulting linkage may be incapable of moving from one precision position to another due to the presence of a toggle condition or other constraint. The toggle condition is undesirable because the linkages can not reach all of the specified design positions without disassembly of the linkages. The reason for the undesired linkages is simply because of the poor ground pivot locations. Sometimes the toggle condition is very useful because it can provide a self locking feature. In order to see whether the resulting linkages will move to all precision points, the animation process can be used.

This software involves three easy steps in the drawing process:
1. Data Entry - involves entering data for the first three position points (P1, P2, and P3) and three angles.
2. Dragging Process - finding a second set of three position points and using them to determine a desired four-bar linkage.
3. Animation Process - the actual process of the kinematic rotation of the four-bar linkage.

DRAWING PROCESS

Drawing Method
1. The method of sketching the graphic using this software is very easy. The computer window such as the one shown in figure 4 will be displayed as soon as the program is executed. Data for x's, y's and angles are to be entered in given fields under 'Menu'. Students are given a second chance to re-enter any data before accepting 'y' (yes) key. The software will start executing the data as soon as the 'y' (yes) key is pressed. The software will execute any data entered, regardless of the values. The actual size of the output display will remain the same. The
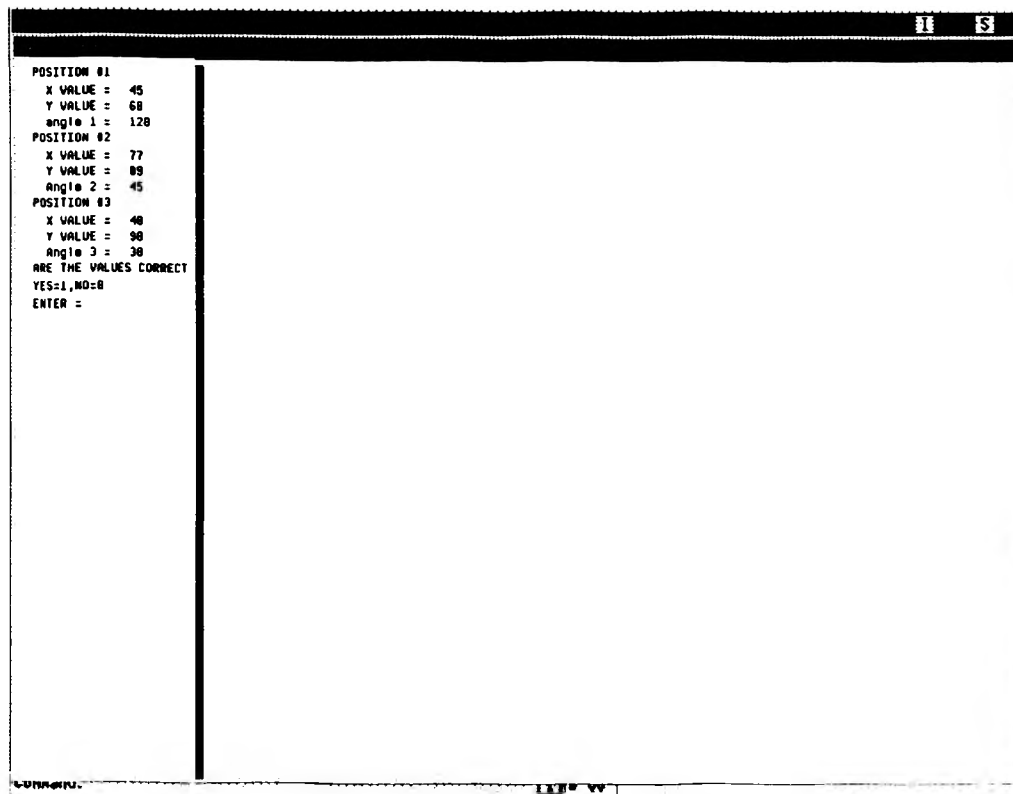
Figure 4. Computer Graphics Screen.

430
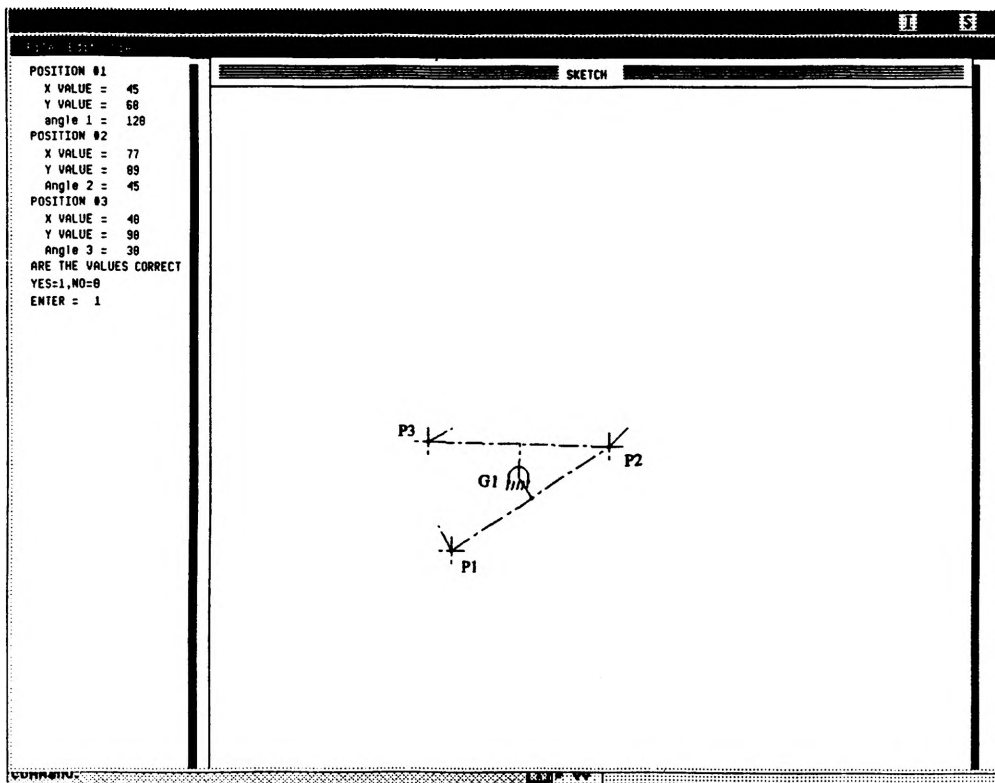
Figure 5. Three Precision Positions Diagram.

program is written to scale the given data to fit in the graphics window.

2.   After all data are entered and accepted, the diagram such as shown in figure 5 will display. Construction lines, perpendicular bisector lines, ground pivot and three position points (P1, P2 and P3) selected will be displayed. Note that there is an extended line at every point. These lines are drawn as a result of the input angles.

3.   In order to construct a four-bar linkage, two moving pivot points must be chosen on the coupler link. One of the points is chosen by default at the precision position. The other moving pivot must be specified in relation to the first precision position. To select the moving pivot, a mouse pointer is used. Once the mouse pointer is clicked, new construction lines will be sketched (figure 6). The moving pivot in its first position (P1') is determined by how far the pointer is dragged away from the first precision position. The second (P2') and third (P3') locations of the moving pivot will be sketched automatically as soon as the first position (P1') is chosen. Simultaneously, the second ground pivot (G2) will be determined. When the mouse button is released, the four-bar linkage will be displayed (figure 6). The sketching for any new construction lines can be repeated by dragging the mouse until the proper linkages and ground pivots are found. The desired dimensions of the linkages (when the mouse button is released) will be stored temporarily for animation purposes.

Animation

There are two types of animation processes, a single-step and a continuous animation through the full range of motion. Animation can be activated by choosing the animation option under the 'View' menu. Single-step animation allows the linkage to move one step at a time when any key is hit; while continuous animation will cause the linkage to rotate continuously around the ground pivots. Beginners are encouraged to select single-step animation because the motion of the linkage is easier to observe and analyze. From this observation, students are able to see whether it is a desired linkage or not, simply by looking at the toggle condition. If the linkage reaches a
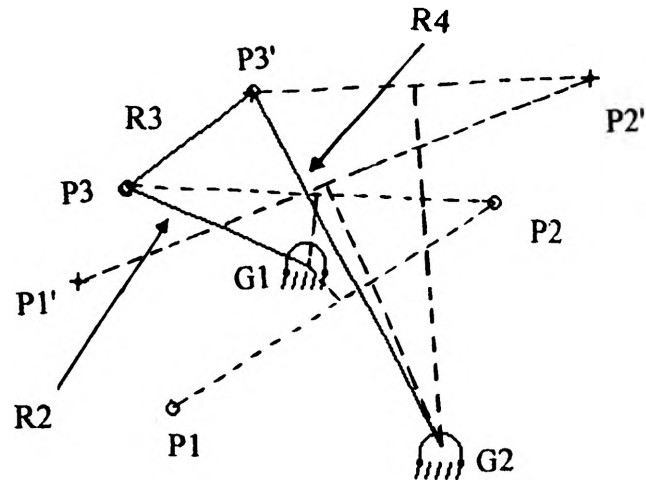
Figure 6. Four-bar Linkage

toggle position, the 't' key can be used to display the linkage on the other side of the toggle position. Figure 7 illustrates a single-step animation.

CONCLUSIONS AND RECOMMENDATIONS

The software supported computer graphic animation shown in this project is expected to improve the method of teaching in the classroom. It should increase interest, depth of understanding, and intuition. More importantly, students have the luxury of visualizing a graphic output of dynamic constructions in a way which can never be done on static blackboards or cardboard modelling. It can also ease the students confusion and difficulties in visualizing the dynamic phenomena.

It is recommended that classes are to be taught with the help of computer graphic animation. Students who have seen the kinematic motion themselves through this software have a deeper image embedded in their mind. This method of teaching is not only limited to classes in

(a)   (b)
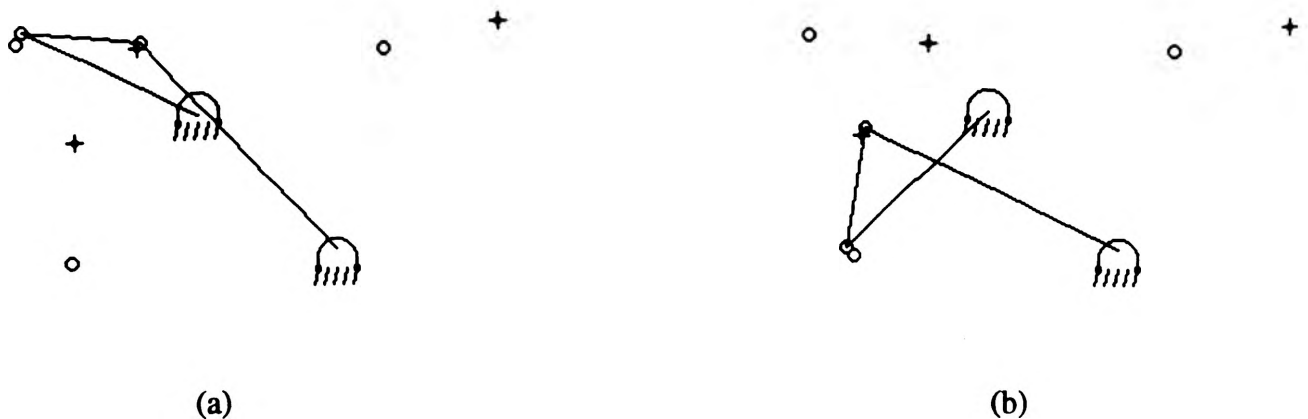
Figure 7. Four-bar Linkage - Single-Step Animation.

engineering fields, but also to other education disciplines. Students will enjoy learning more and have less feelings of frustration.

ACKNOWLEDGMENTS

REFERENCES

1. Nisbett, J. K., Barker, C. R., "A Kinematically Intelligent Blackboard Environment with a Unique Sketch Method," Proceedings of the 1993 Applied Mechanisms and Robotics Conference, Cincinnati, Ohio, Nov. 1993.
2. Norton, Robert L., "Design of Machinery: An Introduction to The Synthesis and Analysis of Mechanisms and Machines". Mc Graw Hill, 1992.